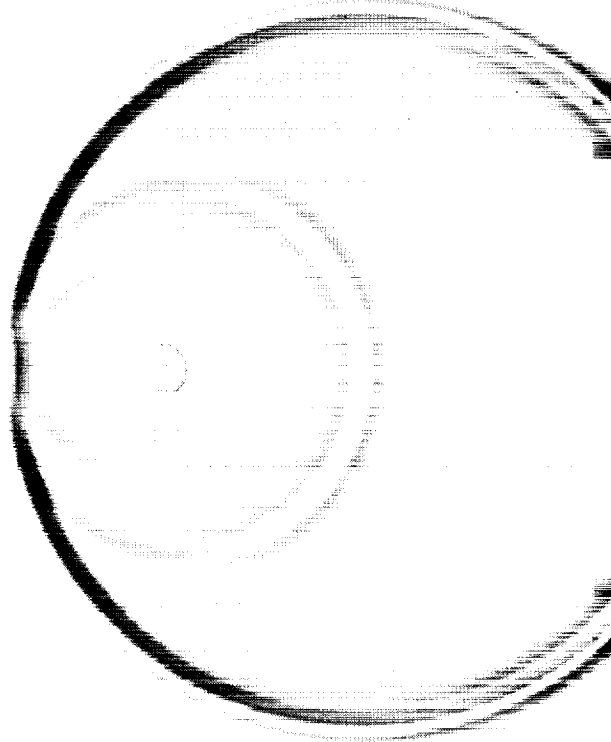


NASA Conference Publication 3352

1N-71
043444

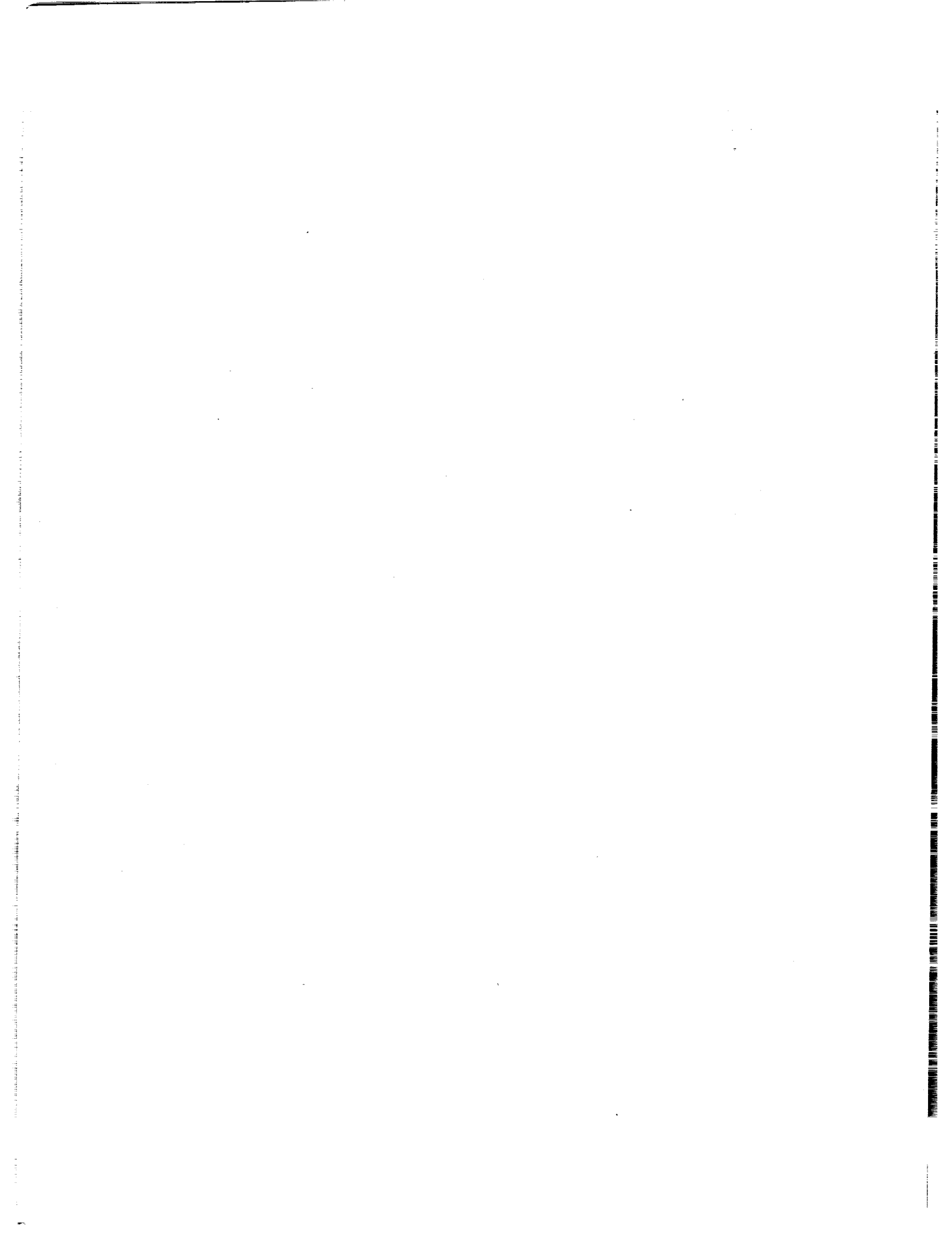
Second Computational Aeroacoustics (CAA) Workshop on Benchmark Problems

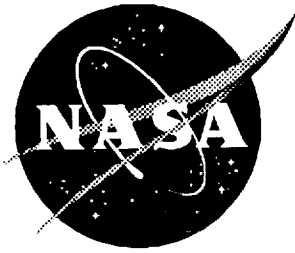
Edited by
C.K.W. Tam and J.C. Hardin



Proceedings of a workshop sponsored by the
National Aeronautics and Space Administration,
Washington, D.C. and the Florida State University,
Tallahassee, Florida
and held in
Tallahassee, Florida
November 4-5, 1996

June 1997





Second Computational Aeroacoustics (CAA) Workshop on Benchmark Problems

Edited by

C. K. W. Tam
Florida State University • Tallahassee, Florida

J. C. Hardin
Langley Research Center • Hampton, Virginia

Proceedings of a workshop sponsored by the
National Aeronautics and Space Administration,
Washington, D. C. and the Florida State University,
Tallahassee, Florida
and held in
Tallahassee, Florida
November 4-5, 1996

National Aeronautics and Space Administration
Langley Research Center • Hampton, Virginia 23681-0001

June 1997

Cover photo
(Contour plot of acoustic pressure field produced by source scattering from cylinder)

Printed copies available from the following:

NASA Center for AeroSpace Information
800 Elkrige Landing Road
Linthicum Heights, MD 21090-2934
(301) 621-0390

National Technical Information Service (NTIS)
5285 Port Royal Road
Springfield, VA 22161-2171
(703) 487-4650

PREFACE

This volume contains the proceedings of the Second Computational Aeroacoustics (CAA) Workshop on Benchmark Problems co-sponsored by Florida State University and NASA Langley Research Center. Computational Aeroacoustics embodies the employment of computational techniques in the calculation of all aspects of sound generation and propagation in air directly from the fundamental governing equations. As such, it enjoys all the benefits of numerical approaches including removal of the restrictions to linearity, constant coefficients, single frequency and simple geometries typically employed in theoretical acoustic analyses. In addition, most importantly from the acoustic viewpoint, sound sources produced by fluid flows arise naturally from the fluid dynamics and do not require modeling. However, these benefits come at the cost of modification of standard computational techniques in order to handle the hyperbolic nature and small magnitude of the phenomenon.

The first Workshop in this series, which was held in 1994, contained benchmark problems designed to demonstrate that the numerical challenges of CAA could be overcome. The successful accomplishment of that goal led to more realistic benchmark problems being chosen for this Second Workshop in an attempt to convince the U.S. Industry that CAA was well on its way to coming of age and would become an important design tool as CFD is today. The benchmark problems are:

Category 1-Acoustic Scattering from a Cylinder or a Sphere. Acoustic scattering from a cylinder is a model of the technologically important problem of propeller noise impinging on the fuselage of an aircraft. The sphere case was included to challenge the community to solve a computationally intensive, fully three-dimensional geometry in which the potential of parallel computations could be demonstrated.

Category 2-Sound Propagation through and Radiation from a Finite Length Duct. Duct acoustics finds application in jet engine and shrouded propeller technology. Classically, such problems have been broken into three parts: source description, duct propagation, and radiation into free space. In these benchmark problems, although the source was specified, the contributor was challenged to solve the duct propagation and farfield radiation problems simultaneously.

Category 3-Gust Interaction with a Cascade. Turbines, such as employed in jet aircraft engines, typically contain cascades of rotor and stator blades. The problems in this category were designed to demonstrate CAA technology, such as computing the sound generation due to the wake of an upstream cascade impinging on a downstream cascade and the ability to faithfully propagate waves through a sliding interface between a stationary and a moving grid, necessary to approach the industrial turbomachinery noise problem.

Category 4-Sound Generation by a Cylinder in Uniform Flow. Aeolian tones which are generated by uniform flow into a cylinder are important in airframe and automobile noise. Further, this geometry is a model of the technologically critical class of high Reynolds number, massively separated flow noise generators. In this problem, the sound source is inherent in the fluid dynamics and would not exist if the flow were inviscid. Thus, the contributor is challenged to attack a fully turbulent flow. Since a direct numerical

simulation cannot be carried out at the Reynolds number requested with present computational capabilities, of particular interest is the success of the turbulent modeling employed and the dimensionality of the solution attempted.

Exact solutions for all but the Category 4 problem are available for comparison and are contained in this volume.

Christopher K.W. Tam, Florida State University
Jay C. Hardin, NASA Langley Research Center

ORGANIZING COMMITTEE

This workshop was organized by a Scientific Committee which consisted of:

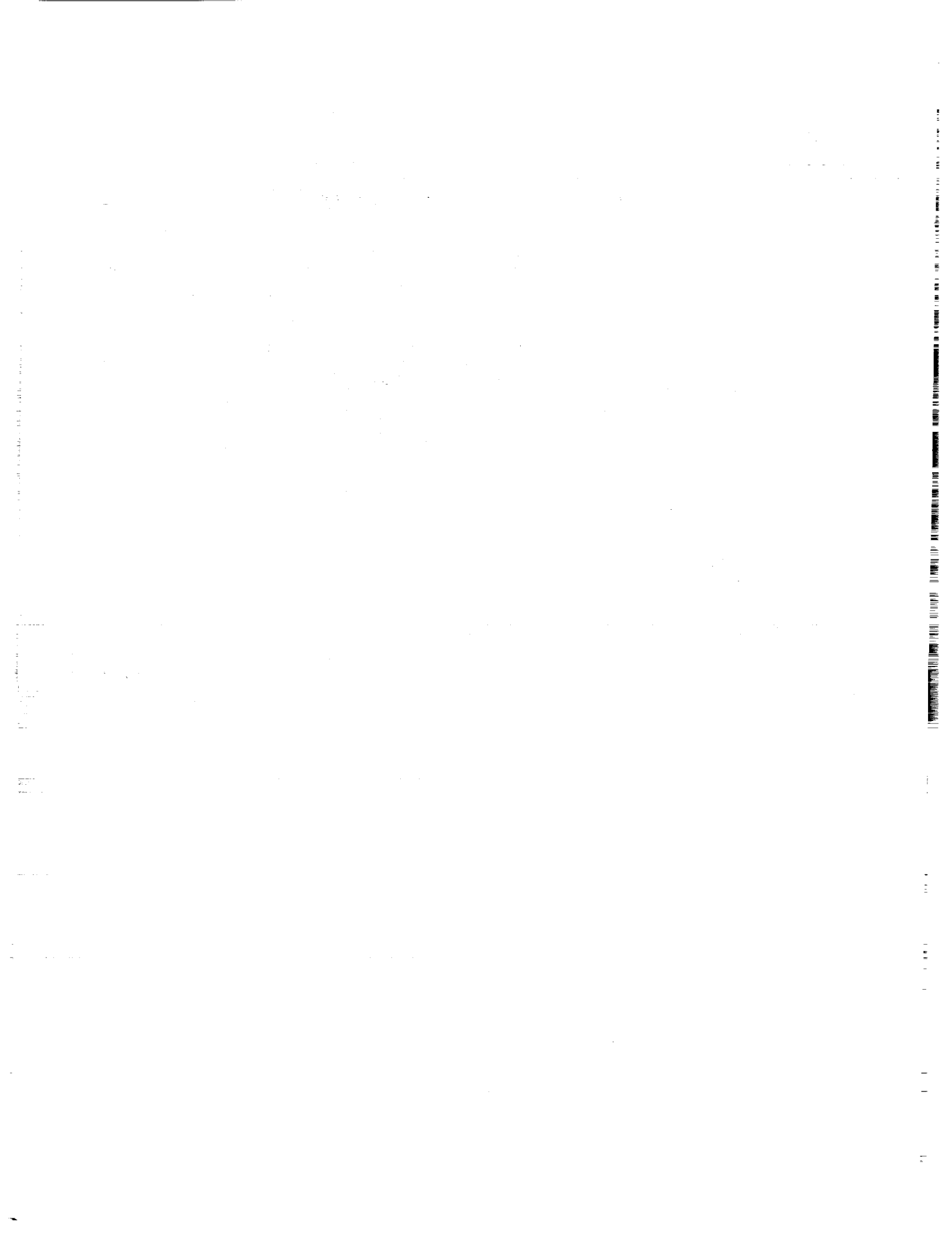
Thomas Barber, United Technologies Research Center
Leo Dadone, Boeing Helicopters
Sanford Davis, NASA Ames Research Center
Phillip Gliebe, GE Aircraft Engines
Yueping Guo, McDonnell Douglas Aircraft Company
Jay C. Hardin, NASA Langley Research Center
Ray Hixon, ICOMP, NASA Lewis Research Center
Fang Hu, Old Dominion University
Dennis Huff, NASA Lewis Research Center
Sanjiva Lele, Stanford University
Phillip Morris, Pennsylvania State University
N.N. Reddy, Lockheed Martin Aeronautical Systems
Lakshmi Sankar, Georgia Institute of Technology
Rahul Sen, Boeing Commercial Airplane Company
Steve Shih, ICOMP, NASA Lewis Research Center
Gary Strumolo, Ford Motor Company
Christopher Tam, Florida State University
James L. Thomas, NASA Langley Research Center

CONTENTS

Preface	iii
Organizing Committee	v <i>omit</i>
Benchmark Problems	1 <i>omit</i>
Analytical Solutions of the Category 1, Benchmark Problems 1 and 2	9 <i>/</i>
Konstantin A. Kurbatskii	
Scattering of Sound by a Sphere: Category 1: Problems 3 and 4	15 <i>-2</i>
Phillip J. Morris	
Radiation of Sound from a Point Source in a Short Duct	19 <i>-3</i>
M. K. Myers	
Exact Solutions for Sound Radiation from a Circular Duct	27 <i>-4</i>
Y. C. Cho and K. Uno Ingard	
Exact Solution to Category 3 Problems-Turbomachinery Noise	41 <i>-5</i>
Kenneth C. Hall	
Application of the Discontinuous Galerkin Method to Acoustic Scatter Problems ..	45 <i>-6</i>
H. L. Atkins	
Computation of Acoustic Scattering by a Low-Dispersion Scheme	57 <i>-7</i>
Oktay Baysal and Dinesh K. Kaushik	
Solution of Acoustic Scattering Problems by a Staggered-Grid Spectral Domain Decomposition Method	69 <i>-8</i>
Peter J. Bismuti and David A. Kopriva	
Application of Dispersion-Relation-Preserving Scheme to the Computation of Acoustic Scattering in Benchmark Problems	79 <i>-9</i>
R. F. Chen and M. Zhuang	
Development of Compact Wave Solvers and Applications	85 <i>-10</i>
K.-Y. Fung	
Computations of Acoustic Scattering off a Circular Cylinder	93 <i>-11</i>
M. Ehtesham Hayder, Gorden Erlebacher, and M. Yousuff Hussaini	
Application of an Optimized MacCormack-type Scheme to Acoustic Scattering Problems	101 <i>-12</i>
Ray Hixon, S.-H. Shih, and Reda R. Mankbadi	
Computational Aeroacoustics for Prediction of Acoustic Scattering	111 <i>-13</i>
Morris Y. Hsi and Fred Périé	

Application of PML Absorbing Boundary Conditions to the Benchmark Problems of Computational Aeroacoustics	119	-14
Fang Q. Hu and Joe L. Manthey		
Acoustic Calculations with Second- and Fourth-Order Upwind Leapfrog Schemes	153	-15
Cheolwan Kim and Phillip Roe		
Least-Squares Spectral Element Solutions to the CAA Workshop Benchmark Problems	165	-16
Wen H. Lin and Daniel C. Chan		
Adequate Boundary Conditions for Unsteady Aeroacoustic Problems	179	-17
Yu. B. Radvogin and N. A. Zaitsev		
Numerical Boundary Conditions for Computational Aeroacoustics Benchmark Problems	191	-18
Christopher K. W. Tam, Konstantin A. Kurbatskii, and Jun Fang		
Testing a Linear Propagation Module on Some Acoustic Scattering Problems	221	-19
G. S. Djambazov, C.-H. Lai, and K. A. Pericleous		
Solution of Aeroacoustic Problems by a Nonlinear, Hybrid Method	231	-20
Yusuf Özyörük and Lyle N. Long		
Three-Dimensional Calculations of Acoustic Scattering by a Sphere: A Parallel Implementation	241	-21
Chingwei M. Shieh and Phillip J. Morris		
On Computations of Duct Acoustics with Near Cut-Off Frequency	247	-22
Thomas Z. Dong and Louis A. Povinelli		
A Computational Aeroacoustics Approach to Duct Acoustics	259	-23
Douglas M. Nark		
A Variational Finite Element Method for Computational Aeroacoustic Calculations of Turbomachinery Noise	269	-24
Kenneth C. Hall		
A Parallel Simulation of Gust/Cascade Interaction Noise	279	-25
David A. Lockard and Phillip J. Morris		
Computation of Sound Generated by Flow over a Circular Cylinder: An Acoustic Analogy Approach	289	-26
Kenneth S. Brentner, Jared S. Cox, Christopher L. Rumsey, and Bassam A. Younis		
Computation of Noise Due to the Flow over a Circular Cylinder	297	-27
Sanjay Kumarasamy, Richard A. Korpus, and Jewel B. Barlow		
A Viscous/Acoustic Splitting Technique for Aeolian Tone Prediction	305	-28
D. Stuart Pope		

Large-Eddy Simulation of a High Reynolds Number Flow around a Cylinder Including Aeroacoustic Predictions	319	-29	
Evangelos T. Spyropoulos and Bayard S. Holmes			
A Comparative Study of Low Dispersion Finite Volume Schemes for CAA Benchmark Problems	329	-30	
D. V. Nance, L. N. Sankar, and K. Viswanathan			
Overview of Computed Results	349	-31	
Christopher K. W. Tam			
Solution Comparisons: Category 1: Problems 1 and 2	351		} omit
Konstantin A. Kurbatskii and Christopher K. W. Tam			
Solution Comparisons. Category 1: Problems 3 and 4. Category 2: Problem 1	359		
Phillip J. Morris			
Solution Comparisons: Category 2: Problem 2	363		
Konstantin A. Kurbatskii and Christopher K. W. Tam			
Solution Comparisons: Category 3	367		
Kenneth C. Hall			
Solution Comparisons: Category 4	373		
Jay C. Hardin			
Industry Panel Presentations and Discussions	377		
N.N. Reddy			



Benchmark Problems

Category 1 — Acoustic Scattering

Problem 1

The physical problem is to find the sound field generated by a propeller scattered off by the fuselage of an aircraft. The pressure loading on the fuselage is an input to the interior noise problem. Computationally, this is a good problem for testing curved wall boundary conditions.

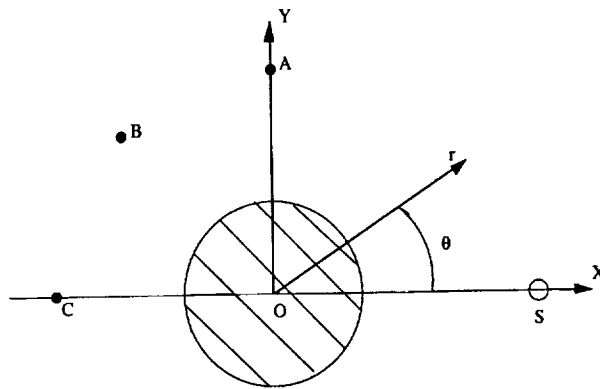


Figure 1

We will idealize the fuselage as a circular cylinder and the noise source (propeller) as a line source so that the computational problem is two-dimensional, figure 1. We will use a polar coordinate system centered at the center of the circular cylinder as shown. Dimensionless variables with respect to the following scales are to be used.

- length scale = diameter of circular cylinder, D
- velocity scale = speed of sound, c
- time scale = $\frac{D}{c}$
- density scale = undisturbed density, ρ_0
- pressure scale = $\rho_0 c^2$

The linearized Euler equations are

$$\frac{\partial u}{\partial t} + \frac{\partial p}{\partial x} = 0 \tag{1}$$

$$\frac{\partial v}{\partial t} + \frac{\partial p}{\partial y} = 0 \tag{2}$$

$$\frac{\partial p}{\partial t} + \frac{\partial u}{\partial x} + \frac{\partial v}{\partial y} = S \tag{3}$$

where

$$S = \exp \left[-\ln 2 \left(\frac{(x-4)^2 + y^2}{(0.2)^2} \right) \right] \sin \omega t.$$

Find the scattered sound field for $\omega = 8\pi$.

Give $D(\theta) = \lim_{r \rightarrow \infty} r \overline{p^2}$ for $\theta = 90^\circ$ to 180° at $\Delta\theta = 1$ degree (— = time average). State your grid specification and Δt used in the computation.

Problem 2

This is the same as problem 1 above except that there is no time periodic source; i.e., $S = 0$ in equation (3). Consider an initial value problem with initial conditions $t = 0$, $u = v = 0$, and

$$p = \exp \left[-\ln 2 \left(\frac{(x-4)^2 + y^2}{(0.2)^2} \right) \right]$$

Find $p(t)$ at the three points A ($r = 5, \theta = 90^\circ$), B ($r = 5, \theta = 135^\circ$), C ($r = 5, \theta = 180^\circ$). Give $p(t)$ from $t = 6$ to $t = 10$ with $\Delta t = 0.01$. State the grid specification and the Δt used in the computation.

Problem 3

Solve the axisymmetric linearized Euler equations to predict the scattering of acoustic waves from a sphere. The governing equations (including the acoustic source) are given by

$$\frac{\partial}{\partial t} \begin{bmatrix} \rho \\ u \\ v \\ p \end{bmatrix} + \frac{\partial}{\partial r} \begin{bmatrix} v \\ 0 \\ p \\ v \end{bmatrix} + \frac{\partial}{\partial x} \begin{bmatrix} u \\ p \\ 0 \\ u \end{bmatrix} = \begin{bmatrix} -\frac{v}{r} \\ 0 \\ 0 \\ -\frac{v}{r} + A \exp(-B(\ln 2)((x-x_s)^2 + r^2)) \cos(\omega t) \end{bmatrix}$$

The length scale is given by the radius of the sphere, R . The ambient speed of sound, a_∞ , and the ambient density, ρ_∞ , are used as the velocity and density scales, respectively. The pressure is nondimensionalized by $\rho_\infty a_\infty^2$ and time is scaled by R/a_∞ . For the source, use $A = 0.01$, $B = 16$, $x_s = 2$ and $\omega = 20\pi$.

There are no constraints on the maximum size of the domain or number of grid points; although, CPU time will be used in part to assess the algorithm.

Submit the RMS pressure along the circle $x^2 + y^2 = 25$ at $\Delta\theta = 1^\circ$, θ measured from the x -axis. The computer used, CPU time per timestep, the number of timesteps per period of the source, the number of grid points and CPU memory per grid point should also be reported.

Problem 4

This is the same as Problem 3 except that the computation is to be carried out in Cartesian coordinates.

Solve the 3-D Cartesian linearized Euler equations to predict the scattering of acoustic waves from a sphere. The governing equations (including the acoustic source) are given by

$$\frac{\partial}{\partial t} \begin{bmatrix} \rho \\ u \\ v \\ w \\ p \end{bmatrix} + \frac{\partial}{\partial x} \begin{bmatrix} u \\ p \\ 0 \\ 0 \\ u \end{bmatrix} + \frac{\partial}{\partial y} \begin{bmatrix} v \\ 0 \\ p \\ 0 \\ v \end{bmatrix} + \frac{\partial}{\partial z} \begin{bmatrix} w \\ 0 \\ 0 \\ p \\ w \end{bmatrix} = \begin{bmatrix} 0 \\ 0 \\ 0 \\ 0 \\ -A \exp(-B(\ln 2)((x - x_s)^2 + y^2 + z^2)) \cos(\omega t) \end{bmatrix}$$

The length scale is given by the radius of the sphere, R . The ambient speed of sound, a_∞ , and the ambient density, ρ_∞ , are used as the velocity and density scales, respectively. The pressure is nondimensionalized by $\rho_\infty a_\infty^2$ and time is scaled by R/a_∞ . For the source, use $A = 0.01$, $B = 16$, $x_s = 2$, and $\omega = 20\pi$.

There are no constraints on the maximum size of the domain or number of grid points; although, CPU time will be used in part to assess the algorithm.

Submit the RMS pressure along the circle $x^2 + y^2 = 25$ at $\Delta\theta = 1^\circ$, θ measured from the x -axis. The computer used, CPU time per timestep, the number of timesteps per period of the source, the number of grid points and CPU memory per grid point should also be reported.

Category 2 — Duct Acoustics

Problem 1

A finite length, both end open cylindrical shell (duct) of zero thickness is placed in a uniform flow at a Mach number of 0.5 as shown in figure 2. A time periodic, distributed but very narrow spherical source is located at the geometrical center of the duct.

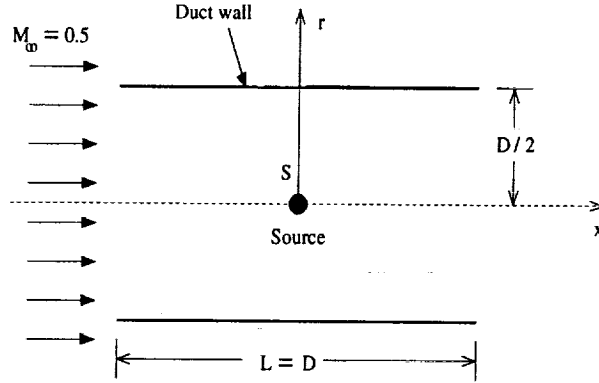


Figure 2

The length L and the diameter D of the shell are equal ($L = D$). The flow variables and the geometrical quantities are nondimensionalized using D as the length scale, the ambient speed of sound a_∞ as the velocity scale, the ambient density ρ_∞ as the density scale, and $\rho_\infty a_\infty^2$ as the pressure scale. Time is made dimensionless by the time scale D/a_∞ . The problem is axisymmetric and should be solved using the linearized Euler equations given, in dimensionless form, as

$$\frac{\partial}{\partial t} \begin{bmatrix} \rho \\ u \\ v \\ p \end{bmatrix} + \frac{\partial}{\partial x} \begin{bmatrix} M_\infty \rho + u \\ M_\infty u + p \\ M_\infty v \\ M_\infty p + u \end{bmatrix} + \frac{\partial}{\partial r} \begin{bmatrix} v \\ 0 \\ p \\ v \end{bmatrix} + \begin{bmatrix} \frac{v}{r} \\ 0 \\ 0 \\ \frac{v}{r} \end{bmatrix} = \begin{bmatrix} S \\ 0 \\ 0 \\ S \end{bmatrix}$$

where the source S is given by

$$S = 0.1 \exp \left[-48(\ln 2) \left(\frac{kD}{2\pi} \right)^2 (x^2 + r^2) \right] \cos(kDt), \text{ with } kD = 16\pi.$$

An equivalent set of equations could also be used. Calculate the intensity of sound, $\overline{p^2}$, along the circular arc $x^2 + r^2 = (5/2)^2$ at $\Delta\theta = 1^\circ$, θ measured from the x -axis. There is no requirement to use a specific domain or number of grid points. However, for algorithm assessment purposes the investigator is asked to report the computer used, the total CPU time, time step size, total number of time steps, total number of grid points, and the size of the physical domain.

Problem 2

Consider the radiation of sound from a thin wall duct as shown in figure 3. The parameters of this problem have been so chosen that unless some fundamental understanding of duct acoustics such as duct modes, cutoff frequencies are incorporated in the design of the computational algorithm, the computed results would, invariably, be quite poor.

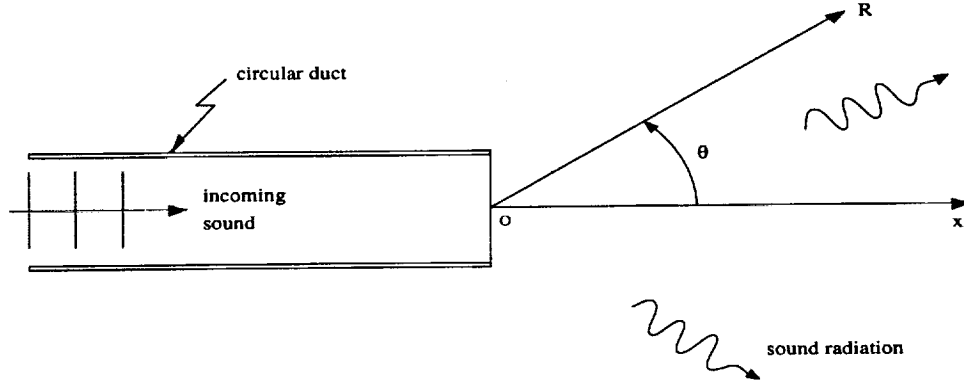


Figure 3

For convenience, we will use a cylindrical coordinate system (r, ϕ, x) inside the duct and a spherical polar coordinate system (R, θ, ϕ) outside the duct. Dimensionless variables with respect to the following scales are to be used.

length scale	=	radius of duct, a
velocity scale	=	speed of sound, c
time scale	=	$\frac{a}{c}$
density scale	=	undisturbed density, ρ_0
pressure scale	=	$\rho_0 c^2$

Consider a semi-infinite long circular duct with infinitesimally thin rigid wall as shown. Small amplitude sound waves enter the duct from the left and radiate out through the open end to the right. The incoming wave is a spinning duct mode with velocity and pressure given by

$$\begin{bmatrix} u \\ v \\ w \\ p \end{bmatrix} = \text{Re} \left\{ \begin{bmatrix} \frac{(\omega^2 - \mu_{nm}^2)^{1/2}}{\omega} J_n(\mu_{nm} r) \\ -i \frac{\mu_{nm}}{\omega} J'_n(\mu_{nm} r) \\ \frac{n}{\omega r} J_n(\mu_{nm} r) \\ J_n(\mu_{nm} r) \end{bmatrix} e^{i[(\omega^2 - \mu_{nm}^2)^{1/2} x + n\phi - \omega t]} \right\}$$

where (u, v, w) are velocity components in the (x, r, ϕ) directions. $J_n(\)$ is the n^{th} order Bessel function. μ_{nm} is the m^{th} zero of J'_n ; i.e., $J'_n(\mu_{nm}) = 0$, $n = 0, 1, 2, \dots$, $m = 1, 2, 3, \dots$

1. Find the directivity, $D(\theta)$, of the radiated sound.

$$D(\theta) \equiv \lim_{R \rightarrow \infty} \overline{R^2 p^2(R, \theta, \phi, t)}, \quad \text{---} = \text{time average.}$$

Give $D(\theta)$ from $\theta = 0$ to $\theta = 180^\circ$ at $\Delta\theta = 1$ degree.

2. Find the pressure envelope inside the duct along the four radial lines $r = 0, 0.34, 0.55, 0.79$. The pressure envelope, $P(x)$, is given by

$$P(x) = \max_{\text{over time}} p(r, \phi, x, t).$$

Give $P(x)$ from $x = -6$ to $x = 0$ at $\Delta x = 0.1$.

For both parts of the problem, consider only $n = 0, m = 2$ and the two cases

(a) $\omega = 7.2$

(b) $\omega = 10.3$

Note: $\mu_{02} = 7.0156$. You are to solve the linearized Euler equations.

Category 3 — Turbomachinery Noise

The purpose of these problems is to study the computational requirements for modeling the aeroacoustic response of typical rotor-stator interactions that generates tonal noise in turbomachinery. You may solve either the full Euler or linearized Euler equations. Be sure to specify the grid size, the total CPU time required, the CPU time per period, and the type of computer used for each problem.

Problem 1

This problem is designed to test the ability of a numerical scheme to model the acoustic response of a cascade to an incident "frozen gust".

Consider the cascade of flat-plate airfoils shown in figure 4. The mean flow is uniform and axial with inflow velocity U_∞ and static density ρ_∞ . The inflow Mach number M_∞ is 0.5. The length (chord) of each plate is c , and the gap-to-chord ratio g/c is 1.0.

We will use non-dimensional variables with U_∞ as velocity scale, c as length scale, c/U_∞ as time scale, ρ_∞ as density scale and $\rho_\infty U_\infty^2$ as pressure scale.

The incident vortical gust, which is carried along by the mean flow, has x and y velocities given by

$$u = - \left(\frac{v_G \beta}{\alpha} \right) \cos(\alpha x + \beta y - \omega t) \quad (1)$$

and

$$v = v_G \cos(\alpha x + \beta y - \omega t) \quad (2)$$

respectively, where $v_G = 0.01$. Consider two cases. For Case 1, the wavenumber β is $5\pi/2$ corresponding to an "interblade phase angle" σ of $5\pi/2$. The frequency ω (same as the reduced frequency based on chord, k) is equal to $5\pi/2$ (≈ 7.864). For Case 2, $\sigma = k = 13\pi/2$ (≈ 20.42). The gust is convected by the mean flow. Therefore, the x -wavenumber α for both cases is equal to ω .

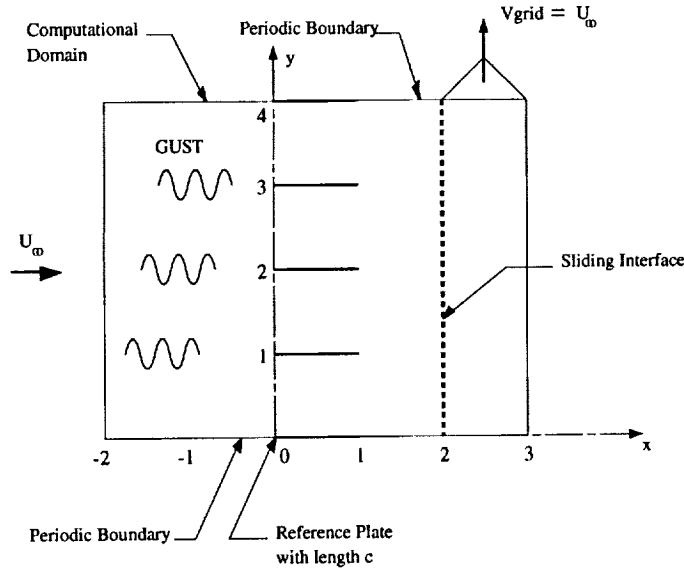


Figure 4

Using the frozen gust assumption, determine the magnitude of the pressure jump across the reference airfoil (the airfoil at $y = 0$) where $\Delta p = p_{\text{lower}} - p_{\text{upper}}$. You need not solve for the gust convection as part of your numerical solution, but instead may simply impose an upwash on the airfoil surfaces given by (2). Also, determine the intensity of the radiated sound \bar{p}^2 along the lines $x = -2$ and $x = +3$. Finally, plot contours of the perturbation pressure at time $t = 2\pi n/\omega$ where n is an integer. If you are using a time marching algorithm, n should be large enough that the solution is temporally periodic. Your contour plots should show the instantaneous nondimensional static pressure p for the entire computational domain.

Problem 2

This problem is designed to test the ability of a numerical scheme to simultaneously model the convection of vortical and acoustic waves in a cascade.

Repeat Problem 1, but this time specify the gust along the upstream boundary of the computational domain. Then use your numerical algorithm to model the convected vortical wave and subsequent interaction with the cascade. Apart from truncation error, your solution should be identical to Problem 1. In other words, be careful to specify the phasing of the incoming gust such that the upwash on the airfoil has the same phase used in Problem 1.

Problem 3

This problem is designed to test the ability of a numerical scheme to model the propagation of acoustic and vortical waves across a sliding interface typical of those used in rotor stator interaction problems.

Repeat Problem 2, but translate the portion of the grid aft of the line $x = 2$ in the positive y -direction with speed 1. If possible, arrange the sliding grid motion so that at times corresponding to the start of each period ($t = 2\pi n/\omega$) the sliding grid is in the original nonsliding position. This will aid in the plotting and evaluation of solutions.

Category 4 — Airframe and Automobile Noise

Aeolian tones, sound generation by flow over a cylinder, are relevant to automobile antenna and airframe noise. The purpose of this problem is to demonstrate computation of sound generation by viscous flows.

Consider uniform flow at Mach number 0.2 over a two-dimensional cylinder of diameter $D = 1.9\text{cm}$ as shown in figure 5. The Reynolds number based on the diameter of the cylinder is 90,000. Perform numerical simulations to estimate the power spectra of the radiated sound in dB (per 20Hz bandwidth) at $r/D = 35$ and $\theta = 60^\circ, 90^\circ, 120^\circ$ over the Strouhal number, $St = \frac{fD}{U_0}$, range of $0.01 \leq St \leq 0.61$ at $\Delta St = 0.002$.

You may use a smaller Reynolds number in your simulation. However, data may not be available for direct validation.

Perform grid and time resolution studies to demonstrate that your solution has converged.

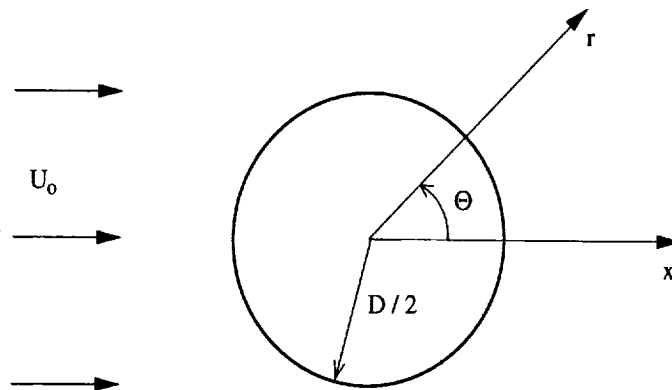


Figure 5

**ANALYTICAL SOLUTIONS OF THE CATEGORY 1,
BENCHMARK PROBLEMS 1 AND 2**

51-64
043 456
p6

Konstantin A. Kurbatskii
Department of Mathematics
Florida State University
Tallahassee, FL 32306-3027

1. ANALYTICAL SOLUTION OF THE PROBLEM 1

The linearized Euler equations are

$$\frac{\partial u}{\partial t} + \frac{\partial p}{\partial x} = 0 \quad (1)$$

$$\frac{\partial v}{\partial t} + \frac{\partial p}{\partial y} = 0 \quad (2)$$

$$\frac{\partial p}{\partial t} + \frac{\partial u}{\partial x} + \frac{\partial v}{\partial y} = S(x, y, t) \quad (3)$$

where

$$S(x, y, t) = e^{-\ln 2((x-x_s)^2+y^2)/w^2} \sin(\omega t) \quad (4)$$

is the time-periodic acoustic source located at $x = x_s$, $y = 0$. Here $x_s = 4$, $w = 0.2$, $\omega = 8\pi$.

Boundary conditions are

1) zero-normal-velocity at the surface of the cylinder

$$\mathbf{v} \cdot \mathbf{n} = 0 \quad \text{at} \quad x^2 + y^2 = (0.5)^2 \quad (5)$$

2) radiation boundary condition for $x, y \rightarrow \infty$, i.e. the solution represents outgoing waves. (6)

By eliminating u and v from (1) to (3), the equation for p is,

$$\frac{\partial^2 p}{\partial t^2} - \left(\frac{\partial^2 p}{\partial x^2} + \frac{\partial^2 p}{\partial y^2} \right) = e^{-b[(x-x_s)^2+y^2]} \text{Im}(i\omega e^{-i\omega t}) \quad (7)$$

$$\text{where} \quad b = \ln 2/w^2 \quad (8)$$

The boundary condition (5) becomes

$$\frac{\partial p}{\partial n} = 0 \text{ at } x^2 + y^2 = 0.25 \quad (9)$$

The solution for pressure, p , can be written as

$$p(x, y, t) = \text{Im}(\hat{p}(x, y)e^{-i\omega t}) \quad (10)$$

Substitution of (10) into (7), (9) gives the problem for $\hat{p}(x, y)$

$$\frac{\partial^2 \hat{p}}{\partial x^2} + \frac{\partial^2 \hat{p}}{\partial y^2} + \omega^2 \hat{p} = -i\omega e^{-b[(x-x_s)^2 + y^2]} \quad (11)$$

$$\frac{\partial \hat{p}}{\partial n} = 0 \text{ at } x^2 + y^2 = 0.25 \quad (12)$$

$$\text{radiation boundary conditions as } x, y \rightarrow \infty \quad (13)$$

(11) is a non-homogeneous Helmholtz equation. The problem (11) - (13) can be solved by the method of superposition. Let

$$\hat{p}(x, y) = p_i(x, y) + p_r(x, y) \quad (14)$$

where p_i is the incident wave generated by the source and p_r is the wave reflected off the cylinder. p_i satisfies

$$\frac{\partial^2 p_i}{\partial x^2} + \frac{\partial^2 p_i}{\partial y^2} + \omega^2 p_i = -i\omega e^{-b[(x-x_s)^2 + y^2]} \quad (15)$$

and the outgoing wave condition. When p_i is found the problem for p_r becomes

$$\frac{\partial^2 p_r}{\partial x^2} + \frac{\partial^2 p_r}{\partial y^2} + \omega^2 p_r = 0 \quad (16)$$

$$\frac{\partial p_r}{\partial n} = -\frac{\partial p_i}{\partial n} \text{ at } x^2 + y^2 = 0.25 \quad (17)$$

To solve for $p_i(x, y)$ we use polar coordinates (r_s, θ_s) with the origin at $x = x_s, y = 0$; thus the solution is independent of θ_s . (16) reduces to the non-homogeneous Bessel equation

$$\frac{d^2 p_i}{dr_s^2} + \frac{1}{r_s} \frac{dp_i}{dr_s} + \omega^2 p_i = -i\omega e^{-br_s^2} \quad (18)$$

with boundary conditions

$$p_i(r_s) \text{ is bounded at } r_s = 0 \quad (19)$$

$$p_i(r_s)e^{-i\omega t} \text{ represents outgoing waves as } r_s \rightarrow \infty \quad (20)$$

The Greens function for (18) - (19) is

$$G(r_s, \xi) = \begin{cases} -\frac{\pi i}{2} \xi J_0(\omega r_s) H_0^{(1)}(\omega \xi), & 0 \leq r_s \leq \xi \\ -\frac{\pi i}{2} \xi J_0(\omega \xi) H_0^{(1)}(\omega r_s), & \xi \leq r_s < \infty \end{cases} \quad (21)$$

where J_0 and $H_0^{(1)}$ are the zeroth order Bessel and Hankel functions respectively.

The solution for $p_i(r_s)$ is

$$p_i(r_s) = \int_0^\infty G(r_s, \xi) [-i\omega e^{-b\xi^2}] d\xi \quad (22)$$

With p_i found, the problem for the reflected wave, p_r , is

$$\frac{\partial^2 p_r}{\partial r^2} + \frac{1}{r} \frac{\partial p_r}{\partial r} + \frac{1}{r^2} \frac{\partial^2 p_r}{\partial \theta^2} + \omega^2 p_r = 0 \quad (23)$$

$$\frac{\partial p_r}{\partial r} = B(\theta) \text{ at } r = 0.5 \quad (24)$$

where $B(\theta)$ is now known.

By separating variables in (23) $p_r(r, \theta)$ is represented by Fourier series

$$p_r(r, \theta) = \sum_{k=0}^{\infty} C_k H_k^{(1)}(r\omega) \cos(k\theta) \quad (25)$$

where $H_k^{(1)}$ is the Hankel function of the first kind. Only cosine terms are retained in (25) because the problem is symmetric about the x-axis.

The coefficients C_k of (25) are found by applying the boundary condition (24). This gives

$$C_k = \frac{\epsilon_k}{\pi\omega \left[\frac{2k}{\omega} H_k^{(1)}(\omega/2) - H_{k+1}^{(1)}(\omega/2) \right]} \int_0^\pi B(\theta) \cos(k\theta) d\theta \quad (26)$$

Here $\epsilon_0 = 1$, $\epsilon_k = 2$, $k = 1, 2, \dots$

Finally, by means of the asymptotic formulas for $H_k^{(1)}$ (see ref.(1)), it is easy to find that the directivity

$$D(\theta) = \lim_{r \rightarrow \infty} r p^2 \text{ is given by}$$

$$D(\theta) = \left| -\sqrt{\frac{\pi\omega}{2}} e^{-i(\omega x_s \cos\theta + \pi/4)} \int_0^\infty \xi J_0(\omega\xi) e^{-b\xi^2} d\xi + \sqrt{\frac{2}{\pi\omega}} \sum_{k=0}^{\infty} C_k e^{-i(k\pi/2 + \pi/4)} \cos(k\theta) \right|^2 \quad (27)$$

1. ANALYTICAL SOLUTION OF THE PROBLEM 2

This is an initial-value problem governed by the linearized Euler equations

$$\frac{\partial u}{\partial t} + \frac{\partial p}{\partial x} = 0 \quad (28)$$

$$\frac{\partial v}{\partial t} + \frac{\partial p}{\partial y} = 0 \quad (29)$$

$$\frac{\partial p}{\partial t} + \frac{\partial u}{\partial x} + \frac{\partial v}{\partial y} = 0 \quad (30)$$

The initial conditions are:

$$u = v = 0 \quad \text{at } t = 0 \quad (31)$$

and

$$p(x, y, 0) = e^{-\ln 2((x-x_s)^2+y^2)/w^2} \quad \text{at } t = 0 \quad (32)$$

Here $x_s = 4, w = 0.2$.

The boundary conditions are:

$$\mathbf{v} \cdot \mathbf{n} = 0 \quad \text{at } x^2 + y^2 = (0.5)^2, \quad (33)$$

and

$$\text{when } x, y \rightarrow \infty \text{ the solution represents outgoing waves.} \quad (34)$$

Solution of the problem (28) - (34) can be found in terms of velocity potential $\phi(x, y, t)$ defined by

$$u = \frac{\partial \phi}{\partial x}, \quad v = \frac{\partial \phi}{\partial y}, \quad p = -\frac{\partial \phi}{\partial t} \quad (35)$$

It is easy to show from (28) - (30) and (35) that the governing equation for ϕ is the wave equation which may be written in polar coordinates (r, θ) as

$$\frac{\partial^2 \phi}{\partial t^2} - \left(\frac{\partial^2 \phi}{\partial r^2} + \frac{1}{r} \frac{\partial \phi}{\partial r} + \frac{1}{r^2} \frac{\partial^2 \phi}{\partial \theta^2} \right) = 0 \quad (36)$$

Initial conditions (31) and (32) are reduced to

$$t = 0: \quad \phi = 0, \quad \frac{\partial \phi}{\partial t} = -e^{-b(r^2+x_s^2-2rx_s \cos \theta)} \quad (37)$$

where $b = \ln 2/w^2$.

Boundary condition (33) becomes

$$\frac{\partial \phi}{\partial r} = 0 \quad \text{at } r = 0.5 \quad (38)$$

The problem (36) - (38) can be solved by the method of superposition. Let

$$\phi(r, \theta, t) = \phi_i(r, \theta, t) + \phi_r(r, \theta, t) \quad (39)$$

where ϕ_i is the incident wave generated by the initial pressure pulse, and ϕ_r is the wave reflected off the cylinder. $\phi_i(r, \theta, t)$ satisfies

$$\frac{\partial^2 \phi_i}{\partial t^2} - \left(\frac{\partial^2 \phi_i}{\partial r_s^2} + \frac{1}{r_s} \frac{\partial \phi_i}{\partial r_s} \right) = 0 \quad (40)$$

with the initial conditions

$$t = 0: \quad \phi_i = 0, \quad \frac{\partial \phi_i}{\partial t} = -e^{-br_s^2} \quad (41)$$

where (r_s, θ_s) are the polar coordinates with the origin at $x = x_s, y = 0$.

The initial value problem of (40) and (41) can be solved by means of the order-zero Hankel transform. The solution is (see ref.(2))

$$\phi_i(r_s, t) = -\frac{1}{2b} \int_0^\infty e^{-b\omega^2/(4b)} J_0(\omega r_s) \sin(\omega t) d\omega$$

or in terms of (r, θ) coordinates

$$\phi_i(r, \theta, t) = \int_0^\infty A_i(r, \theta, \omega) \sin(\omega t) d\omega \quad (42)$$

$$\text{where } A_i(r, \theta, \omega) = -\frac{1}{2b} e^{-b\omega^2/(4b)} J_0(\omega \sqrt{r^2 + x_s^2 - 2rx_s \cos \theta}) \quad (43)$$

The problem for ϕ_r is

$$\frac{\partial^2 \phi_r}{\partial t^2} - \left(\frac{\partial^2 \phi_r}{\partial r^2} + \frac{1}{r} \frac{\partial \phi_r}{\partial r} + \frac{1}{r^2} \frac{\partial^2 \phi_r}{\partial \theta^2} \right) = 0 \quad (44)$$

$$\frac{\partial \phi_r}{\partial r} = -\frac{\partial \phi_i}{\partial r} \quad \text{at } r = 0.5 \quad (45)$$

In view of (42) we will represent the solution for ϕ_r by Fourier sine transform in t ,

$$\phi_r(r, \theta, t) = \int_0^\infty A_r(r, \theta, \omega) \sin(\omega t) d\omega \quad (46)$$

Substitution of (46) into (44), (45) gives

$$\frac{\partial^2 A_r}{\partial r^2} + \frac{1}{r} \frac{\partial A_r}{\partial r} + \frac{1}{r^2} \frac{\partial^2 A_r}{\partial \theta^2} + \omega^2 A = 0 \quad (47)$$

$$\frac{\partial A_r}{\partial r} = B(\theta, \omega) \quad \text{at } r = 0.5 \quad (48)$$

$$\text{where } B(\theta, \omega) = - \left. \frac{\partial A_i}{\partial r} \right|_{r=0.5} \quad (49)$$

(47) can be solved by separation of variables giving,

$$A_r(r, \theta, \omega) = \sum_{k=0}^{\infty} C_k(\omega) H_k^{(1)}(r\omega) \cos(k\theta) \quad (50)$$

The coefficients C_k of (50) are found by applying the boundary condition (48). It is straightforward to find,

$$C_k = \frac{\epsilon_k}{\pi\omega \left[\frac{2k}{\omega} H_k^{(1)}(\omega/2) - H_{k+1}^{(1)}(\omega/2) \right]} \int_0^{\pi} B(\theta, \omega) \cos(k\theta) d\theta \quad (51)$$

Finally, substitution of (50), (51) into (46) and on combining (42), (46), the velocity potential is found,

$$\phi(r, \theta, t) = \int_0^{\infty} A(r, \theta, \omega) \sin(\omega t) d\omega \quad (52)$$

where

$$A(r, \theta, \omega) = - \frac{e^{-b\omega^2/(4b)}}{2b} \left\{ J_0(\omega \sqrt{r^2 + x_s^2} - 2rx_s \cos\theta) + \sum_{k=0}^{\infty} \text{Re} \left[\frac{\epsilon_k H_k^{(1)}(r\omega) \cos(k\theta)}{\pi\omega \left[\frac{2k}{\omega} H_k^{(1)}(\omega/2) - H_{k+1}^{(1)}(\omega/2) \right]} \right] \right. \\ \left. \int_0^{\pi} \frac{(0.5 - x_s \cos\eta) J_1(\omega \sqrt{0.25 + x_s^2} - x_s \cos\eta)}{\sqrt{0.25 + x_s^2} - x_s \cos\eta} \cos(k\eta) d\eta \right\} \quad (53)$$

The pressure field may be calculated by

$$p(r, \theta, t) = - \frac{\partial \phi}{\partial t} = - \int_0^{\infty} A(r, \theta, \omega) \omega \cos(\omega t) d\omega \quad (54)$$

REFERENCES

1. Abramowitz, M.; and Stegun, I.A.: Handbook of Mathematical Functions.
2. Tam, C.K.W.; and Webb, J.C.: Dispersion-Relation-Preserving Finite Difference Schemes for Computational Acoustics. *J. Comput. Phys.*, vol. 107, Aug. 1993, pp. 262-281.

- - 71
043 457
293706
p4

SCATTERING OF SOUND BY A SPHERE: CATEGORY 1: PROBLEMS 3 AND 4.

Philip J. Morris*
Department of Aerospace Engineering
The Pennsylvania State University
University Park, PA 16802

INTRODUCTION

The scattering of sound by a sphere may be treated as an axisymmetric or three-dimensional problem, depending on the properties of the source. In the two problems here, the solution is axisymmetric. The method described below uses a Hankel transform in spherical polar coordinates. Additional details of the solution, including the numerical evaluation of spherical Hankel functions, are given by Morris [3]. This reference also includes solutions for non-rigid spheres. The same method may be applied to cylinder scattering problems as described by Morris [2].

EXACT SOLUTION

Consider the scattering of sound from a spherically-symmetric source by a sphere of radius a . The source is centered at S , a distance x_s from the center of the sphere. A spherical coordinate system (r, θ, ϕ) has its origin at the center of the sphere. The line joining the centers of the sphere and the source defines $\theta = 0$. Thus, the problem is independent of ϕ . The density and speed of sound are ρ_o , c_o respectively. The radial distance from the center of the source is denoted by R .

A periodic solution is sought in the form $e^{-i\omega t}$. The source has a spatial distribution given by $p_s(R)$. The pressure, $p_o(r, \theta)$, satisfies the equation,

$$\frac{1}{r^2} \frac{\partial}{\partial r} \left(r^2 \frac{\partial p_o}{\partial r} \right) + \frac{1}{r^2 \sin \theta} \frac{\partial}{\partial \theta} \left(\sin \theta \frac{\partial p_o}{\partial \theta} \right) + k_o^2 p_o = p_s(R) \quad (1)$$

where, $k_o = \omega/c_o$.

Let the pressure be decomposed into incident and scattered fields: $p_{inc}(R)$ and $p_{sc}(r, \theta)$, respectively. Then $p_{inc}(R)$ satisfies the equation,

$$\frac{1}{R^2} \frac{d}{dR} \left(R^2 \frac{dp_{inc}}{dR} \right) + k_o^2 p_{inc} = p_s(R) \quad (2)$$

*Boeing/A. D. Welliver Professor of Aerospace Engineering

and the scattered field satisfies the homogeneous form of Eq. (1).

The solution for the incident field is obtained here through the use of a Hankel transform, given by

$$G(s) = \frac{2}{\pi} \int_0^{\infty} R^2 j_0(sR) g(R) dR \quad (3)$$

$$g(R) = \int_0^{\infty} s^2 j_0(sR) G(s) ds \quad (4)$$

where $j_n(z)$ is the spherical Bessel function of the first kind and order n . The properties of spherical Bessel functions are given by Abramowitz and Stegun [1].

Now, integration by parts and the use of general expressions for the derivatives of spherical Bessel functions [1], gives

$$\frac{2}{\pi} \int_0^{\infty} R^2 j_0(Rs) \left[\frac{1}{R^2} \frac{d}{dR} \left(R^2 \frac{dg}{dR} \right) \right] dR = -s^2 G(s) \quad (5)$$

So, the Hankel transform of Eq. (2) leads to

$$p_{inc}(R) = - \int_0^{\infty} \frac{s^2 j_0(sR) P_s(s)}{(s^2 - k_o^2)} ds \quad (6)$$

where,

$$P_s(s) = \frac{2}{\pi} \int_0^{\infty} R^2 j_0(sR) p_s(R) dR \quad (7)$$

Now, with $R = \sqrt{r^2 + x_s^2 - 2rx_s \cos \theta}$, Abramowitz and Stegun [1] give an addition theorem for spherical Bessel functions,

$$j_0(sR) = \frac{\sin(sR)}{sR} = \sum_{n=0}^{\infty} (2n+1) j_n(sr) j_n(sx_s) P_n(\cos \theta) \quad (8)$$

where $P_n(\cos \theta)$ is the Legendre polynomial of order n . Thus, from Eqs. (6) and (8),

$$p_{inc}(R) = - \sum_{n=0}^{\infty} (2n+1) P_n(\cos \theta) I_n(r) \quad (9)$$

where,

$$I_n(r) = \int_0^{\infty} \frac{s^2 j_n(sr) j_n(sx_s) P_n(s)}{(s^2 - k_o^2)} ds \quad (10)$$

The general solution for the scattered field may be written in separable form as

$$p_{sc}(r, \theta) = \sum_{n=0}^{\infty} A_n h_n^{(1)}(k_o r) P_n(\cos \theta) \quad (11)$$

where $h_n^{(1)}(z)$ is the spherical Hankel function of the first kind and order n .

At the boundary of the sphere we require that the normal derivative of the pressure be zero. So that,

$$A_n = \frac{(2n+1)}{k_o} \frac{I'_n(a)}{h_n^{(1)'}(k_o a)} \quad (12)$$

where,

$$I'_n(r) = \int_0^\infty \frac{s^3 j'_n(sr) j_n(sx_s) P_s(s)}{(s^2 - k_o^2)} ds \quad (13)$$

$j'_n(z)$ denotes the derivative of $j_n(z)$ with respect to z and is given by

$$j'_n(z) = j_{n-1}(z) - (n+1) j_n(z)/z \quad (14)$$

with $j'_o(z) = -j_1(z)$. Identical forms of expression may be used for the spherical Hankel function derivatives.

Now, consider a spherically-symmetric, spatially-distributed Gaussian source given by

$$p_s(R) = a \exp(-bR^2) \quad (15)$$

Then, from Eq. (7),

$$P_s(s) = \frac{a}{2b\sqrt{\pi b}} \exp(-s^2/4b) \quad (16)$$

In this case, neither the incident field nor the unknown integrals $I_n(a)$ and $I'_n(a)$ may be evaluated analytically. However, they may be obtained numerically. The numerical procedure used involves the use of an integration contour in the complex s plane to include the effect of the pole at $s = k_o$. It is described by Morris [2] and is not repeated here.

In the present problem, where the source is introduced into the linearized energy equation,

$$\begin{aligned} a &= -ik_o A \\ b &= B \end{aligned} \quad (17)$$

and

$$A = 0.01, \quad B = 16, \quad x_s = 2 \quad (18)$$

Different frequencies are considered in the model problems.

REFERENCES

- [1] M. Abramowitz and I. A. Stegun. *Handbook of Mathematical Functions*. Dover, 1965.
- [2] P. J. Morris. The scattering of sound from a spatially-distributed axisymmetric cylindrical source by a circular cylinder. *Journal of the Acoustical Society of America*, 97(5):2651–2656, 1995.
- [3] P. J. Morris. Scattering of sound from a spatially-distributed, spherically-symmetric source by a sphere. *Journal of the Acoustical Society of America*, 98(6):3536–3539, 1995.

RADIATION OF SOUND FROM A POINT SOURCE IN A SHORT DUCT

03-71
043459
293708
p8

M. K. Myers
The George Washington University
Joint Institute for Advancement of Flight Sciences
Hampton, VA

INTRODUCTION

It is the purpose of this paper to provide, in relatively brief form, a summary of a boundary integral approach that has been developed for calculating the sound field radiated from short ducts in uniform axial motion. The method was devised primarily to study sound generated by rotating sources in the duct, as is of current practical interest in connection with ducted-fan aircraft engines. Detailed background on the fan source application of the technique can be found in refs. 1 and 2. The author has not previously discussed the simpler monopole source case of interest in these proceedings. However, readers desiring a more detailed treatment than will be included here should have little difficulty in extracting it from those references after making the relatively minor modifications necessary to adapt the analyses to the monopole case.

It should be noted that other authors have also considered radiation from short ducts. In particular, readers may find the finite-element approach of Eversman [3] of interest as well as the alternate boundary integral method treatments of Martinez [4] and of Dunn, Tweed, and Farassat [5].

BOUNDARY INTEGRAL EQUATION

The problem to be considered is illustrated in fig. 1. An infinitesimally thin, rigid circular cylinder of radius a and length L moves at subsonic speed V in the negative x_3 direction relative to a frame of reference \bar{x} fixed in fluid at rest. The duct encloses a monopole source located at its center, which is taken as the origin of a co-moving system \bar{X} . The monopole emits sound harmonically at circular frequency ω in the moving frame \bar{X} . The objective is to determine the acoustic field radiated into infinite space through the ends of the moving duct.

The field is assumed to be described by the linearized equations of ideal isentropic compressible fluid motion. The problem is expressed in a scattering formulation in which the acoustic pressure is written as $p = p_i + p_s$, where the incident pressure p_i is the free-space field radiated by the monopole source in the absence of the duct. The scattered pressure $p_s(\bar{x}, t)$ is then sought as an outgoing solution to the homogeneous wave equation subject to appropriate boundary conditions on the inner and outer surfaces of the duct.

As shown elsewhere [1, 2], an integral representation of p_s is obtained by utilizing generalized

function theory to account for the fact that p_s is discontinuous across the wall of the duct. The representation is the formal solution of a generalized wave equation satisfied by p_s , which has a source term that arises because of the discontinuity in p_s across the wall. It expresses the scattered pressure at any point in terms of the pressure jump Δp_s across the wall in the form

$$4\pi p_s(\vec{x},t) = -\frac{1}{c} \frac{\partial}{\partial t} \int_{f=0} \left[\frac{\Delta p_s \cos\theta}{r|1-M_r|} \right]_{\tau^*} dS - \int_{f=0} \left[\frac{\Delta p_s \cos\theta}{r^2|1-M_r|} \right]_{\tau^*} dS \quad (1)$$

In eq. (1), $r = |\vec{r}|$ is the radiation distance between a source point on the moving surface $f = 0$ and the observer at \vec{x} , θ is the angle between \vec{r} and the normal to $f = 0$ at the source point, and M_r is the component of the surface Mach number vector in the direction of \vec{r} . The speed of sound in the undisturbed medium is denoted by c , and the subscript τ^* indicates that the integrands in eq. (1) are to be evaluated at the emission time τ^* which satisfies the retarded time equation $t - \tau - r/c = 0$.

The boundary integral equation from which the unknown jump Δp_s along the duct can be determined is obtained by applying condition that the normal component of acoustic particle velocity vanishes on both sides of the duct surface $f=0$. This is equivalent to $\partial p/\partial n = 0$ on $f=0$, or

$$\partial p_s/\partial n = -\partial p_i/\partial n \quad \text{on } f = 0 \quad (2)$$

where n is the direction normal to the surface $f = 0$. Use of eq. (1) in eq. (2) leads to the integral equation

$$-4\pi \frac{\partial p_i}{\partial n} \Big|_{\vec{x}=\vec{x}_0} = \lim_{\vec{x} \rightarrow \vec{x}_0} \frac{\partial}{\partial n} \left\{ -\frac{1}{c} \frac{\partial}{\partial t} \int_{f=0} \left[\frac{\Delta p_s \cos\theta}{r|1-M_r|} \right]_{\tau^*} dS - \int_{f=0} \left[\frac{\Delta p_s \cos\theta}{r^2|1-M_r|} \right]_{\tau^*} dS \right\} \quad (3)$$

in which \vec{x}_0 denotes any observer point on the moving surface $f = 0$. Equation (3) is the boundary integral equation which is solved numerically in the current analysis to find the unknown jump Δp_s across $f = 0$. Once Δp_s is known, then the scattered pressure at any point in space can be calculated using eq. (1) and added to the incident pressure to obtain the radiated field.

ANALYSIS OF BOUNDARY INTEGRAL EQUATION

The integrals in eq. (3) are highly singular when $r = 0$, i.e., when the source point on $f = 0$ coincides with the observer point \vec{x}_0 . To solve the integral equation numerically it is necessary that this singular behavior be analyzed in detail. This is most conveniently done by first expressing eq. (3) in terms of the translating coordinate frame \vec{X} in which, as indicated in fig. 1, cylindrical observer and source coordinates $\vec{X} = (R\cos\phi, R\sin\phi, X_3)$ and $\vec{Y} = (a\cos\phi', a\sin\phi', Y_3)$ are introduced.

The incident pressure emitted by the translating monopole can be obtained, for example, from ref. 6. In complex form it can be written as

$$p_i = \hat{p}(X_3, R) \exp[-i\omega(t + MX_3/c\beta^2)] \quad (4)$$

in which $M = V/c$, $\beta^2 = 1 - M^2$, and the amplitude \hat{p} is given by

$$4\pi\hat{p}(X_3, R) = -\rho c A \left[\frac{i\omega}{c\beta^2} \frac{(-MX_3 + \sqrt{X_3^2 + \beta^2 R^2})}{X_3^2 + \beta^2 R^2} + \frac{MX_3}{(X_3^2 + \beta^2 R^2)^{3/2}} \right] \exp\left(\frac{i\omega}{c\beta^2} \sqrt{X_3^2 + \beta^2 R^2}\right) \quad (5)$$

Here A is the volume strength of the monopole and ρ is the density of the undisturbed medium. It follows that the left side of eq. (3) is

$$-4\pi P(X_3) \exp[-i\omega(t + MX_3/c\beta^2)] \quad (6)$$

where $P(X_3) = \partial\hat{p}/\partial R|_{R=a}$.

Because of the symmetry of the duct, Δp_s will have the same complex form as the expression in (6) when expressed in the moving coordinate frame. Thus Δp_s is written as

$$\Delta p_s = \hat{\pi}(X_3) \exp[-i\omega(t + MX_3/c\beta^2)] \quad (7)$$

The remaining quantities in the integrands of eq. (3) are also easily expressible in the translating cylindrical coordinates, although the details are omitted here. They can be found in refs. 1 and 2. After substitution of eqs. (6 and 7) into eq. (3) and repetition of precisely the same algebraic steps as in refs. 1 and 2, the boundary integral equation (3) assumes the complex form

$$-4\pi P(X_3) = 2a\beta^2 \lim_{R \rightarrow a} \frac{\partial}{\partial R} \int_{-L/2}^{L/2} \hat{\pi}(Y_3) \int_0^\pi \Psi(Y_3, \psi) d\psi dY_3 \quad (8)$$

in which $\Psi(Y_3, \psi)$ is defined by

$$\Psi(Y_3, \psi) = (R \cos \psi - a) \left[\frac{i\alpha}{\xi^2 + B} - \frac{1}{(\xi^2 + B)^{3/2}} \right] \exp(i\alpha \sqrt{\xi^2 + B}) \quad (9)$$

In eq. (9), the abbreviations $\xi = Y_3 - X_3$ and $B = \beta^2(R^2 + a^2 - 2aR \cos \psi)$ have been introduced, with

$$\psi = \phi' - \phi \text{ and } \alpha = \omega/c\beta^2.$$

Equation (8) casts the boundary integral equation in a form from which its singular behavior may be extracted explicitly. The analysis necessary to do so is fairly lengthy, however, and it will be only summarized here in symbolic form; more detail will be found in a forthcoming publication [7]. First, it is seen in eq. (9) that the singularity occurs when $Y_3 = X_3 (\xi = 0)$, $\psi = 0$ and $R - a = h = 0$. Expansion of Ψ for small ξ, ψ, h results in

$$\Psi = h \left[\frac{(i\alpha)^2}{2\sqrt{\xi^2 + B_0}} - \frac{1}{(\xi^2 + B_0)^{3/2}} \right] + \frac{R\psi^2}{(\xi^2 + B_0)^{3/2}} + \dots \quad (10)$$

in which $B_0 = \beta^2(h^2 + a^2\psi^2)$ and the omitted terms are all $O(1)$ or smaller. Let the terms shown in eq. (10) be denoted as $\Psi_0(Y_3, \psi)$ and define $\hat{\Psi} = \Psi - \Psi_0$. This function is completely regular. Then the circumferential integral in eq. (8) is written as

$$\int_0^\pi \hat{\Psi} d\psi + \int_0^\pi \Psi_0 d\psi = I_{ns}(Y_3) + I(Y_3) \quad (11)$$

such that the first integral (I_{ns}) is nonsingular and the second (I) can be evaluated analytically because it contains only quadratic expressions in Ψ . After carrying out this integration it is found that $I(Y_3) = Q_{ns}(Y_3) + Q_s(Y_3)$, where Q_{ns} is also completely nonsingular at $Y_3 = X_3$, $h = 0$. The term Q_s contains the singularity and is discussed further below.

If the results just described are substituted back into eq. (8), that equation becomes

$$-4\pi P(X_3) = 2a\beta^2 \left\{ \int_{-L/2}^{L/2} \hat{\pi}(Y_3) \left[\frac{\partial(I_{ns} + Q_{ns})}{\partial R} \right]_{R=a} dY_3 + \lim_{R \rightarrow a} \frac{\partial I_s}{\partial R} \right\} \quad (12)$$

after the radial derivative of the nonsingular integrals on $R = a$ has been evaluated analytically, and in which

$$I_s = \pi h \int_{-L/2}^{L/2} \left[\frac{\hat{\pi}(Y_3)}{\sqrt{\xi^2 + \beta^2(h^2 + aR\pi^2)}} \right] \frac{dY_3}{\xi^2 + \beta^2 h^2} \quad (13)$$

The entire singular nature of eq. (18) is now isolated in the integral (13) and the final step in the analysis is to remove the singularity from this integral by appropriate expansion about $\xi = 0$ of the nonsingular bracketed factor in the integrand of (13). When this is carried out it is found that the last term on the right of eq. (12) is expressible as

$$\lim_{R \rightarrow a} \frac{\partial I_s}{\partial R} = -\frac{1}{a\beta} \int_{-L/2}^{L/2} \left[\frac{\pi \hat{\pi}(Y_3)}{\sqrt{\xi^2/a^2\beta^2 + \pi^2}} - \hat{\pi}(X_3) - \xi \hat{\pi}'(X_3) \right] \frac{dY_3}{\xi^2} + \frac{\pi \hat{\pi}(X_3)}{2a^2\beta^2} + \frac{1}{a\beta} \left[\frac{\hat{\pi}(X_3)}{\xi} - \hat{\pi}'(X_3) \log \frac{|\xi|}{a\beta} \right]_{\xi^-}^{\xi^+} \quad (14)$$

with $\xi_{\pm} = \pm L/2 - X_3$. The integral remaining in eq. (14) is also nonsingular at $\xi = 0$.

The result of all this is that the integral equation (12) now involves one double integral over Y_3 and ψ and two single integrals over Y_3 , all of which are completely nonsingular. The original singularity in eq. (18) has been integrated analytically and gives rise to the explicit terms on the right side of eq. (14).

NUMERICAL SOLUTION

The solution of the integral equation (12) is obtained numerically using the method of collocation after expressing the unknown $\hat{\pi}(X_3)$ in terms of suitable shape functions. It is known that a unique solution exists only if certain edge conditions are specified, and these are incorporated into $\hat{\pi}$ by enforcing a Kutta condition at the trailing edge of the duct and an inverse square-root singularity at the leading edge. Accordingly, the jump is written as

$$\hat{\pi}(X_3) = a_0 \frac{\sqrt{L/2 - X_3}}{\sqrt{L/2 + X_3}} + \sqrt{1 - 4X_3^2/L^2} \left\{ a_1 + a_2 \frac{X_3}{L} + \sum_{j=3}^J a_j \sin \left[\frac{(j-2)\pi}{L} \left(\frac{L}{2} + X_3 \right) \right] \right\} \quad (15)$$

in which the square-root factor in the numerator guarantees the correct functional form for the vanishing of $\hat{\pi}$ at the trailing edge to comply with the Kutta condition.

The expansion (15) is then substituted into eq.(12) and the integral equation is evaluated at $J + 1$ suitably chosen points along the length of the duct. This results in the algebraic system

$$-4\pi P(X_{3i}) = \sum_{j=0}^J a_j K_j(X_{3i}) \quad i=1, 2, \dots, J+1 \quad (16)$$

from which the $J + 1$ constants a_j are obtained. The coefficients $K_j(X_{3i})$ are calculated from the expressions in the previous section utilizing a four-point Gauss-Legendre quadrature scheme in which the duct surface is discretized into panels based on the wavelengths of oscillation in Ψ and X_3 of the various integrands for each j . A minimum of one panel per wavelength in the circumferential direction and four per wavelength in the axial direction are used, and the scheme has been extensively tested for

accuracy. The number of shape functions J is chosen sufficiently large to capture at least 2-3 times the number of oscillations in \hat{r} expected along the duct; this number can be inferred from the incident field given in eq. (6).

RESULTS

Numerical predictions from the theory outlined in this paper are illustrated in figs. 2 and 3. Figure 2 corresponds to the case of primary interest in the current proceedings: the forward Mach number is 0.5, the duct (D) diameter and length are both 1 m, and the dimensionless circular frequency is $\omega D/c = 16\pi$. On the figure is shown the sound pressure level in dB re $10^{-5}\mu\text{Pa}$ radiated from a monopole for which $\rho c|A| = 1\text{N}$. The polar plot gives the SPL of the incident field alone and that of the total field in the presence of the duct on a spherical radius 2.5m from the origin of \vec{X} . The angles 0° and 180° correspond to the exit and inlet ends of the duct, respectively. As would be expected at this relatively high frequency, the duct causes very little scattering in the axial directions. There is, however, a lateral shielding effect that cuts the SPL about 20dB around the 90° direction as is seen in all problems of this type [1, 2, 7].

Figure 3 illustrates the directivity found for the same case except with the frequency reduced to $\omega D/c = 4.409\pi$ (corresponding to 750 Hz). While the axial scattering is somewhat stronger in this case, the duct obviously affords minimal lateral shielding at the lower frequency.

ACKNOWLEDGMENTS

This research was supported by NASA Langley Research Center under Cooperative Agreement NCC1-14. Essential assistance with computer code development was provided by Mr. Melvin Kosanchick III, Ms. Barbara Lakota and Mr. Jason Buhler.

REFERENCES

1. Myers, M. K. and Lan, J. H., "Sound Radiation from Ducted Rotating Sources in Uniform Motion." AIAA Paper No. 93-4429, October 1993.
2. Myers, M. K., "Boundary Integral Formulations for Ducted Fan Radiation Calculations." Proceedings of First Joint CEAS/AIAA Aerocoustics Conference, Munich, Germany, Vol. I, June 1995, pp. 565-573.
3. Eversman, W., "Ducted Fan Acoustic Radiation Including the Effects of Nonuniform Mean Flow and Acoustic Treatment." AIAA Paper No. 93-4424, October 1993.

4. Martinez, R., "Liner Dissipation and Diffraction for an Acoustically Driven Propeller Duct." AIAA Paper No. 93-4426, October 1993.
5. Dunn, M., Tweed, J. and Farassat, F., "The Prediction of Ducted Fan Engine Noise via a Boundary Integral Equation Method." AIAA Paper No. 96-1770, May 1996.
6. Morse, P. M. and Ingard, K. U., Theoretical Acoustics, McGraw-Hill, New York, 1968, pp. 723-724.
7. Myers, M. K, and Kosanchick, M., "Computation of Sound Radiated from a Fan in a Short Lined Duct." To appear as AIAA Paper No. 97-1711, May 1997.

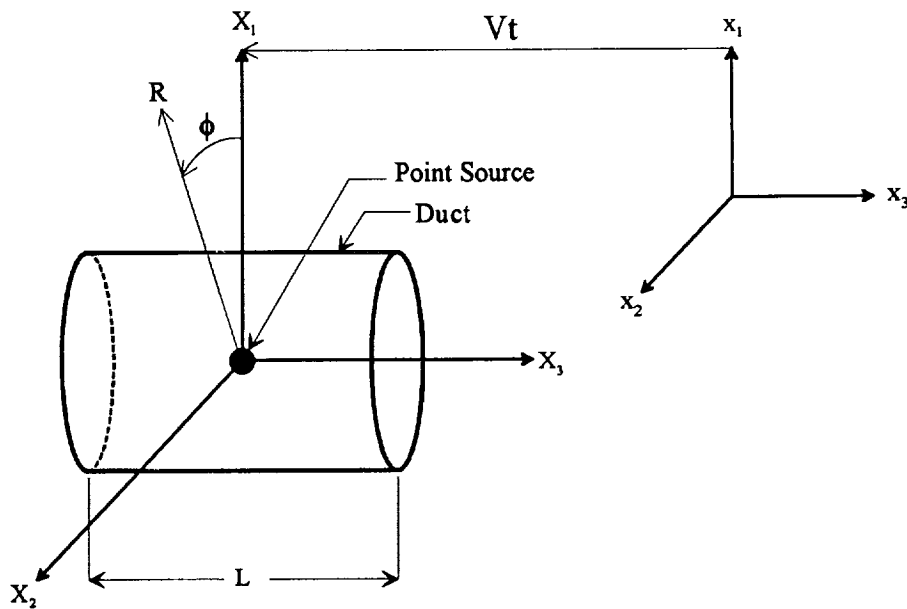


Figure 1. Duct geometry and coordinate systems.

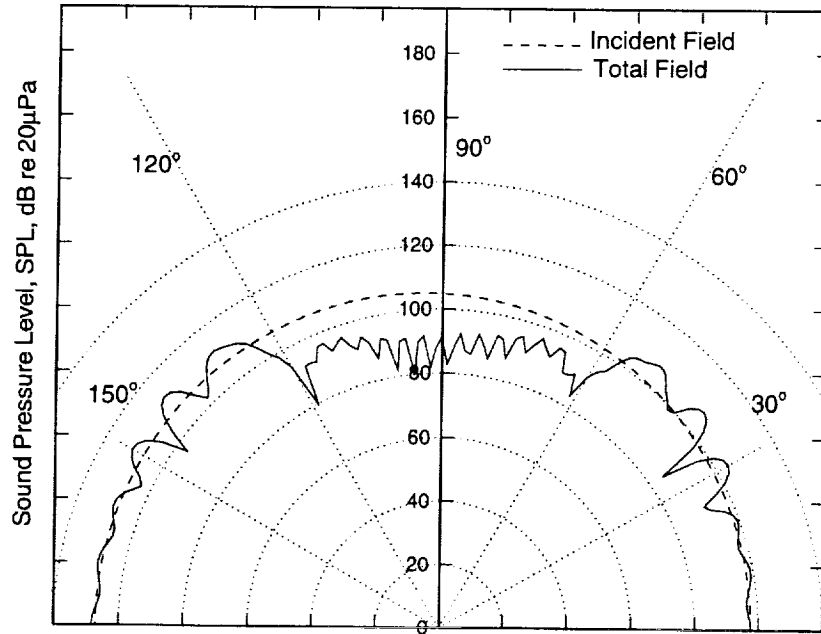


Figure 2. Sound pressure level at spherical radius 2.5m;
 $L=D=1\text{m}$, $M=0.5$, $\omega D/c=16\pi$.

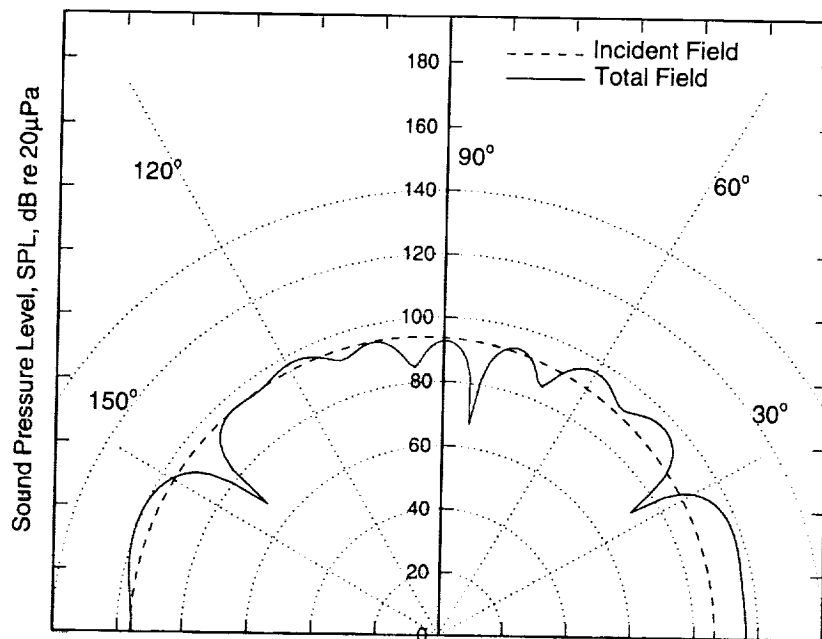


Figure 3. Sound pressure level at spherical radius 2.5m;
 $L=D=1\text{m}$, $M=0.5$, $\omega D/c=4.409\pi$.

54-71
043460
293944
p10

EXACT SOLUTIONS FOR SOUND RADIATION FROM A CIRCULAR DUCT*

Y. C. Cho
NASA Ames Research Center
Mail Stop 269-3, Moffett Field, CA 94035-1000

K. Uno Ingard
Department of Physics
Massachusetts Institute of Technology
Cambridge, MA 02139

SUMMARY

This paper presents a method of evaluation of Wiener-Hopf technique solutions for sound radiation from an unflanged circular duct with infinitely thin duct wall, including mean flows.

1. INTRODUCTION

Sound radiation from circular ducts is a classical acoustics problem. Exact solutions were previously reported: the Wiener-Hopf technique was used for radiation of propagating modes from a circular duct with negligibly thin duct wall, ¹⁻³ and the Hyperboloidal wave function was defined and employed for radiation from duct with various types of termination including a plane flange and horns.⁴ Exact solutions undoubtedly help one to gain physical insight into the problem, and can often be used in practical designs. In this electronic computation age, another significant role of exact solutions is defined as means of cross examination of results of numerical techniques. These techniques, embraced as computational aeroacoustics, are just starting to attract wide-spread attention as a potential tool in attacking important aeroacoustic problems for which quantitative solutions are not available.

Despite the elegance of the closed form solutions with the Wiener-Hopf technique, numerical presentations have been limited to mere demonstrations of its capability. As a matter of fact, no computer program is publicly available for its numerical evaluation. Numerical evaluation of the Wiener-Hopf solution is not straight forward; and it requires the exercise of extreme care, and often sophisticated mathematical tricks. This paper attempts to provide a comprehensive mathematical procedure for evaluation of Wiener-Hopf solutions.

In section 2, acoustic waves will be briefly reviewed for in-duct propagation and radiation. In section 3, the Wiener-Hopf technique is applied to obtain solutions, and Section 4 is devoted to the evaluation of integrals involved in the solutions.

2. REVIEW OF DUCT ACOUSTICS

Duct acoustics will be briefly reviewed here for its aspects relevant to the present problem. This review is also intended for clarification of terminology and nomenclature used in this paper.

The wave equation for the acoustic pressure, p, in flow is

$$\nabla^2 p - \frac{1}{c^2} \left(\frac{\partial}{\partial t} + \vec{V} \cdot \vec{\nabla} \right)^2 p = 0. \tag{1}$$

* Partly based on two consulting reports submitted to Pratt and Whitney Aircraft, May 25, 1976; and December 17, 1976.

Here c is speed of sound, and \bar{V} the mean flow velocity which is assumed to have only the axial component. The analysis is confined to a steady wave with the harmonic time dependence $e^{-i\omega t}$, and axial angle dependence $e^{im\phi}$, where m is an integer called the circumferential mode number. Eq. (1) is then written for circular cylindrical coordinates (r, ϕ, x) as

$$\frac{1}{r} \frac{\partial}{\partial r} \left(r \frac{\partial p}{\partial r} \right) + \frac{\partial^2 p}{\partial x^2} + \left(k + iM \frac{\partial}{\partial x} \right)^2 p - \frac{m^2}{r^2} p = 0 \quad (2)$$

where $k = \omega/c$, and $M = V/c$.

The sound radiation from an unflanged circular duct is schematically displayed in Fig. 1. With reference to this figure, the entire region is divided into two: region 1 for $r < a$, and region 2 for $r > a$, where a is the duct radius. The subscripts 1 and 2 will be used from now on to indicate respectively the region 1 and 2, unless specified otherwise. The mean flow velocities are assumed to be uniform in each region, and denoted by V_1 and V_2 . For $V_1 \neq V_2$, there will be the mean flow mismatch at $r = a$, for $x > 0$. The sound speed can differ for the two regions for reasons such as differences in mean density and temperature. The respective sound speeds, wave constants, air densities, and Mach numbers are denoted by c_1 and c_2 , k_1 and k_2 , ρ_1 and ρ_2 , and M_1 and M_2 , where $k_1 = \omega/c_1$, $k_2 = \omega/c_2$, $M_1 = V_1/c_1$, and $M_2 = V_2/c_2$.

In a hard-wall circular duct, the general solution to Eq. (2) is obtained as

$$p(r, x) = \sum_{n=1}^{\infty} J_m \left(\frac{\mu_{mn} r}{a} \right) \{ A_{mn} e^{ik_{mn}^+ x} + B_{mn} e^{ik_{mn}^- x} \}. \quad (3)$$

Here J_m is the Bessel function of order m , μ_{mn} the n -th zero of $J'_m(x)$, and A_{mn} and B_{mn} constant coefficients. The wave constants k_{mn}^+ and k_{mn}^- correspond to the mode propagations respectively in the positive (to the right) and the negative (to the left) directions, and are given by

$$k_{mn}^{\pm} = \frac{-k_1 M_1 \pm \sqrt{k_1^2 - (1 - M_1^2) \left(\frac{\mu_{mn}}{a} \right)^2}}{1 - M_1^2}. \quad (4)$$

The integer n here is called the radial mode number, and the pair (m, n) is used to represent a single duct mode.

Consider the incident wave of a single mode, say (m, ℓ) ,

$$p_{inc} = J_m \left(\frac{\mu_{m\ell} r}{a} \right) e^{im\phi} e^{ik_{m\ell}^+ x}. \quad (5)$$

This wave is incident from $x = -\infty$ and propagating towards duct termination as in Fig. 1. Upon arriving at the duct termination, it will be partly reflected back into the duct, and partly radiated out of the duct. In general, the reflected wave contains many radial modes including propagating and attenuating modes, and is represented by

$$P_{refl} = e^{im\phi} \sum_{n=1}^{\infty} R_{\ell,n}^m J_m \left(\frac{\mu_{mn} r}{a} \right) e^{ik_{mn} x}. \quad (6)$$

Here $R_{\ell,n}^m$ is the conversion coefficient for the (m, ℓ) mode incident and the (m, n) mode reflected. The reflection problem is completely solved by determining this coefficient for all values of n . The Wiener-Hopf technique yields radiation solutions in terms of the far field, which is represented by

$$P_{rad} = e^{im\phi} f_{m\ell}(\theta) \cdot \frac{1}{k_2 R} e^{i\Lambda(k_2, M_2, R)}. \quad (7)$$

Here R is the radial distance from the center of the duct termination, and θ the polar angle measured from the x -axis (duct axis) as shown in Fig. 1. (R, θ, ϕ) are spherical coordinates. The complex factor $f_{m\ell}(\theta)$ is called the amplitude gain function, which provides the far field directivity of radiation. The phase $\Lambda(k_2, M_2, R)$ of the far field depends on M_2 as well as on k_2 and R . The radiation problem is completely solved by determining $f_{m\ell}(\theta)$ and $\Lambda(k_2, M_2, R)$.

This analysis with a single mode incident can be extended to accommodate incident waves composed of many modes in a straight-forward manner.

3. WIENER-HOPF FORMULATION

The Wiener-Hopf technique involves extensive mathematical manipulation in the Fourier transform space. The Fourier transform of $p(r, x)$ is given by

$$\Phi(r, \alpha) = \frac{1}{\sqrt{2\pi}} \int_{-\infty}^{\infty} p(r, x) e^{i\alpha x} dx, \quad (8)$$

and $p(r, x)$ is restored by the inverse transform

$$p(r, x) = \frac{1}{\sqrt{2\pi}} \int_{-\infty}^{\infty} \Phi(r, \alpha) e^{-i\alpha x} d\alpha. \quad (9)$$

In the process of the Wiener-Hopf formulation, various parameters and functions are defined and derived as follows:

$$\gamma_i(\alpha) = \sqrt{1 - M_i} \sqrt{(\alpha - q_j^-) \cdot (\alpha - q_j^+)}, \quad q_j^\pm = \frac{\pm k_j}{1 \mp M_j} \quad \text{for } i=1, 2, \quad (10)$$

$$W_1(\alpha) = \frac{I_m(\gamma_1 a)}{\gamma_1 a I'_m(\gamma_1 a)}, \quad I_m \text{ being } I - \text{Bessel function of order } m, \quad (11)$$

$$W_2(\alpha) = \frac{K_m(\gamma_2 a)}{\gamma_2 a K'_m(\gamma_2 a)}, \quad K_m \text{ being } K - \text{Bessel function of order } m, \quad (12)$$

$$T_M = \frac{1}{\sqrt{1-M_1^2}} \left[\frac{\rho_1 c_1^2 M_1^2}{\sqrt{1-M_1^2}} + \frac{\rho_2 c_2^2 M_2^2}{\sqrt{1-M_2^2}} \right], \quad (13)$$

$$K(\alpha) = \frac{a}{T_M \gamma_1} \left[\rho_1 c_1^2 (k_1 + \alpha M_1)^2 W_1(\alpha) - \rho_2 c_2^2 (k_2 + \alpha M_2)^2 W_2(\alpha) \right]. \quad (14)$$

In deriving $K(\alpha)$, we have used the condition of the continuity of the acoustic pressure and acoustic displacement at the mean flow mismatch at $r = a$, for $x > 0$. $K(\alpha)$ is factorized into two, one is analytic in the upper half plane (+) and the other in the lower half plane (-) as $K(\alpha) = K_+(\alpha) \cdot K_-(\alpha)$. These factors will be included in the final solutions with arguments representing physical quantities. For the present problem, the factorization is obtained not in closed forms but in integral representations as follows:

$$\text{Log}_e K_+(y_+) = \frac{1}{2\pi i} \int_{C_+} \frac{\text{Log}_e K(\alpha)}{\alpha - y_+} d\alpha, \quad (15)$$

$$\text{Log}_e K_-(y_-) = \frac{-1}{2\pi i} \int_{C_-} \frac{\text{Log}_e K(\alpha)}{\alpha - y_-} d\alpha. \quad (16)$$

Here the integral path is from $-\infty$ to $+\infty$ near the real axis, and the argument y_+ (y_-) is located above (below) the respective integral path, as illustrated in Fig. 2.

Forgoing details of the formulation,⁵ the final results are presented here. The conversion coefficient for the reflection is obtained as

$$R_{\ell,n}^m = \frac{i \rho_1 c_1^2}{a T_M \sqrt{1-M_1^2}} \cdot \frac{J_m(\mu_{m\ell})}{J_m(\mu_{mn})} \cdot \left(1 - \frac{m^2}{\mu_{mn}^2}\right)^{-1} \left[\left(k_{m\ell}^+ + \frac{k_1}{1-M_1} \right) \cdot \left(-k_{m\ell}^- + \frac{k_1}{1+M_1} \right) \right]^{-1/2} \\ \cdot \frac{(k_1 - M_1 k_{mn}^-)^2}{(k_{m\ell}^+ - k_{mn}^-)(k_1 M_1 + (1-M_1^2)k_{mn}^-)} \cdot [K_-(-k_{m\ell}^+) K_+(-k_{mn}^-)]^{-1}. \quad (17)$$

The symmetry between the radial mode numbers ℓ and n is salient, implying that the result satisfies the reciprocity principle,⁶ which can be used to infer the conversion coefficients of a nonpropagating mode.

For the radiation, the phase is obtained as

$$\Lambda(k_2, M_2, R) = \frac{k_2}{\sqrt{1-M_2^2}} \left(R - \frac{M_2 x}{\sqrt{1-M_2^2}} \right), \quad (18)$$

and the amplitude gain function is

$$f_{m\ell}(\theta) = \frac{(-i)^{m+1} J_m(\mu_{m\ell}) \rho_2 c_2^2 k_2^2 (1-M_2 \cos\theta')^2}{\pi T_M (1-M_2^2)^{5/2}} \cdot \left[\sin\theta \cdot H_m^{(1)} \left(\frac{k_2 a \sin\theta'}{\sqrt{1-M_2^2}} \right) \right]^{-1} \\ \cdot \left\{ K_+(-\eta(\theta)) \cdot [k_{m\ell}^+ - \eta(\theta)] \cdot \sqrt{\left(\frac{k_1}{1+M_1} - \eta(\theta) \right)} \cdot K_-(-k_{m\ell}^+) \cdot \sqrt{\left(k_{m\ell}^+ + \frac{k_1}{1-M_1} \right)} \right\}^{-1}, \quad (19)$$

where

$$\eta(\theta) = \frac{k_2(\cos\theta' - M_2)}{1-M_2^2}. \quad (20)$$

Here the modified coordinates R' and θ' are defined as

$$R' = \sqrt{r^2 + \frac{x^2}{1-M_2^2}}, \quad \tan\theta' = \sqrt{1-M_2^2} \tan\theta. \quad (21)$$

$H_m^{(1)}(x)$ is the Hankel function of the first kind, and $H_m^{(1)'}(x)$ is its derivative with respect to x .

Comments are made on the expression of $f_{m\ell}(\theta)$ for two limiting cases. First, as can be shown readily, when θ becomes zero, the quantity in the first square bracket will be infinite except for the case of $m = 0$. In other words, the radiated field is zero for $\theta = 0$ except for the radiation of axi-symmetric modes. Second, as will be seen later, when its argument approaches $-k_{mn}^+$, K_+ in the second square bracket varies as $[k_{m\ell}^+ - \eta(\theta)]^{-1}$. It follows that the radiated field will be zero for the angle satisfying

$$\eta(\theta) = k_{mn}^+ \quad \text{or} \quad \cos\theta' = M_2 + (1-M_2^2) \frac{k_{mn}^+}{k_2}, \quad \text{for } n \neq \ell. \quad (22)$$

However, for the angle corresponding to the incident propagation constant $k_{m\ell}^+$, the radiated field is non-zero, because the term adjacent to K_+ becomes zero in this limit. In fact, the radiated field reaches the maximum in this limit. These findings are all familiar for cases of no mean flows. We will also see later that if its argument approaches $-k_1/(1+M_1)$, K_+ varies in such a way as to compensate the term involving the square root in the same square bracket to maintain the amplitude gain finite.

A remark should be made on the constant T_M . As M_1 and M_2 both become zero, this constant becomes zero, but the expressions for the conversion coefficients and the radiation directivity remains correct, and finite when evaluated as a limit.

4. NUMERICAL EVALUATION

The integrals in Eqs. (15) and (16) cannot be carried out analytically, and thus, we will employ a semi-numerical method. To this end, all the variables are made dimensionless by multiplying or dividing with the duct radius a . For notation simplification, the sub- or superscript m will often be dropped.

$K(\alpha)$ satisfies all the conditions required for its factorization by the integration. Nevertheless, the integrand possesses singular points in the vicinity of the integral paths. These singular points arise as branch points, simple poles, and zeroes of $K(\alpha)$. It should be emphasized that there are no other singularities near the integral paths. The branch points are located at $\alpha = q_1^\pm$. We adopt a rule for determining phase around these branch points, as illustrated in Fig. 3. For example, consider $(\alpha - q_1^-)$. Its phase is 180 degrees for its real part less than zero, and changes clockwise to zero as the real part becomes positive. On the other hand, the phase of $(\alpha - q_1^+)$ is -180 degrees for the real part less than zero, and changes counterclockwise to zero as the real part becomes positive. This rule should be strictly observed for the integrations.

The simple poles of $K(\alpha)$ occur at zeroes of $I'_m(\gamma_1 a)$, which is included through $W_1(\alpha)$ as in Eqs. (11) and (14). These zeroes correspond to the wave constants of duct modes, and one can show that the simple poles of $K(\alpha)$ are located at $\alpha = v_n^\pm \equiv -k_{mn}^\mp$. Note that v_n^+ ($\equiv -k_{mn}^-$) is above the respective integral path, and v_n^- ($\equiv -k_{mn}^+$) below the respective integral path as shown in Fig. 2. $K(\alpha)$ can also possess zeroes near the integral path if $q_1^+ > q_2^+$. The zeroes are located between $\alpha = q_2^+$ and $\alpha = q_1^+$, and above the integral path. The number of zeroes equals that of simple poles between $\alpha = q_2^+$ and $\alpha = q_1^+$, or can be less by one. The zeroes are denoted by z_n , for $n = 1, 2, \dots, n_o$, n_o being the number of zeroes. These zeroes are ordered such that z_1 is the smallest, and z_{n_o} the largest.

The imaginary parts of all the singular points are related to $\mathcal{J}_m(k)$. As the latter tends to zero, all the singular points approach the real axis, and the integral paths are then indented as shown in Fig. 2b.

Consider the integral

$$I = \int_{C_+} \frac{\text{Log}_e K(\alpha)}{\alpha - y} d\alpha. \quad (23)$$

This integral is divided, for convenience, as

$$I = R_- + R_+ + B_- + B_+ + S_- + S_+ + Z + Y + N. \quad (24)$$

R 's are the contribution from the integration over larger arguments as

$$R_- = \int_{-\infty}^{-\chi} \frac{\text{Log}_e K(\alpha)}{\alpha - y} d\alpha, \quad (25)$$

$$R_+ = \int_{\chi}^{\infty} \frac{\text{Log}_e K(\alpha)}{\alpha - y} d\alpha, \quad (26)$$

where $\chi > |q_j^\pm|$.

B 's are the contribution from the integration over small intervals containing the branch points:

$$B_- = \int_{b_1^-}^{b_2^-} \frac{\text{Log}_e K(\alpha)}{\alpha - y} d\alpha, \quad \text{with } b_1^- < q_1^- < b_2^-, \quad (27)$$

$$B_+ = \int_{b_1^+}^{b_2^+} \frac{\text{Log}_e K(\alpha)}{\alpha - y} d\alpha, \text{ with } b_1^+ < q_1^+ < b_2^+. \quad (28)$$

S's are the contribution from the integration over small intervals containing the simple poles:

$$S_{\pm} = \sum_{n=1}^{n_c} S_n^{\pm}, \quad n_c \text{ being the largest propagating radial mode number,} \quad (29)$$

$$S_n^- = \int_{s_{n1}^-}^{s_{n2}^-} \frac{\text{Log}_e K(\alpha)}{\alpha - y} d\alpha, \quad \text{with } s_{n1}^- < v_n^- < s_{n2}^-, \quad (30)$$

$$S_n^+ = \int_{s_{n1}^+}^{s_{n2}^+} \frac{\text{Log}_e K(\alpha)}{\alpha - y} d\alpha, \quad \text{with } s_{n1}^+ < v_n^+ < s_{n2}^+. \quad (31)$$

Z's are the contribution from the integration over small intervals containing the zeroes of $K(\alpha)$:

$$Z = \sum_{n=1}^{n_o} Z_n, \quad (32)$$

$$Z_n = \int_{z_{n1}}^{z_{n2}} \frac{\text{Log}_e K(\alpha)}{\alpha - y} d\alpha, \quad \text{with } z_{n1} < z_n < z_{n2}. \quad (33)$$

Y is the contribution from the interval containing the pole at $\alpha = y$:

$$Y_{\pm} = \int_{y_1}^{y_2} \frac{\text{Log}_e K(\alpha)}{\alpha - y} d\alpha, \quad \text{with } y_1 < y < y_2, \quad (34)$$

where the plus (negative) sign indicates that the pole is above (below) the integral path. This integral needs to be evaluated only if $K(\alpha)$ is free of singularity and zeroes within the integral limit. Otherwise, it should belong to one of B, S, and Z because there are no other singular points than those involved in B, S, or Z.

Finally N is the integral over the whole remaining intervals. There is no singularity at all in these intervals, and thus the integration can be carried out numerically.

$K(\alpha)$ approaches unity as $|\alpha|$ becomes large, that is, $\lim_{\alpha \rightarrow \pm\infty} K(\alpha) = 1.$, and thus, $K(\alpha)$ can be expanded for a large α , as

$$K(\alpha) \cong 1 + \frac{A_1}{\alpha} + \frac{A_2}{\alpha^2}, \quad (35)$$

where the expansion coefficients A_1 and A_2 can be readily obtained. With this substitution to Eqs. (25) and (26), one obtains

$$R_{\pm} = A_1 \left[\frac{\pm d}{y \chi_{\pm}} \mp \frac{1}{y} \left(1 + \frac{d}{y} \right) \text{Log}_e \left(\frac{\chi_{\pm} - y}{\chi_{\pm}} \right) \right], \quad (36)$$

where

$$d = \frac{A_2}{A_1} - \frac{A_1}{2}. \quad (37)$$

Error limits and the expansion coefficients are used to determine the integral limits χ_{\pm} .

The integral near the branch points can be replaced by

$$B_{\pm} = \int \frac{\text{Log}_e Q_{\pm}(\alpha)}{\alpha - y} d\alpha - \frac{1}{2} \int \frac{\text{Log}_e(\alpha - q_1^{\pm})}{\alpha - y} d\alpha, \quad (38)$$

where

$$Q_{\pm}(\alpha) = K(\alpha) \cdot \sqrt{\alpha - q_1^{\pm}}. \quad (39)$$

$Q_{\pm}(\alpha)$ are free of singularity and zeroes within the respective chosen integral limits.

The simple poles of $K(\alpha)$ are separated as follows:

$$S_n^{\pm} = \int \frac{\text{Log}_e L_{\pm}(\alpha)}{\alpha - y} d\alpha - \int \frac{\text{Log}_e(\alpha - v_n^{\pm})}{\alpha - y} d\alpha, \quad (40)$$

where

$$L_{\pm}(\alpha) = K(\alpha) \cdot (\alpha - v_n^{\pm}). \quad (41)$$

$L_{\pm}(\alpha)$ are free of singularity and zeroes within the respective integral limits.

The zeroes of $K(\alpha)$ are similarly separated as

$$Z_n = \int \frac{\text{Log}_e U(\alpha)}{\alpha - y} d\alpha + \int \frac{\text{Log}_e(\alpha - z_n)}{\alpha - y} d\alpha, \quad (42)$$

where

$$U(\alpha) = \frac{K(\alpha)}{\alpha - z_n}. \quad (43)$$

$U(\alpha)$ is free of singularity and zeroes within the respective integral limit.

Now consider the integral

$$H(y) = \int_a^b \frac{\text{Log}_e G(\alpha)}{\alpha - y} d\alpha, \quad (44)$$

Here $G(\alpha)$ is free of singularity and zeroes within the integral limit, and thus represents $Q_{\pm}(\alpha)$ in Eq. (38), $L_{\pm}(\alpha)$ in Eq. (40), $U(\alpha)$ in Eq. (42), or $K(\alpha)$ in Eq. (34) if $K(\alpha)$ is free of singularity in that region. This integral can be written as

$$H(y) = \int_a^b \frac{\text{Log}_e [G(\alpha)/G(y)]}{\alpha - y} d\alpha + \text{Log}_e G(y) \int_a^b \frac{d\alpha}{\alpha - y}. \quad (45)$$

As α approaches y , one readily obtains

$$\frac{\text{Log}_e [G(\alpha)/G(y)]}{\alpha - y} \cong \frac{G'(y)}{G(y)}. \quad (46)$$

Thus, the first integral in Eq. (45) does not involve any singularity, and can be easily evaluated whether y is within the integral limit, or not. The integral contained in the second term yields

$$\begin{aligned} \int_a^b \frac{d\alpha}{\alpha - y_{\pm}} &= \text{Log}_e \left(\frac{b - y_{\pm}}{a - y_{\pm}} \right), \quad \text{for } y_{\pm} < a, \text{ or } y_{\pm} > b, \\ &= \text{Log}_e \left(\frac{b - y_{\pm}}{y_{\pm} - a} \right) \mp i\pi, \quad \text{for } a < y_{\pm} < b, \end{aligned} \quad (47)$$

where (\pm) signs are used to indicate that the simple pole is above (+) or below (-) the integral path, which is indented around the pole like \cup for (+), and \cap for (-).

Consider the integrals

$$\Omega_-^- = \int_a^b \frac{\text{Log}_e(\alpha - \xi_-)}{\alpha - y_-} d\alpha, \quad (48)$$

$$\Omega_+^- = \int_a^b \frac{\text{Log}_e(\alpha - \xi_-)}{\alpha - y_+} d\alpha, \quad (49)$$

$$\Omega_-^+ = \int_a^b \frac{\text{Log}_e(\alpha - \xi_+)}{\alpha - y_-} d\alpha, \quad (50)$$

$$\Omega_+^+ = \int_a^b \frac{\text{Log}_e(\alpha - \xi_+)}{\alpha - y_+} d\alpha. \quad (51)$$

Here, the singular point at $\alpha = \xi$ is within the integral limit, that is, $a < \xi_{\pm} < b$. The subscript on ξ and y is used to indicate that the pole is above (+) or below (-) the integral path. The indented integral paths are shown in Fig. 4. The second integral in each of Eqs. (38), (40), and (42) is identified with one of the integrals in Eqs. (48) - (51). These integrals are evaluated as follows:

For $y < a$,

$$\begin{aligned} \Omega_{\pm}^{\pm} &= \pm i\pi \text{Log}_e \left(\frac{\xi_{\pm} - y_{\pm}}{a - y_{\pm}} \right) - \frac{\pi^2}{3} + \frac{1}{2} \cdot \left[(\text{Log}_e(b - y_{\pm}))^2 + (\text{Log}_e(\xi_{\pm} - y_{\pm}))^2 \right] \\ &\quad - \text{Log}_e(\xi_{\pm} - y_{\pm}) \cdot \text{Log}_e(a - y_{\pm}) + \sum_{j=1}^{\infty} \frac{1}{j^2} \left[\left(\frac{a - y_{\pm}}{\xi_{\pm} - y_{\pm}} \right)^j + \left(\frac{\xi_{\pm} - y_{\pm}}{b - y_{\pm}} \right)^j \right]; \end{aligned} \quad (52)$$

for $y > b$,

$$\begin{aligned}\Omega_{\pm}^{\pm} = & \pm i\pi \operatorname{Log}_e \left| \frac{\xi_{\pm} - y_{\pm}}{a - y_{\pm}} \right| + \frac{\pi^2}{3} - \frac{1}{2} \cdot \left[(\operatorname{Log}_e(y_{\pm} - \xi_{\pm}))^2 + (\operatorname{Log}_e(y_{\pm} - a))^2 \right] \\ & + \operatorname{Log}_e(y_{\pm} - \xi_{\pm}) \cdot \operatorname{Log}_e(y_{\pm} - b) - \sum_{j=1}^{\infty} \frac{1}{j^2} \left[\left(\frac{y_{\pm} - b}{y_{\pm} - \xi_{\pm}} \right)^j + \left(\frac{y_{\pm} - \xi_{\pm}}{y_{\pm} - a} \right)^j \right];\end{aligned}\quad (53)$$

for $a < y < b$,

$$\begin{aligned}\Omega_{-}^{\pm} = & \pm i\pi \operatorname{Log}_e(y_{-} - a) + i\pi [-\operatorname{Log}_e(y_{-} - \xi_{\pm}) \mp \operatorname{Log}_e(y_{-} - \xi_{\pm})] \\ & - \frac{1}{2} \left[(\operatorname{Log}_e(b - \xi_{\pm}))^2 + (\operatorname{Log}_e(y_{-} - a))^2 \right] + \operatorname{Log}_e(b - \xi_{\pm}) \cdot \operatorname{Log}_e(b - y_{-}) \\ & + \frac{\pi^2}{2} - \sum_{j=1}^{\infty} \frac{1}{j^2} \left[\left(\frac{y_{-} - \xi_{\pm}}{b - \xi_{\pm}} \right)^j + \left(\frac{y_{-} - \xi_{\pm}}{y_{-} - a} \right)^j \right],\end{aligned}\quad (54)$$

$$\begin{aligned}\Omega_{+}^{\pm} = & \pm i\pi \operatorname{Log}_e(y_{+} - a) + i\pi [\operatorname{Log}_e(y_{+} - \xi_{\pm}) \mp \operatorname{Log}_e(y_{+} - \xi_{\pm})] \\ & - \frac{1}{2} \left[(\operatorname{Log}_e(b - \xi_{\pm}))^2 + (\operatorname{Log}_e(y_{+} - a))^2 \right] + \operatorname{Log}_e(b - \xi_{\pm}) \cdot \operatorname{Log}_e(b - y_{+}) \\ & + \frac{\pi^2}{2} - \sum_{j=1}^{\infty} \frac{1}{j^2} \left[\left(\frac{y_{+} - \xi_{\pm}}{b - \xi_{\pm}} \right)^j + \left(\frac{y_{+} - \xi_{\pm}}{y_{+} - a} \right)^j \right].\end{aligned}\quad (55)$$

All the integrals involving singular points are analytically evaluated according to Eqs. (47), (52) - (55). For large arguments extending to the infinite, the integral is evaluated according to Eq. (36). The rest involves finite integrals with well-behaved integrands, and thus can be numerically evaluated without any difficulty.

A remark will be made on the results in Eqs. (54) and (55), particularly on the second term on the right. This term vanishes if y and ξ are on the same side (above or below) with respect to the integral path. However, if y and ξ are separated by the integral path, the second term equals $\pm 2\pi i \operatorname{Log}_e(y_{\pm} - \xi_{\mp})$, and diverges as y approaches ξ . Of the K -factors contained in the results in Eqs. (17) and (19), only $K_{+}(-\eta(\theta))$ can have y and ξ separated by the integral path. Its argument is above the integral path according to Eq. (15). As θ varies, the argument can approach a singular point located below the integral path. For this case, the second term above is given by $2\pi i \operatorname{Log}_e(-\eta(\theta) - \xi_{-})$, where ξ_{-} is v_n^{-} or q_1^{-} . Inspecting Eqs. (15), (23), (24), (38), and (55), one obtains, for $-\eta(\theta)$ close to q_1^{-} ,

$$K_{+}(-\eta(\theta)) \propto \frac{1}{\sqrt{-\eta(\theta) - q_1^{-}}}.\quad (56)$$

Similarly, from Eqs. (15), (23), (24), (40), and (55), one obtains, for $-\eta(\theta)$ close to v_n^{-} ,

$$K_{+}(-\eta(\theta)) \propto (-\eta(\theta) - v_n^{-})^{-1}.\quad (57)$$

It follows then that, as $\eta(\theta)$ approaches k_{mn}^+ , $f_{m\ell}(\theta)$ given in Eq. (19) tends to be zero for $n \neq \ell$, and will reach the maximum for $n = \ell$. Also one can see that $f_{m\ell}(\theta)$ will remain finite as $\eta(\theta)$ approaches to $k_1/(1 + M_1)$ as discussed earlier.

CONCLUDING REMARKS

An analysis for evaluation of the Wiener-Hopf solution was presented for sound radiation from an unflanged circular duct with mean flows. This analysis was initially developed for radiation of spinning modes in conjunction with aircraft inlet noise control studies. We have a well working computer code available for such radiation. However, while generating numerical results for the Benchmark problems, we learned that the code needed to be refined for radiation of the axisymmetric modes.

REFERENCES

1. Levine, H.; and Schwinger, J.: On the Radiation of Sound from an Unflanged Circular Duct. Phys. Rev., vol. 73, 1948, pp. 383-406.
2. Weinstein, L. A.: The Theory of Diffraction and the Factorization Method. The Golem Press, 1969.
3. Savakar, S. D.: Radiation of Cylindrical Duct Acoustic Modes with Flow Mismatch. J. of Sound and Vibration, vol. 42, 1975, pp. 363-386.
4. Cho, Y. C.: Rigorous Solutions for Sound Radiation from Circular Ducts with Hyperbolic Horns or Infinite Plane Baffle. J. of Sound and Vibration, vol. 69, 1980, pp. 405-425.
5. Noble, B.: Methods based on The Wiener-Hopf Techniques. The Pergamon Press, 1958.
6. Cho, Y. C.: Reciprocity Principle in Duct Acoustics. J. Acoustical Soc. of Am., vol. 67, 1980, pp. 1421-1426.

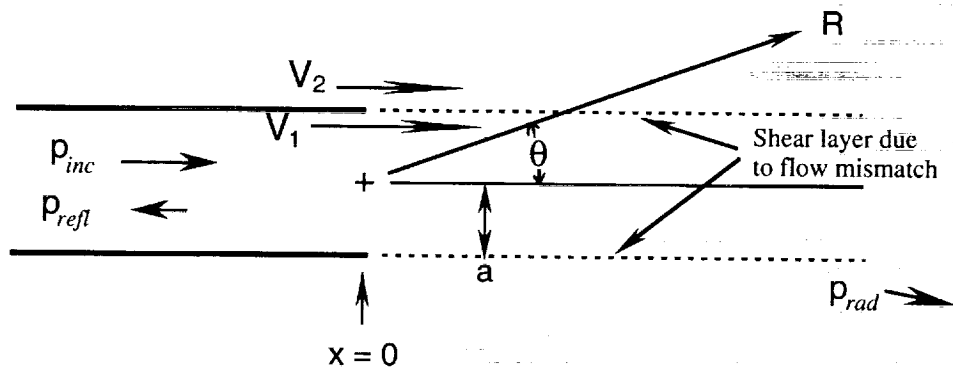


Figure 1. Sound radiation from unflanged circular duct with flow

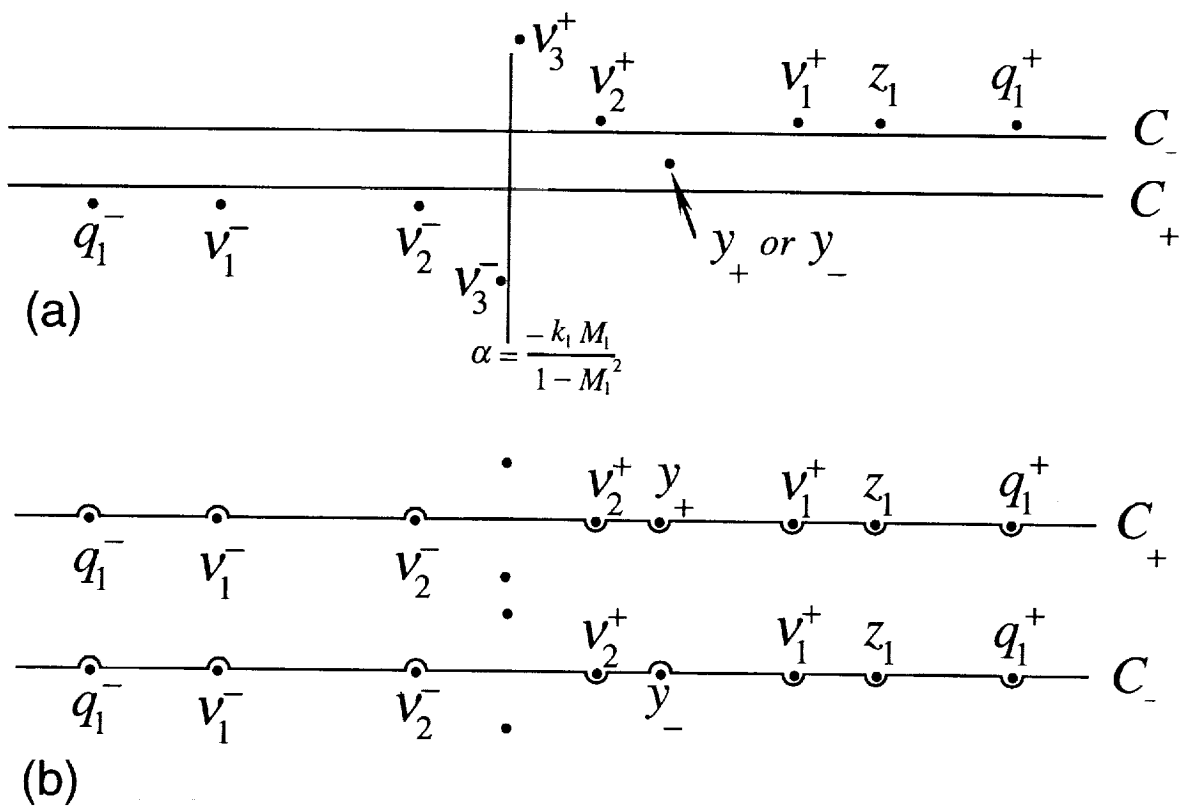


Figure 2. (a) Integral path C_+ and C_- , and singular points: (v_3^\pm correspond to an attenuating mode); (b) indentation of the integral paths as $\text{Im}(k) \rightarrow 0$.

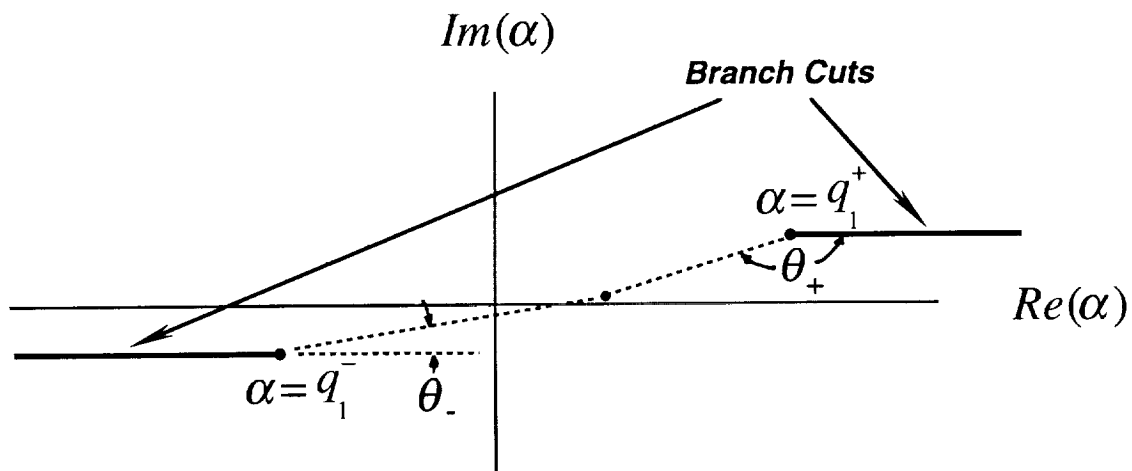


Figure 3. Branch points, branch cuts, and phase convention;
 $0^\circ < \theta_- < 180^\circ$, and $-180^\circ < \theta_+ < 0^\circ$.

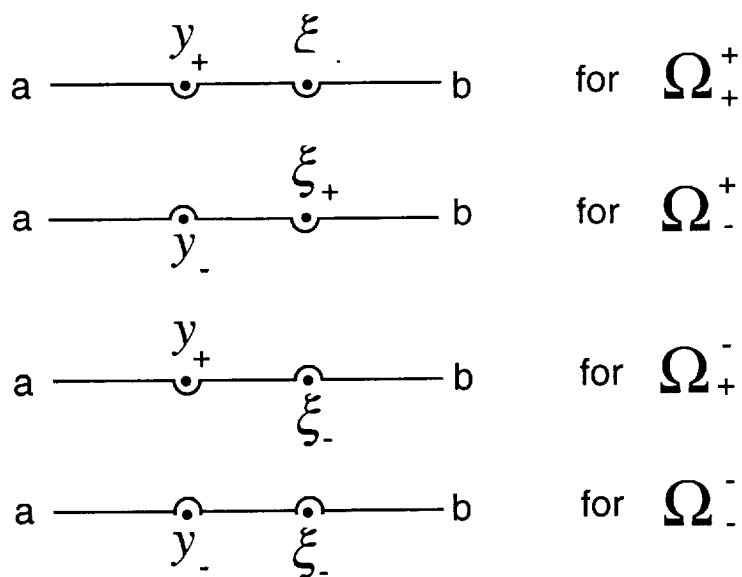


Figure 4. Integral path indentation for integrations involving two singular points at $\alpha = y$ and ξ .

55-71
043462
2 93953
P4

EXACT SOLUTION TO CATEGORY 3 PROBLEMS - TURBOMACHINERY NOISE

Kenneth C. Hall
Duke University
Department of Mechanical Engineering and Materials Science
Durham, NC 27708-0300

In the far-field upstream or downstream of the cascade, the perturbation flow will be composed of pressure waves and vorticity waves. The pressure waves travel away from the cascade, with solutions taking the form

$$p(x, y, t) = \text{Re} \left[\sum_{n=-\infty}^{\infty} p_n e^{jk_n x} e^{j\beta_n y} e^{-j\omega t} \right] \quad (1)$$

where n is the mode index, k_n and β_n are the axial and circumferential wave numbers of the n th outgoing pressure wave, and the coefficient p_n is a complex constant expressing the magnitude and phase of each pressure wave. The circumferential wave number β_n is given by

$$\beta_n = (\sigma + 2n\pi) / G \quad (2)$$

where G is the blade-to-blade gap, which for this problem is equal to unity. The axial wave number k_n is given by

$$k_n = \frac{U(\omega - \beta_n V) \pm a \sqrt{\beta_n^2 (U^2 + V^2 - a^2) + 2\beta_n \omega V + \omega^2}}{U^2 - a^2} \quad (3)$$

where a is the speed of sound, and the root used corresponds to that which produces a wave which propagates away from the cascade in the case superresonant (cut-on) conditions as determined by the group velocity, and which decays away from the cascade in the case of subresonant (cut-off) conditions. Recall from the problem definition that $U = 1$, $V = 0$, and $a = 2.0$. The frequency ω is $5\pi/2$ and $13\pi/2$ for Cases 1 and 2, respectively.

Equation (3) can be rewritten as

$$p(x, y, t) = \frac{1}{2} \sum_{n=-\infty}^{\infty} \left[p_n e^{jk_n x} e^{j\beta_n y} e^{-j\omega t} + \bar{p}_n e^{-j\bar{k}_n x} e^{-j\beta_n y} e^{+j\omega t} \right] \quad (4)$$

where \bar{p}_n is the complex conjugate of p_n . Note that as $|n|$ gets large, the waves tend to be strongly cut off. Thus, the sum in Eq. (4) may be truncated, keeping only cut-on modes and weakly cut-off modes.

To find the mean square value of the pressure, \bar{p}^2 , one takes the square of Eq. (4), integrates over one temporal period T and divides by T , so that

$$\bar{p}^2 = \frac{1}{T} \int_t^{t+T} p \, dt = \frac{1}{4} \sum_{m=-\infty}^{\infty} \sum_{n=-\infty}^{\infty} \left[p_m \bar{p}_n e^{j(k_m - \bar{k}_n)x} e^{j(\beta_m - \beta_n)y} + \bar{p}_m p_n e^{-j(\bar{k}_m - k_n)x} e^{-j(\beta_m - \beta_n)y} \right] \quad (5)$$

Finally, Eq. (5) can be expressed more compactly as

$$\bar{p}^2 = \frac{1}{2} \text{Re} \left[\sum_{m=-\infty}^{\infty} \sum_{n=-\infty}^{\infty} p_m \bar{p}_n e^{j(k_m - \bar{k}_n)x} e^{j(\beta_m - \beta_n)y} \right] \quad (6)$$

Using a modified version of Whitehead's [1] LINSUB computer code, tables containing the "exact" solution to the Category 3 problems have been prepared. Since the LINSUB analysis is based on a semi-analytical theory due to Smith [2] requiring both truncated infinite sums and numerical quadrature, the analysis is in fact approximate. However, the analysis converges very quickly as the number of quadrature points on the airfoils is increased, and for our purposes may be considered exact. Tables 1 and 2 describe the far-field pressure field for Cases 1 and 2, respectively.

Whitehead's LINSUB code also computes the jump in pressure across the airfoil. This information is tabulated in Table 3 for both Cases 1 and 2.

Table 1: Outgoing pressure wave information for Case 1: $\sigma = \omega = 5\pi/2$.

n	β_n	k_n (upstream)	k_n (downstream)	p_n (upstream)	p_n (downstream)
-3	$-7\pi/2$	$-2.6180 - 11.5667j$	$-2.6180 + 11.5667j$	$+0.12147 - 0.03873j$	$-5101.2 + 682.1j$
-2	$-3\pi/2$	$-2.6180 - 1.4810j$	$-2.6180 + 1.4810j$	$+0.53682 - 0.09116j$	$-2.2552 + 0.4629j$
-1	$+\pi/2$	$-7.5298 + 0.0000j$	$+2.2938 + 0.0000j$	$+0.07381 - 0.16809j$	$-0.14795 - 0.15700j$
0	$+5\pi/2$	$-2.6180 - 7.4048j$	$-2.6180 + 7.4048j$	$-0.17443 + 0.04846j$	$+150.37 - 21.37j$
+1	$+9\pi/2$	$-2.6180 - 15.4617j$	$-2.6180 + 15.4617j$	$-0.09719 + 0.03356j$	$+163539 - 21470j$

Table 2: Outgoing pressure wave information for Case 2: $\sigma = \omega = 13\pi/2$.

n	β_n	k_n (upstream)	k_n (downstream)	p_n (upstream)	p_n (downstream)
-6	$-11\pi/2$	$-6.8068 - 14.5858j$	$-6.8068 + 14.5858j$	$+0.05313 - 0.03263j$	$+18415 - 3385j$
-5	$-7\pi/2$	$-11.7186 + 0.0000j$	$-1.8950 + 0.0000j$	$+0.06037 + 0.16068j$	$-0.08366 + 0.04531j$
-4	$-3\pi/2$	$-19.2856 + 0.0000j$	$+5.6720 + 0.0000j$	$+0.01165 + 0.02662j$	$+0.03342 + 0.08047j$
-3	$+\pi/2$	$-20.2990 + 0.0000j$	$+6.6854 + 0.0000j$	$+0.00163 - 0.00941j$	$-0.01837 - 0.02195j$
-2	$+5\pi/2$	$-16.9597 + 0.0000j$	$+3.3462 + 0.0000j$	$-0.01447 - 0.02927j$	$+0.01783 - 0.11869j$
-1	$+9\pi/2$	$-6.8068 - 9.0083j$	$-6.8068 + 9.0083j$	$-0.07713 + 0.04236j$	$-120.370 + 35.98j$

REFERENCES

1. Whitehead, D. S., "Classical Two-Dimensional Methods," in: AGARD Manual on Aeroelasticity in Axial Flow Turbomachines, Volume 1, Unsteady Turbomachinery Aerodynamics (AGARD-AG-298), M. F. Platzer and F. O. Carta, ed., Neuilly sur Seine, France, ch. 3, 1987.
2. Smith, S. N., "Discrete Frequency Sound Generation in Axial Flow Turbomachines," Reports and Memoranda No. 3709, Aeronautical Research Council, London, 1972.

Table 3: Pressure jump across airfoil surface for Cases 1 and 2.

x	Δp (Case 1)	Δp (Case 2)
0.002739	$2.537370 + 5.408126j$	$2.947770 + 2.775677j$
0.010926	$1.325919 + 2.919922j$	$1.396297 + 1.417490j$
0.024472	$0.956211 + 2.171698j$	$0.837480 + 0.969826j$
0.043227	$0.804730 + 1.841727j$	$0.517989 + 0.740339j$
0.066987	$0.745766 + 1.657842j$	$0.287019 + 0.588954j$
0.095492	$0.733135 + 1.523461j$	$0.091642 + 0.467593j$
0.128428	$0.740240 + 1.392526j$	$-0.085729 + 0.361312j$
0.165435	$0.744923 + 1.241506j$	$-0.247446 + 0.265959j$
0.206107	$0.725826 + 1.060468j$	$-0.379861 + 0.183151j$
0.250000	$0.662893 + 0.851991j$	$-0.466097 + 0.106731j$
0.296632	$0.540426 + 0.629459j$	$-0.496350 + 0.026243j$
0.345492	$0.351306 + 0.415466j$	$-0.481046 - 0.066053j$
0.396044	$0.100116 + 0.236820j$	$-0.442407 - 0.155988j$
0.447736	$-0.195112 + 0.119009j$	$-0.391473 - 0.212194j$
0.500000	$-0.505591 + 0.079066j$	$-0.316766 - 0.212000j$
0.552264	$-0.796183 + 0.121177j$	$-0.201247 - 0.167375j$
0.603956	$-1.033825 + 0.234332j$	$-0.056210 - 0.117913j$
0.654509	$-1.193248 + 0.395377j$	$0.075022 - 0.091408j$
0.703368	$-1.263362 + 0.573535j$	$0.148032 - 0.080760j$
0.750000	$-1.246460 + 0.738373j$	$0.152358 - 0.055539j$
0.793893	$-1.157928 + 0.864475j$	$0.115422 + 0.003606j$
0.834565	$-1.019010 + 0.936690j$	$0.075100 + 0.087693j$
0.871572	$-0.854140 + 0.949121j$	$0.054080 + 0.169169j$
0.904509	$-0.683514 + 0.905481j$	$0.052595 + 0.222982j$
0.933013	$-0.523146 + 0.813910j$	$0.059792 + 0.239389j$
0.956773	$-0.381359 + 0.686081j$	$0.063751 + 0.221657j$
0.975528	$-0.261630 + 0.532399j$	$0.058764 + 0.180279j$
0.989074	$-0.161759 + 0.362603j$	$0.044899 + 0.125175j$
0.997261	$-0.076972 + 0.183421j$	$0.024118 + 0.063928j$

26-71
043463
293954
p12

Application of the Discontinuous Galerkin method to Acoustic Scatter Problems

H. L. Atkins
NASA LaRC
Hampton, VA

Introduction

The discontinuous Galerkin method is a highly compact formulation that obtains the high accuracy required by computational aeroacoustics (CAA) on unstructured grids. The use of unstructured grids on these demanding problems has many advantages. Although the computer run times of CAA simulations may take tens of hours, the time required to obtain a structured grid around a complex configuration is often measured in weeks or months. The mesh smoothness constraints imposed by conventional high-order finite-difference methods further complicates the mesh generation process. Furthermore, the impact of poor mesh quality on the accuracy obtained by these high-order methods is not well known.

Unstructured meshes, on the other hand, can be generated in a nearly automated manner in a relatively short time. Unstructured grids often have fewer cells because the cell distribution is more easily controlled. In the case of structured grids, regions of unnecessarily small cells often exist. These small cells can be a waste of computer memory and time; furthermore, in the case of an explicit time-accurate method the small cells may result in an unnecessarily small time step. The use of an unstructured grid allows such cases to be avoided, and the savings usually makes up for the increased cost per cell that is common with most unstructured methods. The use of an unstructured approach also facilitates grid-adaption and refinement techniques, which can further reduce the cost of a simulation.

Although most finite-element methods can be applied to unstructured grids, the property of the discontinuous Galerkin method that distinguishes it from its finite-element counterparts is its compactness. In a typical finite-element method with an order that is greater than 1, the mass matrix is global but sparse; however, the mass matrix becomes more dense as the order of the method is increased because the basis functions, or shape functions, must be globally C^0 functions. The discontinuous Galerkin formulation relaxes this constraint; as a result, the mass matrix becomes local to its generating element. This property makes the approach ideally suited to advection- and propagation-dominated flows for which an explicit time-marching strategy is appropriate.

This article describes the application of the quadrature-free form¹ of the discontinuous Galerkin method to two problems from Category I of the Second Computational Aeroacoustics Workshop on Benchmark Problems. The quadrature-free form imposes several additional constraints and permits an implementation that is more computationally efficient than is otherwise possible. The first part of this article describes the method and boundary conditions relevant to this work; however, details of the implementation can be found in reference 1. The next section describes two test problems, both of which involve the scattering of an acoustic wave off a cylinder. The last section describes the numerical test performed to evaluate mesh-resolution requirements and boundary-condition effectiveness.

Discontinuous Galerkin Method

The discontinuous Galerkin method can be applied to systems of first-order equations in the divergence form

$$\frac{\partial U}{\partial t} + \nabla \cdot \vec{F}(U) = S(U) \quad (1)$$

where $U = \{u_0, u_1, \dots\}$, $\vec{F} = \{\vec{f}_0, \vec{f}_1, \dots\}$, and $S = \{s_0, s_1, \dots\}$, defined on some domain $\bar{\Omega}$ with a boundary $\partial\bar{\Omega}$. The domain is partitioned into a set of nonoverlapping elements Ω_i that cover the domain $\bar{\Omega} = \bigcup_i \Omega_i$. Within each element, the following set of equations is solved:

$$\int_{\Omega_i} b_k \frac{\partial V_i}{\partial t} J_i d\Omega - \int_{\Omega_i} \nabla b_k \cdot \mathbf{J}_i^{-1} \vec{F}(V_i) J_i d\Omega + \int_{\partial\Omega_i} b_k \mathbf{J}_i^{-1} \vec{F}^R \cdot \mathbf{J}_i \vec{d}s = 0 \quad (2)$$

for $k = 0, 1, \dots, N$ where $\{b_k, k = 0, 1, \dots, N\}$ is a set of basis functions,

$$U \approx V_i = \sum_{j=0}^N v_{i,j} b_j, \quad \mathbf{J}_i = \frac{\partial(x, y, z)}{\partial(\xi, \eta, \zeta)}, \quad \text{and} \quad J_i = |\mathbf{J}_i|$$

Equation set (2) is obtained by projecting equation (1) onto each member of the basis set and then integrating by parts to obtain the weak conservation form. In the present work, the basis set is composed of the polynomials that are defined local to the element and are of degree $\leq n$. In two dimensions, for example, the basis set is $\{1, \xi, \eta, \xi^2, \xi\eta, \eta^2, \dots, \xi^n, \xi^{n-1}\eta, \dots, \xi\eta^{n-1}, \eta^n\}$, where (ξ, η) are the local coordinates. The solution U is approximated as an expansion in terms of the basis functions; thus, both V and $\vec{F}(V)$ are discontinuous at the boundary between adjacent elements (hence, the name *discontinuous* Galerkin). The discontinuity in V between adjacent elements is treated with an approximate Riemann flux, which is denoted by \vec{F}^R ; \mathbf{J}_i is the Jacobian of the transformation from the global coordinates (x, y, z) to the local element coordinates (ξ, η, ζ) of element i .

In the usual implementation of the discontinuous Galerkin method^{2, 3, 4} the integrals are evaluated with quadrature formulas. This approach is problematic for even moderately high-order implementations in multidimensions and has limited most efforts to $n = 2$ or 3 . The difficulties are due in part to two considerations; first the integral formulas used in the evaluation of (2) must be exact for polynomials of degree $2n$ (even higher when \vec{F} is nonlinear). Second, multidimensional Gaussian quadrature formulas do not always exist. Near-optimal quadrature formulas that have desirable properties such as symmetry are uncommon, and usually the number of quadrature points exceeds $N + 1$ (the number of terms in the expansion) by a wide margin. The common practice of forming tensor products of one-dimensional Gaussian quadrature formulas is straightforward but also results in considerably more than $N + 1$ quadrature points.

In the quadrature-free form, the integral evaluations are reduced to a summation over the coefficients of the solution expansion, which is an operation of order $N + 1$. To implement this approach, the flux \vec{F} must also be written as an expansion in terms of the basis functions:

$$\vec{F}(U) \approx \vec{G}(V_i) = \sum_{j=0}^N \vec{g}_j(V_i) b_j$$

(a similar expansion is made for the approximate Riemann flux \vec{F}^R). This step is trivially accomplished for linear equations, and several approaches for nonlinear equations are discussed in

reference 1. In addition, the allowed element shapes are limited to those for which the coordinate transformation from a fixed computational element (such as a unit square or an equilateral triangle in two dimensions) to the physical element is linear; thus, \mathbf{J}_i is a constant within the element. With these assumptions, the integrals can be evaluated exactly and efficiently, and equation (2) can be written in matrix form as

$$J_i \mathbf{M} \frac{\partial \mathbf{V}_i}{\partial t} - \vec{\mathbf{A}} \cdot J_i \mathbf{J}_i^{-1} \vec{\mathbf{G}}_i + \sum_{k=1}^{n_e} \mathbf{B}_k \left(J_i \mathbf{J}_i^{-1} \vec{\mathbf{G}}_{i,k}^R \right) \cdot \vec{s}_{i,k} = 0 \quad (3)$$

where n_e is the number of sides around element i , $\vec{s}_{i,k}$ is the outward unit normal on side k , $\mathbf{V}_i = [v_{i,0}, v_{i,1}, \dots]$, $\vec{\mathbf{G}}_i = [\vec{g}_{i,0}, \vec{g}_{i,1}, \dots]$, and $\vec{\mathbf{G}}_{i,k}^R = [\vec{g}_{i,k,0}^R, \vec{g}_{i,k,1}^R, \dots]$. The mass matrix \mathbf{M} and the vector matrix $\vec{\mathbf{A}}$ are given by

$$\mathbf{M} = [m_{k,l}], \quad m_{k,l} = \int_{\Omega} b_{k-1} b_{l-1} d\Omega, \quad \text{and} \quad \vec{\mathbf{A}} = [\vec{a}_{k,l}], \quad \vec{a}_{k,l} = \int_{\Omega} b_{l-1} \nabla b_{k-1} d\Omega$$

for $1 \leq k, l \leq N + 1$. The matrices are the same for all elements of a given type (e.g. the same for all triangles, the same for all squares, etc.) and can be precomputed and stored at a considerable savings.

Derivation of the boundary integral terms is complicated by the fact that the solutions on either side of the element boundary are represented in terms of different coordinate systems. This problem is circumvented by expressing the solution on both sides of the element boundary in terms of a common edge-based coordinate system (a simple coordinate transformation). After some additional algebraic simplification, an edge matrix \mathbf{B}_k is obtained that is the same for similar sides of similar element types. A detailed derivation of the matrices \mathbf{M} , $\vec{\mathbf{A}}$, and \mathbf{B}_k is given in reference 1. Because equation (3) is of the same form for all elements, the element index i is dropped for clarity.

The first two terms of equation (3) depend only on the solution within the element, and communication between adjacent elements occurs only through the Riemann flux $\vec{\mathbf{G}}^R$. The Riemann flux provides this communication in a biased manner by evaluating the flux with data from the "upwind" side of the element boundary. In the case of a system of equations, the upwind side may be different for each characteristic wave component; thus, the flux $\vec{\mathbf{F}}^R$ will usually be a function of the solution on both sides of the element boundary. Cockburn and Shu⁵ have demonstrated that this upwind bias is essential to the stability of the discontinuous Galerkin method.

In this work, the discontinuous Galerkin method is applied to the two-dimensional linear Euler equations given by

$$U \equiv [\rho - P, p, u, v]^T \quad \text{and} \quad \vec{\mathbf{F}} \equiv \vec{M}U + [0, \vec{V}, \hat{i}P, \hat{j}P]^T \quad (4)$$

where $\vec{M} \equiv [M_x, M_y]$, $\vec{V} \equiv [u, v]$, and \hat{i} and \hat{j} are the Cartesian unit vectors $[1, 0]$ and $[0, 1]$, respectively. The dependent variables ρ , p , u , and v are the normalized perturbation values of density, pressure, and the x - and y -components of the velocity, respectively; M_x and M_y are the normalized x - and y -components of the mean flow velocity. The density, pressure, and velocities are normalized with respect to the mean flow density ρ_o , the sound speed of the mean flow c , and $\rho_o c$, respectively. The length scale l_r is problem dependent, and the time scale is given by l_r/c . The source term S is also problem dependent and is described in a later section.

Equation (3) is advanced in time with a three-stage Runge-Kutta method developed by Shu and Osher⁶. Analysis of the stability of this approach, along with many numerical validation tests, can be found in reference 1.

Boundary Conditions

An important feature of the discontinuous Galerkin method is that the Riemann flux is the *only* mechanism by which an element communicates with its surroundings, regardless of whether the element boundary is on the interior of the domain or coincides with the domain boundary. A notable consequence is that the usual interior algorithm is valid at elements that are adjacent to the boundary. In contrast, the interior point operator of most high-order finite-difference and finite-volume methods cannot be applied at points near the boundary without some modifications. These modifications usually result in reduced accuracy, and careful attention is required to prevent the introduction of numerical instabilities⁷. The discontinuous Galerkin method eliminates these problems and, thereby, eliminates a major source of error that is common to most high-order finite-difference and finite-volume methods.

A detailed description of the implementation of boundary conditions for the discontinuous Galerkin method is in preparation⁸. The implementation of the two types of boundary conditions required for the benchmark problems (i.e. hard wall and nonreflecting freestream) are described here. These boundary conditions can be implemented either by supplying the exterior side of the Riemann flux with a complete solution or by reformulating the flux such that it requires only the interior solution and the known boundary data. The later approach is usually more accurate and is used in the present work.

The flux on the element boundary is given by

$$F(U)_b \equiv \vec{F}(U) \cdot \vec{s} = M_n U + [0, V_n, P_x, P_y]^T$$

where $M_n = \vec{M} \cdot \vec{s}$, $V_n = \vec{V} \cdot \vec{s}$, $P_x = P \hat{i} \cdot \vec{s}$, $P_y = P \hat{j} \cdot \vec{s}$, and $\vec{s} = \mathbf{J}^{-1T} J d\vec{s}$ is the boundary-normal vector for an arbitrary edge. At a hard-wall boundary, the flow through the boundary V_n is zero. Also, hard-wall boundary conditions can only be applied at boundaries where $M_n = 0$. After these constraints have been imposed, the flux at a hard wall becomes

$$F(U)_{\text{wall}} = [0, 0, P_x, P_y]_{\text{interior}}^T$$

The pressure contribution to the flux can be attributed to both inbound and outbound acoustic waves. The evaluation of both components by using the interior pressure value corresponds to specifying that the wave entering the domain is the reflection of the wave leaving the domain which is the desired behavior at a hard wall.

Many CAA problems are defined on an infinite or semi-infinite domain; however, limited computational resources require that the numerical simulation be performed on the smallest domain possible. Thus, certain boundaries of the computational domain must behave as if no boundary existed at all. The development of effective nonreflective boundary conditions for treating these boundaries is a critical and ongoing area of study within CAA. The approach used here is a simple variation of standard characteristic boundary conditions that works well in many cases.

In the standard characteristic boundary condition, the flux through the boundary is written in terms of the set of *characteristic variables* Q as $F(U)_b = [A]Q(U)$, where

$$Q(U) = [\rho - P, \alpha v - \beta u, \alpha u + \beta v + P, \alpha u + \beta v - P]^T,$$

$\alpha = \hat{i} \cdot \vec{s}/|\vec{s}|$, and $\beta = \hat{j} \cdot \vec{s}/|\vec{s}|$. Each component of Q corresponds to the strength of a fundamental wave that either enters or leaves the domain along a path that is normal to the boundary. An approximation to the nonreflecting condition is imposed by setting the strength of the wave components that enter the domain to zero. All other components are evaluated from the interior solution values. When characteristic boundary conditions are applied to finite-difference methods, the procedure is usually applied in a differential form such as in the procedure described by Thompson⁹; variations of the differential form are widely used. This differential approach degrades the accuracy of the method because of the need to use one-sided operators near the boundary. The problem is especially severe for high-order methods. Because the discontinuous Galerkin method needs only flux information, the characteristic boundary condition is quite accurate if, in fact, the only waves present are propagating normal to the boundary.

In most cases, however, the waves that leave the domain are not traveling normal to the boundary everywhere. In fact, the waves that reach any particular point on the boundary may be coming from many different directions simultaneously. In these cases, a reflection is produced that depends on the amplitude of the incident wave and the angle between the direction of wave propagation and the boundary normal.

In many flows, the sound emanates from a general area that can be determined a priori. In these instances, a first-order correction to the characteristic boundary conditions just described is to express $F(U)_b$ in terms of the strength of simple waves that are traveling in a prescribed direction instead of in the direction of the boundary normal. These wave strengths are given by the characteristic variables associated with the flux in an arbitrary, but prescribed, direction \vec{w} :

$$Q(U)_{\vec{w}} = [\rho - P, \hat{\alpha}v - \hat{\beta}u, \hat{\alpha}u + \hat{\beta}v + P, \hat{\alpha}u + \hat{\beta}v - P]^T$$

where $\hat{\alpha} = \hat{i} \cdot \vec{w}$ and $\hat{\beta} = \hat{j} \cdot \vec{w}$ (assuming $|\vec{w}| = 1$). As in the standard case, the nonreflecting condition is obtained by setting the inbound components to zero and evaluating the outbound components from the interior. Evaluating the $F(U)_b$ in terms of these characteristic variables results in a significant improvement in many cases. (Note that equation (2) requires the evaluation of the flux through the boundary $\vec{F} \cdot \vec{s}$, even though the characteristic variables are arrived at by considering the flux in an alternate direction $\vec{F} \cdot \vec{w}$.)

Category I Problems

The problems of Category I model the sound field generated by a propeller and scattered off the fuselage of an aircraft. This test case is intended as a good problem for testing curved-wall boundary conditions, but it also poses a challenge to nonreflecting far-field boundary conditions. Although the geometry is by no means complex, this test case still serves to illustrate the advantages of an unstructured method.

The model geometry, shown in figure 1, is defined relative to a polar coordinate system in which the dimensions are normalized by a length scale l_r that equals the fuselage diameter. Fuselage is modeled by a cylinder with a radius of 1/2, the sound source is at $(r, \theta) = (4, 0)$, and measurement points A, B, and C are at $r = 5$, and $\theta = 90, 135$, and 180 respectively.

The flow is governed by the linear Euler equations

$$\frac{\partial u}{\partial t} + \frac{\partial p}{\partial x} = 0$$

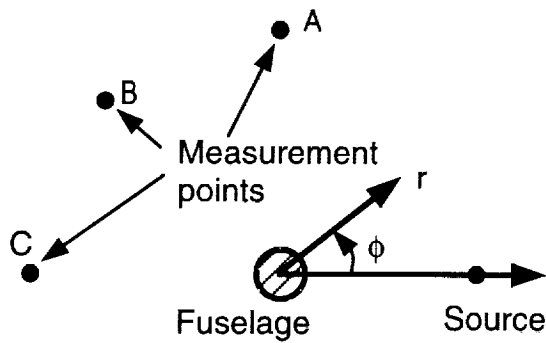


Figure 1. Geometry for problem 2.

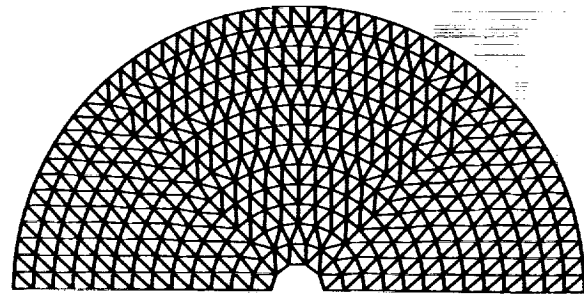


Figure 2. Typical grid with five triangles on cylinder ($N_c = 5$).

$$\begin{aligned} \frac{\partial v}{\partial t} + \frac{\partial p}{\partial y} &= 0 \\ \frac{\partial p}{\partial t} + \frac{\partial u}{\partial x} + \frac{\partial v}{\partial y} &= s \end{aligned}$$

where s is a periodic forcing function that is used to generate sound in problem 1. In problem 2, $s = 0$, and the sound results from a disturbance in the initial solution. This later case results in a discrete wave which facilitates the testing of the boundary conditions. For this reason, the discussion of problem 2 will precede that of problem 1.

The computer program solves the linear Euler equations in the more general form given in equations (1) and (4), with $M_x = M_y = 0$ and $S = [-s, s, 0, 0]^T$. Thus, the continuity equation is solved even though it has no role in this particular problem. All calculations presented use polynomials of degree $n = 4$ (nominally fifth order).

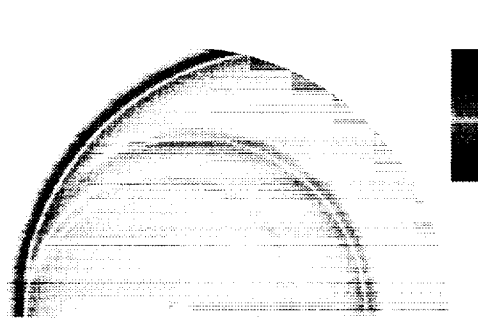
Problem 2

In problem 2 of Category I, a single acoustic pulse is generated by an initial pressure disturbance of the form

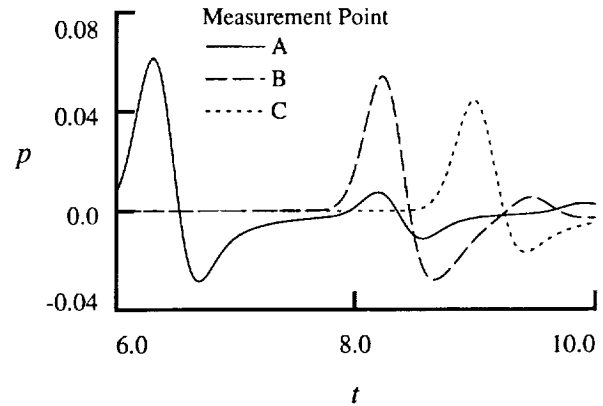
$$p = \exp \left[-\ln(2) \left(\frac{(x-4)^2 + y^2}{(0.2)^2} \right) \right]$$

A typical grid, shown in figure 2, is constructed from triangles of nearly uniform size. The average size of the triangles is set by specifying the number of triangles around the cylinder N_c (e.g., in fig. 2, $N_c = 5$). Note that if a structured polar grid had been used the mesh spacing in the θ direction would have been 10 times smaller on the cylinder than at the measurement points. Thus, the time step of an explicit method would be approximately seven times smaller than necessary to resolve the wave (assuming that the grid spacing and the time step are chosen such that the wave is resolved at the measurement points). The use of an unstructured grid allows the resolution to be uniform over the region of interest. As will be shown later, the use of an unstructured grid permits easy local refinement in special regions without adversely affecting the grid elsewhere.

A baseline solution, which is shown in figure 3, is obtained on a grid with $N_c = 15$ and the outer boundary at $r = 10$. With the outer boundary at this distance, any nonphysical reflections off the outer boundary will not reach the measurement points (A, B, or C, in fig. 1) within the time



(a). Pressure contour at $t = 10$.



(b). Pressure at measurement points A, B, and C.

Figure 3. Baseline solution with $N_c = 15$ and outer boundary at $r = 10$.

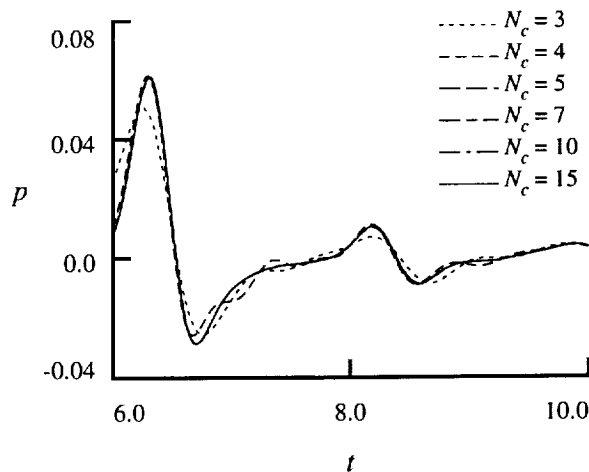


Figure 4. Grid refinement with outer boundary at $r = 5.5$.

span of interest ($t \leq 10$); however, no visible reflection is evident in the solution. The initial pulse generates two reflections that originate from the sides of the cylinder.

Figure 4 shows results at point A from a series of calculations with $N_c = 3, 4, 5, 7, 10,$ and 15 with the outer boundary at $r = 5.5$. The $N_c = 3$ case shows considerable error, but the solution rapidly improves as the grid is refined. The solution of the case in which $N_c = 5$ is indistinguishable from the solution on the finest grid.

In addition to the error that is inherent in the discontinuous Galerkin method, at least three other factors contribute to the error in this particular case: the accuracy of the initial solution, the accuracy of the solid geometry boundary, and the accuracy of the nonreflecting boundary condition. The initial solution within each element is a polynomial defined by a Taylor's series of the prescribed function about the center of the element. Thus as the element gets larger, the initial solution becomes less accurate near the outer edges of the element. Figure 5 shows the initial solution in the neighborhood of the disturbance for $N_c = 3, 4,$ and 5 . The initial solution of the

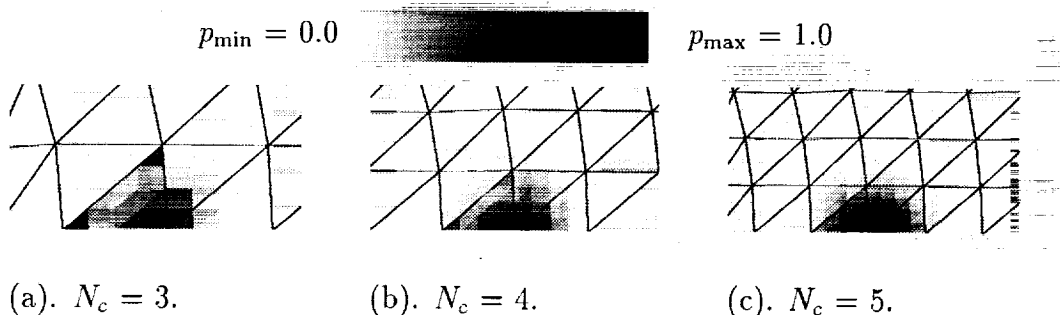


Figure 5. Grid refinement with outer boundary at $r = 5.5$.

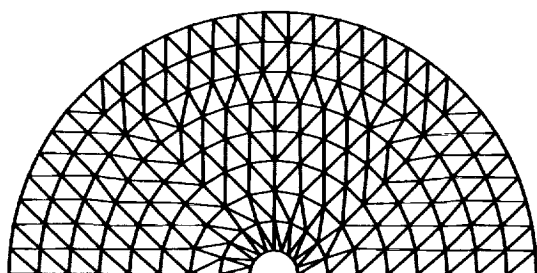


Figure 6. Grid with local refinement near cylinder.

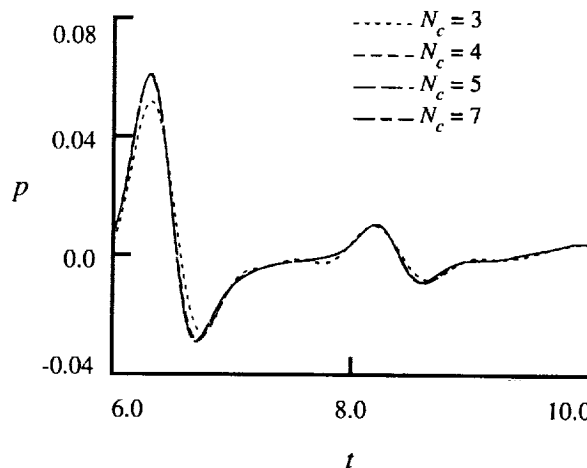


Figure 7. Grid refinement with improved resolution of cylinder (outer boundary at $r = 5.5$).

coarsest grid is clearly not as smooth, which probably accounts for the high-frequency oscillations observed in figure 4.

In regard to the accuracy of the solid geometry boundaries, the current implementation is restricted to triangles or squares with straight sides; consequently, the geometry is represented by linear segments. (Note that this restriction applies only to the current implementation and not to the discontinuous Galerkin method or the quadrature-free form in general.) Thus, with $N_c = 3$ the cylinder is poorly represented, and this poor resolution may produce much of the error. To test this possibility, a second refinement study is performed in which the cylinder is resolved with 10 segments and the resolution away from the cylinder is defined as before. The coarsest grid, $N_c = 3$, is shown in figure 6. A comparison of the solutions (fig. 7) shows that only the solution on the coarsest grid is significantly different from the solution on the finest grid and that $N_c = 4$ provides adequate resolution for this problem.

The last issue, the nonreflecting boundary condition, is examined by placing the outer boundary at different distances from the cylinder and comparing these solutions with the baseline case. Figure 8 shows solutions in which the outer boundary is placed at $r = 5.5, 6, 7, 8,$ and 10 . The last case is the

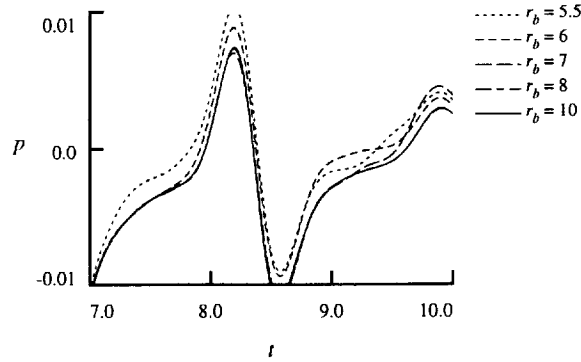


Figure 8. Effect of position of outer boundary on solution accuracy.

baseline solution, in which $N_c = 15$. For the other cases, $N_c = 5$, but the cylinder is resolved with 10 segments (as illustrated in fig. 6). Initially, all five solutions are in agreement. At approximately $t = 7$, the solution with the outer boundary at $r = 5.5$ begins to diverge from the baseline solution. The time at which the other solutions diverge from the baseline increases as the boundary is moved further out. The case with the outer boundary at $r = 8$ agrees well with the baseline solution. This agreement indicates that, at this resolution ($N_c = 5$), all visible error is attributable to the nonreflecting boundary condition. In the case with the outer boundary at $r = 5.5$, the error is less than 5 percent of the amplitude of the initial pulse. Note, however, that the error is not in the form of a compact pulse, as might be expected, but in the form of a shift in the mean value of the solution. This finding suggests that errors in both wavelength and amplitude, relative to a computed mean, may be relatively unaffected by the error produced at the outer boundary.

Problem 1

Problem 1 is similar to problem 2; however, the initial solution is uniform, and the acoustic waves are produced by a temporal forcing. The forcing is given by $S = [-s, s, 0, 0]^T$, where

$$s = \exp \left[-\ln(2) \left(\frac{(x-4)^2 + y^2}{(0.2)^2} \right) \right] \sin(8\pi t)$$

The frequency specified for the workshop results in a wavelength of 0.25, which is smaller than the half-width of the source distribution (0.4). A large transient wave is produced when the forcing is abruptly applied to an otherwise uniform solution. However, because the wavelength is small relative to the size of the source, the amplitude of the periodic acoustic wave is small compared with the amplitude of the forcing (and the initial transient). Consequently, any reflections of this transient off the outer boundary can be quite large relative to the periodic acoustic waves, even if only a fraction of a percent of the energy is reflected.

Simulations were performed at five grid resolutions ($N_c = 5, 7, 10, 15$, and 20) and with the outer boundary at two different positions ($r = 5.5$ and 7.5). Figure 9 compares the solutions at measurement point A obtained with $N_c = 7, 10, 15$, and 20 with the outer boundary at $r = 5.5$. The two finest grids give essentially identical solutions, the case with $N_c = 10$ is only slightly different, and the case with $N_c = 7$ appears to have inadequate resolution. Note, however, that as the grid is coarsened the amplitude of the acoustic wave increases, whereas an underresolved wave would normally be dissipated. Further examination of the solution in the case with $N_c = 7$ reveals that

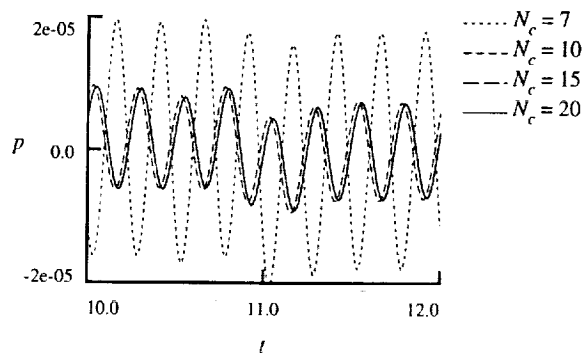


Figure 9. Grid refinement with outer boundary at $r = 5.5$.

the wave is not growing as it propagates and that the wavelength agrees with the wavelength of more well resolved solutions. This observation suggests that the error may be due to insufficient resolution of the source causing an excessive amount of energy to be propagated. This possibility can be resolved by a local refinement at the source; however, this issue is left for future study.

The influence of the initial transient is clearly evident during the time span shown in figure 9. Figure 10 shows a comparison of two solutions at a later time with the outer boundary at $r = 5.5$ and 7.5 . In both cases, $N_c = 15$, and the initial transient has decayed by the time $t = 30$. The two solutions are not distinguishable from one another which suggests that no significant error is produced by the simple, modified characteristic nonreflecting boundary condition used in this work.

The scaled directivity pattern, given by $D(r, \theta) \equiv \overline{rp^2}$, should depend only on the angle θ when r is large (where $\overline{(\)}$ denotes a time average). The workshop requested this quantity in the limit as $r \rightarrow \infty$; however, during the workshop, $D(r, \theta)$ was shown to converge slowly. Thus, the direct computation of the limiting value of $D(r, \theta)$ does not appear feasible because of the large computational domain that would be required. In figure 11, which shows results for 11 values of r averaged over the time span $30 < t < 31$, the phase of the directivity pattern clearly varies with r . However, in figure 12, which shows a contour plot of $D(r, \theta)$, the problem clearly is not that the directivity pattern converges slowly but that the center of the directivity pattern is not at the origin of the grid (which was chosen for convenience but is arbitrary). Figure 13 shows the directivity pattern $D(\bar{r}, \bar{\theta})$ computed from the same simulations, but \bar{r} and $\bar{\theta}$ are measured relative to a point that is halfway between the source and the cylinder. Note that the curves have collapsed to a single directivity pattern.

Conclusions

The discontinuous Galerkin method is applied to problems 1 and 2 from category I of the Second CAA Workshop on Benchmark Problems. Fifth-order elements are used to obtain acceptable resolution with approximately 1.5 elements per wavelength, and mesh independence is obtained with 2 elements per wavelength. The current implementation uses only linear elements; thus, hard-wall boundaries are represented only to second order. However, the hard-wall boundary condition is accurate, provided that the wall curvature is adequately resolved. The method is applicable to elements with curve boundaries, and this extension can improve the surface resolution. The simple modification of the characteristic boundary condition worked well for these problems. No adverse reflections were detected in problem 1, where the acoustic source was periodic. When reflections

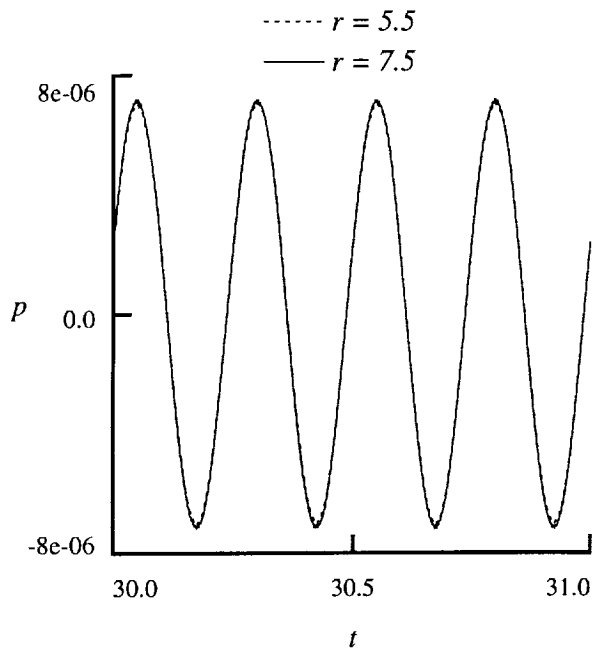


Figure 10. Effect of position of outer boundary.

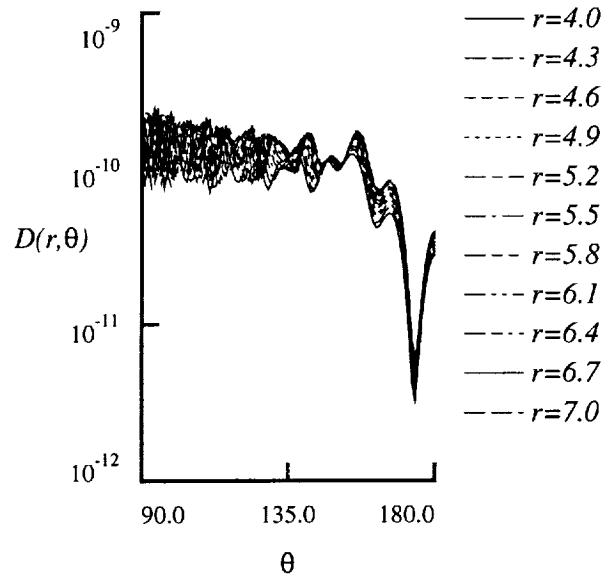


Figure 11. Scaled directivity pattern $D(r, \theta)$ measured from cylinder origin.

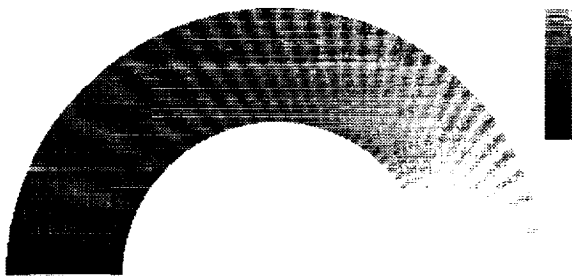


Figure 12. Contour of scaled directivity pattern $D(r, \theta)$ measured from cylinder origin.

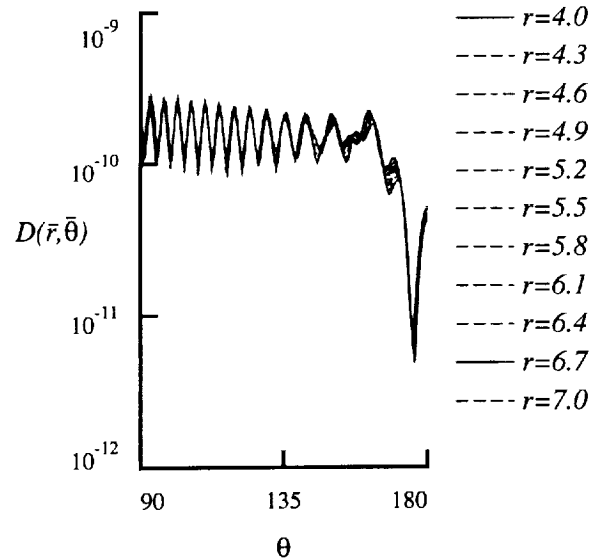


Figure 13. Scaled directivity pattern $D(r, \theta)$ measured from $(2, 0)$.

were detected, the error was in the form of a shift in the average of the solution rather than a discrete pulse. The acoustic directivity pattern can be estimated directly from a simulation on a small domain, provided that the correct center of the pattern is identified.

References

1. H. L. Atkins and Chi-Wang Shu, "Quadrature-Free Implementation of the Discontinuous Galerkin Method for Hyperbolic Equations," AIAA-paper 96-1683, 1996.
2. B. Cockburn, S. Hou, and C.-W. Shu, "The Runge-Kutta local projection discontinuous Galerkin finite element method for conservation laws IV: The multidimensional case," *Mathematics of Computation*, v54 (1990), pp. 545-581.
3. F. Bassi and S. Rebay, "Accurate 2D Euler Computations by Means of a High-Order Discontinuous Finite Element Method," *Proceedings of the 14th international Conference on Numerical Methods in Fluid Dynamics*, Bangalor, India, July 11-15, 1994.
4. R. B. Lowrie, P. L. Roe, and B. van Leer, "A Space-Time Discontinuous Galerkin Method for Time-Accurate Numerical Solution of Hyperbolic Conservation Laws," Presented at the 12th AIAA computational Fluid Dynamics Conference, San Diego, CA, June 19-22, 1995.
5. B. Cockburn and C.-W. Shu, "TVB Runge-Kutta local projection discontinuous Galerkin finite element method for conservation laws II: General framework," *Mathematics of Computation*, v52 (1989), pp. 411-435.
6. C.-W. Shu and S. Osher, "Efficient implementation of essentially non-oscillatory shock-capturing schemes," *Journal of Computational Physics*, v77 (1988), pp. 361-383.
7. B. Gustafson, H.-O. Kreiss, and A. Sundström, "Stability theory of difference approximations for mixed initial-boundary value problems, II," *Mathematics of Computation*, v26 (1972), pp. 649-686.
8. H. L. Atkins, "Continued Development of Discontinuous Galerkin Method for Aeroacoustic Applications " To be presented at the 3rd AIAA/CEAS Aeroacoustic Conference, Atlanta, GA, May 12-14, 1997.
9. Kevin W. Thompson, "Time dependent Boundary Conditions for Hyperbolic Systems," *Journal of Computational Physics*, v68 (1987), pp. 1-24.

57-71
 043465
 293956 p12

COMPUTATION OF ACOUSTIC SCATTERING BY A LOW-DISPERSION SCHEME

Oktay Baysal and Dinesh K. Kaushik

*Department of Aerospace Engineering
 Old Dominion University, Norfolk, Virginia 23529-0247*

Physical problem and background

The objective is the evaluation of a proposed computational aeroacoustics (CAA) method in simulating an acoustic scattering problem. An example may be the sound field generated by a propeller scattered off by the fuselage of an aircraft. The pressure loading on the fuselage would be an input to the interior noise problem. To idealize the problem, the fuselage is assumed to be a circular cylinder and the noise generation by the propeller is represented by a line source.

A typical CFD algorithm may not be adequate for this aeroacoustics problem: amplitudes are an order of magnitude ϑ smaller yet frequencies are ϑ larger than the flow variations generating the sound. For instance, an $\vartheta(2)$ CFD method was previously used for a nonlinear wave propagation problem in unsteady, nonuniform mean flow (Baysal et al., 1994). It was observed that a direct simulation of acoustic waves using a higher-order CFD would become prohibitively expensive, due to the required excessive number of grid points per wavelength (PPM). Also, CAA would need minimal dispersion and dissipation, which would preclude a typical $\vartheta(2)$ CFD method from a long-term wave propagation simulation. Furthermore, a consistent, stable, convergent, high-order scheme is not necessarily dispersion-relation preserving, i.e. no guarantee for a quality numerical solution. Therefore, a baseline $\vartheta(4)$ dispersion-relation-preserving (DRP) method (Tam and Webb, 1993) was investigated (Vanel and Baysal, 1997) for a variety of wave propagation problems, such as, single-, simultaneous-, and successive-acoustic-pulses. Then, a number of algorithmic extensions were performed (Kaushik and Baysal, 1996), when the following were studied: viscous effects by solving the linearized Navier-Stokes equations, low-storage and low-CPU time integration by an optimized Runge-Kutta scheme, generalized curvilinear coordinates for curved boundaries, higher-order accuracy by comparing $\vartheta(4)$ DRP vs. $\vartheta(6)$ DRP, and choice of boundary conditions and differencing stencils. The scheme is now being investigated for nonlinear wave propagation in nonuniform flow (Baysal et al., 1997).

Mathematical approach

The linearized, two-dimensional, compressible, Euler equations were considered in generalized curvilinear coordinates

$$(1) \quad \frac{\partial \hat{U}}{\partial t} = -R(\hat{U}) + S, \quad \text{where} \quad R(\hat{U}) = \frac{\partial \hat{E}}{\partial \xi} + \frac{\partial \hat{F}}{\partial \eta}.$$

The primitive variables, \hat{U} , and the transformed fluxes, \hat{E} and \hat{F} , are,

$$(2) \quad \hat{U} = \frac{1}{J} [\rho \quad u \quad v \quad p]^T, \quad \hat{E} = \frac{1}{J} [\xi_x E + \xi_y F], \quad \hat{F} = \frac{1}{J} [\eta_x E + \eta_y F].$$

and the physical fluxes and the source vector are,

$$(3) \quad E = \begin{bmatrix} u + M_0 \rho \\ M_0 u + p \\ M_0 v \\ M_0 p + u \end{bmatrix}, \quad F = \begin{bmatrix} v \\ 0 \\ p \\ v \end{bmatrix}, \quad S = \begin{bmatrix} 0 \\ 0 \\ 0 \\ S_4 \end{bmatrix}.$$

The perturbed values of density (ρ), pressure (p), and velocity (u, v) are denoted without a subscript, but those of the mean flow are demarcated using the subscript 0. These variables were normalized using the cylinder diameter (D) for length, speed of sound (a_0) for velocity, D/a_0 for time, ρ_0 for density, and $\rho_0(a_0)^2$ for pressure.

Dispersion relation of a proposed numerical scheme should match closely that of eq. (1) for large range of resolution; i.e. $\bar{\alpha}$ and $\bar{\omega}$ be close approximations to α and ω . Assuming $\bar{\alpha}\Delta x$ was a periodic (2π) function of $\alpha\Delta x$ with, Fourier-Laplace transforms rendered,

$$(4) \quad \bar{\alpha} = \frac{-i}{\Delta x} \sum_{j=-L}^M a_j e^{i\alpha j \Delta x} \quad \text{and} \quad \bar{\omega} = \frac{i(e^{-i\omega\Delta t} - 1)}{\Delta t \sum_{j=0}^N b_j e^{i\omega j \Delta t}}.$$

Finite difference coefficients were obtained from Taylor series expansions as one-parameter family, and the remaining coefficient from an error minimization, where the integration limit ε depended on the shortest wavelength to be simulated:

$$(5) \quad \min E_I = \min_{-\varepsilon}^{\varepsilon} \int_{-\varepsilon}^{\varepsilon} |\alpha \Delta x - \bar{\alpha} \Delta x|^2 d(\alpha \Delta x) \quad \text{where} \quad |\alpha \Delta x| < \varepsilon \quad \text{and} \quad \varepsilon = \begin{cases} \pi/2 \\ 1.1 \end{cases} \quad \text{for} \quad \begin{cases} 4.5 \Delta x \\ 7 \Delta x \end{cases}.$$

The time integration of eq. (1) was performed in two different ways. In the first approach, a four-point finite difference, which in a standard sense could be up to third-order accurate, was derived from the Taylor series as a one-parameter family. The remaining coefficient (b_j) was determined, as in the spatial coefficients, by minimizing the discrepancy between the effective and the exact dispersion relations. After discretizing all the terms in eqs. (1)-(3), the resulting $\mathcal{O}(\Delta t^2, \Delta x^{N+M-2})$ DRP scheme was as follows:

$$(6) \quad \hat{U}_{\ell,m}^{n+1} = \hat{U}_{\ell,m}^n + \Delta t \sum_{j=0}^3 b_j R_{\ell,m}^{n-j} \quad \text{where} \quad R_{\ell,m}^n = \frac{-1}{\Delta x} \sum_{j=-N}^M a_j \hat{E}_{\ell+j,m}^n - \frac{1}{\Delta t} \sum_{j=-N}^M a_j \hat{F}_{\ell,m+j}^n.$$

In eq. (6), ℓ and m are the spatial indices and n indicates the time level. For $N=M$, difference is central, for $N=0$, it is fully forward, and for $M=0$, it is fully backward. All the interior cells were computed using central differences with $N=M=3$. However, since these high-order stencils require multiple layers of boundary cells, all combinations between a central and a fully-one-sided difference need also be derived. Only then, it would be possible to always utilize the information from the nearest possible points for better accuracy. In the present computations a fourth-order scheme was used, requiring 7-point stencil: N takes values from 6 to 0, M takes values from 0 to 6, and $N+M=6$.

The numerically stable maximum time step Δt was calculated from the Courant-Friedrichs-Lewy relation. For example, for the fourth-order scheme in Cartesian coordinates, the stable CFL number was found to be 0.4. However, after analyzing the numerical damping of the time integration scheme, the CFL value was set to the more stringent value of 0.19. Since, however, time integration with DRP would require the storage of four time levels, a lower storage alternative, the low-dissipation and low-dispersion

five-stage Runge-Kutta scheme (Hu et al., 1996) was adapted and implemented. The resulting scheme had the spatial integration identical to eq. (6), but the time integration was replaced by the following:

$$(7) \quad \hat{U}^{(0)} = \hat{U}^n, \quad \hat{U}^{(i)} = \hat{U}^{(0)} - \beta_i \Delta t R^{(i-1)}, \quad \hat{U}^{n+1} = \hat{U}^{(p)}, \quad i = 1, 2, \dots, p.$$

The indices n , p and i indicate the time level, and the order and the stage of the Runge-Kutta method, respectively. As for the coefficients, $\beta_1=0$ and the other coefficients β_i were determined from

$$(8) \quad c_i = \prod_{k=2}^i \beta_{p-k+2}, \quad i = 2, \dots, p.$$

The coefficients c_i were computed by considering the amplification factor of the Runge-Kutta scheme, then minimizing the dispersion-relation error. The time steps were determined from the stability as well as the accuracy limits. In the present study, a five-stage Runge-Kutta ($p=5$) was used, which required two levels of storage and it was at least second-order accurate. When it was used with the present 7-point spatial stencil to solve the scalar linear wave equation, the CFL limit from the stability was found to be 3.05, but it was only 1.16 from the accuracy limit. Since, however, this still was larger than the CFL limit of the DRP time integration, this method was also more efficient in processing time.

Usually low-order schemes are used in resolving the highly nonlinear flow or acoustic phenomena. Even with second-order schemes, it is common to have limiters or artificial damping mechanisms, either implicit in the scheme or explicitly added. Since simulating low-amplitude acoustic waves for a long time and for many wavelengths of travel is the objective in CAA, devising such artificial damping mechanisms requires extreme care. For example, constant damping over all wave numbers need to be avoided. Tam et al. (1993) suggested terms, which have small damping over the long wave range but significant damping in the short wave range. The present central-difference scheme includes similar terms with a user specified artificial Reynolds number, to overcome the expected spurious oscillations:

$$(9) \quad D_{\ell,m}^n = \frac{1}{\text{Re}_D} \sum_{j=-N}^N c_j \left[\frac{1}{\Delta \xi^2} \hat{U}_{\ell+j,m}^n + \frac{1}{\Delta \eta^2} \hat{U}_{\ell,m+j}^n \right], \quad \text{where} \quad \text{Re}_D = \frac{\rho_0 a_0 D}{\mu_a}.$$

The boundaries should be transparent to the acoustic disturbances reaching them to avoid any degradation of the numerical solution. From the asymptotic solutions of the finite difference form of the Euler equations, a set of radiation boundary conditions, were derived and implemented. Therefore, following Tam and Webb (1993) and from the asymptotic solutions of the finite difference form of eq. (1), a set of *radiation* boundary conditions were derived,

$$(10) \quad \frac{\partial \hat{U}}{\partial t} + A \frac{\partial \hat{U}}{\partial \xi} + B \frac{\partial \hat{U}}{\partial \eta} + C \hat{U} = 0, \quad \text{where}$$

$$(11) \quad A \equiv V \frac{x \xi_x + y \xi_y}{r}, \quad B \equiv V \frac{x \eta_x + y \eta_y}{r}, \quad C \equiv \frac{V}{2r} \quad \text{and} \quad r = \frac{1}{D} \sqrt{x^2 + y^2}, \quad V = \frac{x}{r} M_0 + \sqrt{1 - (M_0 \frac{y}{r})^2}.$$

For an inviscid solid wall (w) or a symmetry plane, the impermeability condition dictates that the normal contravariant velocity be zero at all times:

$$(12) \quad \hat{v} = \eta_x u + \eta_y v = 0.$$

When this equation was constructed from the η - and ξ -momentum equations, after multiplying them by the appropriate metrics and adding, the wall value of pressure at the ghost point (subscript -1) was obtained,

$$\begin{aligned}
(13) \quad p_{\ell,-1} = & \frac{-\Delta\eta}{a_{\ell,-1}(\eta_x^2 + \eta_y^2)_{\ell,w}} \left\{ \frac{M_0}{\Delta\xi} [(\eta_x \xi_x)_{\ell,w} \sum_{j=-N}^M a_j u_{\ell+j,w} + (\eta_y \xi_x)_{\ell,w} \sum_{j=-N}^M a_j v_{\ell+j,w} \right. \\
& \left. + (\eta_x)_{\ell,w}^2 \sum_{j=w}^{N+M} a_j u_{\ell,j} \right] + \frac{(\eta_x \xi_x + \eta_y \xi_y)_{\ell,w}}{\Delta\xi} \sum_{j=-3}^3 a_j p_{\ell+j,w} \Big\} - \frac{1}{a_{\ell,-1}} \left[\sum_{j=w}^{N+M} a_j p_{\ell,j} \right]
\end{aligned}$$

The coefficients for all the boundary conditions (Tam and Dong, 1994) were derived by an analogous method to that of the boundary region cells. At the corners, two separate ghost points were used, one for each boundary, hence both boundaries' conditions were satisfied.

Results

The present method and its boundary conditions were evaluated by considering a number of reflection or scattering cases (table 1), all in quiescent medium, i.e. $M_0=0$. The acoustic waves were generated either by an initial acoustic pulse introduced to the field at $t=0$ by setting $S=u=v=0$, and

$$(14) \quad p = \hat{p} \exp \left\{ -\ln 2 \left[\frac{(x-x_s)^2 + (y-y_s)^2}{b^2} \right] \right\} \quad (\text{Category 1_Problem 2}),$$

or by a periodic source with $\omega=8\pi$,

$$(15) \quad S_d = \hat{s} \exp \left\{ -\ln 2 \left[\frac{(x-x_s)^2 + (y-y_s)^2}{b^2} \right] \right\} \sin(\omega t) \quad (\text{Category 1_Problem 1}).$$

Table 1. Description of computational cases

Case	Equation	\hat{p} or \hat{s}	b	x_s, y_s	Grid	Δt	Figure
1	14	1.0	3D	4D, 0	H 251x101	1.00E-2	1
2	14	1.0	0.2D	4D, 0	O 401x181	5.00E-3	-
3*	14	1.0	0.2D	4D, 0	O 801x181	5.00E-3	3, 4
4	15	0.01	3D	0, 2D	H 251x101	1.00E-2	5
5	15	1.0	3D	0, 2D	H 251x101	1.00E-2	6
6	15	1.0	0.2D	4D, 0	O 801x181	2.5E-3	7
7**	15	1.0	0.2D	4D, 0	O 361x321	1.25E-3	8, 9

*Category 1_Problem 2

**Category 1_Problem 1

Gaussian pulse: an initial-value problem

In case 1, a coarse H-grid was generated, where the ξ -lines were along the cylinder and the centerline, and the η -lines were perpendicular to the centerline. The transformed computational domain was rectangular with *uniform steps* in each direction and *orthogonal* grid lines, as needed by the DRP scheme. Despite some smearing of the wave front, the initial pulse, its propagation and scattering off the cylinder, were simulated fairly well (fig. 1). However, some oscillations inside the domain and spurious reflections off the boundaries started to emerge.

Then, the grid topology was changed to an O-grid with a radius of 10.5D (cases 2 and 3). The grid had ξ -lines as concentric circles, with the first and last circles being respectively the cylinder and the outer boundary, and the η -lines emanated radially from the cylinder to the outer boundary (fig. 2). The time step $\Delta t = 5.0E-3$ was less than one-half of the accuracy limit for eq. (7) as applied to a linear wave equation, but about five times that needed for eq. (6). Although, the results with the 401 ξ -lines appeared adequate (case 2), doubling these lines rendered a truly symmetric initial pulse (case 3). On an SGI R10K computer in a time-shared mode, case 3 required 24 megabytes of run-time memory and 16 hours of CPU

processing. The unit processing time was computed to be about 0.2 ms/ Δt /node. At three locations, given in their cylindrical coordinates, A(5D, $\pi/2$), B(5D, $3\pi/4$), C(5D, π), the pressure history was recorded from $t = 6$ to $t = 10$ at intervals of 0.01 (fig. 3). The computed results matched the analytical solution very well. The peak reached these points at about $t \approx 6.3, 8.2$ and 9.0 , respectively, and it appeared slightly attenuating (0.06, 0.052, 0.048, respectively) due to the scattering. The peak-trough pair was followed by another set with lower amplitudes. All the waves were crisply simulated with virtually no numerical reflections from the boundaries (fig. 4). This very feature, i.e. the success of the boundary conditions, appeared to be pivotal for this problem.

Periodic source: a limiting-cycle problem

In the preparatory cases of 4 and 5, the equations were solved on an H-grid conforming to the wall shape: a flat plate in the former (fig. 5), and a circular bump on a flat plate in the latter case (fig. 6). The objective was to check the implementation of the boundary conditions and the suitability of the grid. The interference patterns from the cascades of incident and reflected waves reached a periodic state (limiting cycle), after some transient time, as could also be observed by the wall pressure (figs. 5 and 6). Note that the source amplitude was 1% in case 4.

In cases 6 and 7, the scattering off a cylinder was simulated on O-grids and the directivity,

$$(16) \quad D(\theta) = \lim_{r \rightarrow \infty} \left\{ r \overline{p^2} \right\} \cong \frac{R}{n_2 - n_1} \sum_{n_1}^{n_2} p_n^2 \quad ,$$

was computed at $r=R$ and from time step n_1 to n_2 . In case 6, the solution was obtained on a 801x181 O-grid with 10.5D radius. This resulted in 20 PPW radially, and PPW circumferentially were: 28.6 on cylinder, 2.86 at $r=5.0$, and 1.36 at the outer boundary. However, from eq. (5), the theory required 4.5 PPW, which was satisfied for points with $r < 3.18$. Consequently, despite the periodic response attained, e.g. on the cylinder (fig 7), neither the computed directivity pattern nor its amplitudes at $R=10.5D$ were satisfactory.

Hence, another O-grid was generated with 361x321 points and a radius of 8.5D (case 7). This resulted in 10 PPW radially, and PPW circumferentially were: 57.3 on cylinder, 5.73 at $r=5.0$, and 3.37 at the outer boundary. The theoretically required 4.5 PPW was satisfied for points with $r < 6.36$. (Practice may prove the safer requirement to be 8 PPW, which was satisfied for points with $r < 3.58$.) Initially, Δt was 2.5E-3, but after $t=15$, it was reduced to 1.25E-3, which was one-fourth of the accuracy limit for eq. (7) as applied to a linear wave equation, but 2.5 times that needed for eq. (6). At $r = R = 5$ and θ from 0 to $\pi/2$, the periodic response was detected after 100 periods of source excitation, then the results were recorded at $r = R = 5$ and θ from 0 to π at 0.5-deg intervals. The computed directivity is presented in fig. 8. Although, the directivity had not yet attained the limiting cycle values at $t=26.25$, the number of peaks matched analytical values well. Since the results were relatively better for $\theta < \pi/2$, and for $\theta > \pi/2$, they improved with the elapsed time, it was deemed that all the transients had not yet left the domain. Also due to the marginal PPW circumferentially at $r=5$ and the uncertainty about the sufficient artificial viscosity to be used (Re in eq. (9) was set to 1.0E4), some oscillations were detected. This computed scattering pattern is also depicted via its pressure contours at two instants (fig. 9). Finally, on an SGI R10K computer in a time-shared mode, case 7 required 19.2 megabytes of run-time memory and 100 hours of CPU processing. Conceivably, the elapsed time for the scattering shown should have been doubled, which, naturally, would have required twice as much computing time.

Conclusions

By and large, the present simulations of the propagation of acoustic waves, their reflections and scattering, in particular, the initial-value problem with the acoustic pulse, were successful. Two necessary building blocks to success, once a suitable CAA scheme was selected, were the correct boundary conditions, and an

adequate and efficient grid. Notwithstanding the imperfectly orthogonal grids and the required transformation metrics, employing the body-fitted coordinates allowed a straight forward implementation of the boundary conditions. The role of the grid became more accentuated in the periodic source case. The spread of the source (b in eq. (15)) and the intervals that the directivity was requested (1-deg) proved narrow enough to necessitate too fine a grid resolution, which superseded the benefits of a low PPW scheme. A better deployment of the grid points, such as, some sort of domain decomposition, could reduce the required computational resources. Also, since it took longer for the periodic behavior to be established at $\theta=\pi$, it would have been less resource taxing to request the data up to, say, $\theta=3\pi/4$. Further, the definition of directivity included the $r \rightarrow \infty$, leading one to place the outer boundary as far away as possible; however, the benchmark analytical solution was integrated virtually at any $r=R$ value. Finally, a parametric study of the required amount of artificial dissipation proved to be another prerequisite.

References

- Baysal, O., Yen, G.W., and Fouladi, K., 1994, "Navier-Stokes Computations of Cavity Aeroacoustics With Suppression Devices," *Journal of Vibration and Acoustics*, Vol. 116, No. 1, pp. 105-112.
- Baysal, O., Kaushik, D.K., and Idres, M., 1997, "Low Dispersion Scheme for Nonlinear Acoustic Waves in Nonuniform Flow," AIAA Paper 97-1582, *Proceedings of Third CEAS/AIAA Aeroacoustics Conference*, Atlanta, GA.
- Hu, F.Q., Hussaini, M.Y., and Manthey, J., 1996, "Low-dissipation and Low-dispersion Runge-Kutta Schemes for Computational Acoustics," *Journal of Computational Physics*, Vol. 124, pp. 177-191.
- Kaushik, D.K., and Baysal, O., 1996, "Algorithmic Extensions of Low-Dispersion Scheme and Modeling Effects for Acoustic Wave Simulation," *Proceedings The ASME Fluids Engineering Division Summer Meeting*, FED-Vol. 238, San Diego, CA, pp. 503-510.
- Tam, C.K.W., Webb, J.C., and Dong, T.Z., 1993, "A Study of the Short Wave Components in Computational Acoustics," *Journal of Computational Acoustics*, Vol. 1, pp. 1-30.
- Tam, C.K.W., and Dong, Z., 1995 "Radiation and Outflow Boundary Conditions for Direct Computation of Acoustic and Flow Disturbances in a Nonuniform Mean Flow," *ICASE/LaRC Workshop on Benchmark Problems in Computational Aeroacoustics*, NASA Conference Publication 3300, pp. 45-54.
- Tam, C.K.W., and Dong, Z., 1994 "Wall Boundary Conditions for High-Order Finite Difference Schemes in Computational Aeroacoustics," AIAA Paper 94-0457, 32nd Aerospace Sciences Meeting, Reno, NV.
- Tam, C.K. W., and Webb, J. C., 1993, "Dispersion-Relation-Preserving Finite Difference Schemes for Computational Acoustics," *Journal of Computational Physics*, Vol. 107, pp. 262-283.
- Vanel, F. O., and Baysal, O., 1997, "Investigation of Dispersion-Relation-Preserving Scheme and Spectral Analysis Methods for Acoustic Waves," *Journal of Vibration and Acoustics*, Vol. 119, No. 2.

Acknowledgments

This work was supported by NASA Langley Research Center Grant NAG-1-1653. The technical monitor was J.L. Thomas. Authors thank D.E. Keyes for the helpful discussions.

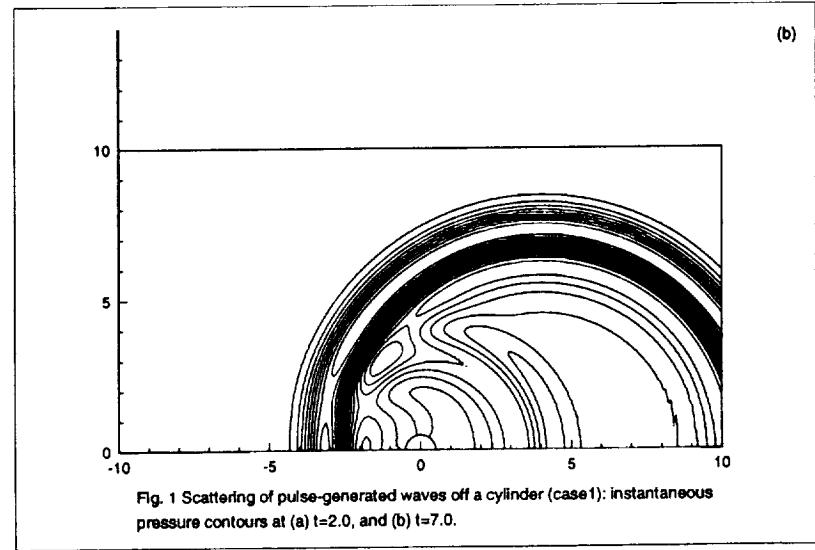
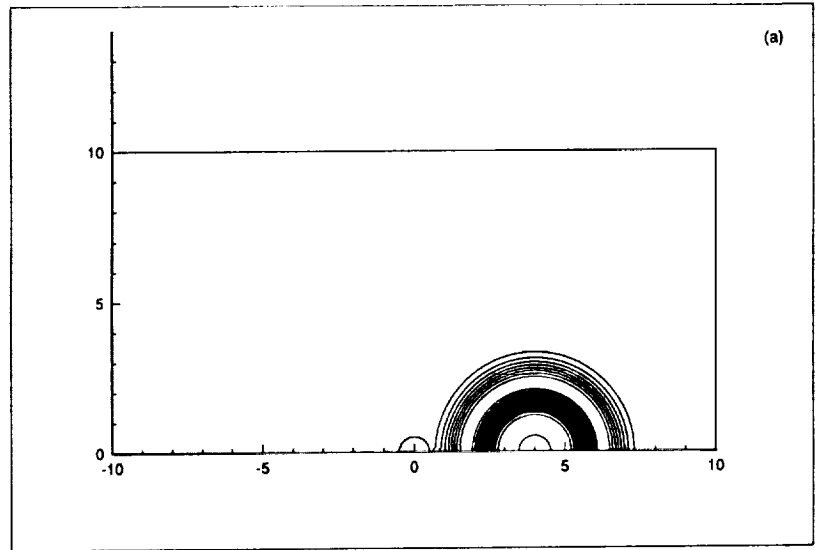


Fig. 1 Scattering of pulse-generated waves off a cylinder (case1): instantaneous pressure contours at (a) $t=2.0$, and (b) $t=7.0$.

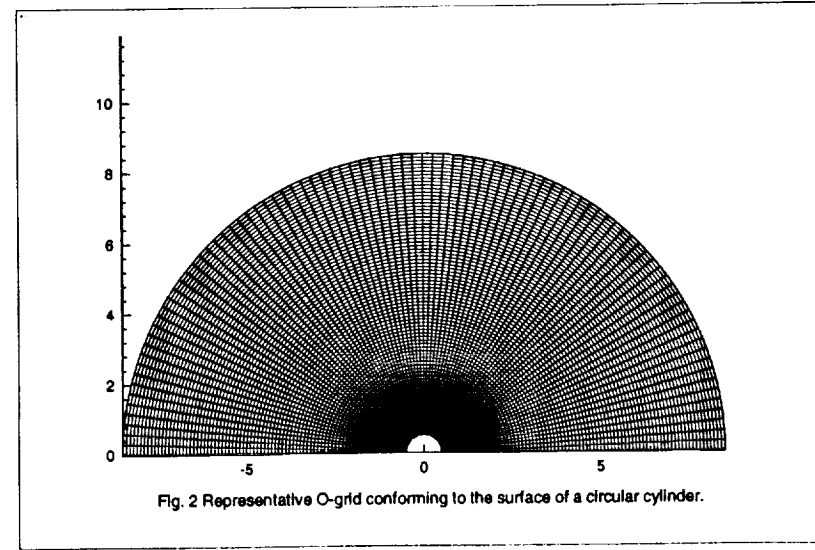


Fig. 2 Representative O-grid conforming to the surface of a circular cylinder.

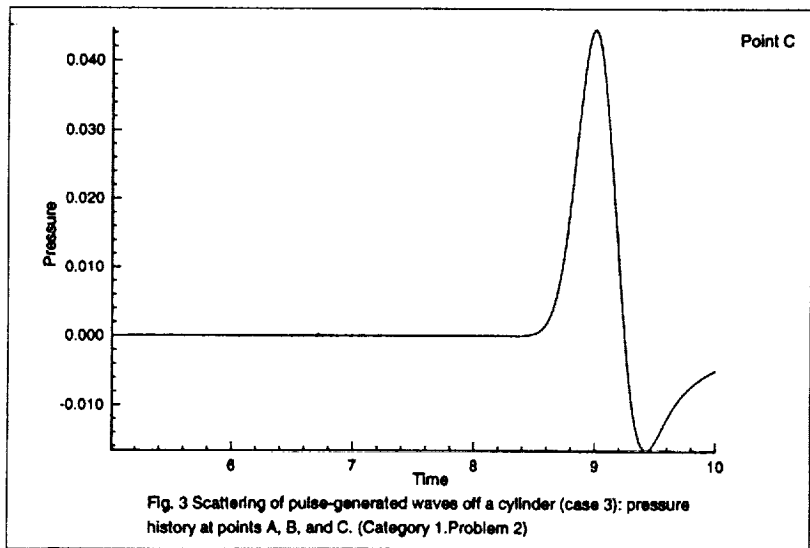
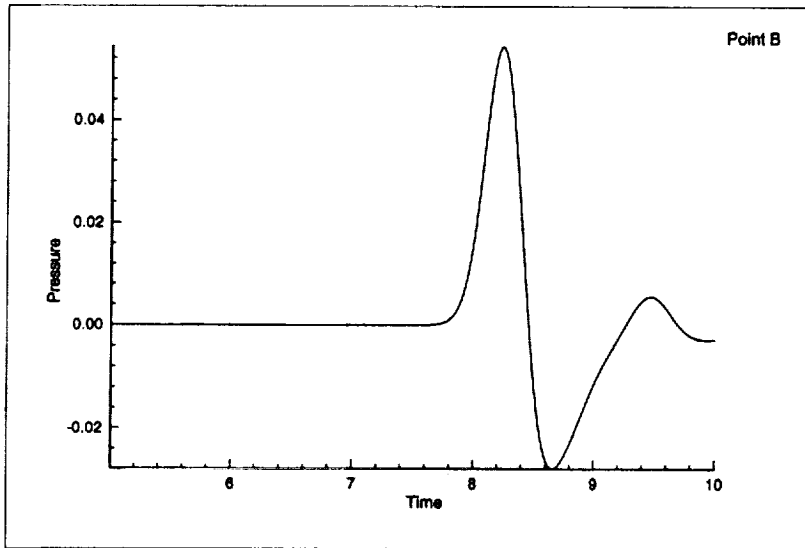
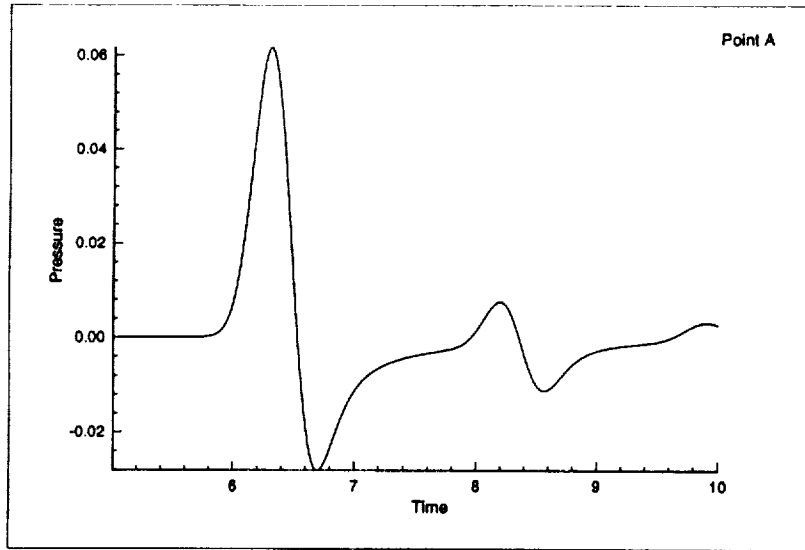


Fig. 3 Scattering of pulse-generated waves off a cylinder (case 3): pressure history at points A, B, and C. (Category 1. Problem 2)

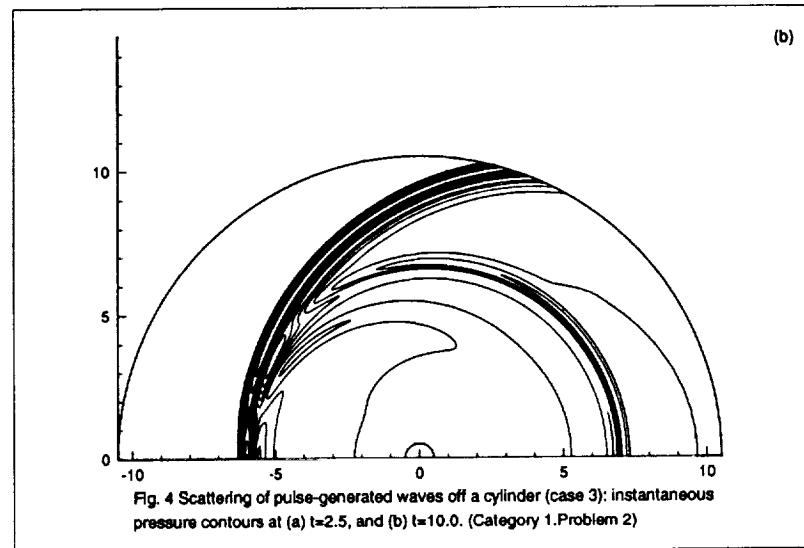
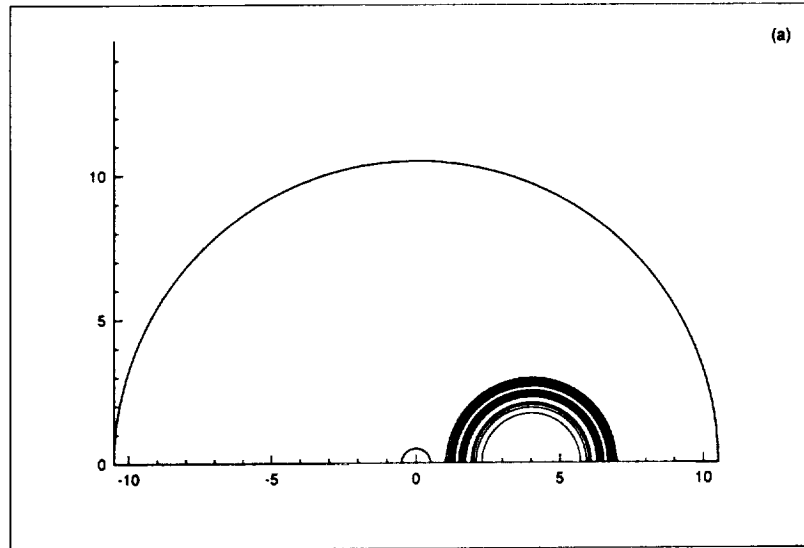


Fig. 4 Scattering of pulse-generated waves off a cylinder (case 3): instantaneous pressure contours at (a) $t=2.5$, and (b) $t=10.0$. (Category 1, Problem 2)

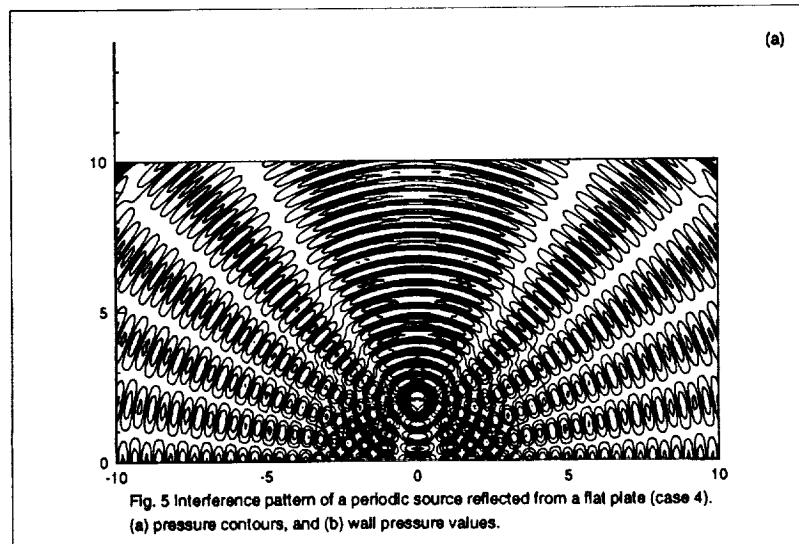


Fig. 5 Interference pattern of a periodic source reflected from a flat plate (case 4). (a) pressure contours, and (b) wall pressure values.

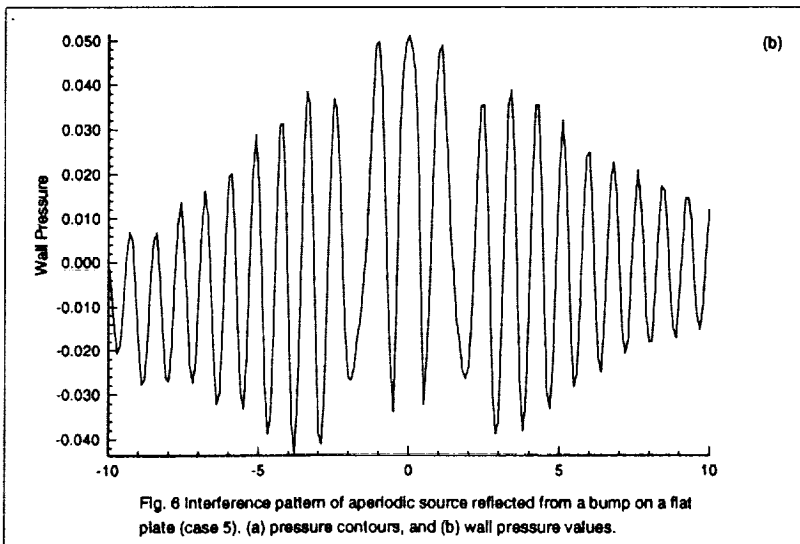
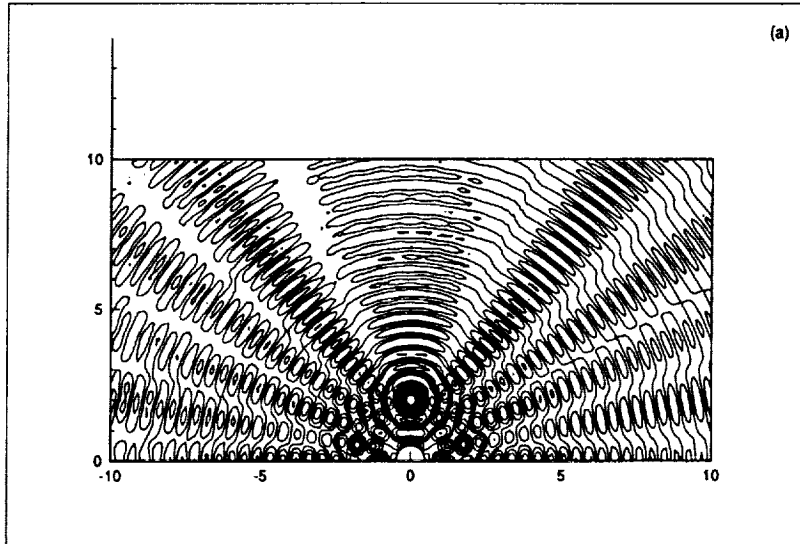
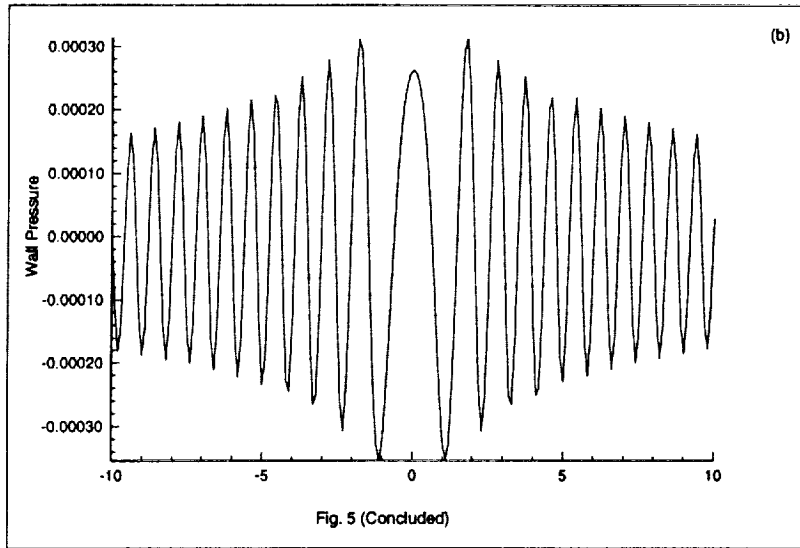
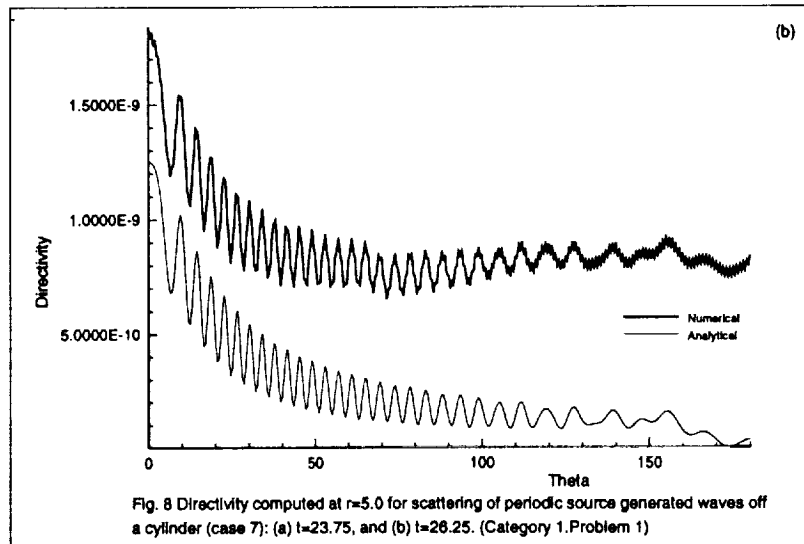
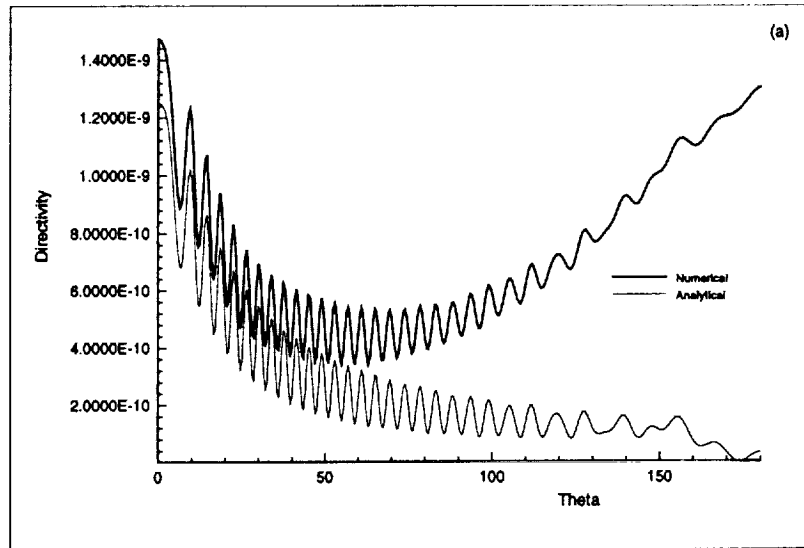
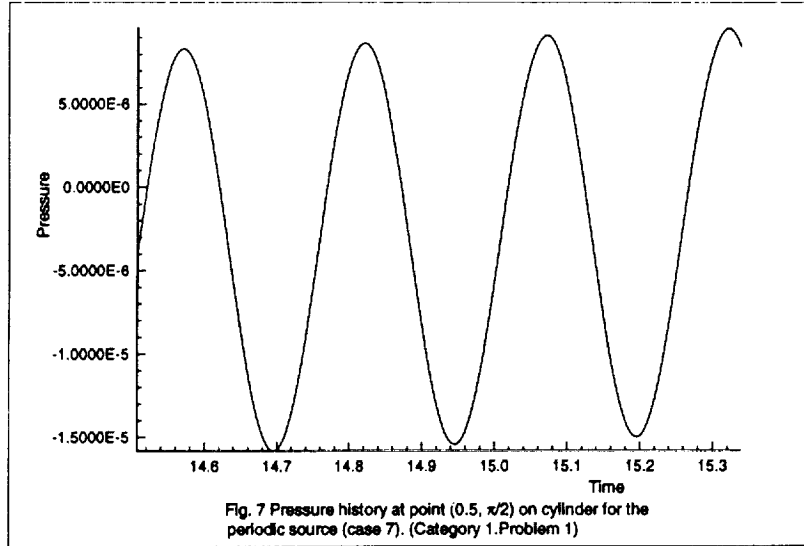


Fig. 6 Interference pattern of aperiodic source reflected from a bump on a flat plate (case 5). (a) pressure contours, and (b) wall pressure values.



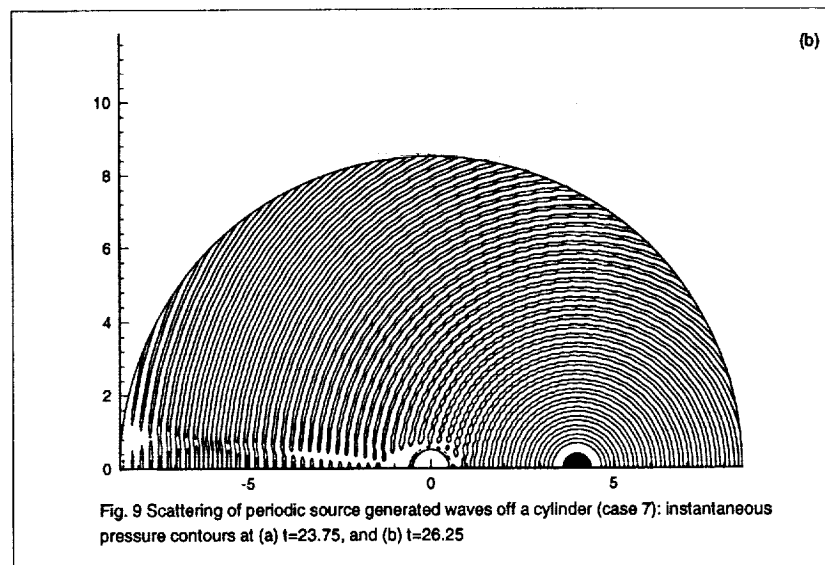
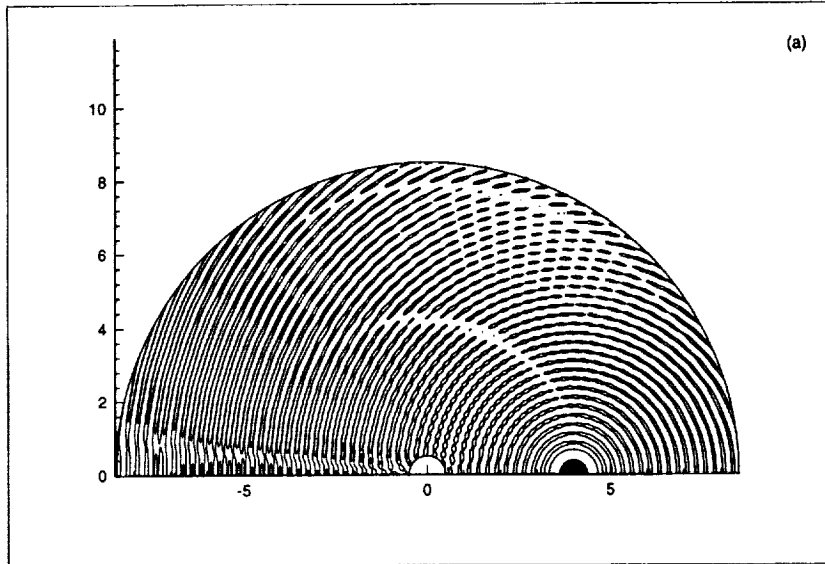


Fig. 9 Scattering of periodic source generated waves off a cylinder (case 7): instantaneous pressure contours at (a) $t=23.75$, and (b) $t=26.25$

028-11
043466
293958

pid

**SOLUTION OF ACOUSTIC SCATTERING PROBLEMS BY
A STAGGERED-GRID SPECTRAL DOMAIN DECOMPOSITION METHOD**

Peter J. Bismuti and David A. Kopriva
Department of Mathematics and Supercomputer Computations Research Institute
Florida State University, Tallahassee, Florida 32306

ABSTRACT

We use a Staggered-Grid Chebyshev spectral multidomain method to solve two of the workshop benchmark problems. The spatial approximation has the ability to compute wave-propagation problems with exponential accuracy in general geometries. The method has been modified by the use of a stretching transformation to extend the range of accurately represented Fourier modes and to increase the allowable time step. We find that the Category 1, Problem 1 solution requested is accurate to 2.6% at $r = 15$ using five points per wavelength. In the second problem, we find that the over the times and angles requested, the maximum error is less than 10^{-6} .

INTRODUCTION

The efficient and accurate approximation of time dependent compressible flow problems requires high order methods both in space and in time [9], [11]. Second order finite difference methods, typically designed for steady-state computational fluid dynamics problems, are strongly dissipative and dispersive unless the number of grid points per wavelength computed is on the order of 20 to 40 [9]. Computing with so many points per wavelength is impractical in problems where waves must be propagated many hundreds of wavelengths. With high order methods, the required number of points per wavelength can be reduced significantly, making accurate multidimensional solutions more practical.

Spectral methods [1] are natural choices for the solution of flow problems where high spatial accuracy is required. They are exponentially convergent for smooth problems. Phase and dissipation errors decay exponentially fast [5]. Special boundary stencils are not required, since spatial derivatives are defined right up to the boundaries.

The advantages of spectral methods are balanced in many peoples' minds by the methods' cost and inflexibility. The cost per grid point is higher than a fixed stencil finite difference method because the cost of computing the spatial derivatives is high, and explicit time marching procedures typically used for wave-propagation problems require a more restrictive time step. Inflexibility is a result of the global polynomial nature of the approximation.

As a means for reducing the high cost and inflexibility of spectral methods, spectral multidomain methods were introduced in the mid 1980's [10], [4]. The basic premise is that high cost

and inflexibility can be reduced by subdividing the computational domain into multiple subdomains on which a spectral approximation is applied. As a result, the method can be used on more complex geometries. The use of lower order approximating polynomials in each subdomain means that matrix multiplication can be both efficient and accurate, and the time step restrictions need not be as severe.

Recently, a staggered-grid spectral approximation method was developed that gives spectral accuracy and geometric flexibility [7], [6]. In this method, the solution and the fluxes are approximated on different grids. Unstructured subdomain decompositions can be used, and connectivity between subdomains is simplified because subdomain corner points are not used as part of the approximation. The use of Chebyshev polynomial approximations gives exponential convergence and simplicity at boundaries. The isoparametric representation of boundaries means that they are approximated to the same accuracy as the solution.

In this paper, we use the staggered-grid multidomain method of [7] to compute solutions to the Category 1 benchmark Problems 1 and 2. To increase the range of accurately approximated wavelengths, and to increase the time step required by the Chebyshev approximation, we use the transformation presented by Kozloff and Tal-Ezer [8]. To treat radiation boundary conditions, we replace the equations in outer subdomains with the Perfectly-Matched-Layer equations of Hu [3].

THE STAGGERED-GRID SPECTRAL MULTIDOMAIN METHOD

The staggered-grid method [7], [6] solves the Euler equations in conservative form,

$$Q_t + F_x + G_y = S \quad (1)$$

where Q is the vector of solution unknowns, S is the source vector, and $F(Q)$ and $G(Q)$ are the flux vectors. In this paper, we solve the linearized Euler equations where

$$Q = \begin{bmatrix} u \\ v \\ p \end{bmatrix} \quad F = \begin{bmatrix} p \\ 0 \\ u \end{bmatrix} \quad G = \begin{bmatrix} 0 \\ p \\ v \end{bmatrix} \quad (2)$$

In the multidomain approximation, we subdivide a computational domain, Ω , into quadrilateral subdomains, $\Omega^k, k = 1, 2, \dots, K$. Under the mapping $\Omega^k \rightarrow [0, 1] \times [0, 1]$, the Euler equations (1) become

$$\tilde{Q}_t + \tilde{F}_x + \tilde{G}_y = \tilde{S} \quad (3)$$

where

$$\begin{aligned} \tilde{Q} &= JQ, \quad \tilde{S} = JS \\ \tilde{F} &= y_Y F - x_Y G, \quad \tilde{G} = -y_X F + x_X G \\ J(X, Y) &= x_X y_Y - x_Y y_X \end{aligned}$$

The staggered-grid approximation computes the solution and source values, \tilde{Q} and \tilde{S} , and the fluxes \tilde{F} and \tilde{G} on separate grids. These grids are tensor products of the Lobatto grid, X_j , and the

Gauss grid, $\bar{X}_{j+1/2}$, mapped onto $[0,1]$

$$X_j = \frac{1}{2} \left(1 - \cos \left(\frac{j\pi}{N} \right) \right) \quad j = 0, 1, \dots, N$$

$$\bar{X}_{j+1/2} = \frac{1}{2} \left(1 - \cos \left(\frac{2j+1}{2N} \pi \right) \right) \quad j = 0, 1, \dots, N-1$$

On the Lobatto and Gauss grids, we define two Lagrange interpolating polynomials

$$\ell_j(\xi) = \prod_{\substack{i=0 \\ i \neq j}}^N \left(\frac{\xi - X_i}{X_j - X_i} \right)$$

and

$$h_{j+1/2}(\xi) = \prod_{\substack{i=0 \\ i \neq j}}^{N-1} \left(\frac{\xi - \bar{X}_{i+1/2}}{\bar{X}_{j+1/2} - \bar{X}_{i+1/2}} \right)$$

We see that $\ell_j(x) \in P_N(x)$, and $h_{j+1/2}(\xi) \in P_{N-1}$, where P_N is the space of polynomials of degree less than or equal to N .

The mapping of each subdomain onto the unit square is done by a static isoparametric transformation. By making the mapping isoparametric, the boundaries are approximated to the same accuracy as is the solution. Let the vector function $g(s)$, $0 \leq s \leq 1$ define a parametric curve. The polynomial of degree N that interpolates g at the Lobatto points is

$$\Gamma(s) = \sum_{j=0}^N g(s_j) \ell_j(s)$$

Four such polynomial curves, $\Gamma_m(s)$, $m = 1, 2, 3, 4$, counted counter-clockwise, bound each subdomain. As in [7], we map each subdomain onto the unit square by the linear blending formula

$$\begin{aligned} x^N(X, Y) &= (1 - Y)\Gamma_1(X) + Y\Gamma_3(X) + (1 - X)\Gamma_4(Y) + X\Gamma_2(Y) \\ &\quad - x_1(1 - X)(1 - Y) - x_2X(1 - Y) - x_3XY \end{aligned}$$

where the x_j 's represent the locations of the corners of the subdomain, counted counter-clockwise.

The solution unknowns are approximated at $(\bar{X}_{i+1/2}, \bar{Y}_{j+1/2})$, $i, j = 0, 1, \dots, N-1$, which we will call the Gauss/Gauss points. The interpolant through these unknowns is a polynomial in $P_{N-1, N-1} = P_{N-1} \otimes P_{N-1}$,

$$\bar{Q}(X, Y) = \sum_{i=0}^{N-1} \sum_{j=0}^{N-1} \frac{\bar{Q}_{i+1/2, j+1/2}}{J_{i+1/2, j+1/2}} h_{i+1/2}(X) h_{j+1/2}(Y) \quad (4)$$

The horizontal fluxes are approximated at the Lobatto/Gauss points $(X_i, \bar{Y}_{j+1/2})$, $i, j = 0, 1, \dots, N$, computed from the polynomial 4

$$\tilde{F}_{i,j+1/2} = y_Y^N(X_i, \bar{Y}_{j+1/2}) F(\bar{Q}(X_i, \bar{Y}_{j+1/2})) - x_Y^N(X_i, \bar{Y}_{j+1/2}) G(\bar{Q}(X_i, \bar{Y}_{j+1/2}))$$

Finally, the vertical fluxes are approximated at the Gauss/Lobatto points $(\bar{X}_{i+1/2}, Y_j)$, $i, j = 0, 1, \dots, N - 1$ and are computed as

$$\tilde{G}_{i+1/2,j} = -y_X^N(\bar{X}_{i+1/2}, Y_j)F(\bar{Q}(\bar{X}_{i+1/2}, Y_j)) + x_X^N(\bar{X}_{i+1/2}, Y_j)G(\bar{Q}(\bar{X}_{i+1/2}, Y_j))$$

It remains now to show how the fluxes are computed at subdomain interfaces and at physical boundaries. The coupling of the subdomains is made by defining interface conditions that compute the interface fluxes. Though the interface points between two neighboring subdomains coincide, the two solutions at the interface need not, since they are computed independently from the interpolant through the Gauss/Gauss points in each subdomain. A unique flux is computed, however, by choosing from the solutions on the forward and backward side of the interface according to the normal characteristics at the interface point. In non-linear problems, this is done using a Roe solver (see [7]). For the linear system (1), we do a linear decomposition of the normal coefficient matrix into forward and backward going waves

$$A = \begin{bmatrix} 0 & 0 & N_x \\ 0 & 0 & N_y \\ N_x & N_y & 0 \end{bmatrix} = A^+ + A^-$$

where $A^+ = \frac{1}{2}(A + |A|)$, and $A^- = \frac{1}{2}(A - |A|)$. Then the normal flux is computed as $F_N = A^+Q^+ + A^-Q^- = F_N^+ + F_N^-$, where Q^\pm refers to the forward and backward solutions along the normal direction. One of the eigenvalues of A is identically zero, and we put that case into A^+ . The flux \tilde{F} or \tilde{G} , depending on which side is being considered, is then computed directly from the normal flux at the interface.

Wall boundary conditions are imposed as simply as they are in a finite volume formulation, through the evaluation of the wall flux. At walls, the reflection condition is imposed by choosing the exterior solution value, Q^+ to have the same pressure, but opposite normal velocity to Q^- when computing the boundary flux.

Radiation boundary conditions are implemented by a buffer-zone technique. Buffer-zone methods are natural for use with multidomain spectral methods, since all that is required is to change the equations in the outer subdomains to ones that will not reflect waves into the interior. It is not as convenient, however, to impose radiation boundary conditions through the solution of a one-way wave equation, since boundary solutions are not part of the approximation.

We will report results using the Perfectly Matched Layer (PML) method of Hu [3]. In this method, the solution vector, \tilde{Q} , is split into two vectors, $\tilde{Q} = \tilde{Q}_1 + \tilde{Q}_2$, where the components satisfy the equations

$$\frac{\partial \tilde{Q}_1}{\partial t} + \tilde{F}_X = -\sigma^X \tilde{Q}_1$$

$$\frac{\partial \tilde{Q}_2}{\partial t} + \tilde{G}_Y = -\sigma^Y \tilde{Q}_2$$

The coefficients, σ^X and σ^Y determine the amount of damping added to the solution. We report solutions using the ramped functions, $\sigma^X = c(X - X_{edge})^m$, and $\sigma^Y = c(Y - Y_{edge})^m$ with $c = 150$, and $m = 10$. After the split variable vectors are updated, we simply add them to form the full solution vector.

Once the fluxes are computed, we form the semi-discrete approximation for the solution on the Gauss/Gauss grid. For each subdomain

$$\left. \frac{d\tilde{Q}}{dt} \right|_{i+1/2, j+1/2} + [\tilde{F}_X + \tilde{G}_Y]_{i+1/2, j+1/2} = S_{i+\frac{1}{2}, j+\frac{1}{2}}, \quad \begin{array}{l} i = 0, 1, \dots, N-1 \\ j = 0, 1, \dots, N-1 \end{array} \quad (5)$$

The derivatives, defined as

$$\begin{aligned} \tilde{F}_X \Big|_{i+1/2, j+1/2} &= \sum_{n=0}^N \tilde{F}_{n, j+1/2} \ell'_n(\bar{X}_{i+1/2}) \\ \tilde{G}_Y \Big|_{i+1/2, j+1/2} &= \sum_{m=0}^N \tilde{G}_{i+1/2, m} \ell'_m(\bar{Y}_{j+1/2}) \end{aligned} \quad (6)$$

are computed by matrix multiplication. Similarly, in the PML subdomains, we solve

$$\begin{aligned} \left. \frac{\partial \tilde{Q}_1}{\partial t} \right|_{i+\frac{1}{2}, j+\frac{1}{2}} + \tilde{F}_X \Big|_{i+\frac{1}{2}, j+\frac{1}{2}} &= -\sigma^X \tilde{Q}_1 \Big|_{i+\frac{1}{2}, j+\frac{1}{2}} \\ \left. \frac{\partial \tilde{Q}_2}{\partial t} \right|_{i+\frac{1}{2}, j+\frac{1}{2}} + \tilde{G}_Y \Big|_{i+\frac{1}{2}, j+\frac{1}{2}} &= -\sigma^Y \tilde{Q}_2 \Big|_{i+\frac{1}{2}, j+\frac{1}{2}} \end{aligned} \quad (7)$$

Equations (5) and (7) are then integrated in time by a fourth order, two-level low-storage Runge-Kutta scheme [2].

To extend the range of wavelengths over which the method is accurate, and to increase the size of the time step allowed by the explicit Runge-Kutta integration, we have also applied the transformation of Kozloff and Tal-Ezer [8]. This transformation makes the change of variables

$$\begin{aligned} X &= \sin^{-1}(\alpha \hat{X}) / \sin(\alpha) \\ Y &= \sin^{-1}(\alpha \hat{Y}) / \sin(\alpha) \end{aligned}$$

where $\alpha \in [0, 1]$ is a parameter that can be used to optimize the approximation. Under the transformation, eq. (5) become

$$\left. \frac{d\tilde{Q}}{dt} \right|_{i+1/2, j+1/2} + \frac{\sin(\alpha)}{\alpha} \left[\sqrt{1 - (\alpha \hat{X})^2} \tilde{F}_{\hat{X}} + \sqrt{1 - (\alpha \hat{Y})^2} \tilde{G}_{\hat{Y}} \right]_{i+1/2, j+1/2} = 0 \quad (8)$$

The limits of the parameter correspond to the pure Chebyshev case when $\alpha = 0$, and to uniform spacing when $\alpha = 1$. We have found $\alpha \approx 0.92$ to be a good choice. The transformation has the effect of reducing the size of the spurious eigenvalues, thus allowing for a larger time step. It also gives a

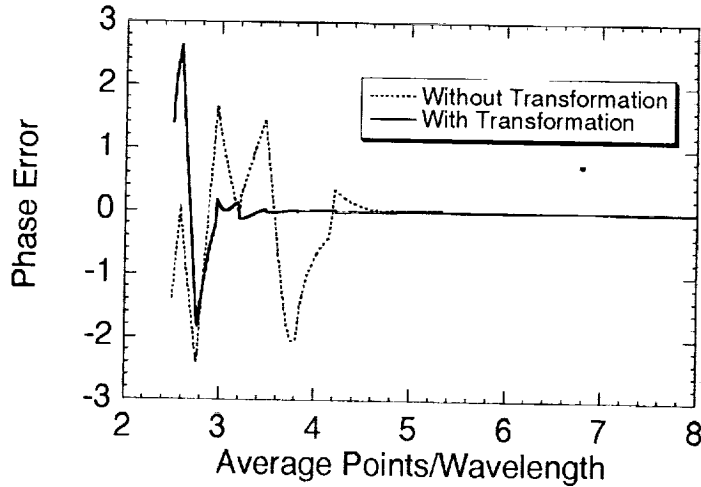


Figure 1: Variation of the maximum phase error across a subdomain as a function of resolution for $N = 20$.

wider range of accurately approximated Fourier modes. To see the latter effect, Fig. 1 shows for $N = 20$, that the accumulated phase error across a subdomain can be substantially reduced for a wider range of frequencies by the use of the transformation.

RESULTS

We present solutions to the first two Category 1 benchmark problems. In the first problem, a line periodic source is placed four diameters from the center of a circular cylinder. In the second, an initial pressure pulse is centered four diameters from the cylinder and allowed to propagate. In both problems, lengths are scaled to the diameter of the circular cylinder, and velocities to the sound speed, c . The time scale is the cylinder diameter divided by the sound speed. Density is scaled to the undisturbed density, ρ_0 . Pressure is scaled to $\rho_0 c^2$. In the first problem, the source is time periodic,

$$S = \sin(\omega t) e^{-\ln 2 \left(\frac{(x-4)^2 + y^2}{0.2^2} \right)}$$

with $\omega = 8\pi$. In the second problem, there is no source, but the initial pressure is

$$p = e^{-\ln 2 \left(\frac{(x-4)^2 + y^2}{0.2^2} \right)}$$

Category 1. Problem 1.

The first Category 1 problem is solved in the region $[-16, 16] \times [0, 16]$ so that only the top half of the problem is computed. The grid is of the form shown in Fig. 2, which shows the skeleton of the subdomains. Overall, the region is subdivided in 514 subdomains, with 32 in the horizontal direction, 16 in the vertical and four around the cylinder itself. Around the exterior, 66 PML subdomains were

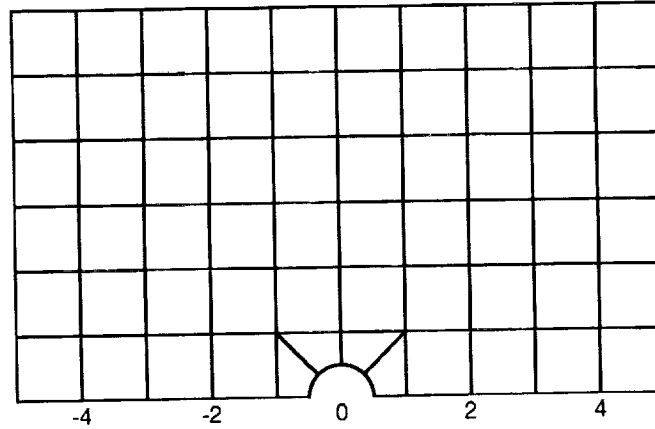


Figure 2: Subdomain decomposition for scattering off a cylinder

added. Except for those around the cylinder, the subdomains were taken to be one unit on a side. A polynomial order of 20 was used in each direction and in each subdomain for a total of 232,000 degrees of freedom. With this grid, the diffracted waves are resolved to an average of five points per wavelength. A stretching factor of $a = 0.92$ was used on this computation. Finally, a time step of 4.17×10^{-3} was used, which corresponds to 60 steps per cycle. The entire computation, which was run for 360 cycles of the source, took approximately 58 hours on a single IBM SP2 node.

Fig. 3 compares the computed and exact values of $\langle P^2 \rangle / r$ at $r = 15$ as a function of angle about the center of the cylinder. At this distance, the reflected wave has travelled roughly 60 wavelengths. The graph indicates excellent precision in both the amplitude and the phase of the solution. The maximum relative error is 2.6%.

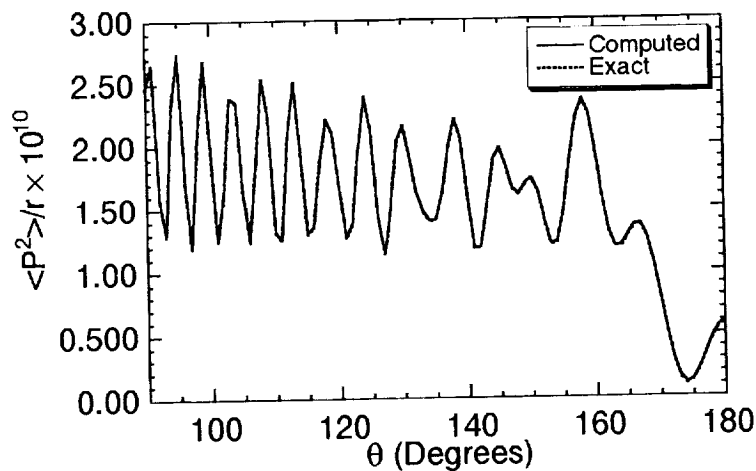


Figure 3: Pressure amplitude as a function of angle at $r = 15$.

Category 1, Problem 2.

We solve the second problem in the region $[-6, 6] \times [0, 6]$ on the grid shown in Fig 2. The Euler equations (5) are solved on 74 subdomains with 12 in the horizontal direction, six in the vertical, and

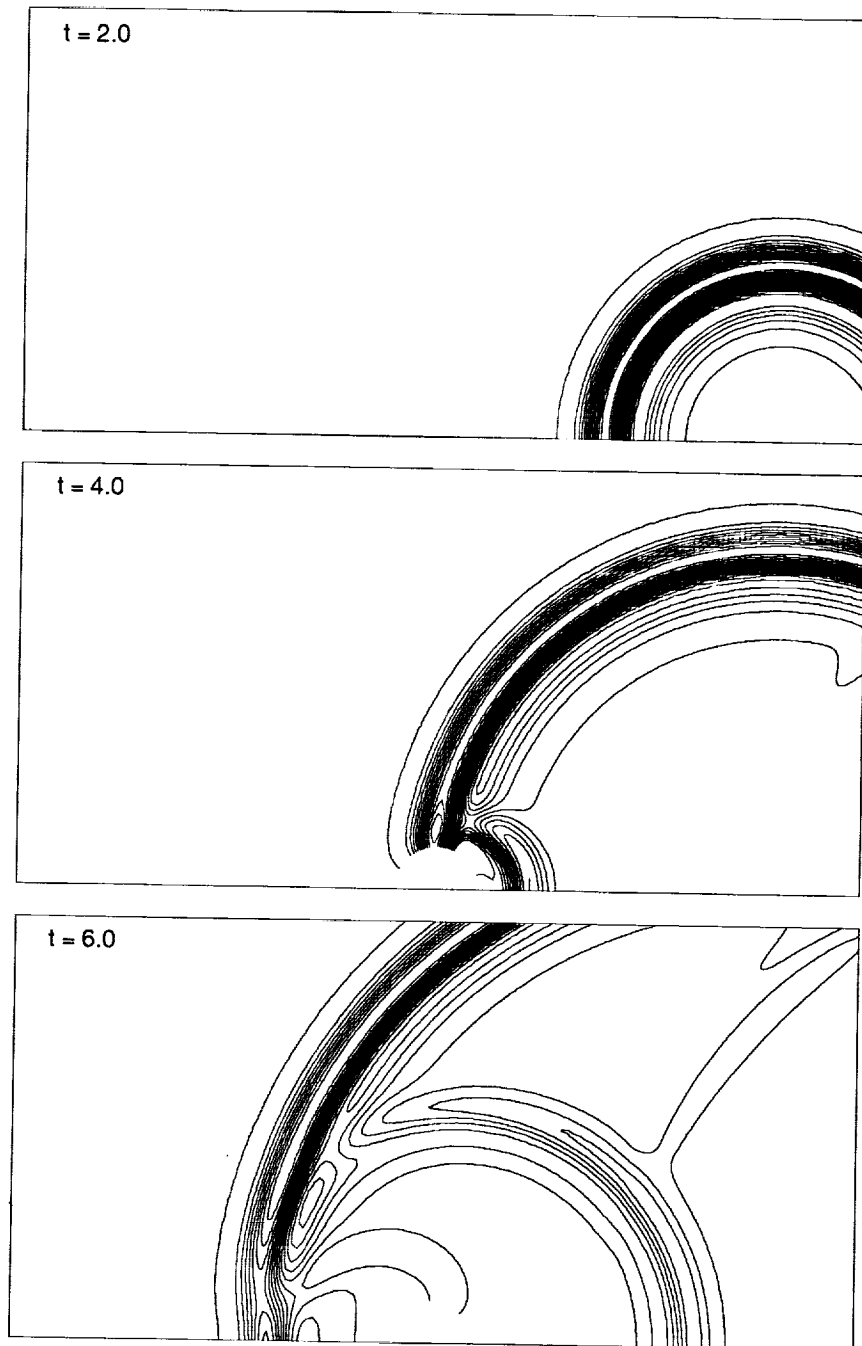


Figure 4: Pressure contours at three times for the scattering of a gaussian pulse off a circular cylinder.

four around the cylinder. The PML equations were applied in an outer ring of 26 subdomains. The subdomains were chosen to be one unit on a side, and twenty points horizontally and vertically were used in each, for a total of about 40,000 degrees of freedom. With this grid, the initial pressure pulse is resolved by 8 grid points. The transformed equations (8) were computed with a transformation parameter $\alpha = 0.92$. The time step was 2.0×10^{-3} . The computation for the time range $0 \leq t \leq 10$ required a total of 48 minutes of CPU time on a single IBM SP2 node. Since the computations were made on a four-variable system that includes the density, we estimate that this corresponds to about 36 minutes for the system defined in the problem statement.

Contours of the pressure at the times $t = 6, 8, 10$ are shown in Fig. 4. We see that the pressure pulse propagates smoothly through the subdomains and out of the grid. Time traces requested in the problem statement at $r = 5$, and $\theta = 90^\circ, 135^\circ, 180^\circ$ for time between 6 and 10 are shown in Fig. 5. Plotted with the computed solutions are the exact solutions. Table 1 shows the maximum errors at the requested probe points over the time interval requested. We see that at five points per wavelength, the maximum error in the three cases is less than 1×10^{-6} .

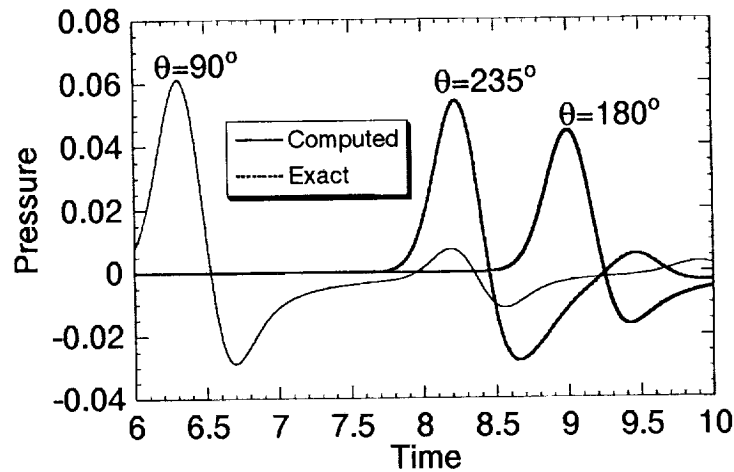


Figure 5: Pressure vs. time for the scattering of a gaussian pulse off a circular cylinder at the three probe points.

θ	Max Error
90°	4.7×10^{-7}
135°	6.2×10^{-7}
180°	7.0×10^{-7}

Table 1: Maximum Error at probe points for Problem 1.2

CONCLUSIONS

We have used a Chebyshev spectral multidomain method to solve two of the workshop benchmark problems. The method, described in detail in [7], has been modified by the use of a stretching transformation to extend the range of accurately represented Fourier modes and to increase the allowable time step. In the first problem, we use an average of five points per wavelength. We find that the Category 1, Problem 1 solution requested is accurate to 2.6% at $r = 15$. In the second problem, with eight points across the width of the initial pulse, we find that over the times and at the angles requested, the maximum error is less than 10^{-6} .

References

- [1] C. Canuto, M. Hussaini, A. Quarteroni, and T. Zang. *Spectral Methods in Fluid Dynamics*. Springer-Verlag, New York, 1987.
- [2] M. Carpenter and C. Kennedy. Fourth-order $2n$ -storage runge-kutta schemes. *SIAM J. Sci. Comp.*
- [3] F. Q. Hu. On absorbing boundary conditions for linearized euler equations by a perfectly matched layer. *J. Comp. Phys.*, 129:201–219, 1996.
- [4] D. A. Kopriva. A spectral multidomain method for the solution of hyperbolic systems. *Appl. Num. Math.*, 2:221–241, 1986.
- [5] D. A. Kopriva. Spectral solution of acoustic wave-propagation problems. 1990. AIAA-Paper 90-3916.
- [6] D. A. Kopriva. A conservative staggered-grid chebyshev multidomain method for compressible flows. ii. a semi-structured method. *J. Comp. Phys.*, 128:475–488, 1996.
- [7] D. A. Kopriva and J. H. Kalias. A conservative staggered-grid chebyshev multidomain method for compressible flows. *J. Comp. Phys.*, 125:244–261, 1996.
- [8] D. Kozloff and H. Tal-Ezer. A modified chebyshev pseudospectral method with $o(n-1)$ time restriction. *J. Comp. Phys.*, 104:457–469, 1993.
- [9] H.-O. Kreiss and J. Oliger. *Methods for the Approximate Solution of Time-Dependent Problems*. World Meteorological Organization, Geneva, 1973. GARP Rept. No.10.
- [10] A. Patera. A spectral element method for fluid dynamics. *J. Comp. Phys.*, 54:468–488, 1984.
- [11] C. Tam. Computational aeroacoustics: Issues and methods. *AIAA J.*, 33:1785, 1995.

59-71
0413 467
293959 p6

Application of Dispersion-Relation-Preserving Scheme to the Computation of Acoustic Scattering in Benchmark Problems

R. F. Chen and M. Zhuang
Department of Mechanical Engineering
Michigan State University
East Lansing, MI 48824

SUMMARY

The results for the first two CAA benchmark problems of the category 1 are presented here. These two problems are designed for testing curved wall boundary conditions. The governing equations for the problems are the linearized Euler equations. For the better treatment of the curved boundary, coordinate transform is used to map the Cartesian coordinate system to polar coordinate system. The governing equations are discretized using the Dispersion-Relation-Preserving (DRP) scheme of Tam and Webb. The DRP schemes with artificial viscosity terms are evaluated as to their suitability for equations in curvilinear coordinate system.

INTRODUCTION

The computation of aeroacoustic problems requires numerical schemes of high accuracy, low dispersion and almost non-dissipation.^{1,2} Recently developed 7-point stencil Dispersion-Relation-Preserving (DRP) scheme of Tam and Webb³ was designed so that the dispersion relation of the finite difference scheme is formally the same as that of original partial differential equations. The DRP method has been shown to be quite successful on calculating linear waves in many acoustic computations^{3,4,5}.

In this work the DRP method is used to solve the acoustic scattering problems in the presence of a curved wall boundary. The physical problem is to find the sound field generated by a propeller scattered off by the fuselage of an aircraft. The fuselage in our computations is idealized as a circular cylinder, and the noise source is given at a specified location. Since the problems are axisymmetric, the computations are conducted only for the upper half of the flow field. Computational domain is chosen as a semi-circular region (see Fig. 1) which is

bounded by an outer semi-circle, the cylinder wall, and the axisymmetric lines. The meshes are generated by the circumferential and radial lines.

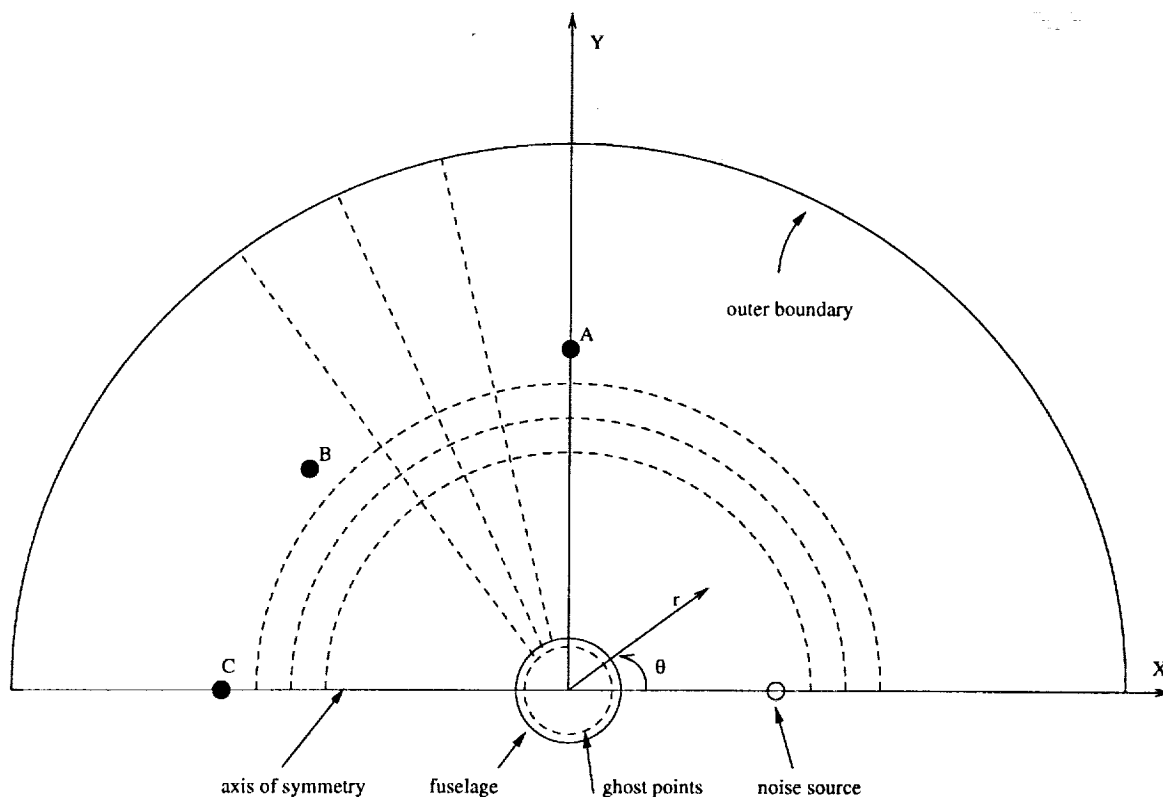


Figure 1: schematic diagram showing the computational domain and boundaries.

Two different noise sources are considered, the first one is a time periodic source and the second one is non-time-periodic source but with a given initial pressure disturbance.

NUMERICAL PROCEDURE

The governing equations with artificial viscosity terms for the transferred polar coordinate system are given as follows:

$$\frac{\partial u}{\partial t} + \cos \theta \frac{\partial p}{\partial r} - \frac{\sin \theta}{r} \frac{\partial p}{\partial \theta} = \nu \left(\frac{\partial^2 u}{\partial r^2} + \frac{1}{r} \frac{\partial u}{\partial r} + \frac{1}{r^2} \frac{\partial^2 u}{\partial \theta^2} \right) \quad (1)$$

$$\frac{\partial v}{\partial t} + \sin \theta \frac{\partial p}{\partial r} - \frac{\cos \theta}{r} \frac{\partial p}{\partial \theta} = \nu \left(\frac{\partial^2 v}{\partial r^2} + \frac{1}{r} \frac{\partial v}{\partial r} + \frac{1}{r^2} \frac{\partial^2 v}{\partial \theta^2} \right) \quad (2)$$

$$\frac{\partial p}{\partial t} + \cos \theta \frac{\partial u}{\partial r} - \frac{\sin \theta}{r} \frac{\partial u}{\partial \theta} + \sin \theta \frac{\partial v}{\partial r} + \frac{\cos \theta}{r} \frac{\partial v}{\partial \theta} = S + \nu \left(\frac{\partial^2 p}{\partial r^2} + \frac{1}{r} \frac{\partial p}{\partial r} + \frac{1}{r^2} \frac{\partial^2 p}{\partial \theta^2} \right) \quad (3)$$

where damping factor $\nu = \epsilon \Delta r \times \Delta \theta$ with the damping coefficient ϵ . Here the artificial viscosity is added to damp out spurious oscillation.

The DRP spatial difference scheme is applied for both the first order derivatives, $\partial/\partial r$ and $\partial/\partial \theta$, and the second order derivatives $\partial^2/\partial r^2$ and $\partial^2/\partial \theta^2$. The derivatives are discretized by seven-point damping stencil of Tam and his colleagues for interior points. Near the boundary standard five-point and three-point central difference schemes are used for the second order derivatives. So the values of time derivatives at grid points are then obtained from the equations and DRP time marching scheme can thus be used to get values of variable at next time level.

BOUNDARY AND INITIAL CONDITIONS

Boundary and initial conditions for the acoustic simulations are given below:

Solid Wall: The pressure derivative condition at the cylinder surface $\frac{\partial p}{\partial r} = 0$ is derived from the governing equations using the no-slip condition, $\vec{V} \cdot \vec{n} = 0$, at the cylinder wall. One row of ghost points for p is placed inside the circle to enforce this condition. Ghost points are shown in figure 1. One-side DRP schemes are used for discretizing velocities u and v near the boundary.

Axis of Symmetry: The symmetric boundary conditions, $u(x, y) = u(x, -y)$, $v(x, y) = -v(x, -y)$ and $p(x, y) = p(x, -y)$, are used near the x-axis.

Outer Boundary: Radiation conditions² are used near the outer boundary. Instead of solving the linearized Euler equations, the following equations are solved:

$$\left(\frac{\partial}{\partial t} + \frac{\partial}{\partial r} + \frac{1}{2r} \right) \begin{bmatrix} u \\ v \\ p \end{bmatrix} = 0. \quad (4)$$

Initial Condition: For both problems, the initial velocity is zero, $u = v = 0$, because of no fluid flow at the beginning. For the problem 1, there is a periodic disturbance source located at $(4, 0)$ described by the expression below:

$$S = \exp\left[-\ln 2 \left(\frac{(x-4)^2 + y^2}{0.2^2} \right)\right] \sin \omega t.$$

For the problem 2, a pressure disturbance located at (4, 0),

$$p = \exp\left[-\ln 2\left(\frac{(x-4)^2 + y^2}{0.2^2}\right)\right],$$

is initially released.

RESULTS AND DISCUSSION

Two sets of grid are used for the problem 1. One is 400×360 with $\Delta r = 0.02$ and $\Delta\theta = 0.5^\circ$ and the other one is 200×180 with $\Delta r = 0.04$ and $\Delta\theta = 1^\circ$. In both cases the outer boundary is chosen as 8 times the diameter of the cylinder. Time step is determined by the formula

$$t = \frac{0.19\Delta r}{1.75\sqrt{1 + (\Delta r/\Delta\theta)^2}}.$$

The damping coefficient ϵ is chosen as $1/60$ after several trials. The result of directivity as a function of the angle θ is shown in Fig. 2. The directivity here is defined by

$$D(\theta) = \lim_{r \rightarrow \infty} r\overline{p^2},$$

where r is chosen as 7.5 and time average of pressure square is obtained over two time periods of t from 39.5 to 40, in which the pressure p is almost periodic. Different patterns shown in the Fig. 2 indicate that the finer grid 400 should be used in order to predict the directivity correctly. In the computation of problem 2, The grid 200×180 with $\Delta r = 0.0375$ and $\Delta\theta = 1^\circ$ are used. The outer boundary is chosen as 7.5 times the diameter of the cylinder with the time step $\Delta t = 0.001$ and the damping coefficient $\epsilon = 1/20$. The Fig. 3 shows the pressure as a function of time for three different points A, B and C shown in figure 1. The profiles of the first wave and its reflection wave can be clearly seen in the Fig. 3.

We should mention that the simulations of both problems can also be proceeded without any artificial viscosity, but spurious short waves is observed with the reflection waves.

CONCLUSIONS

The aeroacoustic computations with curved boundary are presented here. One way to handle this class of problems is to map a non-rectangle domain into a rectangular domain. The

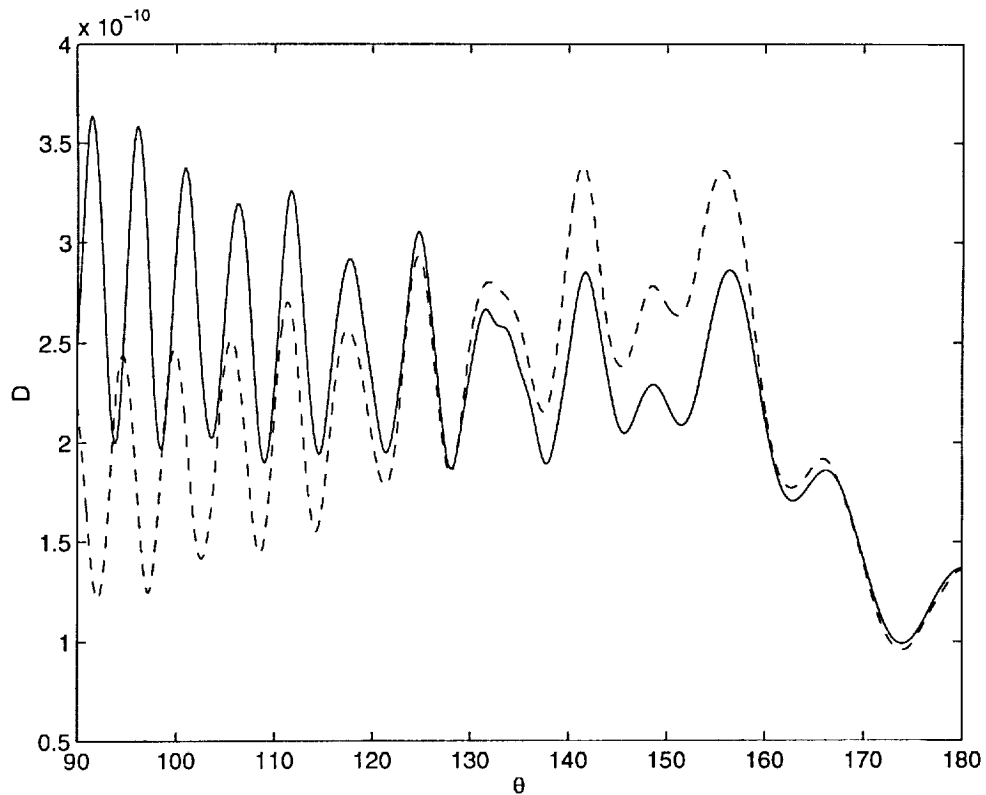


Figure 2: Directivity versus angle for problem 1. Solid line is for 400×360 and dash line is for 200×180

resulting governing equations in curvilinear coordinate systems can then be discretized by the DRP methods. Numerical results in our applications show that this is a valid approach. The DRP methods require explicit artificial viscosity for some complicate flows. Artificial viscosity becomes even more important when there is discontinuous jump in flow field. Different problems require different artificial viscosity factors, the adjustment of which might need many trials.

REFERENCE

1. Tam, C. K. W., "Computational Aeroacoustics: Issues and Methods", *AIAA Journal*, Vol. 33, No. 10, Oct. 1995, pp. 1788-1796.
2. Lockard, D. P., Brentner, K. S. and Atkins, H. L., "High-Accuracy Algorithms for Computational Aeroacoustics", *AIAA Journal*, Vol. 33, No.2, Feb. 1995, pp. 246-251.

3. Tam, C. K. W. and Webb, J. C., "Dispersion-Relation-Preserving Finite Difference Schemes for Computational Acoustics", *J. Comput. Phys.*, Vol. 107, NO. 2, Aug. 1993, pp. 262-281.
4. Tam, C. K. W., Webb, J. C. and Dong, Z., "A Study of The Short Wave Components in Computational Acoustics", *J. Comput. Acoustics*, Vol. 1, No. 1, 1993, pp. 1-30.
5. Tam, C. K. W. and Dong, Z., "Wall Boundary Conditions for High-Order Finite-difference schemes in Computational Aeroacoustics", *Theoret. Comput. Fluid Dynamics*, Vol. 6, 1994, pp. 303-322.

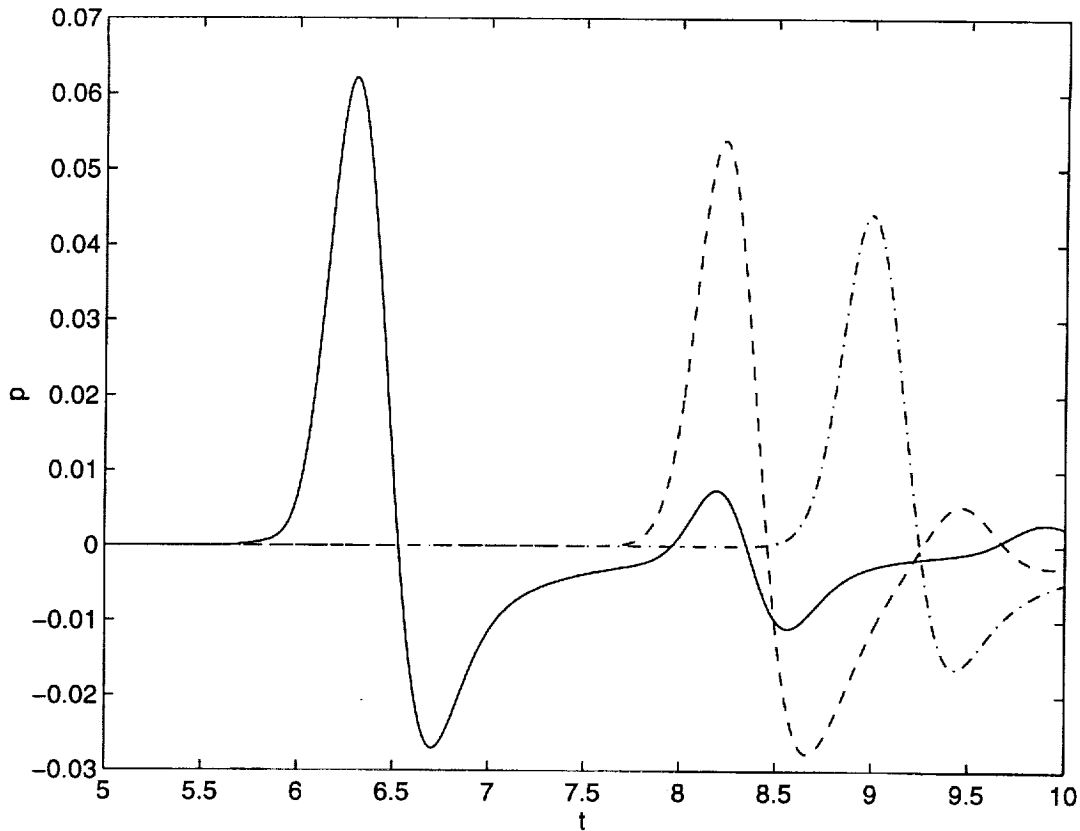


Figure 3: pressure versus time for problem 2. solid line for pressure at point A ($r = 5$, $\theta = 90^\circ$); dash line for pressure at point B ($r = 5$, $\theta = 135^\circ$); dash dot line for pressure at point C ($r = 5$, $\theta = 180^\circ$).

510-32
043468
293961 p8

DEVELOPMENT OF COMPACT WAVE SOLVERS AND APPLICATIONS

K.-Y. Fung

The Hong Kong Polytechnic University

(Voice: 852-2766-6644; Fax: 852-2364-7183; email: mmkyfung@polyu.edu.hk)

ABSTRACT

This paper reports the progress in the development of solvers based on a compact scheme for the computation of waves scattered and diffracted by an arbitrary surface. The formulation that allows the reduction of multidimensional wave problems involving curved surfaces into a set of one-dimensional problems involving line segments will be revisited and the schemes for labeling and enforcing time-domain physical or impedance boundary conditions on an arbitrary surface will be briefly introduced. Applications of these algorithms and benchmarking comparisons with available exact solutions for scattering and diffraction of harmonic and compact wave sources by generic and realistic geometries are presented, and results for Problem 2 of Category 1 are reported.

INTRODUCTION

The major difficulties for time-domain approaches to wave computation are representation of curved surfaces and enforcement of boundary conditions on these surfaces. Current methods can be classified into four types: 1) the use of simple unstructured elements to fill the space restricted by the surface, 2) the mapping of the bounding surface to a coordinate plane, 3) the labeling of boundary points and application of special stencils for them, and 4) the employment of domain inhomogeneities for their desirable reflective or absorptive properties. The use of structured and unstructured surface-conforming grids has been quite successful for steady flow computations. This success is largely due to effective suppression of all physical and spurious waves by artificially added damping during convergence. The technique of adding artificial viscosity for enhanced algorithmic stability can be detrimental for wave computation. Surface-conforming grids may be inappropriate for their often hard-to-control excessive stretching and skewness and the resultant equations after the transformation are so entangled with the coefficients of transformation that only explicit and stability-stringent boundary conditions are practical, compromising the accuracy and effectiveness of the interior scheme. On the other hand, if Cartesian coordinates are used, the management of the points on a curved surface may become too complex for many schemes, particularly implicit ones to operate efficiently. The employment of domain inhomogeneities avoids the management of boundary points for rectangular grids but compromises the accuracy of the surface definition to within a grid cell and correspondingly a reduction of numerical accuracy.

Reference [1] describes the development of a new class of efficient and accurate numerical schemes for computation of waves. It demonstrates that wave propagation in a multi-dimensional medium involving solid boundaries can be efficiently and accurately predicted using an **implicit** scheme on a suitable, finite, not asymptotically large domain without having to apply specific outgoing conditions at the domain boundaries. The advances described in this paper are: 1) development of an essentially fourth-order, unconditionally stable, implicit scheme having a simple three-point, two-level data structure suitable for various nonuniform grids, 2) introduction of an implicit, stable, characteristically exact, easily implementable end scheme for the exit of wave at any end point of a numerical domain, and 3) demonstration of the feasibility of solving multi-

dimensional wave equations as a system of uni-directional wave equations, thus reducing three-dimensional problems with curved surfaces to one-dimensional problems of lines.

We will revisit the idea and rationale behind the reduction of a multi-dimensional problem into a system of one dimensional problems, explore the issues and extend the schemes proposed in [1] to accommodate possible irregularities due to a realistic geometry and the associate boundary condition, and introduce a method for imposing characteristically exact and numerically accurate boundary conditions and the associate data management scheme for solving wave propagation problems involving a realistic geometry on rectangular grids.

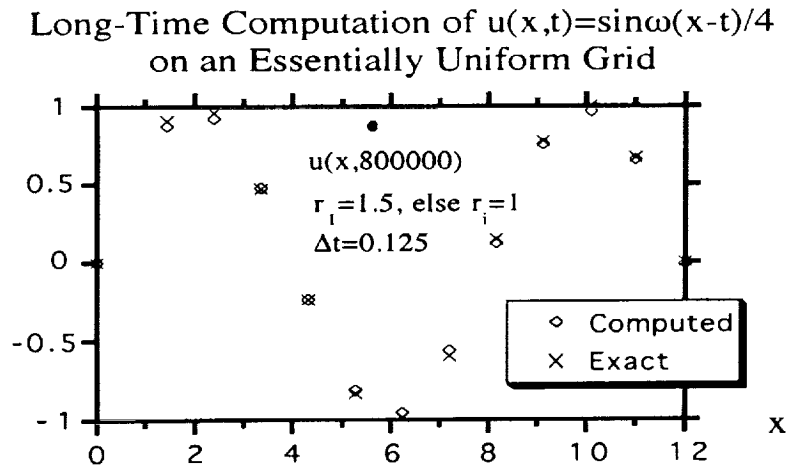


Figure 1 The simple, right-propagating sine wave was computed on an EUG of thirteen points over the domain of 1.5 wavelengths. Similar experiments have been conducted to show same accuracy on EUGs with left or right end grid ratios of $0.5 < r < 1.5$.

NATURAL WAVES IN ONE DIMENSION

The formally third order C3N compact scheme [1], having a three-point two-level data structure closed with a characteristically exact exit condition, forms a numerical simple wave solver for the simple wave equation,

$$(1) \frac{\partial u}{\partial t} + c \frac{\partial u}{\partial x} = 0,$$

and the basis for the approach and extensions here. This robust, accurate, simple wave solver allows a signal to enter at one end and leave cleanly at the other. It has been tested on various grid types and equation models for wave. Once initialized, an array passed into this solver is updated by the specification of the entry wave value $u(a,t)$ as theory requires, where a is the left or right end of the interval depending on the sign of c . Regardless of the grid distribution and time stepping, long-time stable arrays are returned. In particular, numerical experiments have substantiated that fourth-order scheme accuracy (eight grid point per wave length) is achievable on *Essentially Uniform Grids*, EUG, everywhere uniform but the end points. Figure 1 shows the long-time (conveniently chosen at $t=800,000$) computation of a right-running wave with a left EUG of grid ratio $r_1=(x_1-x_0)/(x_2-x_1)=1.5$. The computation can be conducted indefinitely and the RMS error is essentially unchanged after $t > 15$. Similar results with grid ratios $0.5 < r < 1.5$ at both ends have

supported that C3N is long-time stable and fourth order accurate on EUG. This feature of allowing even abrupt nonuniformity in the grid, especially at end points, is essential for extension to multi-dimensional problems involving curved surfaces.

The extension of the simple wave to a system of waves is essential for description of natural wave phenomena. Since an isotropic medium has no preferred direction, propagation of a wave in one direction implies the capability to propagate in the opposite direction, or in any direction in a multi-dimensional space. At a given time when a wave is observed in an infinite one-dimensional space, its future is already determined by solution of a Cauchy problem. For a natural wave to assume a preferred direction with a particular waveform, the directional information must be encoded in the initial data. This is possible only if there are two independent sets of data in a wave. A specific type of combination of the sets excludes propagation in the other direction. Thus, a natural wave in one dimension must have two components which satisfy a set of complementary equations. The extension of the simple wave $u(x-ct)$ to a natural wave system must then be the addition of the complementary component $v(x+ct)$ corresponding to the substitution $c \rightarrow -c$. The simple wave by itself is not natural, since the direction is reference frame dependent. This implies that a natural wave must be governed either by a second-order partial differential equation for one state variable, or equivalently by two first-order PDE for two state variables, i.e.,

$$(2a) \quad \frac{\partial}{\partial t} \begin{pmatrix} u \\ v \end{pmatrix} + \begin{pmatrix} c & 0 \\ 0 & -c \end{pmatrix} \frac{\partial}{\partial x} \begin{pmatrix} u \\ v \end{pmatrix} = \begin{pmatrix} 0 \\ 0 \end{pmatrix}; \text{ or}$$

$$(2b) \quad \frac{\partial^2 \phi}{\partial t^2} - c^2 \frac{\partial^2 \phi}{\partial x^2} = 0; \text{ with } \phi = \alpha u + \beta v.$$

A natural wave is then determined by specification of (α, β) using the boundary and/or initial conditions. The components (u, v) either satisfy Eq. (2a) individually or their linear combination ϕ satisfies Eq. (2b). Therefore, extension from a simple wave to a system of waves is not only necessary, the method of prediction should also be extendible from one wave component to a system. Equation (2) implies that any physical variable ϕ other than the *characteristic* variables (u, v) can only be described by the second-order form Eq. (2b). Hence, any formulation in primitive variable form would have to deal with the difficulty of having to address the appropriate conditions for the two boundaries in each spatial dimension.

It is, therefore, important to consider extension of a simple wave solver to solution of a system of waves. Equally important is the realization that in characteristic form the components (u, v) satisfy distinct equations and are uncoupled on an unbounded domain. On a bounded domain, the components are unrelated everywhere except at the boundaries (i.e., the left and right ends in one dimension). Thus, once initiated, the solution of each component requires only the value at wave entry as determined by the sign of c . If $u(a, t)$ is given at the entry point a , $u(b, t)$ is fully determined at exit end b . Exactly the opposite is true for the complementary component $v(x, t)$ at its entry point b and exit point a . It is then clear that any condition on a physical quantity, i.e., $\phi = \alpha u + \beta v$, at a boundary point must use the boundary-exiting component to determine the boundary-entering component, i.e., $\alpha u(a, t) = -\beta v(a, t) + \phi(a, t)$. The fact that the components u and v are linearly independent assures that any given $\phi(a, t)$, other than the unallowed specification of the exit value $v(a, t)$ (the grossly ill-posed case $\alpha=0$), determines the domain-entering component $u(a, t)$ uniquely. It is also clear that the components of a natural wave system cannot be explicitly specified at a boundary unless they satisfy some compatibility conditions. In any form other than characteristic, the equations are everywhere coupled, allowing lateral communication between components and exchange of error over the entire interval $[a, b]$. Therefore, the only way to avoid unwarranted coupling is to solve the equations in characteristic form. If one end is unbounded, or no waves have reached this end, the solution of a system can easily be obtained by first applying

the simple wave solver to the exiting component for the bounded end and relating the newly updated exit value through the physical constraint to the entry value of the entering component . If both ends are bounded, the proper way to solve the system is to connect the arrays and solve the assembled system, including the boundary conditions at both ends, using a cyclic tridiagonal solver.

MULTI-DIMENSIONAL WAVE SOLVER

The groundwork for extensions to multi-dimensional wave problems has been laid in [1], although none of the examples given there involved curved surfaces. In [1] the two-dimensional Euler equations were split for each spatial dimension into systems of one-dimensional waves and solved using the system wave solver. After a sweep of all wave components in one direction, the variables are converted directly into characteristic form and swept in the other direction. In alternating sweeps, only p is exchanged and, hence, advanced twice. Both u and v are advanced once in x and y , respectively. Therefore, the sweeping order, x - y or y - x , is unimportant. If the sweeps are done alternately, only one array for each variable needs to be stored. If u and v are advanced in parallel (for massively parallel computing systems) an additional array is needed for storing the directional changes in pressure. The latter can be completely symmetrical at the expense of a slight increase in memory and operation count, since u and v are advanced independently and unaffected by the intermediate pressure changes until they are summed. Thus, the only question remaining is the validity of the condition at finite boundaries where values of the domain-entering components must be specified. For generalized curvilinear coordinates, equation splitting and component decoupling may not be effective or possible. How, then, can a general curved surface be taken into consideration in a rectilinear coordinate system?

Once split a wave domain can be seen as an array of straight wave conduits in each spatial direction, the presence of the surface of an object blocks and segments these conduits. Each conduit or line in the simplest case becomes two semi-infinite lines. Again, the rule for bounded domains applies. For each line segment the components propagating towards the wall can be integrated up to the surface point. After all such wall-bound components from all directions are found up to the surface, the physical constraint there is sufficient to determine the domain-entering components (i.e., the reflections). Some grid lines may not intersect the object and thus remain unbounded. Thus, the grid lines are divided into bounded and unbounded grid line blocks. Strategies for solution sweeping on unbounded and bounded grid blocks are different. Operator symmetry, and direction and order of sweep may affect accuracy. However, the best strategy for sweeping a partially bounded domain can be numerically determined, and directional symmetry can be ascertained by exchanging indices in the data management of the sweeps.

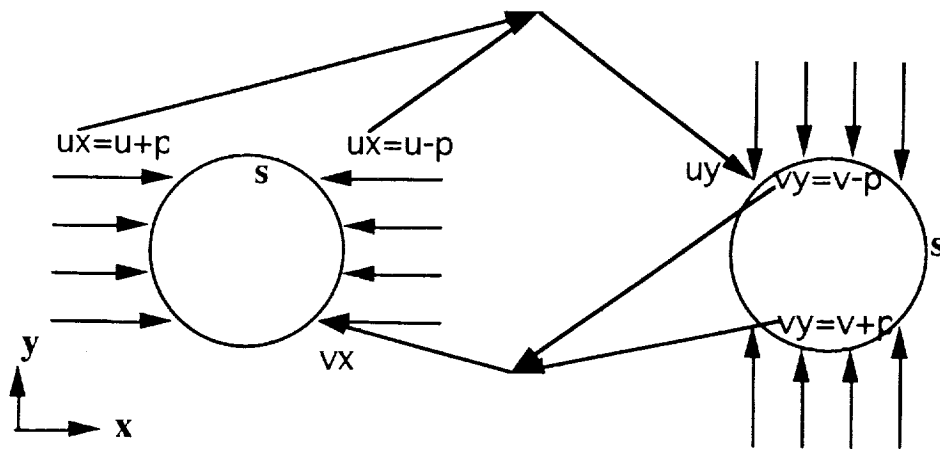


Figure 2. Data flow of wall-bound values from x-lines to y-lines.

Figure 2 shows intersections of horizontal and vertical grid lines with a circle, which is a convex object and allows two intersection points per grid line. Even when a line is tangent to the circle, it can still be considered as two numerically distinct points. For concave or wavy surfaces, multiple intersections by one grid line are possible, forming two types of segments, finite and semi-infinite. Solution logic and sweeping strategy may be different, depending on the segment type. Given an arbitrary curve, a routine can be written to search for the intersection points (xx,yy) , denoting the (x,y) pairs in an x -grid line. These points in general do not coincide with a grid node. The distance Δx_s between a surface point and the closest grid point is greater than zero but less than a full grid step Δx . To avoid the extreme case where Δx_s is close to machine zero, logic can be built in to extend the next grid point to the surface point $\{- - + - + - + - -\}$ or add the surface point as an additional grid point $\{- - + - + - + -\}$. Thus, the ratio between neighboring steps satisfies $\Delta x_s/\Delta x = r \leq 1.5$ when the regular grid point is extended, and $r > 0.5$ when a grid point is added. Since the spacing of the grid near the ends of a segmented grid line may change abruptly, the importance of a robust solver for nonuniform grids is clear. If the last grid point is extended, the value at the eliminated point is retrieved by interpolation from the newly updated solution, as if the solution had been computed on the original grid.

Separate arrays $ux(xx,yy)$, $vx(xx,yy)$ for the wave components at surface points $(xx(s),yy(s))$ along the surface coordinate s are stored for enforcement of boundary conditions. Here ux and vx denote the vector wave components at a surface point intersected by an x -grid line. After the first x -sweep the set of wall-bound values ux at the surface is computed and transferred by interpolation to the set of values uy at the surface points (xy,yy) intersected by y -lines, and similarly (xz,yz) by z -lines. After all sweeps for the wall-bound components from all directions are computed and transferred, each surface point on a grid line will have all components of the wave vector (e.g., u - p and v - p) stored as (ux,vx) for a bounded x -line and (uy,vy) for a bounded y -line. Each pair together with the surface normal vector (e_x, e_y) is sufficient to satisfy a physical constraint, such as $ue_x + ve_y = 0$, determine the unknown temporal variation p , and form the domain-entering characteristics $(u+p, v+p)$. A subroutine can be written to transform the surface values from wall-bound to domain-entering variables, and vice versa, and enforce numerically exact boundary conditions.

APPLICATIONS

Figure 3 shows the diffraction (left) of a harmonic plane wave train by the cylinder of radius $R=5$ computed on a 120×120 uniform rectangular grid filling the 15×15 domain as exactly shown without employing a buffer zone or outgoing boundary condition. The directivity pattern (right) evaluated at the computational boundaries compares well with the analytical solution [2]. Figures 4a and 4b show the computed pressure contours of a plane Gaussian pulse diffracted by a projected contour of the Sikorsky S-70 on a 100×100 uniform grid, at $t=10$ and 20 , respectively, following initiation at $t=0$ (when the wave centerline is at a distance of 12.5 units from the grid center). The entire computational domain is shown; no buffer zone was used. The incident wave enters the top and left boundaries and leaves the right and bottom boundaries. The diffracted wave is quite clear, as well as the satisfaction of the wall boundary condition, having contours normal to the true surface. Both domain-entering and -exiting waves are allowed on each boundary without spurious reflections. Figures 4c and 4d show essentially same contours except that the incident pulse and the fuselage are rotated -45° with respect to the grid. Since the body is defined by marking the surface points on the grid lines, its movements with respect to the grid can easily be effected by changing the markings. Thus, the formidable body-conforming grid generation problem which often leads to solution degradation, especially in three dimensions, is avoided. The contour used was represented by a set of points taken from a photograph. To avoid the development of spurious waves due to abrupt changes of contour slope, a damping of $\epsilon=0.001$ was added as a default value for a range of computations, including that for Fig. 3. This damping was later found to be excessive for high frequencies after the presentation of Problem 2 of

Category I at the Workshop. Figure 5 shows the same computation as presented but without the defaulted damping, which is not needed. Good agreement with the analytical solution is found for the solution computed on a 281x281 rectangular grid over a domain of 14x14 centered about the cylinder using a time step of 0.02. The recomputation of Problem I of Category I has not been completed by the deadline for submission.

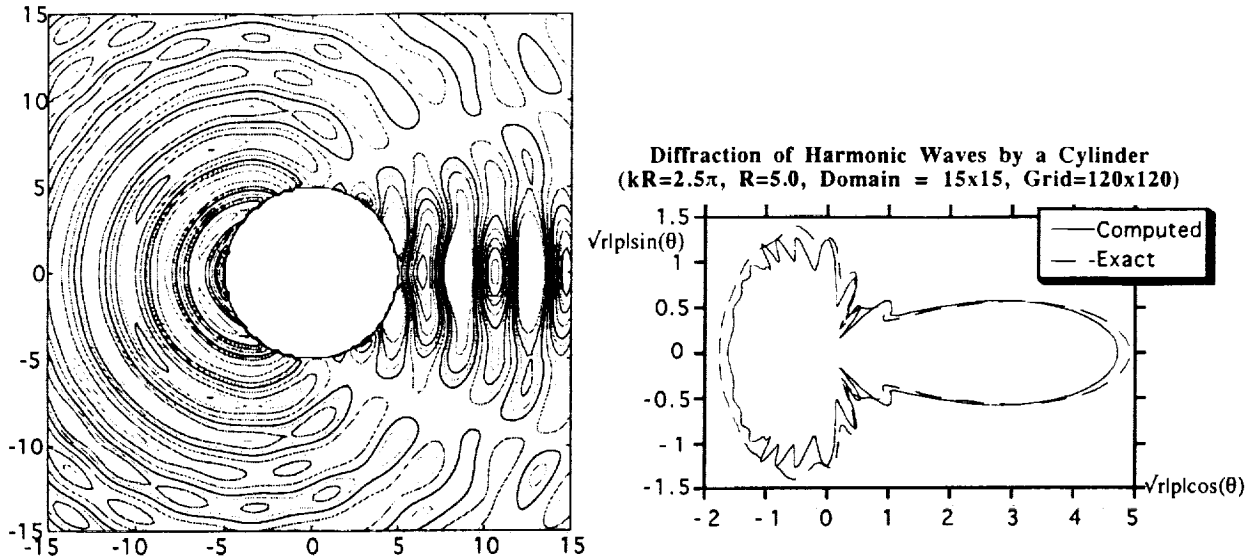


Figure 3. Computed diffraction pressure field of a plane harmonic wave train impinging on the cylinder (left), and corresponding comparison with the exact directivity pattern (right).

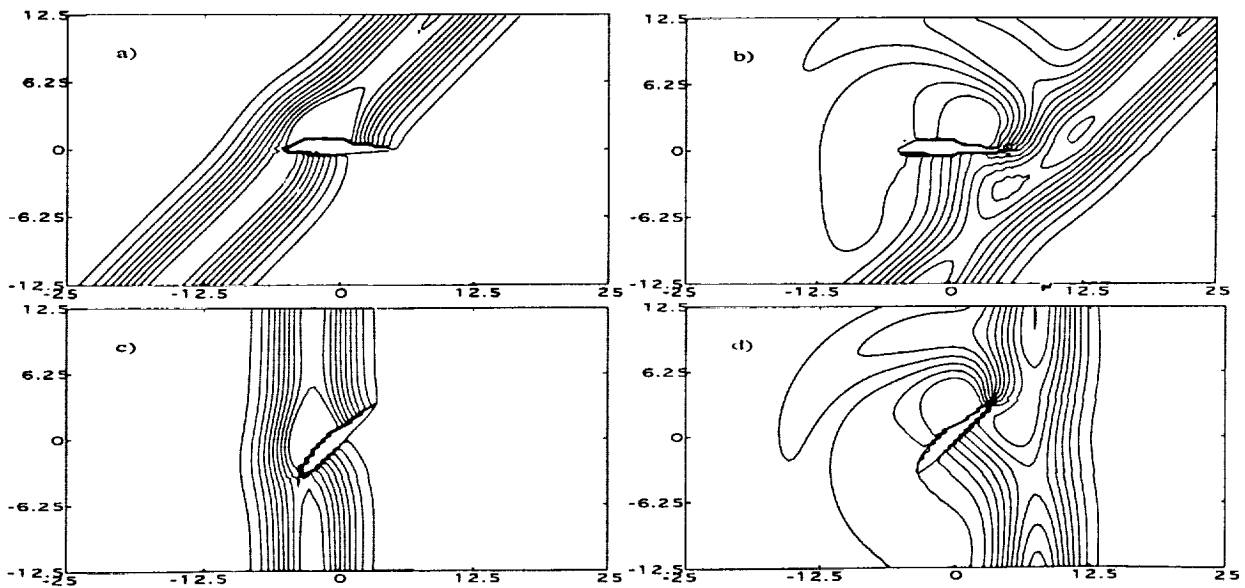


Figure 4. Pressure contours of a plane Gaussian pulse diffracted by a projected fuselage of the Sikorsky S-70 at $t=10$ (left figures) and $t=20$ (right figures). Top figures were computed with fuselage aligned with the horizontal x-axis and incident wave at 45° ; bottom figures with fuselage and wave rotated -45° but computed on the same 100x100 uniform grid.

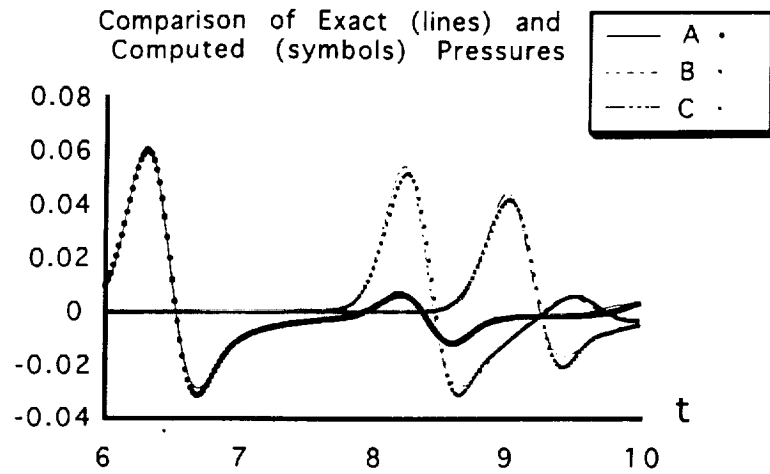


Figure 5, Comparison of Solutions for Problem 2 of Category 1

REFERENCES

1. K.-Y. Fung, R. Man and S. Davis; "An Implicit High-Order Compact Algorithm for Computational Acoustics," Vol. 34, No. 10, pp. 2029-2037, *AIAA J.*
2. Morse, P. M. and Ingard, K. U., "Theoretical Acoustics," McGraw-Hill, New York, 1968.

511-71

043469

Computations of acoustic scattering off a circular cylinder 293962

p8

M. Ehtesham Hayder

Institute for Computer Applications in Science and Engineering
MS 403, NASA Langley Research Center, Hampton, VA 23681-0001

Gordon Erlebacher and M. Yousuff Hussaini

Program in Computational Science & Engineering
Florida State University, Tallahassee, FL 32306-3075

Abstract

We compute the sound field scattered off a circular cylinder as given in category 1. The linearized Euler equations are solved using a multi-block algorithm. A Low-Dissipation and Low-Dispersion Runge-Kutta Scheme is adopted for the time integration, while spatial derivatives are discretized with a combination of spectral and 6th order compact schemes. In this study, spectral discretization is performed in the radial direction in domains adjacent to the cylinder. Away from the cylinder and in the azimuthal direction we use compact differencing. Explicit filtering of the solution field is avoided. We exploit the symmetry of the problem and only compute the solution in the upper half plane. Symmetry boundary conditions are built into the derivative operators. Absorbing layers near the computational boundary at large radii minimize numerical reflections. The absorbing-layer equations are based on the Perfectly Matched Layer (PML) formulation of Hu (1996).

Problem Formulation

Problems in category 1 model the sound field generated by a propeller and scattered by the fuselage of an aircraft. The model consists of a line noise source (propeller) and a circular cylinder (fuselage). The governing equations are the linear Euler equations:

$$\begin{aligned}\frac{\partial u}{\partial t} + \frac{\partial p}{\partial x} &= 0 \\ \frac{\partial v}{\partial t} + \frac{\partial p}{\partial y} &= 0 \\ \frac{\partial p}{\partial t} + \frac{\partial u}{\partial x} + \frac{\partial v}{\partial y} &= S(x, y, t).\end{aligned}$$

where $S(x, y, t)$ is an acoustic source term.

The above equations are transformed to polar coordinates through $x = r \cos \theta$, $y = r \sin \theta$ which leads to the transformed Euler equations

$$\frac{\partial U}{\partial t} + \frac{\partial p}{\partial r} = 0$$

$$\frac{\partial V}{\partial t} + \frac{1}{r} \frac{\partial p}{\partial \theta} = 0$$

$$\frac{\partial p}{\partial t} + \frac{1}{r} \frac{\partial(rU)}{\partial r} + \frac{1}{r} \frac{\partial V}{\partial \theta} = S$$

where U and V are velocity components in the radial and azimuthal directions respectively. Boundary conditions on the cylinder demand a zero normal velocity.

We consider problem 1 for which

$$S(x, y, t) = \exp \left[-\ln 2 \left(\frac{(x-4)^2 + y^2}{(0.2)^2} \right) \right] \sin(8\pi t)$$

and problem 2 for which $S(x, y, t) = 0$. Initial conditions in problem 2 are given by $u = v = 0$ and

$$p = \exp \left[-\ln 2 \left(\frac{(x-4)^2 + y^2}{(0.2)^2} \right) \right].$$

Numerical Method

The governing equations are solved with a recently developed multi-block algorithm. In each domain, and in each coordinate direction, derivatives are either spectral or 6th order compact. On domains which abut a solid boundary, spectral discretization is chosen normal to the boundary to improve the dissipation characteristics of the derivative operator. Away from wall, and in the azimuthal direction, a compact discretization is preferred for reasons of computational efficiency. If N is the number of points along a coordinate direction, the cost of a derivative computation is $O(N)$ for compact schemes, and $O(N^2)$ for spectral methods. Spectral domains are often limited to a maximum of 15 points in each direction, leading to a high number of domains. Higher densities of grid points on spectral discretizations are also detrimental to explicit time stepping algorithms.

Compact difference schemes in general lack adequate numerical damping and filtering is often required to eliminate high frequency errors in the computational domain. However, we prefer to avoid explicit filtering of the solution. There is no general prescription on how the filtering should be applied or how often. These decisions are often left to the intuition of the numerical analyst. Time integration is implemented with a Low-Dissipation and Low-Dispersion Runge-Kutta Scheme [Hu et al., 1996].

The problem is symmetric about $\theta = 0$; we only compute the solution for $0 \leq \theta \leq \pi$. To this end, the compact operator stencil is modified at the symmetry plane to maintain 6th order accuracy. In the radial direction, we use then standard $5^2 - 6 - 5^2$ scheme [Carpenter et al., 1993].

We use a non-staggered uniform mesh in the coordinate directions used by the compact derivative stencils, and a Gauss-Lobatto grid in the directions used by the spectral differentiation. Along the domain edges, continuity of the fluxes is imposed normal to the domain interfaces. As a consequence, only two domains are taken into account at all boundary points, including corners (by continuity). Continuity of normal fluxes is imposed at

the boundary interface (in computational space), which leads to discontinuous values of the primitive variables. Except for the grid and the discretization, the scheme partially follows that of Kopriva (1996).

To minimize numerical reflections in the far field direction, we implement an absorbing layer technique in the radial direction. The absorbing-layer equations are obtained by operator-splitting the governing equations in the two coordinate directions and by introducing absorption coefficients in each split equation. Since we use the symmetry condition in the azimuthal direction, our model problem has only one absorbing layer (see Figure 1). This layer is located at large r . The equations inside the absorbing layer are

$$\begin{aligned}\frac{\partial U}{\partial t} + \frac{\partial p_1}{\partial r} &= -\sigma_r U \\ \frac{\partial V}{\partial t} + \frac{1}{r} \frac{\partial p_2}{\partial \theta} &= -\sigma_\theta V \\ \frac{\partial p_1}{\partial t} + \frac{1}{r} \frac{\partial(rU)}{\partial r} &= -\sigma_r p_1 \\ \frac{\partial p_2}{\partial t} + \frac{1}{r} \frac{\partial V}{\partial \theta} &= -\sigma_\theta p_2\end{aligned}$$

where $p = p_1 + p_2$, $\sigma_\theta = 0$, $\sigma_r = \sigma_0 z^2$ where z increases linearly from 0 at the interior/absorbing layer interface to 1 at the exterior computational boundary. In general one may also have a layer which is parallel to the radial direction, i.e., at a constant azimuthal location. In those layers, σ_θ is positive and σ_r is zero. Further details on the formulation of absorbing layers and their effectiveness and limitations are given by Hu, 1996 and Hayder et al., 1997. Note that the source term in the pressure equation decays rapidly from its center (i.e., $x=4$ and $y=0$, or $r=4$, $\theta=0$). It is set to zero inside the absorbing layer.

Results and discussion

The computational domain is shown in Figure 1. We use two computational blocks and an absorbing layer. For the oscillatory source in problem 1, we obtain a flow field with interference patterns. A snapshot of pressure is shown in Figure 2. This computations was done with 671 points in the radial direction (46 points in block-1 and 625 points in block-2) and 361 points in the azimuthal direction. For simplicity, we used a polar grid with the origin at the center of the cylinder. The edge of the buffer domain is at $r = 12.5$. Unfortunately, the grid spacing at the cylinder boundary is extremely tight in the azimuthal direction which forces the time step to be very small. On the other hand, although the resolution is very fine near the cylinder, it becomes coarse at large radii. Poor azimuthal resolution in the far field for our choice of grid is a weakness of the present study. This shortcoming may be overcome by increasing the number of points in the azimuthal direction at large radii (possibly through the use of multiple blocks). The absorbing layer is very effective and the oscillations vanish smoothly inside this layer. At $r = 12$ and with 361 azimuthal points, there are 48π waves around the outer boundary, which is 2.4 points per wavelength. The wavefront is almost

parallel to the radial direction, so the waves are more resolved than is indicated. Nonetheless, there is a lack of resolution at large r in the azimuthal direction as seen from Figure 3, which shows the computed and analytical $D(\theta)$ at $r = 11.44$; the analytical solution was obtained from Hu (1997). In addition to results with 361 azimuthal points (ny), we also show results with 181 azimuthal points. Lack of sufficient resolution in the azimuthal direction probably is a major cause for the disagreements between the analytical and computed solutions.

Temporal variations of pressure at point A in the problem 2 is shown in figures 4 and 5. Results for 671x361 and 671x181 grid resolutions are visually indistinguishable, and are also indistinguishable from the exact solution. This indicates sufficient azimuthal resolution at $r = 5$. However, when the number of radial points is halved, noticeable discrepancies in the solution are visible.

References

- Carpenter, M.H., Gottlieb, D. & Abarbanel, S., "The Stability of Numerical Boundary Treatments for Compact High-Order Finite-Difference Schemes." *J. Comp. Phys.* **108**, No. 2, 1993.
- Hu, F. Q., Hussaini, M. Y. and Manthey, J. L., "Low-Dissipation and Low-Dispersion Runge-Kutta Schemes for Computational Acoustics" *J. Comp. Phys.*, **124**, 177-191, 1996.
- Hu, F. Q., "On Absorbing Boundary Conditions for Linearized Euler Equations by a Perfectly Matched Layer", *J. Comp. Phys.*, **129**, 201-219. 1996.
- Hayder, M. E., Hu, F. Q. and Hussaini, M. Y., "Towards Perfectly Absorbing Boundary Conditions for Euler Equations", AIAA paper 97-9075, 13th AIAA CFD Conference, 1997.
- Hu, F. Q., Private Communications, 1997.
- Kopriva, D. A., "A Conservative Staggered-Grid Chebyshev Multidomain Method for Compressible Flows. II: A Semi-Structured Method," NASA CR-198292, ICASE Report No. 96-15, 1996, 27 p.

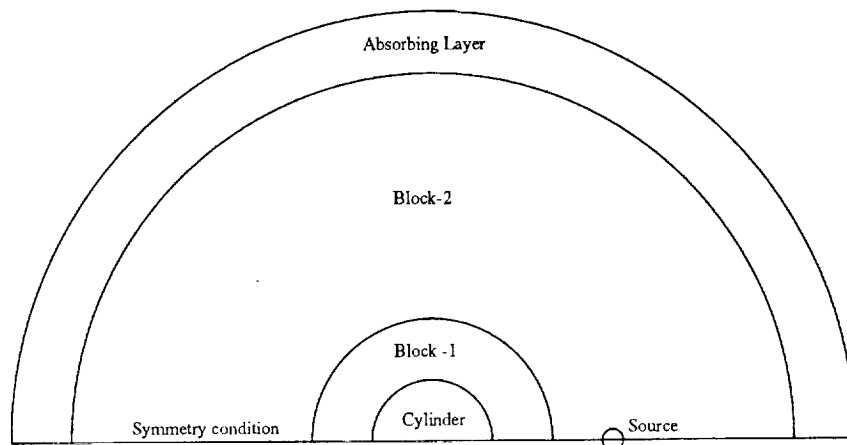


Figure 1: Computational domain

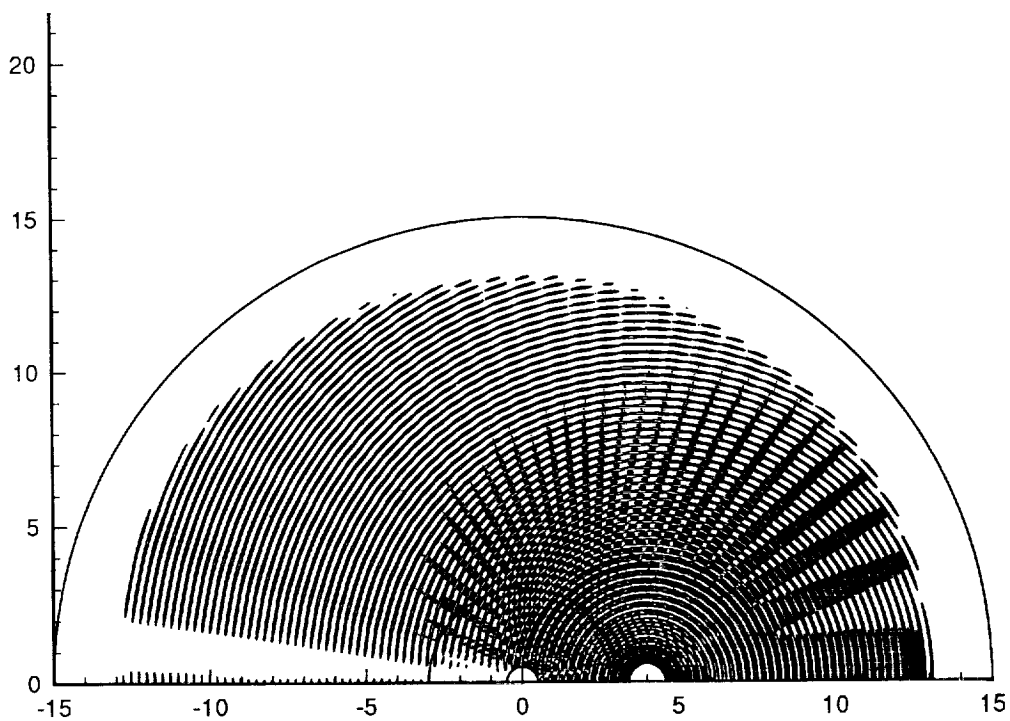


Figure 2: Snapshot of pressure

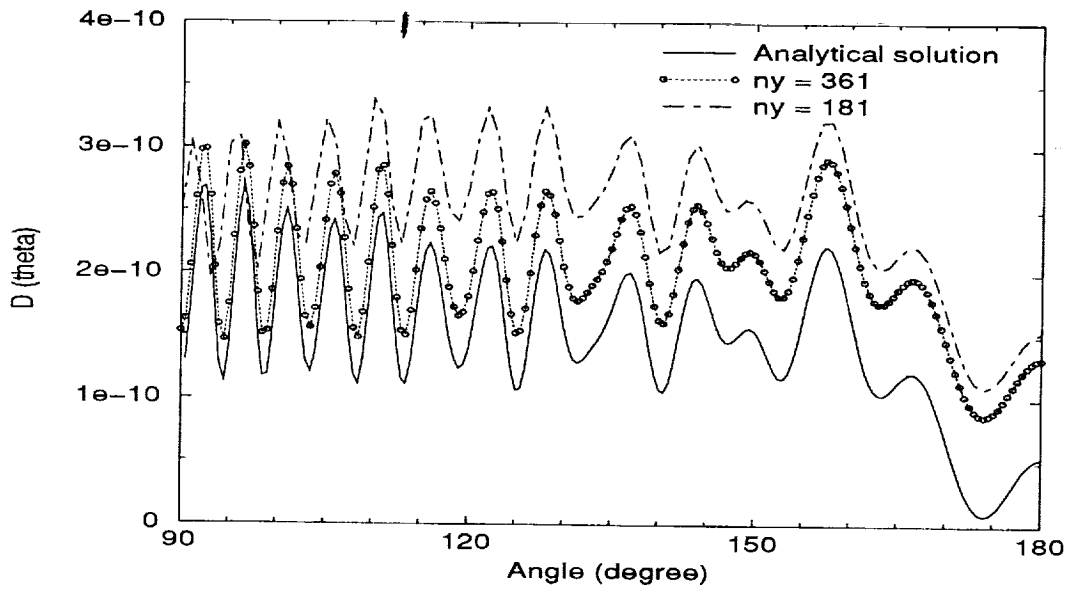


Figure 3: Directivity

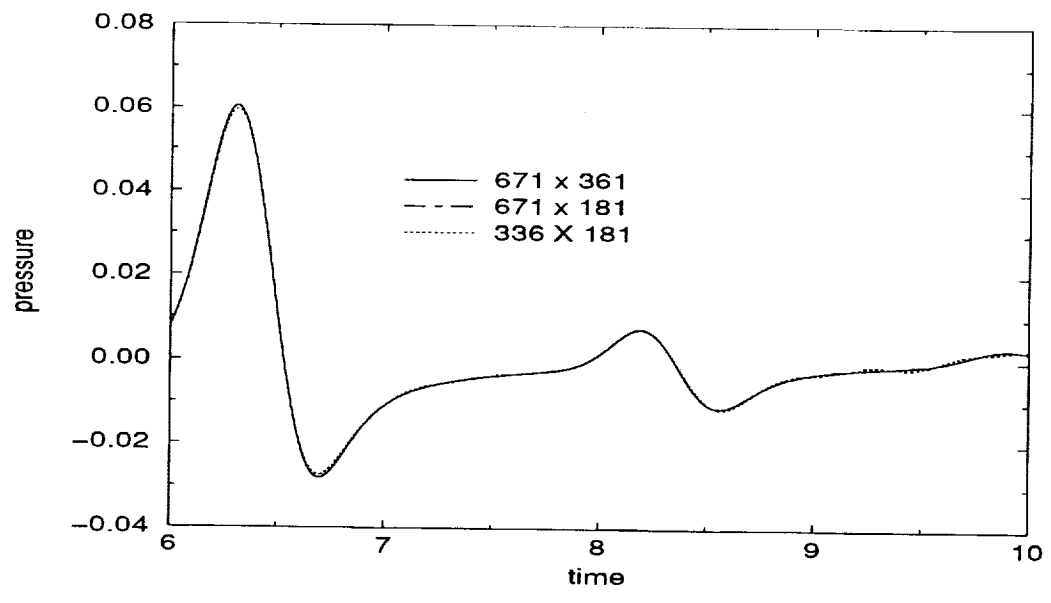


Figure 4: Pressure at point A

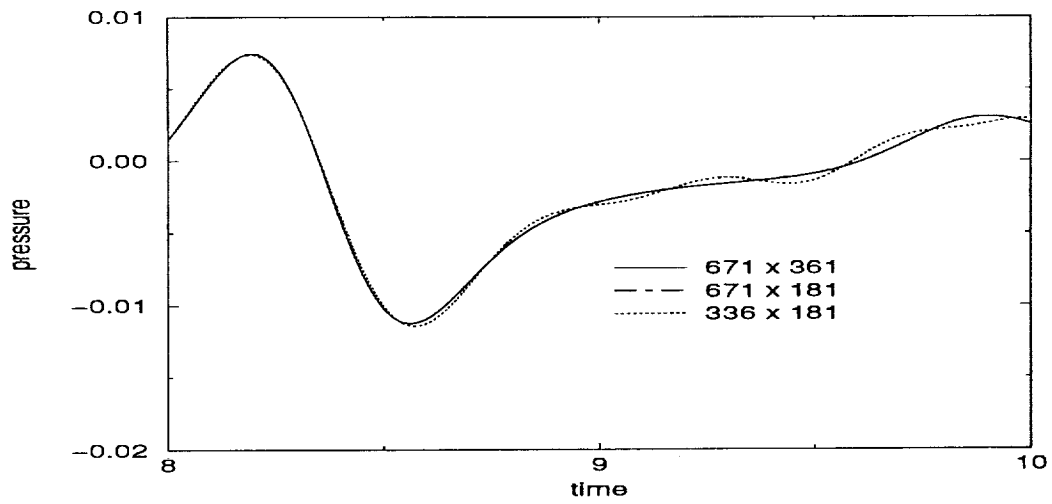


Figure 5: Details of pressure variation at point A

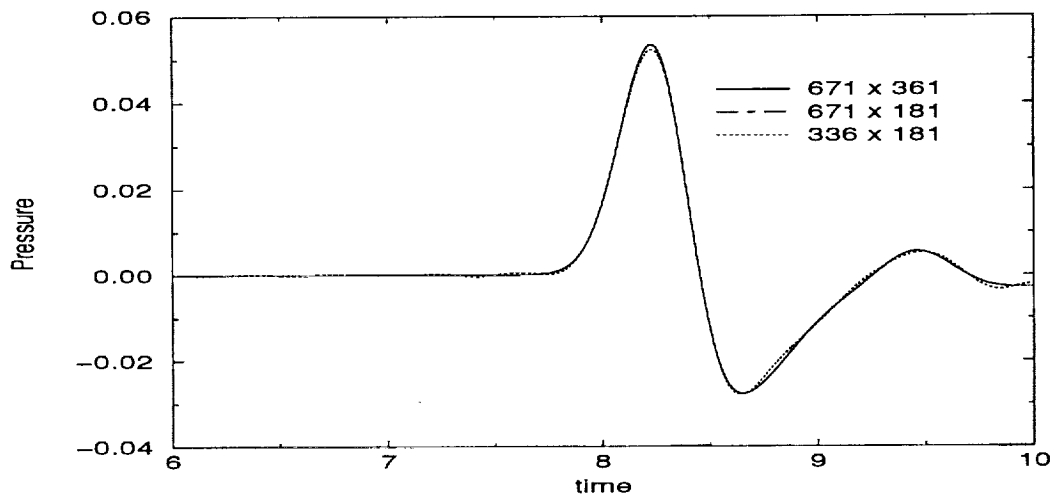


Figure 6: Pressure at point B

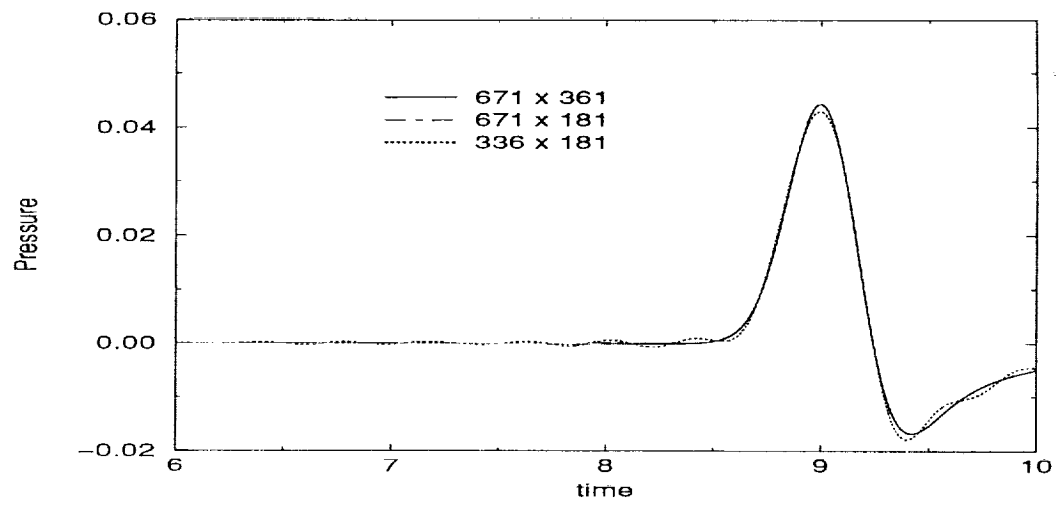


Figure 7: Pressure at point C

APPLICATION OF AN OPTIMIZED MACCORMACK-TYPE SCHEME TO ACOUSTIC SCATTERING PROBLEMS

Ray Hixon and S.-H. Shih
Institute for Computational Mechanics in Propulsion
NASA Lewis Research Center
Cleveland, OH 44135

Reda R. Mankbadi
Mechanical Power Engineering Dept.
Cairo University
Cairo, Egypt

512-71
043478
293966
p8

Abstract

In this work, a new optimized MacCormack-type scheme, which is 4th order accurate in time and space, is applied to Problems 1 and 2 of Category 1. The performance of this new scheme is compared to that of the 2-4 MacCormack scheme, and results for Problems 1 and 2 of Category 1 are presented and compared to the exact solutions.

Introduction

In the past, the 2-4 MacCormack scheme of Gottlieb and Turkel¹ has been used for aeroacoustics computations. It is a scheme that is robust and easily implemented, with reasonable accuracy. Past experience has shown that the 2-4 scheme requires 25 points per wavelength for accurate wave propagation.

Recently, a new family of MacCormack-type schemes have been developed², using the Dispersion Relation Preserving methodology of Tam and Webb³ for guidance. These schemes have been tested on 1-D wave propagation, showing a significant improvement over the existing 2-4 and 2-6 schemes⁴. As an initial test of this new scheme, Problems 1 and 2 of Category 1 were chosen.

These problems require accurate propagation of high-frequency low-amplitude waves for a considerable distance, with curved-wall boundary conditions adding to the difficulties. The performance of the new scheme as well as the results obtained will be shown and discussed.

Governing Equations

In this work, the linearized Euler equations are solved in non-conservative form

over a half-plane. The equations used are:

$$\begin{Bmatrix} v_r' \\ v_\theta' \\ p' \end{Bmatrix}_r + \begin{Bmatrix} p' \\ 0 \\ v_r' \end{Bmatrix}_r + \frac{1}{r} \begin{Bmatrix} 0 \\ p' \\ v_\theta' \end{Bmatrix}_\theta + \frac{1}{r} \begin{Bmatrix} 0 \\ 0 \\ v_r' \end{Bmatrix}_\theta = S \quad (1)$$

For Problem 1, S is a simple harmonic source, given by:

$$S = \begin{Bmatrix} 0 \\ 0 \\ \exp\left(-\ln(2) \frac{(x-4)^2 + y^2}{(0.2)^2}\right) \sin(8\pi t) \end{Bmatrix} \quad (2)$$

In Problem 2, S is an initial disturbance at time $t = 0$, given by:

$$S|_{t=0} = \begin{Bmatrix} 0 \\ 0 \\ \exp\left(-\ln(2) \frac{(x-4)^2 + y^2}{(0.2)^2}\right) \end{Bmatrix} \quad (3)$$

Numerical Formulation

The scheme used is a new variant of the 2-4 MacCormack-type scheme¹, which is optimized in both space and time for improved wave propagation and accuracy². Tam and Webb's Dispersion Relation Preserving scheme³ is used to specify the spatial derivatives, and Hu, et. al.'s Low Dissipation and Dispersion Runge-Kutta scheme⁴ is used for the time marching. The scheme can be written as follows:

$$\begin{aligned} \bar{Q}^{(1)} &= \bar{Q}^k \\ \bar{Q}^{(2)} &= \bar{Q}^k + \begin{pmatrix} 1/2 \\ .353323 \end{pmatrix} \Delta t F(\bar{Q}^{(1)}) \\ \bar{Q}^{(3)} &= \bar{Q}^k + \begin{pmatrix} 1/2 \\ .353323 \end{pmatrix} \Delta t F(\bar{Q}^{(2)}) \\ \bar{Q}^{(4)} &= \bar{Q}^k + \begin{pmatrix} 1 \\ .240823 \end{pmatrix} \Delta t F(\bar{Q}^{(3)}) \\ \bar{Q}^{(5)} &= \bar{Q}^k + \begin{pmatrix} 0 \\ .240823 \end{pmatrix} \Delta t F(\bar{Q}^{(4)}) \\ \bar{Q}^{(6)} &= \bar{Q}^k + \begin{pmatrix} 0 \\ .341148 \end{pmatrix} \Delta t F(\bar{Q}^{(5)}) \end{aligned}$$

$$\bar{Q}^{k+1} = \bar{Q}^k + \Delta t \begin{bmatrix} \left(\begin{array}{c} 1/6 \\ -0.766927 \end{array} \right) F(\bar{Q}^{(1)}) + \\ \left(\begin{array}{c} 1/3 \\ -0.519328 \end{array} \right) F(\bar{Q}^{(2)}) + \\ \left(\begin{array}{c} 1/3 \\ 0.147469 \end{array} \right) F(\bar{Q}^{(3)}) + \\ \left(\begin{array}{c} 1/6 \\ -0.140084 \end{array} \right) F(\bar{Q}^{(4)}) + \\ \left(\begin{array}{c} 0 \\ 1.11946 \end{array} \right) F(\bar{Q}^{(5)}) + \\ \left(\begin{array}{c} 0 \\ 1.15941 \end{array} \right) F(\bar{Q}^{(6)}) \end{bmatrix} \quad (4)$$

where the values of the upper coefficients are used in the four stage step and those of the lower coefficients are used in the six-stage step. Each derivative uses biased differencing, either forward or backward, providing inherent dissipation for the solver. Unlike the earlier MacCormack-type schemes, the stencil is not fully one-sided, allowing the magnitude and behavior of the dissipation to be modified using an optimization technique.

Using a radial derivative at point j as an example,

Forward:

$$\left. \frac{\partial \bar{Q}}{\partial r} \right|_j = \frac{-1}{\Delta r} \begin{pmatrix} .30874 \bar{Q}_{i-1} + .6326 \bar{Q}_i \\ -1.2330 \bar{Q}_{i+1} + .3334 \bar{Q}_{i+2} \\ -.04168 \bar{Q}_{i+3} \end{pmatrix}^k \quad (5)$$

Backward:

$$\left. \frac{\partial \bar{Q}}{\partial r} \right|_j = \frac{1}{\Delta r} \begin{pmatrix} .30874 \bar{Q}_{i+1} + .6326 \bar{Q}_i \\ -1.2330 \bar{Q}_{i-1} + .3334 \bar{Q}_{i-2} \\ -.04168 \bar{Q}_{i-3} \end{pmatrix}^k \quad (6)$$

The sweep directions are reversed between each stage of the time marching scheme to avoid biasing, and the first sweep direction in each time step is alternated as well. This gives a four-step time marching cycle:

$$\begin{aligned} Q^{k+1} &= L_{BFBF} Q^k \\ Q^{k+2} &= L_{FBFBFB} Q^{k+1} \\ Q^{k+3} &= L_{FBFB} Q^{k+2} \\ Q^{k+4} &= L_{BFBFBF} Q^{k+3} \end{aligned} \quad (7)$$

At the computational boundaries, flux quantities outside the boundaries are needed to compute the spatial derivatives, and the methods used to predict these fluxes are given below.

The resulting scheme is capable of resolving waves of 7 points per wavelength for large distances while taking much larger time steps than the original 2-4 scheme. The advantage of using this type of scheme is that the one-sided differences both add in desirable dissipation at high frequencies and cost less to evaluate than the corresponding central differences.

The performance of this new scheme is compared with the 2-4 scheme in Figures 1 and 2. Figure 1 shows the dispersion error per wavelength of travel for a 1-D wave as a function of the number of points per wavelength. The time accuracy of the new scheme is illustrated by the lack of error at larger time steps. Figure 2 shows the dissipation error per wavelength of travel; notice that the optimization of the one-sided differences gives a reduction in dissipation of nearly three orders of magnitude at 10 points per wavelength. The CFL range shown in Figures 1 and 2 are $.1 \leq \text{CFL} \leq .6$ for the 2-4 scheme, and $.2 \leq \text{CFL} \leq 1.4$ for the new scheme.

Boundary Conditions

There are three boundary conditions which are used. At the cylinder surface ($r = 0.5$), the Thompson solid wall boundary condition is used, and the equations become:

$$\begin{Bmatrix} v_r' \\ v_\theta' \\ p' \end{Bmatrix}_t + \begin{Bmatrix} 0 \\ 0 \\ v_r' - p' \end{Bmatrix}_r + \frac{1}{r} \begin{Bmatrix} 0 \\ p' \\ v_\theta' \end{Bmatrix}_\theta + \frac{1}{r} \begin{Bmatrix} 0 \\ 0 \\ v_r' \end{Bmatrix} = S \quad (8)$$

In this computation, three ghost points are used inside the surface for the radial derivative; their values are set as:

$$\begin{Bmatrix} v_r' \\ v_\theta' \\ p' \end{Bmatrix}_{1-j} = \begin{Bmatrix} -v_r' \\ 0 \\ p' \end{Bmatrix}_{1+j} \quad (9)$$

In the far field ($r = R_{\max}$), the acoustic radiation condition is used:

$$\begin{Bmatrix} v_r' \\ v_\theta' \\ p' \end{Bmatrix}_t + \begin{Bmatrix} v_r' \\ 0 \\ p' \end{Bmatrix}_r + \frac{1}{2r} \begin{Bmatrix} v_r' \\ 0 \\ p' \end{Bmatrix} = S \quad (10)$$

For the radial derivative at the outer boundary, three ghost points are used. The values of the variables at these ghost points are determined using third-order extrapolation from the interior values.

At the symmetry planes ($\theta = 0$ and $\theta = \pi$), a symmetry condition is used. For

example, around $i = 1$:

$$\begin{Bmatrix} v_r' \\ v_\theta' \\ \rho' \end{Bmatrix}_{1-i} = \begin{Bmatrix} v_r' \\ -v_\theta' \\ \rho' \end{Bmatrix}_{1+i} \quad (11)$$

where i is the index in the azimuthal direction.

Computational Grid

For Problem 1, a 801 (radial) x 501 (azimuthal) grid was used, covering a domain of $0.5 \leq r \leq 20.5$ in the radial direction, and $0 \leq \theta \leq \pi$. Since the wavelength of the disturbance is 0.25, this grid results in 7-10 points per wavelength. The exact results were given at the $r = 15$ line, giving a maximum of 76 wavelengths of travel at $\theta = \pi$.

For Problem 2, a 201 (radial) x 301 (azimuthal) grid was used, covering a domain of $0.5 \leq r \leq 10.5$ in the radial direction, and $0 \leq \theta \leq \pi$. Since the transient problem only requires data from $6 \leq t \leq 10$, the outer radial boundary only has to be far enough away such that no reflections can reach any of the three data points during this time period.

Results

Results for Problem 1 are given in Figure 3. In order to avoid problems with the very large initial transient, a polynomial function was used to smoothly increase the amplitude of the forcing function. The time step used was limited by the stability of the solid wall boundary; for these calculations a CFL number of 0.1 was used ($\Delta t = .00245$). The calculation was run to a time of 32.09, with results being taken from $31.59 \leq t \leq 32.09$. This calculation took a total of 6.27 hours of CPU time on a Cray Y/MP, running at 191 Mflops. The results are given at $r = 15$ D, and compare very well with the exact solution.

Results for Problem 2 are given in Figures 4-6. The results agree very well with the exact solution. This calculation, using a Δt of .0025 in order to print out the required results, took a total of 469 CPU seconds on a Cray Y/MP, running at 175.5 Mflops. However, the code could run stably at a CFL number of 0.1 ($\Delta t = .0045$), requiring 261 CPU seconds. With more stable solid wall boundary conditions, it is expected that the scheme can recover the CFL = 1.4 time step that has been seen previously.

Grid refinement studies were conducted for Problem 2; the effect of halving and doubling the grid are shown for Point C in Figures 7 and 8. Point C was chosen because it was the most distant point from the initial location of the pulse. In Figure 7, three computed results are shown: a half grid (101 x 151), the grid used (201 x 301), and a doubled grid (401 x 601). The two denser grids have nearly identical results, and compare very well with the exact solution. The coarsest grid, however, shows leading and trailing waves, some traveling much faster than the physical wave. This is due to the low

resolution of the grid causing the solver to incorrectly allow high-frequency waves to travel faster than the speed of sound.

Figure 8 shows the transient peak at point C. The effect of increased grid is illustrated in this graph; the transient peak becomes closer and closer to the exact solution as the grid becomes denser. At this extreme amplification, it can be seen that the transient peak velocity is very slightly off with the grid used, but the answer is well within expected tolerances for this case.

Conclusions

A new optimized MacCormack-type scheme was used to solve Problems 1 and 2 of Category 1. This scheme performed very well, requiring less than 10 points per wavelength to accurately propagate waves for a distance of 100 wavelengths. This scheme has been validated on supersonic jet noise calculations, and is currently being applied to parametric calculations of coannular jet noise⁶.

Acknowledgements

This work was performed under cooperative agreement NCC3-483 with NASA Lewis Research Center. Dr. L. A. Povinelli was the Technical Monitor.

References

1. Gottlieb, D. and Turkel, E., 'Dissipative Two-Four Method for Time Dependent Problems', *Mathematics of Computation*, Vol. 30, No. 136, 1976, pp. 703-723.
2. Hixon, R. 'On Increasing the Accuracy of MacCormack Schemes for Aeroacoustic Applications', paper submitted to the 3rd AIAA/CEAS Aeroacoustics Conference, May 12-14, 1997.
3. Tam, C. K. W. and Webb, J. C., 'Dispersion-Relation-Preserving Schemes for Computational Acoustics', *J. Comp. Physics*, **107**, 1993, p. 262-281.
4. Bayliss, A., Parikh, P., Maestrello, L., and Turkel, E., 'Fourth Order Scheme for the Unsteady Compressible Navier-Stokes Equation', ICASE Report 85-44, Oct. 1985.
5. Hu, F. Q., Hussaini, M. Y., and Manthey, J., 'Low-Dissipation and -Dispersion Runge-Kutta Schemes for Computational Acoustics', ICASE Report 94-102, Dec. 1994.
6. Hixon, R., Shih, S.-H., and Mankbadi, R. R., 'Effect of Coannular Flow on Linearized Euler Equation Predictions of Jet Noise', AIAA Paper 97-0284, Jan. 1997.

Figures

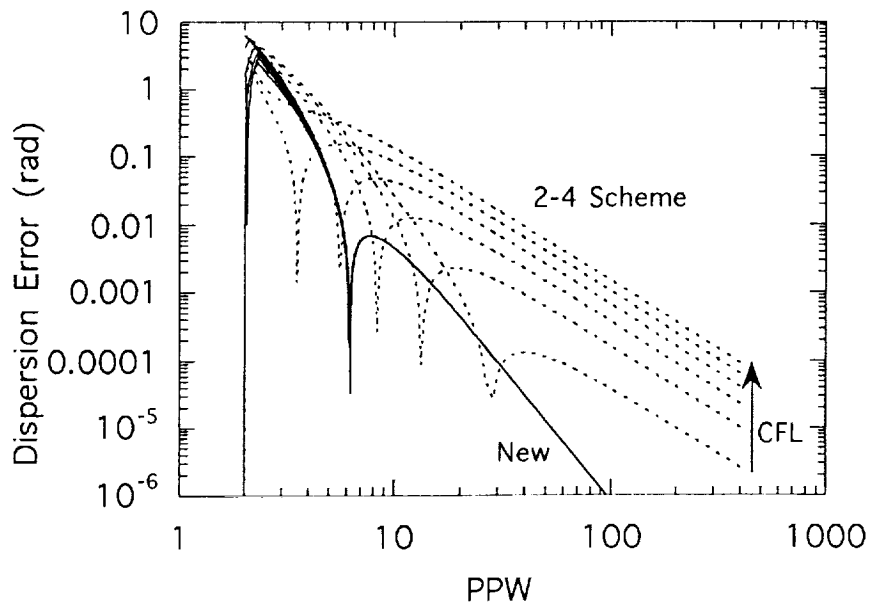


Figure 1. Comparison of dispersion error per wavelength of travel

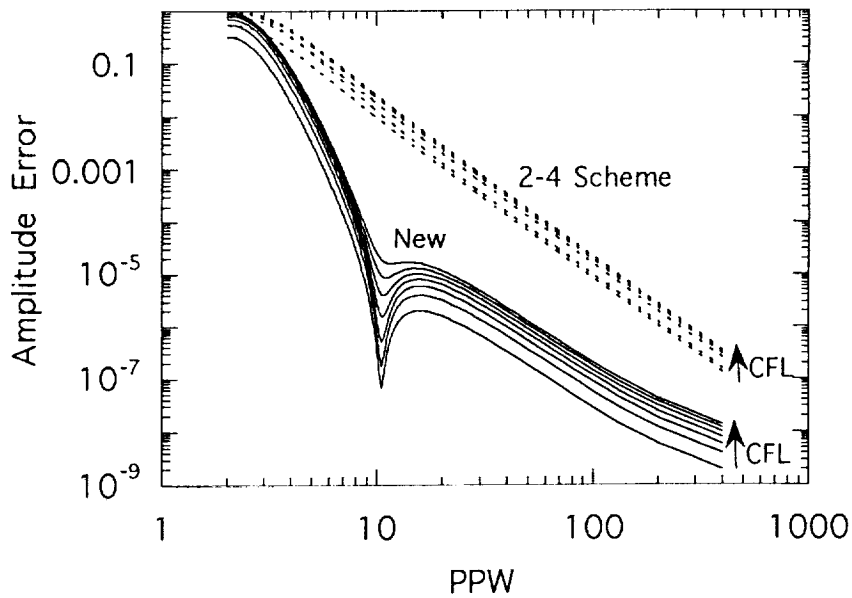


Figure 2. Comparison of amplitude error per wavelength of travel

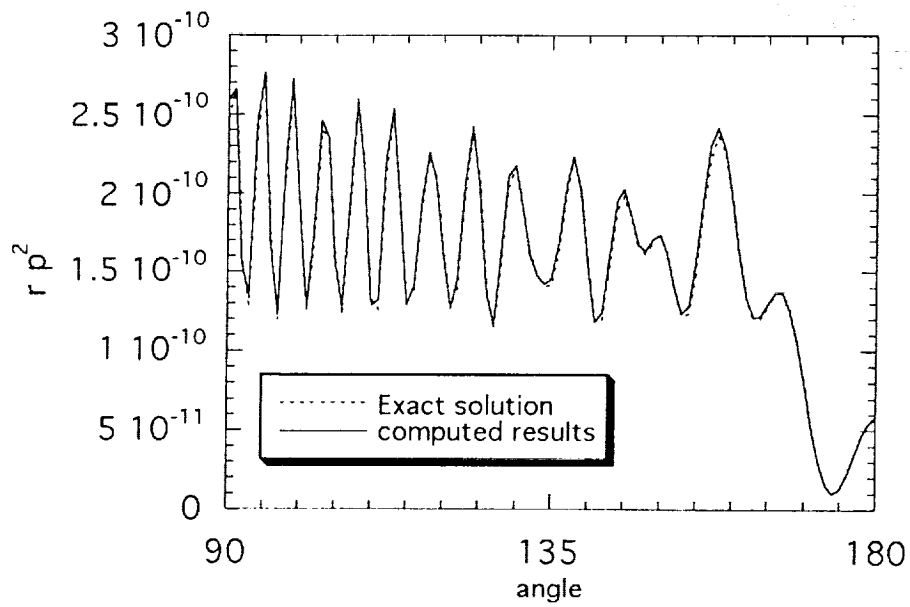


Figure 3. Computed solution of Problem 1 at $r = 15$.

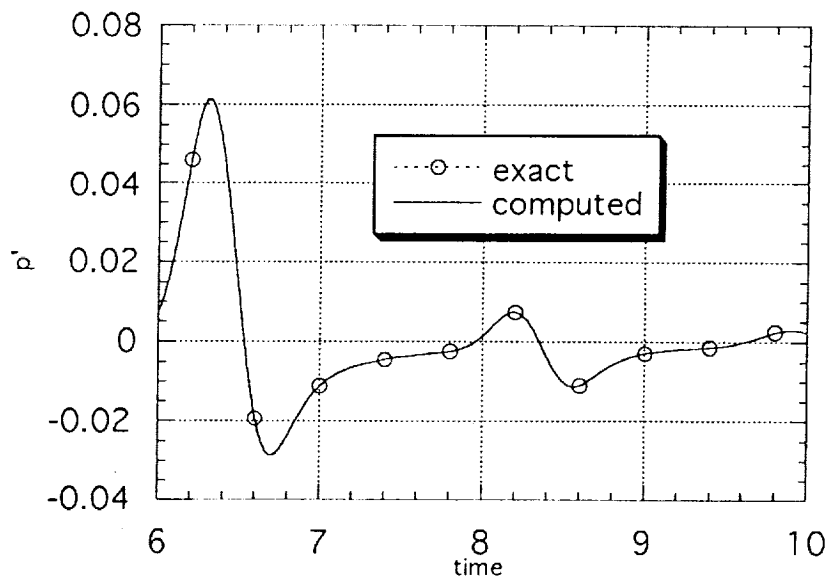


Figure 4. Computed solution of Problem 2 at point A

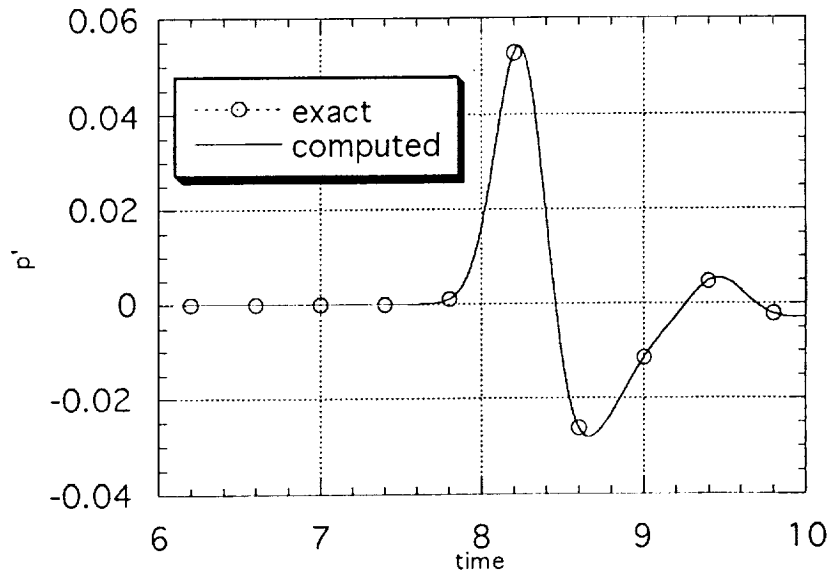


Figure 5. Computed solution of Problem 2 at point B

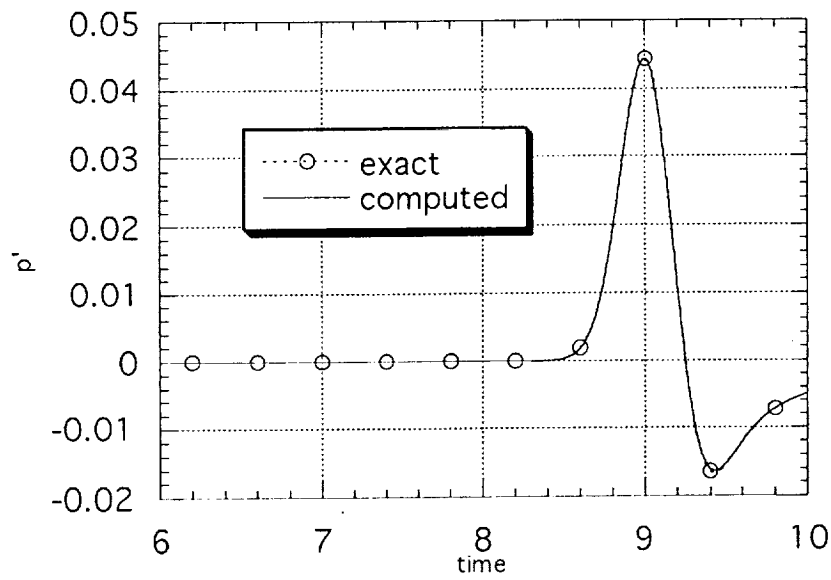


Figure 6. Computed solution of Problem 2 at point C

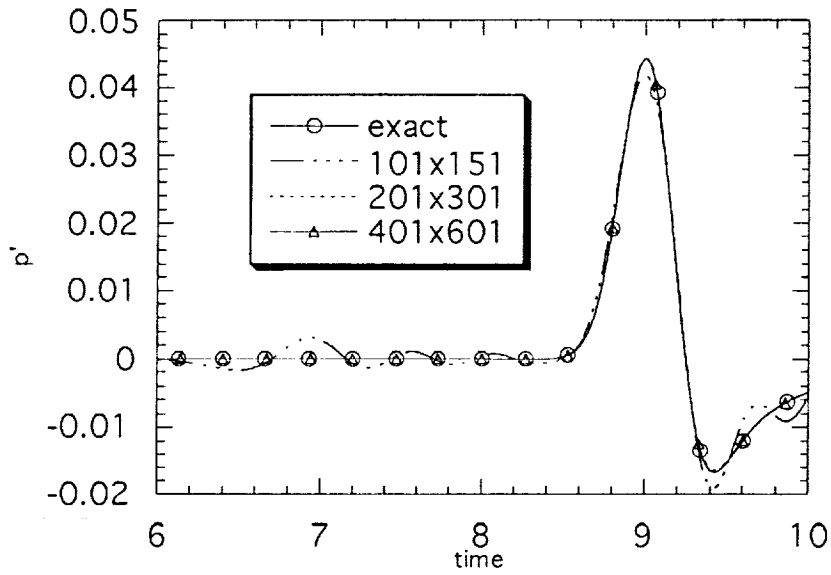


Figure 7. Effect of grid density on computed solution at point C

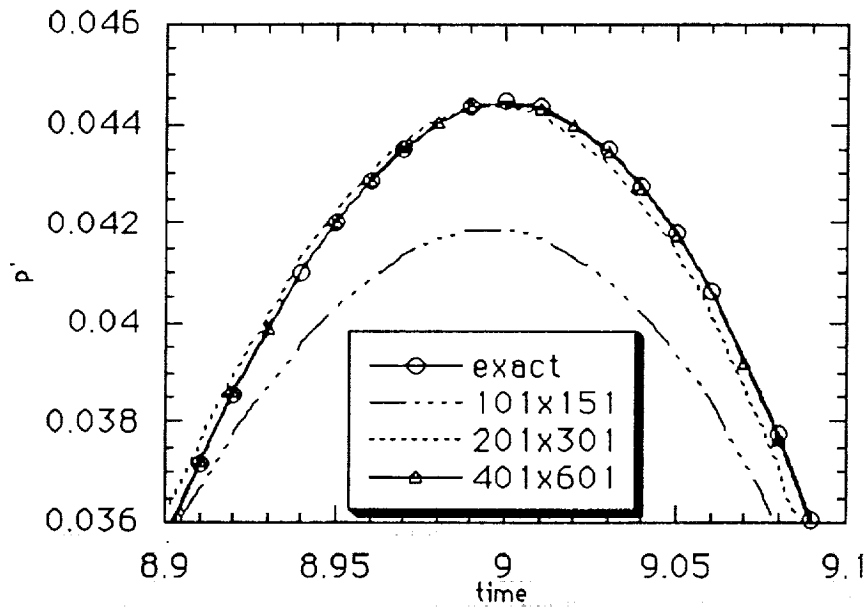


Figure 8. Effect of grid density on computed solution for transient peak at point C

COMPUTATIONAL AEROACOUSTICS FOR PREDICTION OF ACOUSTIC SCATTERING

Morris Y. Hsi
Ford Motor Company
Dearborn, Michigan
e-mail: mhsi@ford.com

513-71
043471
293971
p8

Fred Périé
Mecalog
Paris, France
e-mail: fperie@mecalog.fr

ABSTRACT

Two problems are investigated : Category 1 – Acoustic Scattering, Problems 1 and 2. RADIOSS CFD, an industrial software package is the solver used. The computations were performed on a HP9000 Model 735 workstation. No slip conditions are imposed on the surface of the cylinder body and non reflecting boundary conditions are utilized at the artificial boundary of the computational domain. Numerical results were reported in the specified format for comparison and assessment.

NUMERICAL MODEL

RADIOSS CFD finite element code includes several formulations that can solve a wide variety of problems ranging from transient fluid flow to fully coupled fluid structure interaction. These formulations include Lagrangian, Eulerian as well as Arbitrary Lagrangian Eulerian (ALE) [1] representations of the compressible Navier–Stokes equations. To solve the proposed linearized Euler equations, an explicit time integration and a Lagrangian Finite Element representation were chosen, because the associated algorithm involves theoretically no numerical dissipation and minimizes dispersion effects [2]. In practice, some numerical dissipation is artificially introduced to avoid zero energy modes (shear modes).

Outer domain boundaries are treated using the silent boundary of Bayliss and Turkell [3]

$$\partial p / \partial t = \rho c (\partial v_n / \partial t - v_n \operatorname{div} [\mathbf{v} - v_n \mathbf{n}]) + c (p_\infty - p) / 2l_c$$

where \mathbf{v} is velocity vector, \mathbf{n} normal vector at boundary, v_n normal velocity, p_∞ pressure at infinity, l_c characteristic length for low frequency filtering. Here $p_\infty = 0$ and $l_c = \infty$.

For both problems (1 & 2 of Category 1), no slip conditions are applied at the surface of the circular cylinder, and nodes on x-axis are constrained in y to take advantage of the symmetry of the problem. The mesh used for both problems is unstructured and contains roughly 112000 elements, whose sizes range from $h=0.01$ to 0.04 , with most of them being close to 0.025 (corresponding to an average of ten elements per wave length in Problem 1). As usual in explicit methods, time step is governed by Courant's stability condition :

$$\Delta t \leq \text{Min}(h/c)$$

$\Delta t=0.01$ is used in all the calculations presented here.

The above assumptions (formulation, mesh size, boundary conditions) were first evaluated for a monodimensional acoustic problem described below.

PRELIMINARY TEST

A rectangle (Fig. 1) is loaded with white noise propagating horizontally. The length of the model is $L=2.5$ whereas the height is $H=0.25$; the total number of elements of the mesh is roughly 1000, with mesh size comparable to that in Problems 1 and 2. The purpose of this test is to evaluate the transfer function resulting from the numerical algorithm and the spatial discretization of waves propagating over 100 elements.

Inlet and outlet velocity signals can be decomposed using Fourier's transform,

$$v_i(t) = \sum_{\omega} \hat{v}_i(\omega) e^{j(\omega t - \varphi_i)}$$

$$v_o(t) = \sum_{\omega} \hat{v}_o(\omega) e^{j(\omega t - \varphi_o)}$$

and the transfer function error can then be displayed in terms of dissipation error e_d and dispersion error (phase velocity error) e_{φ} [4]:

$$e_d(\omega) = 20 \text{Log}(\hat{v}_o/\hat{v}_i)$$

$$e_{\varphi}(\omega) = (\varphi_o - \varphi_i)/kL - 1$$

Results are presented in Figures 2 and 3. Spectra are averaged as usual when dealing with white noise. The cut-off frequency of the model is close to frequency $f=6$; there is less than 1dB attenuation and 3% dispersion error for $f=4$. This shows that the mesh size chosen for the two problems presented hereafter should be good enough. For these problems, waves will indeed propagate over roughly 200 elements and 2dB attenuation and 6% dispersion error can a priori be expected.

PROBLEM 1.1

The transient simulation was run until convergence was obtained at time 30. Isocontours of pressure (Fig.4) show an image of the waves propagating through the mesh. No major reflection can be observed at the outer boundary of the domain. The size of computational domain and the behavior of the silent boundary seem good enough for this problem. The visible interference patterns are however altered by region of lower intensities, whose origin is unclear. There are strong indications though, that this problem stems from the discretization of the source region. Contours of pressure near the source (Fig.5) clearly show that the wave shape is influenced by the square nature of the mesh. A much finer mesh of this region should improve the solution. Figure 6 compares the computed results with the reference data provided by the Workshop Committee. It is noted that the reported results are at $r=5$, boundary of the computational domain. This boundary is obviously too close to allow the numerical results there to approximate the solution at infinity. An extrapolation could have been made using a Boundary Element Method, which would be in conflict with the underlying purposes of this benchmark. Differences can be observed between the computed and the reference results at $r=5$, in particular around $\theta=120^\circ$; this is probably due to the source modelization problem mentioned above. Orders of magnitude are anyhow relevant.

More work will be undertaken to improve the model of the source region and to evaluate the influence of the size of computational domain and of the amount of numerically added dissipation.

PROBLEM 1.2

Figure 7 shows the comparison between computed results at three locations ($\theta=90^\circ$, 135° and 180°) and the reference data provided by the Workshop Committee. A reasonably good correlation can be observed. Presence of higher frequencies and early arrival of first peaks can be noted. This appears consistent with the positive error in terms of phase velocity, that was noticed in the preliminary test (Fig.3). This defect is inherent to the central difference nature of space and time derivatives used in this simulation.

CONCLUSION

This work shows a promising application of time domain simulations to acoustics. Main limitations lie in the dispersive and to some extent diffusive character of the method at high frequencies. Investigations should be undertaken on how to improve accuracy, specially for Problem 1 in Category 1, including sensitivity to computational domain, mesh size and source modelization, as well as methods for extrapolating results to region away from the mesh boundaries.

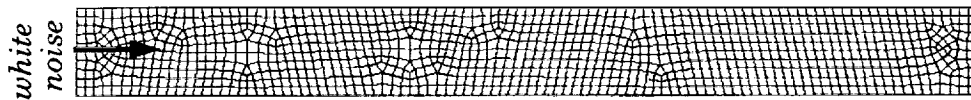


Fig.1 : 1D problem – Unstructured grid used in 1D test

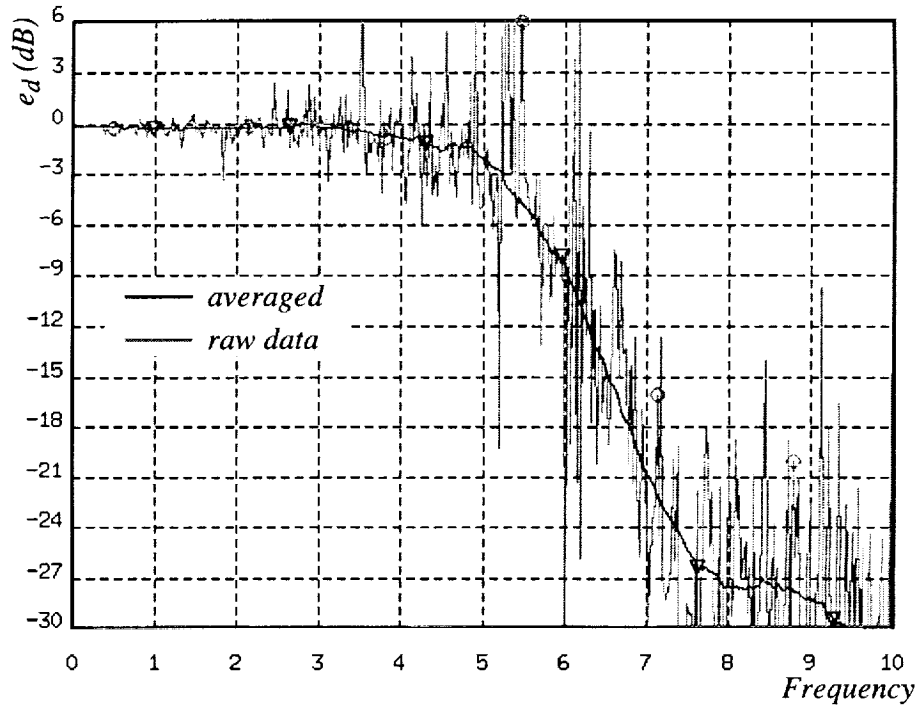


Fig 2 : 1D problem –Dissipation error at outlet of 1D test

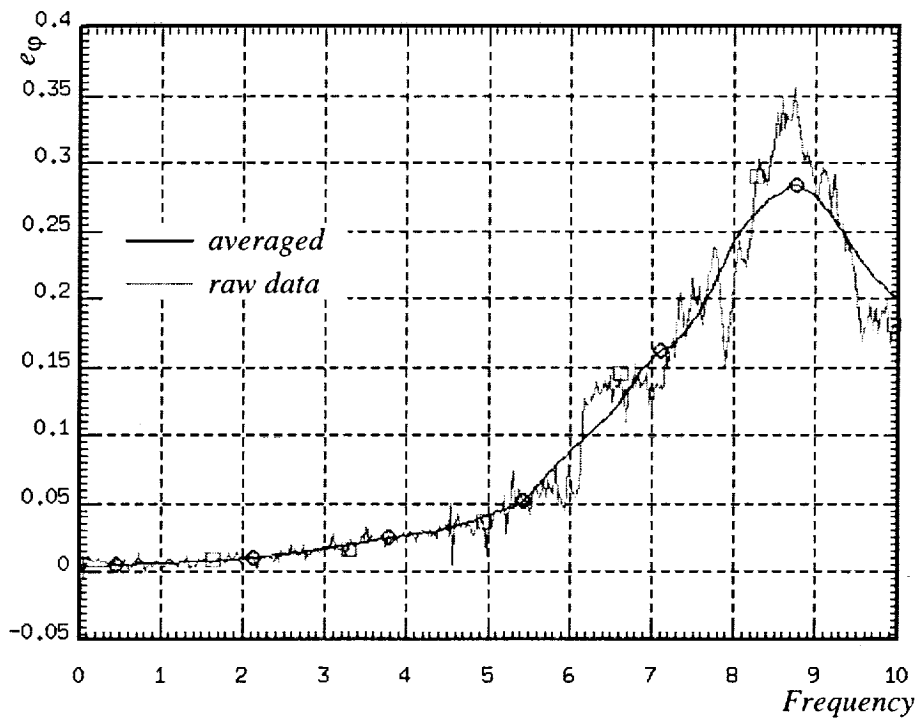


Fig 3 : 1D problem – Dispersion error at outlet of 1D test

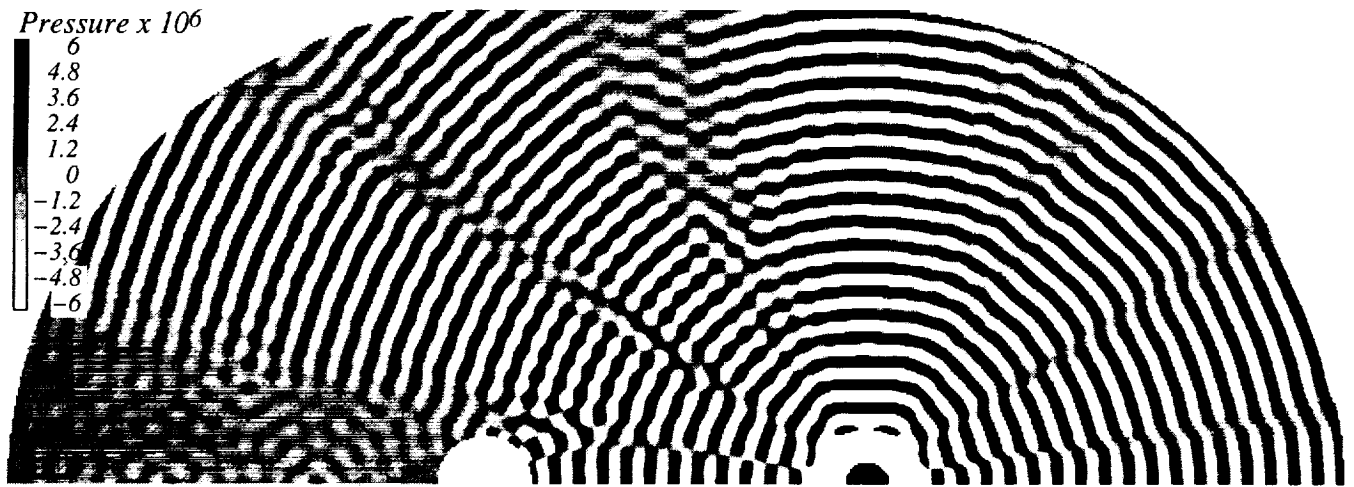


Fig 4 : Problem 1.1 – Isocontours of pressure at time 39.75

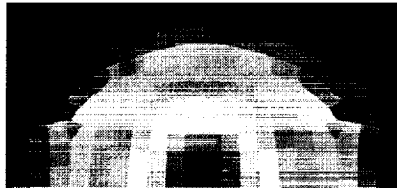


Fig 5 : Problem 1.1 – wave shape near source

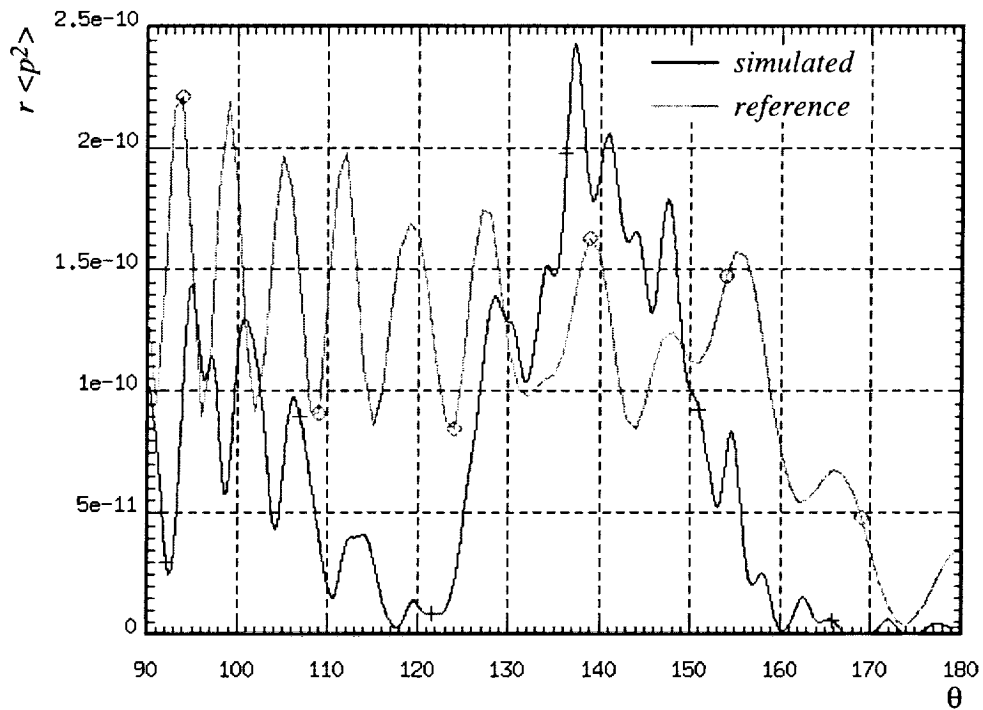
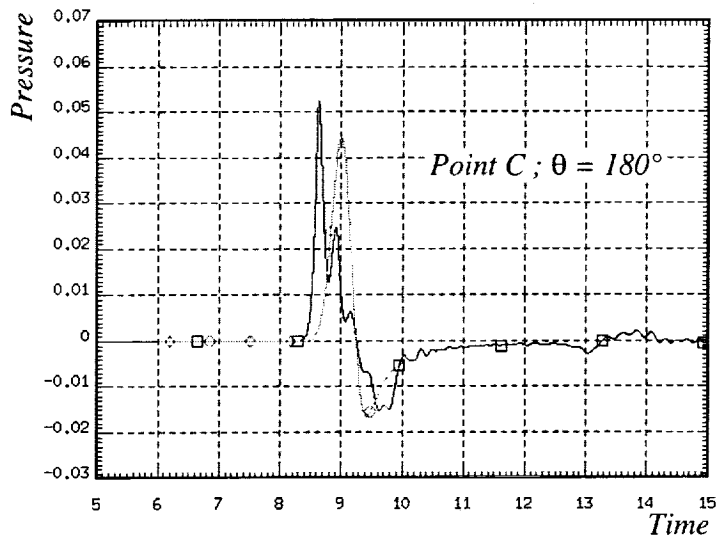
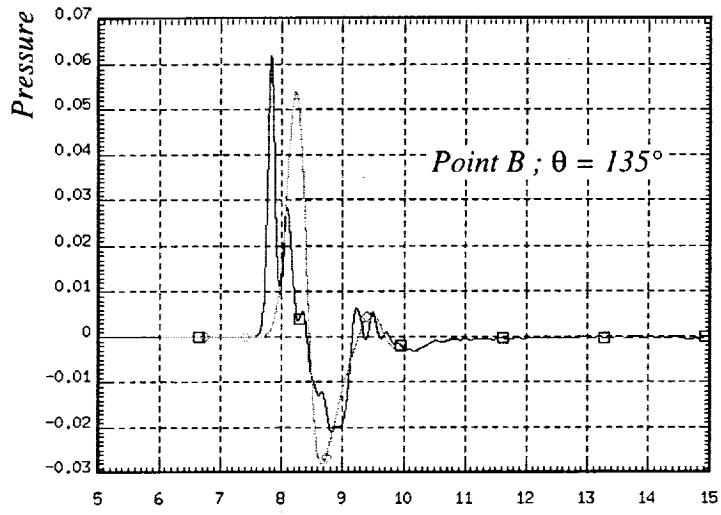
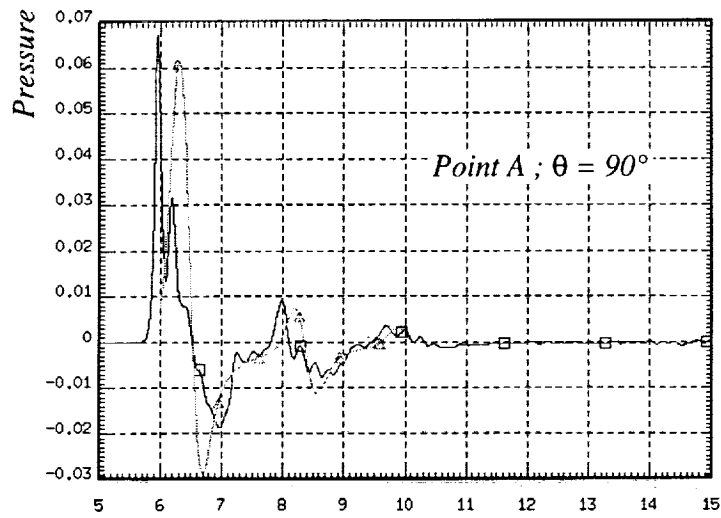


Fig 6 : Problem 1.1 – Comparison of $r \langle p^2 \rangle$ with reference data at $r=5$



— simulated
— reference

Fig 7 : Problem 1.2 – Pressure time histories at Reference Points A, B and C

REFERENCES

- [1] J. Donea, "*Arbitrary Lagrangian–Eulerian Finite Element Methods*", Computational Methods in Mechanics. Vol. 1, No 10 (1983)
- [2] T. Belytschko, "*Overview of semidiscretization*", Computational Methods in Mechanics Vol.1, No1 (1983)
- [3] A. Bayliss and E. Turkell, "*Outflow Boundary Conditions for Fluid Dynamics*", SIAM J. SCI. STAT. COMPUT. Vol. 3, No 2 (1982)
- [4] H.L. Schreyer, "*Dispersion of Semidiscretized and Fully Discretized Systems*", Computational Methods in Mechanics Vol.1, No 6 (1983)

1
2
3
4
5
6
7
8
9
10
11
12
13
14
15
16
17
18
19
20
21
22
23
24
25
26
27
28
29
30
31
32
33
34
35
36
37
38
39
40
41
42
43
44
45
46
47
48
49
50
51
52
53
54
55
56
57
58
59
60
61
62
63
64
65
66
67
68
69
70
71
72
73
74
75
76
77
78
79
80
81
82
83
84
85
86
87
88
89
90
91
92
93
94
95
96
97
98
99
100

514-71
043 472
293977
p34

**Application of PML Absorbing Boundary Conditions
to the Benchmark Problems of Computational Aeroacoustics**

Fang Q. Hu and Joe L. Manthey
Department of Mathematics and Statistics, Old Dominion University
Norfolk, VA 23529

ABSTRACT

Accurate numerical non-reflecting boundary condition is important in all the proposed benchmark problems of the Second Workshop. Recently, a new absorbing boundary condition has been developed using Perfectly Matched Layer (PML) equations for the Euler equations. In this approach, a region with a width of a few grid points is introduced adjacent to the non-reflecting boundaries. In the added region, Perfectly Matched Layer equations are constructed and applied so that the out-going waves are absorbed inside the layer with little reflection to the interior domain. It will be demonstrated in the present paper that the proposed absorbing boundary condition is quite general and versatile, applicable to radiation boundaries as well as inflow and outflow boundaries. It is also easy to implement. The emphasis of the paper will be on the application of the PML absorbing boundary condition to problems in Categories 1, 2, and 3. In Category 1, solutions of problems 1 and 2 are presented. Both problems are solved using a multi-domain polar grid system. Perfectly Matched Layer equations for a circular boundary are constructed and their effectiveness assessed. In Category 2, solutions of problem 2 are presented. Here, in addition to the radiation boundary conditions at the far field in the axisymmetric coordinate system, the inflow boundary condition at duct inlet is also dealt with using the proposed Perfectly Match Layer equations. At the inlet, a PML domain is introduced in which the incident duct mode is simulated while the waves reflected from the open end of the duct are absorbed at the same time. In Category 3, solutions of all three problems are presented. Again, the PML absorbing boundary condition is used at the inflow boundary so that the incoming vorticity wave is simulated while the outgoing acoustic waves are absorbed with very little numerical reflection. All the problems are solved using central difference schemes for spatial discretizations and the optimized Low-Dissipation and Low-Dispersion Runge-Kutta scheme for the time integration. Issues of numerical accuracy and efficiency are also addressed.

1. INTRODUCTION

Recently, a new absorbing boundary condition has been developed using Perfectly Matched Layer (PML) equations for the Euler equations^{1,2,3}. In this approach, a region with a width of a few grid points is introduced adjacent to the non-reflecting boundaries. In the added region, Perfectly

Matched Layer equations are constructed and applied so that the out-going waves are absorbed inside the layer with little reflection to the interior domain. The emphasis of the paper will be on the application PML technique to the Benchmark Problems of the workshop, as accurate numerical non-reflecting boundary condition is important in all the proposed benchmark problems. It will be demonstrated that the proposed absorbing boundary condition is quite general and versatile, applicable to radiation boundaries as well as inflow and outflow boundaries.

We present results of problems in categories 1, 2 and 3 are presented in sections 2, 3 and 4 respectively. Section 5 contains the conclusions.

2. CATEGORY 1 — PROBLEMS 1 AND 2

In Problems 1 and 2, scattering of acoustic waves by a circular cylinder is to be computed directly from the time-dependent Euler equations. To simplify the implementation of boundary conditions on the surface of the cylinder, a polar coordinate system will be used. In polar coordinates (r, θ) , the linearized Euler equations are

$$\frac{\partial u}{\partial t} + \frac{\partial p}{\partial r} = 0 \quad (1.1)$$

$$\frac{\partial v}{\partial t} + \frac{1}{r} \frac{\partial p}{\partial \theta} = 0 \quad (1.2)$$

$$\frac{\partial p}{\partial t} + \frac{\partial u}{\partial r} + \frac{1}{r} \frac{\partial v}{\partial \theta} + \frac{u}{r} = S(r, \theta, t) \quad (1.3)$$

where p is the pressure, and u and v are the velocities in the r and θ directions, respectively. The circular cylinder has a radius of 0.5 and centered at $r = 0$. The computational domain is as shown in Figure 1.

Equations (1.1)-(1.3) will be discretized by a hybrid of finite difference⁴ and Fourier spectral methods⁵ and time integration will be carried out by a optimized Runge-Kutta scheme⁶. In addition, numerical non-reflecting, or absorbing, boundary condition is needed for grid termination at the outer boundary. This is achieved by using the Perfectly Matched Layer technique^{1,2,3} in th present paper.

In what follows, we will first discuss the spatial and temporal discretization schemes used in solving (1.1)-(1.3). Then the absorbing boundary condition to be used at the far field is proposed and its efficiency is investigated. These are followed by the numerical results of Problems 1 and 2 and their comparisons with the exact solution whenever possible.

2.1 Discretization

2.1.1 Mesh

From numerical discretization point of view, it is convenient to use a mesh with fixed spacings Δr and $\Delta \theta$. However, such a mesh will not be desirable for the present problem for two reasons.

First, the grid points will be over concentrated near the cylinder while relatively sparse at the far field. Consequently, in order to resolve the waves at the far field, it will result in a needlessly dense grid distribution near the cylinder. Secondly, and perhaps more importantly, the overly dense mesh near the cylinder will reduce the CFL number and thus lead to a very small time step in explicit time integration schemes such as the Runge-Kutta schemes.

To increase the computational efficiency, a multi-domain polar grid system will be used, as shown in Figure 2. In this system, the number of grid points in the θ direction is different in each sub-domains. For instances, suppose that the entire computational domain is divided into 3 sub-domains and that there are M points in the θ direction of the inner most sub-domain, then $\Delta\theta$ will be taken as follows :

$$\Delta\theta = \frac{2\pi}{M} \quad \text{for } 0.5 \leq r < r_1 \quad (2.1)$$

$$\Delta\theta = \frac{2\pi}{2M} \quad \text{for } r_1 \leq r < r_2 \quad (2.2)$$

$$\Delta\theta = \frac{2\pi}{4M} \quad \text{for } r_2 \leq r \leq r_3 \quad (2.3)$$

The Spacing in r , Δr , will be fixed for all sub-domains.

2.1.2 Spatial discretization

The spatial derivatives will be discretized using a hybrid of finite difference (in r direction) and Fourier spectral (in θ direction) methods on the grid system described above. In particular, a 7-point 4-th order central difference scheme (as in the DRP scheme⁴) is used for the derivatives in the r direction. For grid points near the computational boundary where a central difference can not be applied, backward differences are used. For numerical stability with backward differences, a 11-point 10th order numerical filter is all applied in all the computations. The details are referred to ref [2]. This is largely a straightforward process. However, at any interface of two sub-domains, extra values are needed in the inner sub-domain for the stencils extended from the outer sub-domain, as shown in Figure 3. These values are obtained by interpolation using Fourier expansion of the inner sub-domain values⁵.

2.1.3 Time integration

Time integration will be carried out using an optimized Low-Dissipation and Low-Dispersion Runge-Kutta (LDDRK) scheme⁶. The Runge-Kutta scheme is an explicit single-step multi-stage time marching scheme. Let the time evolution equation, after the spatial discretization, be written as

$$\frac{d\mathbf{U}}{dt} = F(\mathbf{U}, t) \quad (3)$$

where the right hand side is now time dependent when the forcing term is present. Then, a p -stage scheme advances the solution from \mathbf{U}^n to \mathbf{U}^{n+1} as follows :

1. For $i = 1, 2, \dots, p$, compute ($\beta_1 = 0$) :

$$\mathbf{K}_i = \Delta t F(\mathbf{U}^n + \beta_i \mathbf{K}_{i-1}, t_n + \beta_i \Delta t) \quad (4.1)$$

2. Then

$$\mathbf{U}^{n+1} = \mathbf{U}^n + \mathbf{K}_p \quad (4.2)$$

The optimized coefficients β_i are given in ref [6]. In particular, the LDDRK 5-6 scheme is used in all the computations.

2.2 Perfectly Matched Layer

At the far field boundary, non-reflective boundary condition is needed to terminate the grids. In the present paper, we introduce a Perfectly Matched Layer around the outer boundary for this purpose, so that the out-going waves are absorbed in the added Perfectly Matched Layer domain while giving very little reflection to the interior domain.

The Perfectly Matched Layer equations to be used in the absorbing region will be constructed by splitting the pressure p into two variables p_1 and p_2 and introducing the absorption coefficients. This results in a set of modified equations to be applied in the added absorbing layer. The following PML equations are proposed :

$$\frac{\partial u}{\partial t} + \sigma_r u = -\frac{\partial p}{\partial r} \quad (5.1)$$

$$\frac{\partial v}{\partial t} = -\frac{1}{r} \frac{\partial p}{\partial \theta} \quad (5.2)$$

$$\frac{\partial p_1}{\partial t} + \sigma_r p_1 = -\frac{\partial u}{\partial r} \quad (5.3)$$

$$\frac{\partial p_2}{\partial t} = -\frac{1}{r} \frac{\partial v}{\partial \theta} - \frac{u}{r} \quad (5.4)$$

in which $p = p_1 + p_2$ and σ_r is the absorption coefficient. We note that when $\sigma_r = 0$, (5.1)-(5.4) reduce to the Euler equations (1.1)-(1.3).

The above PML equations are easy to implement in finite difference schemes since the spatial derivative in r involves only the total pressure p , which is available in both the interior and PML domains. Thus the difference operator can be applied across the interface of the interior and PML domains in a straight forward manner. Inside the PML domain, the value of σ_r is increased gradually since a wide stencil has been used in the finite difference scheme. In particular, σ_r varies as

$$\sigma_r = \sigma_m \left(\frac{r - r_o}{D} \right)^\beta \quad (6)$$

where D is the thickness of the PML domain and r_o is the location of the interface between the interior and PML domain.

2.3 Numerical results

2.3.1 Results of Problem 1

In Problem 1, a time periodic acoustic source is located at $(r, \theta) = (4, 0)$. The source term in equation (1.3) is given as

$$S(r, \theta, t) = \sin(\omega t) e^{-(\ln 2)[(r \cos \theta - 4)^2 + (r \sin \theta)^2]/0.2^2}$$

where $\omega = 8\pi$.

For the results presented below, the grid spacing in radial direction is $\Delta r = 0.03125$ and the mesh is terminated at $r_{max} = 13.0$. This results in 401 points in the r direction. The computational domain of $r \times \theta = [0.5, 13] \times [0, 2\pi]$ is divided into 3 sub-domains with the r range as $[0.5, 1.5)$, $[1.5, 3)$ and $[3, 13]$ respectively. The value of $\Delta\theta$ in each sub-domain is as shown below :

$$\Delta\theta = \frac{2\pi}{90} \quad \text{for} \quad 0.5 \leq r < 1.5$$

$$\Delta\theta = \frac{2\pi}{180} \quad \text{for} \quad 1.5 \leq r < 3.0$$

$$\Delta\theta = \frac{2\pi}{360} \quad \text{for} \quad 3.0 \leq r \leq 13.0$$

This yields a mesh with 135480, or approximately 351^2 , total grid points.

The time integration is carried out by an optimized Low-Dissipation and Low-Dispersion Runge-Kutta scheme as detailed in section 2.1.3. The time step is $\Delta t = 0.02083$.

A PML domain of 16 grid points in the radial direction is used around the outer boundary. That is, the Euler equations (1.1)-(1.3) are used for $0.5 \leq r < 12.5$ and the PML equations (5.1)-(5.4) are used for $12.5 \leq r < 13.0$. σ_r varies as given in (6) with $\bar{\sigma}_m \Delta r = 2$ and $\beta = 2$.

Figure 4 shows instantaneous pressure contours at $t = 30$. The resolution of the grid system is about 8 points per wavelength. To assess the effectiveness of the absorbing boundary condition, the pressure history was also monitored at a set of selected locations near the PML domain. Figure 5(a)-(c) plot the pressure as a function of time at $r = 11.6875$ and $\theta = 0, \pi/2$ and π , respectively. It is seen that the pressure history first shows large initial transient generated by the startup of the source term. However, after the transient has passed the monitoring points, time periodic responses are observed. We point out that the periodic oscillations had much smaller magnitudes compared with the transient and, yet, the time periodic state is established very quickly after the transient signal. This indicates that the absorbing boundary condition is quite effective and the reflection is indeed very small. The reflection error will be further quantified in problem 2.

The directivity pattern of the acoustic field is shown in Figure 6 where \bar{p}^2 was computed as

$$\bar{p}^2 = \frac{1}{T} \int_{t_0}^{t_0+T} p^2 dt$$

where $t_0 = 25$ and $T = 1$ has been used, which includes four periods. Also shown in Figure 6 is the exact solution in dotted line. Excellent agreement is observed.

2.3.2 Results of Problem 2

In problem 2, the source term in (1.3) is not present, i.e. $S(r, \theta, t) = 0$, and the acoustic field is initialized with a pressure pulse given as

$$p = e^{-(\ln 2)[(r \cos \theta - 4)^2 + (r \sin \theta)^2]/0.2^2}, \quad u = v = 0$$

For the results presented below, $\Delta r = 0.05$ and the mesh is truncated at $r_{max} = 8.5$. Thus the number of grid points in the r direction is 161. Again, the computational domain is divided into three sub-domains and the values of $\Delta \theta$ are

$$\begin{aligned} \Delta \theta &= \frac{2\pi}{64} \quad \text{for} \quad 0.5 \leq r < 1.5 \\ \Delta \theta &= \frac{2\pi}{128} \quad \text{for} \quad 1.5 \leq r < 3.0 \\ \Delta \theta &= \frac{2\pi}{256} \quad \text{for} \quad 3.0 \leq r \leq 8.5 \end{aligned}$$

This yields a mesh with 33536, or approximately 183^2 , total grid points. Time step is $\Delta t = 0.03125$.

Figure 7 shows the instantaneous pressure contours at select times. The out-going waves are absorbed in the PML domain giving no visible reflection to the interior domain. A PML domain of 10 points in the radial direction is used for this problem. Thus the domain where the PML equations are applied is for $8 < r \leq 8.5$. Pressure responses at three chosen locations are shown in Figure 8.

To further quantify the numerical reflection error at the artificial boundary, the current solution is compared with a reference solution. The reference solution is computed using a larger computational domain so that its solution is not affected by the grid truncation. The differences of the computed solutions using PML domains and the reference solution are plotted in Figure 9. We observe that, first, the reflection errors are small when PML domains of 10 or more points are used. Second, the reflection errors, however, does not show order-of-magnitude improvements as the thickness of PML domain increases. This is a different behavior as compared to that of Cartesian PML equations^{1,2,3}.

3. CATEGORY 2 — PROBLEM 2

In this problem, CAA technique is applied to compute sound radiation from a circular duct (Figure 10). The progressive duct wave mode is specified at the duct inlet and the radiated sound field is to be calculated. In particular, sound directivity pattern and pressure envelope inside the duct are to be determined. For the given problem, the duct mode has been chosen to be axisymmetric.

In cylindrical coordinates (x, r, θ) , the Linearized Euler Equations for the axisymmetric disturbances are

$$\frac{\partial u}{\partial t} + \frac{\partial p}{\partial x} = 0 \tag{7.1}$$

$$\frac{\partial v}{\partial t} + \frac{\partial p}{\partial r} = 0 \quad (7.2)$$

$$\frac{\partial p}{\partial t} + \frac{\partial u}{\partial x} + \frac{\partial v}{\partial r} + \frac{v}{r} = 0 \quad (7.3)$$

where p is the pressure, u and v are the velocities in the x and r directions respectively.

As in the previous section, the spatial derivatives will be discretized by the 7-point 4th-order central difference scheme and the time integration will be carried out by the LDDRK 5-6 scheme. These are the same as those used for the First Workshop Problems, ref [7], including the solid wall and centerline treatments. The emphasis of this section will be on the implementation of the non-reflective boundaries in the current problem.

There are two types of non-reflective boundaries encountered in the present problem, as shown in Figure 10. One is the far field non-reflecting boundary condition for the termination of grids. The numerical boundary condition should be such that the out-going waves are not reflected. The second type is the inflow boundary condition at the duct inlet. At the inlet of the duct, we wish to feed-in the progressive duct mode and at the same time absorb the waves reflected from the open end of the duct. In the present paper, both types of non-reflective boundary conditions are implemented using the Perfectly Matched Layer technique. The details are given below.

3.1 PML absorbing boundary condition

To absorb the out-going waves, we introduce a PML domain around the outer boundary of the computational domain, similar to that used in the previous section only that the form of PML equations will be different. For the linearized Euler equations (7.1)-(7.3) in cylindrical coordinates, we proposed the following PML equations :

$$\frac{\partial u}{\partial t} + \sigma_x u = -\frac{\partial p}{\partial x} \quad (8.1)$$

$$\frac{\partial v}{\partial t} + \sigma_r v = -\frac{\partial p}{\partial r} \quad (8.2)$$

$$\frac{\partial p_1}{\partial t} + \sigma_x p_1 = -\frac{\partial u}{\partial x} \quad (8.3)$$

$$\frac{\partial p_2}{\partial t} + \sigma_r p_2 = -\frac{\partial v}{\partial r} - \frac{v}{r} \quad (8.4)$$

where $p = p_1 + p_2$ and the absorption coefficients σ_x and σ_r have been introduced for absorbing the waves that enter the PML domain. The above form follows the PML equations for the Cartesian coordinates given in refs [1, 2]. Here we need only to split the pressure since no mean flow is present. We note that, the Euler equations (7.1)-(7.3) can be recovered from the PML equations (8.1)-(8.4) with $\sigma_x = \sigma_r = 0$ by adding the split equations. Consequently, the interior domain where the Euler equations are applied is regarded as absorption coefficients being zero.

The absorption coefficients σ_x and σ_r are *matched* in a special way, namely, σ_x will remain the same across a horizontal interface and σ_r will remain the same across a vertical interface, as

shown in Figure 11 and described in detail in ref [1, 2]. Within the PML domain, σ_x or σ_r are increased gradually as discussed in the previous section.

3.2 Inflow Boundary Condition

At the inlet of the duct, we wish to feed-in the progressive duct modes and at the same time absorb the waves reflected from the open end of the duct, as shown in Figure 12. For this purpose, a PML domain is also introduced at the inlet. In this region, referred to as the *inflow-PML domain*, we treat the solution as a summation of the incoming and out-going waves and apply the PML equations (8.1)-(8.4) to the out-going part. That is, we express and store the variables as

$$\begin{pmatrix} u \\ v \\ p \end{pmatrix} = \begin{pmatrix} u_{in} \\ v_{in} \\ p_{in} \end{pmatrix} + \begin{pmatrix} u' \\ v' \\ p' \end{pmatrix} \quad (9)$$

in which u_{in} , v_{in} , and p_{in} are the "incoming wave", traveling to the right, and u' , v' , and p' are the "out-going" wave, reflected from the open end and traveling to the left. Since the incoming wave satisfies the linearized Euler equation, it follows that the out-going reflected wave will also satisfy (7.1)-(7.3). To absorb the "out-going" part in the inflow-PML domain, we apply the PML equations (8.1)-(8.4) to the reflected waves. This results in following equations for u' , v' and p' :

$$\frac{\partial u'}{\partial t} + \sigma_x u' = \frac{\partial p}{\partial x} - \frac{\partial p_{in}}{\partial x} \quad (10.1)$$

$$\frac{\partial v'}{\partial t} + \sigma_r v' = \frac{\partial p}{\partial r} - \frac{\partial p_{in}}{\partial r} \quad (10.2)$$

$$\frac{\partial p'_1}{\partial t} + \sigma_x p'_1 = \frac{\partial u}{\partial x} - \frac{\partial u_{in}}{\partial x} \quad (10.3)$$

$$\frac{\partial p'_2}{\partial t} + \sigma_r p'_2 = \frac{\partial v}{\partial r} - \frac{\partial v_{in}}{\partial r} + \frac{v}{r} - \frac{v_{in}}{r} \quad (10.4)$$

where $p' = p'_1 + p'_2$ and u , v , p are those given in (9). Since the inflow-PML domain involves only a vertical interface between the interior and PML domains, it results in $\sigma_r = 0$ in (10.1)-(10.4). The right hand sides of (10.1)-(10.4) have been written in such a way that they can be readily evaluated in finite difference schemes. In particular, we note that, first, since the incoming wave is known, there should be no difficulty in computing their spatial derivatives. Second, the other spatial derivative terms involve only the total u , v and p which are available in the interior domain as well as the inflow-PML domain by using (9).

3.3 Numerical Results

For the results given below, the computational domain is $x \times r = [-9, 9] \times [0, 9]$ in the cylindrical coordinate system. The duct centerline is at $r = 0$ and the radius of the duct is unity. The open end of the duct is located at $x = 0$. For both the low and high frequency cases, we have used a uniform grid with $\Delta x = \Delta r = 0.05$. This results in a 361×181 grid system. The time step that ensures both accuracy and stability is $\Delta t = 0.0545$ in the LDDRK 5-6 scheme.

To absorb the out-going waves at the far field, PML domains with a width of 10 grid points are used around the outer boundaries of the computational domain. In addition, an inflow-PML domain is employed at the duct inlet with the same width as in the far field.

Figure 13 shows the instantaneous pressure contours at $t = 87.2$ and $\omega = 7.2$ (low frequency case). It is seen that the waves decay rapidly in the PML domain. As in the previous section, the pressure as a function of time is monitored at a set of chosen points. Figure 14 shows the pressure histories at two points near the interior-PML interfaces $(x, r) = (8, 0), (0, 8)$, and two points inside the duct $(x, r) = (-2, 0), (-4.5, 0)$. We observe that, while the pressure responses at the far field quickly become time periodic after the initial transients have passed, it takes a longer time for the pressure inside the duct to reach the periodic state. This is believed to be due to the reflection of the transient at the open end of the duct which has to be absorbed by the inflow-PML domain before a periodic state can be established.

Numerical reflection error has also been assessed by comparing the computed solution using PML absorbing boundary condition to a reference solution using a larger computational domain. The maximum difference of the two solutions around the outer boundaries is plotted in Figure 15 for $n = 10$ and 20 where n is the width of the PML domain used. It is seen that satisfactory results are obtainable with a width of 10 points and the reflection error is further reduced significantly by increase the width of the PML domain.

Figure 16 shows the directivity pattern of the radiated sound field. The envelopes of the pressure distribution inside the duct are given in Figure 17. Results for the high frequency case, $\omega = 10.3$, are shown in Figures 18-21.

4. CATEGORY 3

In this category, CAA technique is applied to a turbomachinery problem in which the sound field generated by a gust passing through a cascade of flat plates is to be computed directly from the time-dependent Euler equations :

$$\frac{\partial u}{\partial t} + M \frac{\partial u}{\partial x} + \frac{\partial p}{\partial x} = 0 \quad (11.1)$$

$$\frac{\partial v}{\partial t} + M \frac{\partial v}{\partial x} + \frac{\partial p}{\partial y} = 0 \quad (11.2)$$

$$\frac{\partial p}{\partial t} + M \frac{\partial p}{\partial x} + \frac{\partial u}{\partial x} + \frac{\partial v}{\partial y} = 0 \quad (11.3)$$

where M is the Mach number of the mean flow. In the above, the velocities have been non-dimensionalized by the speed of sound a_o and pressure by $\rho_o a_o^2$ where ρ_o is the density scale. The problem configuration is as shown in Figure 22. In non-dimensional scales, the chord length and the gap-to-chord ratio are both unity. In addition, periodicity is assumed for the top and bottom boundaries. A uniform mean flow is present which has a Mach number of 0.5. The

incident vortical gust is given as

$$u_{in} = -\frac{V_g \beta}{\alpha} \cos(\alpha x + \beta y - \omega t) \quad (12.1)$$

$$v_{in} = V_g \cos(\alpha x + \beta y - \omega t) \quad (12.2)$$

$$p_{in} = 0 \quad (12.3)$$

where $V_g = 0.005$.

In all three problems posed in this category, the sound field scattered by the plates as well as the loadings on the plates are to be determined. In Problem 1, the solutions are to be calculated by using a frozen gust assumption. In problem 2, the convected gust is to be simulated together with the scattered sound field. In problem 3, a sliding interface is introduced and the grids down stream of the interface are moving vertically with a given speed V_s . Problems in this category include several important and challenging issues in developing CAA techniques, such as the inflow and out flow conditions, solid boundaries and moving zones. In the present paper, the inflow and outflow conditions are implemented by the PML technique. The details of the boundary conditions as well as the sliding zone treatments are described below.

4.1 Outflow condition

At the downstream outflow boundary, the out-going waves consist of the acoustic waves scattered from the plates and the vorticity waves convected by the mean flow. To absorb these waves with as little reflection as possible, a PML domain is used at the outflow boundary. For the linear Euler equations (11.1)-(11.3) with a uniform mean flow in the x direction, the following equations are applied in the added PML domain :

$$\frac{\partial u}{\partial t} + \sigma_x u = -M \frac{\partial u}{\partial x} - \frac{\partial p}{\partial x} \quad (13.1)$$

$$\frac{\partial v_1}{\partial t} = -\frac{\partial p}{\partial y} \quad (13.2)$$

$$\frac{\partial v_2}{\partial t} + \sigma_x v_2 = -M \frac{\partial p}{\partial x} \quad (13.3)$$

$$\frac{\partial p_1}{\partial t} + \sigma_x p_1 = -M \frac{\partial p}{\partial x} + \frac{\partial u}{\partial x} \quad (13.4)$$

$$\frac{\partial p_2}{\partial t} = -\frac{\partial v}{\partial y} \quad (13.5)$$

where v and p have been split into v_1 , v_2 and p_1 , p_2 , i.e., $v = v_1 + v_2$ and $p = p_1 + p_2$. Note that, since now the top and bottom boundaries are periodic, only one absorption coefficient, σ_x , is needed. In addition, the u velocity may not be split. For the Cartesian coordinates, it has been shown that the PML domain so constructed is reflectionless for all the linear waves supported by the Euler equations and the waves that enter the PML domain decay exponentially. The details are referred to ref. [1, 2].

4.2 Inflow condition

At the inflow, two types of waves co-exist, namely, the downstream propagating vorticity waves (the gust) and the upstream propagating acoustic waves (scattered from the plates). A successful inflow condition should simulate the downstream connection of the vorticity waves and at the same time be non-reflective for the upstream acoustic waves. As in the previous section (category 2), the inflow condition is implemented by introducing a PML domain at the inflow boundary. In the inflow-PML domain, the variables u , v and p are expressed and stored as a summation of the "incoming" vorticity wave and "out-going" acoustic waves as those given in (9). The incoming wave u_{in} , v_{in} and p_{in} is as given in (12.1)-(12.3). The PML equations (13.1)-(13.5) are then applied to the "out-going" waves u' , v' and p' . Thus, in the inflow-PML domain, we solve

$$\frac{\partial u'}{\partial t} + \sigma_x u' = -M \frac{\partial u}{\partial x} - \frac{\partial p}{\partial x} + M \frac{\partial u_{in}}{\partial x} + \frac{\partial p_{in}}{\partial x} \quad (14.1)$$

$$\frac{\partial v'_1}{\partial t} = -\frac{\partial p}{\partial y} + \frac{\partial p_{in}}{\partial y} \quad (14.2)$$

$$\frac{\partial v'_2}{\partial t} + \sigma_x v'_2 = -M \frac{\partial p}{\partial x} + M \frac{\partial p_{in}}{\partial x} \quad (14.3)$$

$$\frac{\partial p'_1}{\partial t} + \sigma_x p'_1 = -M \frac{\partial p}{\partial x} - \frac{\partial u}{\partial x} + M \frac{\partial p_{in}}{\partial x} - \frac{\partial u_{in}}{\partial x} \quad (14.4)$$

$$\frac{\partial p'_2}{\partial t} = -\frac{\partial v}{\partial y} + \frac{\partial v_{in}}{\partial y} \quad (14.5)$$

Again, the right hand sides have been written in a way that the spatial derivatives can be readily evaluated in finite difference schemes. The implementation of above is similar to that in section 3.2.

4.3 Sliding Zone Treatments

In problem 3, a sliding interface is added to the computational domain and the grids downstream of the sliding interface is moving vertically with a speed V_s , Figure 23. That is, after each time step, the grids in the sliding zone advance vertically by $V_s \Delta t$. Due to this movement, the grids in the two zones are not necessary aligned in the horizontal direction. This will obviously give rise to difficulties in finite difference schemes when the stencils extend across the interface. Extra grid points are created as shown in Figure 24. In the present paper, values of variables on these points are obtained by interpolation using Fourier expansions in the vertical direction. For instance, let the values of pressure p on the regular grids be denoted as $p(j\Delta x, k\Delta y)$. Then the values of p on a point $(j\Delta x, y)$, not on a regular grid point, will be computed as

$$p(j\Delta x, y) = \sum_{n=-N/2}^{N/2-1} \hat{p}_{jn} e^{i \frac{2\pi n}{L} y}$$

where \hat{p}_{jn} is the Fourier transform of $p(j\Delta x, k\Delta y)$ in the y direction and N is the number of grid points ($N = L/\Delta y$). The Fourier expansions are implemented efficiently using FFT. It is well known that Fourier interpolation is highly accurate, better than any polynomial interpolations. Indeed, we found that, using Fourier interpolation, the results with sliding zone (Problem 3) are virtually identical to those without a sliding interface (Problem 2).

4.4 Numerical Results

Since solutions of all three problems in this category are similar, we will concentrate on numerical results of Problem 2 in particular and present the results of Problems 1 and 3 as references.

4.4.1 Effectiveness of the inflow-PML boundary condition

We first demonstrate the validity and effectiveness of the inflow-PML boundary condition described in section 4.2 by a numerical example plane wave simulation. In this example, a plane vorticity wave, convecting with the mean flow, will be simulated. The computational domain is the same as that of problem 2 except that now no plate is present. The flow field is initialized as follows :

At $t = 0$:

$$\begin{aligned} u &= -\frac{V_g\beta}{\alpha} \cos(\alpha x + \beta y - \omega t)H(x + 1) \\ v &= V_g \cos(\alpha x + \beta y - \omega t)H(x + 1) \\ p &= 0 \end{aligned}$$

where $H(x)$ is a step function which has a value of zero for $x > 0$ and unity for $x < 0$.

Figure 25 shows instantaneous pressure contours at the initial state $t = 0$ and subsequent moments at $t = 4.8$ and 14.4 . The inflow-PML domain described in 4.2 is applied at the inflow boundary. It is seen that a plane vorticity wave is established. Figure 26 shows the v -velocity and pressure as functions of time at a point $(x, y) = (-2, 0)$. Notice that while the velocity is periodic, the pressure is not exactly zero as a plane vorticity wave should behave. This is due to our initial flow field being not exact along the cut-off line $x = -1$ which generates small pressure waves. Although these pressure waves are eventually absorbed by the PML domains at both the inflow and out-flow boundaries, the decay of the pressure is slow due to periodicity of the top and bottom boundaries. However, the magnitude of these pressure waves is small as shown in Figure 25.

Simulation of a plane acoustic wave has also been performed with similar results.

4.4.2 Low frequency gust

For the low frequency case, $\omega = 5\pi/4$, $\alpha = \beta = 5\pi/2$. The computational domain is $[-3.5, 4.5] \times [0, 4]$. A uniform grid with $\Delta x = \Delta y = 0.05$ is used and time step used is $\Delta t = 0.044$. The PML domains contain 20 points in the x -direction. Thus the interior domain in which the Euler equations are applied is $[-2.5, 3.5] \times [0, 4]$. Figure 27 shows the instantaneous pressure

and v -velocity contours. In the velocity contours, also visible is the trailing vorticity waves from the plates due to numerical viscosity in the finite difference scheme. The pressure intensity along $x = -2$ and $x = 3$ are shown in Figure 28, along with the results of Problems 1 and 3. Close agreement is found. Especially, results of Problems 2 and 3 are identical.

4.4.3 High frequency gust

For the high frequency case, $\omega = 13\pi/4$, $\alpha = \beta = 13\pi/2$. The computational domain is $[-3.5, 4.5] \times [0, 4]$ and $\Delta x = \Delta y = 0.03125$. Time step $\Delta t = 0.028$.

Pressure and v -velocity contours are shown in Figure 29. We point out that it appears that the out-going waves are not absorbed as efficiently, as in the low frequency case as they enter the out-flow PML domain. However, the waves reflected from the end of the PML domain are absorbed more effectively so the solutions in the interior domain are not affected. Results for sound intensity are shown in Figure 30.

5. CONCLUSIONS

Problems in Categories 1, 2 and 3 have been solved by a finite difference method. Numerical schemes have been optimized for accuracy and efficiency. Perfectly Matched Layer technique for Euler equations have been successfully applied to all the problems as a general treatment for non-reflecting boundaries. It is demonstrated that the proposed PML technique is applicable to radiation boundaries as well as out-flow and inflow boundaries and can be effective for non-Cartesian grids. The accuracy and efficiency of the PML absorbing boundary conditions are also addressed.

Acknowledgment

This work was supported by the National Aeronautics and Space Administration under NASA contract NAS1-19480 while the authors were in the residence at the Institute for Computer Application in Science and Engineering, NASA Langley Research Center, VA 23665, USA.

References

1. F. Q. Hu, "On absorbing boundary conditions for linearized Euler equations by a Perfectly Matched Layer", *Journal of Computational Physics*, Vol 128, No. 2, 1996.
2. F. Q. Hu' "On perfectly matched layer as an absorbing boundary condition", *AIAA paper 96-1664*, 1996.
3. J-P Berenger, "A Perfect Matched Layer for the absorption of electromagnetic waves", *Journal of Computational Physics*, Vol 114, 185, 1994.
4. C. K. W. Tam and J. C. Webb, "Dispersion-relation-preserving schemes for computational acoustics" *Journal of Computational Physics*, Vol 107, 262-281, 1993.

5. C. Canuto, M. Y. Hussainin, A. Quarteroni and T. A. Zang, *Spectral Methods in Fluid Dynamics*, Springer-Verlag, 1988.
6. F. Q. Hu, M. Y. Hussaini, J. L. Manthey, "Low-dissipation and low-dispersion Runge-Kutta schemes for computational acoustics", *Journal of Computational Physics*, Vol 124, 177-191, 1996.
7. F. Q. Hu, M. Y. Hussaini, J. L. Manthey, " Application of low-dissipation and low-dispersion Runge-Kutta schemes to Benchmark Problems in Computational Aeroacoustics", *ICASE/LaRC Workshop on Benchmark Problems in Computational Aeroacoustics*, Hardin et al Eds, NASA CP 3300, 1995.

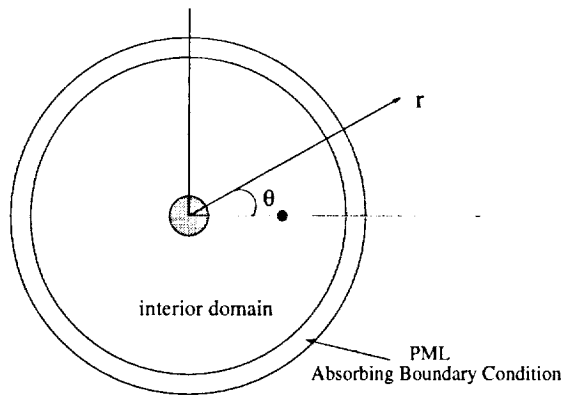


Figure 1. Schematic of the computational domain in cylindrical coordinates. A PML domain is introduced at outer boundary.

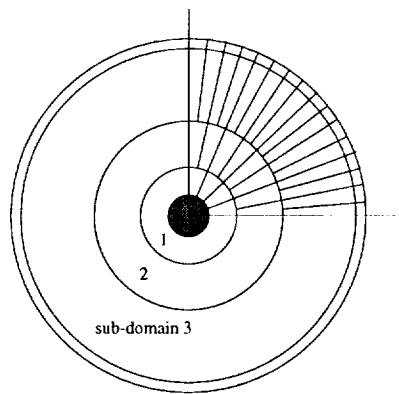


Figure 2. A schematic showing variable spacing in θ direction in sub-domains.

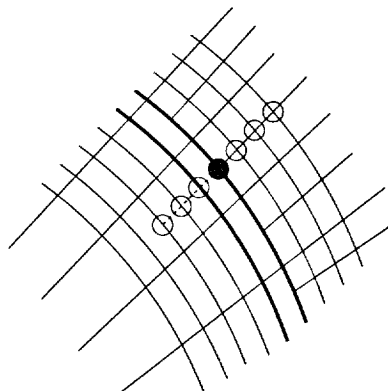


Figure 3. Extra values near the interface of sub-domains.

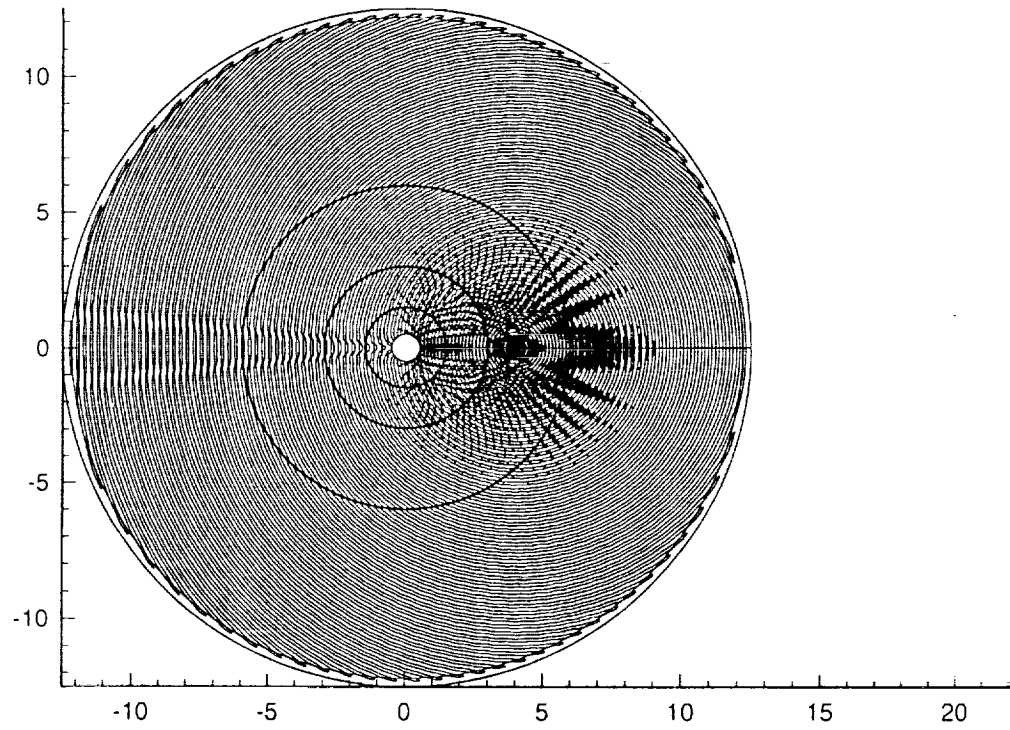


Figure 4. Instantaneous pressure contours. Problem 1.

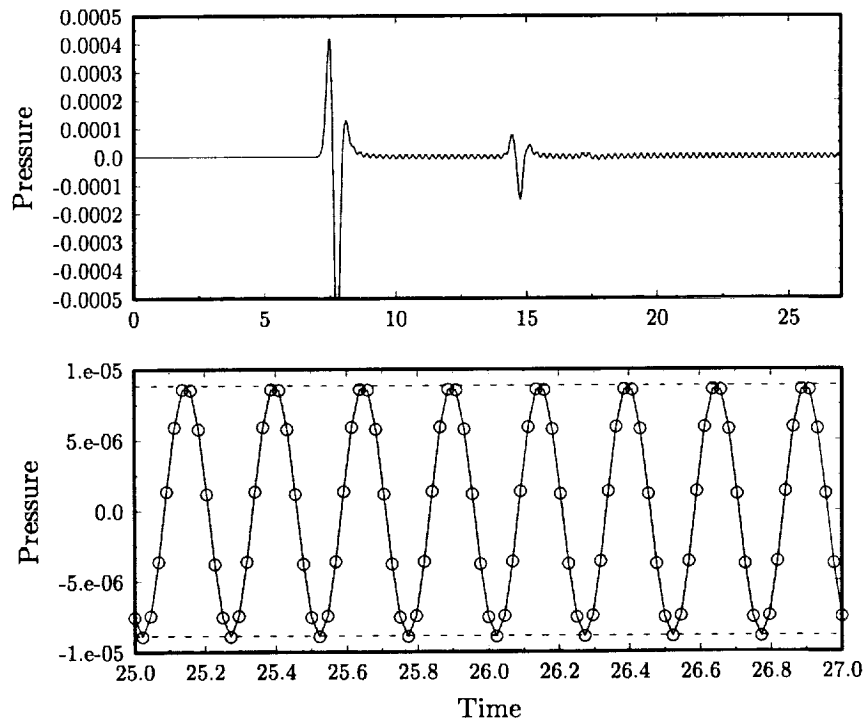


Figure 5a. Pressure as a function of time at $r = 11.6875$, $\theta = 0$.

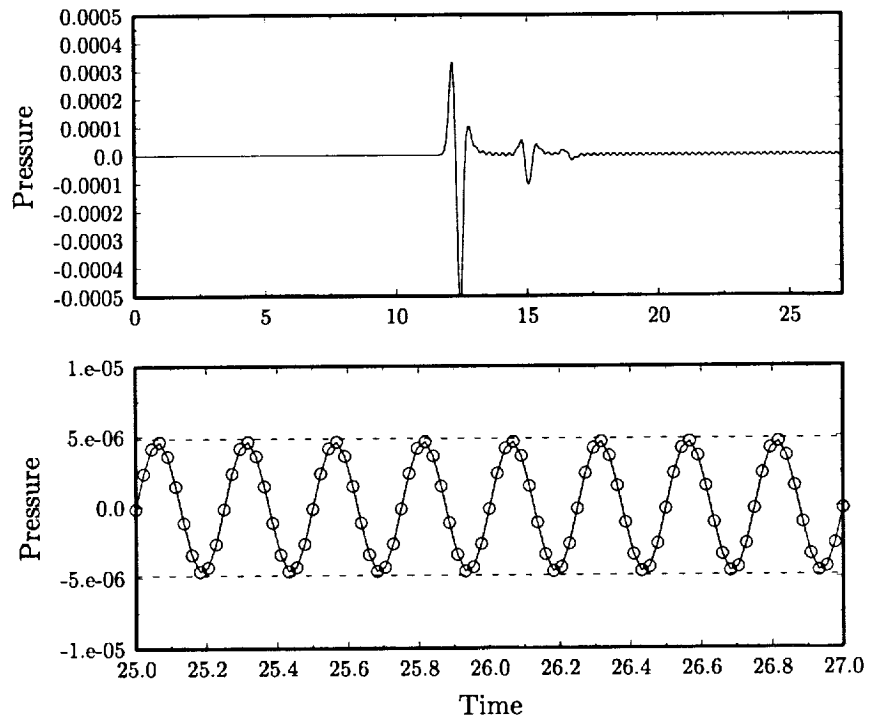


Figure 5b. Pressure as a function of time at $r = 11.6875$, $\theta = \pi/2$.

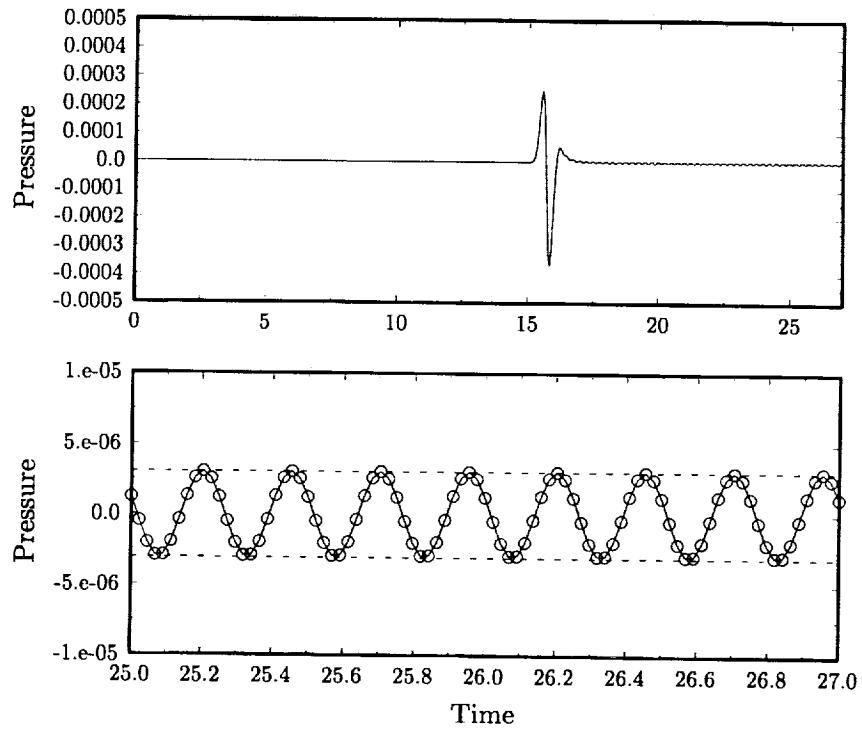


Figure 5c. Pressure as a function of time at $r = 11.6875$, $\theta = \pi$

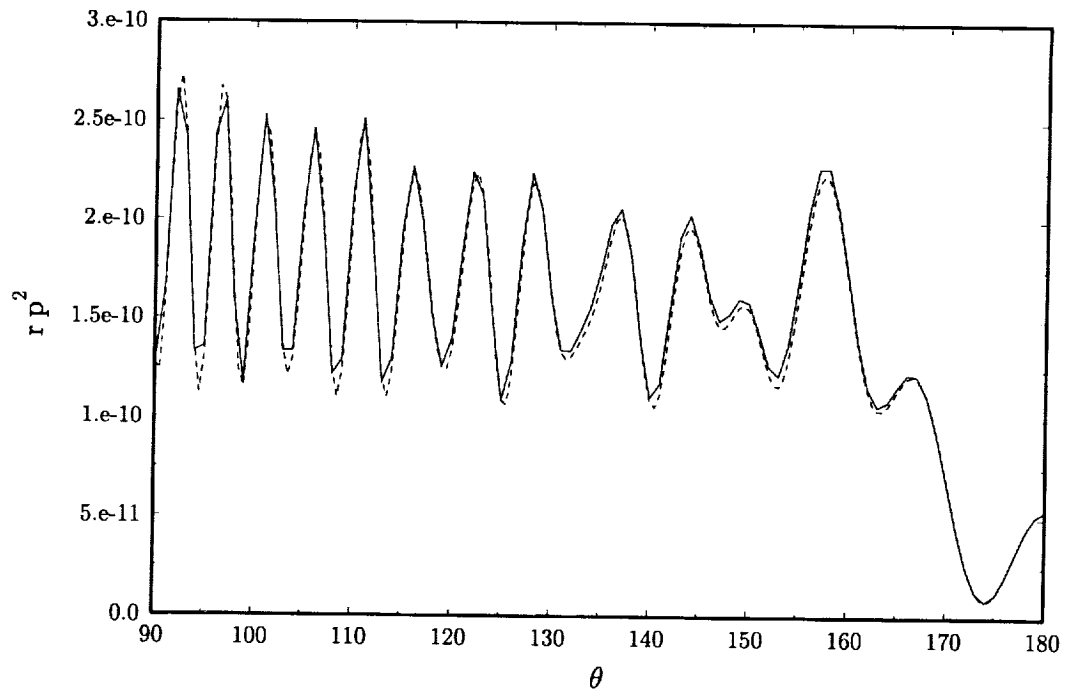


Figure 6. Directivity computed at $r = 11.6875$. ——— computed, - - - exact.

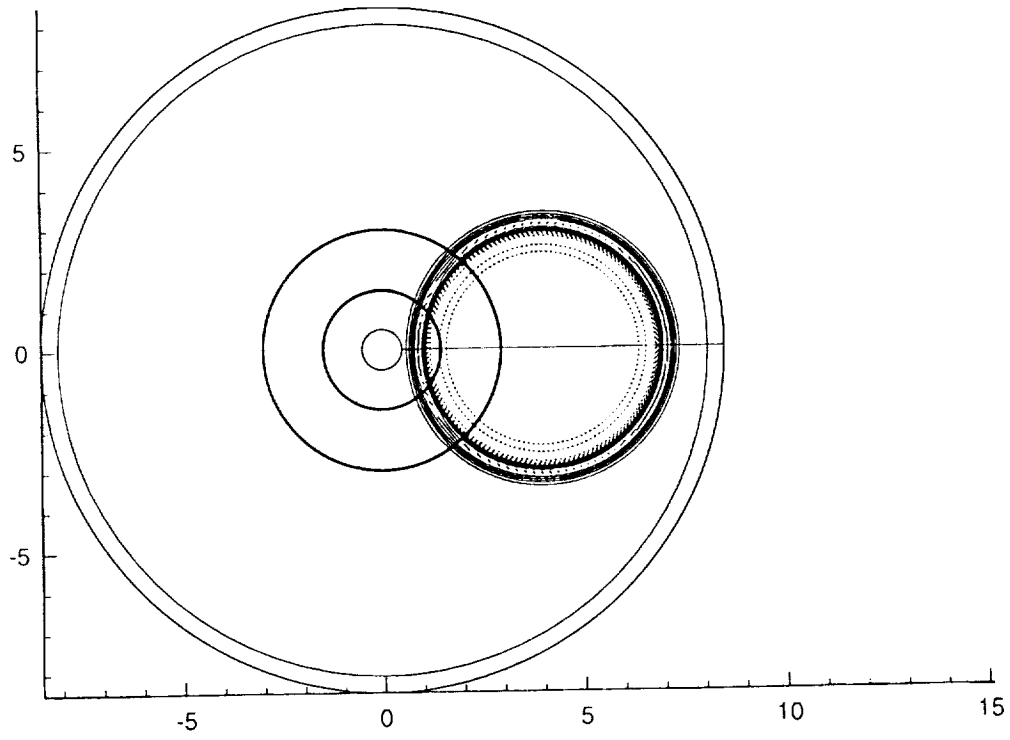


Figure 7a.

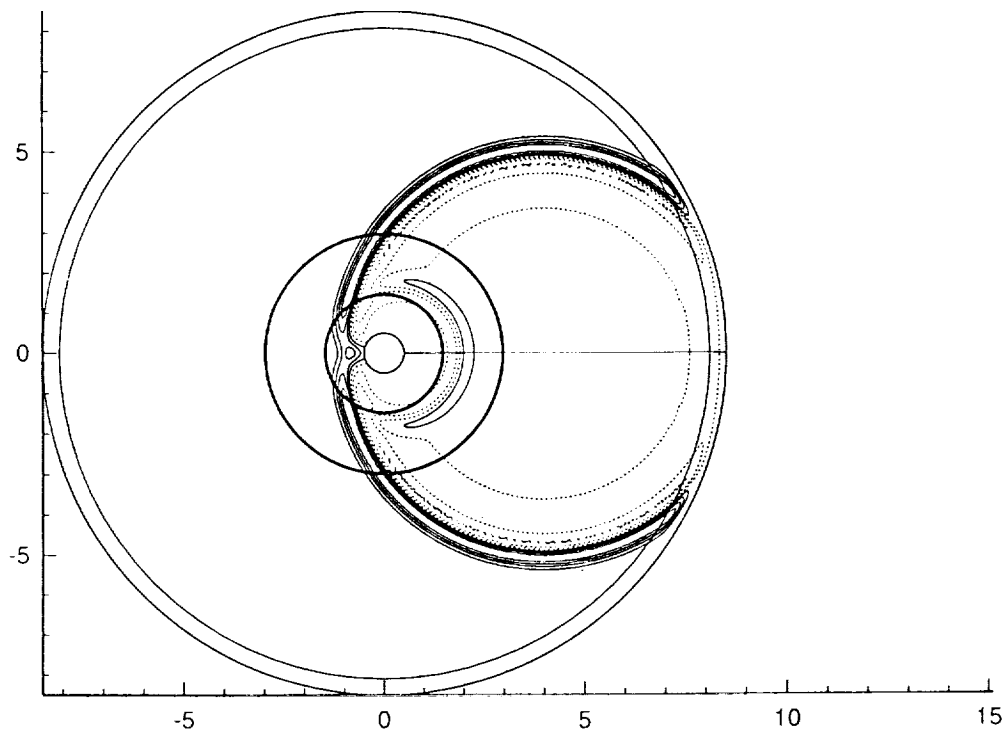


Figure 7b.

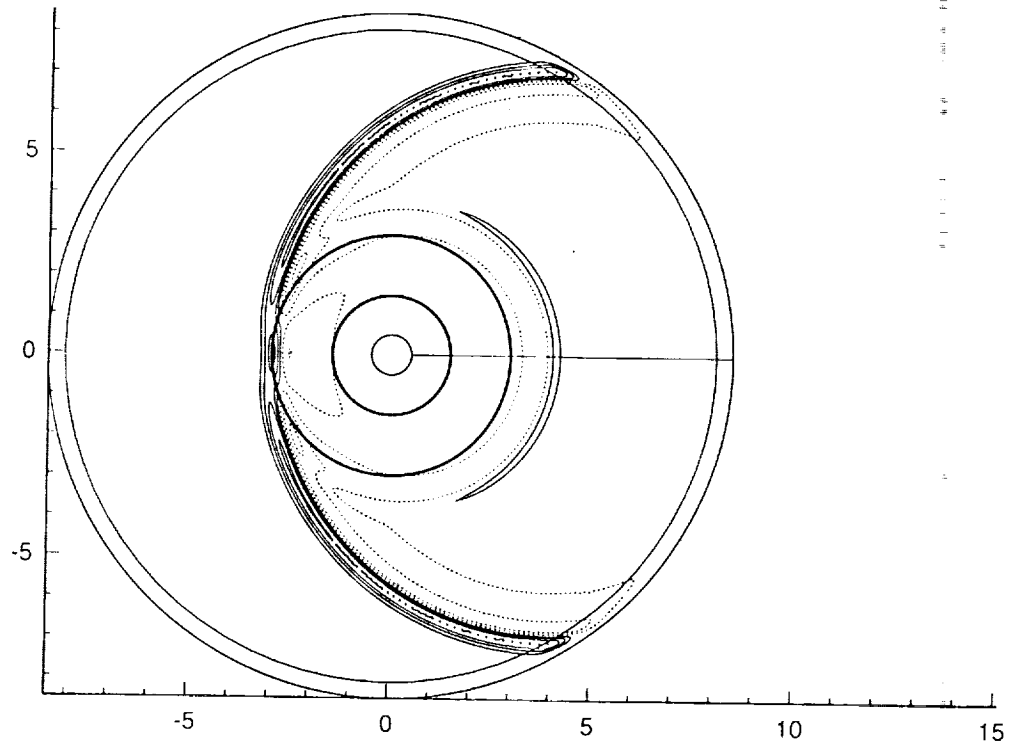


Figure 7c

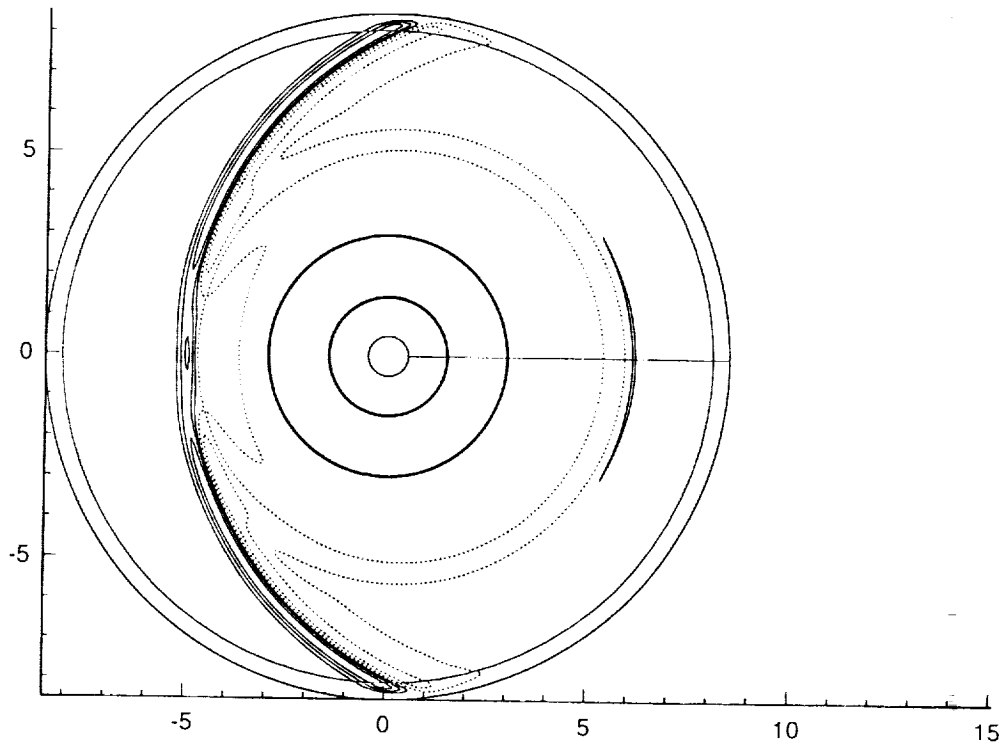


Figure 7d.

Figure 7 Instantaneous Pressure contours. Problem 2. (a) $t = 3$; (b) $t = 5$; (c) $t = 7$; (d) $t = 9$.

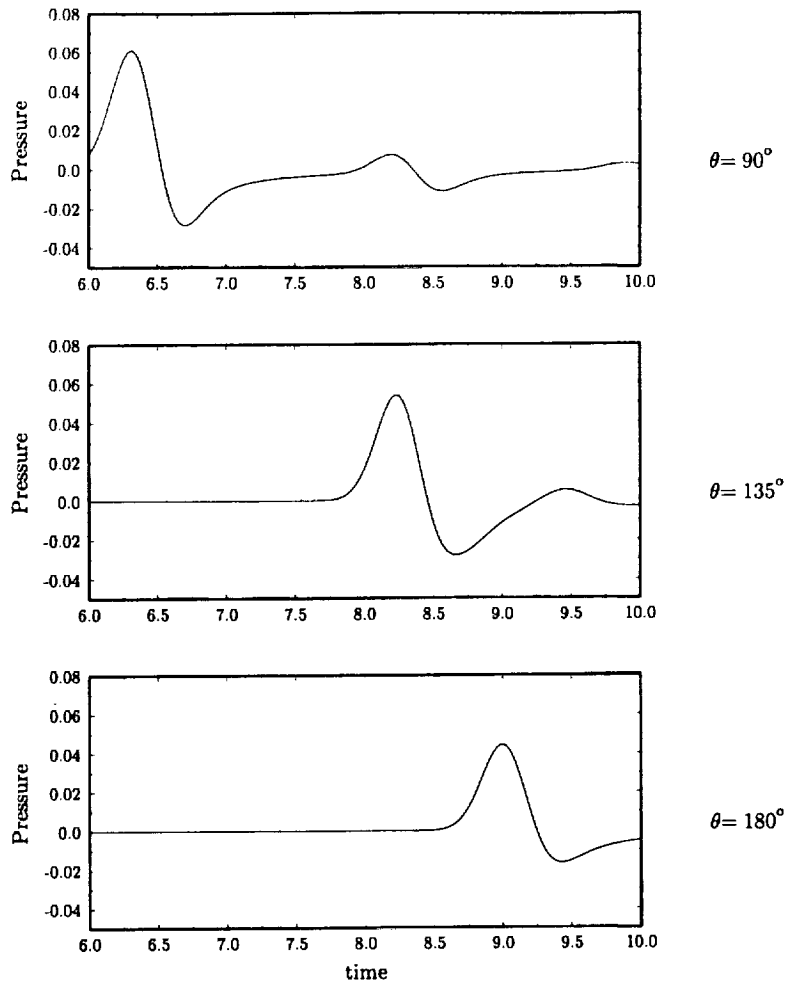


Figure 8. Pressure history at three chosen locations. $r = 5$.

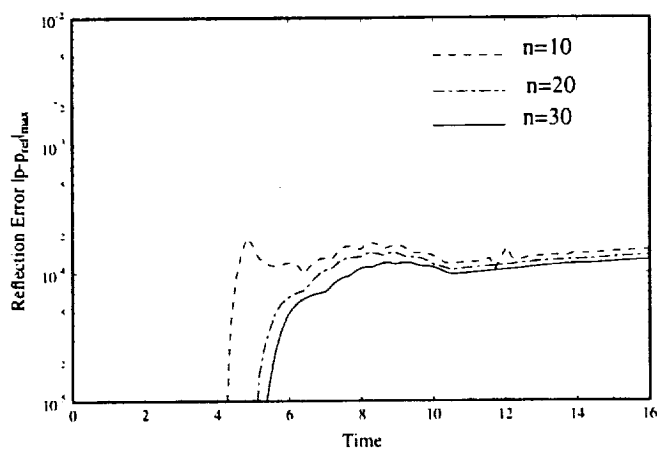


Figure 9. Maximum umerical reflection error as compared to a reference solution. The reference solution is obtained using a larger computational domain. Indicated are the width of PML domain.

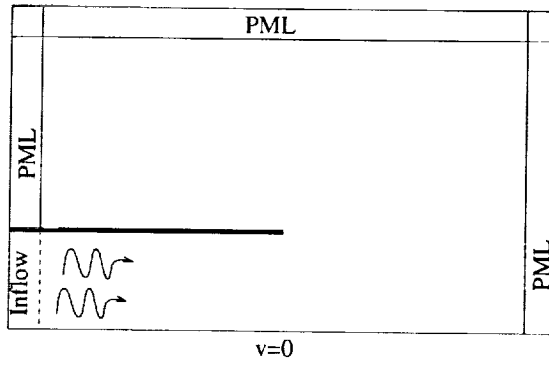


Figure 10. Schematic of the computational domain for Category 2, Problem 2. PML absorbing domains are introduced at the far field, as well as an inflow-PML domain at the inlet.

$\sigma_x \neq 0$ $\sigma_r \neq 0$	$\sigma_x = 0$ $\sigma_r \neq 0$	$\sigma_x \neq 0$ $\sigma_r \neq 0$	r_p
$\sigma_x \neq 0$ $\sigma_r = 0$	$\sigma_x = \sigma_r = 0$	$\sigma_x \neq 0$ $\sigma_r = 0$	
x_p			

Figure 11. Schematic of absorbing coefficients in the interior and PML domains.

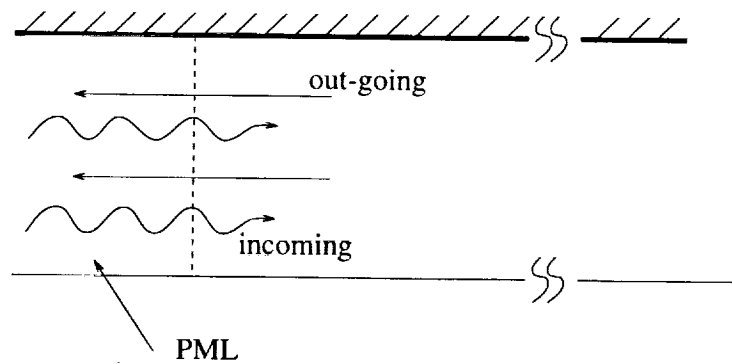


Figure 12. At the duct inlet, incoming and out-going waves co-exist. An inflow-PML domain is introduced inside the duct at the inlet to absorb the out-going wave only.

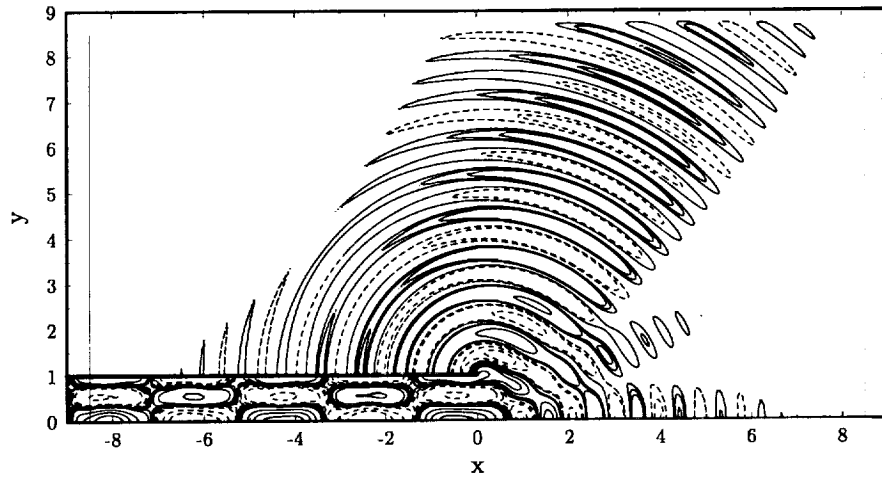


Figure 13. Pressure contours at $t = 87.2$, $\omega = 7.2$.

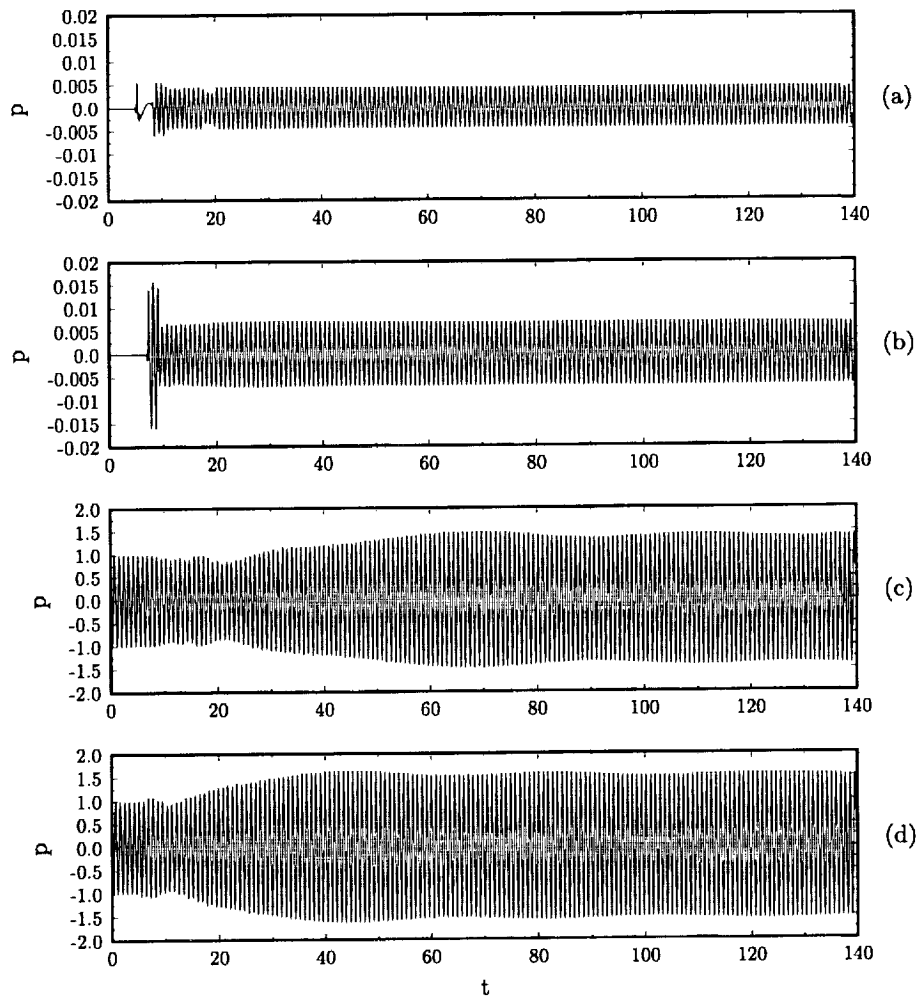


Figure 14. Pressure history at four locations, $\omega = 7.2$, (a) $(x, r) = (8, 0)$, (b) $(0, 8)$, (c) $(-2, 0)$, (d) $(-4.5, 0)$.

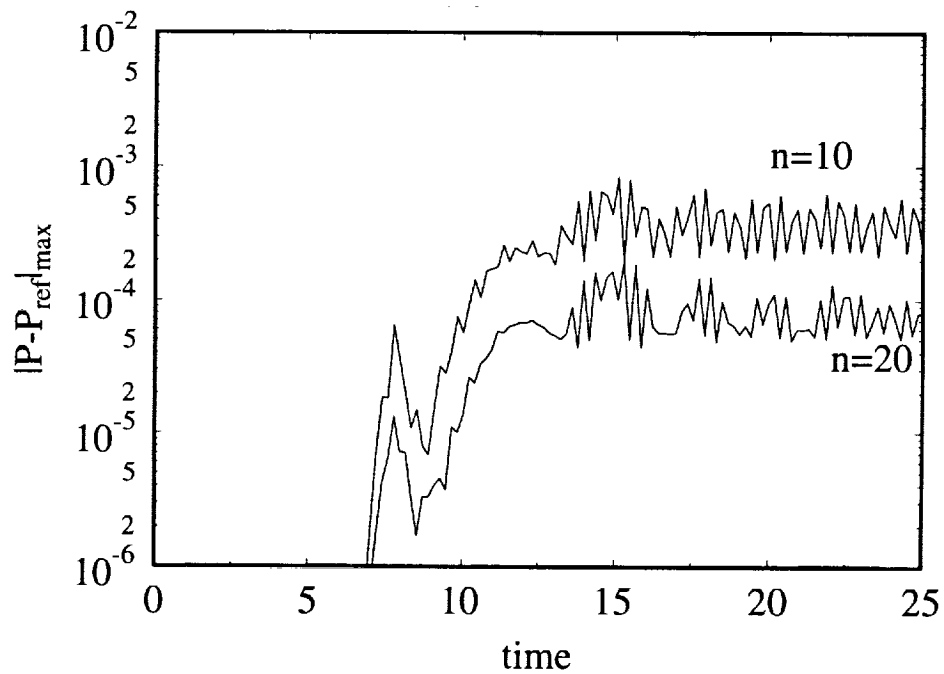


Figure 15. Maximum reflection error on the far field boundaries. The reference solution is obtained by using a larger computational domain. n indicates the width of the PML domain used.

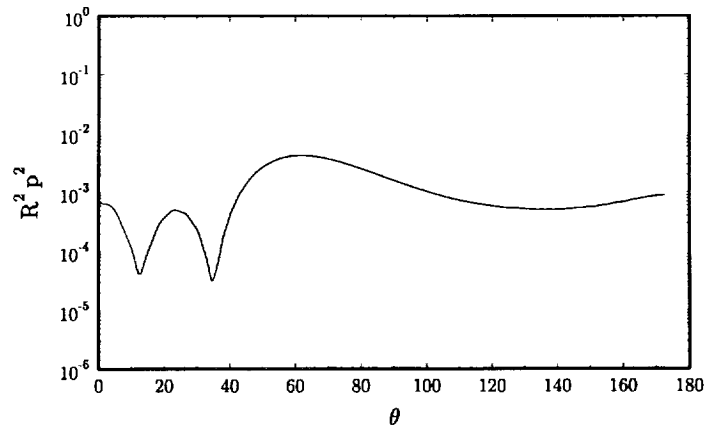


Figure 16. Directivity of radiated sound. $\omega = 7.2$.

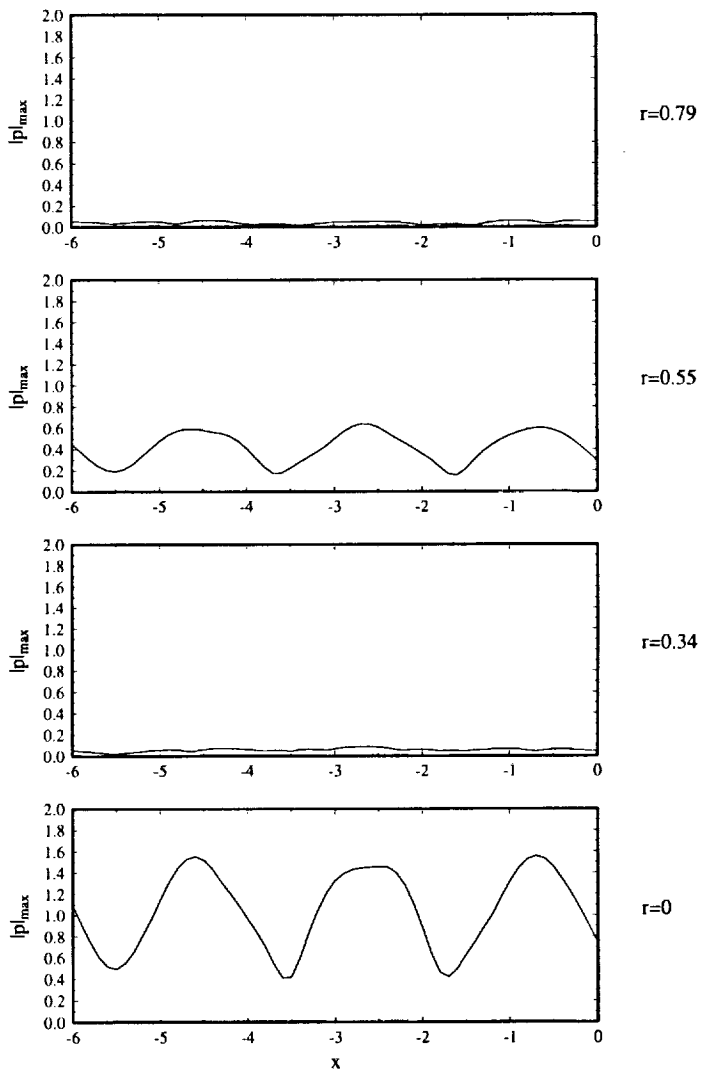


Figure 17. Pressure envelopes inside the duct at indicated values of r . $\omega = 7.2$

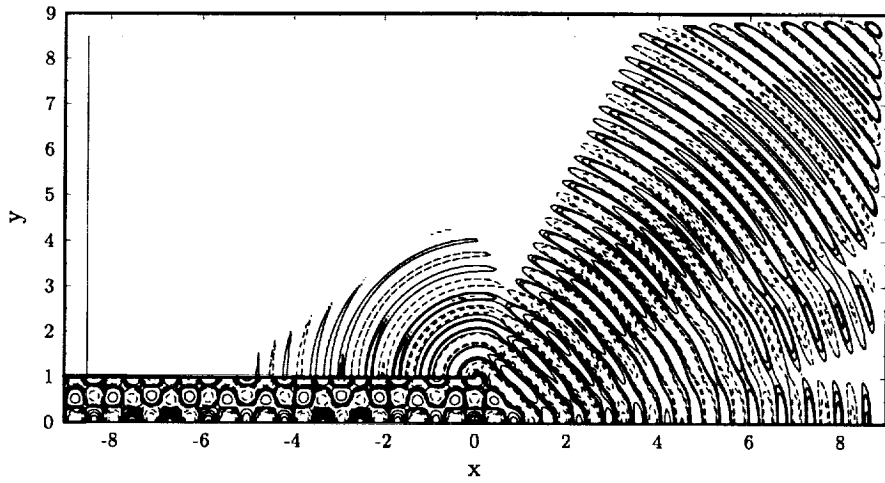


Figure 18. Pressure contours at $t = 87.2$, $\omega = 10.3$.

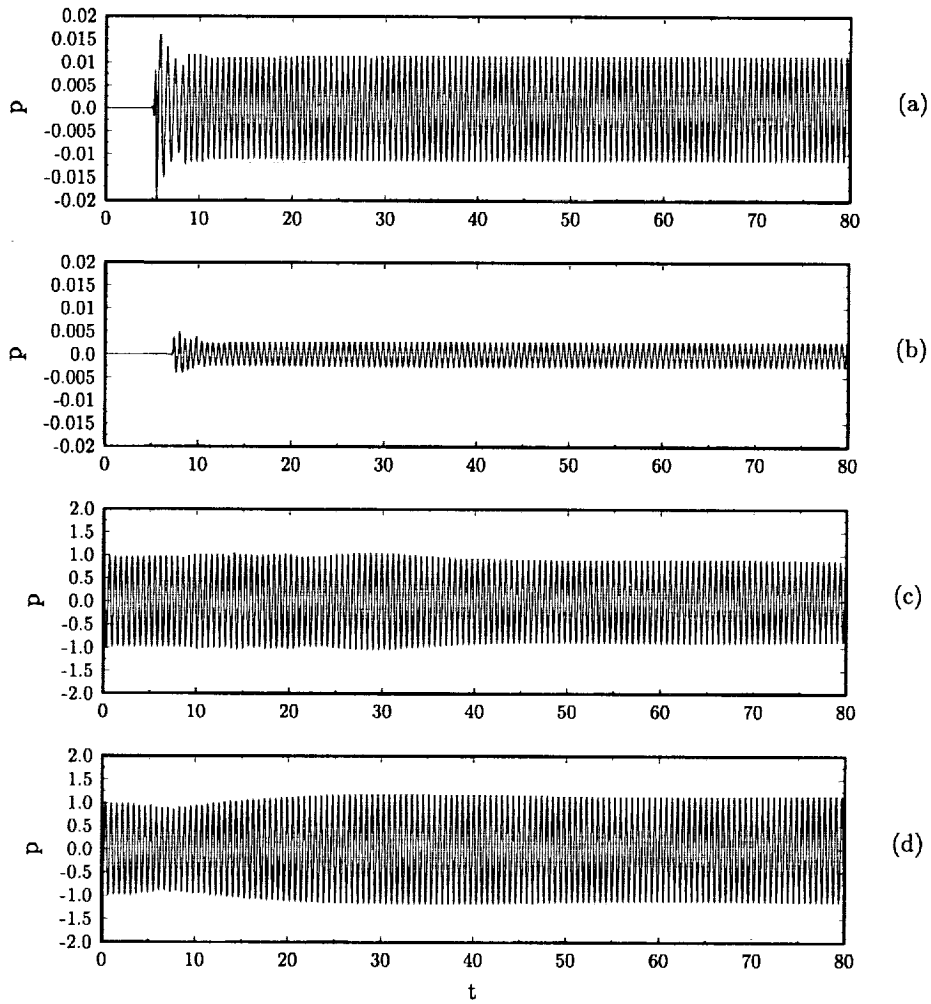


Figure 19. Pressure history at four locations, $\omega = 10.3$, (a) $(x, r) = (8, 0)$, (b) $(0, 8)$, (c) $(-2, 0)$, (d) $(-4.5, 0)$.

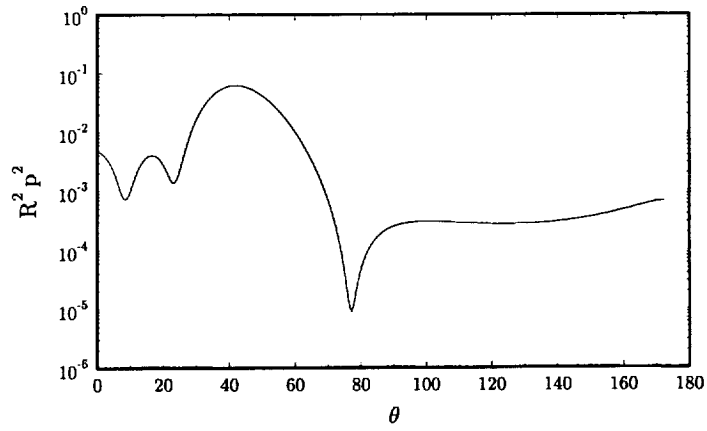


Figure 20. Directivity of radiated sound. $\omega = 10.3$.

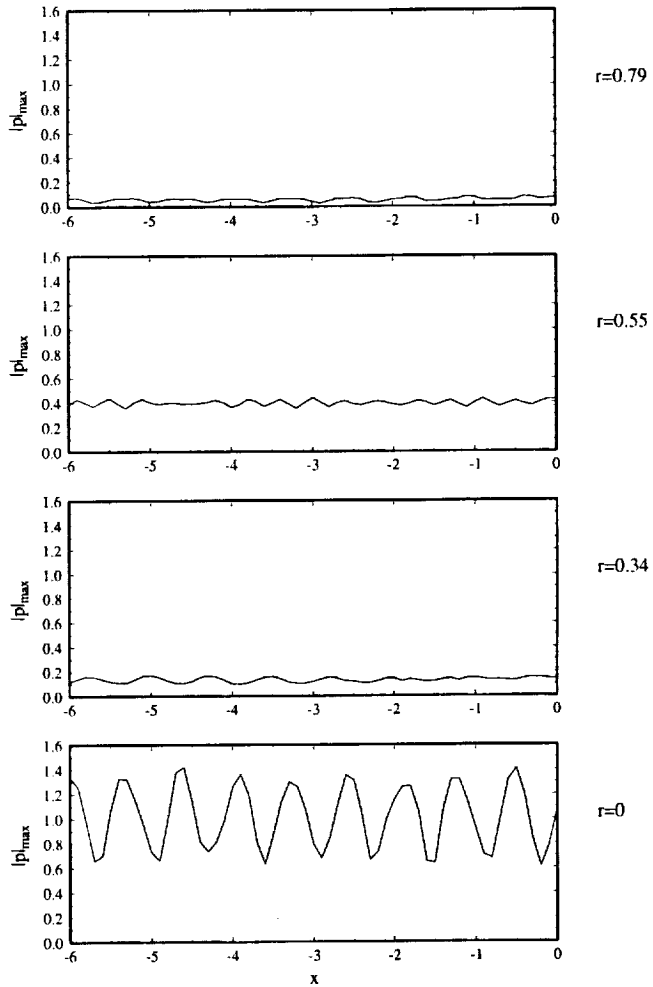


Figure 21. Pressure envelopes inside the duct at indicated values of r . $\omega = 10.3$

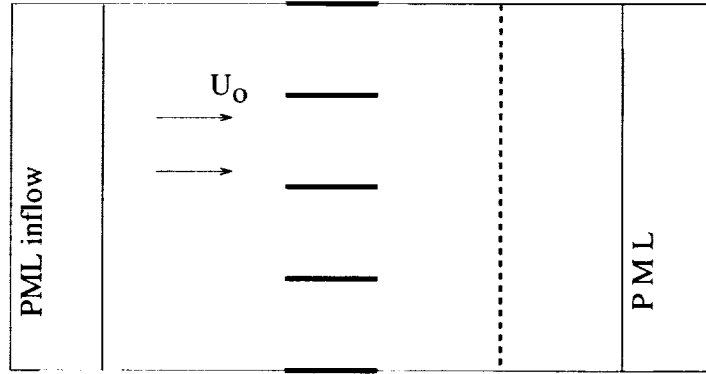


Figure 22. Schematic of the computational domain for Category 3.

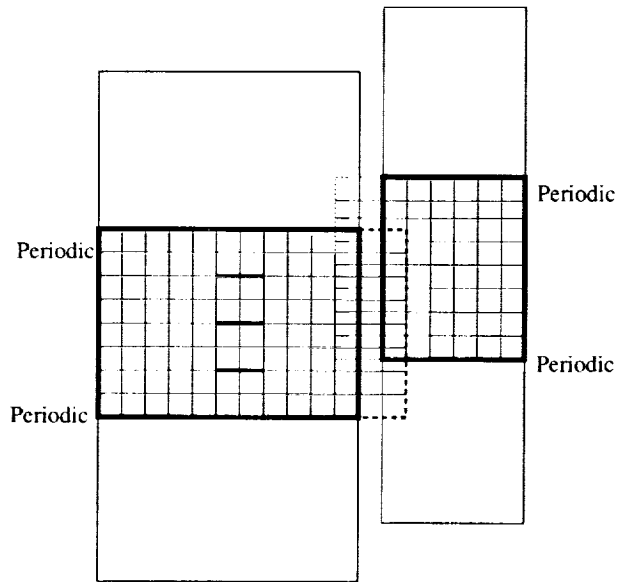


Figure 23. Sliding zone.

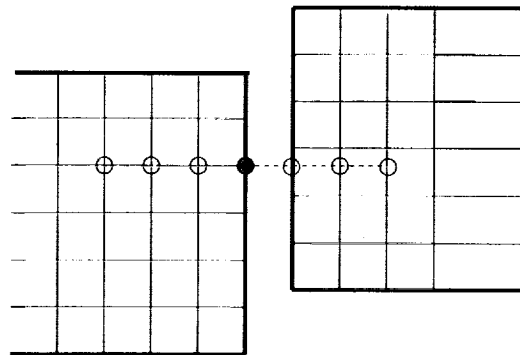


Figure 24. Extra grid points near the sliding interface for a central difference scheme.

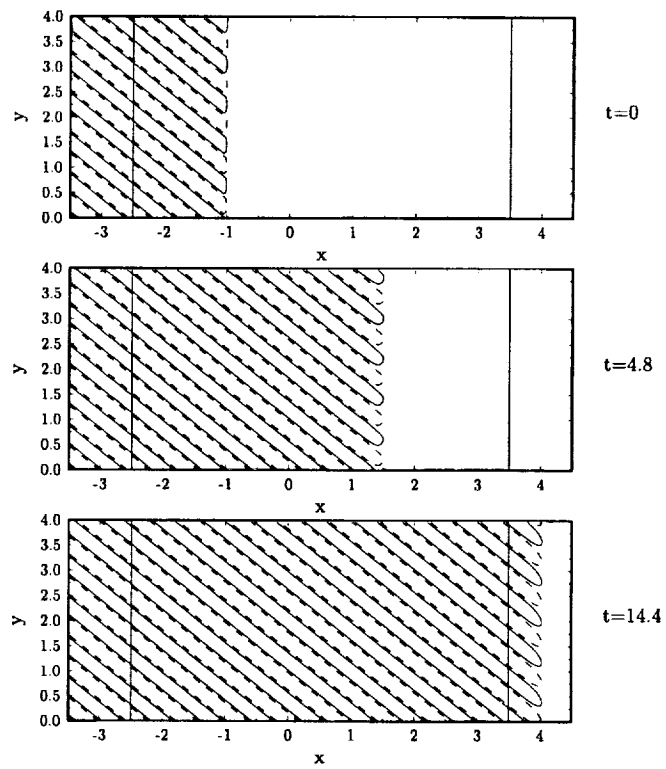


Figure 25. Instantaneous velocity contours at indicated moments, simulating a plane vorticity wave convecting with the mean flow.

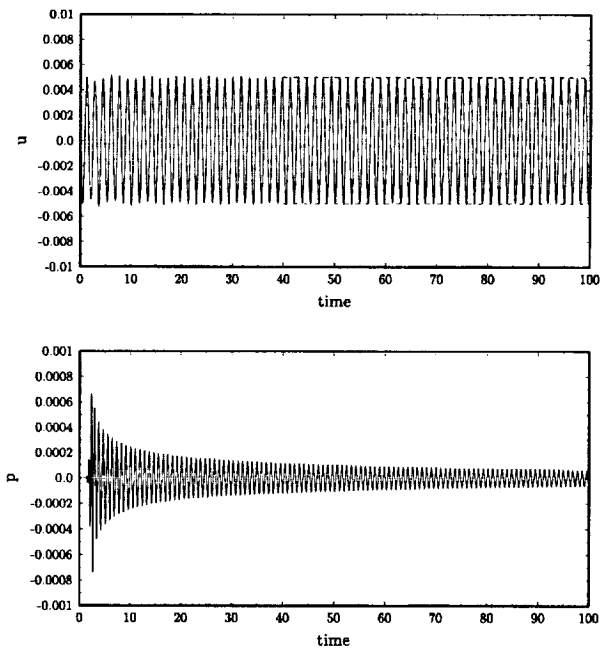


Figure 26. Velocity and pressure history at $(x, y) = (-2, 0)$.

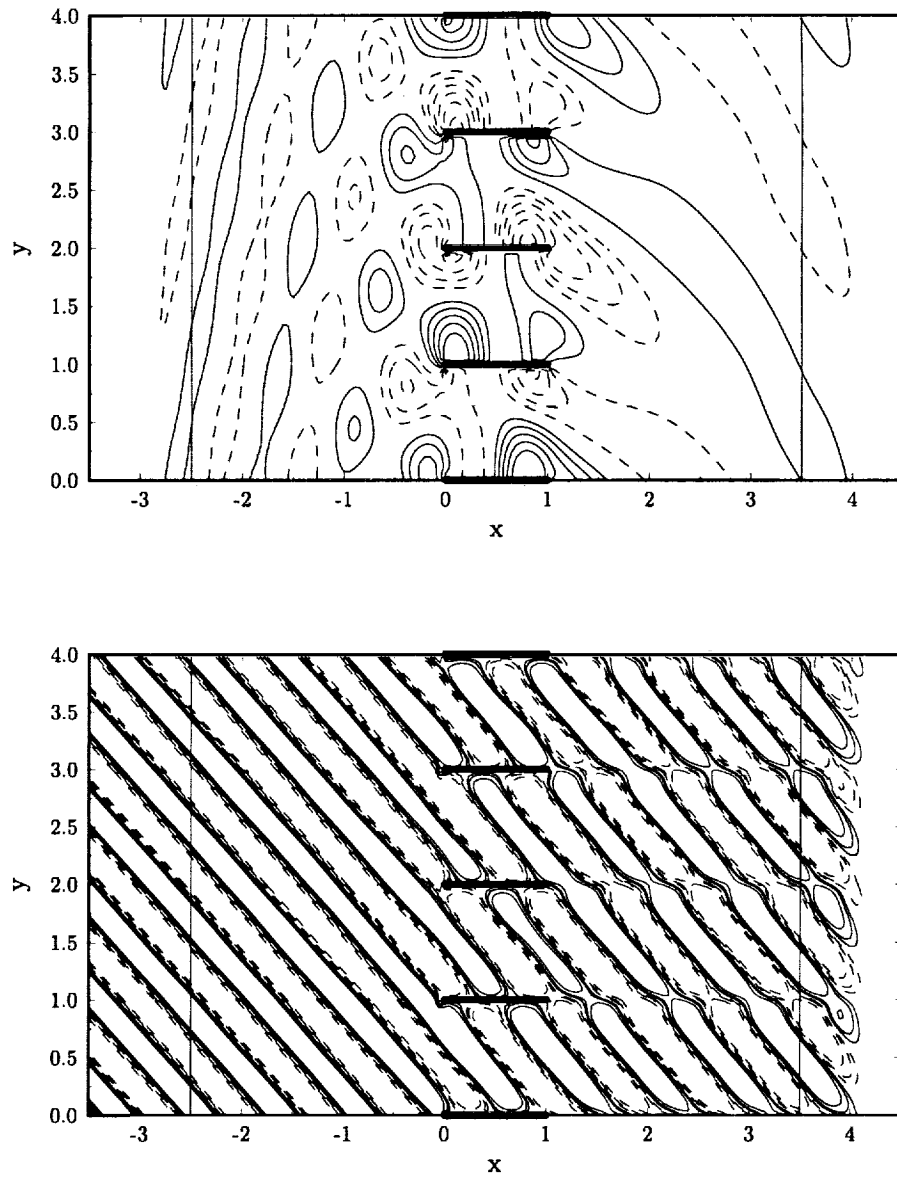


Figure 27. Instantaneous v -velocity and pressure contours. Problem 2, low frequency case.

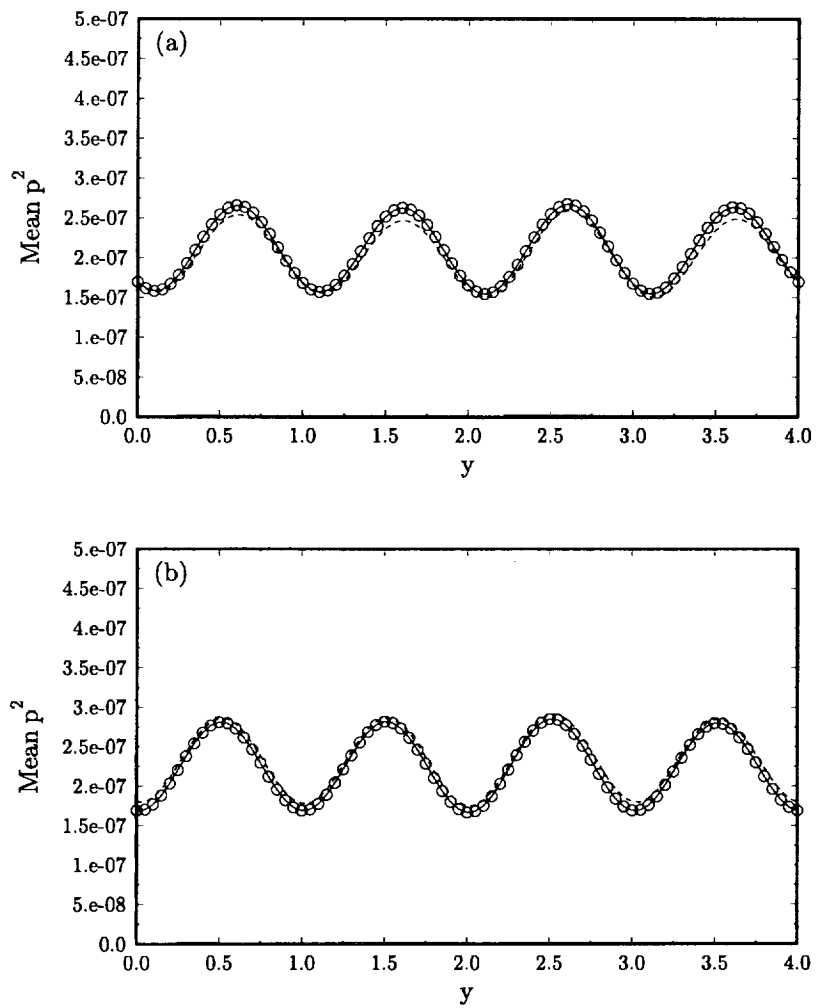


Figure 28. Sound intensity. Low frequency case. (a) $x = -2$, (b) $x = 3$. - - - - Problem 1, ———, Problem 2, o Problem 3.

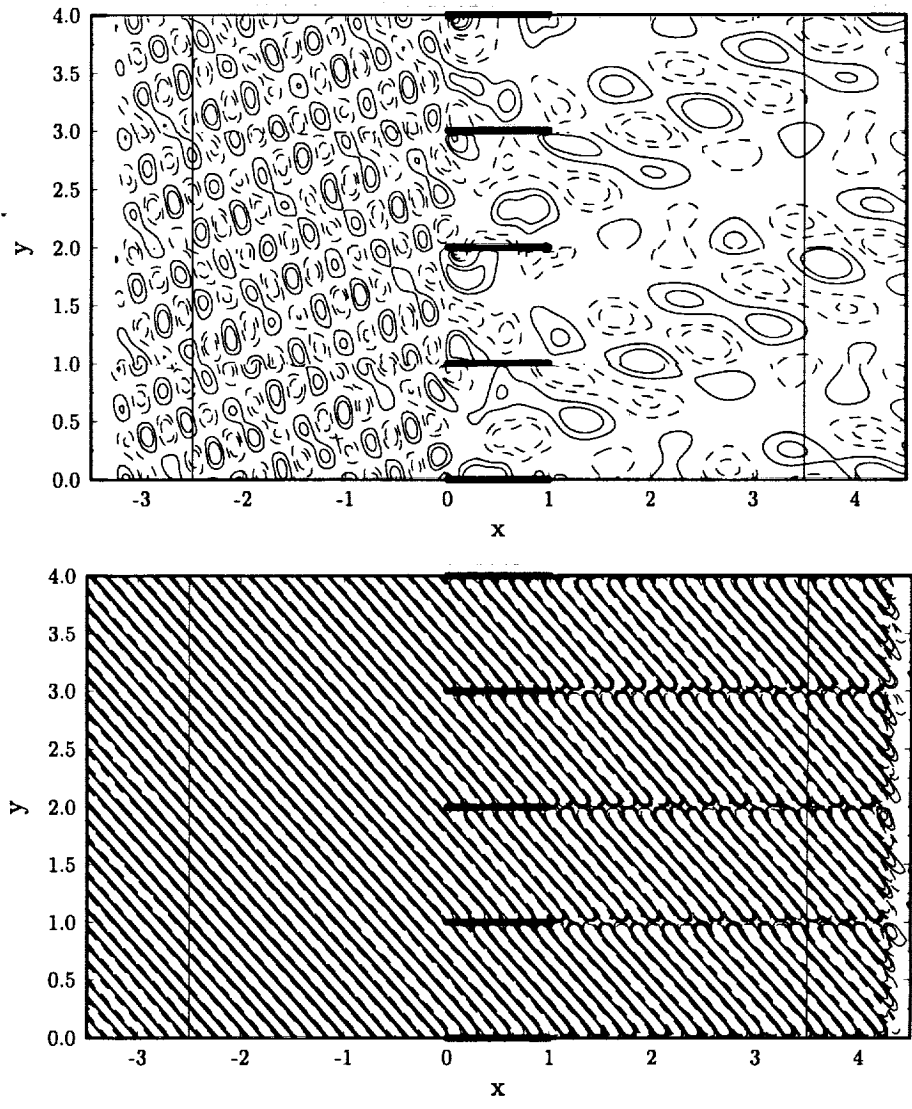


Figure 29. Instantaneous pressure (top) and v -velocity (bottom) contours. High frequency case.

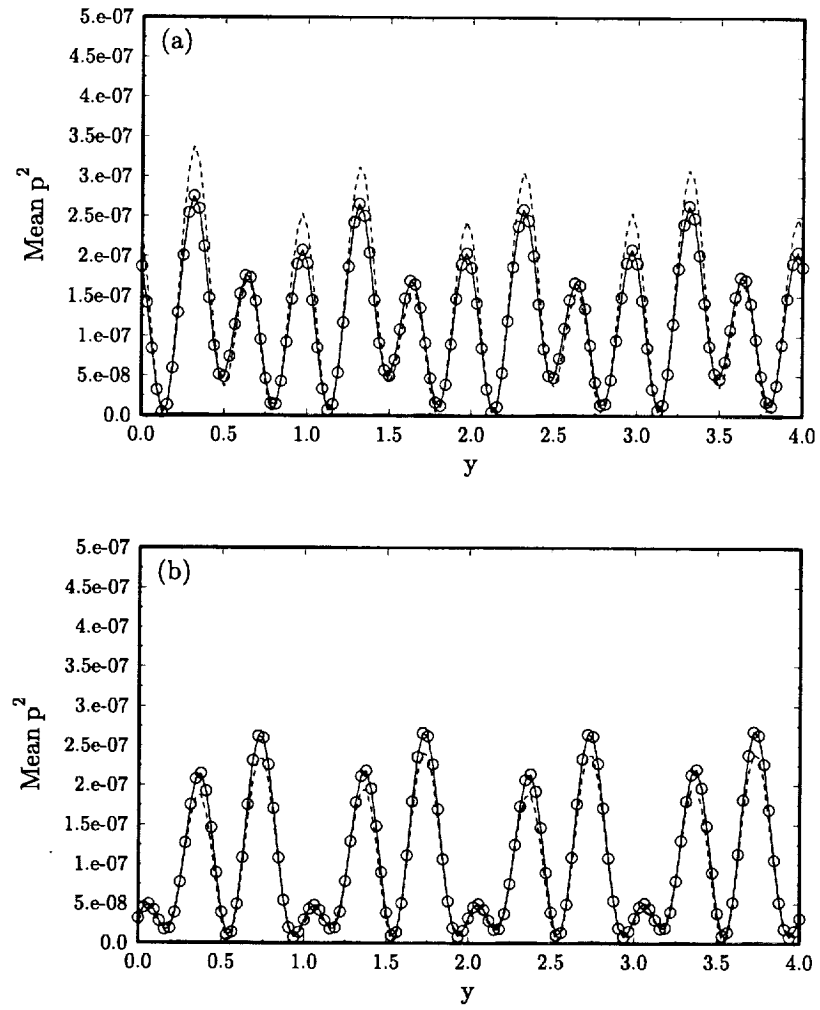
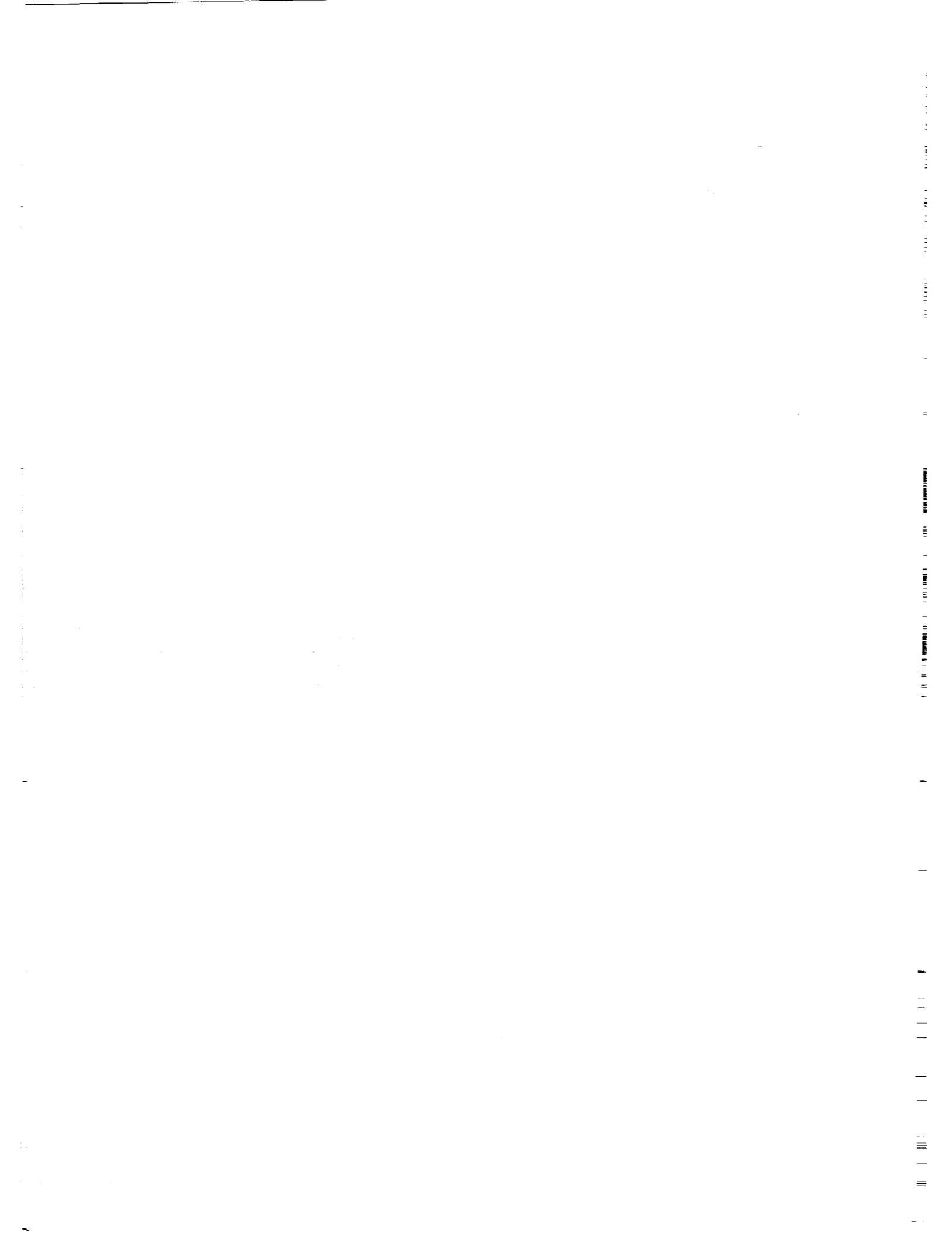


Figure 30. Sound intensity. High frequency case. (a) $x = -2$, (b) $x = 3$. - - - Problem 1, ———, Problem 2, o Problem 3.



515-71
043473

ACOUSTIC CALCULATIONS WITH SECOND- AND FOURTH-ORDER UPWIND LEAPFROG SCHEMES

293985
p10

Cheolwan Kim and Philip Roe
W. M. Keck Foundation Laboratory for Computational Fluid Dynamics,
Department of Aerospace Engineering, University of Michigan, Ann Arbor MI
48109-2118.

INTRODUCTION

Upwind leapfrog schemes were devised by Iserles [1] for the one-dimensional linear advection equation and the second-order version was extended to multidimensional linear wave systems by Roe and Thomas [2,3] using bicharacteristic theory. Fourth-order versions on square grids were presented by Thomas [4] and Nguyen [5] for acoustics and electromagnetic waves respectively. In the present paper we describe experience implementing the second- and fourth-order methods on polar grids for two of the workshop test cases.

THE SECOND-ORDER ALGORITHM

In polar coordinates (r, θ, t) with velocity components u, v the acoustic equations in dimensionless form are

$$p_t + u_r + \frac{1}{r}v_\theta + \frac{u}{r} = 0, \quad (1)$$

$$u_t + p_r = 0, \quad (2)$$

$$v_t + \frac{1}{r}p_\theta = 0. \quad (3)$$

Bicharacteristic versions of these equation, describing respectively radial and circumferential wave propagation, are

$$(\partial_t \pm \partial_r)(p \pm u) + \frac{1}{r}\partial_\theta v = -\frac{u}{r} \quad (4)$$

$$(\partial_t \pm \frac{1}{r}\partial_\theta)(p \pm v) + \partial_r u = -\frac{u}{r} \quad (5)$$

Compared with their Cartesian counterparts, these equations have 'source terms' on the right-hand-side, which require careful treatment to avoid exciting long-term instabilities, as noted in [2,3].

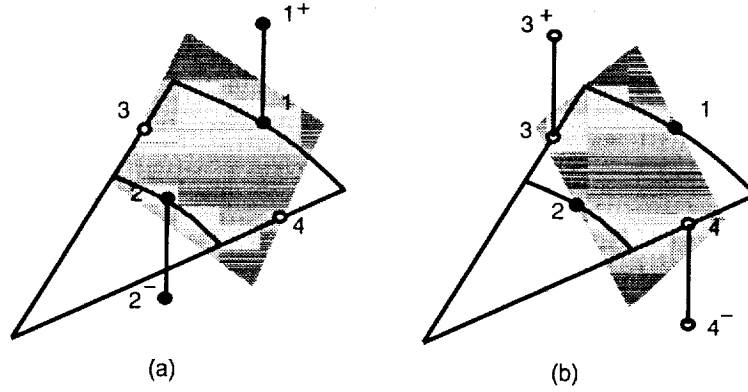


Figure 1: Basic second-order stencils for waves running in the $+r$ and $+\theta$ directions. Quantities u, p are stored at the black grid points and v, p at the white ones.

The basic philosophy of the method is to discretize each bicharacteristic equation by using points that cluster as closely as possible around the plane wave that it describes, as shown in Fig 1. This also motivates the use of staggered storage. To discretize the equation (4⁺) on the stencil of Fig 1(a), the time derivative of u , for example, is taken as the average of the two differences

$$u_t \simeq \frac{u_{1+} - u_1 + u_2 - u_{2-}}{2\Delta t}.$$

The spatial derivatives are evaluated in the only possible way, and the ‘source term’ is evaluated in a way that was found to eliminate instability in [2,3] as

$$\frac{u_{1+} + u_{2-}}{r_1 + r_2}.$$

The equations for circumferential wave motion are treated analogously, except that no special treatment of the source term is required.

We offer the following comments on this discretization

- Because the weightings are equal for points symmetrically disposed with respect to the centroid of the stencil, the discretization is time-reversible and has even-order accuracy. In this simple case the accuracy is second-order.
- For every mesh point, two variables are stored, and two bicharacteristic equations are available. The scheme is therefore explicit. It is found to be stable up to a Courant number of 0.5.
- The scheme can be applied directly at computational boundaries. The equation describing any wave entering the domain at the boundary is unavailable, but is simply replaced by the appropriate boundary condition. A point on the outer boundary is updated by any outgoing wave, but there are no incoming waves.

- Because the discretization connects three time levels there exist, as with all leapfrog schemes, spurious (non-physical) solutions.
- Because the pressure is stored twice, there is a possible error mode in which the pressures stored at the black and white mesh points become uncoupled.
- It is an easy consequence of the governing equations that the vorticity should not change with time. However, this is not enforced by the discretization, so another spurious mode may appear that is linked to vorticity.

The first three of these properties are desirable; the last three constitute potential problems.

Like any other leapfrog method, we need a special starting procedure for the first time step. This is important, because errors generated at that moment can be inherited by all later times. At present, however, we use a very crude starting procedure. We put $u^1 \equiv u^0$, and then advance to u^2 with one half of the regular timestep. It is easy to show that this effectively advances u^0 to u^2 with the regular timestep according to a first-order upwind scheme.

THE FOURTH-ORDER ALGORITHM

Construction of this is straightforward in principle. Each of the quantities appearing in the second-order scheme can be replaced by its Taylor expansion (with respect to the centroid of the stencil) to give the equivalent equation of the scheme. The higher derivatives that appear can be regarded as error terms and are mixtures of space and time derivatives. The time derivatives are due to expansions like

$$\frac{u_{1+} - u_1 + u_2 - u_{2-}}{2\Delta t} = \partial_t u + \frac{h^2}{8} \partial_{xxt} u + \frac{hk}{4} \partial_{xtt} u + \frac{k^2}{8} \partial_{ttt} u + \mathcal{O}(h^4, k^4).$$

from which the terms involving time can be eliminated, in the spirit of Lax-Wendroff methods, by using the governing equations to convert time derivatives to space derivatives. The outcome is an estimate of the truncation error entirely in terms of space derivatives. Evaluating these merely to second order is enough to eliminate the errors, because they come already multiplied by second-order factors. If the error terms are kept in a form that preserves the symmetry with respect to the centroid of the stencil, it is guaranteed that no third-order terms will be introduced. The resulting scheme will be fourth-order, time-reversible, and fully discrete. All of the above algebraic manipulations can be carried out using symbolic manipulation, and the necessary FORTRAN expressions can be generated in the same way.

Unfortunately the resulting scheme may not be stable; numerical experiments indicate that instability is usually encountered, although it may be very mild and may not be apparent until after several hundred time steps. Because the schemes are time-reversible, the instability always takes the form of a bifurcation where two neutrally stable modes split into one stable mode and one unstable mode. In the language of Fourier analysis, the complex amplification factors move off the unit circle. In fact a Fourier analysis will reveal eight¹ modes, each of which has an amplification factor depending on a vector wavenumber \vec{k} , on the (possibly unequal) mesh spacings, on the Courant number, and on the magnitude of the source term (assumed locally constant). Three of the eight modes are physical, corresponding to acoustic waves travelling in one of two directions plus a stationary vorticity mode. The other five are spurious modes which may be excited by boundary conditions, or starting errors, or by rounding error.

There seems to be no analytical method for checking stability, and no simplifying assumptions that are useful (for example, the bifurcations do not always begin at the highest wavenumbers). Therefore we have had to resort to a numerical search in the parameter space. One fact that influences stability is that the discretizations available to remove the second-order errors are far from unique. A term like $\partial_{rrr}u$ can be performed using a single row of radial points or by averaging over more than one row (this situation is familiar in other contexts; for example there are, in higher dimensions, families of Lax-Wendroff schemes sharing the same stencil). We had hoped by trial and error, or inspired insight, to find the correct choices that lead to stable schemes. So far this has not happened, and we have had to introduce smoothing operators.

SMOOTHING OPERATORS

An ideal smoothing operator is one that attacks only the spurious modes, leaving the physical modes untouched. To accomplish this rigorously would require a decomposition of the numerical solution into its eigenmodes, and that would be very expensive. However, intuitive reasons were given above for supposing that the method might support spurious modes involving either pressure decoupling or vorticity. We do not in fact find modes exhibiting either type of behaviour in a pure form, but damping out such behaviour does have a powerful effect on the spurious modes. It is simple to do this by focussing on the control volumes shown in Fig 2. In control volume D pressure decoupling is detected by comparing the average pressures along each diagonal. The high pair are adjusted downward, and vice versa. Every pressure value takes part in four such comparisons, and the net effect can be shown to be a fourth-order adjustment that does not damage the formal accuracy of the scheme. In control volume V the vorticity ω can be evaluated. If it turns out to be positive (as

¹There are four unknowns in two dimensions; the two velocity components and the pressure counted twice. Recognizing that the variables stored at odd and even time levels are independent gives eight.

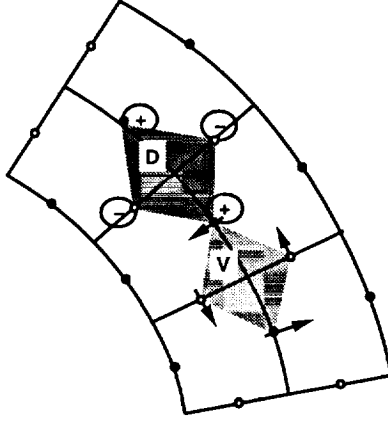


Figure 2: Control volumes for detecting pressure decoupling and vorticity modes.

shown) then small equal corrections are made to each of the four velocities so as to reduce it. The effect of this can be described by the partial differential equation

$$\partial_t \vec{u} = \epsilon \operatorname{curl} \vec{\omega},$$

which has no effect on the divergence, but applies a Laplacian smoothing to the vorticity. Since the vorticity is anyway zero to truncation error, there is again no harm to the accuracy of the scheme. An analysis of this form of dissipation can be found in [6].

It has proved possible to determine the coefficients of these smoothing operators by performing the Fourier analysis numerically on Cartesian grids, but at the present time none of our analysis is systematic enough to justify recommending any universal values.

GRID REFINEMENT

We decided to attempt some of the workshop problems involving diffraction around a cylinder, and to employ a polar grid for the purpose. This would simplify the surface boundary conditions, and also be the first implementation of the upwind leapfrog methods on a non-Cartesian grid. There were no problems with maintaining accuracy, but the appearance of source terms, accompanied by slight uncertainty how best to discretize them, triggered weak instabilities that had to be removed by the smoothing operators just described.

There is a geometric problem, however, inevitably associated with trying to use polar grids on large domains. If we employ uniform intervals $\Delta r, \Delta \theta$ on a domain $r_1 \leq r \leq r_2$, then the aspect ratio of the cells will change by a factor r_2/r_1 and so the grid will contain cells whose aspect ratio is at least $\sqrt{r_2/r_1}$. These high-aspect-ratio

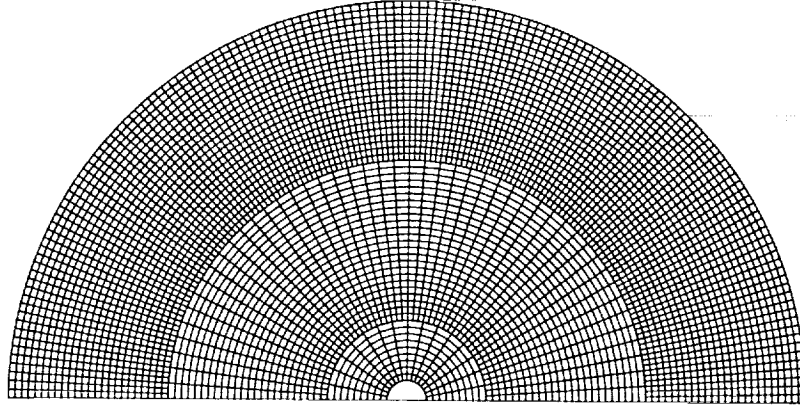


Figure 3: A typical (but rather coarse) grid ($\Delta r = \frac{1}{6}$).

cells significantly degraded both the accuracy and, in some cases, the stability of the code.

Therefore we divided the grid into three subgrids (as in Fig 3) so that in each outer grid there were three times as many radial lines as in the inner grid. This meant that for some grid points on an interface we lack the information required to provide the update due to the outgoing wave. This was determined simply by constructing two rings of ‘ghost points’ inside the interface and interpolating onto them with cubic polynomials. This worked very straightforwardly and gives good reason to hope that automatic adaptive mesh refinement (AMR) could be easily incorporated into the method at some future time.

BOUNDARY CONDITIONS

For the inner (cylinder) boundary, we again created two rings of ghost points, this time inside the cylinder surface. We extrapolated radially onto these points assuming that $u_r = 0$ and $\partial_r p = 0$ at the surface. Although we realise that the second of these conditions is only justified for $u_\theta = 0$, the results that we obtain appear to be fourth-order accurate away from the surface (see below).

At the outer boundary, the second-order method comes equipped with a default boundary condition, as mentioned above. Simply doing nothing special at the outer boundary means that no update is received from incoming waves, but the outgoing wave is updated by the outgoing radial bicharacteristic equation. It can be shown that this is effectively Tam’s second boundary condition.

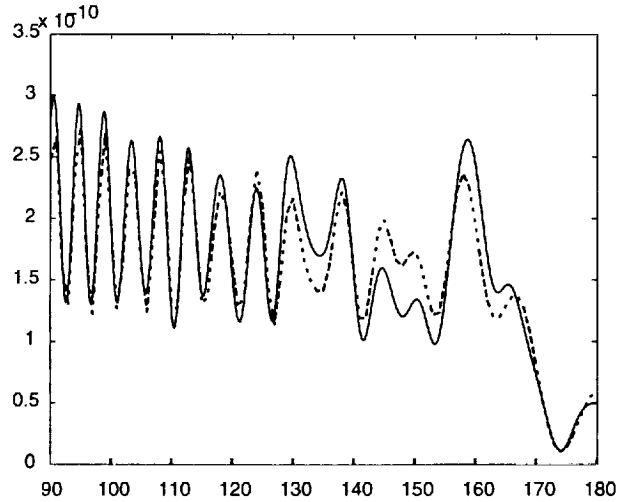


Figure 4: The mean square pressure $\overline{r|p^2|}$ at $r = 15.0$ for problem 1. The dashed line is the exact solution and the solid line is the numerical prediction on a grid with 10 points per wavelength ($\Delta r = \frac{1}{40}$).

RESULTS

CATEGORY 1, PROBLEM 1. We obtained results for this problem using grids defined radially by 8 and 10 grid points per wavelength. Using 8 points did not seem to be enough and we present only our results with 10 points. This translates to $\Delta r = \frac{1}{40}$. The frequency is $\omega = 8\pi$ and the solution is given in Figure 4 for $r = 15.0$. The computational domain was $0.5 \leq r \leq 16.0$. The directivity pattern seems to be very well predicted, but the amplitude is less satisfactory. Partly we attribute this to the effect of the small damping terms we had to introduce to cure instability due to the source terms arising from the non-Cartesian grid. It is possible that dealing with this more systematically would improve the agreement. We estimate that a calculation with 12 points per wavelength would be much better, but with our code still undergoing modification as the deadline approaches, we have not yet been able to perform such a calculation. There is moreover the possibility that we have some interference due to spurious reflections from the computational boundary. In the future we hope to implement some of the ideas described at this meeting by Radvogin and by Goodrich.

CATEGORY 1, PROBLEM 2. This problem is distinctly easier and we are able to make a fairly thorough comparison of results from different schemes on different grids. Figure 5 shows a snapshot of the pressure at $t = 6.0$, according to the fourth-order scheme with $\Delta r = \frac{1}{20}$. The main purpose of including this is to show that no wave reflections are visible from the grid refinement lines at $r = 2.0$ and $r = 6.0$. Next we give time histories of the pressure at the points A,B,C. First we show results from the second-order scheme for grid sizes $\Delta r = \frac{1}{24}, \frac{1}{32}, \frac{1}{40}$. The heavy dashed line is the ‘exact’ solution, and it can be seen that not even on the finest grid is there really close

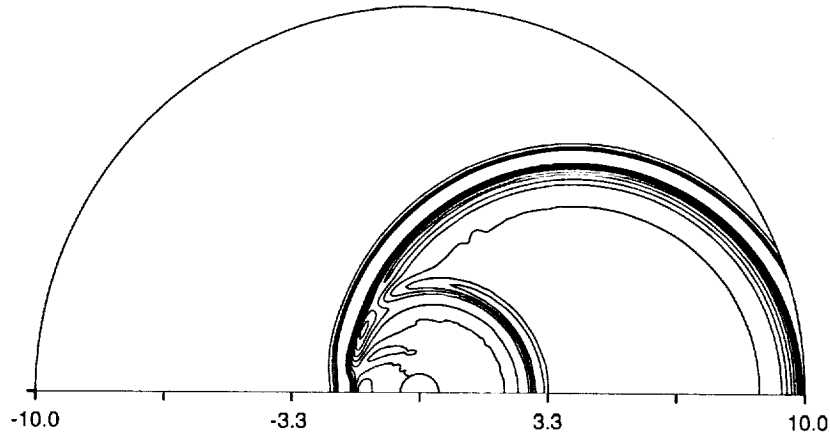


Figure 5: Pressure contours at $t = 6.0$ for Problem 2.

agreement. By contrast, Fig 7 shows results from the fourth-order method on grids with $\Delta r = \frac{1}{12}, \frac{1}{18}, \frac{1}{24}$. Although the grid with $\Delta r = \frac{1}{12}$ produces noticeable precursor oscillations, the results with $\Delta r = \frac{1}{18}$ are difficult to distinguish from the exact solution, and those with $\Delta r = \frac{1}{24}$ match it to plotting accuracy.

To confirm that these results do in fact have the formal accuracy that we expect, we have plotted the pressure at one particular place and time versus the second or fourth power of the mesh size. Such a plot should of course yield a straight line whose intercept at $h = 0$ is the “deferred approach to the limit”, our best numerical estimate of the exact solution.

In Fig 8 results from the second-order scheme for point A at the time of arrival ($t = 6.7$) of the first pressure minimum are plotted on the left against Δr^2 for $1/\Delta r = 20(4)40$. The cross on the vertical axis is the ‘exact’ solution; clearly the numerical solution is converging to something not far from this, but a precise estimate would be hard to give. On the right we plot results from the fourth-order scheme against Δr^4 for $1/\Delta r = 14(2)26$. As we would hope, the errors are very much lower, and there is now no doubt that a grid-converged solution would be very close indeed to the exact one.

Because the first minimum comes from the wave directly transmitted to A it gives no information about how well the reflections are treated. Therefore in Fig 9 the exercise is repeated for the second pressure minimum (at $t = 8.6$) at point A. Again the fourth-order results are much more accurate and convincing. They seem to be headed rather precisely for the exact solution. Any tiny discrepancy might be due to small errors in the ‘exact’ calculation, or to errors in the code. We concede above that neither our starting procedure nor our surface boundary condition is beyond reproach, but the effect of these appear to be so small numerically that the code behaves for all practical purposes ‘as if’ it were fourth-order accurate.

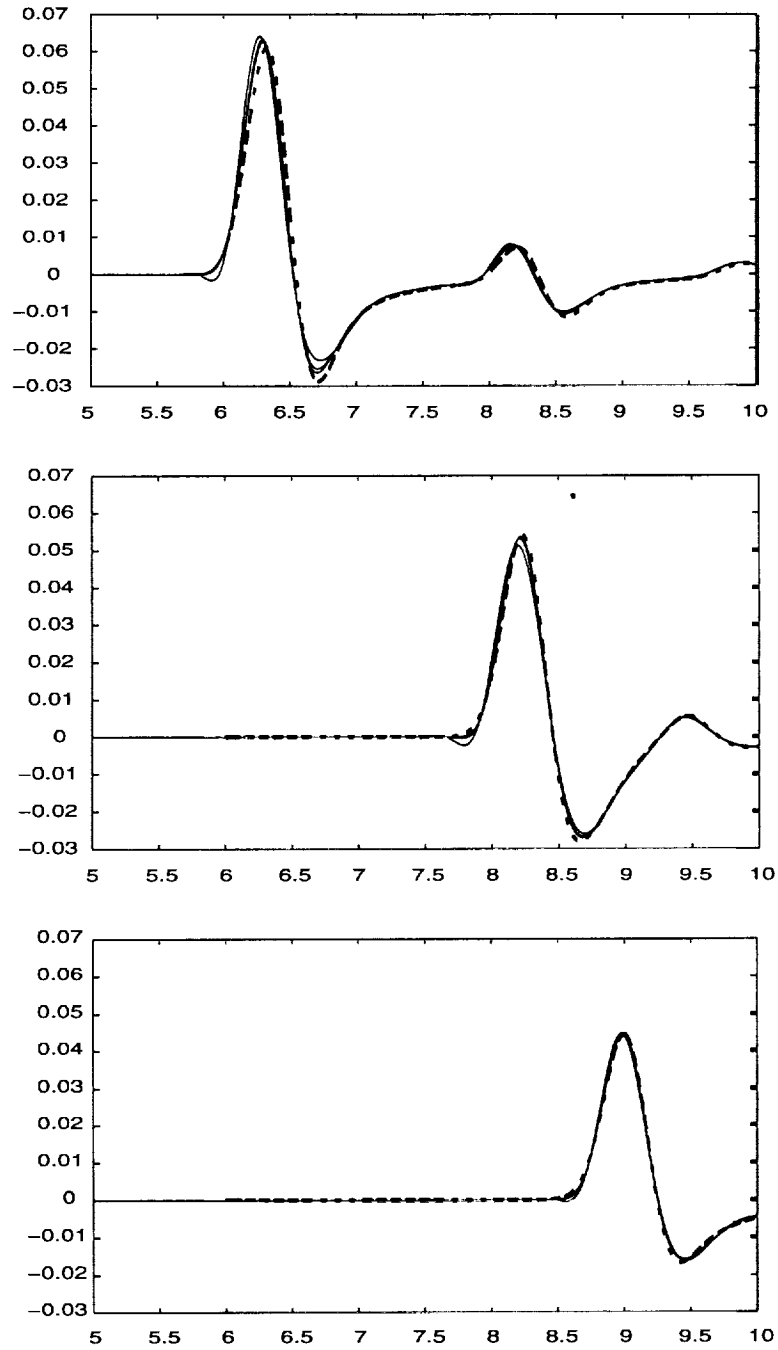


Figure 6: Pressure-time histories at points A (top), B (center), and C (bottom) from the second-order method. The grid sizes are $\Delta r = \frac{1}{24}, \frac{1}{32}, \frac{1}{40}$.

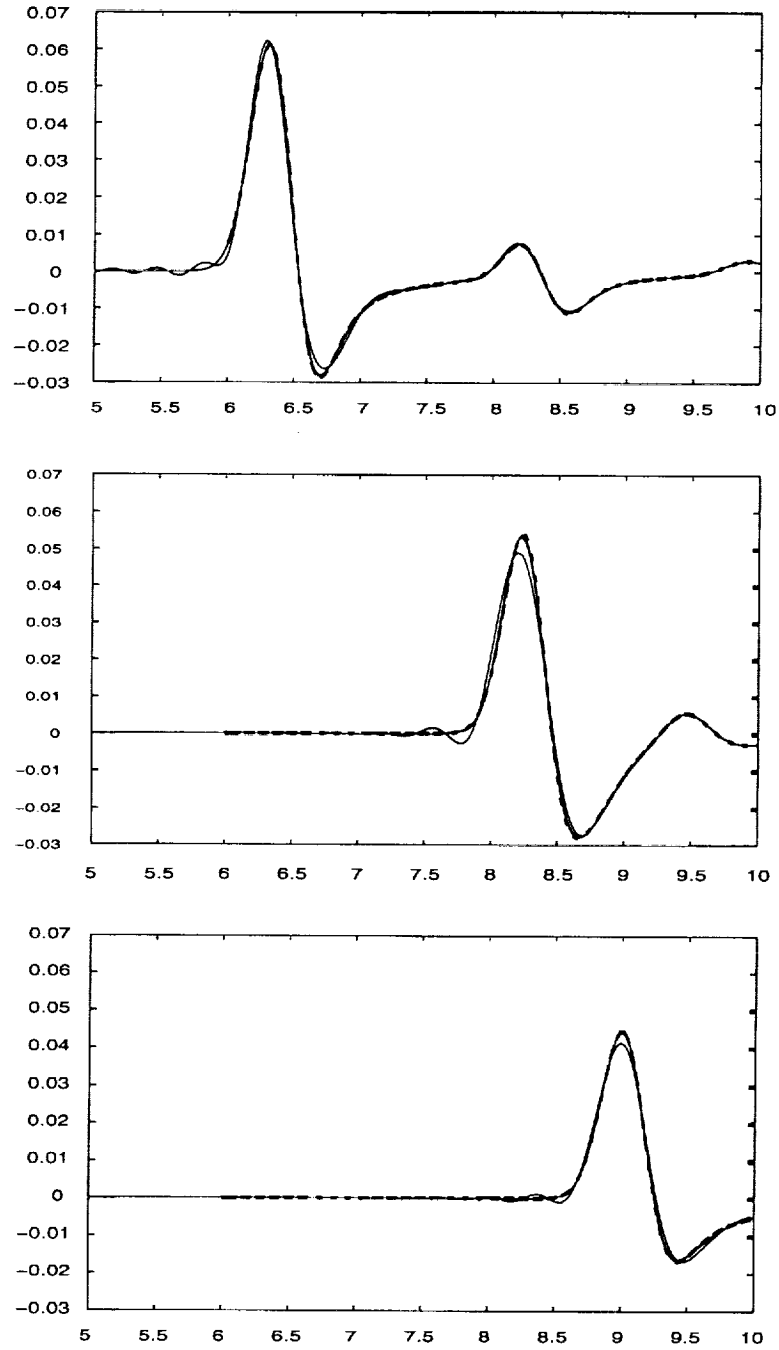


Figure 7: Pressure-time histories at points A (top), B (center), and C (bottom) from the fourth-order method. The grid sizes are $\Delta r = \frac{1}{12}, \frac{1}{18}, \frac{1}{24}$

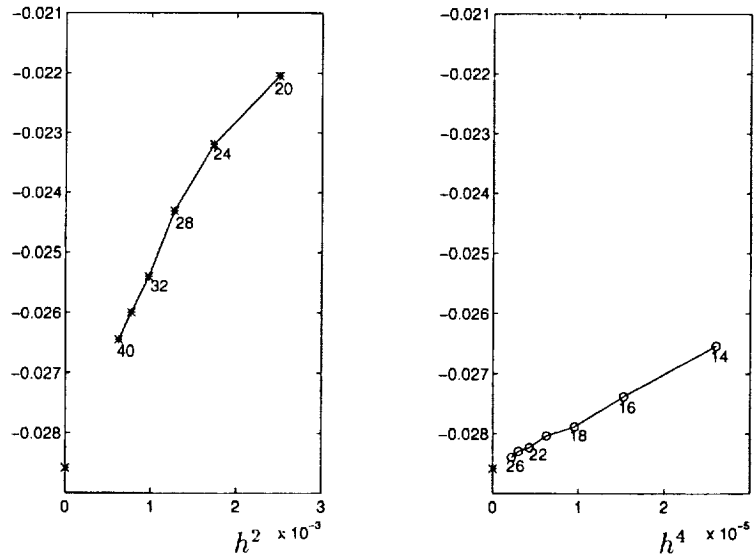


Figure 8: Grid-convergence studies for the pressure at point A as the first pressure minimum arrives.

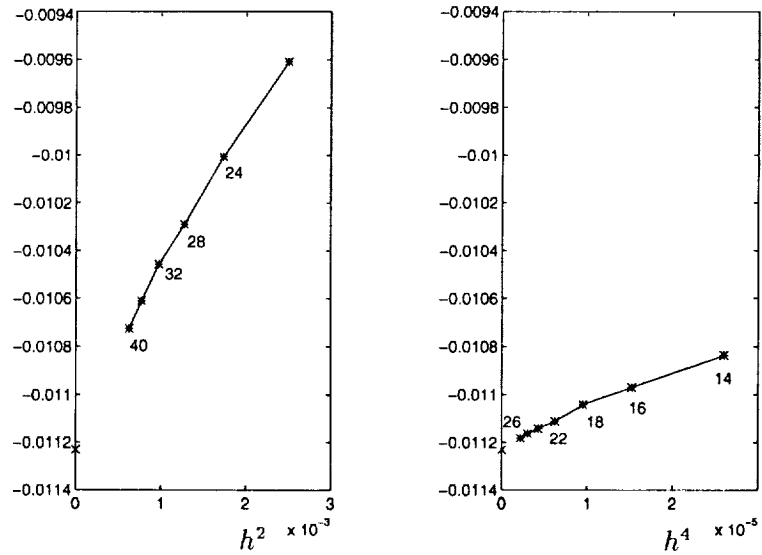


Figure 9: Grid-convergence studies for the pressure at point A as the second pressure minimum arrives.

CONCLUSIONS

We have presented a progress report giving the outcome of applying to two of the Workshop problems a fourth-order version of the upwind leapfrog method. The exercise has proved very useful in developing the method and we are grateful to the organisers for providing test cases that were originally just beyond our reach, together with independent solutions against which to measure our progress.

We feel encouraged by the outcome, especially by our results for Problem 2 where a careful analysis of the error is possible. We find that the fourth-order method is a very substantial improvement beyond the second-order version and amply repays the additional costs. The ability to implement the scheme on non-Cartesian grids with local refinement is a new and valuable feature to which we have been impelled by our efforts to solve the workshop problems. However, we have much to do to make the scheme more systematic, and we hope eventually to eliminate the need for smoothing operators with arbitrary coefficients. Current work aims to develop the schemes not only for acoustic and electromagnetic problems, but for linear elastodynamics also. We hope to achieve a general methodology, first for long-range linear wave propagation, and eventually for weakly non-linear waves also.

REFERENCES

1. A. ISERLES, Generalised leapfrog schemes, *IMA Journal of Numerical Analysis*, **6**, 1986.
2. P. L. ROE, Linear bicharacteristic schemes without dissipation, ICASE Report 94-65, 1994, *SIAM J. Scientific Computing*, to appear, 1997.
3. J. P. THOMAS, P. L. ROE, Development of non-dissipative numerical schemes for computational aeroacoustics, *AIAA paper 93-3382*, 1993.
4. J. P. THOMAS, Ph.D. Thesis, Department of Aerospace Engineering, University of Michigan. 1996.
5. B. T. NGUYEN, Ph.D. Thesis, Department of Aerospace Engineering, University of Michigan. 1996.
6. H. R. STRAUSS, An artificial viscosity for 2D hydrodynamics, *J. Comput. Phys.* **28**, 1978.

LEAST-SQUARES SPECTRAL ELEMENT SOLUTIONS TO THE CAA WORKSHOP BENCHMARK PROBLEMS

Wen H. Lin and Daniel C. Chan
Rocketdyne Division, Boeing North American, Inc.
Canoga Park, CA 91309-7922

516-64
043474
293993
p14

ABSTRACT

This paper presents computed results for some of the CAA benchmark problems via the acoustic solver developed at Rocketdyne CFD Technology Center under the corporate agreement between Boeing North American, Inc. and NASA for the Aerospace Industry Technology Program. The calculations are considered as benchmark testing of the functionality, accuracy, and performance of the solver. Results of these computations demonstrate that the solver is capable of solving the propagation of aeroacoustic signals. Testing of sound generation and on more realistic problems is now pursued for the industrial applications of this solver.

Numerical calculations were performed for the second problem of Category 1 of the current workshop problems for an acoustic pulse scattered from a rigid circular cylinder, and for two of the first CAA workshop problems, i. e., the first problem of Category 1 for the propagation of a linear wave and the first problem of Category 4 for an acoustic pulse reflected from a rigid wall in a uniform flow of Mach 0.5. The aim for including the last two problems in this workshop is to test the effectiveness of some boundary conditions set up in the solver. Numerical results of the last two benchmark problems have been compared with their corresponding exact solutions and the comparisons are excellent. This demonstrates the high fidelity of the solver in handling wave propagation problems. This feature lends the method quite attractive in developing a computational acoustic solver for calculating the aero/hydrodynamic noise in a violent flow environment.

INTRODUCTION

Accurate determination of sound generation, propagation, and attenuation in a moving medium is vital for noise reduction and control, especially for the design of quiet devices and vehicles. Currently, a sophisticated tool to accurately predict the noise generation and propagation is still lacking even though the aerodynamic noise theory has been extensively studied since Sir James Lighthill's famous paper on sound generated aerodynamically appeared in 1952 [1]. The major difficulty in computational aeroacoustics is caused by inaccurate calculations of the amplitude and phase of an acoustic signal. Because of its relatively small magnitude compared with its carrier - the flow field - an acoustic signature is not easily computed without distortion and degradation. Nowadays it is relatively easy to compute a steady flow field at most speeds with reasonable accuracy but it is still quite difficult to accurately compute an acoustic signature associated with a violent flow field. The basic reason for this difficulty is caused by the dispersion and dissipation effects introduced by most numerical methods for stability control in performing numerical computations. To circumvent the deficiency of current numerical methods for computational aeroacoustics, we have proposed a spectrally accurate method to compute the reference flow field and the generation and propagation of sound in an unsteady flow.

The method is based on a least-squares spectral element method. This method solves the linearized acoustic field equations by firstly expanding the acoustic variables in terms of some basis (or trial) functions and unknown coefficients. Then, the method minimizes the integral of the squares of the residual over the domain of influence. The resultant equations are a set of linear algebraic equations for the unknown coefficients. These algebraic equations incorporate the system derivatives of the acoustic field equations in integral forms. The spatial derivatives are discretized by the use of Legendre polynomials, and the time derivative is performed by a three-level time stepping method. The resultant matrix equation is solved by a Jacobi preconditioned conjugate gradient method.

Along with the field equations is a set of boundary conditions, including the nonreflecting and radiation conditions, to be satisfied for a given problem. These boundary conditions were explicitly implemented in the acoustic solver. For instance, the normal velocity component is set equal to zero for an acoustically rigid wall. Testing of the solver has been begun on the second problem of Category 1 for the current workshop benchmark and the first problems of Categories 1 and 4 for the first CAA workshop benchmark. Results of the last two computations compare very well with the analytic results. These calculations were considered as benchmark testing on the functionality, accuracy, and performance of the solver.

MATHEMATICAL FORMULATION

Consider an inhomogeneous, partial differential equation of the form

$$[\mathbf{L}] \{\mathbf{u}\} = \{\mathbf{f}\}, \quad (1)$$

where \mathbf{L} is the first-order partial differential operator, $\{\mathbf{u}\}$ the column vector of unknown variables, and $\{\mathbf{f}\}$ the column vector of forcing functions. The aim of working with the first-order derivatives is to ensure C^0 continuity in field variables at element interfaces. Next, we divide the domain of influence, \mathcal{D} , into \mathcal{S} elements and assume an approximate solution to Eq. (1) for a typical element can be written as

$$\{\mathbf{u}^e\} = \sum_{j=1}^N \{\mathbf{a}_j\} \phi_j^e, \quad (2)$$

where ϕ_j^e are linearly independent basis (or trial) functions, \mathbf{a}_j the expansion coefficients for the unknown variables, and N the total number of basis functions (or degrees of freedom) in an element. It should be noted that the same basis functions are used for all unknown variables. This feature is a characteristic of the proposed method and it simplifies the mathematical formulation and numerical implementation. In general, the basis functions are arbitrary and need not satisfy the differential equation or the boundary conditions. However, they must be differentiable once in the domain \mathcal{D} and at the boundaries. The basis functions used in the current study are Legendre polynomials of the independent variables.

Substituting Eq. (2) into Eq. (1), forming the residual, and applying the method of *least squares* with respect to the expansion coefficients, one leads to

$$\sum_{j=1}^N \mathbf{K}_{ij} a_j = \mathbf{F}_i \quad (3)$$

for each element, where $\mathbf{K}_{ij} = \int_{\mathcal{D}}^{(e)} (\mathbf{L}^T \phi_i) (\mathbf{L} \phi_j) d\mathcal{D}$, and

$$\mathbf{F}_i = \int_{\mathcal{D}}^{(e)} (\mathbf{L}^T \phi_i) \mathbf{f} d\mathcal{D}$$

where \mathcal{D} is the domain of interest, and \mathbf{L}^T the transpose of \mathbf{L} . Therefore, the original partial differential equation becomes an algebraic equation with its coefficients in terms of the derivatives of basis functions. The forcing functions are also weighted by the basis functions.

In order to evaluate the above integrals via the Gauss quadrature rules, we used a rectilinear relations to transform the coordinates, ranging from -1 to 1, of a computational element onto the coordinates of a physical element. The interior points in the computational element are determined as Legendre-Gauss-Lobatto collocation points [2], which are the roots of the derivatives of the Legendre polynomial. Details of the transformation and integration can be found in [3]. In the following paragraph we briefly present the governing equations in the matrix form for the benchmark problems we solved. For the acoustic scattering problem of Category 1 of the current workshop, the semi-discrete equation is

$$\begin{pmatrix} \alpha_1 & \Delta t \frac{\partial}{\partial x} & \Delta t \frac{\partial}{\partial y} & p^{n+1} \\ \Delta t \frac{\partial}{\partial x} & \alpha_1 & 0 & u^{n+1} \\ \Delta t \frac{\partial}{\partial y} & 0 & \alpha_1 & v^{n+1} \end{pmatrix} = \begin{pmatrix} \alpha_2 p^n + \alpha_3 p^{n-1} \\ \alpha_2 u^n + \alpha_3 u^{n-1} \\ \alpha_2 v^n + \alpha_3 v^{n-1} \end{pmatrix} \quad (4)$$

For the acoustic reflection problem of Category 4 of the first workshop, the semi-discrete equation is

$$\begin{pmatrix} \alpha_1 + M \Delta t \frac{\partial}{\partial x} & \Delta t \frac{\partial}{\partial x} & \Delta t \frac{\partial}{\partial y} & p^{n+1} \\ \Delta t \frac{\partial}{\partial x} & \alpha_1 + M \Delta t \frac{\partial}{\partial x} & 0 & u^{n+1} \\ \Delta t \frac{\partial}{\partial y} & 0 & \alpha_1 + M \Delta t \frac{\partial}{\partial x} & v^{n+1} \end{pmatrix} = \begin{pmatrix} \alpha_2 p^n + \alpha_3 p^{n-1} \\ \alpha_2 u^n + \alpha_3 u^{n-1} \\ \alpha_2 v^n + \alpha_3 v^{n-1} \end{pmatrix} \quad (5)$$

where M being the free-stream Mach number (equal to 0.5 in this case), n denoting the n^{th} time step. In these semi-discrete equations the accuracy is second order in time with the application of a backward difference scheme in which $\alpha_1 = 1.5$, $\alpha_2 = -2$, and $\alpha_3 = 0.5$.

For the linear wave problem of Category 1 of the first CAA workshop benchmark, the semi-discrete equation is

$$(1 - \alpha \Delta t \frac{\partial}{\partial x}) u = (1 + [1 - \alpha] \Delta t \frac{\partial}{\partial x}) u^0, \quad (6)$$

where u^0 denotes the initial condition, and α is a parameter representing various time-marching algorithms; for example, if $\alpha = 0.5$, the algorithm is the Crank-Nicolson scheme [4]; and if $\alpha = 1$, the algorithm is the backward difference scheme. In our calculations the value of α was set to 0.5. Therefore, the accuracy of the time integration for this problem is also second order.

NUMERICAL RESULTS AND DISCUSSION

Problem 2 of Category 1 - Acoustic Scattering

Totally, the computational grid used for the calculation has 14,651 nodes, which includes 9 elements in the radial direction and 16 elements in the angular direction. Within each element, 11 collocation points were used in each direction for the interpolation. The radius of the circular cylinder was set as unity and the location of the acoustic pulse was at $r = 4$ from the origin of the cylinder. The outer boundary for the computational domain was at $r = 10$. The time step used for this calculation was $\Delta t = 0.01$ from the initial state. Before time, t , reached six, data for every 20 time steps were stored; and starting from $t = 6$ to $t = 10$, data for every time step were stored for postprocessing.

Results are shown in Fig. 1 for the computational grid and the pulse location, in Fig. 2 the contours of pressures at $t = 6, 7.25, 8.65$, and 10, and in Fig. 3 the instantaneous pressures at three points as designated in the benchmark problem. In this benchmark calculation there is no effect of reference (base) flow. The aim of this study is to investigate the effectiveness of curvilinear wall boundary condition and farfield nonreflecting condition.

Originally the acoustic pulse is released at the spatial point and free to expand in space. The cylinder is on the way of pulse passage and reflects the pulse when both encounter each other. As seen from Figure 2, the pulse expands and hits the cylinder when time increases. As the pulse touches the cylinder it is scattered from the cylinder. The original pulse interacts with the scattered wave, continues to spread omni-directionally, and travels across the farfield boundary. The fact of no reflection from the outer boundary indicates that the farfield nonreflecting condition is effective to pass the waves. This benchmark testing shows that the acoustic solver of CAAS is capable of handling the curvilinear spectral element for sound wave propagation, where CAAS standing for Computational Aeroacoustic Analysis System developed at Rocketdyne for NASA Aerospace Industry Technology Program (AITP).

The First CAA Benchmark Problems:

Problem 1 of Category 1 - Linear Waves

In this one-dimensional wave propagation problem the domain was divided into 30 elements between -20 and 450 and within each element there were 16 collocation points; therefore, the total grid nodes were 451. The time step for the calculation of this problem was $\Delta t = 0.1$. Results are presented in Fig. 4 for the pulse at $t = 100, 200, 300$, and 400, and in Fig. 5 for detailed comparisons between the numerical and exact solutions. As seen from the figures, the comparisons at these time instants are excellent. It indicates that the numerical algorithm of the CAAS solver is accurate enough for predicting wave propagation.

Problem 1 of Category 4 - Acoustic Pulse Reflection from a Wall

For this problem the computational domain is a square, namely, x ranging from -100 to 100 and y from 0 to 200. The grid used for the calculation has 5929 nodes, which includes 4 elements in both x and y directions. Within each element there are 20 collocation points used for the interpolation. The time step used in the calculation was $\Delta t = 0.1$.

Results shown in Figs. 6 and 7 are the time history of the pulse reflected from the wall at $t = 15, 30, 45, 60, 75, 90, 100,$ and 150 . As seen from the plots, for $t = 150$ there are still some small variations of the lower-level pressure contours at the downstream boundary. This may indicate that the non-reflecting boundary condition at the outflow is not perfect. We have tried both Tam's and Webb's [5] and Giles' [6] outflow boundary conditions in the calculations for this problem and found that Tam's and Webb's boundary conditions produced slightly better results. A numerical sponge layer is now being investigated for its effectiveness of absorbing the undesirable wave energy at the outflow boundaries.

Figure 8 shows the pressure waveform along the line $x = y$ at $t = 30, 60, 75,$ and 100 . In each figure the exact pressure field was also plotted for comparison, where $s = (x^2 + y^2)^{.5}$. The computed pressures compare very well with the exact pressures; only at $t = 100$, there is a small discrepancy happening between $s = 130$ and $s = 135$. This good comparison again shows that the numerical algorithm used in the solver is quite accurate for handling sound wave propagation.

CONCLUDING REMARKS

An aeroacoustic solver has been developed in the framework of CAAS developed at Rocketdyne for predicting aerodynamic sound generation and propagation. The mathematical formulation of the solver is based on the linearized acoustic field equations and the numerical algorithm is based on the least-squares weighted residual method. The two-dimensional version of the solver has been tested with some of the ICASE Workshop benchmark problems. The numerical results obtained via the CAAS acoustic solver compare very well with the known analytical results. Testing of the solver for the three-dimensional problems and for sound generation is now being pursued.

REFERENCES

1. Lighthill, M. J. (1952) "On Sound Generated Aerodynamically: I. General Theory," Proc. Royal Soc., Series A, Vol. 211, pp. 564-587.
2. Canuto, C., Hussaini, M. Y., Quarteroni, A., and Zang, T. A. (1988) "Spectral Methods in Fluid Dynamics," pp 60-65, Springer-Verlag, Berlin & Heidelberg.
3. Chan, D. C (1995) "Unstructured Implicit Flow Solver (UniFlo)," Rocketdyne CFD Technology Center.
4. Huebner, K. H., and Thornton, E. A. (1982) "The Finite Element Method for Engineers," pp. 292-295, John Wiley & Sons, Inc.
5. Tam, C. K. W., and Webb, J. C. (1993) "Dispersion-relation-preserving finite difference schemes for computation acoustics," *J. Comp. Physics*, **107**, pp. 262-281.
6. Giles, M. B. (1990) "Non-reflecting boundary conditions for Euler equation calculations," *J. AIAA*, **28**, pp. 2050-2058.

FIG.1 PROBLEM 2 OF CATEGORY 1 – ACOUSTIC SCATTERING; COMPUTATIONAL GRID AND LOCATION OF THE ACOUSTIC PULSE

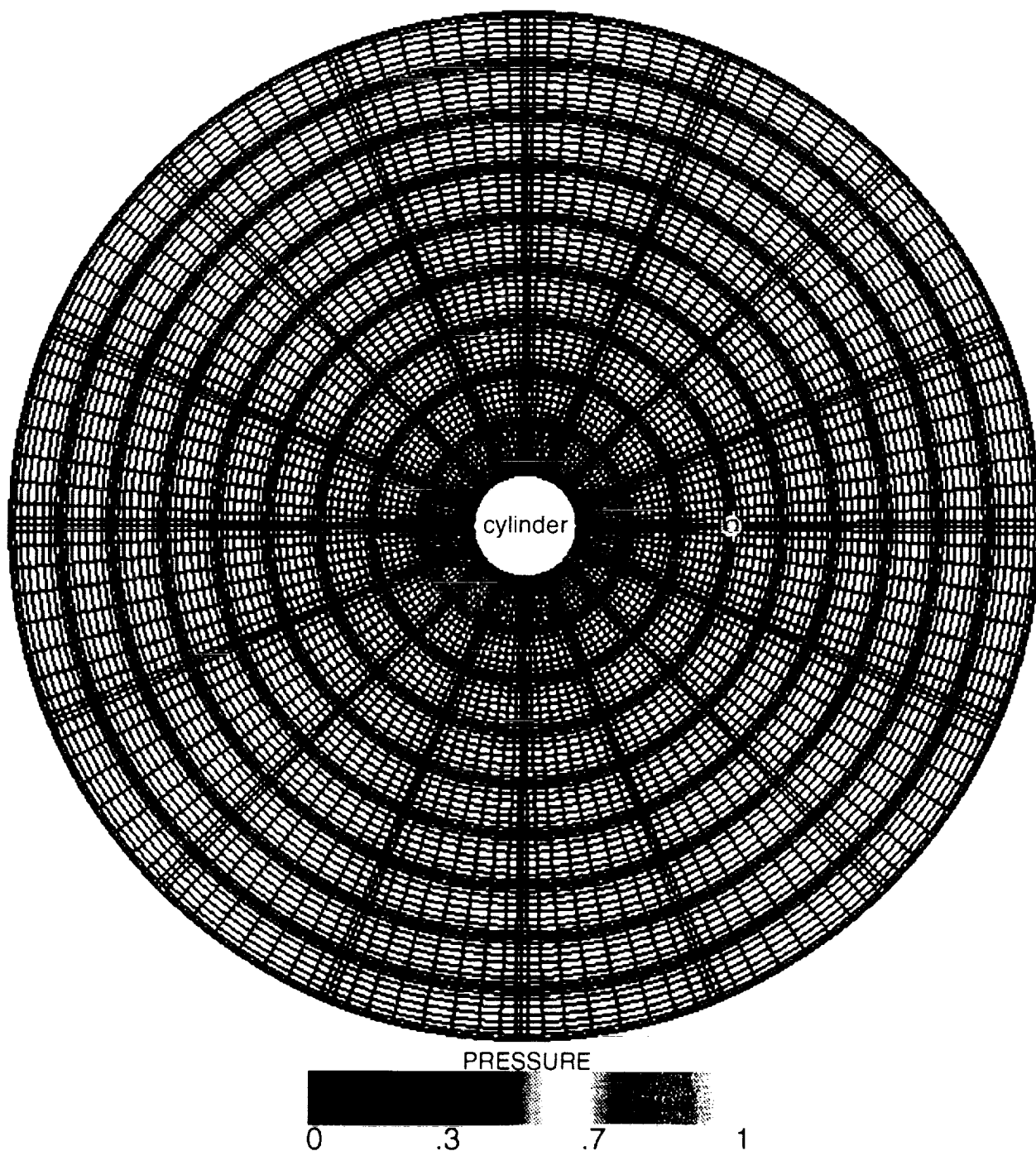


FIG. 2 SCATTERING OF AN ACOUSTIC PULSE FROM A CIRCULAR CYLINDER

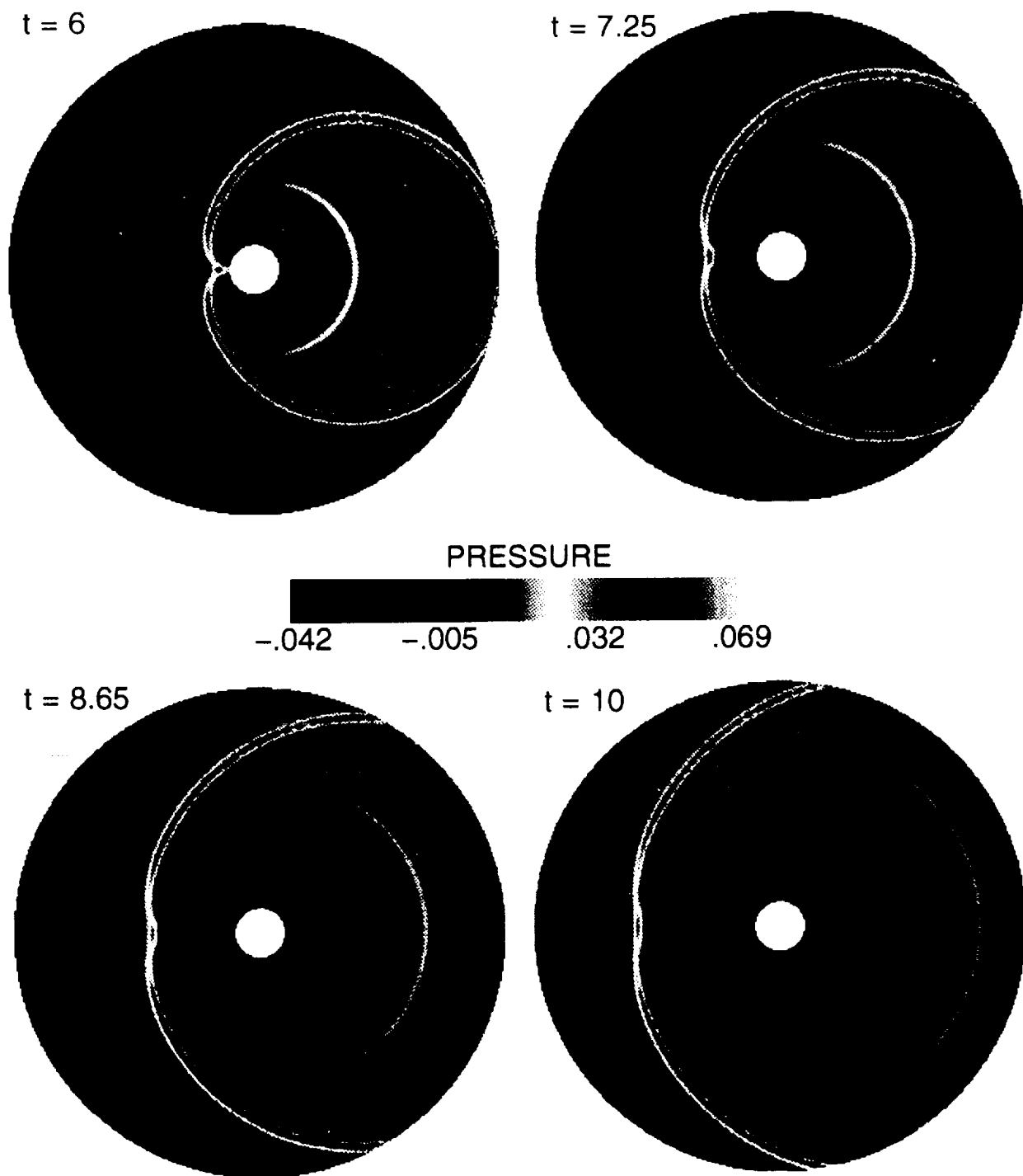


Fig. 3 Instantaneous Pressures At Points

$A(r=5, \theta=90)$, $B(r=5, \theta=135)$, $C(r=5, \theta=180)$

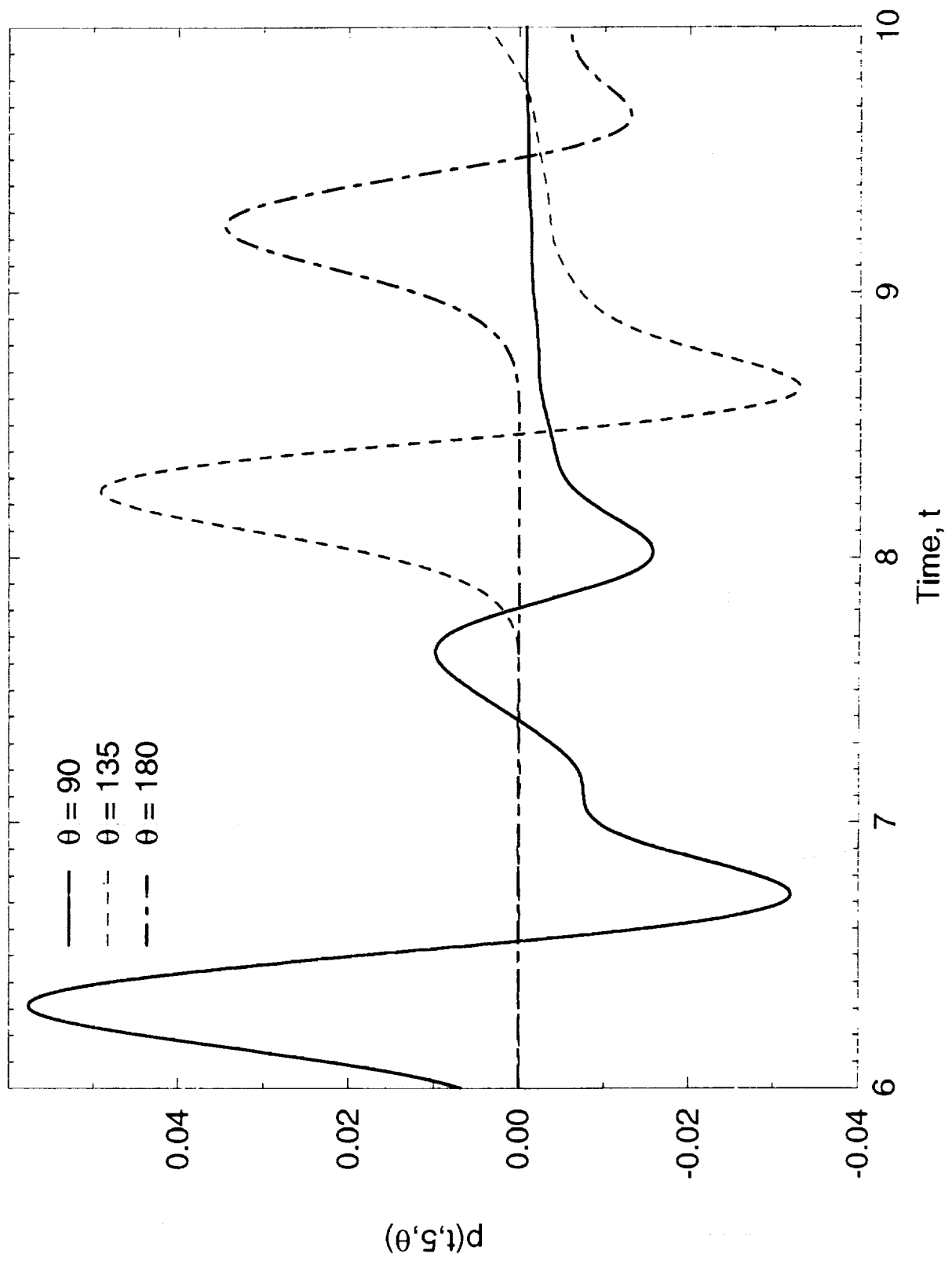


Fig. 4 CAAS Solutions for the Pulse at
 $t = 100, 200, 300, 400$, with $\Delta t = 0.1$

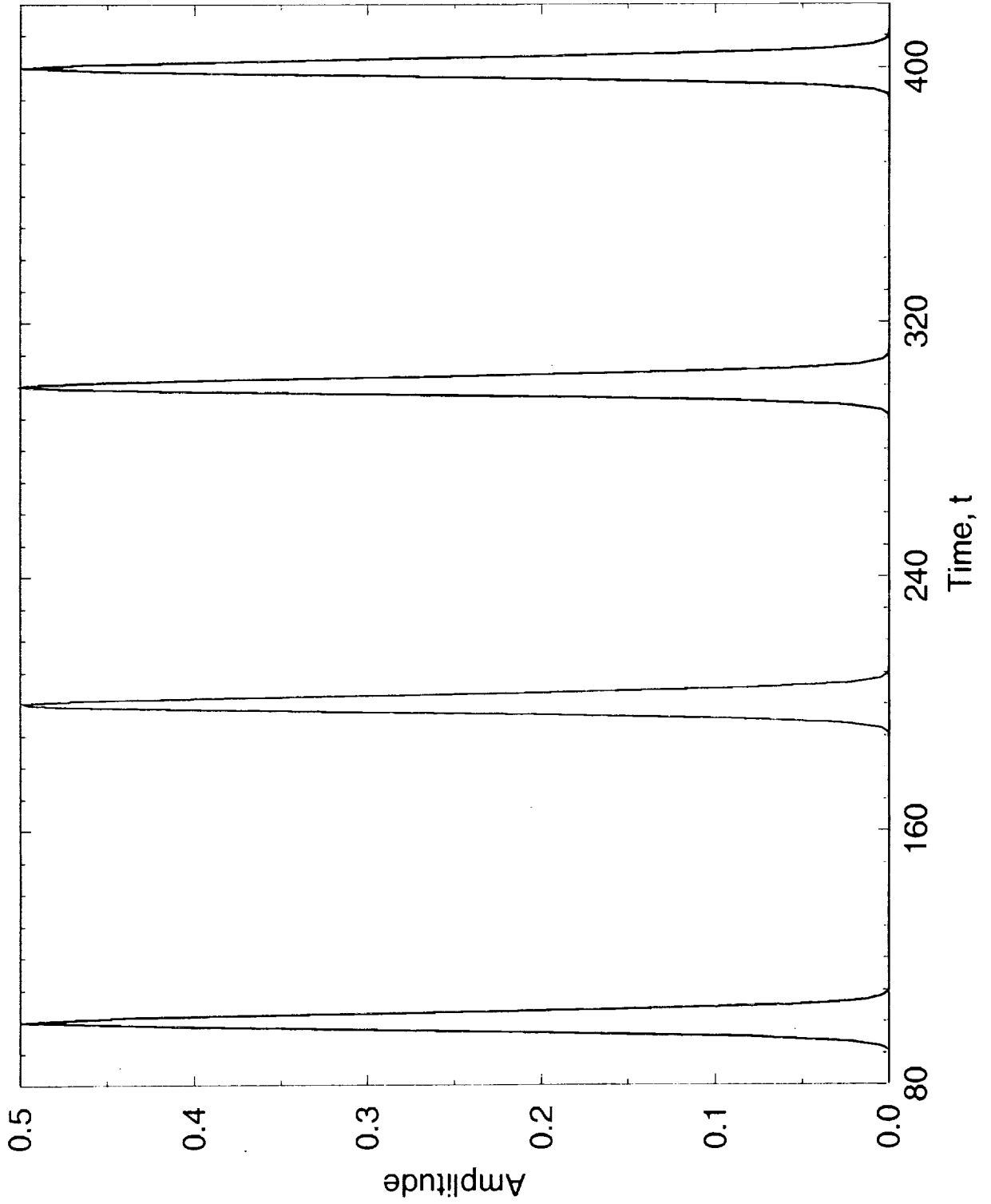


Fig. 5 Comparisons of Numerical and Exact Solutions

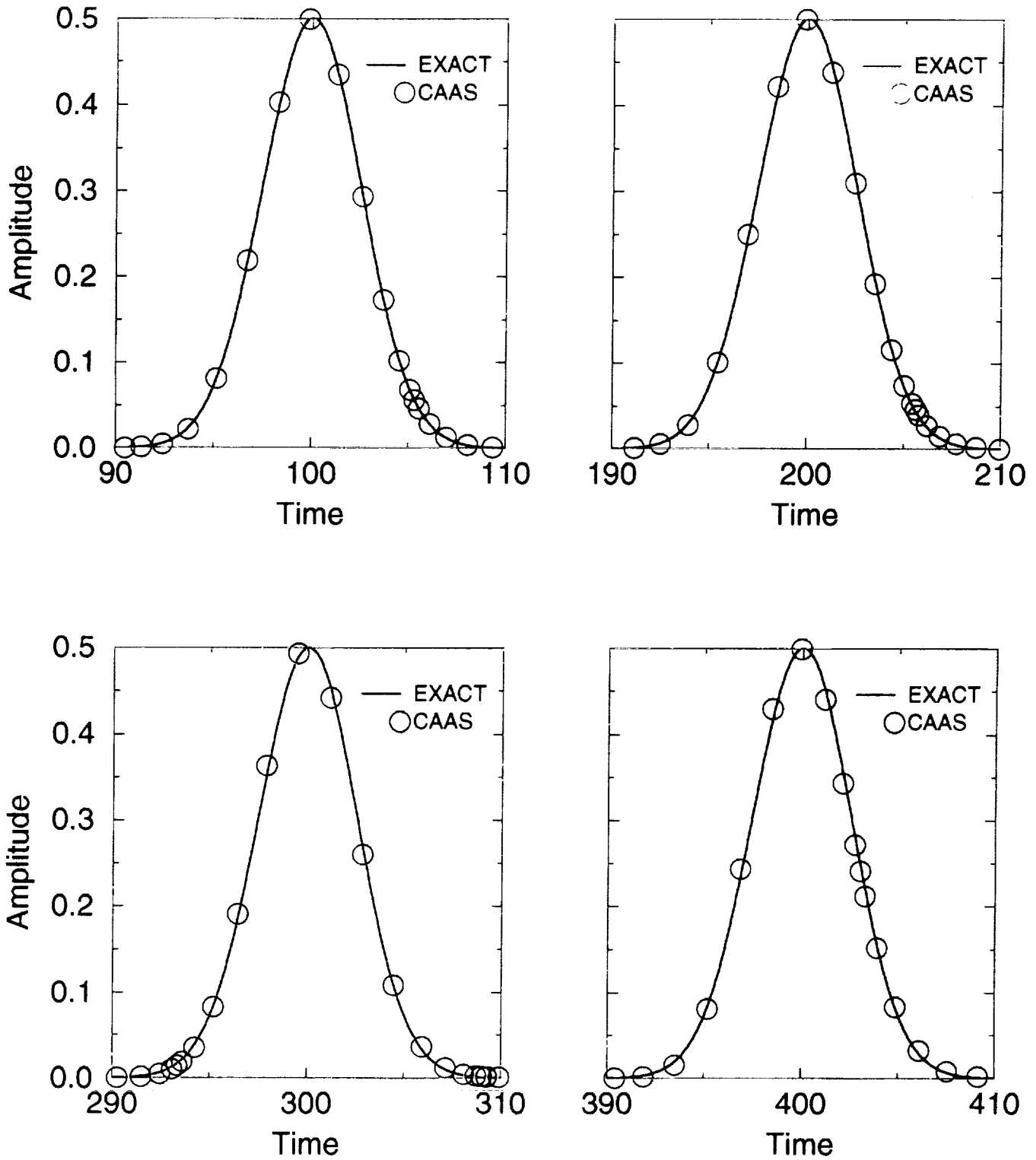


FIG. 6 TIME HISTORY OF AN ACOUSTIC PULSE REFLECTED FROM A HARD WALL IN A UNIFORM FLOW OF MACH 0.5

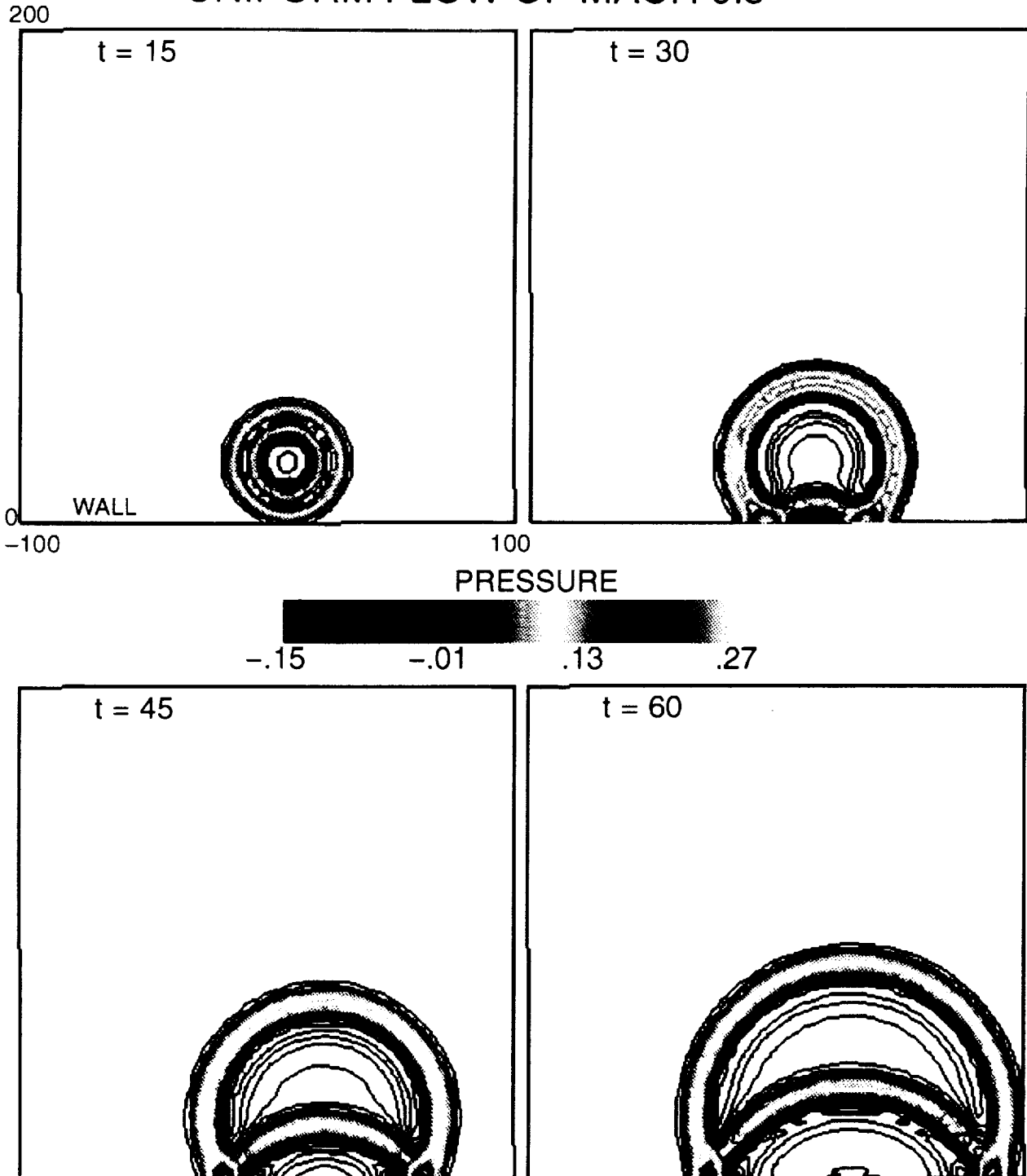


FIG. 7 TIME HISTORY OF AN ACOUSTIC PULSE REFLECTED FROM A HARD WALL IN A UNIFORM FLOW OF MACH 0.5

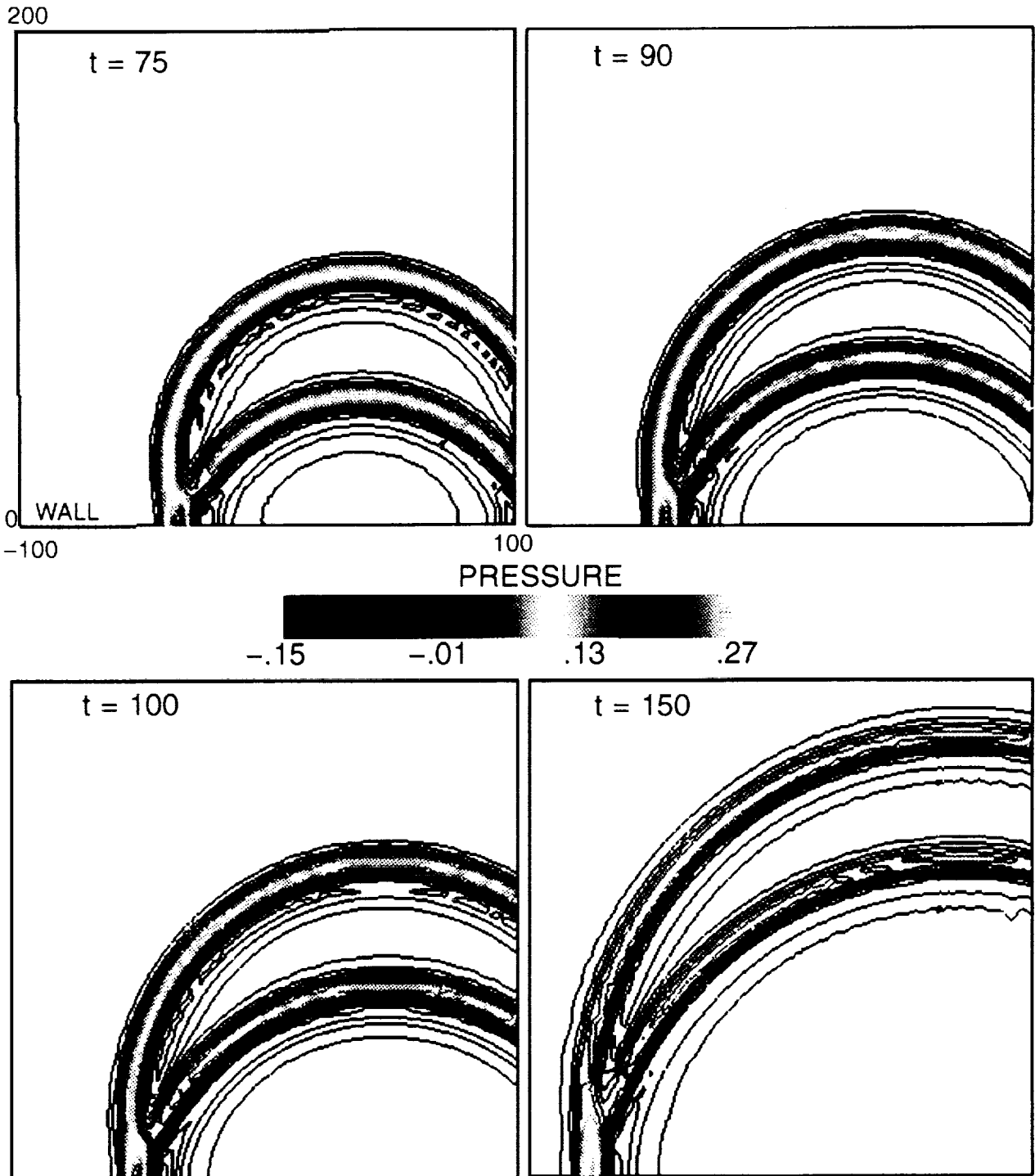
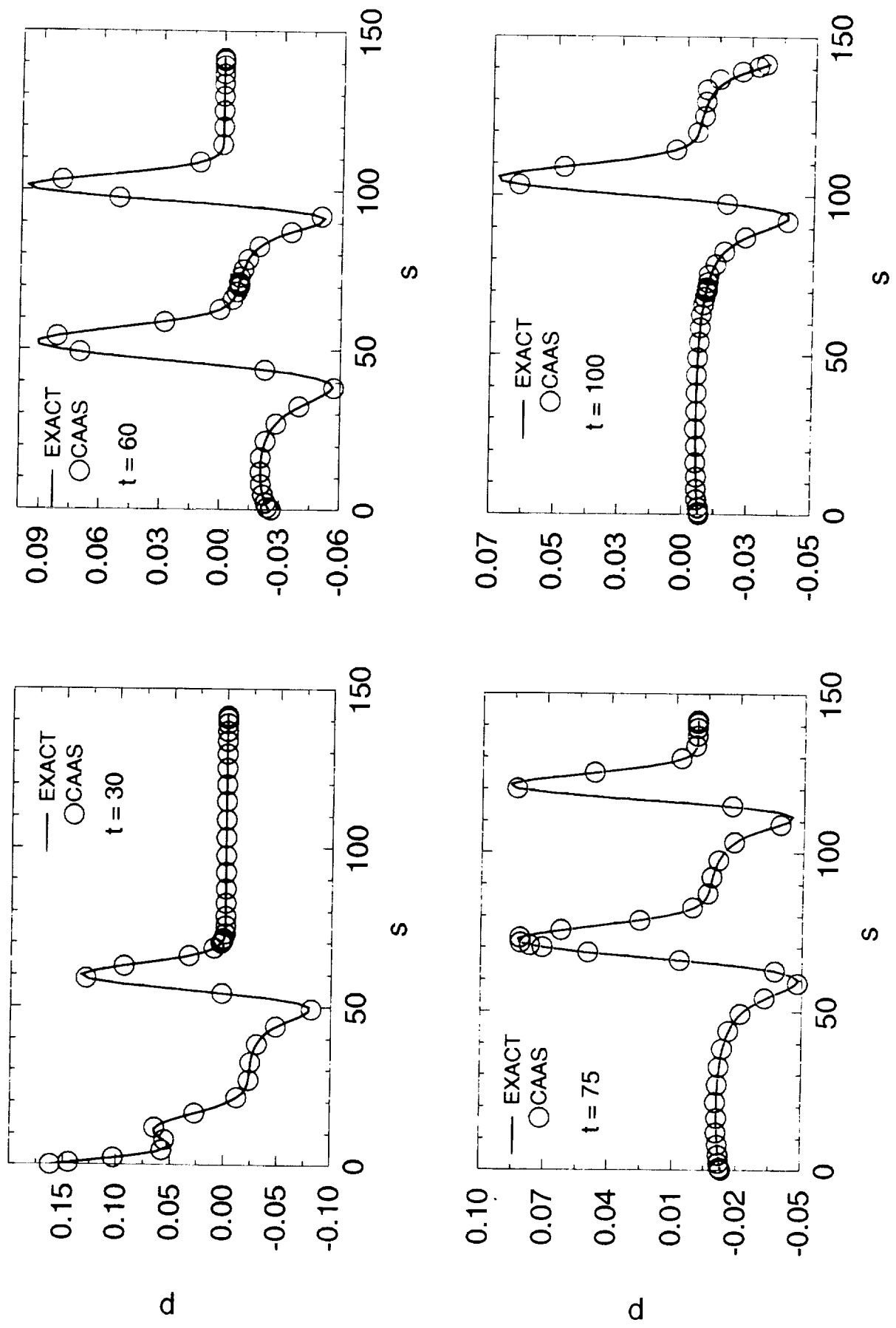


Fig. 8 Pressure Waveform Along the Line $x = y$





517-71
043475
293998
p12

**ADEQUATE BOUNDARY CONDITIONS
FOR UNSTEADY AEROACOUSTIC PROBLEMS**

Yu. B. Radvogin, N. A. Zaitsev
Keldysh Institute of Applied Mathematics
Miusskaya Sq. 4, Moscow, 125047, Russia
E-mail: radvogin@spp.keldysh.ru, zaitsev@spp.keldysh.ru

ABSTRACT

The strict formulation of the Adequate Boundary Conditions in the case of the wave equation is presented. The nonlocal ABC are obtained by means of Riemann's method. The corresponding Riemann's functions can be used to create ABC for each Fourier mode. Approximate boundary conditions are also presented. First order accurate BC coincides with the well-known Tam's BC. Second order accurate BC provide more exact numerical solutions. Comparison analysis of the exact solution and both of approximations as applied to the Category I, Problem 2 demonstrates the advantages of second order accurate BC. Some results relating to steady problems are also presented.

INTRODUCTION

One of the important elements of a numerical algorithm for solving aeroacoustic problems is the formulation of radiation and outflow boundary conditions and their numerical implementation. In one-dimensional problems, the corresponding conditions can be easily constructed using characteristics of the governing system. This problem becomes rather complicated for the multidimensional case.

This paper is mainly devoted to the simplest problem of this kind. The main purpose is the formulation of the exact boundary conditions (so-called adequate boundary conditions, ABC). As a rule, such conditions are too complicated. In many cases, one can use one or another approximate conditions. Only this approach is optimal for a wide class of aeroacoustic problems.

ADEQUATE BOUNDARY CONDITIONS FOR THE WAVE EQUATION

We consider the 2D wave equation in polar coordinates

$$\frac{\partial^2 P}{\partial t^2} - \frac{\partial^2 P}{\partial r^2} - \frac{1}{r} \frac{\partial P}{\partial r} - \frac{1}{r^2} \frac{\partial^2 P}{\partial \varphi^2} = 0. \quad (1)$$

Let $P(r, \varphi, 0)$ and $P_t(r, \varphi, 0)$ be the initial data which are compactly supported in the circle C_R of radius R . We denote by D and ∂D the cylinder $C \times [0, t]$ and its boundary, respectively.

Our goal is to construct ABC on ∂D such that the solution of this mixed problem coincides in D with the solution of the original Cauchy problem.

First, we use the Fourier expansion and obtain

$$p_{tt}^{(k)} - p_{rr}^{(k)} - \frac{1}{r} p_r^{(k)} + \frac{k^2}{r^2} p^{(k)} = 0, \quad (2)$$

where $p^{(k)}(r, t)$ are the corresponding Fourier coefficients.

The initial data transform into the form

$$p^{(k)}(r, 0) = p_0(r), \quad p_t^{(k)}(r, 0) = p_1(r). \quad (3)$$

We note that p_0 and p_1 are also compactly supported functions. Now we can formulate the problem for each $p^{(k)}(r, t)$. Namely, to construct ABC on the boundary $\partial g : r = R$, such that the mixed problem in the strip $g : (r \leq R, t > 0)$ coincides with the solution of the Cauchy problem (2) - (3).

In order to deal with self-adjoint operators we introduce the new unknown functions $u^{(k)} = \sqrt{r}p^{(k)}$. Then we obtain the following problem

$$L^{(k)}u^{(k)} = 0, \quad L^{(k)} = \frac{\partial^2}{\partial t^2} - \frac{\partial^2}{\partial r^2} + \frac{a^{(k)}}{r^2}, \quad a^{(k)} = k^2 - 1/4; \quad (4)$$

$$u^{(k)}(r, 0) = u_0(r), \quad u_t^{(k)}(r, 0) = u_1(r). \quad (5)$$

To construct the desired boundary conditions we shall use the well-known Riemann method. Let $t = \tau$ be fixed. Consider the triangle ABP , see Fig. 1, where AP and BP are the upper and lower characteristics, respectively. Clearly,

$$u^{(k)}|_{AP} = 0. \quad (6)$$

We introduce the Riemann function $v^{(k)}(r, t, \tau)$ as the function satisfying the following conditions:

$$L^{(k)}v^{(k)} = 0, \quad (7)$$

$$v^{(k)}|_{BP} = 1. \quad (8)$$

Combining (5) and (7) we obtain

$$vLu - uLv = 0$$

(for simplicity we omit all superscripts "k").

By integration this identity over the triangle ABP we obtain

$$\iint_{ABP} (vLu - uLv) d\sigma = \oint_{ABP} (vu_t - uv_t) dr + (vu_r - uv_r) dt = 0.$$

Using (6) and (8) we have

$$\int_A^B (vu_r - uv_r) dt + u(B) = 0.$$

Finally, for each k we obtain the desired boundary conditions

$$u(r, \tau) = \int_0^\tau [u(R, t)v_r(R, t) - u_r(R, t)v(R, t)] dt. \quad (9)$$

It remains to turn back to the original function $P = \sum_k p^{(k)} e^{ik\varphi} \sqrt{r}$.

It should be pointed out that the presented above ABC is nonlocal in both time and space.

We note that each $v^{(k)}$ is determined not uniquely. To find $v^{(k)}$ we have to define $v^{(k)}(R, t)$, for example. Thus, we can choose Riemann's functions in a convenient way, which is important for applications.

We also note that despite the non-uniqueness all AB conditions lead to the same solution of mixed problem.

Some of Riemann's functions are connected with Legendre functions. For example, let $v(r, t, \tau) = v(\xi)$, where $\xi = (R + \tau - t)/r$. Then

$$(\xi^2 - 1) \frac{d^2 v}{d\xi^2} + 2\xi \frac{dv}{d\xi} + k^2 - 1/4 = 0. \quad (10)$$

Therefore $v(\xi) = P_{k-1/2}(\xi)$.

Boundary condition (9) can be rewritten in the following way. Since u_t is also a compact supported function, it follows that we can rewrite (9) replacing u by u_t :

$$u_t(R, \tau) = \int_0^\tau (u_t v_r - u_{rt} v) dt = [u v_r - u_r v]_0^\tau - \int_0^\tau (u v_{rt} - u_r v_t) dt.$$

In other words,

$$u_t(R, \tau) + u_r(R, \tau) = u(R, \tau) v_r(R, \tau) - \int_0^\tau (u v_{rt} - u_r v_t) dt. \quad (11)$$

Further we shall consider Riemann's functions satisfying the condition

$$v(R, t) \equiv 1. \quad (12)$$

In this case $v_r(R, \tau) = 0$ and $v_t \equiv 0$. Therefore ABC (11) takes the form

$$u_t + u_r = - \int_0^\tau u v_{rt} dt. \quad (13)$$

We shall call $V(r, t)$ the base function if

$$LV = 0 \quad \text{and} \quad V = 1 \quad \text{for} \quad t = r - R.$$

It is obvious that $V(r, t)$ gives the correspondent Riemann's function $v(r, t, \tau) = V(r, \tau - t)$.

Some properties of $V(r, t)$ were investigated numerically and analytically. In particular, it was found that $\lim_{t \rightarrow \infty} V_{rt}(R, t) = 0$ and $\lim_{t \rightarrow \infty} V_r(R, t) = -(k - 1/2)$ in the case $V(R, t) \equiv 1$. Only these $V(r, t)$ will be considered below.

APPROXIMATE BOUNDARY CONDITIONS

The exact ABC (13) is too complicated for practical use. In many cases one can apply approximate boundary conditions. In order to construct such conditions we consider the approximations of v_{rt} in (13).

(i) As the first approximation we put $V \equiv 1$. Then $v \equiv 1$ and $v_{rt} \equiv 0$. As a result we obtain boundary condition in the form

$$u_t + u_r = 0, \quad r = R. \quad (14)$$

However, $u^{(k)} = p^{(k)}\sqrt{r}$. Thus, we have

$$p_t^{(k)} + p_r^{(k)} + \frac{p^{(k)}}{2R} = 0.$$

We recall that $p^{(k)}$ are the Fourier coefficients. Clearly, this condition remains the same for the original function $p(r, t, \varphi)$:

$$p_t + p_r + \frac{p}{2R} = 0. \quad (15)$$

Note that condition (15) coincides with the well-known Tam's condition [1].

(ii) The second approximation can also be easily obtained:

$$V(r, t) = 1 - \frac{a}{2R^2}(r - R)(t + R - r)$$

This leads to

$$v(r, t) = 1 - \frac{a}{2R^2}(r - R)(\tau - t + R - r)$$

and

$$v_{rt} = \frac{a}{2R^2}, \text{ i.e. } v_{rt}^{(k)} = \frac{k^2 - 1/4}{2R^2}.$$

From (13) we obtain

$$u_t^{(k)}(R, \tau) + u_r^{(k)}(R, \tau) = -\frac{k^2 - 1/4}{2R^2} \int_0^\tau u^{(k)}(R, t) dt. \quad (16)$$

Turning back to $p^{(k)}(r, t)$ we obtain

$$p_t^{(k)} + p_r^{(k)} + \frac{1}{2R}p^{(k)} = -\frac{k^2 - 1/4}{2R^2} \int_0^\tau p^{(k)}(R, t) dt.$$

Finally, we have

$$P_t + P_r + \frac{P}{2R} = \frac{1}{2R^2} \int_0^t (P_{\varphi\varphi} + P/4) d\tau, \quad r = R. \quad (17)$$

(Here we interchanged t and τ for convenience.)

Further we use approximate boundary conditions only. Thus, we shall denote by ABC an approximate BC.

One can show that the truncation error $\delta = O(\tau^2)$ for ABC (17) unlike $\delta = O(\tau)$ for ABC (15).

In accordance with these estimates, boundary conditions (15) or (17) will be denoted 1ABC and 2ABC, respectively.

FORMULATION OF THE PROBLEM AND THE NUMERICAL ALGORITHM

We consider the linearized Euler system for $M_\infty = 0$ in the form

$$\begin{aligned}\frac{\partial u}{\partial t} + \frac{\partial P}{\partial r} &= 0, \\ \frac{\partial v}{\partial t} + \frac{1}{r} \frac{\partial P}{\partial \varphi} &= 0, \\ \frac{\partial P}{\partial t} + \frac{\partial u}{\partial r} + \frac{1}{r} \left(u + \frac{\partial v}{\partial \varphi} \right) &= 0.\end{aligned}\tag{18}$$

where P is the pressure, u and v are the polar components of velocity.

The initial data equal zero outside the circle C_R of radius R . Since this system can be reduced to the wave equation with respect to p , it follows that the foregoing construction does apply. Using ABC we replace the Cauchy problem in the whole plane by the mixed problem in C_R .

Thus we have the boundary condition on ∂C_R in the form

$$P_t + P_r + \frac{P}{2R} = F(P),\tag{19}$$

where

$$F(P) \equiv 0$$

which corresponds to the first order approximation (1ABC), see (15), or

$$F(P) = \frac{1}{2R^2} \int_0^t (P_{\varphi\varphi} + P/4) d\tau$$

which corresponds to the second order approximation (2ABC), see (17).

We note that, as a rule, additional boundary conditions can lead to an ill-posed problem.

The numerical algorithm we apply is a modification of our method [2]. The original second order accurate difference scheme belongs to the TVD-type class and uses the minimal stencil. In order to create a third order accurate scheme we apply the well-known Runge's rule.

We write the initial scheme in the form

$$U_h^{n+1} = R_h U_h^n.$$

The first step of the desired scheme is a reconstruction of U^n at the intermediate points $(m + 1/2, k + 1/2)$. It can be done using the cubic interpolation. As a result we obtain "the fine" grid. Then according to Runge's rule we have

$$U_h(t^n + \tau) = \frac{1}{3} [4U_h(t^n + \tau) - U_{h/2}(t^n + \tau)].$$

Since $U_h(t^n + \tau) = R_h U_h^n$, $U_{h/2}(t^n + \tau) = R_{h/2}^2 U_{h/2}^n$ we obtain the resulting scheme in the form

$$U_h^{n+1} = \frac{1}{3} (4R_h U_h^n - R_{h/2}^2 U_{h/2}^n).\tag{20}$$

To calculate (P, u, v) at the boundary one can use a difference approximation of two characteristic relations

$$\frac{\partial(u+P)}{\partial t} + \frac{\partial(u+P)}{\partial r} + \frac{1}{r} \left(u + \frac{\partial v}{\partial \varphi} \right) = 0,$$

$$\frac{\partial v}{\partial t} + \frac{1}{r} \frac{\partial P}{\partial \varphi} = 0,$$

and ABC (19).

NUMERICAL RESULTS

In this section, results for the Category I, Problem 2 are presented. To estimate the validity of the method including approximate BC we present three sets of numerical data.

The computational domain is the ring G_R : $r_0 \leq r \leq R$; $r_0 = 0.5$. The grid size in the φ direction is constant. As for size in the r direction, we use a nonuniform grid. Namely,

$$r = r_0 e^{\alpha(\rho-r_0)}, \quad \alpha = \frac{1}{R-r_0} \ln \frac{R}{r_0}.$$

This method allows to deal with practically square cells over the whole domain, which leads to the improvement of the numerical results.

Each variant is defined by three constants: R , $\Delta\varphi$ and $\Delta\rho$ and the type of BC.

The first variant: $R = 5$ (this is the minimal size of the computational region because of given coordinates of the points A, B, C); $\Delta\varphi = \pi/600$, $\Delta\rho = 1/440$; 1ABC.

The second variant differs from the first one by ABC only. Here we use 2ABC.

Finally, for the third variant we apply the same $\Delta\varphi$ and $\Delta\rho$ but $R = 10.40284$; 2ABC. Since in this case the boundary ∂G_{10} does not affect the solution in G_5 up to $t = 10$, it follows that we can consider this solution "exact".

Comparing all these solutions one can estimate the role of the type of ABC.

The time histories of P at A, B, C are plotted in Figs 2 - 4, respectively. It is seen that 2ABC-results look at A and B better then 1ABC-results.

The superiority of 2ABC over 1ABC is considerably more visible in Figs 5 - 8. Here we show spatial distributions of pressure on some semi-infinite lines: Fig. 5: $\varphi = 0^\circ$, $t = 2$; Fig. 6: $\varphi = 45^\circ$, $t = 4$; Fig. 7: $\varphi = 90^\circ$, $t = 7$; Fig. 8: $\varphi = 135^\circ$, $t = 10$. In all these Figures "exact" solutions are plotted up to $r = 10$. This gives an indication of the structure of the solution.

As for the accuracy of the difference method we examined it using calculations with fine grid $\Delta\tilde{\varphi} = \Delta\varphi/2$, $\Delta\tilde{\rho} = \Delta\rho/2$. It was found that the third-order accuracy is achieved and results for both grids are practically the same. Thus, we can omit quotes and call the third variant the exact solution.

CONCLUSION

The presented method of constructing ABC can be generalized to the case $M_\infty \neq 0$ as well as to a wide class of hyperbolic systems. One can use the exact ABC if the problem admits the Fourier expansion. Otherwise we are forced to use the approximate ABC like it was shown above.

We also note that this approach can be applied to the steady-state problems. The case of the wave equation outside G is presented in the Appendix.

APPENDIX

We consider the following problem in the whole plane

$$LP = f,$$

where

$$L = \begin{cases} \partial^2/\partial t^2 - \Delta & \text{outside } G_R, \\ L_{int} & \text{in } G_R. \end{cases}$$

$$f = \begin{cases} 0 & \text{outside } G_R \\ f_{int} & \text{in } G_R. \end{cases}$$

Suppose that

- (i) The initial data are compactly supported;
- (ii) This problem is well-posed;
- (iii) There exists the limit solution \bar{P} as $t \rightarrow \infty$.

Then the adequate boundary condition at ∂G for the steady-state problem can be presented in the form

$$\bar{P}_t + \bar{P}_r + \frac{\bar{P}}{2R} = \frac{1}{2R^2} \left(\frac{1}{2}\bar{P} + \mathcal{H}(\bar{P}) \right),$$

where $\mathcal{H}(P)$ is the Hilbert operator

$$\mathcal{H}(P)(\varphi) = \frac{1}{2\pi} \int_0^{2\pi} \frac{P(\xi)d\xi}{\tan \frac{\xi-\varphi}{2}}.$$

REFERENCES

1. Tam, C. K. W. and Webb, J. C., "Dispersion-Relation-Preserving Difference Schemes", for Computational Acoustics", J. Comp. Phis. **107**, 262 – 281, 1993.
2. Radvogin, Yu. B. and Zaitsev, N. A., "Multidimensional Minimal Stencil Supported Second Order Accurate Upwind Schemes for Solving Hyperbolic and Euler Systems", Preprint of Keldysh Inst. of Appl. Math., #22, Moscow, 1996.

FIGURE CAPTIONS

Figure 1. Sketch for Riemann's method

The following Figures illustrate the solution of the Problem 2, Category I.

Figure 2. Time history of pressure p at the point A ($\varphi = 90^\circ$, $r = 5$). Short dashed line corresponds to boundary condition (15) (1ABC, i.e. Tam's BC). Long dashed line corresponds to boundary condition (17) (2ABC). Solid line corresponds to the numerical solution in the expanded region, $R = 10.4$ ("exact").

Figure 3. The same for the point B ($\varphi = 135^\circ$, $r = 5$).

Figure 4. The same for the point B ($\varphi = 135^\circ$, $r = 5$).

Figure 5. Spatial distribution of p on the ray $\varphi = 0^\circ$ at $t = 2$.

Figure 6. The same for $\varphi = 45^\circ$ at $t = 4$.

Figure 7. The same for $\varphi = 90^\circ$ at $t = 7$.

Figure 8. The same for $\varphi = 135^\circ$ at $t = 10$.

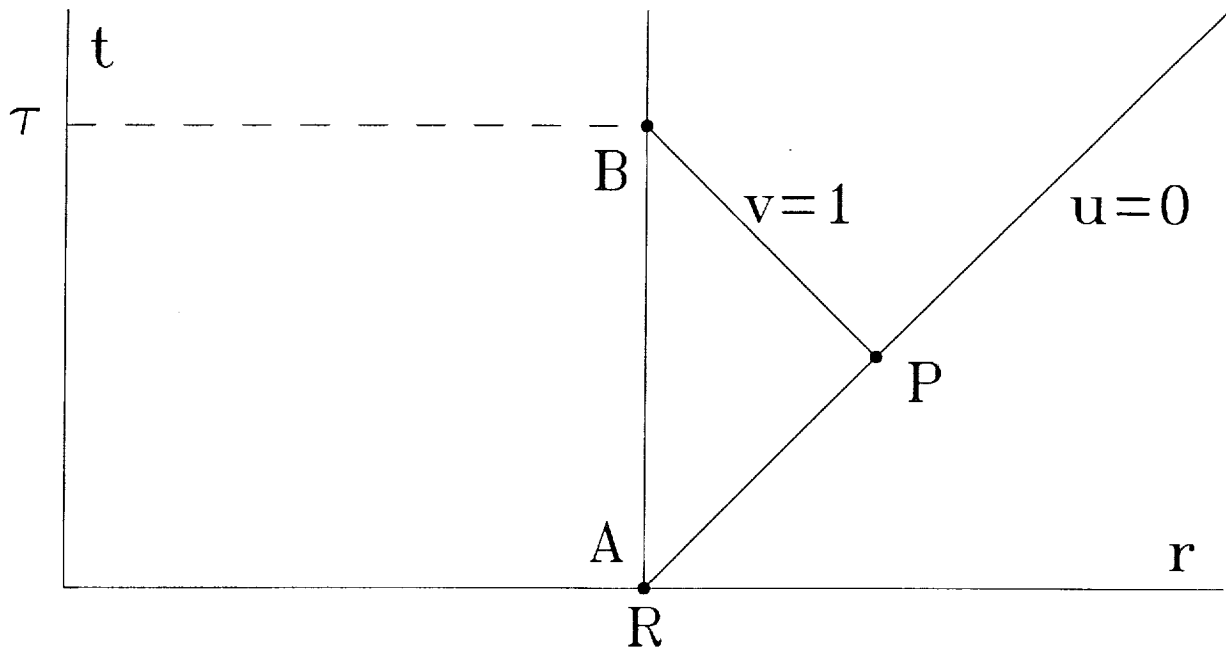


Fig. 1.

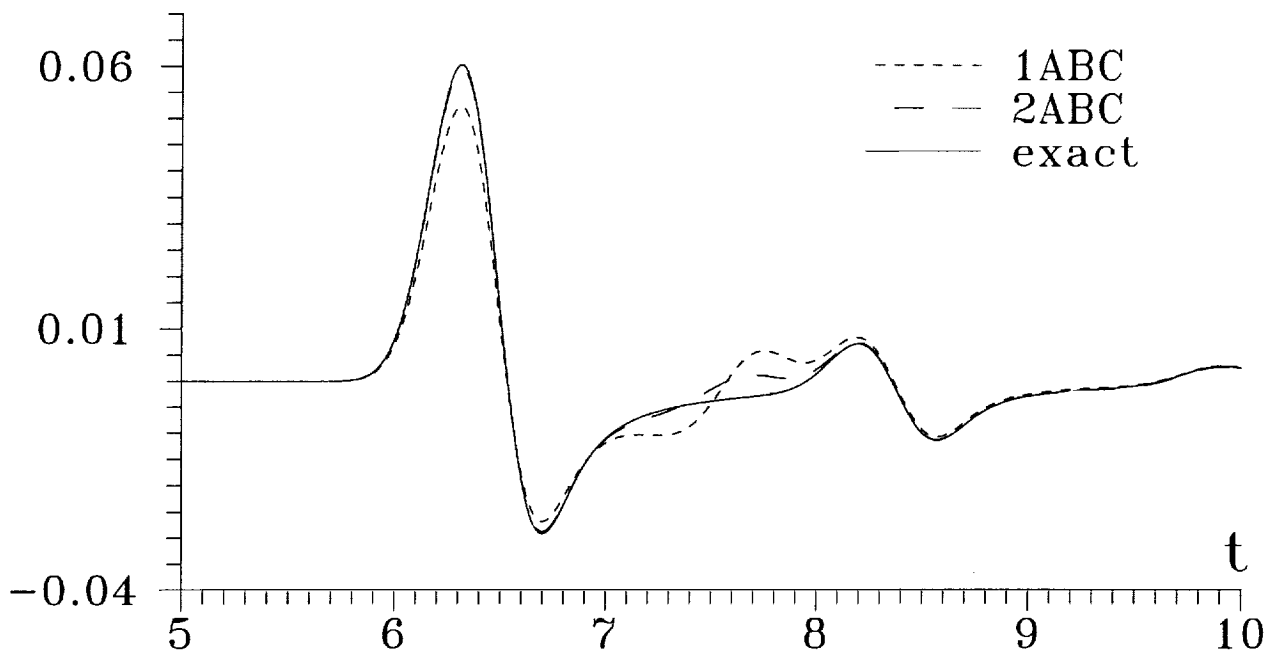


Fig. 2.

$\varphi=90^\circ, r=5$

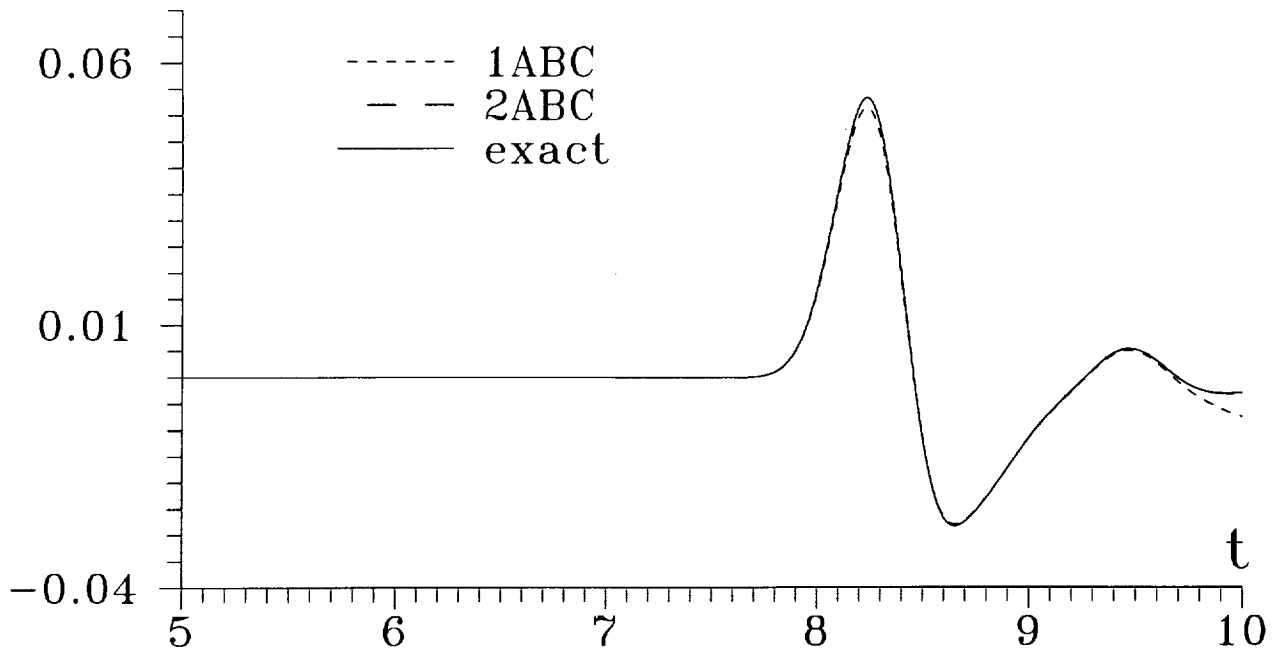


Fig. 3. $\varphi = 135^\circ$, $r = 5$

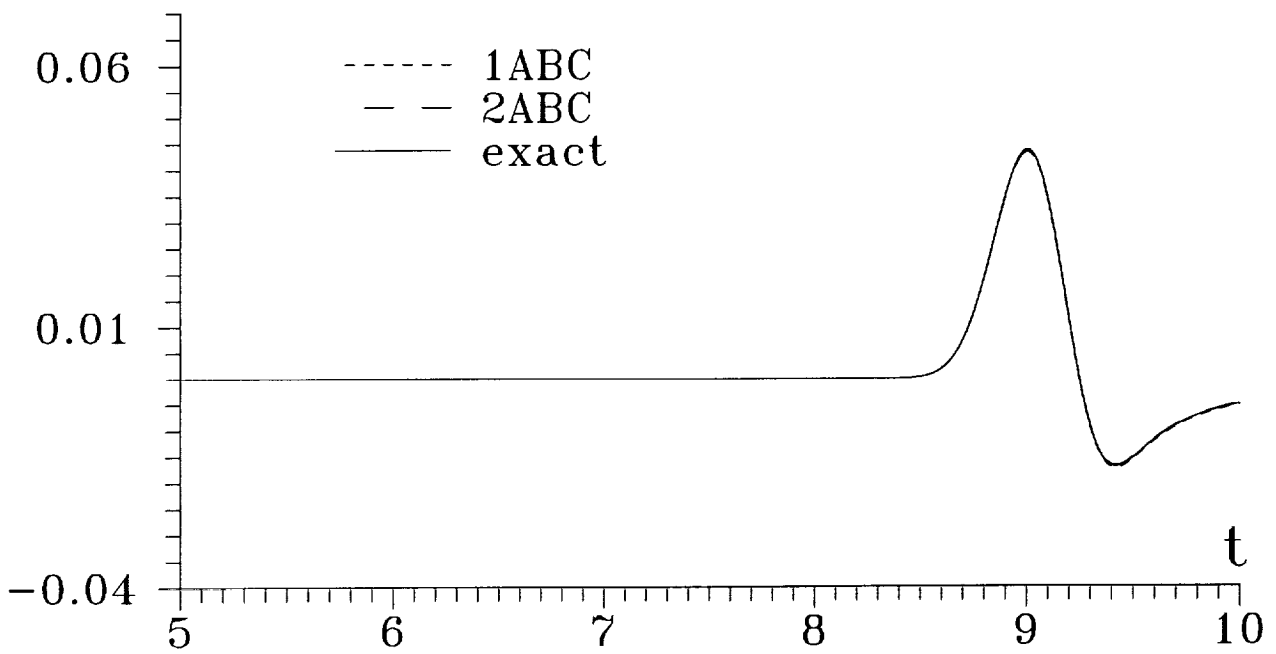


Fig. 4. $\varphi = 180^\circ$, $r = 5$

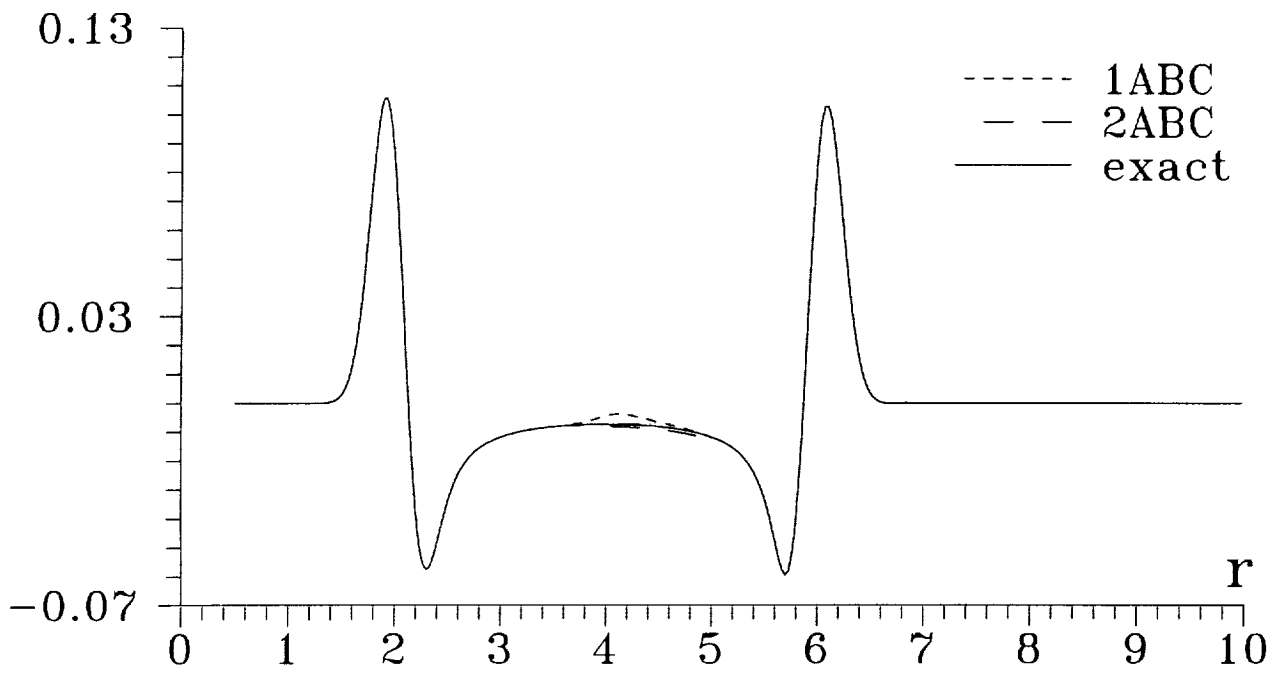


Fig. 5. $\varphi=0^\circ, t=2$

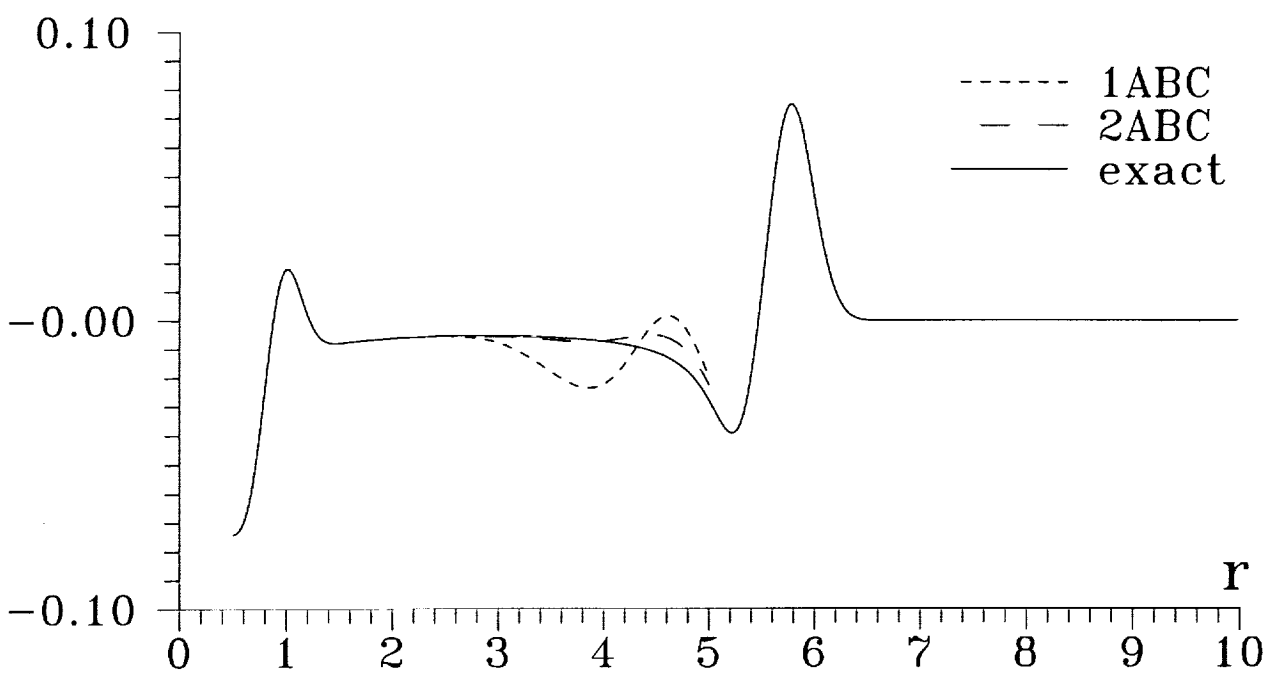


Fig. 6. $\varphi=45^\circ, t=4$

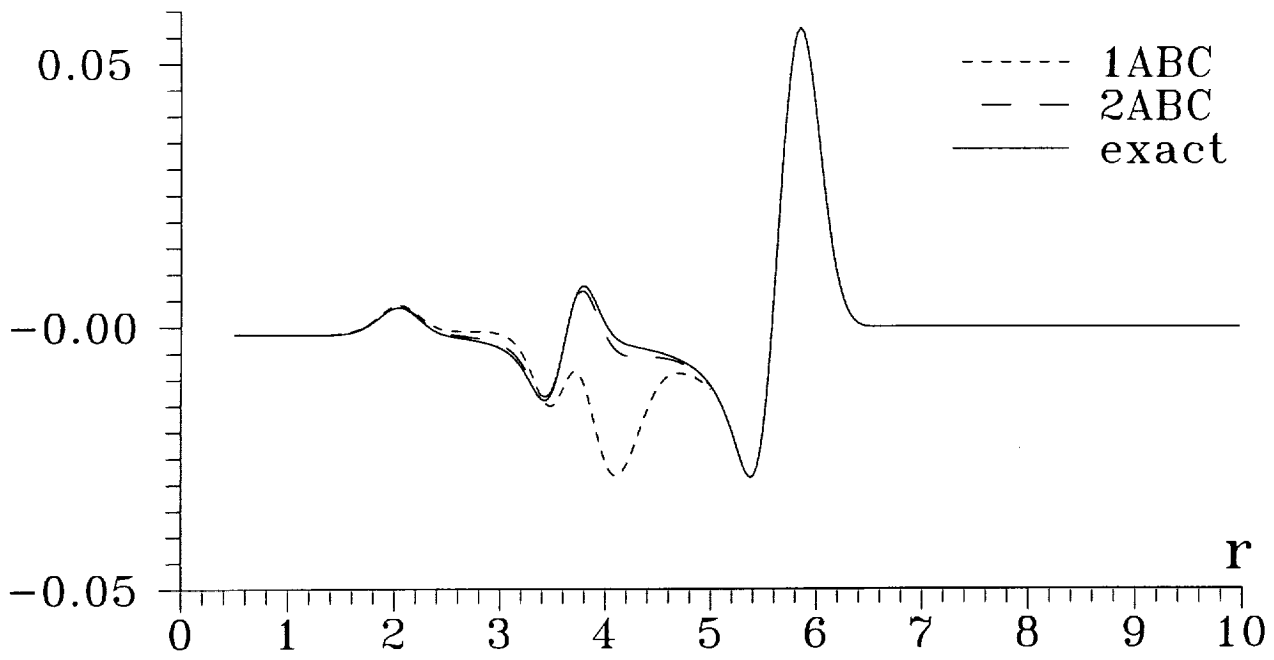


Fig. 7. $\varphi=90^\circ, t=7$

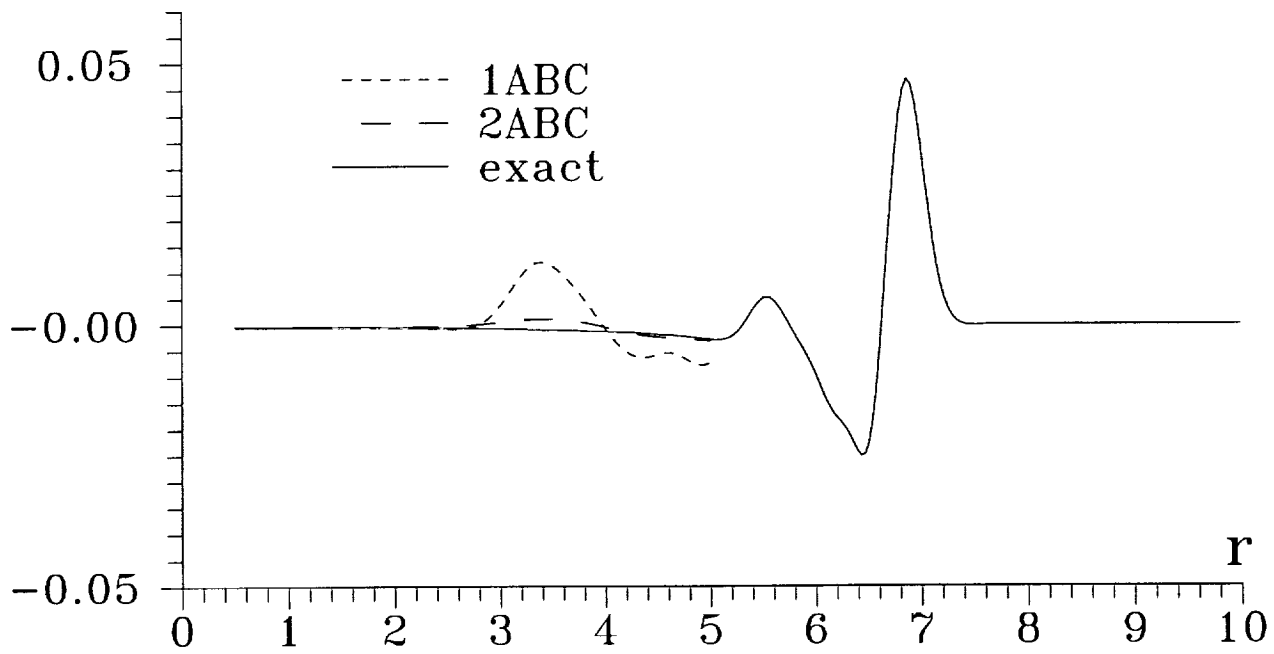


Fig. 8. $\varphi=135^\circ, t=10$



NUMERICAL BOUNDARY CONDITIONS FOR COMPUTATIONAL AEROACOUSTICS BENCHMARK PROBLEMS

Chritsopher K.W. Tam, Konstantin A. Kurbatskii, and Jun Fang
Department of Mathematics
Florida State University
Tallahassee, FL 32306-3027

S 18-64
043476
294000
p30

SUMMARY

Category 1, Problems 1 and 2, Category 2, Problem 2, and Category 3, Problem 2 are solved computationally using the Dispersion-Relation-Preserving (DRP) scheme. All these problems are governed by the linearized Euler equations. The resolution requirements of the DRP scheme for maintaining low numerical dispersion and dissipation as well as accurate wave speeds in solving the linearized Euler equations are now well understood. As long as 8 or more mesh points per wavelength is employed in the numerical computation, high quality results are assured. For the first three categories of benchmark problems, therefore, the real challenge is to develop high quality numerical boundary conditions. For Category 1, Problems 1 and 2, it is the curved wall boundary conditions. For Category 2, Problem 2, it is the internal radiation boundary conditions inside the duct. For Category 3, Problem 2, they are the inflow and outflow boundary conditions upstream and downstream of the blade row. These are the foci of the present investigation. Special non-homogeneous radiation boundary conditions that generate the incoming disturbances and at the same time allow the outgoing reflected or scattered acoustic disturbances to leave the computation domain without significant reflection are developed. Numerical results based on these boundary conditions are provided.

1. INTRODUCTION

The governing equations of the Category 1, 2 and 3 benchmark problems are the linearized Euler equations. Recent works have shown that the linearized Euler equations can be solved accurately by the 7-point stencil time marching Dispersion-Relation-Preserving (DRP) scheme (Tam and Webb, ref. 1) using 8 or more grid points per wavelength. At such a spatial resolution, the numerical dispersion and dissipation of the scheme is minimal. Also, the scheme would support waves with wave speeds almost the same as those of the original linearized Euler equations. Thus, from a purely computational point of view, all these problems are the same except for their boundary con-

ditions. The formulation and implementation of the appropriate numerical boundary conditions for the solutions of these problems are the primary focus of the present paper.

For spatial discretization, the 7-point stencil DRP scheme uses central difference approximation with optimized coefficients. For instance, the first derivative $\frac{\partial f}{\partial x}$ at the ℓ^{th} node of a grid with spacing Δx is approximated by,

$$\left(\frac{\partial f}{\partial x}\right)_{\ell} = \frac{1}{\Delta x} \sum_{j=-3}^3 a_j f_{\ell+j} \quad (1)$$

where the coefficients a_j (see Tam and Shen, ref. 2) are:

$$a_0 = 0$$

$$a_1 = -a_{-1} = 0.770882380518$$

$$a_2 = -a_{-2} = -0.166705904415$$

$$a_3 = -a_{-3} = 0.020843142770.$$

For time marching, the DRP scheme uses a four levels marching algorithm. Let Δt be the time step. We will use superscript n to indicate the time level. To advance the solution $f(t)$ to the next time level the DRP scheme uses the formula,

$$f^{(n+1)} = f^{(n)} + \Delta t \sum_{j=0}^3 b_j \left(\frac{df}{dt}\right)^{(n-j)} \quad (2)$$

where the coefficients b_j are:

$$b_0 = 2.302558088838$$

$$b_1 = -2.491007599848$$

$$b_2 = 1.574340933182$$

$$b_3 = -0.385891422172.$$

In (2) the functions $\left(\frac{df}{dt}\right)^{(n-j)}$ are provided by the governing equation.

The DRP scheme, just as all the other high-order finite difference schemes, supports short wavelength spurious numerical waves. These spurious waves are often generated at computation boundaries (both internal and external), at interfaces and by nonlinearities. They are pollutants of the numerical solution. When excessive amount of spurious waves is produced, it leads not only to the degradation of the quality of the numerical solution but also, in many instances, to numerical instability. To obtain a high quality numerical solution, it is, therefore, necessary to eliminate the

short wavelength spurious numerical waves. This can be done by adding artificial selective damping terms in the finite difference equations. The idea of using artificial damping to smooth out the profile of a shock is not new (ref. 3 and 4). In ref. 5, Tam *et al.* refined the idea by developing a way to adjust the coefficients of the damping terms specifically to eliminate only the short waves. The long waves (with $\alpha\Delta x < 1.0$, where α is the wavenumber) are effectively unaffected.

Consider the linearized u -momentum equation discretized on a regular mesh of spacing Δx . At the ℓ^{th} mesh point, the discretized equation including artificial selective damping terms may be written as,

$$\frac{du_\ell}{dt} = -\frac{1}{\rho_0\Delta x} \sum_{j=-3}^3 a_j p_{\ell+j} - \frac{\nu_a}{(\Delta x)^2} \sum_{j=-3}^3 d_j u_{\ell+j} \quad (3)$$

where d_j are the damping coefficients and ν_a is the artificial kinematic viscosity. Let a_0 be the speed of sound. The artificial mesh Reynolds number $R_{\Delta x}$ will be defined as

$$R_{\Delta x} = \frac{a_0\Delta x}{\nu_a}. \quad (4)$$

In computing the numerical solution below, a suitable value for $R_{\Delta x}^{-1}$ will be assigned in each problem. The choice of the numerical value of $R_{\Delta x}^{-1}$ is largely dictated by the size of the computation domain and the complexity of the boundaries of the problem. Near a wall or at the boundaries of the computation domain, there may not be enough room for a seven-point stencil. In that case, a smaller five-point or a three-point damping stencil may be used. The coefficients of the damping stencils may be found in ref. 6.

2. CATEGORY 1 PROBLEMS

2.1. Problem 1

The acoustic field produced by the oscillating source in the presence of a rigid circular cylinder is computed using the 7-point stencil DRP scheme on a Cartesian grid. By using a spatial resolution of 8 or more mesh points per wavelength we are assured that the numerical results are of high quality.

On the outer boundary of the computation domain (see figure 1), the asymptotic radiation boundary conditions of Bayliss and Turkel (ref. 7) or Tam and Webb (ref. 1) is used. Let (r, θ) be the polar coordinates. The two-dimensional asymptotic radiation boundary conditions are,

$$\frac{\partial}{\partial t} \begin{bmatrix} u \\ v \\ p \end{bmatrix} + \frac{\partial}{\partial r} \begin{bmatrix} u \\ v \\ p \end{bmatrix} + \frac{1}{2r} \begin{bmatrix} u \\ v \\ p \end{bmatrix} = 0. \quad (5)$$

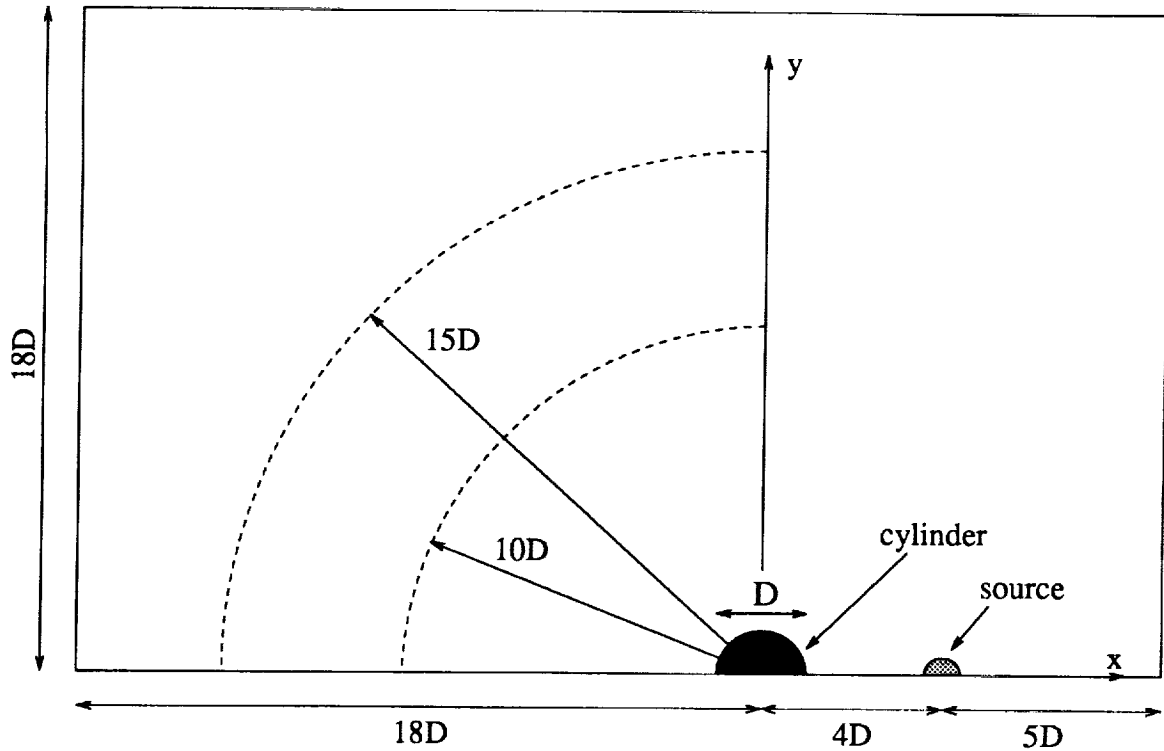


Figure 1. Computational domain for Category 1, Problem 1.

The problem is symmetric about the x -axis. Thus only the solution in the upper half $x-y$ -plane needs to be computed. A symmetric boundary condition is imposed at $y = 0$.

On the surface of the cylinder, we implement the Cartesian boundary treatment of curved walls developed by Kurbatskii and Tam (ref. 8). This boundary treatment is designed for use in conjunction with high-order finite difference schemes. In this method, ghost points, behind the wall outside the physical domain, are included in the computation. On following the suggestion of Tam and Dong (ref. 9), ghost values of pressure are assigned at the ghost points. These ghost values of pressure are then chosen so that the normal component of the fluid velocity at the wall is zero. Details of the method are discussed in Reference 8 and, therefore, will not be elaborated upon here.

To remove spurious short wavelength numerical waves and to provide numerical stability near the solid surface, artificial selective damping terms are added to the computation scheme. An inverse mesh Reynolds number, $R_{\Delta x}^{-1}$, of 0.01 is applied everywhere. In the region surrounding the cylinder, additional damping is needed for numerical stability. This is provided by an additional Gaussian distribution of $R_{\Delta x}^{-1}$ with a maximum value of 0.25 at the wall. The half width of the Gaussian is 3 mesh spacings.

Figure 1 shows the dimensions of the computation domain. The numerical results reported here use a spatial resolution of 8 mesh points per acoustic wave length in both x - and y -directions. For the present problem, the far field directivity of radiated sound is dictated by the interference pattern formed between the directly radiated sound and the scattered sound field centered at the

cylinder. The separation distance between the source and the cylinder is quite large so that to achieve an accuracy of one degree in calculating $\lim_{r \rightarrow \infty} r \overline{p^2}$ the computation must be extended to a distance of $r \simeq 150$. For this reason, comparisons with the exact solution will be carried out in the near field only. Figure 2 shows the computed directivity function $D(\theta) = r \overline{p^2}$ at $r = 10$. The computed results are obtained by time marching to a time periodic state. It is easily seen that there is uniformly good agreement with the exact solution. Figure 3 shows the computed and the exact directivity at $r = 15$. Again, the agreement is very good. The good agreement obtained suggests that the Cartesian boundary treatment of Reference 8 is effective and accurate.

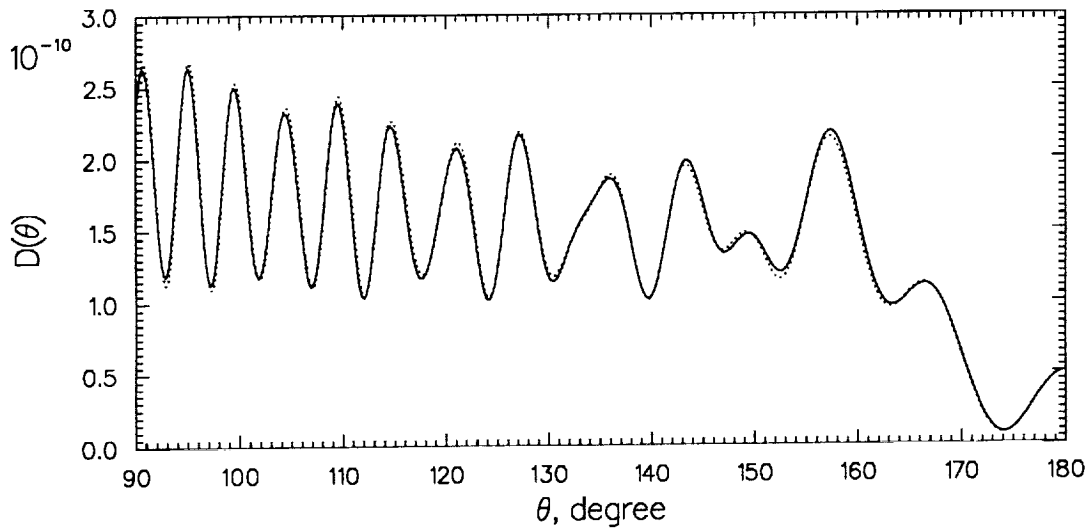


Figure 2. Directivity of radiated sound, $D(\theta) = r \overline{p^2}$, $r = 10$.
 ————— numerical solution, exact solution.

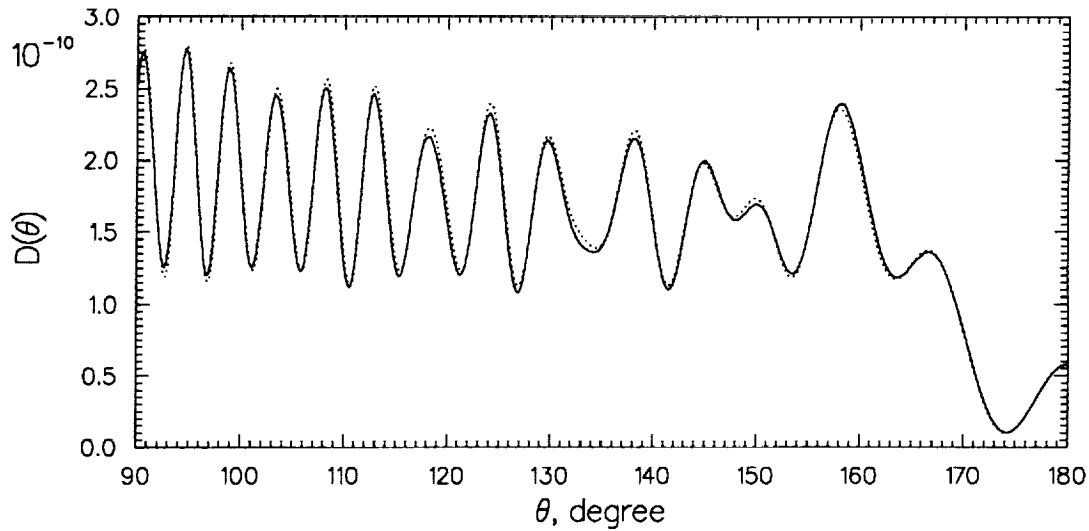


Figure 3. Directivity of radiated sound, $D(\theta) = rp^2$, $r = 15$.
 — numerical solution, exact solution.

2.2. Problem 2

The initial value problem is solved by the DRP scheme on a Cartesian grid in exactly the same manner as in Problem 1. The same curved wall boundary treatment and radiation boundary condition are used. Figure 4 shows a picture of the computed acoustic wave pattern at $t = 7$. There are three wave fronts. The one that is farthest from the cylinder is the wave front created by the initial condition. The next front is wave reflected off the right surface of the cylinder directly facing the initial pulse. The wave front closest to the cylinder is generated when the two parts of the initial wave front, split by the cylinder, collided and merged to the left of the surface of the cylinder. This wave front is weak relative to the other two.

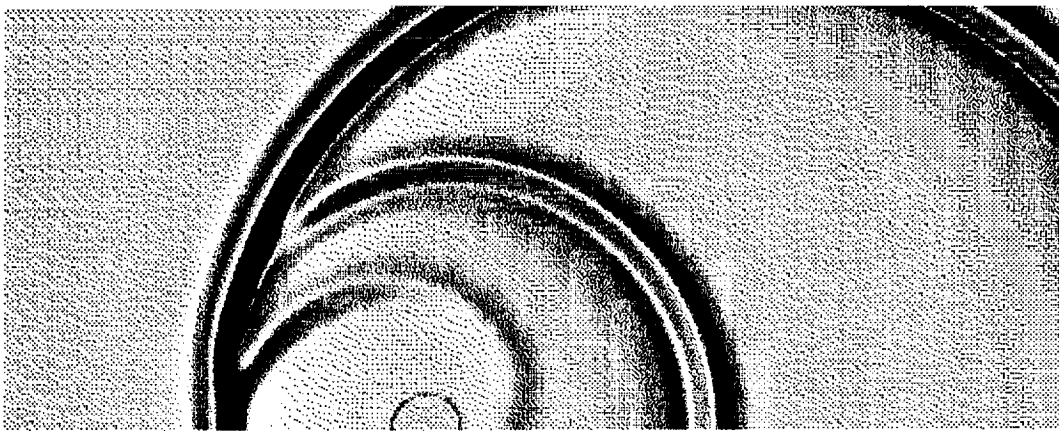


Figure 4. Acoustic wave pattern at $t = 7$.

Figures 5a, b, c show the time history of pressure variation at the prescribed measurement points A , B and C . Plotted in these figures are the exact solutions. There is excellent agreement between the computed and the exact time histories. This is, perhaps, not surprising when one examines the Fourier transform of the initial disturbance. The wavelengths of the main part of the spectrum are very long, significantly longer than that of Problem 1.

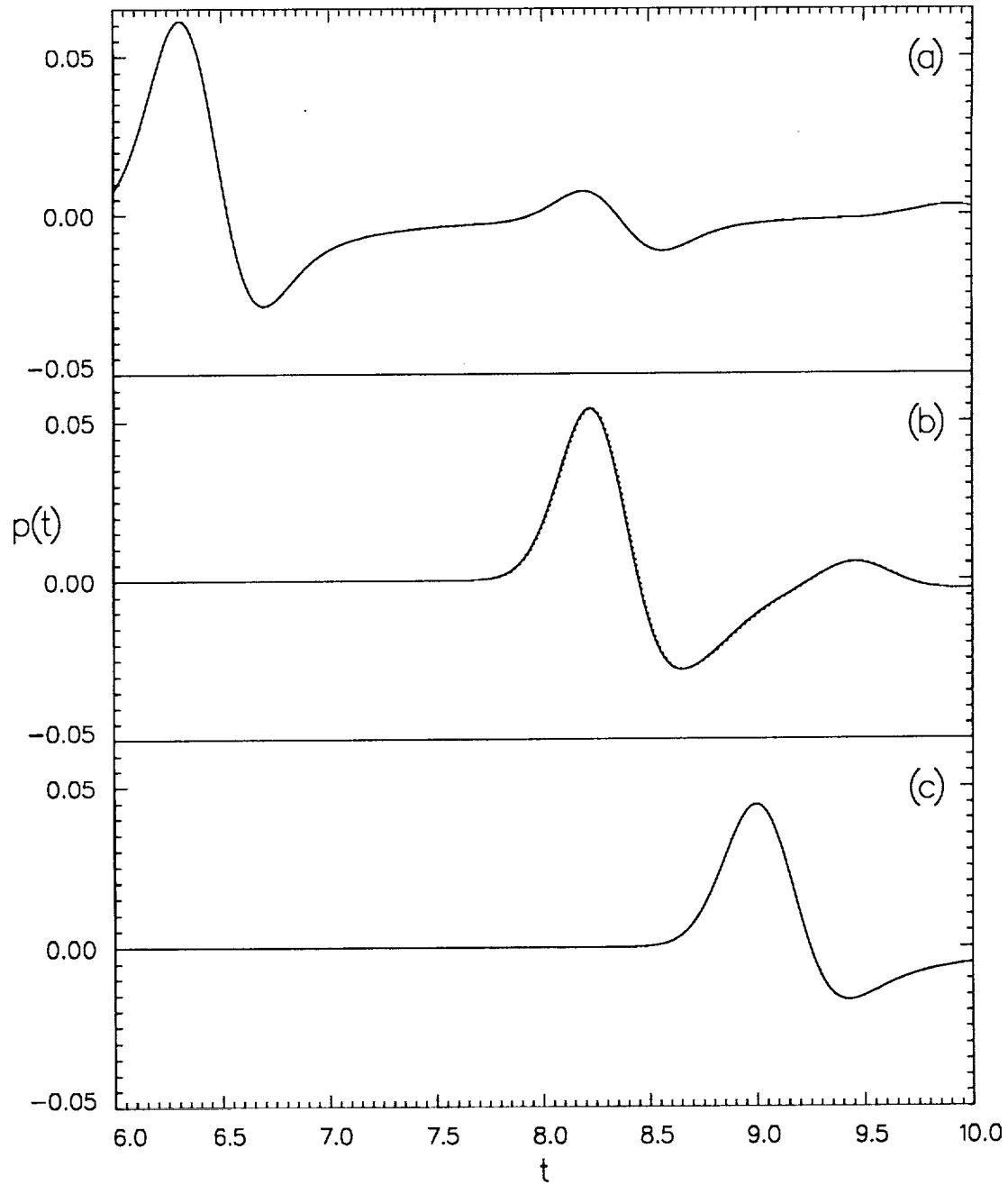


Figure 5. Time history of pressure fluctuation. (a) at A , (b) at B , (c) at C .
 ————— numerical solution, exact solution.

3. CATEGORY 2, PROBLEM 2

The axisymmetric linearized Euler equations in cylindrical coordinates are,

$$\frac{\partial u}{\partial t} = -\frac{\partial p}{\partial x} \quad (6)$$

$$\frac{\partial v}{\partial t} = -\frac{\partial p}{\partial r} \quad (7)$$

$$\frac{\partial p}{\partial t} = -\left(\frac{\partial u}{\partial x} + \frac{\partial v}{\partial r} + \frac{v}{r}\right). \quad (8)$$

We solve these equations in the $r-x$ -plane using the 7-point stencil DRP scheme. The computational domain is as shown in figure 6. To carry out the time marching computation, various types of boundary conditions are required. Along the external boundary $ABCDE$ radiation boundary conditions are needed. On both sides of the duct wall FEH , the imposition of wall boundary conditions is necessary. It is noted that equation (8) has an apparent singularity at the x -axis where $r = 0$. A special duct axis treatment is needed to avoid the problem of division by zero. Finally, at the computation boundary FG , a set of radiation boundary conditions for a ducted environment is required. These radiation boundary conditions must create the prescribed incoming acoustic mode and at the same time allow the reflected waves to exit smoothly out of the computation domain. The formulation and implementation of these various types of boundary conditions are discussed below.

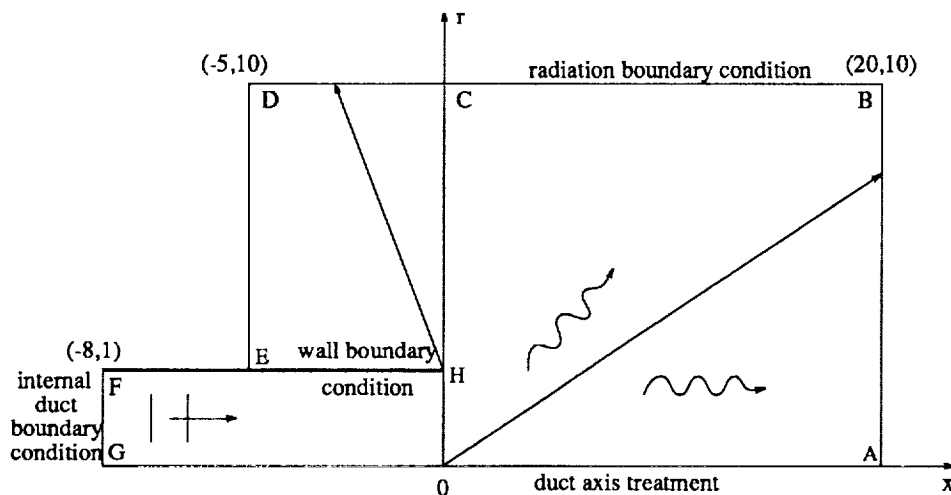


Figure 6. Computational domain for calculating acoustic radiation from the open end of a circular duct.

3.1. Radiation Boundary Conditions

The following three-dimensional asymptotic radiation boundary conditions are used along the open boundary $ABCDE$.

$$\frac{\partial}{\partial t} \begin{bmatrix} u \\ v \\ p \end{bmatrix} + \frac{\partial}{\partial R} \begin{bmatrix} u \\ v \\ p \end{bmatrix} + \frac{1}{R} \begin{bmatrix} u \\ v \\ p \end{bmatrix} = 0 \quad (9)$$

where R is the distance from the center to the boundary point. The presence of the duct wall EH requires a slight adjustment in the implementation of these radiation boundary conditions. This is needed so as to allow the outgoing acoustic waves in the vicinity of E to propagate out parallel to the duct wall. In this work, for the boundary ABC , the center used to compute R in (9) is taken to be at O . For the boundary CDE , the center is taken to be at H . Numerical experiments indicate that the change in the $\frac{1}{R}$ factor in the last term of (9) does not lead to any noticeable degradation of the numerical results.

3.2. Wall Boundary Conditions

To enforce the no throughflow boundary condition at the duct wall, the ghost point method of Tam and Dong (ref. 9) is employed. For each side of the duct wall, a row of ghost points is introduced. For mesh points within two rows of the duct wall, backward difference approximation is used. To compute $\frac{\partial p}{\partial r}$, the stencil is allowed to extend to the ghost point. The ghost value p is chosen so that the wall boundary condition of no throughflow is satisfied.

3.3. Treatment of Singularity at the Axis of the Duct

Equation (8) has an apparent singularity at $r = 0$. One way to avoid the singularity is to replace the last term by its limit value; i.e.,

$$\lim_{r \rightarrow 0} \frac{v}{r} = \frac{\partial v}{\partial r}. \quad (10)$$

At $r = 0$, (8) becomes

$$\frac{\partial p}{\partial t} = - \left(\frac{\partial u}{\partial x} + 2 \frac{\partial v}{\partial r} \right). \quad (11)$$

Tam *et al.* (ref. 10) used this limit value method in one of the benchmark problems of the previous computational aeroacoustics workshop. One not so desirable consequence is that there is a change in the governing equations between the row of points on the duct axis and the first row

off the axis. Such a change often results in the generation of spurious short wavelength numerical waves. Thus the imposition of stronger artificial selective damping is needed around the duct axis.

In this work, the limit value method is not used. Instead, we make use of the Half-Mesh Displacement method. Here the computation mesh is laid so that the first row of mesh points is at a half-mesh distance from the duct axis. This is shown in figure 7. For this mesh, the problem of $r = 0$ never arises. Thus there is no need to switch governing equation. In fact, the computation stencil can be extended into the $r < 0$ side of the mesh. For the values of the variables in the negative r region, we use symmetric extension about the duct axis for u and p and antisymmetric extension for v . In this way, the tendency to produce spurious waves near the axis region is greatly reduced.

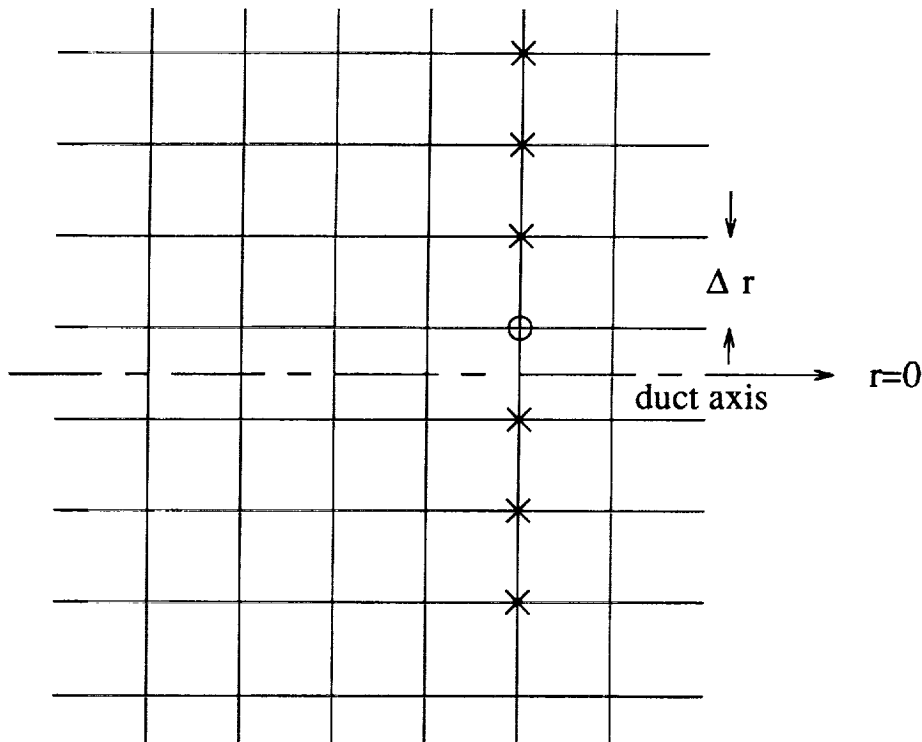


Figure 7. Lay-out of the mesh for the Half-mesh point displacement method.

3.4. Radiation Boundary Conditions Inside a Duct

The radiation boundary conditions, to be imposed along boundary FG , (see figure 6) must perform two important functions. First, they are to create the incoming acoustic wave mode specified by the problem. Second, they are to allow the waves reflected back from the open end of the duct to leave the computational domain smoothly. As far as we know, boundary conditions of this type are not available in the literature.

By eliminating u and v from equations (6)–(8), it is easy to find that the governing equation for p is,

$$\frac{\partial^2 p}{\partial t^2} - \left(\frac{\partial^2 p}{\partial r^2} + \frac{1}{r} \frac{\partial p}{\partial r} + \frac{\partial^2 p}{\partial x^2} \right) = 0. \quad (12)$$

Let us look for propagating wave solutions of the form,

$$p(r, x, t) = \text{Re} \left[\hat{p}(r) e^{i(\alpha x - \omega t)} \right]. \quad (13)$$

Substitution of (13) into (12) together with the wall boundary condition $\frac{\partial p}{\partial r}(r = 1) = 0$ leads to the following eigenvalue problem.

$$\frac{d^2 \hat{p}}{dr^2} + \frac{1}{r} \frac{d\hat{p}}{dr} + (\omega^2 - \alpha^2) \hat{p} = 0 \quad (14)$$

$$\frac{d\hat{p}}{dr}(1) = 0 \quad (15)$$

The eigenvalues ($\alpha = \pm \alpha_n$, $n = 0, 1, 2, \dots$) and eigenfunctions are,

$$\alpha_n = (\omega^2 - \kappa_n^2)^{\frac{1}{2}} \quad (16)$$

$$\hat{p}_n = J_0(\kappa_n r) \quad (17)$$

where κ_n are the roots of Bessel functions of order 1; i.e.,

$$J_1(\kappa_n), \quad n = 1, 2, 3, \dots$$

and J_0 is Bessel function of order zero. The corresponding duct mode solution is,

$$\begin{bmatrix} u \\ v \\ p \end{bmatrix} = \text{Re} \left\{ A_n \begin{bmatrix} \frac{\alpha_n}{\omega} J_0(\kappa_n r) \\ \frac{i\kappa_n}{\omega} J_1(\kappa_n r) \\ J_0(\kappa_n r) \end{bmatrix} e^{i(\alpha_n x - \omega t)} \right\}. \quad (18)$$

The first four roots of J_1 are,

$$\kappa_0 = 0$$

$$\kappa_1 = 3.83171$$

$$\kappa_2 = 7.01559$$

$$\kappa_3 = 10.17347$$

For propagating modes, α must be real. From (16), it is clear that for case (a) with $\omega = 7.2$, there are three propagating modes and for case (b) with $\omega = 10.3$, there are four propagating modes.

In the space below, we will concentrate on developing the radiation boundary conditions for case (b). In the region of the duct away from the open end (see figure 6), the solution consists of the incoming wave and the outgoing wave modes (the wave modes propagating in the negative x -direction have $\alpha = -\alpha_n$, $n = 0, 1, 2, 3$). That is,

$$\begin{bmatrix} u \\ v \\ p \end{bmatrix} = \left\{ \begin{array}{l} \frac{\alpha_2}{\omega} J_0(\kappa_2 r) \cos(\alpha_2 x - \omega t) \\ -\frac{\kappa_2}{\omega} J_1(\kappa_2 r) \sin(\alpha_2 x - \omega t) \\ J_0(\kappa_2 r) \cos(\alpha_2 x - \omega t) \end{array} + \sum_{n=0}^3 A_n \begin{bmatrix} \frac{\alpha_2}{\omega} J_0(\kappa_n r) \cos(\alpha_n x + \omega t + \phi_n) \\ \frac{\kappa_2}{\omega} J_1(\kappa_n r) \sin(\alpha_n x + \omega t + \phi_n) \\ J_0(\kappa_n r) \cos(\alpha_n x + \omega t + \phi_n) \end{bmatrix} \right\}. \quad (20)$$

The reflected wave amplitudes A_n ($n = 0, 1, 2, 3$) and phases ϕ_n ($n = 0, 1, 2, 3$) are unknown.

Let us consider the u -velocity component. By differentiating (20), we find

$$\frac{\partial u}{\partial t}(r, x, t) = \alpha_2 J_0(\kappa_2 r) \sin(\alpha_2 x - \omega t) - [\omega, \alpha_1 J_0(\kappa_1 r), \alpha_2 J_0(\kappa_2 r), \alpha_3 J_0(\kappa_3 r)] \mathbf{A}$$

where $\mathbf{A} = \begin{bmatrix} A_0 \sin(\omega x + \omega t + \phi_0) \\ A_1 \sin(\alpha_1 x + \omega t + \phi_1) \\ A_2 \sin(\alpha_2 x + \omega t + \phi_2) \\ A_3 \sin(\alpha_3 x + \omega t + \phi_3) \end{bmatrix}$ (21)

If the column vector, \mathbf{A} , of (21) is known, then this equation can be used to update the value of u at the boundary region. To find vector \mathbf{A} , let us differentiate (20) with respect to x to obtain,

$$\frac{\partial u}{\partial x}(r, x, t) = -\frac{\alpha_2^2}{\omega} J_0(\kappa_2 r) \sin(\alpha_2 x - \omega t) - \left[\omega, \frac{\alpha_1^2}{\omega} J_0(\kappa_1 r), \frac{\alpha_2^2}{\omega} J_0(\kappa_2 r), \frac{\alpha_3^2}{\omega} J_0(\kappa_3 r) \right] \mathbf{A}. \quad (22)$$

We will assume that the mesh lay-out inside the duct near the boundary of the computation domain is as shown in figure 8. Equation (22) holds true for $r = (m + \frac{1}{2})\Delta r$, $m = 0, 1, 2, \dots, M$. This yields $(M + 1)$ linear algebraic equations that may be written in the matrix form,

$$\mathbf{C}\mathbf{A} = \mathbf{b} \quad (23)$$

where \mathbf{C} is a $(M + 1) \times 4$ matrix and \mathbf{b} is a $(M + 1)$ column vector.

$$\mathbf{C} = \begin{bmatrix} \omega & \frac{\alpha_1^2}{\omega} J_0(0.5\kappa_1 \Delta r) & \frac{\alpha_2^2}{\omega} J_0(0.5\kappa_2 \Delta r) & \frac{\alpha_3^2}{\omega} J_0(0.5\kappa_3 \Delta r) \\ \omega & \frac{\alpha_1^2}{\omega} J_0(1.5\kappa_1 \Delta r) & \frac{\alpha_2^2}{\omega} J_0(1.5\kappa_2 \Delta r) & \frac{\alpha_3^2}{\omega} J_0(1.5\kappa_3 \Delta r) \\ \omega & \frac{\alpha_1^2}{\omega} J_0(2.5\kappa_1 \Delta r) & \frac{\alpha_2^2}{\omega} J_0(2.5\kappa_2 \Delta r) & \frac{\alpha_3^2}{\omega} J_0(2.5\kappa_3 \Delta r) \\ \vdots & \vdots & \vdots & \vdots \\ \omega & \frac{\alpha_1^2}{\omega} J_0((M + 0.5)\kappa_1 \Delta r) & \frac{\alpha_2^2}{\omega} J_0((M + 0.5)\kappa_2 \Delta r) & \frac{\alpha_3^2}{\omega} J_0((M + 0.5)\kappa_3 \Delta r) \end{bmatrix} \quad (24)$$

$$\mathbf{b} = \begin{bmatrix} \frac{\partial u}{\partial x}(0.5\Delta r, x, t) + \frac{\alpha_2^2}{\omega} J_0(0.5\kappa_2 \Delta r) \sin(\alpha_2 x - \omega t) \\ \frac{\partial u}{\partial x}(1.5\Delta r, x, t) + \frac{\alpha_2^2}{\omega} J_0(1.5\kappa_2 \Delta r) \sin(\alpha_2 x - \omega t) \\ \vdots \\ \frac{\partial u}{\partial x}((M + 0.5)\Delta r, x, t) + \frac{\alpha_2^2}{\omega} J_0((M + 0.5)\kappa_2 \Delta r) \sin(\alpha_2 x - \omega t) \end{bmatrix} \quad (25)$$

In (25) the x -derivatives are to be found by finite difference approximation.

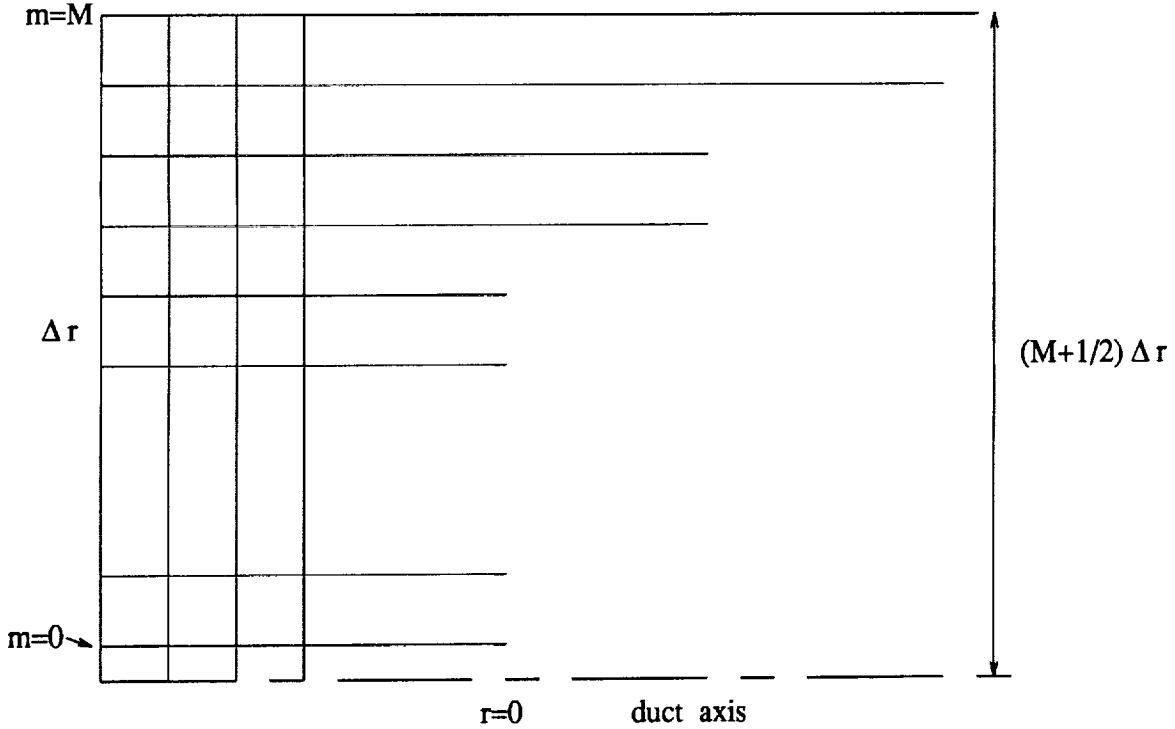


Figure 8. Mesh lay-out inside the duct near the boundary of the computational domain.

(23) is an overdetermined system for \mathbf{A} . Such a system may be solved by the least squares method (ref. 11, Chapter 5). This leads to the normal equation, the solution of which gives,

$$\mathbf{A} = (\mathbf{C}^T \mathbf{C})^{-1} \mathbf{C}^T \mathbf{b} \quad (26)$$

where \mathbf{C}^T is the transposition of \mathbf{C} .

Finally, by substitution of (26) into (21), we obtain a nonhomogeneous radiation boundary condition for the ducted environment.

$$\frac{\partial u}{\partial t}(r, x, t) = \alpha_2 J_0(\kappa_2 r) \sin(\alpha_2 x - \omega t) - [\omega, \alpha_1 J_0(\kappa_1 r), \alpha_2 J_0(\kappa_2 r), \alpha_3 J_0(\kappa_3 r)] (\mathbf{C}^T \mathbf{C})^{-1} \mathbf{C}^T \mathbf{b}. \quad (27)$$

In applying (27), it is noted that for a given column of mesh points, the matrix $(\mathbf{C}^T \mathbf{C})^{-1} \mathbf{C}^T$ need be calculated only once in the entire computation. At each time step, once the vector \mathbf{b} is updated, it can be used for all the mesh points in the column.

For the variable p and v , boundary conditions similar to (27) can be easily derived following the steps above.

3.5. Numerical Results

Three mesh sizes with $\Delta x = \frac{1}{16}, \frac{1}{24}, \frac{1}{32}$ and $\Delta r = \frac{1}{16.5}, \frac{1}{24.5}, \frac{1}{32.5}$ are used in the computation. This allows us to monitor numerical convergence. Artificial selective damping is included in the computation. An inverse mesh Reynolds number of 0.05 is applied to every mesh point. Additional damping is imposed around the boundaries shown in figure 9. The maximum value of the inverse mesh Reynolds number of the additional damping is displayed. This value is reduced to zero through a Gaussian distribution with a half-width of three mesh points in the normal direction.

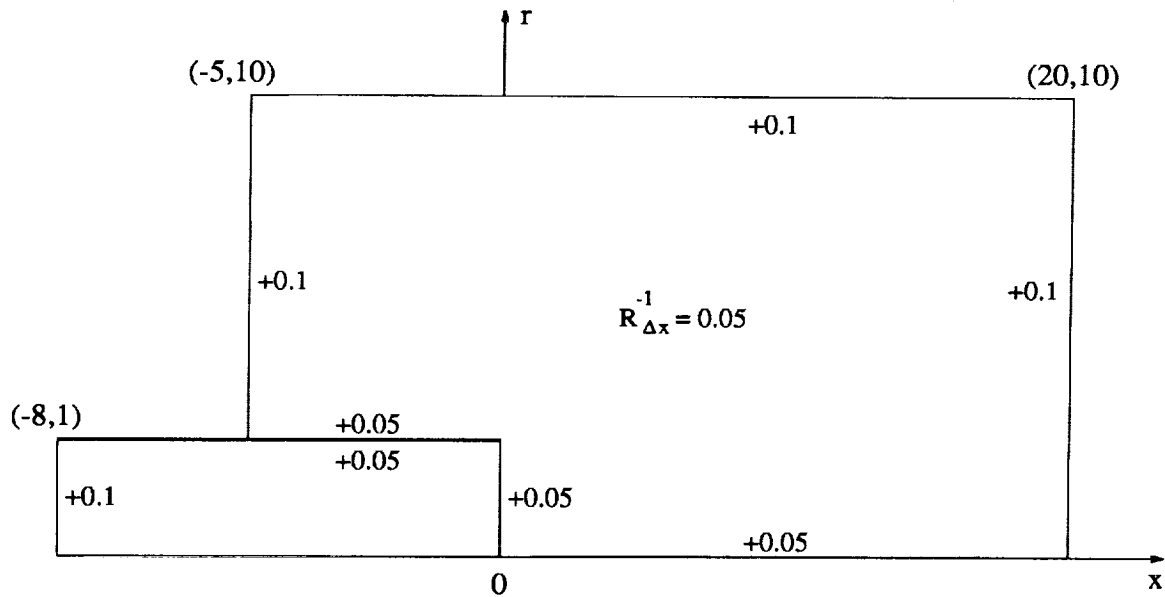


Figure 9. Distribution of $R_{\Delta x}^{-1}$ used in the computation.

Figure 10 shows the computed directivity of the radiated sound at $\omega = 7.2$ using $\Delta x = \frac{1}{32}$ and $\Delta r = \frac{1}{32.5}$. There is a peak radiation around $\theta = 60$ deg. Figure 11 shows the pressure envelope inside the duct at $r = 0, 0.34, 0.55$ and 0.79 . The peaks and valleys of the envelope are formed by strong reflection off the open end of the duct. Such strong reflection arises because the wave frequency is quite close to the cut-off frequency of the second radial mode. The radial variation of the amplitude of the pressure envelope follows the spatial distribution of the eigenfunction of the second radial mode. For this problem, this mode is the dominant of the four cut-on modes.

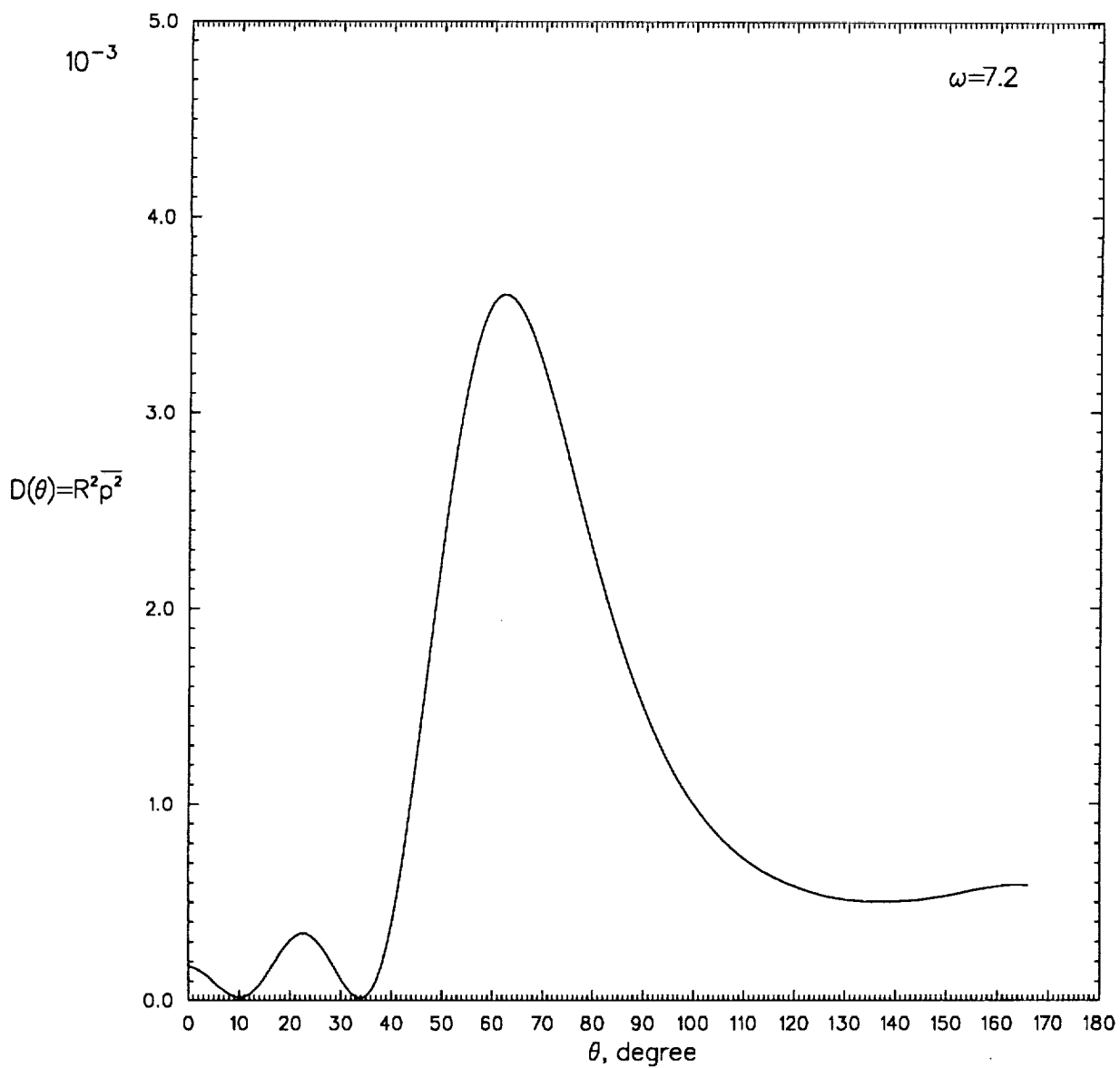


Figure 10. Directivity of radiated sound at $\omega = 7.2$.

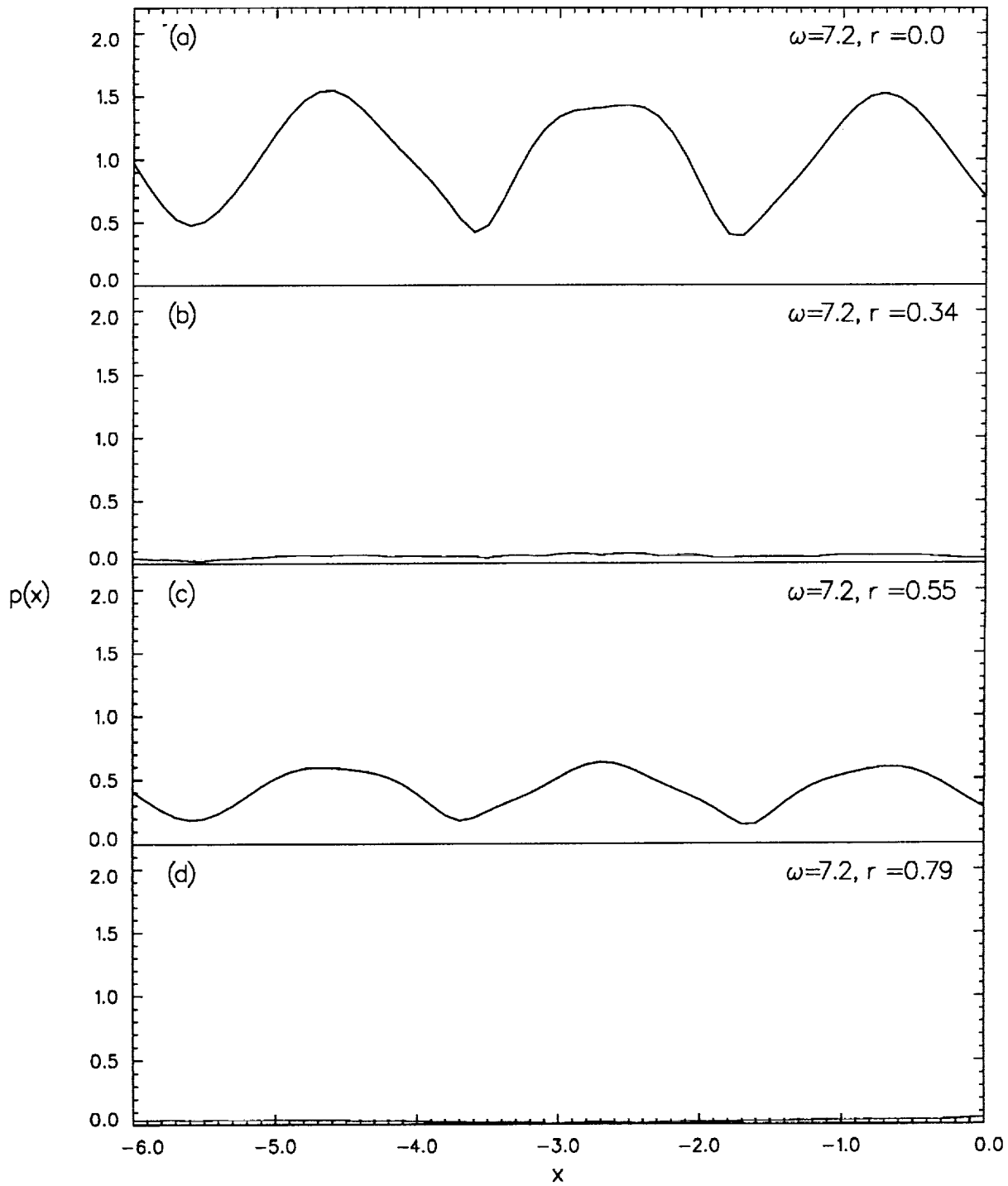


Figure 11. Pressure envelope inside the duct at $\omega = 7.2$.
 (a) $r = 0.0$, (b) $r = 0.34$, (c) $r = 0.55$, (d) $r = 0.79$.

Figure 12 is the computed directivity of the radiated sound at $\omega = 10.3$. Figure 13 shows the pressure envelope inside the duct at this higher frequency. These results are qualitatively similar to those at $\omega = 7.2$.

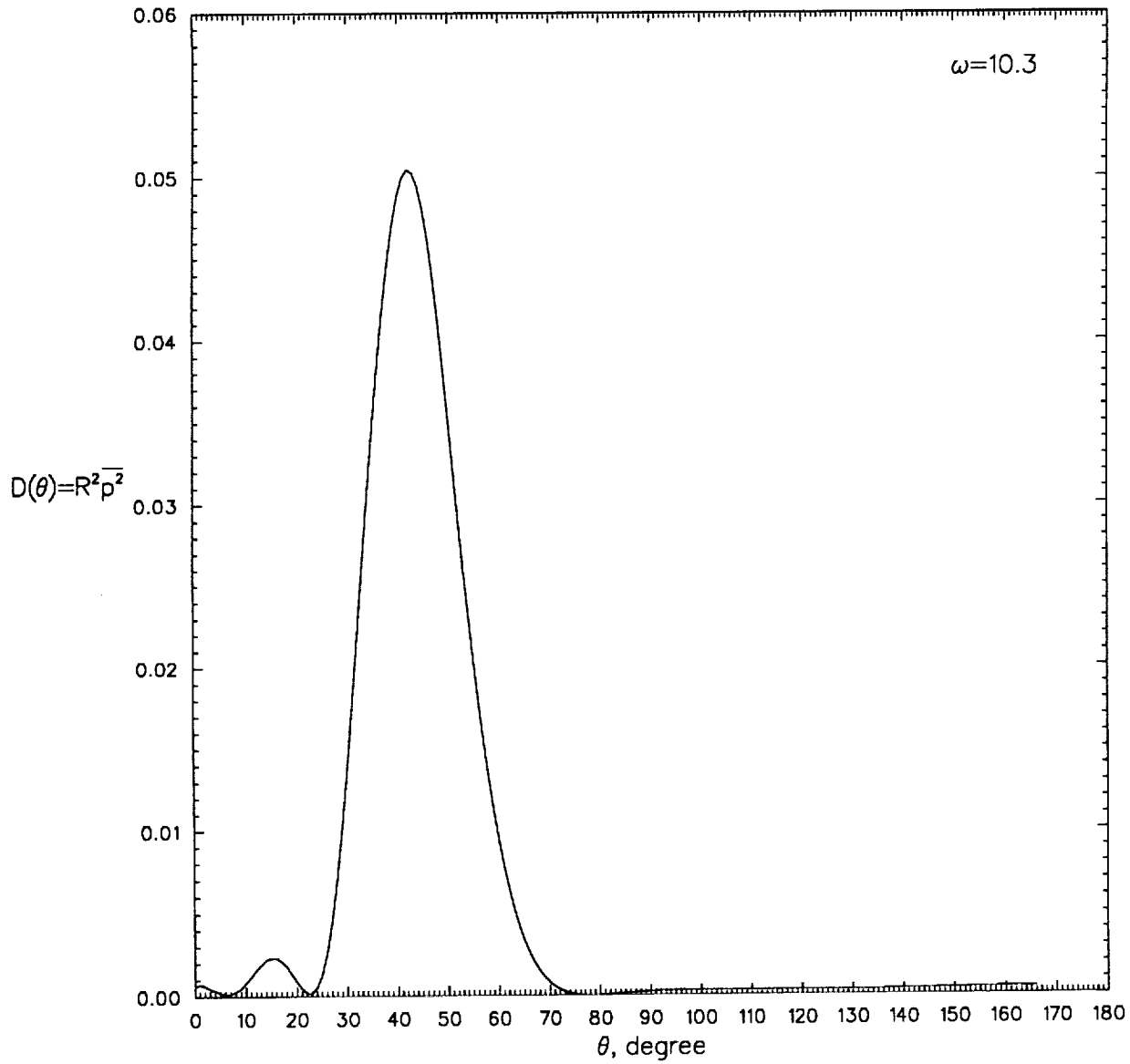


Figure 12. Directivity of radiated sound at $\omega = 10.3$.

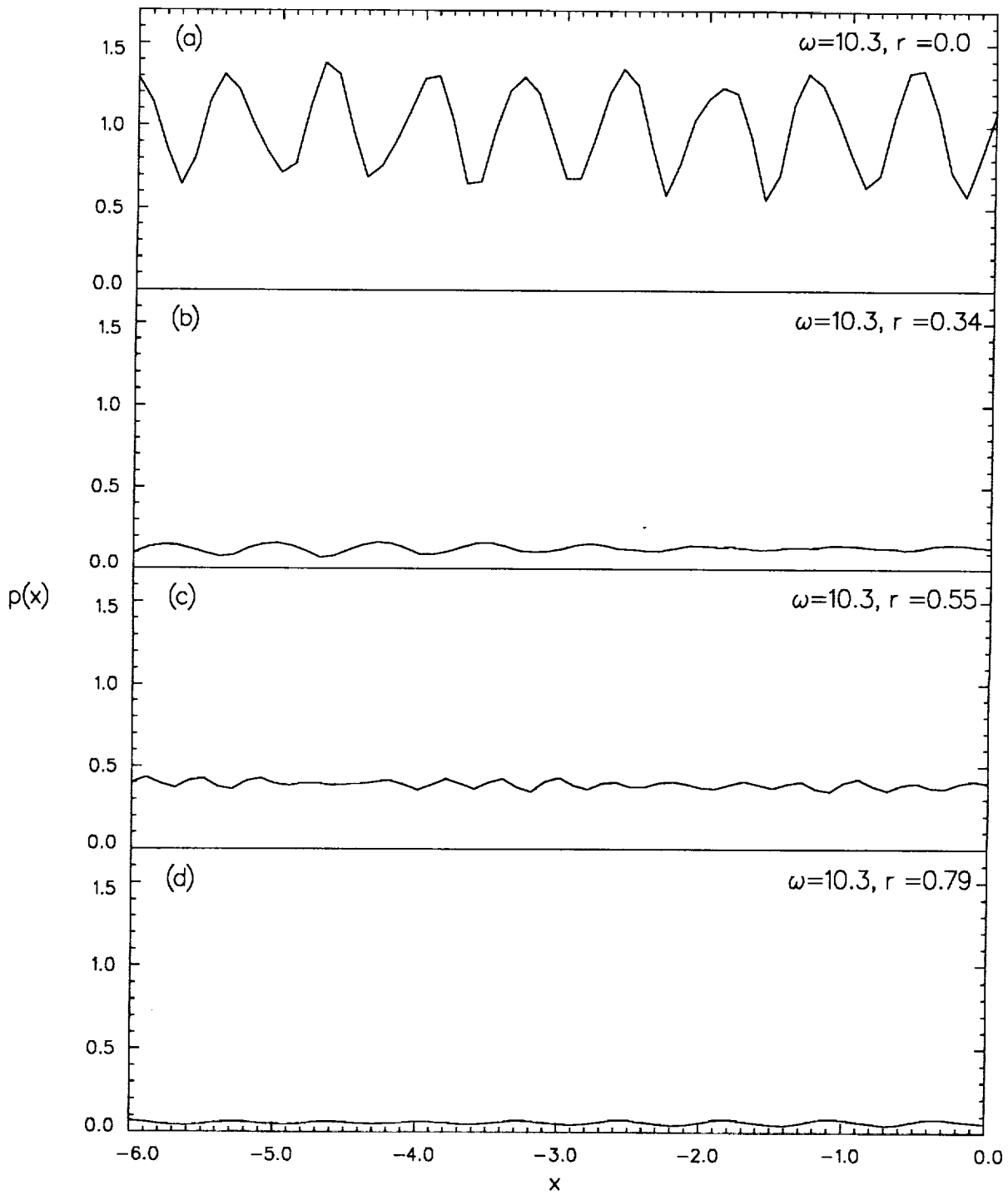


Figure 13. Pressure envelope inside the duct at $\omega = 10.3$.
 (a) $r = 0.0$, (b) $r = 0.34$, (c) $r = 0.55$, (d) $r = 0.79$.

4. CATEGORY 3, PROBLEM 2

This problem, strictly speaking, is quite similar to Category 2, Problem 2. For this reason, only the formulation of the inflow and outflow boundary conditions will be discussed.

The linearized Euler equations are,

$$\frac{\partial u}{\partial t} + \frac{\partial u}{\partial x} = -\frac{\partial p}{\partial x} \quad (28)$$

$$\frac{\partial v}{\partial t} + \frac{\partial v}{\partial x} = -\frac{\partial p}{\partial y} \quad (29)$$

$$\frac{\partial p}{\partial t} + \frac{\partial p}{\partial x} + \frac{1}{M^2} \left(\frac{\partial u}{\partial x} + \frac{\partial v}{\partial y} \right) = 0 \quad (30)$$

where M is the mean flow Mach number. (28) to (30) support two types of waves, namely, the vorticity and the acoustic waves.

For the vorticity waves, the general solution can be written as,

$$u = \frac{\partial \phi}{\partial y}(x-t, y), \quad v = -\frac{\partial \phi}{\partial x}(x-t, y), \quad p = 0 \quad (31)$$

where ϕ is an arbitrary function that is periodic in y .

The computation domain is shown in figure 14. Because of the periodic boundary condition, the acoustic waves propagate in the x -direction in the form of duct modes. By eliminating u and v from (28) to (30), the equation for p is,

$$\left(\frac{\partial}{\partial t} + \frac{\partial}{\partial x} \right)^2 p - \frac{1}{M^2} \left(\frac{\partial^2 p}{\partial x^2} + \frac{\partial^2 p}{\partial y^2} \right) = 0. \quad (32)$$

The duct modes can be found by expanding the solution as a Fourier series in y with a period of 4; i.e.,

$$p(x, y, t) = \text{Re} \left\{ \sum_{n=-\infty}^{\infty} A_n e^{i(\alpha_n x + \frac{n\pi y}{2} - \omega t)} \right\} \quad (33)$$

Substitution of (33) into (32), it is easy to find that the wavenumber α_n is given by

$$\alpha_n^{\pm} = \frac{-\omega M^2 \pm \left[\omega^2 M^2 - (1 - M^2) \frac{n^2 \pi^2}{4} \right]^{\frac{1}{2}}}{(1 - M^2)}. \quad (34)$$

α_n^+ s are for waves propagating in the x -direction while α_n^- s are for waves propagating in the negative x -direction. It is clear that the waves become damped if the square root term of (34) is purely imaginary. In other words,

$$n > \frac{2\omega M}{\pi(1 - M^2)^{\frac{1}{2}}}.$$

For the case $\omega = \frac{5\pi}{2}$, there are three propagating modes corresponding to $n = 0, 1$ and 2 . Thus at the inflow boundary the outgoing acoustic waves are,

$$\begin{aligned}
 u &= \sum_{n=0}^2 \left[A_n \frac{\alpha_n^-}{(\omega - \alpha_n^-)} \cos\left(\frac{n\pi y}{2}\right) \cos(\alpha_n^- x - \omega t + \phi_n) \right. \\
 &\quad \left. + B_n \frac{\alpha_n^-}{(\omega - \alpha_n^-)} \sin\left(\frac{n\pi y}{2}\right) \cos(\alpha_n^- x - \omega t + \psi_n) \right] \\
 v &= \sum_{n=1}^2 \left[A_n \frac{\frac{n\pi}{2}}{(\alpha_n^- - \omega)} \sin\left(\frac{n\pi y}{2}\right) \sin(\alpha_n^- x - \omega t + \phi_n) \right. \\
 &\quad \left. - B_n \frac{\frac{n\pi}{2}}{(\alpha_n^- - \omega)} \cos\left(\frac{n\pi y}{2}\right) \sin(\alpha_n^- x - \omega t + \psi_n) \right] \\
 p &= \sum_{n=0}^2 \left[A_n \cos\left(\frac{n\pi y}{2}\right) \cos(\alpha_n^- x - \omega t + \phi_n) + B_n \sin\left(\frac{n\pi y}{2}\right) \cos(\alpha_n^- x - \omega t + \psi_n) \right]
 \end{aligned} \tag{35}$$

where A_n, B_n are the unknown amplitudes and ϕ_n, ψ_n are the unknown phases. Similarly, at the outflow boundary, the outgoing acoustic waves are,

$$\begin{aligned}
 u &= \sum_{n=0}^2 \left[C_n \frac{\alpha_n^+}{(\omega - \alpha_n^+)} \cos\left(\frac{n\pi y}{2}\right) \cos(\alpha_n^+ x - \omega t + \chi_n) \right. \\
 &\quad \left. + D_n \frac{\alpha_n^+}{(\omega - \alpha_n^+)} \sin\left(\frac{n\pi y}{2}\right) \cos(\alpha_n^+ x - \omega t + \lambda_n) \right] \\
 v &= \sum_{n=1}^2 \left[C_n \frac{\frac{n\pi}{2}}{(\alpha_n^+ - \omega)} \sin\left(\frac{n\pi y}{2}\right) \sin(\alpha_n^+ x - \omega t + \chi_n) \right. \\
 &\quad \left. - D_n \frac{\frac{n\pi}{2}}{(\alpha_n^+ - \omega)} \cos\left(\frac{n\pi y}{2}\right) \sin(\alpha_n^+ x - \omega t + \lambda_n) \right] \\
 p &= \sum_{n=0}^2 \left[C_n \cos\left(\frac{n\pi y}{2}\right) \cos(\alpha_n^+ x - \omega t + \chi_n) + D_n \sin\left(\frac{n\pi y}{2}\right) \cos(\alpha_n^+ x - \omega t + \lambda_n) \right]
 \end{aligned} \tag{36}$$

where C_n, D_n are the unknown amplitudes and χ_n, λ_n are the unknown phases.

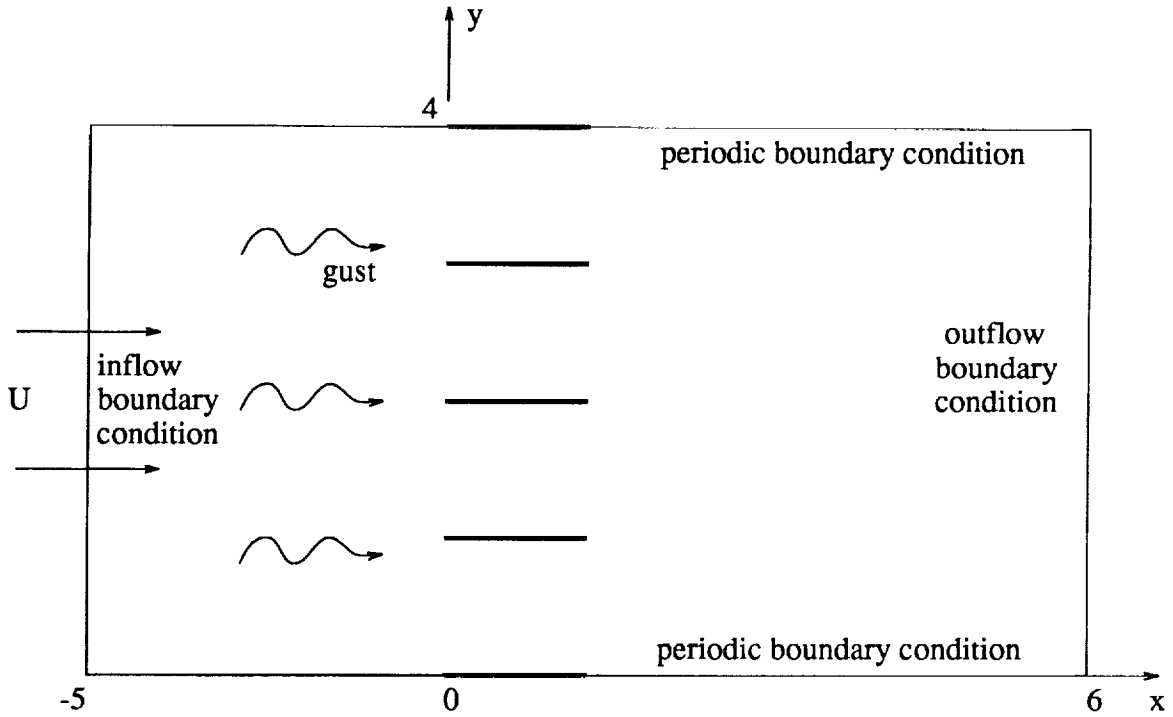


Figure 14. Computational domain for the turbomachinery noise problem.

4.1. Inflow Boundary Conditions

In the inflow boundary region, the disturbances consist of the prescribed incident gust,

$$u = - \left(\frac{v_g \beta}{\omega} \right) \cos(\omega x + \beta y - \omega t), \quad v = v_g \cos(\omega x + \beta y - \omega t) \quad (37)$$

and the outgoing acoustic waves of (35). It is easy to see that the desired inflow boundary conditions are very similar to the radiation boundary conditions in a ducted environment discussed in Section 3. Thus a set of radiation boundary condition for the inflow region can be derived accordingly. For example, let the computation domain in the y -direction be divided into $(M+1)$ intervals, the inflow boundary condition for the u -velocity component may be written as,

$$\begin{aligned} \frac{\partial u}{\partial t} = & -v_g \beta \sin(\omega t + \beta y - \omega t) \\ & + \left[\frac{\omega \alpha_0^-}{(\omega - \alpha_0^-)}, \frac{\omega \alpha_1^-}{(\omega - \alpha_1^-)} \cos\left(\frac{\pi y}{2}\right), \frac{\omega \alpha_2^-}{(\omega - \alpha_2^-)} \cos(\pi y), \frac{\omega \alpha_1^-}{(\omega - \alpha_1^-)} \sin\left(\frac{\pi y}{2}\right), \frac{\omega \alpha_2^-}{(\omega - \alpha_2^-)} \sin(\pi y) \right] \end{aligned} \quad (38)$$

$$\cdot (\mathbf{E}^T \mathbf{E})^{-1} \mathbf{E}^T \mathbf{d}$$

where \mathbf{E} is an $(M + 1) \times 5$ matrix and \mathbf{d} is a column vector of length $(M + 1)$

$$\mathbf{E} = \begin{bmatrix} -\frac{(\alpha_0^-)^2}{(\omega - \alpha_0^-)} & -\frac{(\alpha_1^-)^2}{(\omega - \alpha_1^-)} & -\frac{(\alpha_2^-)^2}{(\omega - \alpha_2^-)} & 0 & 0 \\ -\frac{(\alpha_0^-)^2}{(\omega - \alpha_0^-)} & -\frac{(\alpha_1^-)^2}{(\omega - \alpha_1^-)} \cos\left(\frac{\pi \Delta y}{2}\right) & -\frac{(\alpha_2^-)^2}{(\omega - \alpha_2^-)} \cos(\pi \Delta y) & -\frac{(\alpha_1^-)^2}{(\omega - \alpha_1^-)} \sin\left(\frac{\pi \Delta y}{2}\right) & -\frac{(\alpha_2^-)^2}{(\omega - \alpha_2^-)} \sin(\pi \Delta y) \\ \vdots & \vdots & \vdots & \vdots & \vdots \\ -\frac{(\alpha_0^-)^2}{(\omega - \alpha_0^-)} & -\frac{(\alpha_1^-)^2}{(\omega - \alpha_1^-)} \cos\left(\frac{M\pi \Delta y}{2}\right) & -\frac{(\alpha_2^-)^2}{(\omega - \alpha_2^-)} \cos(M\pi \Delta y) & -\frac{(\alpha_1^-)^2}{(\omega - \alpha_1^-)} \sin\left(\frac{M\pi \Delta y}{2}\right) & -\frac{(\alpha_2^-)^2}{(\omega - \alpha_2^-)} \sin(M\pi \Delta y) \end{bmatrix}$$

$$\mathbf{d} = \begin{bmatrix} \frac{\partial u}{\partial x}(x, 0, t) - v_g \beta \sin(\omega x - \omega t) \\ \frac{\partial u}{\partial x}(x, \Delta y, t) - v_g \beta \sin(\omega x + \beta \Delta y - \omega t) \\ \vdots \\ \frac{\partial u}{\partial x}(x, M\Delta y, t) - v_g \beta \sin(\omega x + \beta M\Delta y - \omega t) \end{bmatrix}$$

4.2. Outflow Boundary Conditions

In the outflow region, the outgoing disturbances consist of a linear superposition of the as yet unknown vorticity wave, equation (31), and the downstream propagating acoustic waves of (36). The presence of the unknown vorticity waves requires the outflow boundary conditions to be formulated slightly differently than the inflow boundary conditions. However, there is no pressure fluctuations associated with vorticity waves. Therefore, for p the outflow boundary condition can be derived as in the case of inflow boundary conditions. On proceeding as before, it is straightforward to find,

$$\frac{\partial p}{\partial t}(x, y, t) = \left[\omega, \omega \cos\left(\frac{\pi y}{2}\right), \omega \cos(\pi y), \omega \sin\left(\frac{\pi y}{2}\right), \omega \sin(\pi y) \right] (\mathbf{F}^T \mathbf{F})^{-1} \mathbf{F}^T \mathbf{p} \quad (39)$$

where \mathbf{F} is an $(M + 1) \times 5$ matrix and \mathbf{p} is a column vector of length $(M + 1)$.

$$\mathbf{F} = \begin{bmatrix} -\alpha_0^+ & -\alpha_1^+ & -\alpha_2^+ & 0 & 0 \\ -\alpha_0^+ & -\alpha_1^+ \cos\left(\frac{\pi \Delta y}{2}\right) & -\alpha_2^+ \cos(\pi \Delta y) & -\alpha_1^+ \sin\left(\frac{\pi \Delta y}{2}\right) & -\alpha_2^+ \sin(\pi \Delta y) \\ -\alpha_0^+ & -\alpha_1^+ \cos\left(\frac{2\pi \Delta y}{2}\right) & -\alpha_2^+ \cos(2\pi \Delta y) & -\alpha_1^+ \sin\left(\frac{2\pi \Delta y}{2}\right) & -\alpha_2^+ \sin(2\pi \Delta y) \\ \vdots & \vdots & \vdots & \vdots & \vdots \\ -\alpha_0^+ & -\alpha_1^+ \cos\left(\frac{M\pi \Delta y}{2}\right) & -\alpha_2^+ \cos(M\pi \Delta y) & -\alpha_1^+ \sin\left(\frac{M\pi \Delta y}{2}\right) & -\alpha_2^+ \sin(M\pi \Delta y) \end{bmatrix} \quad (40)$$

$$\mathbf{p} = \begin{bmatrix} \frac{\partial p}{\partial x}(x, 0, t) \\ \frac{\partial p}{\partial x}(x, \Delta y, t) \\ \vdots \\ \frac{\partial p}{\partial x}(x, M\Delta y, t) \end{bmatrix} \quad (41)$$

Also, in the course of deriving (39), the following relationship is established.

$$\mathbf{e} = \begin{bmatrix} C_0 \sin(\alpha_0^+ x - \omega t + \chi_0) \\ C_1 \sin(\alpha_1^+ x - \omega t + \chi_1) \\ C_2 \sin(\alpha_2^+ x - \omega t + \chi_2) \\ D_1 \sin(\alpha_1^+ x - \omega t + \lambda_1) \\ D_2 \sin(\alpha_2^+ x - \omega t + \lambda_2) \end{bmatrix} \quad (42)$$

$$\mathbf{e} = (\mathbf{F}^T \mathbf{F})^{-1} \mathbf{F}^{-1} \mathbf{p} \quad (43)$$

Now in the outflow region, the velocity component u of the outgoing disturbances is represented by,

$$\begin{aligned} u(x, y, t) &= \frac{\partial \phi}{\partial y}(x - t, y) \\ &+ \left[\frac{\alpha_0^+}{\omega - \alpha_0^+}, \frac{\alpha_1^+}{\omega - \alpha_1^+} \cos\left(\frac{\pi y}{2}\right), \frac{\alpha_2^+}{\omega - \alpha_2^+} \cos(\pi y), \frac{\alpha_1^+}{\omega - \alpha_1^+} \sin\left(\frac{\pi y}{2}\right), \frac{\alpha_2^+}{\omega - \alpha_2^+} \sin(\pi y) \right] \\ &\begin{bmatrix} C_0 \cos(\alpha_0^+ x - \omega t + \chi_0) \\ C_1 \cos(\alpha_1^+ x - \omega t + \chi_1) \\ C_2 \cos(\alpha_2^+ x - \omega t + \chi_2) \\ D_1 \cos(\alpha_1^+ x - \omega t + \lambda_1) \\ D_2 \cos(\alpha_2^+ x - \omega t + \lambda_2) \end{bmatrix} \end{aligned} \quad (44)$$

To eliminate the unknown function ϕ , we apply $(\frac{\partial}{\partial t} + \frac{\partial}{\partial x})$ to (44) and rewrite as,

$$\frac{\partial u}{\partial t}(x, y, t) = -\frac{\partial u}{\partial x}(x, y, t) + \left[\alpha_0^+, \alpha_1^+ \cos\left(\frac{\pi y}{2}\right), \alpha_2^+ \cos(\pi y), \alpha_1^+ \sin\left(\frac{\pi y}{2}\right), \alpha_2^+ \sin(\pi y) \right] \mathbf{e}. \quad (45)$$

The outflow boundary condition can be obtained by replacing \mathbf{e} in (45) by (43). Hence

$$\begin{aligned} \frac{\partial u}{\partial t}(x, y, t) &= -\frac{\partial u}{\partial x}(x, y, t) \\ &+ \left[\alpha_0^+, \alpha_1^+ \cos\left(\frac{\pi y}{2}\right), \alpha_2^+ \cos(\pi y), \alpha_1^+ \sin\left(\frac{\pi y}{2}\right), \alpha_2^+ \sin(\pi y) \right] \\ &(\mathbf{F}^T \mathbf{F})^{-1} \mathbf{F}^T \mathbf{p}. \end{aligned} \quad (46)$$

The v -velocity component in the outflow region is given by

$$\begin{aligned}
v = & -\frac{\partial\phi}{\partial x}(x-t, y) \\
& + \left[\frac{\frac{\pi}{2}}{(\alpha_1^+ - \omega)} \sin\left(\frac{\pi y}{2}\right), \frac{\frac{\pi}{2}}{(\alpha_2^+ - \omega)} \sin(\pi y), \frac{\frac{\pi}{2}}{(\alpha_1^+ - \omega)} \cos\left(\frac{\pi y}{2}\right), \frac{\frac{\pi}{2}}{(\alpha_2^+ - \omega)} \cos(\pi y) \right] \\
& \cdot \begin{bmatrix} C_1 \sin(\alpha_1^+ x - \omega t + \chi_1) \\ C_2 \sin(\alpha_2^+ x - \omega t + \chi_2) \\ D_1 \sin(\alpha_1^+ x - \omega t + \lambda_1) \\ D_2 \sin(\alpha_2^+ x - \omega t + \lambda_2) \end{bmatrix}.
\end{aligned} \tag{47}$$

Upon eliminating ϕ by applying $(\frac{\partial}{\partial t} + \frac{\partial}{\partial x})$ to (47) it is found,

$$\begin{aligned}
\frac{\partial v}{\partial t}(x, y, t) = & -\frac{\partial v}{\partial x}(x, y, t) + \left[\frac{\pi}{2} \sin\left(\frac{\pi y}{2}\right), \pi \sin(\pi y), \frac{\pi}{2} \cos\left(\frac{\pi y}{2}\right), \pi \cos(\pi y) \right] \\
& \cdot \begin{bmatrix} C_1 \cos(\alpha_1^+ x - \omega t + \chi_1) \\ C_2 \cos(\alpha_2^+ x - \omega t + \chi_2) \\ D_1 \cos(\alpha_1^+ x - \omega t + \lambda_1) \\ D_2 \cos(\alpha_2^+ x - \omega t + \lambda_2) \end{bmatrix}.
\end{aligned} \tag{48}$$

To determine the last column vector of (48), we may start by differentiating p of (36) with respect to y . This yields,

$$\frac{\partial p}{\partial y}(x, y, t) = \left[-\frac{\pi}{2} \sin\left(\frac{\pi y}{2}\right), -\pi \sin(\pi y), \frac{\pi}{2} \cos\left(\frac{\pi y}{2}\right), \pi \cos(\pi y) \right] \begin{bmatrix} C_1 \cos(\alpha_1^+ x - \omega t + \chi_1) \\ C_2 \cos(\alpha_2^+ x - \omega t + \chi_2) \\ D_1 \cos(\alpha_1^+ x - \omega t + \lambda_1) \\ D_2 \cos(\alpha_2^+ x - \omega t + \lambda_2) \end{bmatrix}. \tag{49}$$

The unknown column vector can now be evaluated as an overdetermined system by enforcing (49) at $y = m\Delta y$, $m = 0, 1, 2, \dots, M$. Once this vector is found in terms of a column vector of $\frac{\partial p}{\partial y}$, it is inserted into (48) to provide the desired outflow boundary condition for v .

4.3. Numerical Results

We carried out numerical computation for the case $\omega = \frac{5\pi}{2}$ using two size meshes with $\Delta x = \Delta y = \frac{1}{20}$ and $\frac{1}{30}$. The distribution of inverse mesh Reynolds number associated with the artificial selective damping is shown in figure 15. A $R_{\Delta x}^{-1} = 0.05$ is used for general background damping. Extra damping is added near the flat plate. A Gaussian distribution of inverse mesh

Reynolds number with a maximum equal to 1.5 at the surfaces of the plate and a half-width of 3 mesh points is used.

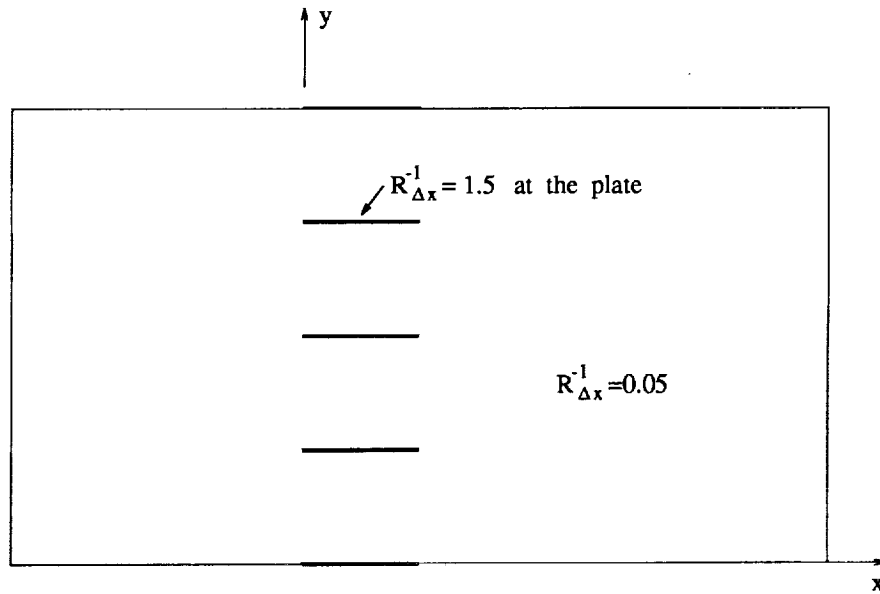


Figure 15. Distribution of inverse mesh Reynolds number used in the numerical solution of Category 3, Benchmark problem 2.

The computation starts with zero initial conditions and marches in time until a time periodic solution is reached. Figure 16 shows the zero pressure contour at the beginning of a cycle. As can be seen, there is very little difference between using the coarse or the fine mesh. Thus mesh size convergence is assured.

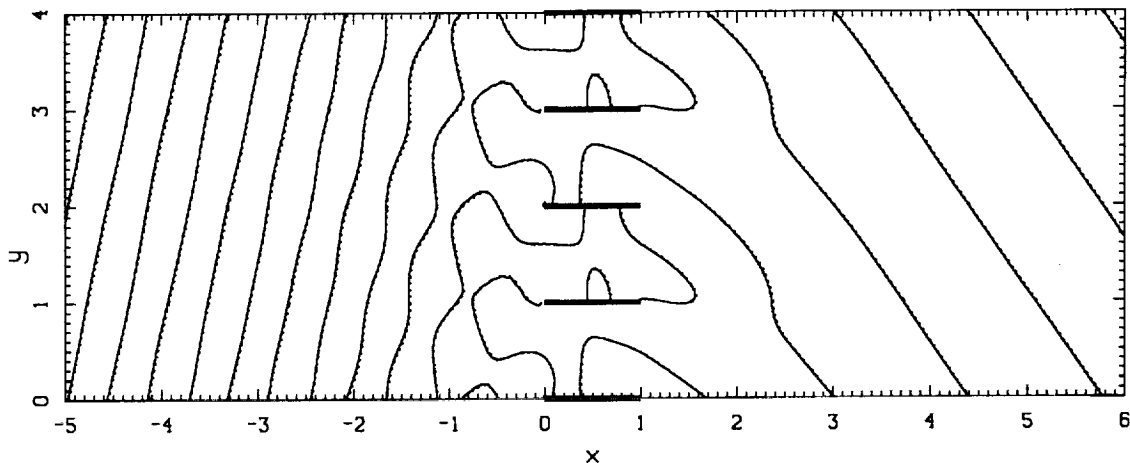


Figure 16. Zero pressure contour map at the beginning of a cycle.

- solution using $20\Delta x$ per plate length,
- solution using $30\Delta x$ per plate length.

Figure 17 shows the calculated pressure distribution along the lines $y = 0, 1, 2$ and 3 at the beginning of a cycle. The full line indicates the pressure on the bottom side of a flat plate and the dotted line gives the pressure on the top side of the plate. The pressure loading on the plate at the beginning of a cycle is shown in figure 18. There is good agreement between the results computed using $\Delta x = \frac{1}{20}$ and $\frac{1}{30}$ except near the leading edge singularity. Figures 19 and 20 give the root mean square pressure distributions along $x = -2$ and $x = 3$, respectively. Again, the computed results using the coarse and the fine resolution are essentially the same. Judging by the above results. We believe that the inflow and outflow boundary conditions have performed remarkably well.

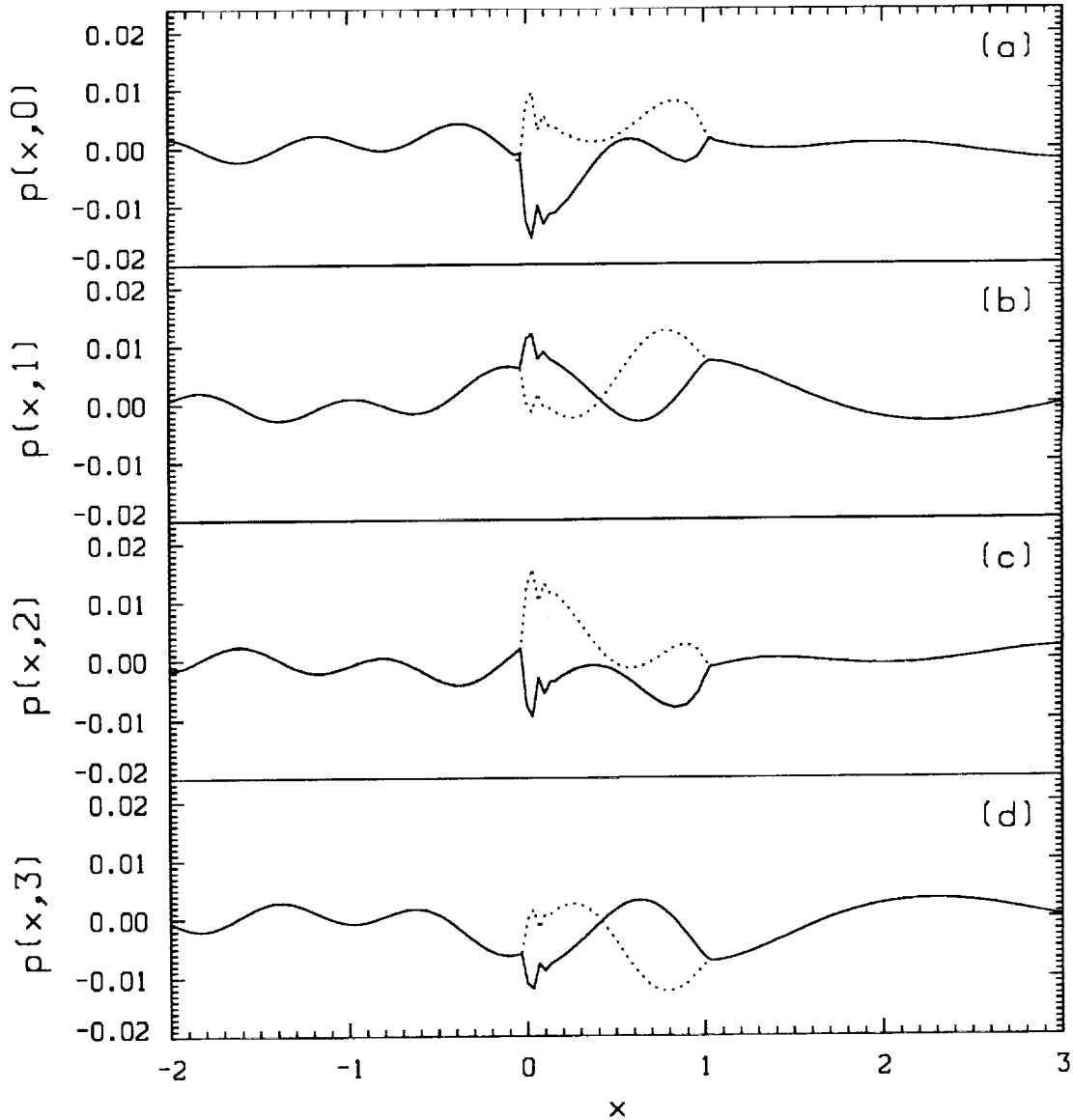


Figure 17. Pressure distribution at the beginning of a cycle of oscillation along: (a) $y=0$, (b) $y=1$, (c) $y=2$, (d) $y=3$. ————— pressure along the bottom side of a plate, pressure along the top side of a plate.

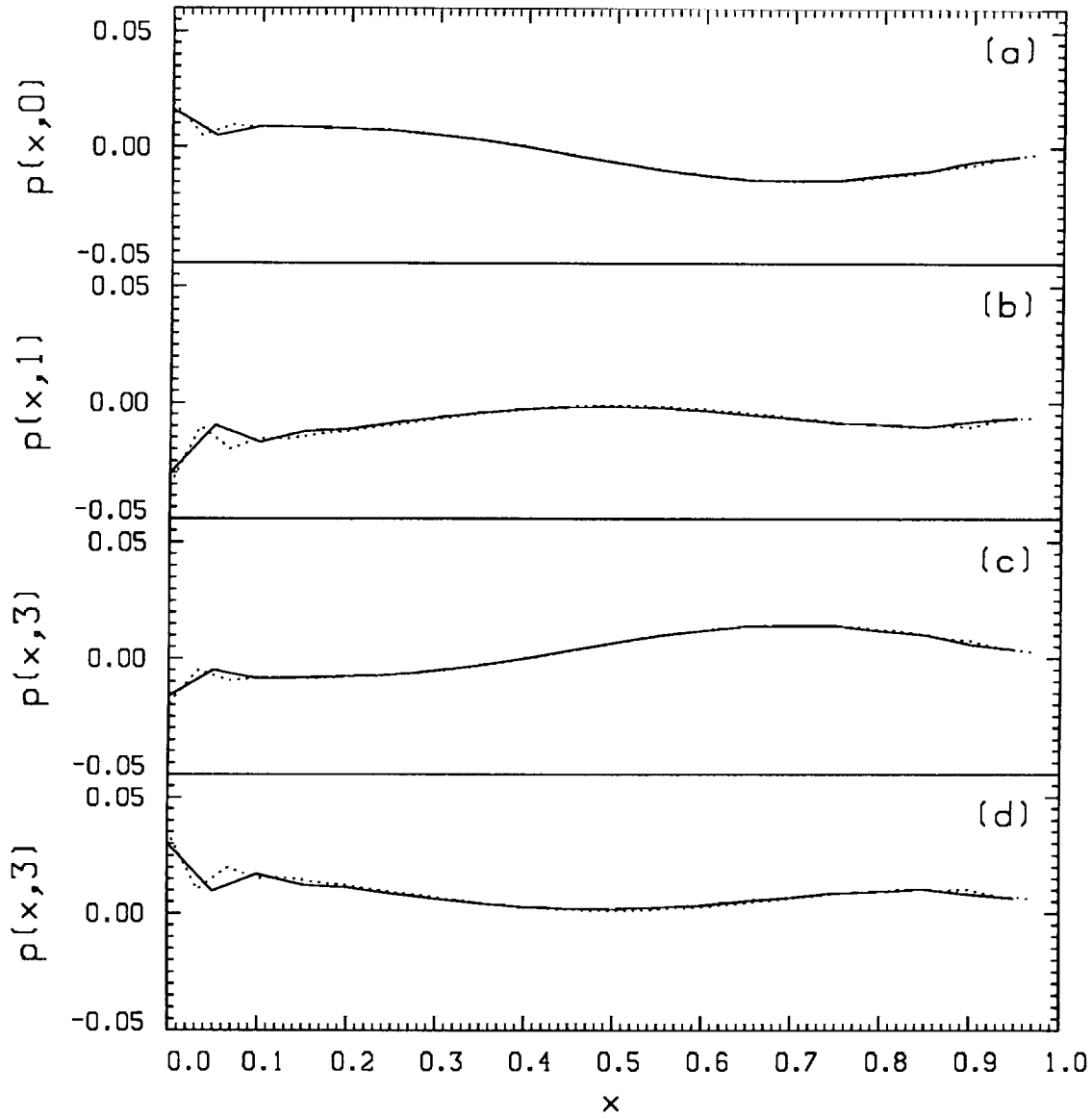


Figure 18. Distribution of $\Delta p = p_{bottom} - p_{top}$ across the flat plates at the beginning of a cycle of oscillation. (a) $y=0$, (b) $y=1$, (c) $y=2$, (d) $y=3$. — solution using $20\Delta x$ per plate length, solution using $30\Delta x$ per plate length.

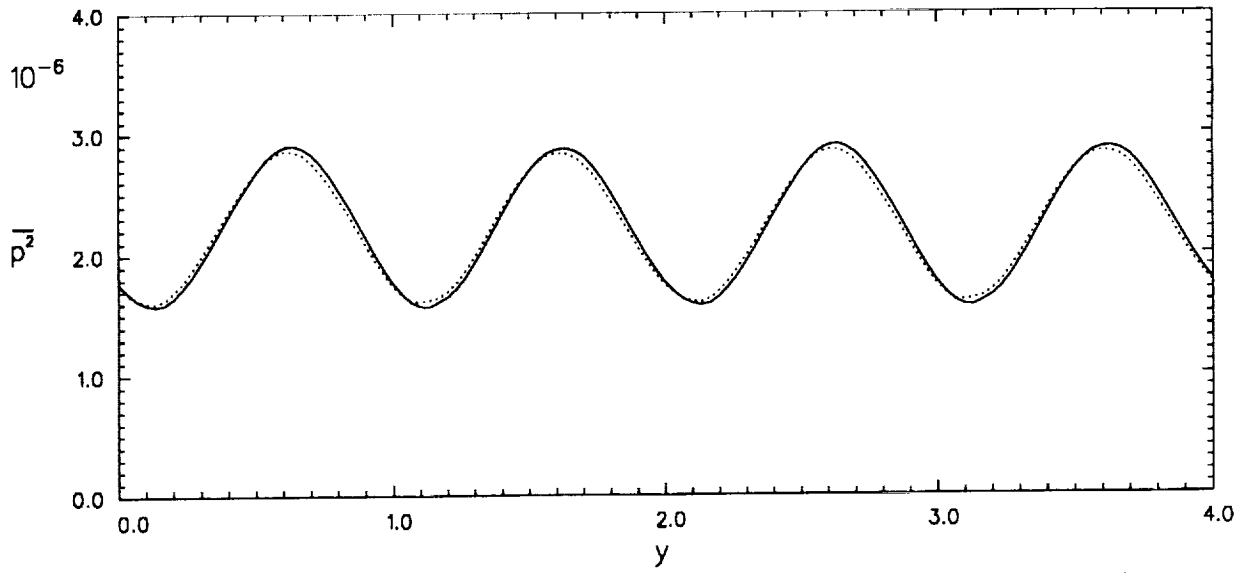


Figure 19. Intensity of radiated sound, \bar{p}^2 , along $x = -2$.
 — solution using $20\Delta x$ per plate length,
 solution using $30\Delta x$ per plate length.

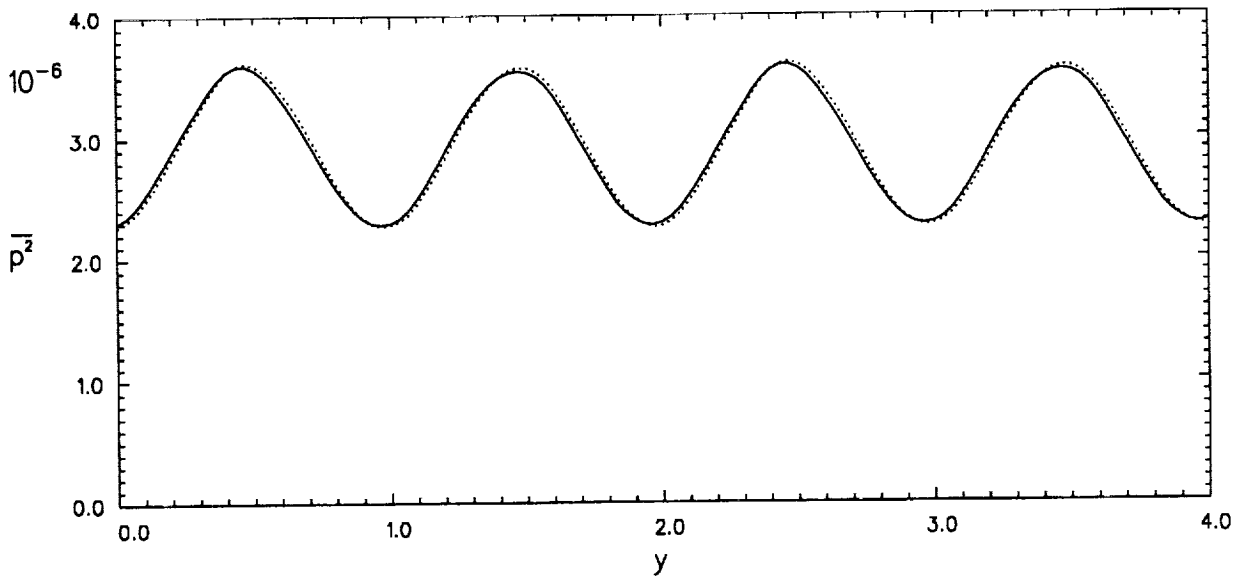


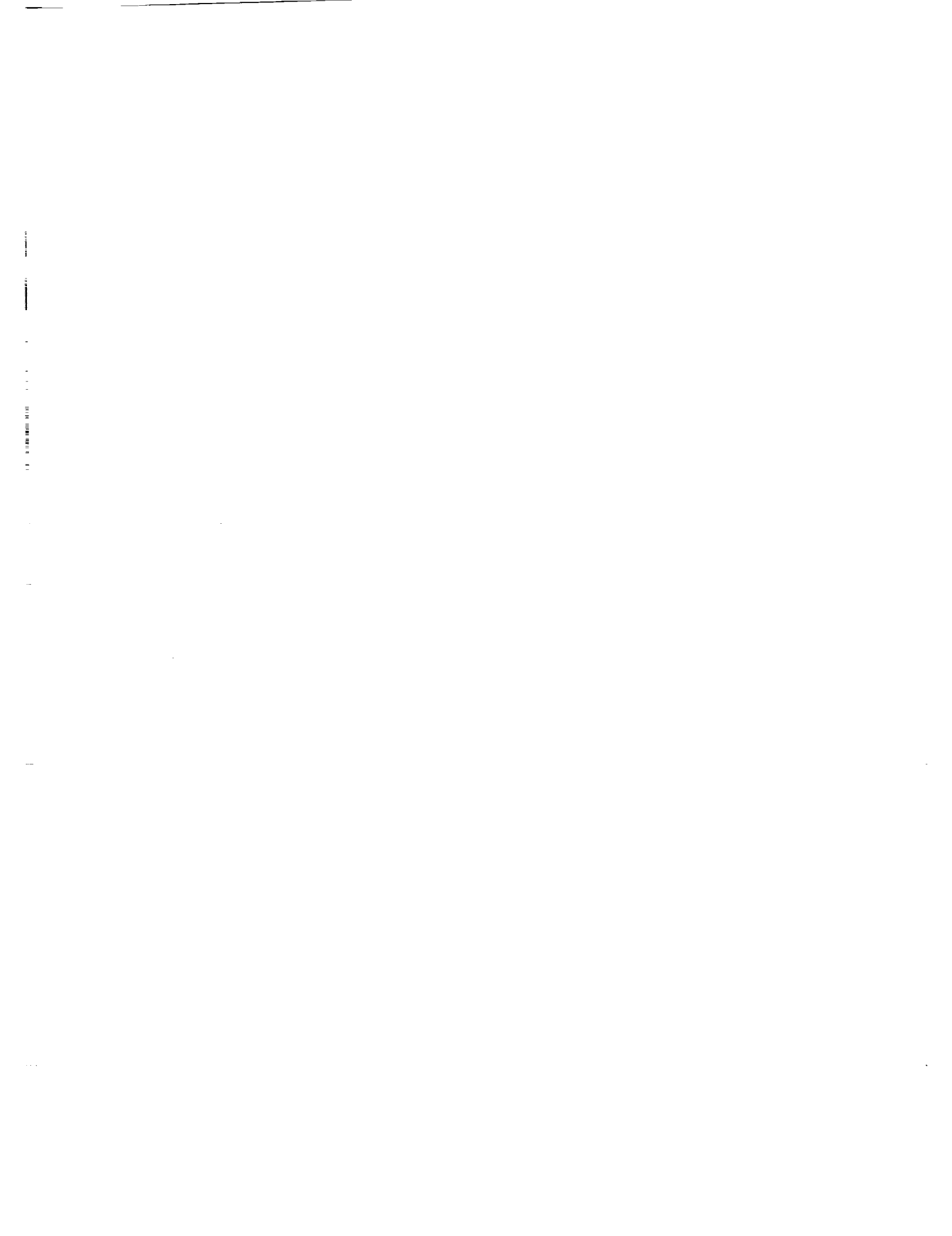
Figure 20. Intensity of radiated sound, \bar{p}^2 , along $x = 3$.
 — solution using $20\Delta x$ per plate length,
 solution using $30\Delta x$ per plate length.

ACKNOWLEDGMENT

This work was supported by the NASA Langley Research Center Grant NAG 1-1776.

REFERENCES

1. Tam, C.K.W.; and Webb, J.C.: Dispersion-Relation-Preserving Finite Difference Schemes for Computational Acoustics. *J. Comput. Phys.*, vol. 107, Aug. 1993, pp. 262-281.
2. Tam, C.K.W.; and Shen, H.: Direct Computation of Nonlinear Acoustic Pulses Using High-Order Finite Difference Schemes. AIAA-93-4325, Oct. 1993.
3. Von Neumann, J.; and Richtmyer, R.D.: A Method for the Numerical Calculation of Hydrodynamic Shocks. *J. Appl. Phys.*, vol 21, Mar. 1950, pp. 232-237.
4. Jameson, A.; Schmidt, W.; and Turkel, F.: Numerical Solutions of the Euler Equations by Finite Volume Methods Using Runge-Kutta Time Stepping Schemes. AIAA-81-1259, June 1981.
5. Tam, C.K.W.; Webb, J.C.; and Dong, Z.: A Study of the Short Wave Components in Computational Acoustics. *J. Comput. Acoustics*, vol. 1, Mar. 1993, pp. 1-30.
6. Tam, C.K.W.: Computation Aeroacoustics: Issues and Methods. *AIAA J.*, vol. 33, Oct. 1995, pp. 1788-1796.
7. Bayliss, A.; and Turkel, E.: Radiation Boundary Conditions for Wave-Like Equations. *Commun. Pure and Appl. Math.*, vol. 33, Nov. 1980, pp. 707-725.
8. Kurbatskii, K.A.; and Tam, C.K.W.: Cartesian Boundary Treatment of Curved Walls for High-Order Computational Aeroacoustics Schemes. *AIAA J.*, vol. 35, Jan. 1997, pp. 133-140.
9. Tam, C.K.W.; and Dong, Z.: Wall Boundary Conditions for High-Order Finite-Difference Schemes in Computational Aeroacoustics. *Theoret. Comput. Fluid Dynamics*, vol. 6, Oct. 1994, pp. 303-322..
10. Tam, C.K.W.; Shen, H.; Kurbatskii, K.A.; Auriault, L.; Dong, Z.; and Webb, J.C.: Solutions to the Benchmark Problems by the Dispersion-Relation-Preserving Scheme. ICASE/LaRC Workshop on Benchmark Problems in Computational Aeroacoustics. NASA CP 3300, May, 1995, pp. 149-171.
11. Hager, W.W.: Applied Numerical Linear Algebra. 1988, Prentice Hall.



519-71

043477

294003 p/0

TESTING A LINEAR PROPAGATION MODULE ON SOME ACOUSTIC SCATTERING PROBLEMS

G.S. Djambazov, C.-H. Lai, K.A. Pericleous

School of Computing and Mathematical Sciences, University of Greenwich
Wellington Street, Woolwich, London SE18 6PF, UK

ABSTRACT

Finite volume discretization of the Linearized Euler Equations on a fully staggered computational grid results in an efficient semi-implicit numerical scheme which can be used in the 'near field' of aerodynamic noise problems.

INTRODUCTION

Since sound is a form of fluid motion, when solving aeroacoustic problems it is desirable to use existing Computational Fluid Dynamics (CFD) codes as much as possible. They can simulate any flow field but, due to numerical diffusion, they tend to smear the noise signal close to its source. That is why they have to be combined with some other method to produce accurate acoustic results. Traditionally the Acoustic Analogy [1] has been used as a complementary technique [2, 3]. The alternative Computational Aeroacoustics (CAA) approach provides additional flexibility and simplicity when handling complex and/or moving geometries.

To reduce the computational cost Domain Decomposition methods are used to define the 'near field' containing the noise generation region with nonlinear acoustic effects and the 'far field' of linear sound propagation [4, 2]. Special high accuracy CAA methods [5] or Kirchhoff's surface integral method [6] can be used in the far field.

In the near field commercial CFD codes cannot do the aeroacoustic simulation alone because of the highly diffusive nature of the CFD algorithms. This 'near field' has to be large enough to contain *all* the nonlinearities of the sound field, and no CFD code can carry the acoustic signal that far. This problem has been addressed at the University of

Greenwich [7] by creating an acoustic software module which can be combined with a CFD code to solve aerodynamic noise problems. The code can also be used on its own in smaller domains of linear propagation or it can be combined with some structural acoustics software for internal noise problems.

The code has been applied to the first two problems in "Category 1 - Acoustic Scattering" of the Second CAA Workshop on Benchmark Problems. The method and results are described below.

METHOD

With the popular approach of splitting the flow variables into mean-flow and perturbation parts [8, 9] the Linearized Euler Equations are obtained to describe the sound field. If the mean flow is uniform, or if there is no mean flow at all, the relative form of these equations can be used, and in two dimensions they can be written as:

$$\frac{\partial p}{\partial t} + c \left(\frac{\partial u}{\partial x} + \frac{\partial v}{\partial y} \right) = q$$

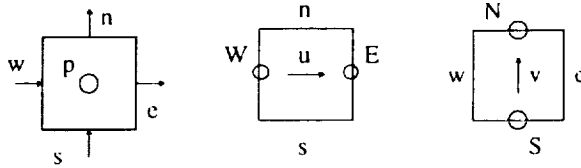
$$\frac{\partial u}{\partial t} + c \frac{\partial p}{\partial x} = f_x, \quad u = \rho_0 c v_x \quad (1)$$

$$\frac{\partial v}{\partial t} + c \frac{\partial p}{\partial y} = f_y, \quad v = \rho_0 c v_y$$

$$\frac{\partial p}{\partial \rho} = c^2 = \gamma \frac{p_0}{\rho_0}, \quad \gamma_{air} = 1.4 \quad (2)$$

Perturbation velocity components along the axes x and y are denoted v_x and v_y respectively, c is the speed of sound, ρ_0 is the density of undisturbed air, p_0 is the atmospheric pressure, and p is the pressure perturbation. The right-hand sides q, f_x, f_y are considered known functions of x, y and time t .

When discretizing the three unknown functions p, u and v , a fully staggered (along both space and time) grid has been chosen. This is done because it allows (as shown below) a fully explicit, stable, second-order accurate scheme to be formulated. Its accuracy can then be extended to third order by allowing the scheme to become implicit while retaining a strong diagonal dominance that guarantees fast convergence.



Using this cell-centered regular Cartesian mesh and the notation pictured above, a finite-volume set of equations has been obtained by successive integration of (1) along each of the axes x, y and t :

$$\begin{aligned}
 & \int_{cell} (p - p_{old}) dx dy + \\
 + c & \left[\int_{old}^{new} dt \int_s^n (u_e - u_w) dy + \int_{old}^{new} dt \int_w^e (v_n - v_s) dx \right] = \int_{old}^{new} dt \int_{cell} q dx dy \quad (3) \\
 & \int_{cell} (u - u_{old}) dx dy + c \int_{oldM}^{newM} dt \int_s^n (p_E - p_W) dy = \int_{oldM}^{newM} dt \int_{cell} f_x dx dy \\
 & \int_{cell} (v - v_{old}) dx dy + c \int_{oldM}^{newM} dt \int_w^e (p_N - p_S) dx = \int_{oldM}^{newM} dt \int_{cell} f_y dx dy
 \end{aligned}$$

The solved-for values of pressure are stored in the cell centers (with upper case indexes), while velocity components are stored on cell faces (lower case indexes) in the *middle* of each time step ($t_{oldM} = t_{old} + \Delta t/2$, $t_{newM} = t_{new} + \Delta t/2$). The storage locations are shown in Figure 1.

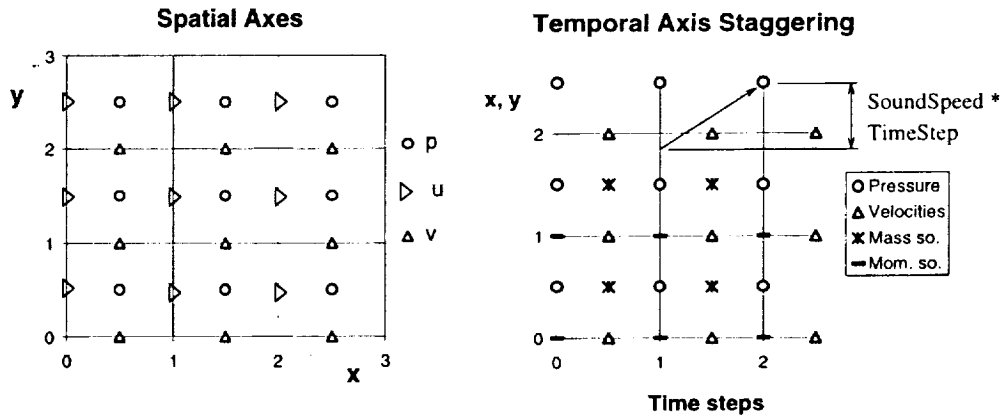


Figure 1: Computational grid and radiating boundary interpolation

The integrals in (3) are first evaluated through mean values providing an easy-to-program, second-order accurate, **fully explicit numerical scheme**:

$$\begin{aligned}
 p &= p_{old} - \sigma_x(u_e - u_w) - \sigma_y(v_n - v_s) + q\Delta t \\
 u &= u_{old} - \sigma_x(p_E - p_W) + f_x\Delta t \\
 v &= v_{old} - \sigma_y(p_N - p_S) + f_y\Delta t \\
 \sigma_x &= \frac{c\Delta t}{\Delta x}, \quad \sigma_y = \frac{c\Delta t}{\Delta y}
 \end{aligned} \tag{4}$$

This scheme is accurate enough within about 5 wavelengths, accumulating not more than 8 % error, and it can be used on its own in small domains, e. g. with internal noise problems.

A second-order approximation of all the functions in all the integrals in (3) can be employed to extend the accuracy of the method. Instead of $I(x_0, h) = hf(x_0)$ now we have

$$\begin{aligned}
 I(x_0, h) &= \int_{x_0 - \frac{h}{2}}^{x_0 + \frac{h}{2}} f(x)dx = \\
 &= h[Af(x_0 - h) + (1 - 2A)f(x_0) + Af(x_0 + h)], \\
 A &= \frac{1}{24}
 \end{aligned} \tag{5}$$

applied to all integrals. In 2D this means

$$\int_{cell} f(x, y)dx dy = \left[A \sum_{nb} f_{nb} + (1 - 4A)f_{cell} \right] \Delta x \Delta y \tag{6}$$

with 'nb' used to denote all four neighboring cells.

This **semi-implicit scheme** proved to be accurate enough to take the sound generated out of the 'near field'. The resulting linear system is solved iteratively at each time step starting with a very good initial guess computed using the explicit scheme (4). Only one level of neighboring cells are involved, and not second or further neighbors. The boundary cells are processed with the explicit scheme only. With the discretization of those integrals containing time as one of the arguments, 'future' and 'past'

neighbors are involved. Both of them are determined at each iterative step by the fully explicit scheme. Stored 'past' values at the cell faces cannot be used because of the Courant limit when the time step is adjusted to whole cells.

The algorithm described above has been tested with one-dimensional plane wave propagation showing maximum error of about 5 percent of the amplitude over about 100 wavelengths in 2000 time steps.

Acoustic radiation **boundary conditions** are implemented assuming *plane wave* propagation in the boundary region: velocity components at the boundary faces are computed from the velocity field at the previous step by interpolation at the appropriate points inside the domain (see Figure 1). The direction of radiation has to be prescribed for each boundary cell. Then the interpolation point inside the domain can be determined based on the distance the wave covers in one time step.

Solid boundaries are represented in a stepwise manner as shown in Figure 2. The corresponding velocity components perpendicular to the boundary cell faces are set to zero.

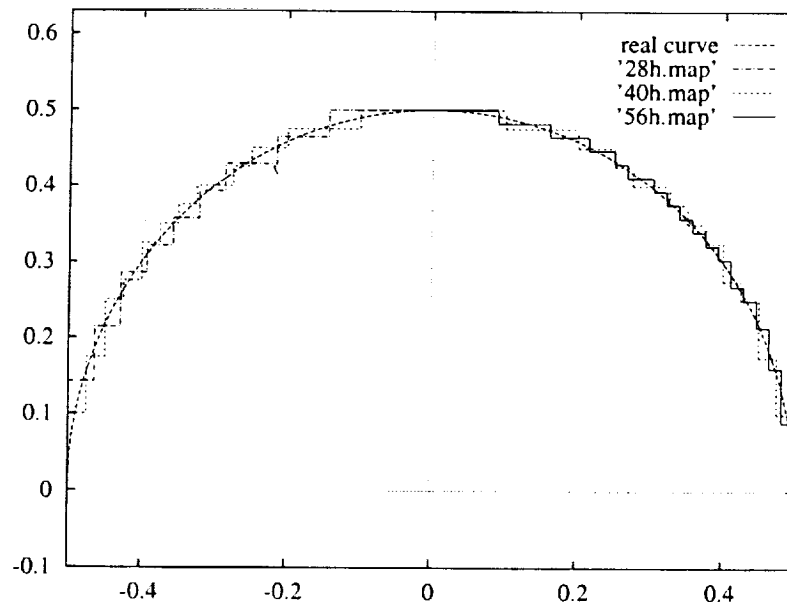


Figure 2: Solid boundary and mesh refinement

RESULTS

Benchmark **Problem 1** in **Category 1** has been attempted using a regular Cartesian grid of 800×100 cells over a domain of approx. 14×7 units (Fig. 3). The cell size is 0.01786, and the time step is 0.0125 units. The cylinder is represented by a stepwise boundary mapped onto 56×28 cells. Symmetry (no flux) boundary conditions have been imposed on the bottom boundary of the domain. Averaging along two semi-circles with radii respectively 5 and 7 units produced oscillating values which differ considerably in some regions. Both sets of data have been submitted for comparison.

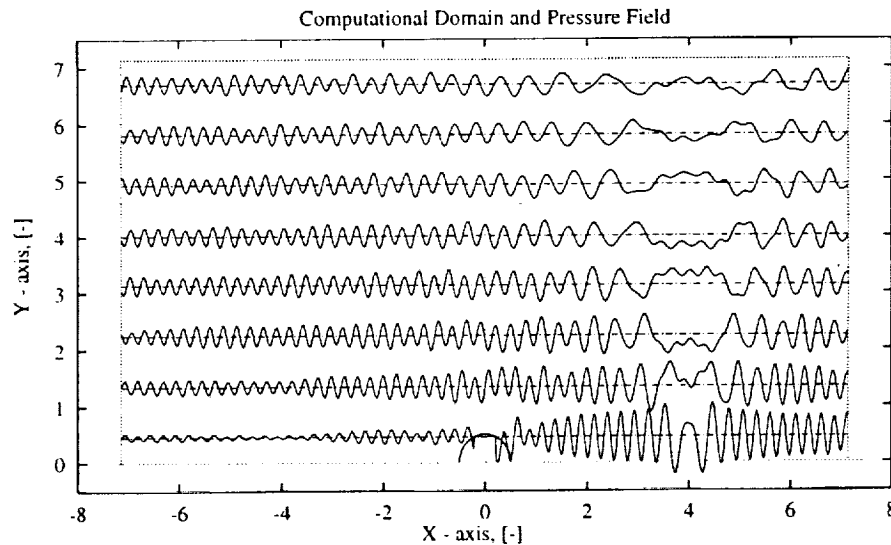


Figure 3: Sound pressure amplitude scaled to fit the plot area

The outer ($r = 7$) averaging locations are shown in Figure 4, and a comparison between the results for the two close semi-circles (r_1 being the outer one) are presented in Figure 5. The greater oscillations in the graphs are due to the standing wave pattern that develops around the cylinder (because the diameter and the distance to the source are proportional to the wavelength). There can be two reasons for the minor oscillations and for the difference between the two graphs: some numerical inaccuracy and/or coordinate truncation when cell centers have been picked as averaging locations instead of the exact points on the circles.

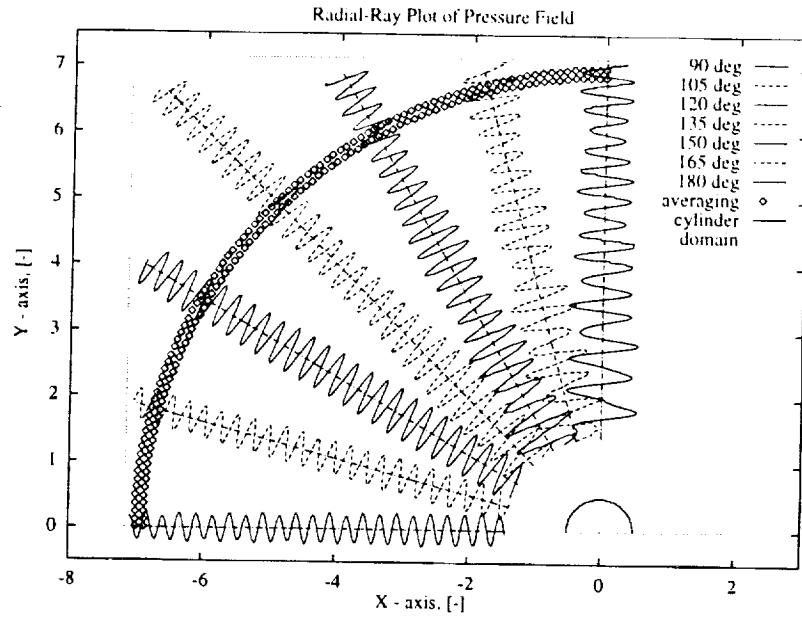


Figure 4: Instantaneous pressure and averaging locations

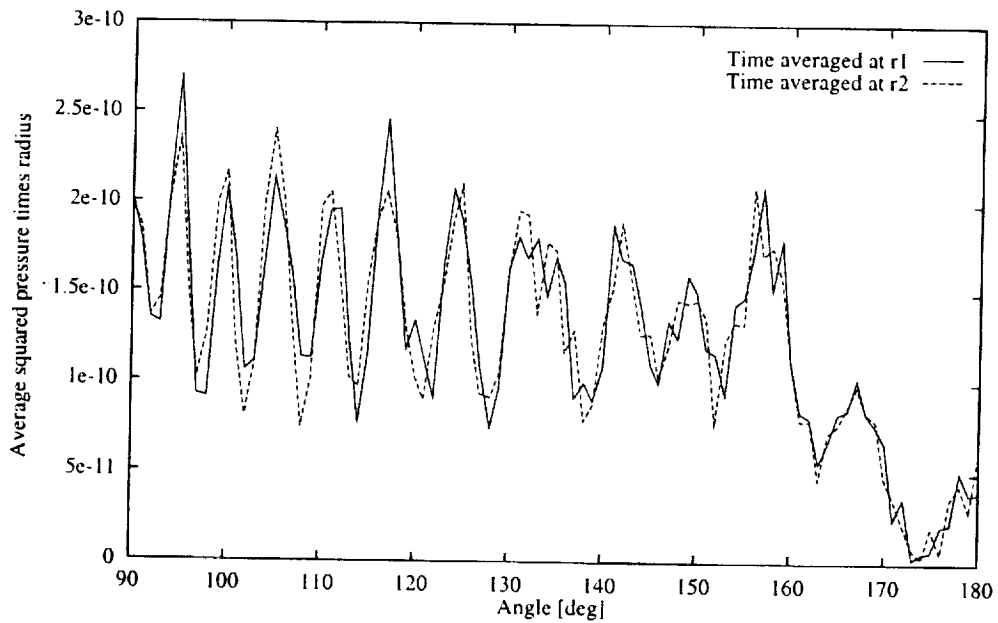


Figure 5: Problem 1: Results

Benchmark **Problem 2** in **Category 1**, has been solved with the same grid spacing ($h = D/56$), time step and solid boundary mapping as Problem 1 in a domain of 600×300 cells - just enough to contain the target semi-circle with radius 5. These results (in solid lines on Figure 6) have been submitted to the workshop. Later computations on coarser meshes

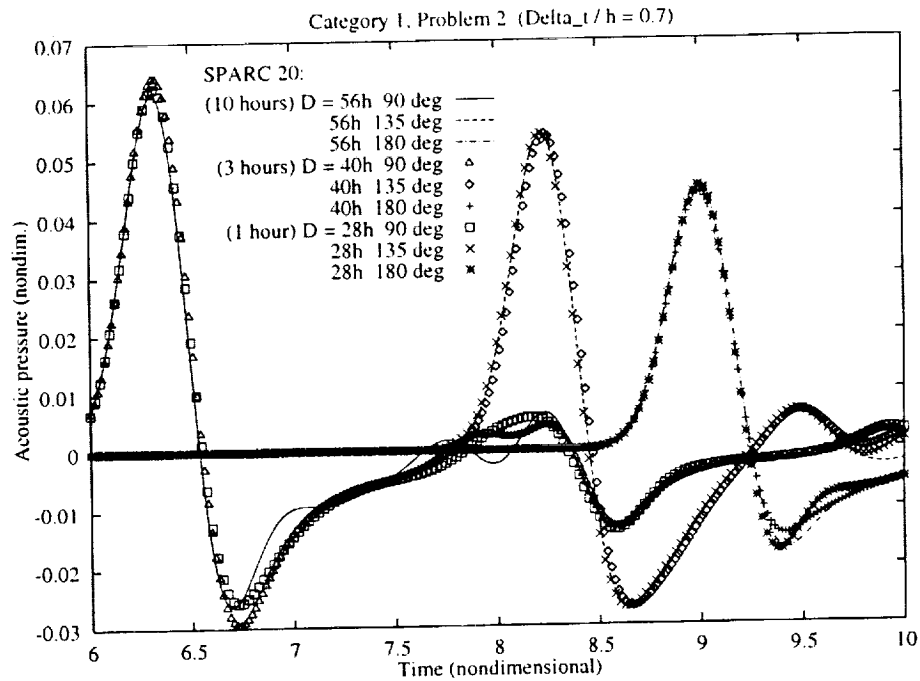


Figure 6: Mesh refinement results

($h = D/40$ and $h = D/28$) were carried out for comparison. In all three cases the mesh is fine enough to resolve the pressure pulse but the stepwise discretization of the cylinder is different (see Fig. 2). At the workshop it has turned out that the finer-mesh results are wrong, and the organizers have shown how to determine the optimal grid spacing.

CONCLUSIONS

The finite volume discretization of the linearized Euler equations presented here is accurate enough to handle the 'near field' of aerodynamic noise problems. Mesh refinement to fit curved boundaries has to be done most carefully as false oscillations may occur.

Future work involves the inclusion of the convection and *nonlinear* terms from the Navier-Stokes Equations to produce a code capable of simulating the generation of aerodynamic noise.

References

- [1] Lighthill, M.J., 1952. "On sound generated aerodynamically. Part I: General theory", *Proc. Roy. Soc. A*, Vol. 211, pp. 564-587.
- [2] Sankar, S. and Hussaini, M.Y., 1993, "A hybrid direct numerical simulation of sound radiated from isotropic turbulence". *ASME FED* Vol. 147, pp. 83-89.
- [3] Zhang, X., Rona, A., Lilley, G.M., "Far-field noise radiation from an unsteady supersonic cavity flow", *CEAS/AIAA Paper* 95-040.
- [4] Shih, S.H., Hixon, D.R. and Mankbadi, R.R., 1995, "A zonal approach for prediction of jet noise", *CEAS/AIAA Paper* 95-144.
- [5] Tam, K. W. and J. C. Webb, 1993, "Dispersion-relation-preserving finite difference schemes for computational aeroacoustics", *J. Comp. Phys.*, Vol. 107, pp. 262-281.
- [6] Lyrantzis, A.S., 1993, "The use of Kirchhoff's method in computational aeroacoustics", *ASME FED* Vol. 147, pp. 53-61.
- [7] Djambazov, G.S., Lai, C.-H., Pericleous, K.A., 1996, "Development of a domain decomposition method for computational aeroacoustics", *Proc. of the 9-th Conf. on Domain Decomposition*, Bergen, Norway, June 1996, Editor P.Bjorstad, M.Espedal and D.Keyes.
- [8] Viswanathan, K. and Sankar, L.N., 1995, "Numerical simulation of airfoil noise", *ASME FED*, Vol. 219, pp. 65-70.
- [9] Hardin, J., Invited Lecture given at the *ASME Forum on Computational Aeroacoustics and Hydroacoustics*, June 1993.

1
2
3
4
5
6
7
8
9
10
11
12
13
14
15
16
17
18
19
20
21
22
23
24
25
26
27
28
29
30
31
32
33
34
35
36
37
38
39
40
41
42
43
44
45
46
47
48
49
50
51
52
53
54
55
56
57
58
59
60
61
62
63
64
65
66
67
68
69
70
71
72
73
74
75
76
77
78
79
80
81
82
83
84
85
86
87
88
89
90
91
92
93
94
95
96
97
98
99
100

1
2
3
4
5
6
7
8
9
10
11
12
13
14
15
16
17
18
19
20
21
22
23
24
25
26
27
28
29
30
31
32
33
34
35
36
37
38
39
40
41
42
43
44
45
46
47
48
49
50
51
52
53
54
55
56
57
58
59
60
61
62
63
64
65
66
67
68
69
70
71
72
73
74
75
76
77
78
79
80
81
82
83
84
85
86
87
88
89
90
91
92
93
94
95
96
97
98
99
100

1
2
3
4
5
6
7
8
9
10
11
12
13
14
15
16
17
18
19
20
21
22
23
24
25
26
27
28
29
30
31
32
33
34
35
36
37
38
39
40
41
42
43
44
45
46
47
48
49
50
51
52
53
54
55
56
57
58
59
60
61
62
63
64
65
66
67
68
69
70
71
72
73
74
75
76
77
78
79
80
81
82
83
84
85
86
87
88
89
90
91
92
93
94
95
96
97
98
99
100

1
2
3
4
5
6
7
8
9
10
11
12
13
14
15
16
17
18
19
20
21
22
23
24
25
26
27
28
29
30
31
32
33
34
35
36
37
38
39
40
41
42
43
44
45
46
47
48
49
50
51
52
53
54
55
56
57
58
59
60
61
62
63
64
65
66
67
68
69
70
71
72
73
74
75
76
77
78
79
80
81
82
83
84
85
86
87
88
89
90
91
92
93
94
95
96
97
98
99
100

520-71-

043478

294005 p/10

SOLUTION OF AEROACOUSTIC PROBLEMS BY A NONLINEAR, HYBRID METHOD*

Yusuf Özyörük[†] and Lyle N. Long[‡]
Department of Aerospace Engineering
The Pennsylvania State University
University Park, PA 16802

ABSTRACT

Category 1, problem 3 (scattering of sound by a sphere) and category 2, problem 1 (spherical source in a cylindrical duct subject to uniform flow) are solved in generalized coordinates using the nonlinear Euler equations together with nonreflecting boundary conditions. A temporally and spatially fourth-order accurate finite-difference, Runge-Kutta time-marching technique is employed for the near-field calculations and a Kirchhoff method is employed for the prediction of far-field sound. Computations are all performed on parallel processors using the data-parallel paradigm.

INTRODUCTION

Past several years have witnessed a significant activity [1] to develop computational tools for aeroacoustic applications. This has been so because of the increasing availability of powerful computers to the computational sciences community as well as the continuous need for further understanding of the physics of flow associated noise and its accurate prediction for quiet engineering designs. This activity ranged from the development of high level algorithms [2, 3] to high level applications [4, 5, 6]. Recently, the present authors have developed a nonlinear, fourth-order accurate (both in space and time), hybrid, parallel code [4, 7, 8] for the prediction of ducted fan noise. This code solves the full Euler equations in the near field and uses a Kirchhoff method for the prediction of far-field sound. This code has been shown to be able to make accurate predictions. It is the purpose of this paper to describe the application of this code to the solutions of the benchmark problems of the Second Computational Aeroacoustics (CAA) Workshop. Particularly, problem 3 of category 1, and problem 1 of category 2 are solved. It is shown here that even relatively simple problems, such as these, could be computationally intense and demanding if the far-field sound is of interest. Therefore, far-field extrapolation techniques, such as the Kirchhoff method, must be used for feasible solutions.

*Work sponsored by NASA grant NAG-1-1367

[†]Postdoctoral Scholar

[‡]Associate Professor

NONLINEAR, HYBRID CODE

The hybrid ducted fan noise radiation code [7, 4] solves the 3-D Euler equations on a 3-D body-fitted coordinate system and passes the near-field acoustic pressure to a Kirchhoff method based on the formulation of Farassat and Myers [9] to predict the far-field sound. The governing equations are solved in a relatively small domain using nonreflecting boundary conditions based on the works of Bayliss and Turkel [10] and Tam and Webb [2]. For realistic engine inlet geometries an orthogonal mesh system is created through a sequence of conformal mappings [11] and the governing equations are formulated in cylindrical coordinates to effectively treat the grid singularity at the centerline. Fourth-order accurate, cell-centered finite differencing and four-stage, noncompact R-K time integration are performed to advance the solution. Adaptive artificial dissipation [12] is used to suppress high-frequency spurious waves. The Euler solver and the Kirchhoff method are coupled such that as soon as the Euler solution becomes available, the Kirchhoff surface integrations are performed in a forward-time-binning manner to predict the far-field noise. All calculations are carried out on parallel computers using the data parallel paradigm. Ref. [7] describes the fourth-order flow solver with emphasis on the hybrid code's parallel aspects. Ref. [4] discusses the acoustic source model and the Kirchhoff coupling issues for engine inlet noise predictions. The hybrid code utilizes a spatially fourth-order accurate multigrid procedure for efficient calculations of the mean flow and this procedure is described in Ref. [8].

The boundary conditions routines of this code have been modified to accommodate the present workshop problems. Also, the Kirchhoff routine of this code has been improved for time-periodic problems. In such cases, after the transients are gone, the near-field Euler solution is obtained only for one time period and this solution is replicated in the Kirchhoff routine for longer time periods so that the forward-time-binning procedure [4] can be completed for a converged far-field solution. This approach results in significant CPU time savings.

RESULTS AND DISCUSSION

Solution of Category 1, Problem 3

This problem requires the solution of the acoustic field driven by a spherical (Gaussian) source plus its scattered field from a sphere. The source and sphere centers are separated from each other by a distance of one sphere diameter. Since this problem is axisymmetric, it is solved on a polar mesh in a constant θ plane (i.e. $x-r$ plane, (x, r, θ) denote cylindrical coordinates) with an (x, r) -to- (ξ, η) coordinate transformation. This mesh is constructed such that there exist 384 grid points along the half-sphere wall (ξ) and 256 grid points in the normal direction to the sphere wall (η). The physical size of the computational domain is taken to be about 6 sphere radii so that a direct Euler solution on a 5-radius circular arc on the mesh could be obtained and compared with the Kirchhoff solution. The Kirchhoff surface is chosen to be at about 3 radii, where the source strength is diminished. This mesh has approximately 18 grid points per wavelength in both curvilinear coordinate directions in the vicinity of the Kirchhoff surface so that the acoustic waves are well resolved on the Kirchhoff surface.

Figure 1 shows a snapshot of the acoustic pressure contours in the domain for a nondimensional

circular frequency of 4π . The scattered pressure pattern is well defined. The Kirchhoff surface location is also indicated in this figure. Although the Euler solution was obtained only in the $x - r$ plane, a closed Kirchhoff surface was constructed by a 360 degree rotation of the circular arc shown as the Kirchhoff surface in the figure about the x -axis so that the surface integrations could be performed. This surface had 64 elements in the rotational direction. The integrations were performed at every 16th Runge-Kutta iteration. The Kirchhoff solution is shown in Fig. 2 together with the direct solution. Both results agree excellently validating the modified Kirchhoff routine for time-periodic problems.

Solution of Category 2, Problem 1

This problem involves the solution of the acoustic field generated by a spherically distributed Gaussian source placed at the geometrical center of a finite, both-end-open, cylindrical duct subject to a Mach 0.5 uniform flow parallel to the duct axis. Specifically, the sound pressure levels are sought on a 2.5-duct diameter circular arc in the $x - r$ plane ((x, r, θ) represent cylindrical coordinates). This problem is axisymmetric as it is stated.

Because of the simple geometrical shape of the duct, it is convenient to solve the problem on a mesh constructed by families of constant x and constant r grid lines. If the solution on this 2.5-diameter arc, which we will call here as the far field, is to be obtained directly from the Euler calculations, the mesh resolution has to be sufficient all the way out from the source to the far field. This in turn dictates an extremely high number of grid points in both x and r directions for the specified nondimensional frequency. For example, if the mesh were designed to have 14 points per wavelength, the required number of grid points would be more than 1000 in the x and more than 500 in the r coordinate directions, indicating an excessive total number of grid points for such an axisymmetric problem. Therefore, mesh stretching is used and the Kirchhoff method is employed for the solution of the far-field sound. The stretched mesh system is shown in Fig. 3. Uniform mesh spacing is used in the duct and its immediate surrounding, and the mesh is stretched exponentially outward. The uniform portion of the mesh has about 14 points per wavelength in the upstream direction. A total of 512 grid points is used in the x direction and a total of 256 grid points is used in the r direction. The Kirchhoff surface is placed just outside the duct as shown in the figure. Again the problem is solved in two dimensions, i.e. in the $x - r$ plane, but the Kirchhoff integrations are performed on a closed surface formed by the rotation of the mesh.

A snapshot of the acoustic pressure contours is shown in Fig. 3. Because of the strong stretching and poor grid resolution in the far field, the solution is inaccurate there. Also the downstream outer boundary caused some reflections because of the high aspect ratio cells. However, the Kirchhoff solution is expected to be accurate because the waves are reasonably well resolved in the near field. The Kirchhoff results are compared with the point-source boundary-element solution of Myers [13] in Fig. 4. Myers' solution was scaled to match the present calculations at about 90 degrees from the duct axis. Both solutions agree very well in the most silent region. In fact, the solution in this region is due to the effects of the duct leading and trailing edges behaving as point sources that account for the diffracted waves, and this behavior is well represented by both methods. However, the differences in the other regions are mainly because of the differences between the specified sources. This is shown in Fig. 5, where a narrower Gaussian source was used to simulate the point source. The solutions

agree better now although there are still differences at about 60 and 120 degrees. This is probably due to Myers' boundary element method using singular functions at the duct leading and trailing edges. It should be pointed out that it is always difficult to treat a point source in a finite difference algorithm. The workshop problem, therefore, proposed the use of a distributed source.

The present calculations for this high-frequency case required about 9 CPU hours on a 32-node CM-5. It should be noted that these calculations were carried out by a slightly modified version of the ducted fan noise code and there is some overhead associated with this.

Calculations for a low-frequency case were also carried out. The nondimensional frequency chosen for this case was 4.409π . The comparison shown in Fig. 6 again indicates some differences between the point source solution of Myers and the present calculation, which used a distributed source. The effects of various parameters on the current solution are shown in Fig. 7. This figure essentially presents the effects of the grid and time step resolutions as well as the system of equations used. Since the frequency for this case was significantly lower, we were also able to obtain the solution using 18 points per wavelength without grid stretching. This improvement in the grid resolution did not result in significant change in the solution. Also, the solution was found using a significantly reduced time step size. The effect of this is also very minor. The use of the linearized Euler equations versus the nonlinear equations did not alter the solution significantly. A narrower Gaussian source test was also performed and the solution was compared with Myers' point source solution. This is shown in Fig. 8. Good agreement between both solutions is now evident from this figure. A conclusion from this is that the distributed sources had some noncompactness effects in their respective numerical solutions.

CONCLUDING REMARKS

A nonlinear, hybrid—the combination of Euler and Kirchhoff methods was used to solve two linear CAA benchmark problems—cat 1, prob 3 and cat 2, prob 1. Although these problems were relatively simple, they still required significant computational resources, even for moderate frequencies. Therefore, the real applications of CAA must utilize far-field extrapolation techniques such as the Kirchhoff method if feasible solutions are to be attained.

ACKNOWLEDGEMENTS

The authors would like to acknowledge the National Center for Supercomputing Applications at the University of Illinois for providing the computational resources (CM-5). Also, the authors would like to thank M. K. Myers of the George Washington University for providing his boundary element solutions to problem 1 of category 2.

References

- [1] Hardin, J. C., Ristorcelli, J. R., and Tam, C. K. W., editors. *ICASE/LaRC Workshop on Benchmark Problems in Computational Aeroacoustics (CAA)*, NASA CP-3300, NASA Langley

Research Center, Hampton, VA, May 1995.

- [2] Tam, C. K. W., and Webb, J. C. Dispersion-relation-preserving finite difference schemes for computational acoustics. *Journal of Computational Physics*, **107**, pp. 262–281, 1993.
- [3] Hu, F. Q., Hussaini, M. Y., and Manthey, J. Low-dissipation and low-dispersion Runge-Kutta schemes for computational acoustics. *Journal of Computational Physics*, **124(1)**, pp. 177–191, 1996.
- [4] Özyörük, Y., and Long, L. N. Computation of sound radiating from engine inlets. *AIAA Journal*, **34(5)**, pp. 894–901, May 1996.
- [5] Chyczewski, T. S., and Long, L. N. Numerical prediction of the noise produced by a perfectly expanded rectangular jet. AIAA paper 96-1730, 2nd AIAA/CEAS Aeroacoustics Conference, State College, PA, May 1996.
- [6] Bangalore, A., Morris, P. J., and Long, L. N. A parallel three-dimensional computational aeroacoustics method using non-linear disturbance equations. AIAA Paper 96-1728, 2nd AIAA/CEAS Aeroacoustics Conference, State College, PA, May 1996.
- [7] Özyörük, Y., and Long, L. N. A new efficient algorithm for computational aeroacoustics on parallel processors. *Journal of Computational Physics*, **125(1)**, pp. 135–149, April 1996.
- [8] Özyörük, Y., and Long, L. N. Multigrid acceleration of a high-resolution computational aeroacoustics scheme. *AIAA Journal*, **35(3)**, March 1997.
- [9] Farassat, F., and Myers, M. K. Extension of Kirchhoff's formula for radiation from moving surfaces. *Journal of Sound and Vibration*, **123**, pp. 451–460, 1988.
- [10] Bayliss, A., and Turkel, E. Far field boundary conditions for compressible flow. *Journal of Computational Physics*, **48**, pp. 182–199, 1982.
- [11] Özyörük, Y. *Sound Radiation From Ducted Fans Using Computational Aeroacoustics On Parallel Computers*. Ph.D. thesis, The Pennsylvania State University, December 1995.
- [12] Swanson, R. C., and Turkel, E. Artificial dissipation and central difference schemes for the Euler and Navier-Stokes equations. AIAA Paper 87-1107, 1987.
- [13] Myers, M. K. Boundary integral formulations for ducted fan radiation calculations. CEAS/AIAA Paper 95-076, 1995.

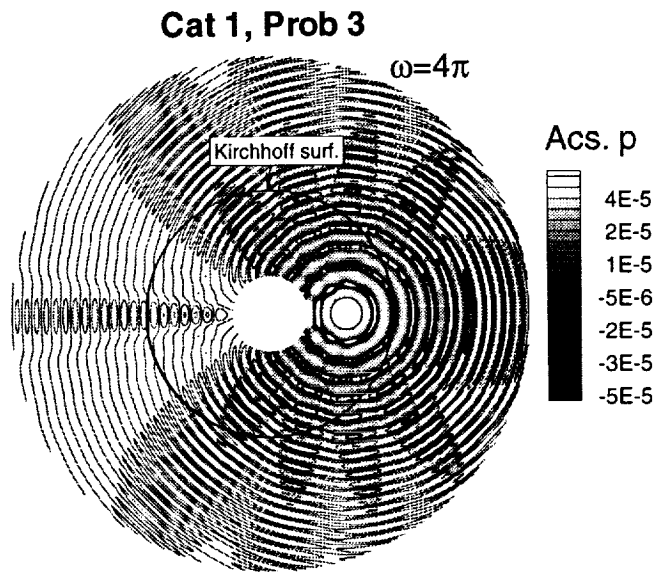


Figure 1: Snapshot of the acoustic pressure contours (Cat 1, Prob 3 with $\omega = 4\pi$).

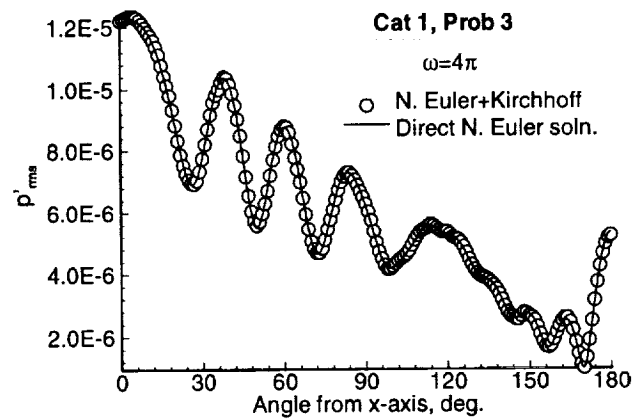


Figure 2: Comparison of the direct Euler solution with the Kirchhoff solution on a $x^2 + r^2 = 5^2$ circular arc (Cat 1, Prob 3 with $\omega = 4\pi$).

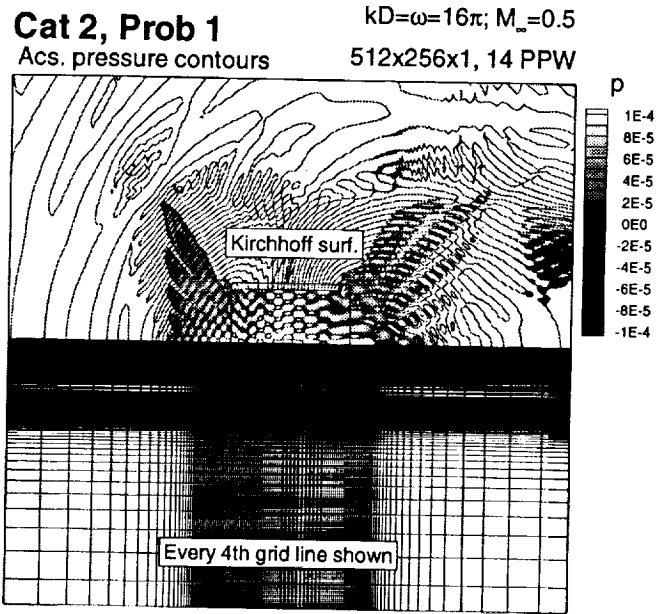


Figure 3: The nonuniform 512×256 grid system and the acoustic field (Cat 2, Prob 1 with $kD = 16\pi$).

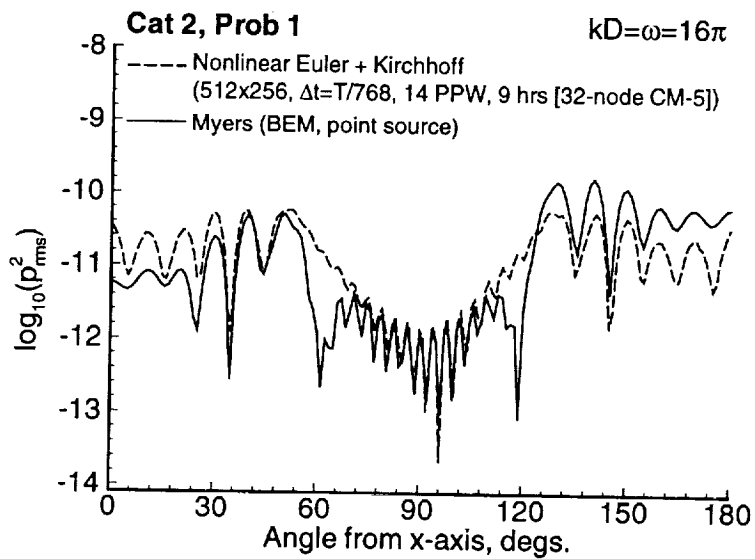


Figure 4: Comparison of the hybrid code's solution with Myers' point source solution on a $x^2 + r^2 = (5/2)^2$ circular arc (Cat 2, Prob 1 with $kD = 16\pi$).

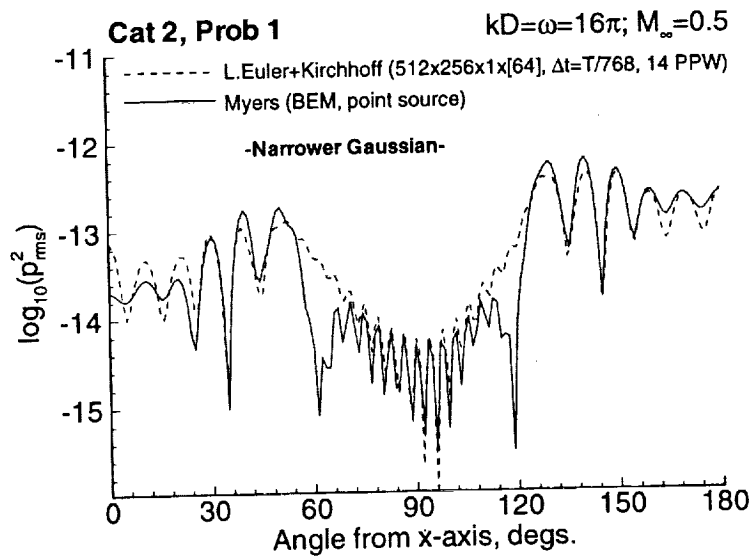


Figure 5: Comparison of the hybrid code's solution with Myers' point source solution for a narrower Gaussian source on a $x^2 + r^2 = (5/2)^2$ circular arc (Cat 2, Prob 1 with $kD = 16\pi$).

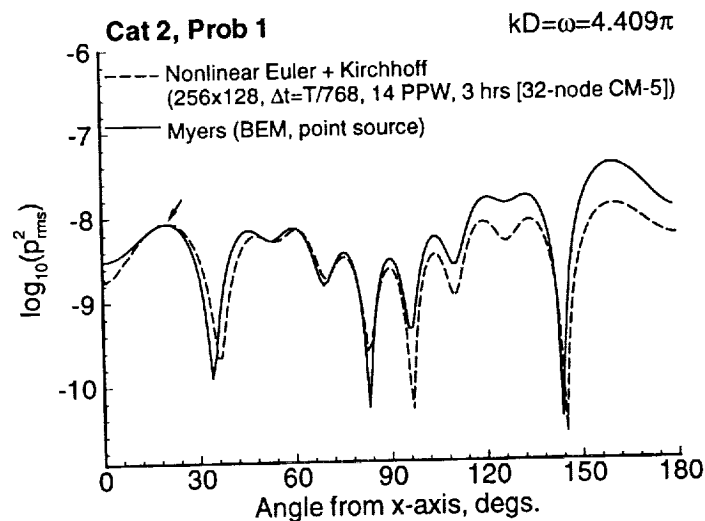


Figure 6: Comparison of the hybrid code's solution with Myers' point source solution on a $x^2 + r^2 = (5/2)^2$ circular arc (Cat 2, Prob 1 with $kD = 4.409\pi$).

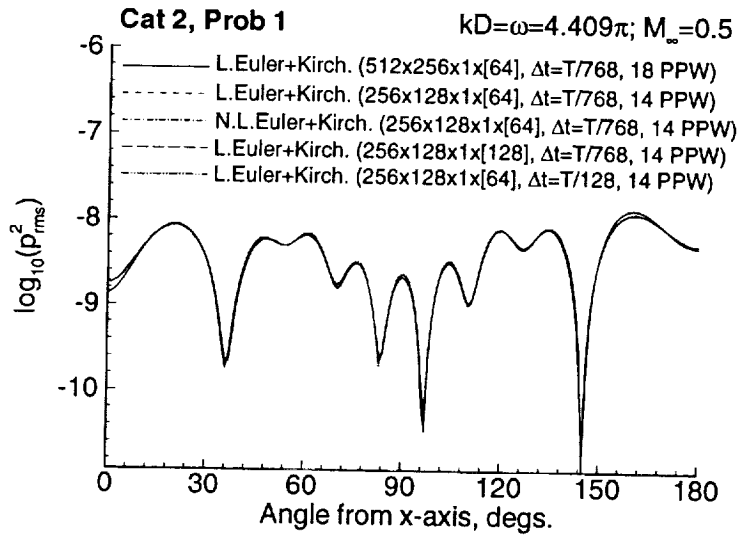


Figure 7: Effects of various parameters on the solution of Cat 2, Prob 1 with $kD = 4.409\pi$.

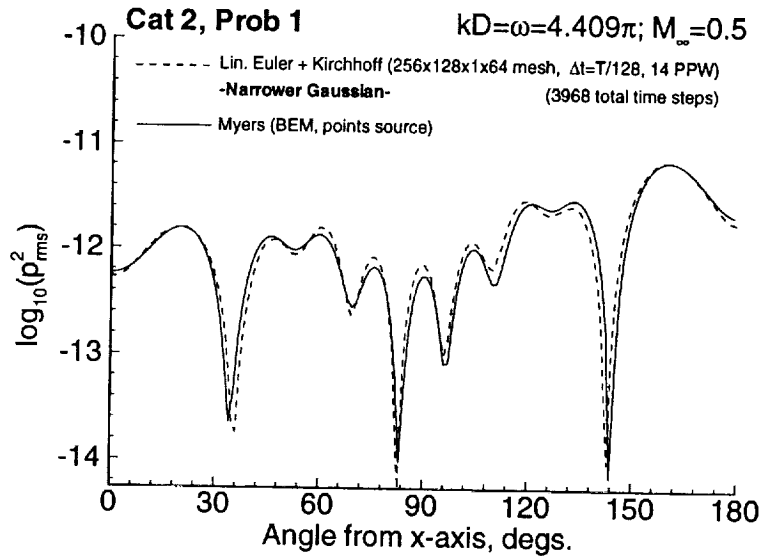


Figure 8: Comparison of the hybrid code's solution with Myers' point source solution for a narrower Gaussian source on a $x^2 + r^2 = (5/2)^2$ circular arc (Cat 2, Prob 1 with $kD = 4.409\pi$).

201-71 -
043479
294007 p6

THREE-DIMENSIONAL CALCULATIONS OF ACOUSTIC SCATTERING BY A SPHERE: A PARALLEL IMPLEMENTATION

Chingwei M. Shieh* and Philip J. Morris[†]
Department of Aerospace Engineering
The Pennsylvania State University
University Park, PA 16802

ABSTRACT

In this paper, the problem of acoustic scattering by a sphere is considered. The calculations are carried out with the use of a high-order, high-bandwidth numerical scheme and explicit time integration. Asymptotic non-reflecting radiation boundary conditions are applied at the outer boundaries of the computational domain, and the Impedance Mismatch Method (IMM) developed by Chung and Morris¹ is implemented in order to treat solid wall boundaries. Since a three-dimensional simulation of moderate source frequency is desired, parallel computation is exploited in order to decrease the computation time required. This study further demonstrates that in order for realistic CAA calculations to be performed, the computational power of parallel computers has to be harnessed.

INTRODUCTION

The scattering of sound from a spatially distributed, spherically symmetric source by a sphere is an excellent test case for numerical simulations in CAA. While the phenomenon is well understood, three-dimensional calculations of such problem with a moderate to high frequency source are still a daunting task because of the number of grid points per wavelength needed in order to resolve the acoustic waves. In this paper, such simulations are performed with the utilization of parallel computation. Numerical results are compared with the analytical solutions derived by Morris², and excellent agreement has been found.

NUMERICAL ALGORITHM

In the section, the governing equations that describe the acoustic scattering problem are given. The solution algorithm, with the implementation of non-reflecting boundary conditions and the IMM for the solid wall boundaries, are mentioned only briefly. The parallel numerical algorithm is also discussed briefly, and data from a scalability study are presented to demonstrate the improvement in performance using parallel computations.

*Graduate research assistant
[†]Boeing Professor of Aerospace Engineering

Governing Equations

The problem of acoustic scattering is governed by the linearized Euler equations. In a three-dimensional Cartesian co-ordinate system, the equations can be written as

$$\frac{\partial}{\partial t} \begin{bmatrix} \rho' \\ p' \\ u' \\ v' \\ w' \end{bmatrix} + \frac{\partial}{\partial x} \begin{bmatrix} \rho_0 u' \\ \rho_0 u' \\ p'/\rho_0 \\ 0 \\ 0 \end{bmatrix} + \frac{\partial}{\partial y} \begin{bmatrix} \rho_0 v' \\ \rho_0 v' \\ 0 \\ p'/\rho_0 \\ 0 \end{bmatrix} + \frac{\partial}{\partial z} \begin{bmatrix} \rho_0 w' \\ \rho_0 w' \\ 0 \\ 0 \\ p'/\rho_0 \end{bmatrix} = \begin{bmatrix} 0 \\ A_p \\ 0 \\ 0 \\ 0 \end{bmatrix} \quad (1)$$

where it is assumed that there is no mean flow. In the above equations, all quantities are non-dimensionalized by the radius of the sphere, R , the ambient speed of sound, a_∞ , and the ambient density, ρ_∞ , as the length, velocity, and density scales, respectively. The characteristic scales for the pressure and time are $\rho_\infty a_\infty^2$ and R/a_∞ , and the source term, A_p , is given by

$$A_p = -A \exp \left\{ -B(\log 2)[(x - x_s)^2 + y^2 + z^2] \right\} \cos(\omega t) \quad (2)$$

where $A = 0.01$, $B = 16$, $x_s = 2$, and $\omega = 2\pi$. ρ_0 is the non-dimensional mean density equal to unity exterior to the body.

Solution Algorithm

In the present study, a high-order, high-bandwidth numerical scheme is implemented for the spatial discretization of the governing equations. This scheme, the Dispersion-Relation-Preserving (DRP) method developed by Tam and Webb³, is an optimized third-order finite difference operator with the use of a seven-point stencil. A standard fourth-order Runge-Kutta time integration algorithm has been applied for explicit time stepping. It has been shown in various CFD studies that central difference operators are inherently unstable. Therefore, in order to circumvent this problem, a filter is added explicitly. A sixth derivative is used as a smoother, as proposed by Lockard and Morris⁴; however, since a uniform computational grid is used, and it is expected that the problem does not possess any nonlinear effects, the artificial dissipation model has been further simplified so that only a constant coefficient filter is applied. This decreases the computational time significantly without sacrificing the integrity of the data.

Asymptotic non-reflecting radiation boundary conditions, first developed by Tam and Webb³ in two dimensions and later extended to three-dimensional cases by Chung and Morris¹, are applied at the outer boundaries of the computational domain. The Impedance Mismatch Method (IMM) is introduced to treat the solid wall boundaries. This is achieved by simply setting a different value of ρ_0 inside the sphere. Further details are given by Chung and Morris¹.

Parallel Implementation and Performance

The parallel implementation employed in the present study follows the same strategy outlined by Lockard and Morris⁴. The code is written in Fortran 90 with the Message Passing Interface (MPI) on

the IBM SP2. The computational domain is decomposed in a single direction only in order to simplify coding. The asymptotic non-reflecting radiation boundary conditions are applied at the outer surfaces of the computational domain, as shown in figure 1. Along the interface between each sub-domain, a message passing boundary condition is applied. Data are transferred from one sub-domain to another with the use of the MPI. Since a seven point finite difference stencil is used, a three-point overlap region is constructed along the interface of each sub-domain.

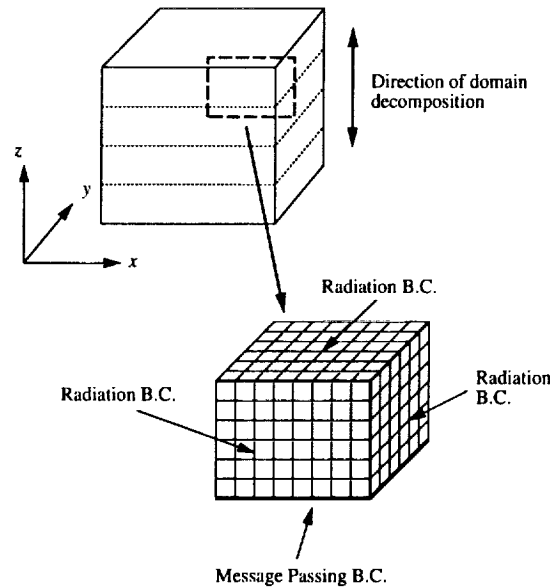


Figure 1: A schematic representation of the domain decomposition strategy.

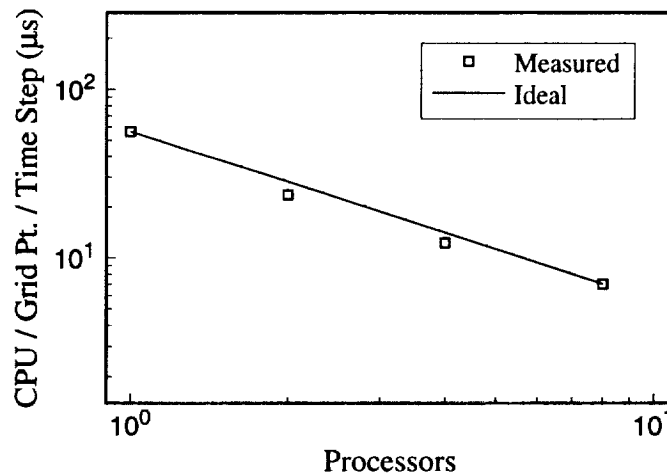


Figure 2: Scalability study and comparison of the increase in performance with a parallel implementation.

The increase in performance of the code with parallel implementation is summarized in figure 2. A logarithmic plot of the CPU time per grid point per time step in micro-seconds versus the number of processors used in the calculation is shown in this figure. Nearly ideal speed-up is seen to be achieved for up to eight processors. This is due to the minimization of the overhead in communication between

each processor that is associated with the parallelization, as discussed by Lockard and Morris⁴. Based on similar computations by Lockard and Morris⁴, additional ideal speed-up may be expected for at least 128 processors.

RESULTS AND DISCUSSIONS

The sphere is placed at the center of the computational domain, with the source located at $(2, 0, 0)$. The acoustic wave is generated by a time periodic source in the energy equation, as shown in equation (1). The domain extends from -5 to 5 in each direction, with $101 \times 101 \times 101$ grid points. This corresponds to approximately seven grid points per wavelength along a diagonal.

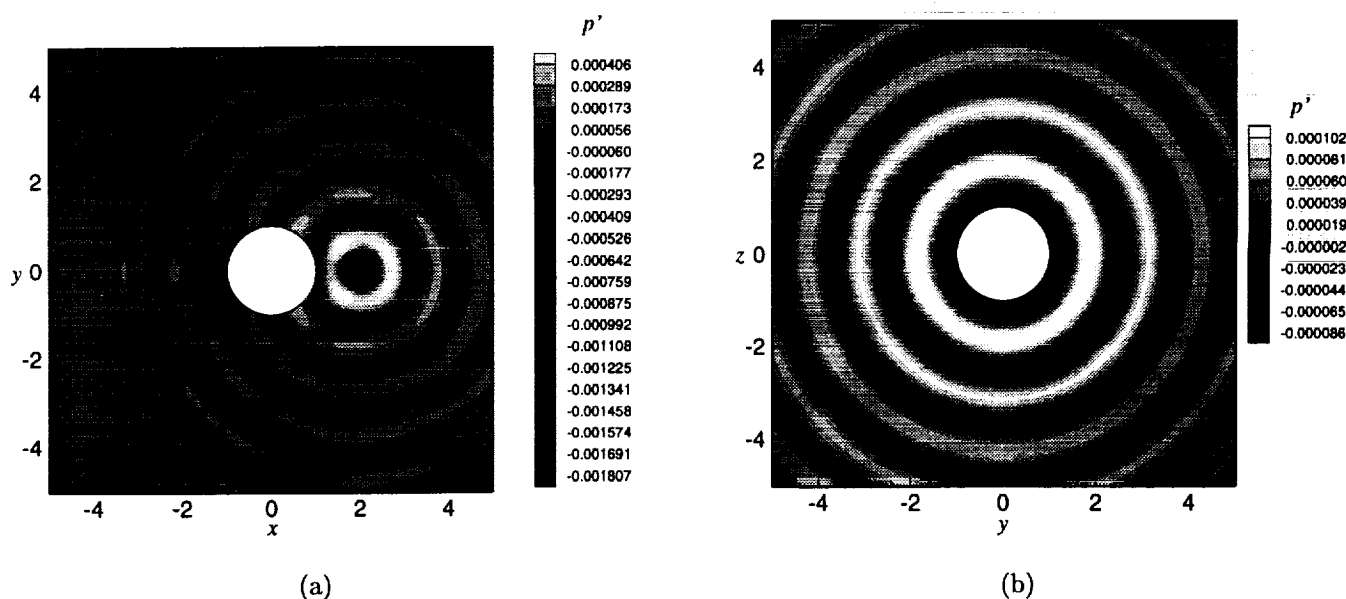


Figure 3: Contour level of instantaneous pressure at the beginning of a period: (a) along the plane $z = 0$; (b) along the plane $x = 0$.

Inside the sphere, ρ_0 is set to $1/30$ in the implementation of the IMM for the solid wall boundary condition. The definition of the sphere surface is approximated by a staircase boundary. Figure 3(a) shows the instantaneous pressure contours along the plane $z = 0$, a plane that intersects the center of the sphere and the acoustic source, at the beginning of a period. The axisymmetric property of the problem is evident in figure 3(b). The contour levels of the instantaneous pressure are plotted along the plane $x = 0$ that cuts through the center of the sphere. The concentric pattern of the pressure is a clear indication that the physical phenomenon has been faithfully reproduced in the simulation.

Comparisons between the numerical results and the analytic solutions derived by Morris² are shown in figure 4. Along the line in which the center of the source and the sphere are located, as shown in figure 4(a), an excellent agreement between the numerical and the analytic solutions has been achieved. Only slight discrepancies are observed near the vicinity of the sphere. The disagreement is more prominent when the instantaneous pressure is plotted along the line that

intersects the center of the sphere only, as shown in figure 4(b). Most of the disagreement occurs because of the staircase boundary that defines the sphere and the relatively coarse grid used in the present study.

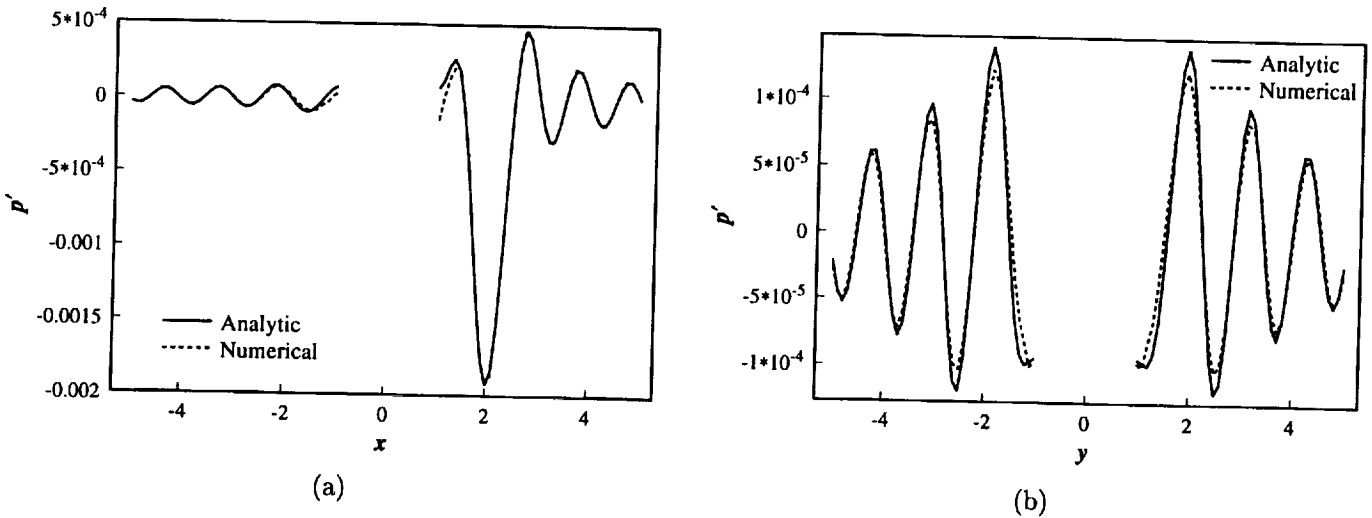


Figure 4: Comparison of the analytic and numerical solutions of the scattered acoustic field: (a) along the line at $y = 0$ and $z = 0$; (b) along the line at $x = 0$ and $z = 0$.

The root-mean-square (RMS) pressure is calculated by sampling the pressure data after a periodic state of the pressure has been obtained. This RMS pressure is then plotted along a circle of radius $r = 5$ at $\Delta\theta = 1^\circ$, as shown in figure 5. The discrepancies between the numerical and the analytic solutions may be due to post-processing, where the RMS data have been interpolated from a Cartesian grid to a circle. However, the difference is very small to be of any significance when sound pressure levels are considered.

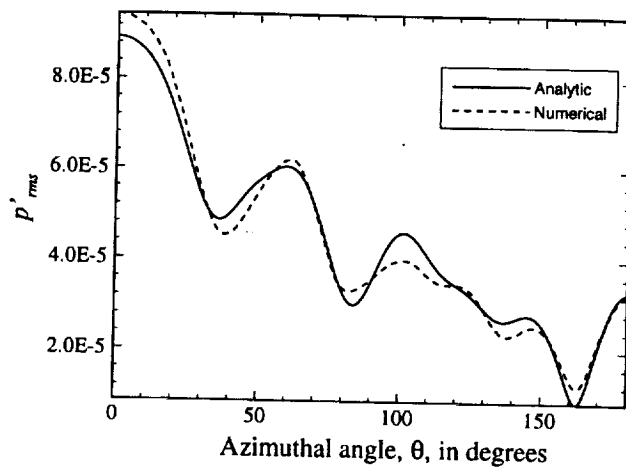


Figure 5: Plot of the root-mean-square pressure along the circle $x^2 + y^2 = 25$ at $\Delta\theta = 1^\circ$.

CONCLUSIONS

In this paper, a three-dimensional calculation of acoustic scattering by a sphere has been performed with a parallel implementation. It has been demonstrated that parallel computing can be exploited for CAA calculations in order to achieve better computation time. The treatment of solid wall boundaries with the use of the IMM has been implemented in the present computation. This method has many advantages over traditional solid wall boundary conditions, such as simplicity in coding, increase in speed of computation, and the ability to treat curved boundaries in Cartesian grids. Good agreement between the numerical and the analytic solutions has been observed.

REFERENCES

- [1] Chung, C., and Morris, P. J. Acoustic scattering from two- and three-dimensional bodies. CEAS/AIAA Paper 95-008. Submitted to *Journal of Computational Acoustics*.
- [2] Morris, P. J. Scattering of sound from a spatially distributed, spherically symmetric source by a sphere. *Journal of Acoustical Society of America*, **98**, pp. 3536-3539, 1995.
- [3] Tam, C. K. W., and Webb, J. C. Dispersion-relation-preserving finite difference schemes for computational aeroacoustics. *Journal of Computational Physics*, **107**, pp. 262-281, 1993.
- [4] Lockard, D., and Morris, P. J. A parallel implementation of a computational aeroacoustic algorithm for airfoil noise. AIAA Paper 96-1754, 1996. To appear in *Journal of Computational Acoustics*.

522-71
043 480 294010

ON COMPUTATIONS OF DUCT ACOUSTICS WITH NEAR CUT-OFF FREQUENCY

p12

Thomas Z. Dong*

NASA Lewis Research Center, Cleveland, Ohio 44135

Louis A. Povinelli

NASA Lewis Research Center, Cleveland, Ohio 44135

ABSTRACT

The cut-off is a unique feature associated with duct acoustics due to the presence of duct walls. A study of this cut-off effect on the computations of duct acoustics is performed in the present work. The results show that the computation of duct acoustic modes near cut-off requires higher numerical resolutions than others to avoid being numerically cut off. Duct acoustic problems in Category 2 are solved by the DRP finite difference scheme with the selective artificial damping method and results are presented and compared to reference solutions.

1. Introduction

Duct acoustics are sound waves transmitted along the interior of a duct. Once generated, the waves which do not propagate in the axial direction of the duct reflect from the walls of the duct and interact with each other. Because of this, waves with only special patterns defined as the duct acoustic modes are allowed in the duct. It is found that for a given frequency only a finite number of duct acoustic modes can propagate through the duct. The rest are blocked out by the duct walls. An illustration of this phenomenon as results of interference of waves with different propagation angles can be found in the book by Morse and Ingard¹. This unique feature was defined as the cut-off of duct acoustics. A parameter called cut-off ratio was introduced to study this phenomenon quantitatively so that waves with cut-off ratio greater than unity propagate while waves with cut-off ratio less than unity are cut off. This brings up a new difficulty for direct numerical simulations of duct acoustics involving waves with cut-off ratio near unity as a wave with cut-off ratio slightly above unity could be cut off by the errors in the numerical approximations.

On the other hand, an analysis of a numerical scheme designed for acoustic computations often suggests that the accuracy of the numerical solutions is in general an increasing

* This work was performed while the author held a National Research Council-(NASA Lewis Research Center) Research Associateship.

function of the number of mesh points per wave length. This implies that more accurate solutions will be produced for waves containing more mesh points than those containing less. So if a scheme can produce an accurate solution for a wave with say eight points per wave length, one would expect better or least equally accurate solutions for waves containing more mesh points. For computations of duct acoustics, this is not necessarily the case. In the present work, it will be shown that poor numerical solutions could be produced for duct acoustic waves near cut-off, although the waves are well in the accurate solution range. Higher resolutions are required for these duct acoustic waves in order to produce the expected accuracy.

In the next section, we start with a brief review of linear duct acoustics including the definitions of cut-off ratio, group velocity. In Section 3, a duct acoustic inflow boundary condition is derived. The numerical simulations and a discussion of the results are given in Section 4.

2. Linear Duct Acoustics

Consider a uniform subsonic mean flow with Mach number M_0 in an infinitely long circular duct with radius R . The linear duct acoustics is governed by the linearized Euler's equations which can be further simplified to give the convective wave equation for acoustic pressure p

$$\left(\frac{\partial}{\partial t} + M_0 \frac{\partial}{\partial x}\right)^2 p - \nabla^2 p = 0 \quad (1)$$

and the boundary condition at $r = R$

$$\frac{\partial p}{\partial r} = 0 \quad (2)$$

The flow variables are non-dimensionalized by a_0 , ρ_0 and $\rho_0 a_0^2$ where a_0 and ρ_0 are the speed of sound and density of the mean flow.

A single eigen-solution or duct acoustic solution to the above system can be written as

$$p_{mn}(r, \theta, x, t) = P_{mn} J_m(\mu_{mn} r) e^{i(\lambda x + m\theta - \omega t)} \quad (3)$$

where m is the circumferential mode number and n is the radial mode number. The eigenvalue μ_{mn} is the n th zero of the derivative of the m th order Bessel function J_m , namely

$$J'_m(\mu_{mn} R) = 0 \quad (4)$$

The variable k is the axial wave number and ω is the angular frequency. They are related by the dispersion relation of equation (1)

$$D(k, \omega) = (\omega - M_0 k)^2 - k^2 - \mu_{mn}^2 = 0 \quad (5)$$

It can be easily seen that duct acoustic waves are dispersive. The group velocity of the duct acoustics can be obtained from the above equation as

$$V_g(\omega, k) = \frac{d\omega}{dk} = M_0 + \frac{k}{\omega - M_0 k} \quad (6)$$

The axial wave number can be solved as

$$k_{\pm} = \frac{1}{(1 - M_0^2)} \left[-M_0 \omega \pm \sqrt{\omega^2 - (1 - M_0^2) \mu_{mn}^2} \right] \quad (7)$$

where k_+ represents waves propagating downstream and k_- represents waves traveling upstream. For

$$\frac{\omega^2}{(1 - M_0^2) \mu_{mn}^2} \geq 1$$

k_{\pm} are real. Waves propagate both upstream and downstream without attenuation. For

$$\frac{\omega^2}{(1 - M_0^2) \mu_{mn}^2} < 1$$

k_{\pm} are a pair of conjugate complex numbers. Waves in both directions are attenuated exponentially with distance. This means no waves with these wave numbers can be observed away from the source region in both upstream and downstream directions. These waves are defined as being cut off while the waves propagating without attenuation are referred as to being cut on. A special parameter "cut-off ratio" is therefore introduced as

$$\beta_{mn} = \frac{\omega}{\mu_{mn} \sqrt{1 - M_0^2}}$$

Waves with cut-off ratio greater than unity are cut on and waves with cut-off ratio less than unity are cut off. For waves with cut-off ratio less than or equal to unity, the group velocities are equal to zero. This means that the waves which are cut-off are not propagating and waves with cut-off ratio only slightly greater than unity will propagate very slowly.

3. Duct Acoustics Inflow Boundary Condition

In numerical simulations of duct acoustics radiation, where the duct acoustic waves are generated inside the duct and propagate through the duct and radiate to the ambient from the duct open end, the duct must have a finite length. The boundary condition imposed at the inflow boundary or the inner boundary of the duct, for problem 2 of Category 2, serves two purposes. First, it simulates a noise source to generate duct acoustic waves propagating towards the open end. Second, it must allow the acoustic waves reflected

from the open end to travel out of the computational domain. The acoustic solution there can be written as a sum of the incident and reflected waves, namely

$$p = p_{in} + p_{re} \quad (8)$$

Assuming a single angular frequency ω , the reflected wave must be in the form

$$p_{re} = \sum_{m,n} p_{m,n} J_m(\mu_{mn} r) e^{i(k_{mn} x + m\theta - \omega t)} \quad (9)$$

The axial wave number k_{mn} can be computed from the dispersion relation

$$\frac{k_{mn}}{\omega} = \frac{1}{1 - M_0^2} \left[-M_0 \pm \sqrt{1 - (1 - M_0^2) \left(\frac{\mu_{mn}}{\omega} \right)^2} \right] \quad (10)$$

For reflected waves the plus sign in the above equation should be taken.

Differentiating equation (9) with respect to x and t yields

$$\frac{\partial p}{\partial x} = \frac{\partial p_{in}}{\partial x} + i \sum_{mn} p_{mn} J_m(\mu_{mn} r) k_{mn} e^{i(k_{mn} x + n\theta - \omega t)} \quad (11)$$

and

$$\frac{\partial p}{\partial t} = \frac{\partial p_{in}}{\partial t} - i\omega p_{re} \quad (12)$$

Since only the cut-on modes of the reflected waves are considered, we must have $(\sqrt{1 - M_0^2})\mu_{mn}/\omega \leq 1$. A Taylor series approximation leads to

$$\sqrt{1 - (1 - M_0^2) \left(\frac{\mu_{mn}}{\omega} \right)^2} = 1 + O\left((1 - M_0^2) \left(\frac{\mu_{mn}}{\omega} \right)^2 \right) \quad (13)$$

Therefore, by combining equations (11)-(13), we obtain the boundary equation for p

$$\frac{\partial p}{\partial t} + (1 + M_0) \frac{\partial p}{\partial x} = \frac{\partial p_{in}}{\partial t} + (1 + M_0) \frac{\partial p_{in}}{\partial x} \quad (14)$$

Similarly, boundary equations for other variables with the same form can be obtained.

4. Numerical Simulations of Duct Acoustics

In this section, the duct acoustics problems in Category 2 were solved by the DRP scheme with the selective artificial damping method in reference²⁻³. Schematic diagrams of the computational domains for both problem 1 and 2 are shown in Figure 1-2. The duct wall thickness was set to be Δr instead of zero to eliminate the ambiguity in numerical approximation of x derivatives at points near the tips. The length scale L is set to be

the duct diameter D for problem 1 and the radius R for problem 2. The time scale is L/a_0 . The damping coefficient μ was set to be 0.05. To remove the singularities at the tips of the duct wall due to the inviscid approximation, larger damping coefficients were used at the tips ($\mu_t = 1.0$) and along the wall ($\mu_w = 0.1$). A Gaussian function with half width equal to three mesh points was used to make a smooth transition of the damping. The time step was set to be $\Delta t = 0.05\Delta x$. The amplitude of the source was multiplied by a time dependent factor $1 - e^{-(n\Delta t/2000\Delta t)^2}$ to make a smooth transient. The governing equations are the Euler's equations. A numerical treatment of solid wall boundary condition with the minimum number of ghost points for high order schemes, developed by Tam and Dong⁴, was applied to the solid surfaces of the duct walls. The computations are done on IBM RS/6000-590 workstations.

For problem 1, a harmonic source function with a narrow Gaussian spatial distribution located at the center of the duct was added to the continuity and energy equations as specified by the problem. The acoustic radiation boundary condition was used at the inflow and top boundaries and the outflow boundary condition was used at the outflow boundary. These boundary conditions can be found in reference² by Tam and Webb. Two cases with angular frequency $\omega = 4.409507\pi$ and 16π were computed. The mesh size for the lower frequency case was $\Delta x = \Delta r = D/51$. The shortest acoustic wave contains about $12\Delta x$. The mesh size for the higher frequency case was set to be $\Delta x = \Delta r = D/159$. The shortest wave in this case is about $10\Delta x$. The computational domain contains 272×136 and 801×401 mesh points for the lower and higher frequency cases respectively. The solutions took a long time to reach a good periodic state. This could be partially due to the fact that the modes near cut-off took long time to travel out of the duct. The $\omega = 4.409507\pi$ case took 12 CPU hours and the $\omega = 16\pi$ case took about 200 CPU hours. The sound pressure levels ($p_{ref} = 2 \times 10^{-5} Pa$) for both cases are measured along a circular arc $x^2 + r^2 = (5D/2)^2$ and plotted in Figure 3-4. The computed results in general agree with the reference solutions which are computed by boundary element method with a point source and rescaled with the computed solutions at a point. Because of the mean flow, acoustic waves take longer time to travel upstream. More loss in sound pressure level due to the numerical dissipation is expected in the upstream region (θ near 180°) than in the downstream region (θ near 0°).

The results from problem 2 are more interesting. The Mach number of the mean flow is zero. The same acoustic radiation boundary condition was used at the boundaries of the ambient region as shown in Figure 2. A single incoming duct acoustic mode was specified at the inflow boundary of the duct as follows

$$\begin{bmatrix} \rho \\ u \\ v \\ w \\ p \end{bmatrix}_{in} = \epsilon Re \left\{ \begin{bmatrix} J_m(\mu_{mn}r) \\ \frac{(\omega^2 - (\mu_{mn})^2)^{1/2}}{\omega} J_m(\mu_{mn}r) \\ -\frac{i\mu_{mn}}{\omega} J'_m(\mu_{mn}r) \\ \frac{n}{\omega} J_m(\mu_{mn}r) \\ J_m(\mu_{mn}r) \end{bmatrix} \times e^{i[(\omega^2 - \mu_{mn}^2)^{1/2}x + m\theta - \omega t]} \right\} \quad (15)$$

The mode numbers are $m = 0$ and $n = 2$. Cases with $\omega = 7.2$ and $\omega = 10.3$ are considered. The mesh size was $\Delta x = \Delta r = R/15.5$. So the wave with the lower frequency has about

13.5 Δx per wave length in the free space and the one with high frequency has about 9.5 Δx . Waves in both cases are in the well resolved long wave range for the chosen scheme and mesh size according to the analysis in reference³.

The computed results are compared with the reference solutions with mesh size $\Delta x = \Delta r = R/32$ which is smaller than half of the mesh size used in the present work. The reference solution was computed by Tam. Figures 5-6 show the pressure envelope, which is defined as the maximum amplitude of pressure, inside the duct along four radial lines $r = 0, 0.34, 0.55, 0.79$. For the second radial mode ($n=2$), these are the locations of peak and trough. It can be seen that the computed solutions agree in general with the reference solutions except that the computed solutions have less interactions between the incident and reflected waves. This could be due to the fact that the lip of the duct wall in the present work is Δr instead of zero which is used by the reference solution. The directivity $D(\theta)$ (θ is the polar angle measured from the center of the duct exit plane as shown in Figure 2) of the radiated sound, which is defined by

$$D(\theta) = \overline{R^2 p^2(R, \theta, \phi, t)}$$

where the bar denotes the time average, is measured along the outer boundary of the computational domain and plotted in Figure 7-8.

It is observed from Figure 7-8 that solutions of both cases predict the locations of the lobes and nodes very well. The solutions of the present computations predict higher level of sound in the forward direction than the reference solution. Again this could be caused by a finite thickness of the duct wall. The solution with the high frequency in general matches the reference solution very well as expected. The solution with the lower frequency loses more than 30% of sound in the direction of the peak comparing to the reference solution which is in contradiction with the analysis as both solutions have enough grid resolutions. If this is caused by the numerical damping, the lower frequency solution should still perform better than the higher one.

With a close look at the parameters, it is observed that the radial eigenvalue μ_{02} is equal to 7.0156. This makes the lower frequency $\omega = 7.2$ very close to the cut-off frequency $\omega_c = 7.0156$ with $M_0 = 0$. The group velocity computed from equation (6) is equal to about 0.2 while the group velocity for the higher frequency solution is about 0.7. This means that the amount of time for the lower frequency solution to propagate through the duct is 3.5 times the amount needed for the higher frequency solutions. Therefore, much more numerical dissipation is experienced by the lower frequency solution.

In addition to the numerical dissipation, it is well known that on a discrete grid a single wave spreads its spectrum to the adjacent frequencies. This spreading is usually not a major concern as the propagation properties like dispersion, dissipation and wave speeds are continuous functions of wave numbers. But for duct acoustics, if part of the energy of the solution is spread to the adjacent modes which are cut off, a loss of sound level could happen. In this particular case, any energy leaked to the next higher radial mode ($n=3$) will be cut off by the duct wall.

To fix this problem, a multi-domain multiple time-step method⁵ was used to double the grid resolution only inside the duct. Since the artificial damping rate decreases faster than a linear function as $k\Delta x$ decreases, a reduction of Δx should decrease the amount of damping. In addition, an increase of grid resolution should also reduce the spreading of energy to the neighboring modes. With the use of this multi-domain multiple time step method, the doubling of grid resolution inside the duct only increased the amount of computation by 58% while an overall increase of resolution will make a 700% increase since the resolution in time also needs to be increased to maintain the numerical stability. With the new grid resolution, the computed results agree favorably with the reference solution as shown by the dashed curves in Figure 5 and 7.

5. Conclusion

A study of numerical simulations of the radiation of duct acoustics with near cut-off frequency was carried out in the present paper. The results show that the computation of duct acoustics with near cut-off frequency requires higher grid resolution than the requirement from the dispersion and dissipation error analysis due to their very low group velocity and possible spreading of energy to the adjacent modes which are cut off. To avoid an overall increase of grid resolution, multi-domain methods which allow for different grid resolutions in different sub-domains should be considered.

REFERENCE

- ¹ Morse, P.M.; Ingard, K.U., *Theoretical Acoustics*, McGraw-Hill, New York, 1968.
- ² Tam, C.K.W.; Webb, J.C.: "Dispersion-Relation-Preserving finite difference schemes for computational acoustics", *J. Comput. Phys.*, Vol. 107, Aug. 1993, pp. 262-281.
- ³ Tam, C.K.W.; Webb, J.C; and Dong, T.Z.: "A study of the short wave components in computational acoustics," *J. Comput. Acoustics*, Vol 1, 1993, pp. 1-30.
- ⁴ Tam, C.K.W.; Dong, T.Z., "Wall boundary conditions for high-order finite difference schemes in computational aeroacoustics," *Theoret. Comput. Fluid Dynamics*, Vol. 6, 1994, pp. 303-322.
- ⁵ Dong, T.Z., "Fundamental problems in computational acoustics", Ph.D Dissertation, Chapter IV, 1994, pp.78-105.

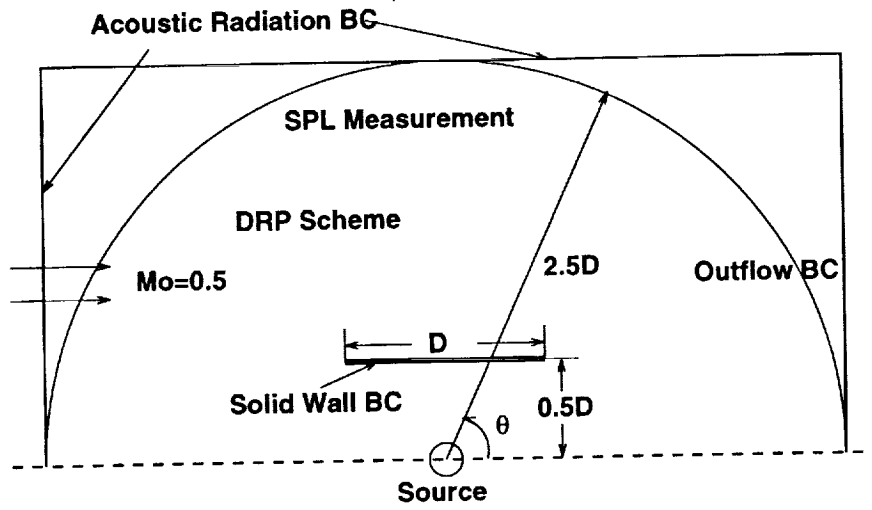


Figure 1. Computational domain of problem 1.

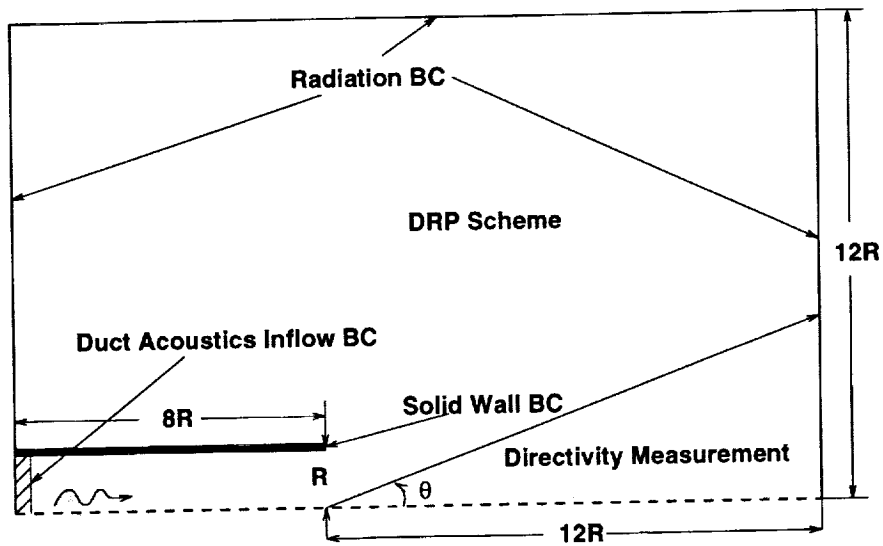


Figure 2. Computational domain of problem 2.

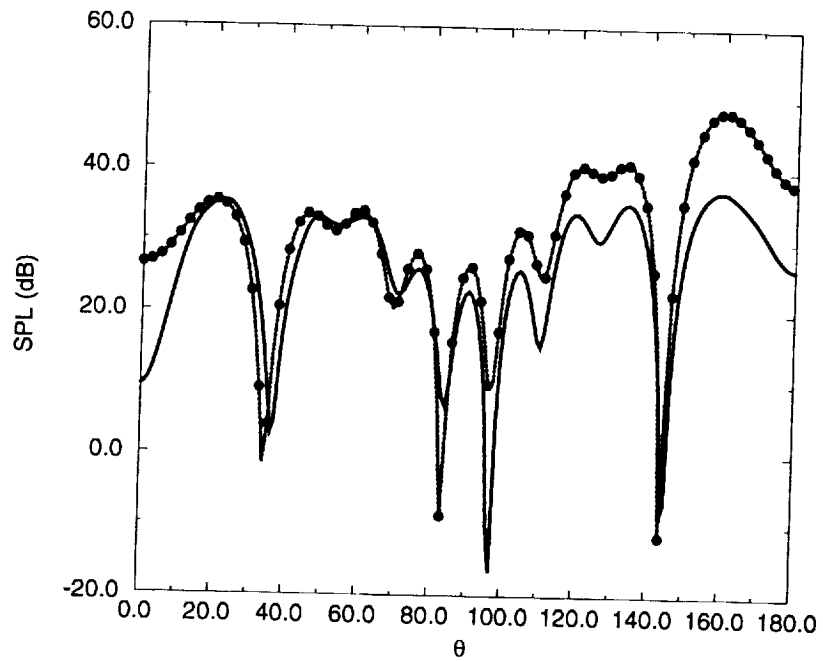


Figure 3. Sound pressure level with $\omega = 4.4\pi$. Computed solution (solid line), reference solution (dotted line).

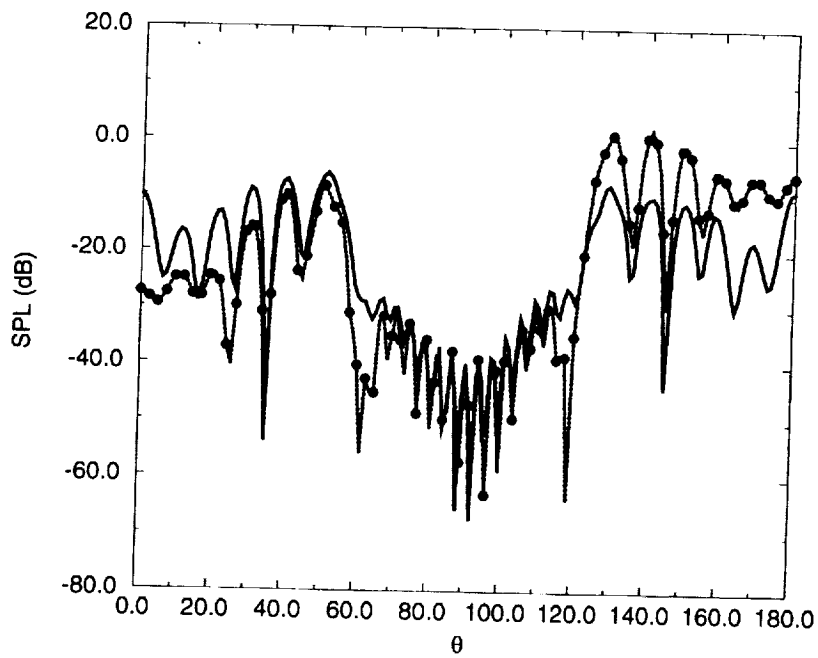


Figure 4. Sound pressure level with $\omega = 16\pi$. Computed solution (solid line), reference solution (dotted line).

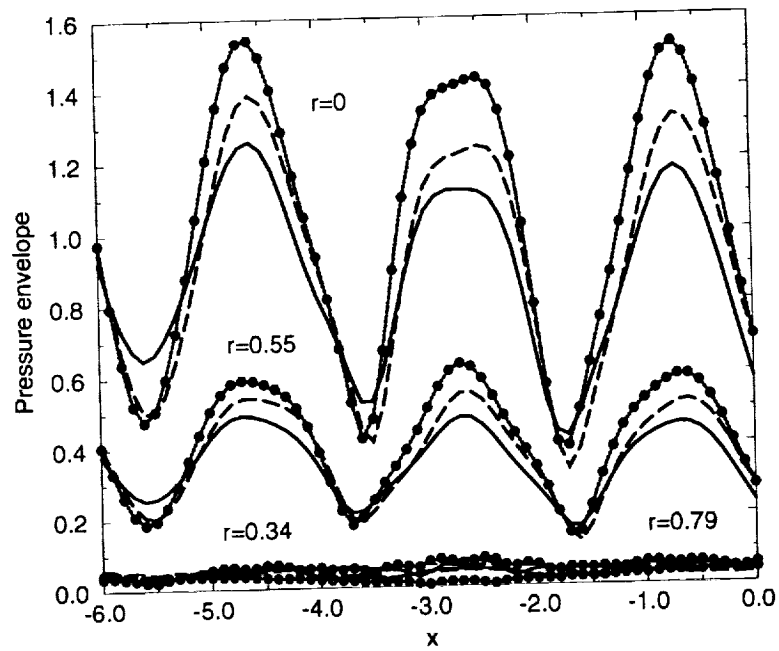


Figure 5. Pressure envelope at various r locations ($\omega = 7.2$). $\Delta x = R/15.5$ (solid line), Reference solution (dotted line), Multi-domain solution (dashed line).

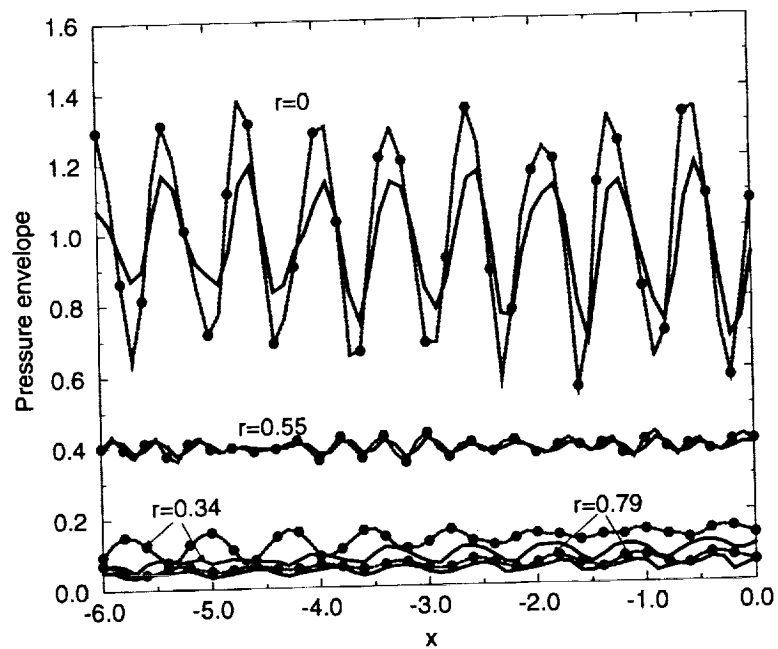


Figure 6. Pressure envelope at various r locations ($\omega = 10.3$). $\Delta x = R/15.5$ (solid line), Reference solution (dotted line).

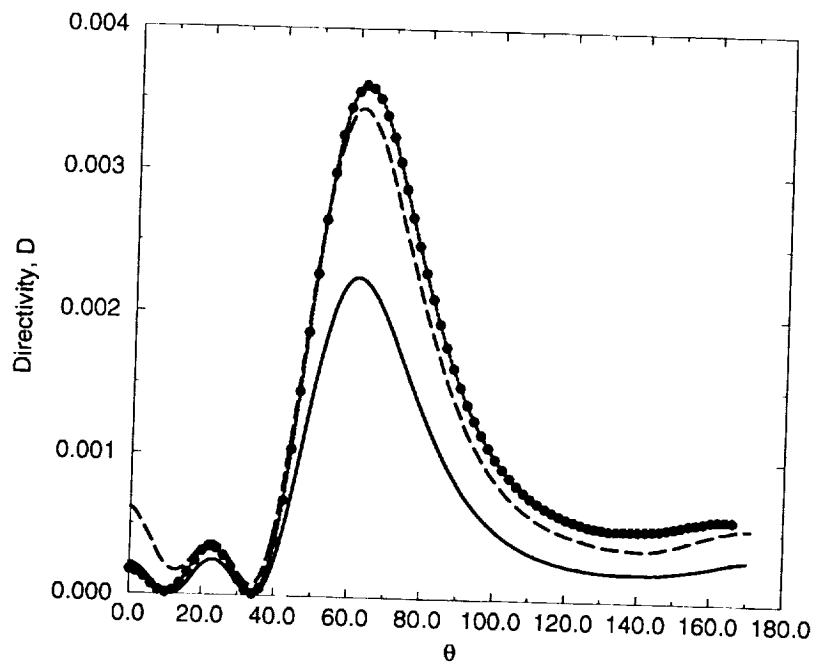


Figure 7. Directivities D ($\omega = 7.2$). $\Delta x = R/15.5$ (solid line), Reference solution (dotted line), Multi-domain solution (dashed line).

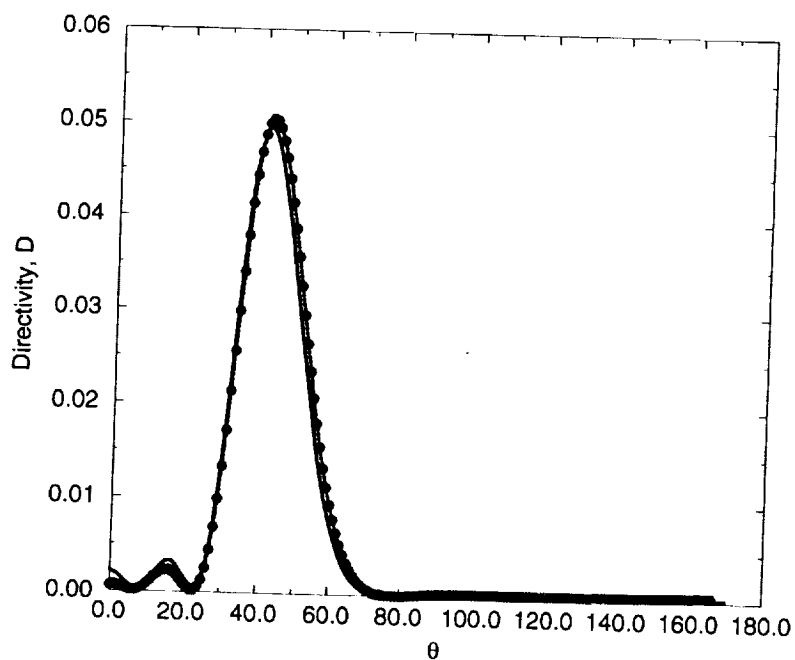
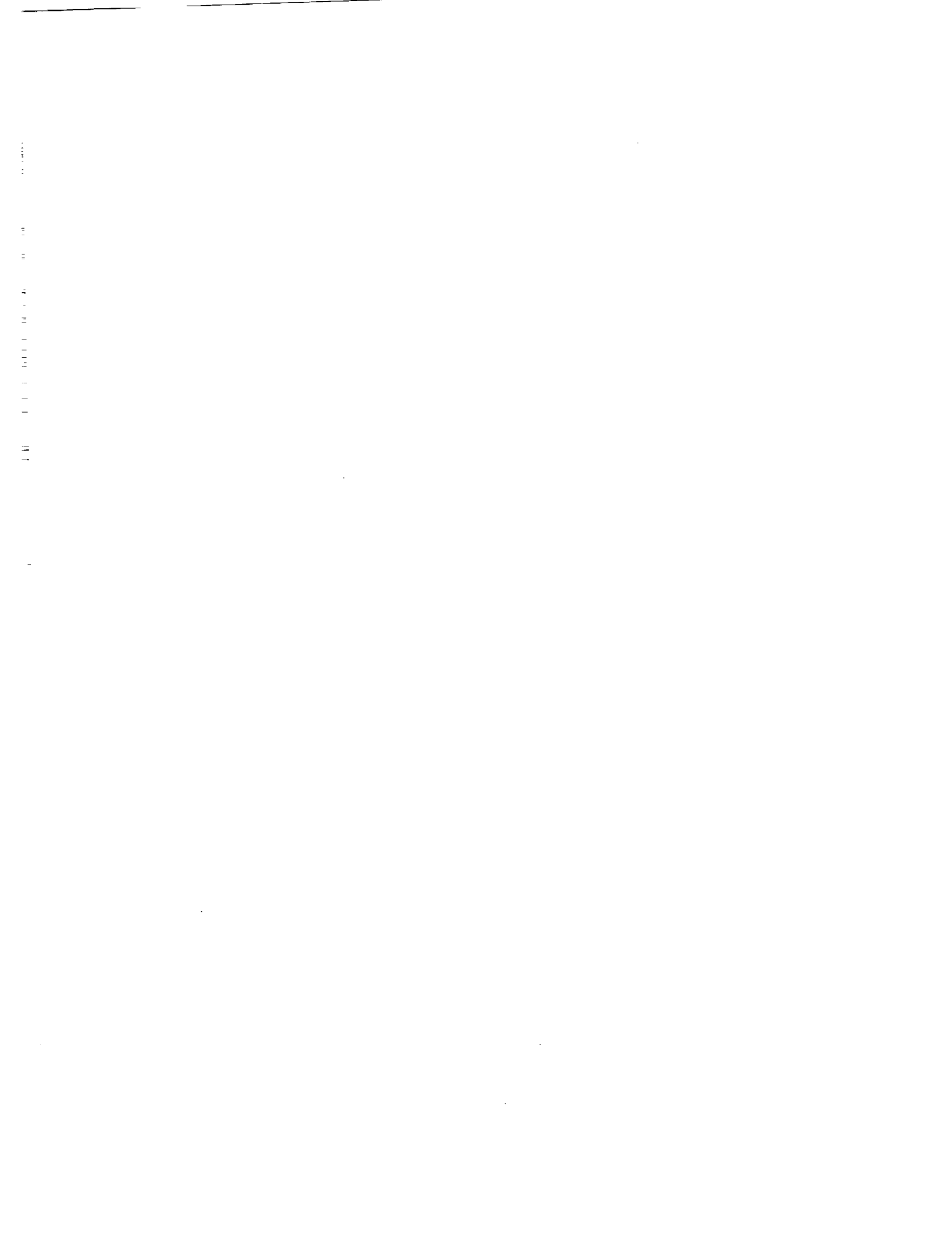


Figure 8. Directivities D ($\omega = 10.3$). $\Delta x = R/15.5$ (solid line), Reference solution (dotted line).



223-71
043481
294011 P10

A COMPUTATIONAL AEROACOUSTICS APPROACH TO DUCT ACOUSTICS

Douglas M. Nark *
Joint Institute for Advancement of Flight Sciences
The George Washington University
Hampton, Virginia 23681

SUMMARY

A staggered finite difference approach is utilized in studying benchmark duct acoustics problems (category 2). The numerical boundaries are handled through the use of buffer zones which may be formulated to allow inflow while absorbing any outgoing waves. In addition, the use of grid compression and some effects on solution quality are investigated.

INTRODUCTION

This work focuses on the application of a staggered finite difference scheme to the solution of two benchmark problems in duct acoustics (category 2). These problems were chosen in order to assess the use of such an approach in solving duct problems and to further validate the performance of 'buffer zones' at computational boundaries. Additionally, the geometries involved provide an opportunity to examine the effects of grid stretching and compression on the quality of the solutions obtained.

The finite difference scheme employs a fourth order spatial discretization with fourth order Runge-Kutta time integration which was chosen in light of results for previous benchmark problems [1]. The staggered approach involves calculation of the flow variables at different grid points in the computational domain. This may be illustrated by considering a grid square or 'cell'. This 'cell' is comprised of five grid points; one in the center, and one point at the midpoint of each of the walls. This is shown for cylindrical coordinates in figure 1. Scalar quantities are calculated at the center of the cell and the components of the vector quantities are calculated at the sides. The vector components in the r -direction are computed on the right and left sides, whereas the components in the z -direction are computed on the top and bottom. The entire computational domain may be thought of as a collection of these cells with the variables at the specified points. The next issue is the treatment of the physical and numerical boundaries, and although the geometries of the two problems are similar, it may be best to discuss that aspect of the problems separately.

PROBLEM 1

This problem involves the calculation of the acoustic field produced by a spherical source in the geometrical center of a finite length open-ended cylindrical duct placed in a uniform mean flow. Taking advantage of the axisymmetry of the geometry, the problem is cast in cylindrical coordinates with the z -axis being an axis of symmetry (figure 2). Along this axis, the r -component of velocity and the partial derivative of the pressure, p , with respect to r , $\frac{\partial p}{\partial r}$, are set equal to zero. Application of the fourth order stencil requires some special attention at this

*This is a portion of research being conducted in partial satisfaction of the requirements for the Degree of Doctor of Science with the School of Engineering and Applied Science of The George Washington University.

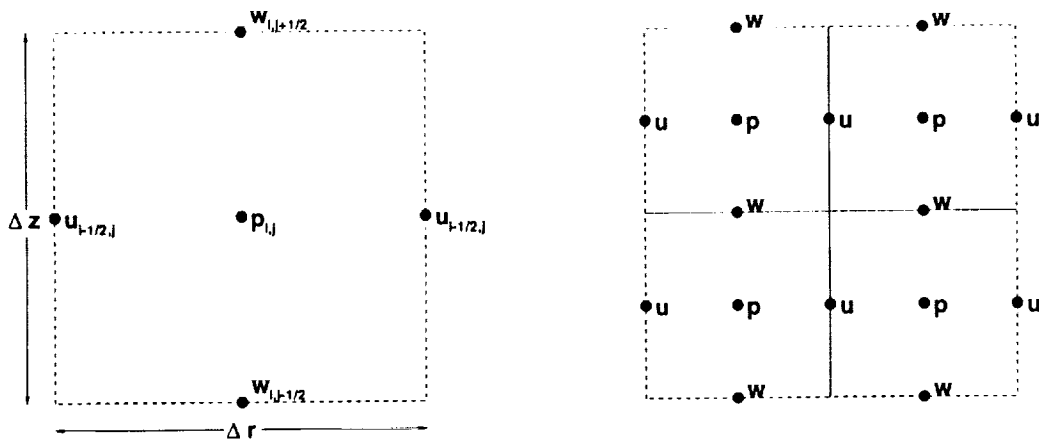


Figure 1: A portion of the computational domain

location because the finite difference stencils can extend beyond the axis. In this case, the condition on the pressure is used to obtain ghost values, and a full stencil may be used for $\frac{\partial p}{\partial r}$. The radial derivatives of the other variables are then shifted so that they include only interior points. The conditions on the duct wall are treated in much the same way following a procedure similar to that given by Tam and Dong [2]. Here, ghost points for pressure are obtained by using the w -momentum equation along the boundary. This allows a full stencil to be used for the term $\frac{\partial p}{\partial r}$. The stencils for the remaining variables are shifted so that they require only known data points.

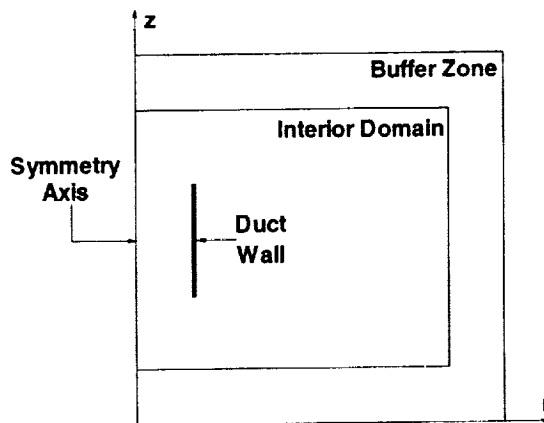


Figure 2: Problem 1 geometry

The remaining computational boundaries are a result of truncation of the infinite domain of propagation and are also illustrated in figure 2. These require outflow conditions which result in minimal reflection. Here, a technique involving an absorbing buffer zone was employed. In this formulation, a number of points is added to the computational domain to form a buffer zone. In this region, the original equations are modified in such a way that no wave will be reflected from the outer boundary of the buffer zone [3]. The construction of the modified equations in the buffer zone is accomplished by changing the domain of dependence for the problem, or equivalently by changing the dispersion relation near the boundary. The change from the interior domain, where

the original equations hold, to the outer edges of the buffer zone must be done in a smooth way in order to eliminate reflection caused by the inhomogeneity introduced.

One further aspect of this problem should be addressed before presenting results. The presence of the mean flow causes disparate wavelengths on the upstream and downstream sides of the acoustic source and therefore differing grid resolution requirements. A uniform grid would require a mesh spacing tailored to the shorter wavelengths and would be finer than necessary in regions where waves of longer wavelength were propagating. Thus, it would seem reasonable to employ a variable computational grid, which is compressed upstream of the source and stretched downstream, in order to minimize the total number of grid points and reduce computation time. This may be accomplished by applying independent variable transformations of the form

$$\begin{aligned}\xi &= \xi(r, z) \\ \zeta &= \zeta(r, z).\end{aligned}\quad (1)$$

The partial derivatives with respect to r and z then become

$$\begin{aligned}\frac{\partial}{\partial r} &= \frac{\partial \xi}{\partial r} \frac{\partial}{\partial \xi} + \frac{\partial \zeta}{\partial r} \frac{\partial}{\partial \zeta} = \xi_r \frac{\partial}{\partial \xi} + \zeta_r \frac{\partial}{\partial \zeta} \\ \frac{\partial}{\partial z} &= \frac{\partial \xi}{\partial z} \frac{\partial}{\partial \xi} + \frac{\partial \zeta}{\partial z} \frac{\partial}{\partial \zeta} = \xi_z \frac{\partial}{\partial \xi} + \zeta_z \frac{\partial}{\partial \zeta}.\end{aligned}\quad (2)$$

Since the duct walls are straight, the problem requires only a transformation which provides refinement near an interior point (*ie.* the source location or duct wall). One may be found in Anderson *et al* [4] and in this case is written as

$$\xi(r) = B_1 + \frac{1}{\tau_1} \sinh^{-1} \left[\left(\frac{r}{r_c} - 1 \right) \sinh(\tau_1 B_1) \right] \quad (3)$$

$$\zeta(z) = B_2 + \frac{1}{\tau_2} \sinh^{-1} \left[\left(\frac{z}{z_c} - 1 \right) \sinh(\tau_2 B_2) \right] \quad (4)$$

where

$$B_1 = \frac{1}{2\tau_1} \ln \left[\frac{1 + (\exp^{\tau_1} - 1)(r_c/h)}{1 + (\exp^{-\tau_1} - 1)(r_c/h)} \right] \quad 0 < \tau_1 < \infty$$

$$B_2 = \frac{1}{2\tau_2} \ln \left[\frac{1 + (\exp^{\tau_2} - 1)(z_c/h)}{1 + (\exp^{-\tau_2} - 1)(z_c/h)} \right] \quad 0 < \tau_2 < \infty.$$

Here, τ_1 and τ_2 are stretching parameters which produce more refinement at $r = r_c$ and $z = z_c$ for larger values (zero produces no stretching). If this transformation is applied to the governing equations, the following set is obtained

$$\frac{\partial \mathbf{A}}{\partial t} + \xi_r \frac{\partial \mathbf{B}}{\partial \xi} + \zeta_z \frac{\partial \mathbf{C}}{\partial \zeta} + \mathbf{D} = 0 \quad (5)$$

where \mathbf{A} , \mathbf{B} , \mathbf{C} , and \mathbf{D} are vectors given by

$$\mathbf{A} = \begin{Bmatrix} \rho \\ u \\ w \\ p \end{Bmatrix}$$

$$\mathbf{B} = \begin{Bmatrix} u \\ p \\ 0 \\ u \end{Bmatrix}$$

$$\mathbf{C} = \begin{Bmatrix} M_\infty \rho + w \\ M_\infty v \\ M_\infty w + p \\ M_\infty p + w \end{Bmatrix}$$

$$\mathbf{D} = \begin{Bmatrix} \frac{u}{r} - S \\ 0 \\ 0 \\ \frac{u}{r} - S \end{Bmatrix}.$$

Here, p and ρ are the pressure and density, (u, w) are the velocity components in the (r, z) directions, and S is the source given by

$$S = 0.1 \exp \left[-48 (\ln 2) \left(\frac{kD}{2\pi} \right)^2 (x^2 + y^2) \right] \cos(kDt). \quad (6)$$

Having discussed the numerical solution technique, it is possible to present results and examine some of the possible effects that variable grids may have on solution quality.

Results

Initially, the source was given by equation (6) with $kD = 16\pi$. The pressure contours for this case are presented in figure 3 to offer some guide to the form of the directivity pattern. Here, the pipe has been turned on its side (with the positive z -axis directed to the right) and a uniform mean flow at a Mach number of 0.5 is present in this direction. The disparate wavelengths caused by the mean flow may be seen clearly. Also presented in this figure is a plot of the RMS pressure, $\overline{p^2}$, along a circular arc $x^2 + y^2 = (2.5)^2$ at $\Delta\theta = 1^\circ$, where the angle θ is measured from the positive z -axis ($\theta = 0$ corresponds to the downstream side of the source). It is evident from these plots that the radiated pressure drops off considerably around $\theta = 90^\circ$.

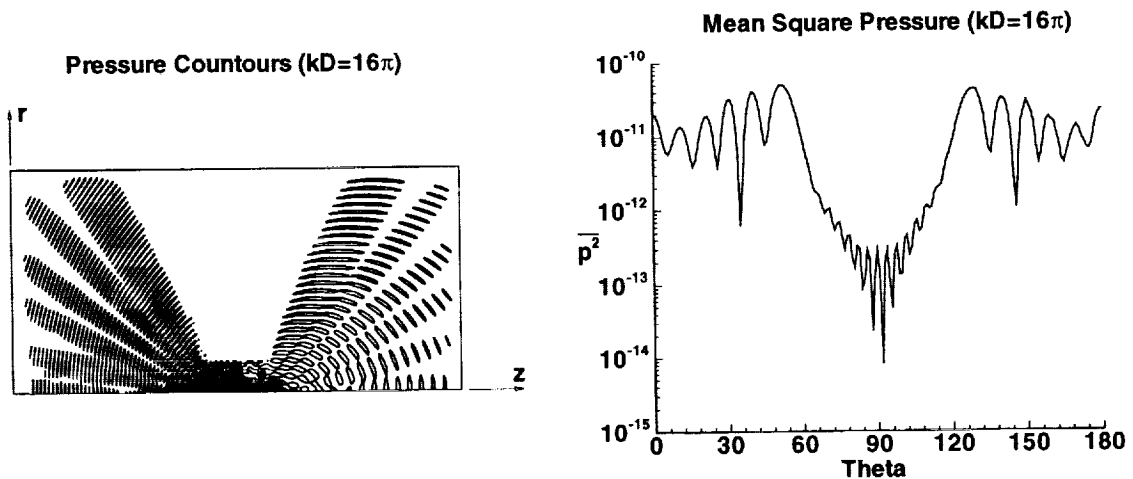


Figure 3: Pressure contours and RMS pressure along $r = 2.5$ for $kD = 16\pi$

Although reasonable results may be obtained for the case given by $kD = 16\pi$, a significant amount of computation time was required. Therefore, a source characterized by equation (6) with $kD = 4.409507\pi$ was studied. With this lower frequency, computation time was decreased and various grids more easily studied. Figure 4 shows the pressure contours and RMS pressure for this case on a uniform grid. One feature to be noticed from these plots is that the radiated pressure appears to be much more uniform and the null around $\theta = 90^\circ$ is much smaller than in the previous case. At this point, it was then possible to look at results obtained on grids compressed by differing amounts around the duct wall and upstream end. As an example, figure 5 shows the pressure contours, as well as the actual grid for the situation in which $\tau_1 = 2.0$ and $\tau_2 = 5.0$ in equations (3) and (4). Comparison of the pressure contours in figures 4 and 5 shows that similar results are obtained. However, this is simply a qualitative comparison and a better understanding of the effects of the variable grid is gathered by comparing the plots of RMS pressure $\overline{p^2}$ versus θ .

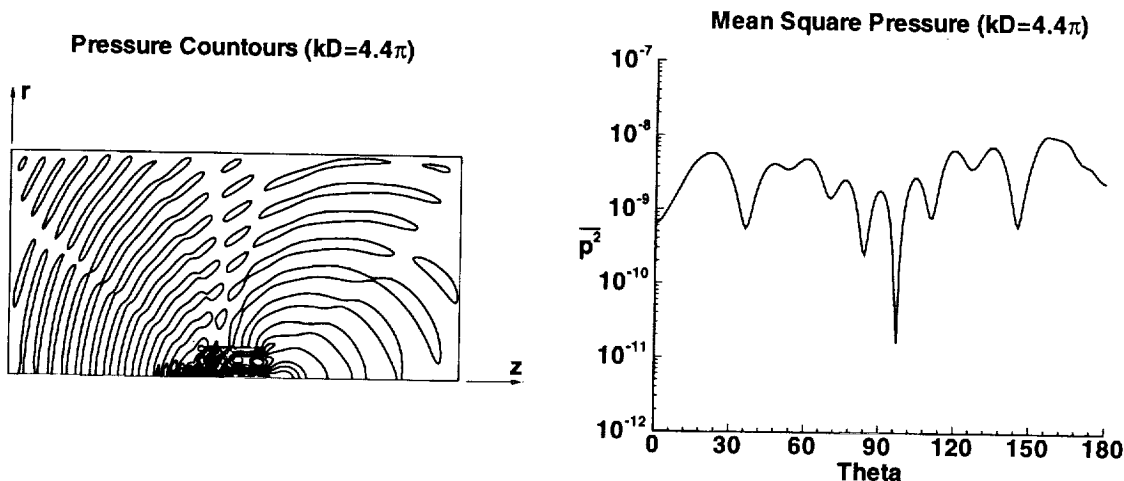


Figure 4: Pressure contours and RMS pressure along $r = 2.5$ for $kD = 4.4\pi$

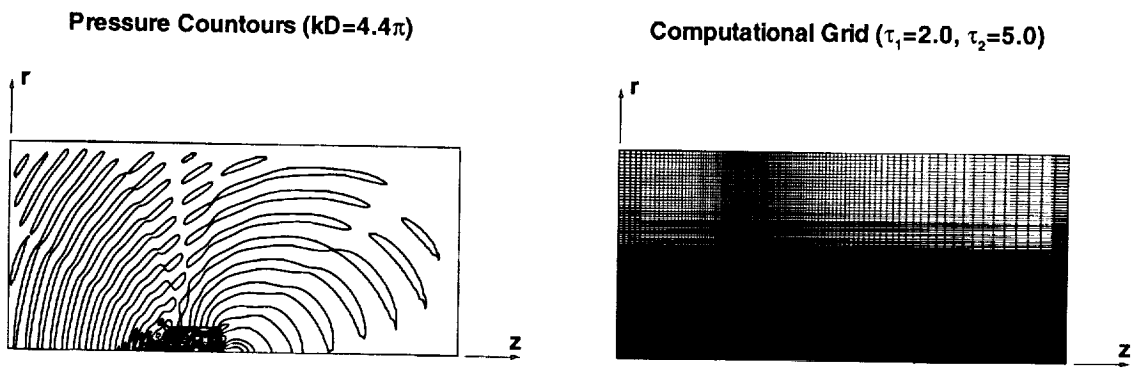


Figure 5: Pressure contours and computational grid for $kD = 4.4\pi$ with $\tau_1 = 2.0$, $\tau_2 = 5.0$

Several different grids of varying configurations (*ie* different values of τ_1 and τ_2) were employed in solving the $kD = 4.409507\pi$ case, however the results for only four of the grids are required to bring an issue to light. The size of these grids and the stretching parameters are included in table 1. Figure 6 shows the results for two uniform grids, and one compressed the same amount around the duct wall and upstream end. In this plot, run 1 may be considered a

baseline case, as it employed a very fine uniform mesh. The total number of grid points was then reduced in run 2. And in run 3, the number of grid points was reduced even further, but compression was then applied. As can be seen in figure 6, the results for run 3 match the baseline case much better than run 2 and overall it appears that the variable grid performed effectively. There does, however, appear to be some oscillation in the solution as θ approaches 180° . This may be further studied by utilizing a grid which is identical to run 3 except that it is compressed even further around the upstream end of the duct. These cases are plotted in figure 7 and appear to be similar over a range of θ .

Run	Grid Size	τ_1	τ_2
1	250x500	0.0	0.0
2	160x350	0.0	0.0
3	106x228	2.0	2.0
4	106x228	2.0	5.0

Table 1: Grid parameters for various cases

However, there is again some oscillation evident as θ approaches 180° which is more prevalent for run 4. A possible cause of this oscillation may be that the acoustic waves are actually propagating through a fine grid which becomes coarser as the distance from the duct end increases. Thus, as the grid is compressed further (*ie* larger values of τ), this transition from fine to coarse grid becomes more abrupt and the possibility of introducing numerical error increased. It would then seem that grid refinement may be applied effectively, with the understanding that compressing the grid too much may lead further error. With these ideas in mind, the second problem in this category may be discussed.

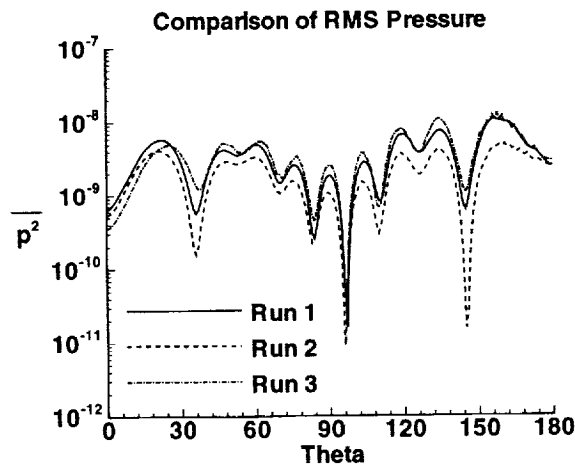


Figure 6: Comparison of RMS pressure for various grid configurations

PROBLEM 2

This problem involves the propagation of sound waves through a semi-infinite circular duct and the subsequent radiation to an unbounded domain. At first glance, this problem appears to require a much different computational domain than problem 1. However, the form of the

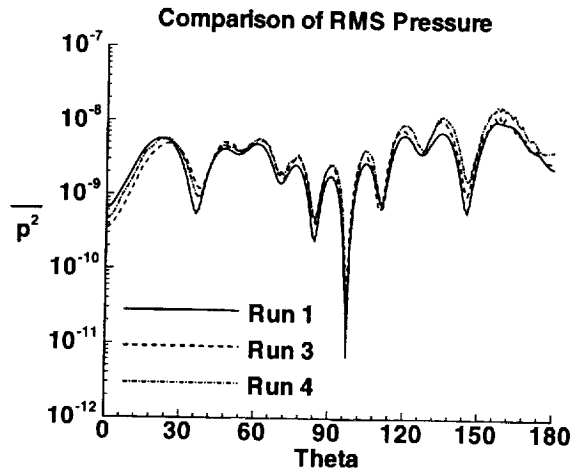


Figure 7: Comparison of RMS pressure for various grid configurations

incoming wave allows some simplification to be made. This incoming sound wave is taken to be a radial duct mode (specifically $n = 0, m = 2$) given by

$$\begin{bmatrix} u \\ v \\ w \\ p \end{bmatrix} = \text{Re} \left\{ \begin{bmatrix} -i \frac{\mu_{02}}{\omega} J_0'(\mu_{02}r) \\ 0 \\ \frac{\sqrt{\omega^2 - \mu_{02}^2}}{\omega} J_0(\mu_{02}r) \\ J_0(\mu_{02}r) \end{bmatrix} \exp \left[\sqrt{\omega^2 - \mu_{02}^2} z - \omega t \right] \right\} \quad (7)$$

where p is the pressure and (u, v, w) are the velocity components in the radial, azimuthal, and longitudinal directions respectively. Thus, the problem may be taken to be axisymmetric and a domain similar to that for problem 1 may be employed. Figure 8 shows various components of the problem geometry. Again, the z -axis is a symmetry axis and the other boundaries are a result of the truncation of the infinite physical domain. All of these boundaries, as well as the solid duct walls, are treated in the same way as problem 1.

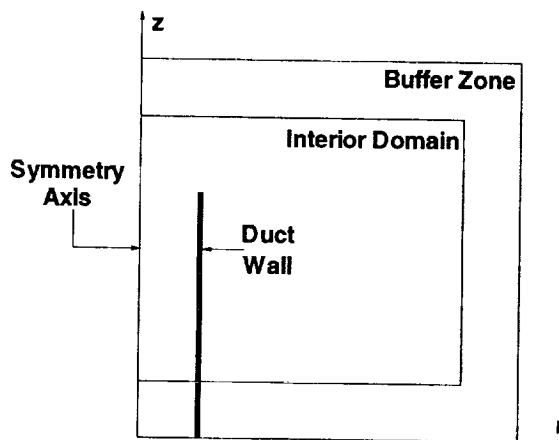


Figure 8: Problem 2 geometry

There is some difficulty in the treatment of the incoming duct mode within the buffer zone. In this region, the governing equations are solved only for the outgoing waves by simply subtracting

the incoming wave solution from the full set of equations. If this procedure were not carried out, then an incoming mode specified at the boundary of the domain, or within the buffer zone, would never reach the actual computational domain. In effect, these waves would be swept out of the domain by the buffer zone and the duct would not see a disturbance. Once the incoming mode is specified, a computational grid is constructed keeping in mind that the radial mode requires differing resolution in the r and z directions.

Results

The first case attempted was that for which $\omega = 10.3$ in equation (7). In figure 9, the pressure contours are presented to aid in qualitatively understanding the directivity pattern. In addition, a plot of the actual directivity, $D(\theta)$, versus θ is included. Here, θ is the angle measured from the z -axis and the directivity is defined as

$$D(\theta) \equiv \lim_{R \rightarrow \infty} \overline{R^2 p^2(R, \theta, t)},$$

where the overline denotes the time average of the quantity. Since the computational domain can not extend to infinity, the directivity was calculated at $R = 6$. Also included for this case are plots of the pressure envelope in figures 10 and 11. The pressure envelope is given by

$$P(z) = \max_{\text{over time}} p(r, z, t)$$

and was calculated from $z = -6$ to $z = 0$, with $z = 0$ being the outflow duct end.

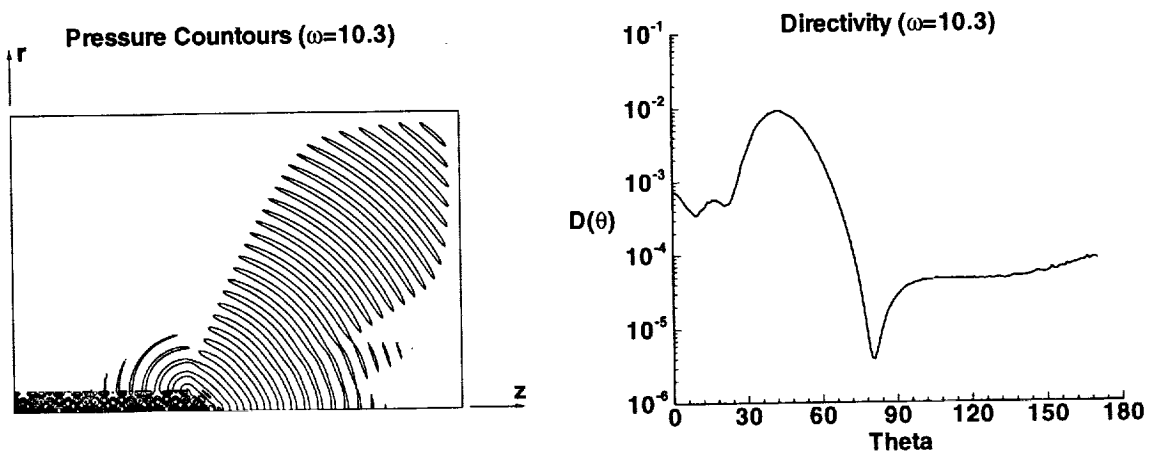


Figure 9: Pressure contours and directivity for $\omega = 10.3$

Another set of calculations was performed in which $\omega = 7.2$ in equation (7). This frequency is very close to the cutoff frequency of the duct making the calculation more difficult. The numerical approach appears to give reasonable results as seen in the pressure contour and directivity plots of figure 12 and the pressure envelope plots of figures 13 and 14.

DISCUSSION

The results from these problems presented above show that the staggered finite difference approach can be applied effectively to some duct acoustics problems, provided that specific

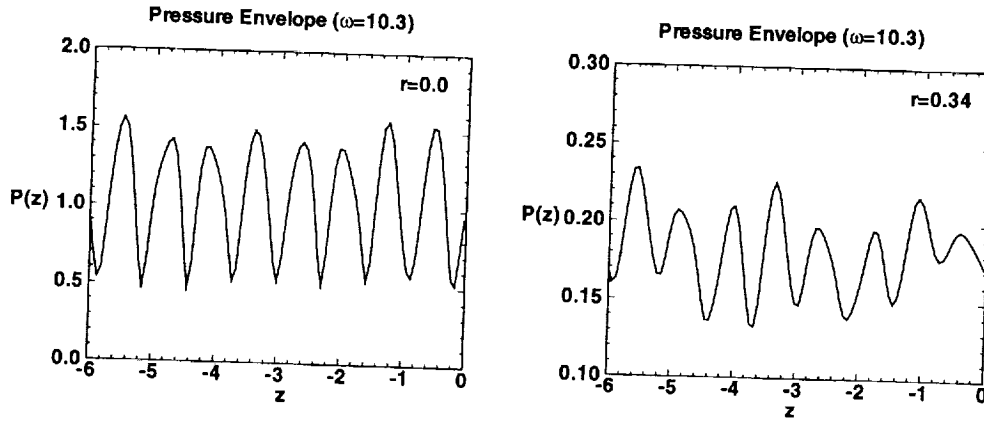


Figure 10: Pressure envelope at various locations

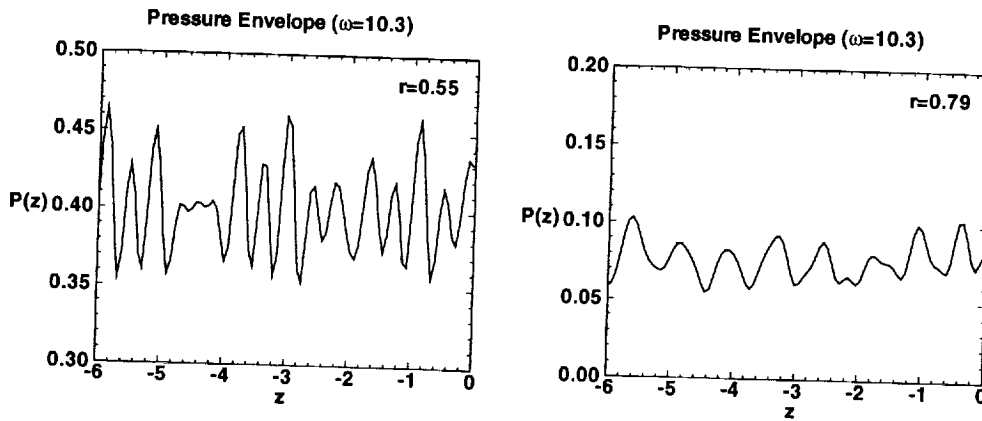


Figure 11: Pressure envelope at various locations

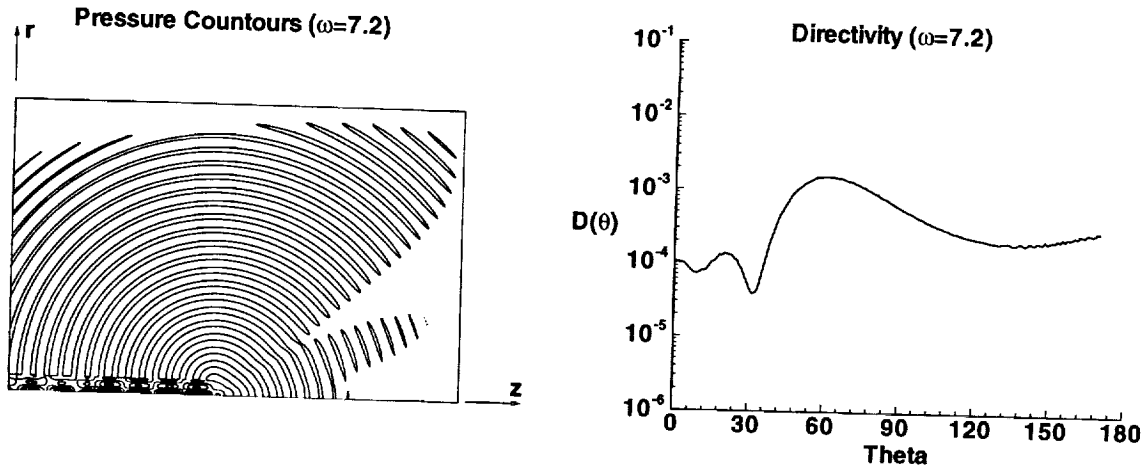


Figure 12: Pressure contours and directivity for $\omega = 7.2$

requirements inherent to the geometries (*ie.* mean flows, cutoff modes) are taken into account. In addition, the buffer zone approach handled both problems well, including the introduction of an incoming duct mode while sweeping other waves out of the domain. Finally, as evidenced by results from problem 1, grid compression must be carried out carefully so that the transition from

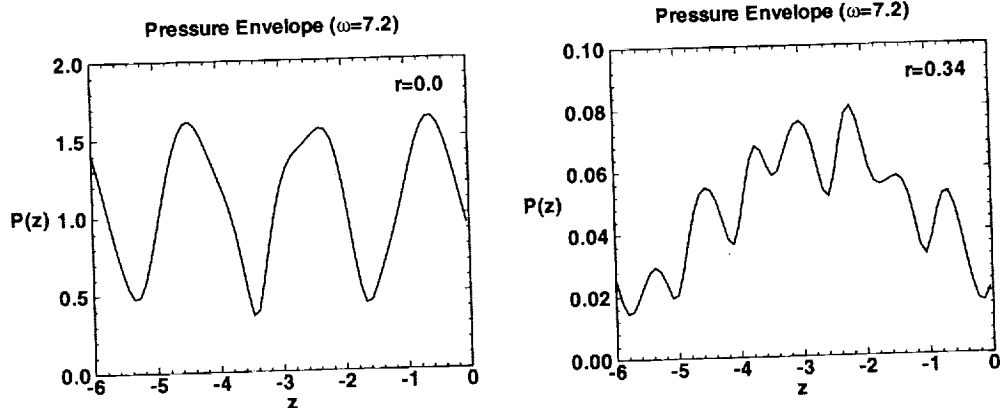


Figure 13: Pressure envelope at various locations

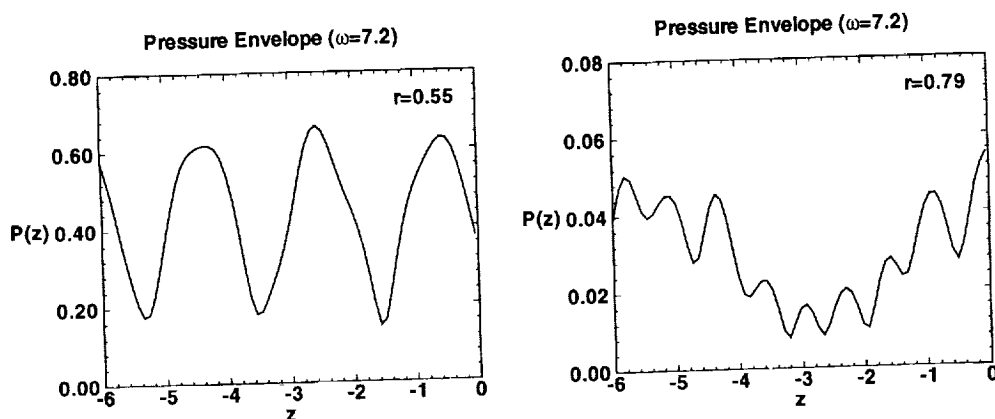


Figure 14: Pressure envelope at various locations

a 'fine' to 'coarse' grid takes place gradually. Overall, however, it was found that this technique may be effective in providing more efficient calculations by reducing the total number of grid points while maintaining solution quality.

REFERENCES

- [1] Nark, D. M., "The Use of Staggered Schemes and an Absorbing Buffer Zone for Computational Aeroacoustics", *ICASE/LaRC Workshop on Benchmark Problems in Computational Aeroacoustics (CAA)*, NASA C.P. 3300, Hardin, J. C., Ristorcelli, J. R., and Tam, C. K. W., (eds), pp. 233-244, (May 1995).
- [2] Tam, C. K. W., and Dong, Z., "Solid Wall Boundary Conditions for Computational Aeroacoustics". *Proceedings of the Forum on Computational Aero- and Hydro- Acoustics*, Washington, DC, June 20-24, 1993.
- [3] Ta'asan, S., and Nark, D. M. "An Absorbing Buffer Zone Technique for Acoustic Wave Propagation", AIAA paper no. 95-0164, 1995.
- [4] Anderson, D. A., Tanehill, J. C., and Pletcher, R.H., *Computational Fluid Mechanics and Heat Transfer*, McGraw Hill, 1984.

524-71
043 482
294012 P10

A VARIATIONAL FINITE ELEMENT METHOD FOR COMPUTATIONAL AEROACOUSTIC CALCULATIONS OF TURBOMACHINERY NOISE

Kenneth C. Hall¹
Department of Mechanical Engineering and Materials Science
Duke University
Durham, NC 27708-0300

ABSTRACT

A variational method for computing the unsteady aeroacoustic response of turbomachinery blade rows to incident vortical gusts is presented. A variational principle which describes the harmonic small disturbance behavior of the full potential equations about a uniform mean flow is developed. Four-node isoparametric finite elements are used to discretize the variational principle, and the resulting discretized equations are solved efficiently using LU decomposition. Results computed using this technique are found to be in excellent agreement with those obtained using semi-analytical methods.

INTRODUCTION

In this paper, an extension of Bateman's [1] variational principle – previously derived by Hall [2] for aeroelastic calculations and later extended by Lorence and Hall [3] for aeroacoustic applications – is used to solve for the aeroacoustic response of a two-dimensional cascade of airfoils subjected to an incident vortical gust. The variational principle describes the small disturbance behavior of the compressible full potential equation. The small-disturbance variational principle is discretized using bilinear four-node isoparametric finite elements, and the resulting set of linear equations is solved using LU decomposition to obtain the unknown perturbation velocity potential.

Also presented is a numerically exact far-field boundary condition. To prevent spurious reflections of outgoing waves as they pass through the far-field computational boundary, so-called nonreflecting boundary conditions must be applied. Previous investigators have found the analytical behavior of the unsteady flow field and matched these solutions to the computational solution at the far-field boundary [4, 5, 6, 7]. In this paper, the exact far-field behavior of the *discretized* small disturbance equations is found by performing an eigenanalysis of the discretized equations in the far-field. The resulting eigenmodes are then used to construct perfectly nonreflecting boundary conditions.

The present variational finite element method is both accurate and computationally efficient. For example, typical aeroacoustic calculations require less than one minute of CPU on a modern desktop workstation computer. A number of computational examples are presented; results computed using the present method are shown to be in excellent agreement with exact solutions.

THEORY

In the present analysis, the flow through a compressor or turbine blade row is assumed to be inviscid, isentropic, and two-dimensional. Furthermore, the fluid is assumed to be an ideal gas with constant specific heats. For the Category 3 turbomachinery problem, defined for the Second Computational Aeroacoustics Workshop on Benchmark Problems, the cascade is composed of flat plate airfoils which do no steady turning so that the mean or steady flow is uniform. Thus, the unsteady flow through the cascade of airfoils can be modelled as the sum of three parts: a uniform steady flow, an unsteady

¹Copyright © 1997 by Kenneth C. Hall. Published by NASA with permission.

vortical disturbance, and an unsteady perturbation velocity. The unsteady perturbation velocity flow is irrotational (except in the wake) so that the perturbation velocity may be represented by the gradient of a scalar velocity potential, ϕ . Thus the total velocity $\hat{\mathbf{V}}$ may be expressed as

$$\hat{\mathbf{V}}(x, y, z) = \mathbf{U} + \mathbf{v}_R(x, y, t) + \nabla\phi(x, y, t) \quad (1)$$

where \mathbf{U} is the (uniform) steady or mean flow, $\mathbf{v}_R(x, y)$ is the velocity associated with a divergence free vorticity field, and $\phi(x, y)$ is the unsteady perturbation potential. Note that here we have assumed that the unsteady quantities \mathbf{v}_R and $\nabla\phi$ are small compared to the mean flow \mathbf{U} . Note also that since the mean flow is uniform, the vortical disturbance is simply convected through the cascade without distortion, and further, there is no unsteady pressure associated with the vorticity itself.

Next, the expression for the velocity field, Eq. (1), is substituted into the conservation of mass, which is given by

$$\frac{\partial \hat{\rho}}{\partial t} + \nabla \cdot (\hat{\rho} \hat{\mathbf{V}}) = 0 \quad (2)$$

where $\hat{\rho}$ is the density of the fluid. Collecting terms which are first order in the unsteady quantities, one obtains

$$\frac{\partial \rho}{\partial t} + \nabla \cdot (R \nabla \phi + \rho \mathbf{U}) = 0 \quad (3)$$

where R and ρ are the steady flow (zeroth-order) density and unsteady perturbation (first-order) density, respectively. Integrating the momentum equation and making use of the isentropic assumption, one can obtain expressions for the unsteady perturbation pressure p and density ρ in terms of the perturbation potential, i.e.

$$p = -R \frac{D\phi}{Dt} = -R \left(\frac{\partial \phi}{\partial t} + \mathbf{U} \cdot \nabla \phi \right) \quad (4)$$

and

$$\rho = -\frac{R}{C^2} \frac{D\phi}{Dt} = -\frac{R}{C^2} \left(\frac{\partial \phi}{\partial t} + \mathbf{U} \cdot \nabla \phi \right) \quad (5)$$

where D/Dt is the linearized substantial derivative operator, and C is the steady flow speed of sound. Equation (4) is recognized as the linearized Bernoulli equation. Finally, substitution of Eq. (5) into the conservation of mass, Eq. (3), gives the desired linearized potential equation,

$$\nabla \cdot R \nabla \phi - \nabla \cdot \left[\frac{R}{C^2} \left(\mathbf{U}^T \nabla \phi + \frac{\partial \phi}{\partial t} \right) \mathbf{U} \right] - \frac{R}{C^2} \left(\mathbf{U}^T \nabla \frac{\partial \phi}{\partial t} + \frac{\partial^2 \phi}{\partial t^2} \right) = 0 \quad (6)$$

To complete the specification of the problem, boundary conditions must be specified on the surface ∂D bounding the solution domain D (see Fig. 1). On the airfoil surfaces, there can be no mass flux through the airfoil surface so that

$$R \frac{\partial \phi}{\partial n} = -R \mathbf{v}_R \cdot \mathbf{n} \quad (7)$$

where \mathbf{n} is the unit normal to the airfoil. The wake may also be thought of as an impermeable surface. However, since the wake will in general oscillate unsteadily, Eq. (7) must be slightly modified to account for the upwash produced by the wake motion. On either side of the wake, we require

$$R \frac{\partial \phi}{\partial n} = R \left(-\mathbf{v}_R \cdot \mathbf{n} + \frac{\partial r}{\partial t} + V \frac{\partial r}{\partial s} \right) \quad (8)$$

where $r = r(s, t)$ is the displacement of the wake normal to its mean position, s is distance along the wake, and V is the magnitude of the steady velocity aligned with the mean wake position. To

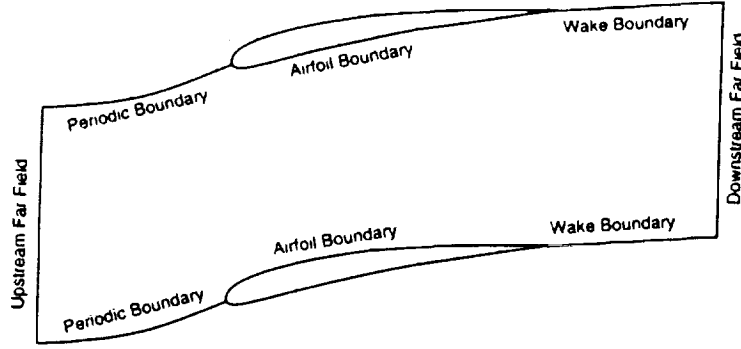


Figure 1: Computational domain D bounded by surface ∂D .

provide closure for the wake position, an additional condition is required, that is, the pressure must be continuous across the wake. Hence,

$$[p] = \left[\left[-R \frac{D\phi}{Dt} \right] \right] = 0 \quad (9)$$

where $[p]$ denotes the pressure jump across the wake. At the trailing edge of the airfoil, the wake displacement is prescribed to be zero. This requirement is equivalent to the Kutta condition.

At the periodic boundaries, the complex periodicity condition

$$\phi(x, y + g) = \phi(x, y)e^{j\sigma} \quad (10)$$

is applied, where g is the blade-to-blade gap. This boundary condition permits us to reduce the computational domain to a single blade passage significantly reducing the computational effort required to compute the unsteady flow field.

Finally, boundary conditions are required at the upstream and downstream far-field boundaries to prevent outgoing waves from being reflected back into the computational domain. These conditions will be discussed in the following section.

In an earlier paper, Hall [2] showed that the linearized potential equation, Eq. (6), is the Euler-Lagrange equation of a variational principle which states that the Π is stationary, where

$$\Pi = \frac{1}{T} \int_T \int \int_D \frac{1}{2} R \left[-\nabla \phi^T \nabla \phi + \frac{1}{C^2} (\mathbf{U}^T \nabla \phi + \phi_t)^2 \right] dx dy dt + \frac{1}{T} \int_T \oint_{\partial D} q \phi ds \quad (11)$$

and where T is the temporal period of the unsteadiness, and ∂D is the surface bounding the spatial domain D . Taking the variation of Π with respect to the unknown ϕ and setting the result to zero gives,

$$\delta \Pi = \frac{1}{T} \int_T \int \int_D R \left[-\nabla \phi^T \nabla \delta \phi + \frac{1}{C^2} (\mathbf{U}^T \nabla \phi + \phi_t) (\mathbf{U}^T \nabla \delta \phi + \delta \phi_t) \right] dx dy dt + \frac{1}{T} \int_T \oint_{\partial D} q \delta \phi ds = 0 \quad (12)$$

Application of various forms of Gauss' theorem and integration by parts gives

$$\begin{aligned} \delta \Pi = \frac{1}{T} \int_T \int \int_D \left\{ \nabla \cdot R \nabla \phi - \nabla \cdot \left[\frac{R}{C^2} \left(\mathbf{U}^T \nabla \phi + \frac{\partial \phi}{\partial t} \right) \mathbf{U} \right] - \frac{R}{C^2} \left(\mathbf{U}^T \nabla \frac{\partial \phi}{\partial t} + \frac{\partial^2 \phi}{\partial t^2} \right) \right\} \delta \phi dx dy dt \\ - \frac{1}{T} \int_T \oint_{\partial D} \left(R \frac{\partial \phi}{\partial n} - q \right) \delta \phi ds = 0 \end{aligned} \quad (13)$$

In the interior of the domain D , the integrand of the first integral must vanish for arbitrary variations $\delta \phi$. Thus, the Euler-Lagrange equation is just given by Eq. (6). On the boundary of the computational

domain ∂D , the second integral will vanish if ϕ is specified (Dirichlet conditions), or if $R\partial\phi/\partial n - q = 0$ (Neumann conditions). The latter condition is used to include the influence of upwash on the airfoil induced by the vortical gust \mathbf{v}_R and the wake motion τ [Eqs. (7) and (8)].

For gust disturbances which are temporally harmonic, the unsteady perturbation potential ϕ will also be harmonic. Thus, it will be convenient to let

$$\phi(x, y, t) \rightarrow \text{Re} [\phi(x, y)e^{-j\omega t}] = \frac{1}{2} [\phi(x, y)e^{-j\omega t} + \bar{\phi}(x, y)e^{+j\omega t}] \quad (14)$$

where $\phi(x, y)$ is now the complex amplitude of the perturbation potential, and $\bar{\phi}(x, y)$ is its complex conjugate.

Substitution of the simple harmonic motion assumption into the functional Π yields the functional for the variational principle which describes the behavior of the harmonic small disturbance potential, ϕ . The result is

$$\begin{aligned} \Pi_{\text{shm}} = \frac{1}{2} \iint_D R \left\{ -\nabla\bar{\phi}^T \nabla\phi + \frac{1}{C^2} \left[\nabla\bar{\phi}^T \mathbf{U} \mathbf{U}^T \nabla\phi - j\omega (\nabla\bar{\phi}^T \mathbf{U}\phi - \bar{\phi} \mathbf{U}^T \nabla\phi) + \omega^2 \bar{\phi}\phi \right] \right\} dx dy \\ + \frac{1}{T} \int_T \int_{\partial D} q \bar{\phi} ds + \text{complex conjugate terms} \end{aligned} \quad (15)$$

Taking the variation of Eq. (15) and setting the result to zero and applying the divergence theorem as before gives the desired Euler-Lagrange equation and boundary conditions which describe the harmonic small disturbance behavior of the flow. The Euler-Lagrange is given by

$$\nabla \cdot R \nabla\phi - \nabla \cdot \left[\frac{R}{C^2} (\mathbf{U}^T \nabla\phi - j\omega\phi) \mathbf{U} \right] + \frac{R}{C^2} (j\omega \mathbf{U}^T \nabla\phi + \omega^2\phi) = 0 \quad (16)$$

As expected, Eq. (16) is identical to Eq. (6) with the operator $\partial/\partial t$ replaced by $-j\omega$. On the boundaries of the domain, we have the natural boundary condition

$$R \frac{\partial\phi}{\partial n} - q = 0 \quad (17)$$

which can be used to describe the upwash due to the wake or the periodic boundary conditions. For additional details on the modifications to the variational principle required to compute unsteady flows in cascade, the interested reader is referred to Hall [2].

NUMERICAL SOLUTION TECHNIQUE

Because the unsteady solutions are spatially periodic, the solution domain can be reduced to a single blade passage. Within a single passage, an H-grid of quadrilateral cells is generated algebraically. The unsteady variational principle, Eq. (15), is then discretized using conventional finite element techniques. In the present work, a four-node isoparametric element is used. Consider the n th quadrilateral element in the computational domain. The values of the unsteady velocity perturbation at the corners of the element, $\{\phi\}_n$, are interpolated into the interior of the element using an interpolation of the form

$$\phi(x, y) = [\mathbf{N}]_n \{\phi\}_n \quad (18)$$

where $[\mathbf{N}]_n$ is a row vector of interpolation functions. Then, for example, the local stiffness matrix is given by

$$\begin{aligned} [\mathbf{k}]_n = \iint_{\Omega_n} \left\{ -[\mathbf{N}'^T]_n [\mathbf{N}]_n + \frac{1}{C^2} \left[[\mathbf{N}'^T]_n \nabla' \Phi \nabla' \Phi^T [\mathbf{N}]_n \right. \right. \\ \left. \left. - j\omega ([\mathbf{N}'^T]_n \nabla' \Phi [\mathbf{N}]_n - [\mathbf{N}]_n^T \nabla' \Phi^T [\mathbf{N}'^T]_n) + \omega^2 [\mathbf{N}]_n^T [\mathbf{N}]_n \right] \right\} dx dy \end{aligned} \quad (19)$$

where

$$[\mathbf{N}']_n = \begin{bmatrix} \frac{\partial N_1}{\partial x} & \frac{\partial N_2}{\partial x} & \frac{\partial N_3}{\partial x} & \frac{\partial N_4}{\partial x} \\ \frac{\partial N_1}{\partial y} & \frac{\partial N_2}{\partial y} & \frac{\partial N_3}{\partial y} & \frac{\partial N_4}{\partial y} \end{bmatrix}_n$$

The local stiffness matrix, Eq. (19), is identical to that found by Whitehead using a Galerkin method (c.f. Eq. (25) of Ref. [5]). For cells which are located on the computational boundary, additional contributions to the stiffness matrix and/or an inhomogeneous "force vector" \mathbf{b}_n arise for those regions in which Neumann conditions are applied (along the airfoil and wake surfaces).

Having computed the local stiffness matrices and force vectors, the global system of equations is assembled. The assembly process is simplified because of the regular structure afforded by the H-grid. To provide wake closure, auxiliary finite difference equations are applied along the wake to enforce pressure continuity, and one equation is introduced at the trailing edge that specifies that the wake must remain attached to the trailing edge ($r = 0$). The resulting finite element scheme is spatially second-order accurate.

For unsteady flow computations, nonreflecting boundary conditions are required at the far-field boundaries so that the flow field may be computed on a computational domain of finite extent. Without nonreflecting boundary conditions, outgoing waves would produce spurious reflections at the far-field boundary that would corrupt the solution. Previous investigators have found the exact analytical behavior of the linearized potential [4, 5] and linearized Euler [6] equations and matched these analytical solutions to numerical solutions at the far-field boundary. In this paper, the exact far-field behavior of the *discretized* small disturbance equations is found by performing an eigenanalysis of the discretized equations in the far-field. The resulting eigenmodes are then used to construct perfectly nonreflecting boundary conditions (see also Ref. [8]).

The computational grid used in the present analysis is an H-grid. If in the far-field the grid spacing in the axial direction is uniform and the "streamline" grid lines are parallel, then the discretized equations are identical from axial grid line to axial grid line as one moves away from the cascade. The discretized equations at the i th axial station in the far field are

$$[\mathbf{A}]\{\Phi_{i-1}\} + [\mathbf{B}]\{\Phi_i\} + [\mathbf{C}]\{\Phi_{i+1}\} = 0 \quad (20)$$

where $\{\Phi_i\}$ is the solution at the nodes of the i th axial station and contains not only the unsteady perturbation potential, but also the wake motion r in the downstream region. The matrices $[\mathbf{A}]$, $[\mathbf{B}]$, and $[\mathbf{C}]$ are sparse matrices which do not vary from axial station to axial station in the far-field. At the upstream far-field boundary ($i = 1$) the discretized equations are

$$[\mathbf{A}]\{\Phi_0\} + [\mathbf{B}]\{\Phi_1\} + [\mathbf{C}]\{\Phi_2\} = 0 \quad (21)$$

The $i = 0$ station corresponds to a line of false nodes. Hence the solution Φ_0 is not actually calculated but must be expressed in terms of the solution at stations $i = 1$ and $i = 2$.

Because of the periodic nature of this equation, one can hypothesize that solutions in the far field are of the form

$$\{\Phi_i\} = \sum_{n=1}^N z_n^i \{\bar{\Phi}_n\} \quad (22)$$

where N is the number of unknowns per station. Substitution of Eq. (22) into Eq. (20) gives

$$\sum_{n=1}^N z_n^{i-1} \left[[\mathbf{A}] + z_n[\mathbf{B}] + z_n^2[\mathbf{C}] \right] \{\bar{\Phi}_n\} = 0 \quad (23)$$

For this series to be zero, each term in the series must vanish so that

$$\left[[\mathbf{A}] + z_n[\mathbf{B}] + z_n^2[\mathbf{C}] \right] \{\bar{\Phi}_n\} = 0 \quad (24)$$

This is recognized as an eigenvalue problem for the eigenmode $\{\bar{\Phi}_n\}$ and the corresponding eigenvalues z_n . The problem is put into a more conventional form by recasting Eq. (24) in state-space form, i.e.,

$$\begin{bmatrix} 0 & \mathbf{I} \\ -\mathbf{A} & -\mathbf{B} \end{bmatrix} \begin{Bmatrix} \bar{\Phi}_n \\ z_n \bar{\Phi}_n \end{Bmatrix} = z_n \begin{bmatrix} \mathbf{I} & 0 \\ 0 & \mathbf{C} \end{bmatrix} \begin{Bmatrix} \bar{\Phi}_n \\ z_n \bar{\Phi}_n \end{Bmatrix} \quad (25)$$

By examining the eigenvalues of Eq. (25), one can determine whether the n th eigenmode is travelling away from or toward the cascade. On physical grounds, no acoustic waves should travel toward the cascade since such waves would originate outside the computational domain or would be due to artificial reflections at the far-field boundary. At the upstream far-field boundary, eigenmodes with eigenvalues with a magnitude less than unity represent incoming waves which decay as they move toward the cascade, and hence, should be excluded from the solution. If the magnitude of the eigenvalue is greater than unity, the corresponding eigenmode is an outgoing mode which decays as it moves away from the cascade. Such a wave is allowed. Finally, if the magnitude of the eigenvalue is unity, then the direction that the wave travels is determined by its group velocity and again incoming waves are to be excluded.

If the solution is known at station i and $i+1$ of the far field, then one can compute the solution at some other set of stations j and $j+1$ by decomposing the solution at station i and $i+1$ into eigenmodes, propagating the individual eigenmodes to stations j and $j+1$, and then recombining the eigenmodes. Mathematically this is expressed as

$$\begin{Bmatrix} \Phi_j \\ \Phi_{j+1} \end{Bmatrix} = \begin{bmatrix} \mathbf{T}_{11} & \mathbf{T}_{12} \\ \mathbf{T}_{21} & \mathbf{T}_{22} \end{bmatrix}^{j-i} \begin{Bmatrix} \Phi_i \\ \Phi_{i+1} \end{Bmatrix} \quad (26)$$

where

$$[\mathbf{T}] = [\mathbf{E}][\mathbf{Z}][\mathbf{E}]^{-1}$$

and where $[\mathbf{E}]$ is the matrix of eigenvectors and $[\mathbf{Z}]$ is a diagonal matrix whose n th entry is the n th eigenvalue z_n , found by solving Eq. (25).

To implement the far-field boundary conditions, say at the upstream far-field boundary, the transition matrix $[\mathbf{T}]$ is computed as above but with those eigenvalues z_n which correspond to incoming modes set to zero thereby eliminating incoming eigenmodes. Substitution of the upper half of Eq. (26) into Eq. (21) yields the desired nonreflecting boundary conditions at the upstream far-field boundary, i.e.,

$$[\tilde{\mathbf{B}}]\{\Phi_1\} + [\tilde{\mathbf{C}}]\{\Phi_2\} = 0 \quad (27)$$

where

$$[\tilde{\mathbf{B}}] = [\mathbf{B}] + [\mathbf{A}][\mathbf{T}_{11}] \quad \text{and} \quad [\tilde{\mathbf{C}}] = [\mathbf{C}] + [\mathbf{A}][\mathbf{T}_{12}]$$

Note that, in general, $[\tilde{\mathbf{B}}]$ and $[\tilde{\mathbf{C}}]$ will be fully populated. The nonreflecting boundary condition at the downstream boundary is constructed in a similar fashion.

The implementation of the far-field boundary conditions completes the discretization of the linearized potential equations. Because an H-grid is used, the resulting matrix is block tridiagonal and can be solved efficiently using an LU-decomposition algorithm which takes advantage of the block-tridiagonal structure. In the next section, some typical results of the present analysis are presented.

RESULTS

In this section, results computed using the present method are compared to the "exact" solutions for Category 3, Problem 1. For this problem, a vortical gust washes over a cascade of unstaggered flat plate airfoils. The mean flow is uniform with speed U_∞ and density ρ_∞ . The inflow Mach number M_∞ is 0.5. The length (chord) of each blade is c . The gap-to-chord ratio g/c is 1.0. We consider the case of an incident vortical gust which has x and y velocity components given by

$$u = -\frac{v_0 j^2}{\alpha} \exp[j(\alpha x + \beta y - \omega t)] \quad (28)$$

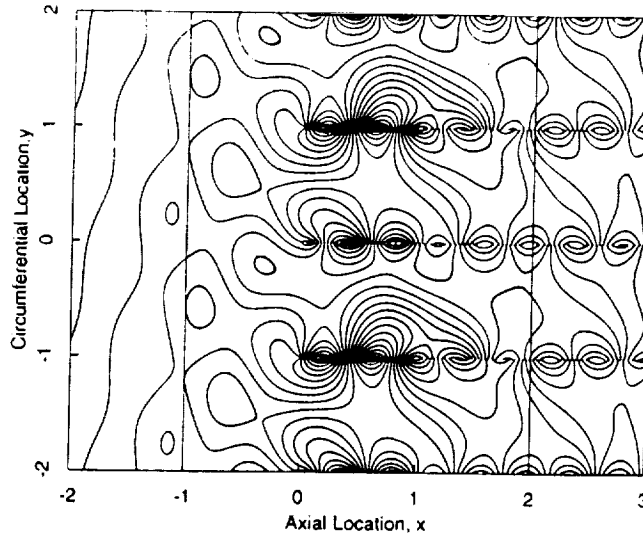


Figure 2: Contours of unsteady perturbation potential, $\omega = \sigma = 5\pi/2$ (Category 3, Problem 1). Note: two solutions are overlaid, one computed on a grid extending from $x = -2$ to $+3$, and one extending from $x = -1$ to $+2$.

$$v = v_G \exp[j(\alpha x + \beta y - \omega t)] \quad (29)$$

respectively, where β is the prescribed circumferential wave number equal to σ/g where σ is the so-called interblade phase angle. In the following, all lengths have been nondimensionalized by c , and pressures by $\rho_\infty U_\infty v_G$.

For the first case, a vortical gust with interblade phase angle σ of $5\pi/2$ impinges on the cascade with a reduced frequency ω of $5\pi/2$. The mean or steady flow through the cascade is uniform with a Mach number of 0.5. In the original problem description, four blade passages are required to achieve periodicity. However, because we impose complex periodicity at the periodic boundaries, the computational grid used here spans a single blade passage.

Figure 2 shows the computed contours of unsteady perturbation potential computed using two computational grids: a 241×49 node H-grid extending from approximately two chords upstream to two chords downstream of the airfoil, and a 145×49 node H-grid extending from one chord upstream to one chord downstream of the airfoil. The solution computed on the 241×49 node grid required 44 sec of CPU time on a Silicon Graphics Power Indigo 2 R8000 workstation. Note that the two solutions are nearly identical in the region where they overlap. If the far-field boundary conditions were not perfectly nonreflecting, some differences would be seen when the location of the far-field boundary is changed. Also note the jump in potential across the airfoil and wake. Figure 3 shows contours of unsteady perturbation pressure for the smaller computational grid. One can clearly see that a single pressure wave is cut on upstream and downstream of the cascade.

Next, the solutions computed using the present method are compared to the "exact" solution computed using Whitehead's LINSUB code [9]. Shown in Fig. 4 is the (nondimensional) pressure jump across the reference airfoil (located at $y = 0$). Note the present solution and the exact solution are in almost perfect agreement at this moderate reduced frequency. Similarly, Fig. 5 shows the computed mean square pressure of the acoustic response at $x = -2$ and $x = +3$ (two chords upstream and downstream of the cascade). Again, the agreement between the present method and the exact solution is excellent.

Next, we consider the same gust response example, but with $\omega = \sigma = 13\pi/2$. Again, the 241×49 node H-grid is used to compute the aeroacoustic response. Figure 6 shows the computed pressure difference

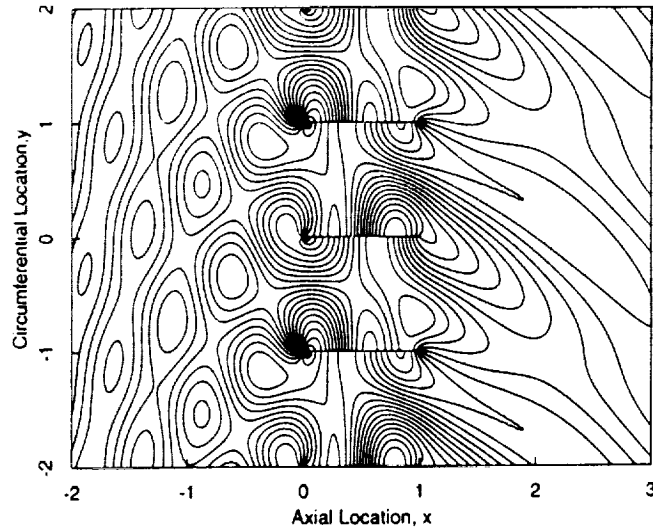


Figure 3: Contours of unsteady perturbation pressure, $\omega = \sigma = 5\pi/2$ (Category 3, Problem 1).

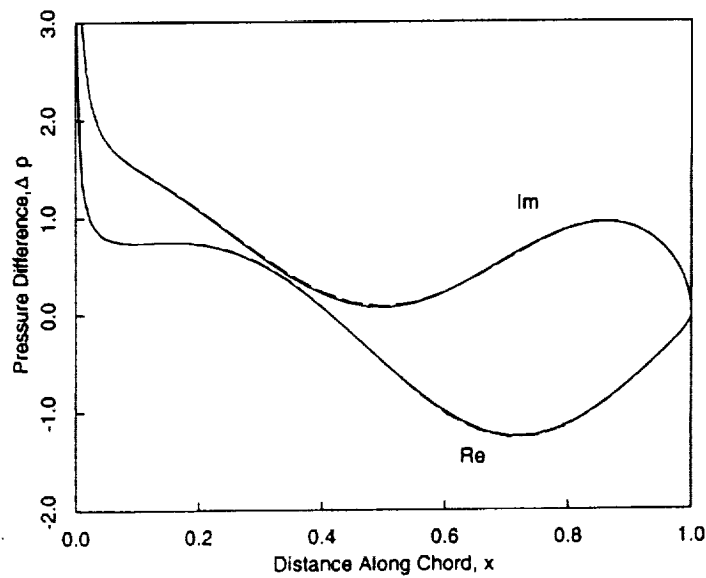


Figure 4: Nondimensional pressure loading on airfoil, $\omega = \sigma = 5\pi/2$ (Category 3, Problem 1). —, present method; - - - -, exact solution.

across the reference airfoil. The agreement between the present method and the exact theory, while still acceptable, is clearly not as good as in the lower frequency example. This is to be expected since at higher frequencies the acoustic disturbances will have shorter wavelengths. Thus, more grid resolution will be required to achieve the same level of accuracy.

Finally, shown in Fig. 7 is the computed upstream and downstream mean square acoustic pressure. Again, the agreement is acceptable, but clearly not as good as in the lower frequency example.

CONCLUSIONS

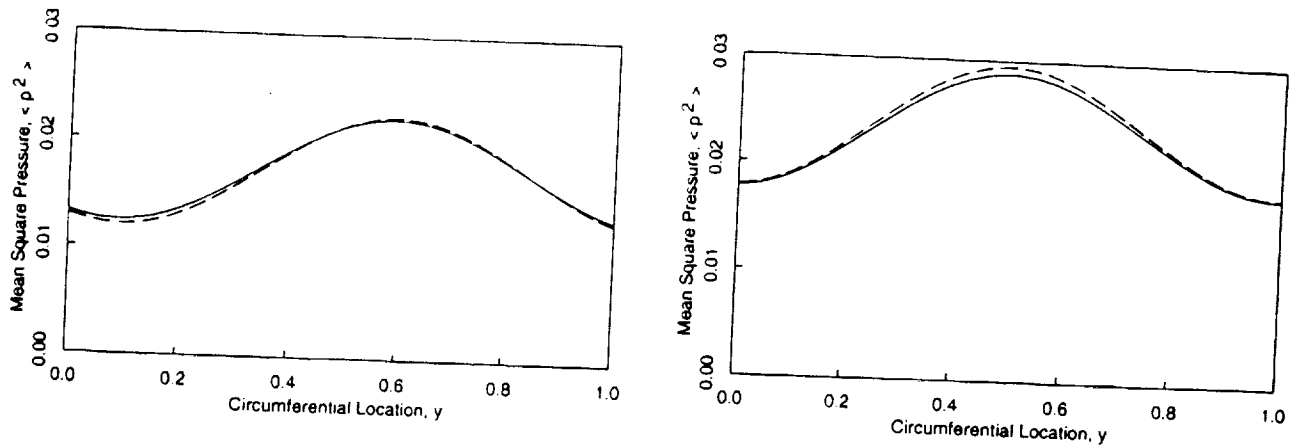


Figure 5: Mean square pressure upstream ($x = -2$) and downstream ($x = 3$) of cascade, $\omega = \sigma = 5\pi/2$ (Category 3, Problem 1). —, present method; - - - -, exact solution.

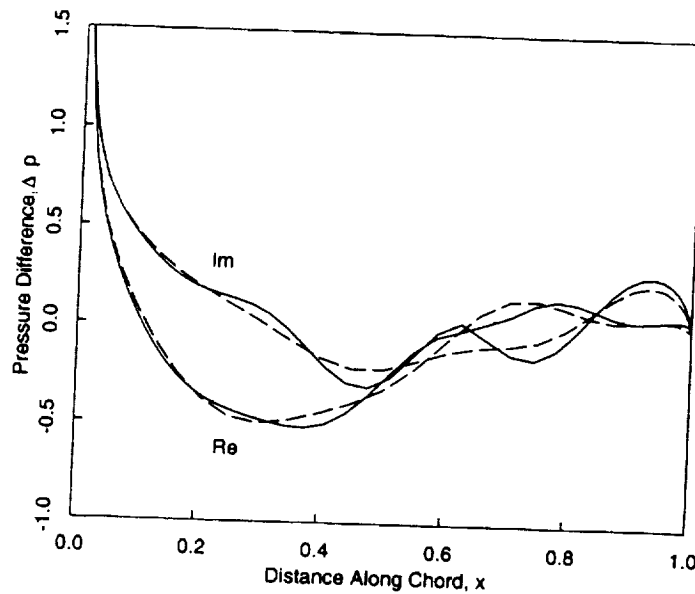


Figure 6: Nondimensional pressure loading on airfoil, $\omega = \sigma = 13\pi/2$ (Category 3, Problem 1). —, present method; - - - -, exact solution.

In this paper, a finite element method for calculating the aeroacoustic response of turbomachinery cascades to incident gusts is presented. The method is based on a linearized version of Bateman's variational principle. The variational principle is discretized on a computational grid of quadrilateral cells using standard finite element techniques. Two novel features are used to improve the accuracy of the computed results. The first is the use of wake fitting to model the motion of the wake and the jump in potential across the wake. Wake fitting allows the discontinuity in potential across the wake to be modelled quite accurately with only moderate grid resolution, and also automatically incorporates the Kutta condition. The second novel feature is the use of numerically exact far-field boundary conditions. In the present method, the far-field boundary conditions are based on the eigenmodes of the discretized potential equations, rather than on the eigenmodes of the analytical model. Thus, the boundary conditions are exact (to within round-off error) with no truncation error.

The present method is computationally efficient, with typical aeroacoustic calculations requiring

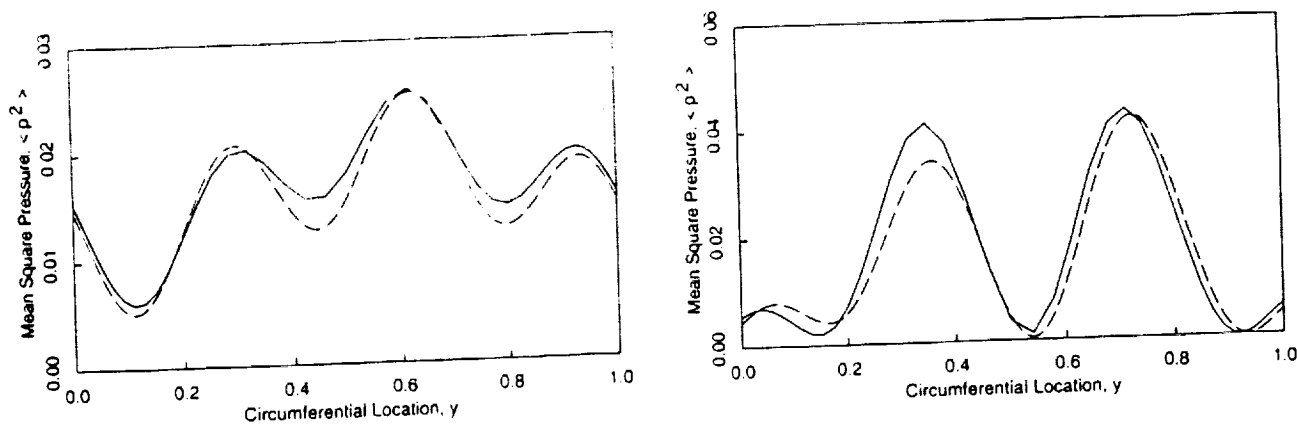


Figure 7: Mean square pressure upstream ($x = -2$) and downstream ($x = 3$) of cascade, $\omega = \sigma = 13\pi/2$ (Category 3, Problem 1). —, present method; - - -, exact solution.

less than one minute of CPU time on a Silicon Graphics Power Indigo 2 R8000 workstation. The method also gives results which are in excellent agreement with the exact solution, despite being only second-order accurate in space.

Finally, in this paper, only flows with uniform mean flows were considered. However, the present method can be extended to the more general problem of nonuniform mean flows using rapid distortion theory to model the distortion of the vortical velocity component [3, 10].

REFERENCES

1. Bateman, H., "Irrotational Motion of a Compressible Fluid," Proc. National Academy of Sciences, Vol. 16, 1930, p. 816.
2. Hall, K. C., "Deforming Grid Variational Principle for Unsteady Small Disturbance Flows in Cascades," AIAA Journal, Vol. 31, No. 5, May 1993, pp. 891-900.
3. Lorence, C. B., and Hall, K. C., "Sensitivity Analysis of Unsteady Aerodynamic Loads in Cascades," AIAA Journal, Vol. 33, No. 9, September 1995, pp. 1604-1610.
4. Verdon, J. M., and Caspar, J. R., "Development of a Linear Unsteady Aerodynamic Analysis for Finite-Deflection Subsonic Cascades," AIAA Journal, Vol. 20, No. 9, September 1982, pp. 1259-1267.
5. Whitehead, D. S., "A Finite Element Solution of Unsteady Two-Dimensional Flow in Cascades," International Journal for Numerical Methods in Fluids, Vol. 10, 1990, pp. 13-34.
6. Hall, K. C., and Crawley, E. F., "Calculation of Unsteady Flows in Turbomachinery Using the Linearized Euler Equations," AIAA Journal, Vol. 27, No. 6, June 1989, pp. 777-787.
7. Giles, M. B., "Nonreflecting Boundary Conditions for Euler Equation Calculations," AIAA Journal, Vol. 28, No. 12, December 1990, pp. 2050-2058.
8. Hall, K. C., Clark, W. S., and Lorence, C. B., "Nonreflecting Boundary Conditions for Linearized Unsteady Aerodynamic Calculations," AIAA Paper 93-0882, presented at the 31st Aerospace Sciences Meeting and Exhibit, Reno, Nevada, January 11-14, 1993.
9. Whitehead, D. S., "Classical Two-Dimensional Methods," Chapter II in AGARD Manual on Aeroelasticity in Axial-Flow Turbomachines, Vol. 1, Unsteady Turbomachinery Aerodynamics, M.F. Platzer and F.O. Carta (eds.), AGARD-AG-298, March 1987.
10. Hall, K. C., and Verdon, J. M., "Gust Response Analysis for Cascades Operating in Nonuniform Mean Flows," AIAA Journal, Vol. 29, No. 9, September 1991, pp. 1463-1471.

525-71

043483

294013 PID

A PARALLEL SIMULATION OF GUST/CASCADE INTERACTION NOISE

David P. Lockard* and Philip J. Morris†
Department of Aerospace Engineering
The Pennsylvania State University
University Park, PA 16802

INTRODUCTION

The problem of an incompressible vortical gust encountering a cascade of flat plate airfoils is investigated using parallel computers. The Euler equations are used to model the flow. A high-accuracy, finite-difference algorithm is used to solve the equations in a time accurate manner. Two frequencies of the incident gust are investigated. The sensitivity of the solution to the boundary conditions and run times are examined. In addition, the influence of the spacing between the blades is demonstrated. Although the use of parallel computers significantly reduces the turnaround time for these calculations, the difficulties in properly specifying the boundaries and obtaining a periodic state still makes them challenging.

SOLUTION METHODOLOGY

Extensive testing of CFD methodology has identified high-order algorithms as the most efficient for acoustic calculations. Runge-Kutta time integration and central differences in space have been chosen for the present work. In this section, the governing equations are presented as well as the details of the numerical scheme.

Governing Equations

The Euler equations are normally associated with acoustic phenomena and are used for the present simulations. The dimensionless equations of motion in two dimensions may be written as

$$\begin{aligned} \frac{\partial \rho}{\partial t} + u \frac{\partial \rho}{\partial x} + v \frac{\partial \rho}{\partial y} + \rho \left(\frac{\partial u}{\partial x} + \frac{\partial v}{\partial y} \right) &= 0, & \frac{\partial p}{\partial t} + u \frac{\partial p}{\partial x} + v \frac{\partial p}{\partial y} + \frac{1}{M^2} \left(\frac{\partial u}{\partial x} + \frac{\partial v}{\partial y} \right) &= 0, \\ \frac{\partial u}{\partial t} + u \frac{\partial u}{\partial x} + v \frac{\partial u}{\partial y} + \frac{1}{\rho} \frac{\partial p}{\partial x} &= 0, & \frac{\partial v}{\partial t} + u \frac{\partial v}{\partial x} + v \frac{\partial v}{\partial y} + \frac{1}{\rho} \frac{\partial p}{\partial y} &= 0. \end{aligned} \quad (1)$$

Here, ρ and p are the instantaneous density and pressure, respectively. The Cartesian velocity components are u and v , and t is time. M is the Mach number, and γ is the ratio of specific heats and is taken as 1.4. Since our primary interests are flows in air, the fluid is assumed to be an ideal gas. The inflow velocity, U_∞ is used as the velocity scale. The pressure is nondimensionalized by $\rho_\infty U_\infty^2$, and the density by its freestream value. The length scale is taken to be the airfoil chord.

A transformation from (x, y) to (ξ, η) space is applied to the equations by expanding the spatial derivatives using the chain rule. For example, the derivative in the x direction is given by $\frac{\partial}{\partial x} = \xi_x \frac{\partial}{\partial \xi} + \eta_x \frac{\partial}{\partial \eta}$. The subscripts on the generalized coordinates denote differentiation. The resulting equations can be solved efficiently by grouping like terms. J denotes the Jacobian of the transformation.

*Graduate Research Assistant

†Boeing Professor of Aerospace Engineering

Numerical Algorithm

Equations (1) can be placed in the semi-discrete, compact form

$$\frac{\partial \mathbf{Q}}{\partial t} = -[\mathcal{F}(\mathbf{Q}) - \mathcal{D}(\mathbf{Q})] = -\mathcal{R}(\mathbf{Q}). \quad (2)$$

Here, \mathcal{F} represents the discrete form of all the spatial derivatives appearing in eqs. (1). \mathcal{D} denotes the artificial dissipation. Runge-Kutta time-integration of the form

$$\begin{aligned} \mathbf{Q}^{(0)} &= \mathbf{Q}^n, \\ \mathbf{Q}^{(s)} &= \mathbf{Q}^n - \alpha_s \Delta t [\mathcal{F}(\mathbf{Q}^{(s-1)}) - \mathcal{D}(\mathbf{Q}^{(0)})], \\ \mathbf{Q}^{n+1} &= \mathbf{Q}^{s_{max}} \end{aligned} \quad (3)$$

is used to advance the solution in time. The local time step is chosen based on a Courant-Freidrichs-Lewy (CFL) constraint.

Time integration is performed using the alternating five-six stage Runge-Kutta (RK56) time integration of Hu *et al.*[1]. The smallest Δt for the entire domain is used globally. Although the method of Hu *et al.* is technically fourth-order accurate only for linear problems, the results have been found to compare well with those from the classical fourth-order method. The primary advantage of the alternating scheme is to increase the allowable CFL number based on accuracy requirements. For the present scheme, this is 1.1 compared with 0.4 for the classical method. The spatial operator can either be sixth-order or possess the dispersion-relation-preserving (DRP) property developed by Tam and Webb[2]. All of the results in this paper are obtained using the DRP coefficients given by Lockard *et al.*[3]

Since central difference operators do not possess any implicit dissipation, a filter has been added explicitly. A higher-order version of the adaptive dissipation of Jameson[4] has been implemented for this purpose. An optimized smoother using a seven point stencil is used as a background dissipation rather than the fourth derivative used in Jameson's implementation. This smoother is given by Tam[5] for a Gaussian half width of $\sigma = 0.3\pi$. A detailed description of the dissipation is given in a previous paper by the authors[6].

Boundary Conditions

Nonreflecting boundary conditions are necessary for acoustic simulations since nonphysical reflections of waves back into the computational domain can alter the solution significantly. The specified problems provide a stern test for nonreflecting boundary conditions since some of the acoustic wavefronts are nearly normal to the boundaries. Furthermore, some of the cutoff modes decay very slowly. The present simulations use Giles[7] linearized inflow and outflow conditions. However, the location of the outer boundaries is found to have a strong influence the solution. Other boundary conditions for unbounded domains and one-dimensional flows were found to perform poorly. Thompson's[8] wall boundary conditions based on a characteristics analysis are used for solid surfaces. The normal derivatives at the boundary used in the boundary treatment are discretized using third-order fully biased operators for stability reasons.

Gust Specification

The source of the noise in the problem is the interaction of an oblique, vortical gust with a cascade. Since it is often difficult to impose arbitrary disturbances at curved boundaries and still minimize reflections of

outgoing waves, an alternate approach has been developed to generate the gust inside the domain. The gust defined by

$$u = -\left(\frac{v_G \beta}{\alpha}\right) \cos(\alpha x + \beta y - \omega t), \quad v = v_g \cos(\alpha x + \beta y - \omega t) \quad (4)$$

is introduced inside the domain by adding a source function to the governing equations. Since the gust is incompressible and vortical, only the momentum equations need to be modified. The equations that include the source have the form

$$\frac{\partial u}{\partial t} \dots = \frac{\partial \Psi}{\partial y} \sin(\omega t), \quad \frac{\partial v}{\partial t} \dots = -\frac{\partial \Psi}{\partial x} \sin(\omega t) \quad (5)$$

where

$$\Psi = \frac{v_G}{\pi} (1 + \cos[0.5\alpha(x - x_o)]) \cos(\alpha x + \beta y) \quad (6)$$

in the range $|x - x_o| < 2\pi/\alpha$. The source is similar to a stream function so that the induced vortical gust velocities are solenoidal to linear order. Thus, the gust should not produce any noise.

RESULTS

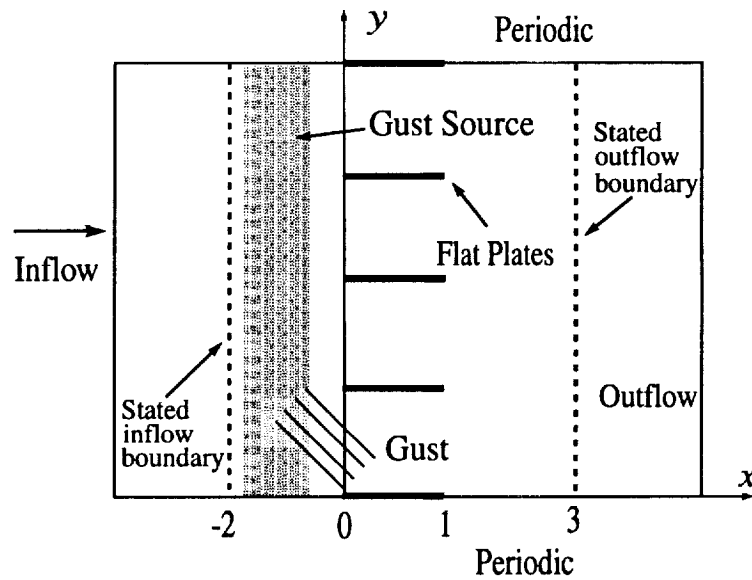


Figure 1: Geometry for the cascade problem.

The problem involves the interaction of a vortical gust with a cascade of flat plate airfoils as shown in figure 1. The gust amplitude $v_G = 0.01$, and the mean flow Mach number in the x direction is $M = 0.5$. The wavenumbers are $\alpha = \beta = \omega$. The upper and lower surfaces of the flat plates are represented by adjacent grid lines. Thus, the spacing between the blades changes as the grid is refined. Although calculations on stretched grids have been performed, only results from uniform grids will be presented due to space limitations. The solutions on grids clustered near the edges of the plate are slightly better near the singularities, but smaller time steps had to be used. The periodic boundaries are implemented by exchanging data from one side of the domain to the other.

The results are divided into different sections for the specified frequencies of $\omega = 5\pi/2$ and $\omega = 13\pi/2$. The effect of the domain length and the grid size are investigated. In addition, the influence on the rms values of the starting time and sampling duration are examined.

Low Frequency

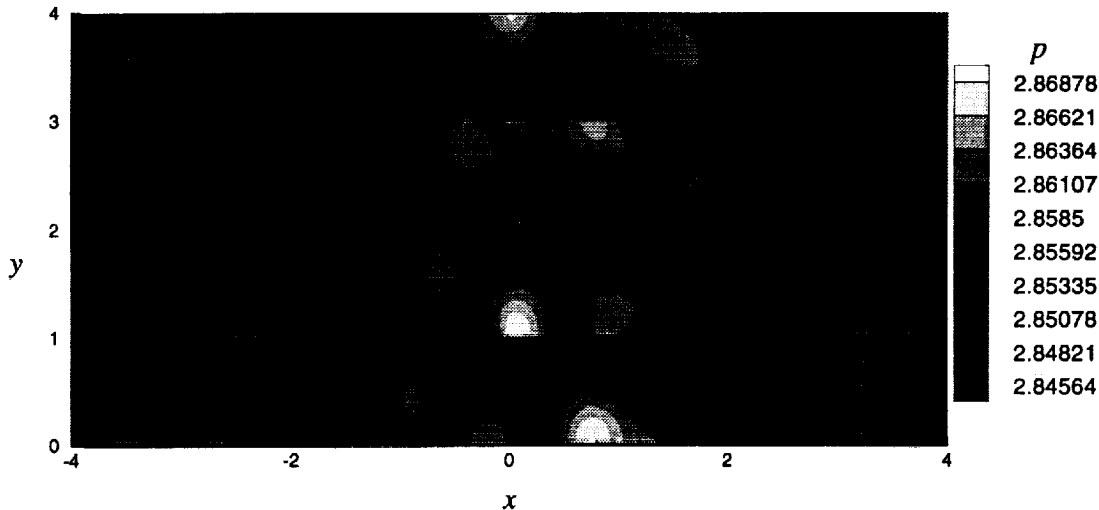


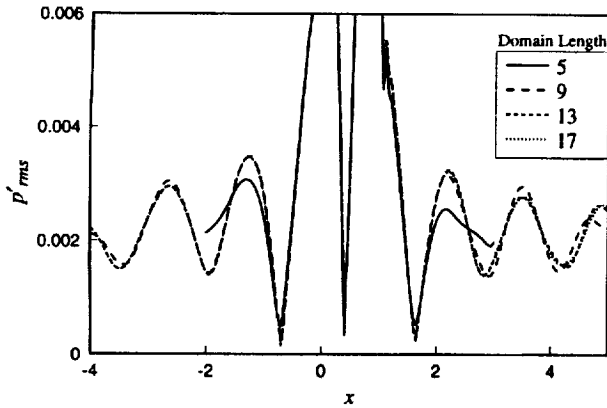
Figure 2: Instantaneous total pressure distribution for $\omega = 5\pi/2$.

The instantaneous total pressure distribution for $\omega = 5\pi/2$ at the beginning of a period is given in figure 2. The interference between different modes is clearly seen on the upstream side. It is also evident that one of the modes is decaying as the pattern becomes dominated by a single mode away from the cascade.

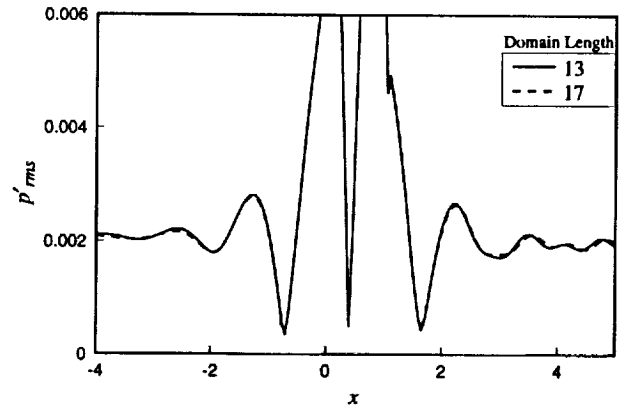
To examine the effect of the boundary conditions on the solution, the rms profiles of the perturbation pressure along the plate at $y = 0$ are given in figure 3 for different domain lengths in the x direction. A temporal period of the gust frequency is represented by T . A domain length of five, which corresponds to the minimum necessary to obtain solutions at $x = -2$ and $x = 3$, is shown to be very different from the longer domains in 3(a). Domain lengths of 13 and 17 yield similar results. 3(b) compares the solutions for the two longest domains when the starting sampling time is much later and for much longer sampling times. Again the solutions are similar, but they are considerably different away from the plate from those in 3(a).

Obtaining truly periodic solutions numerically for this problem is extremely challenging for a time-marching algorithm. The problem can be conceptualized as an infinite distribution of sources in the y direction which all turn on at the same time. Hence, one must wait until all of the sources have had enough time for their radiated field to reach the modeled domain. Since the problem is two-dimensional, the radiated field will decay like $1/r$. Thus, many of the sources must be included to obtain the correct periodic state. This argument is also valid for startup transients and reflections at boundary conditions. Thus, the problem is extremely sensitive to the run time and numerical errors.

Figure 4(a) shows the variation in the solution with sampling time. Sampling for less than 20 periods is inadequate. The solutions for $20T$ and $40T$ are nearly identical, but sampling for $40T$ produces some variation. Examination of the temporal signal shows a slight beating type phenomena that approximately repeats every $20T$. This may be caused by nonlinearities, the singularities at the leading and trailing edges of the plates, or numerical errors. Although one would prefer to sample for an extremely long time to completely



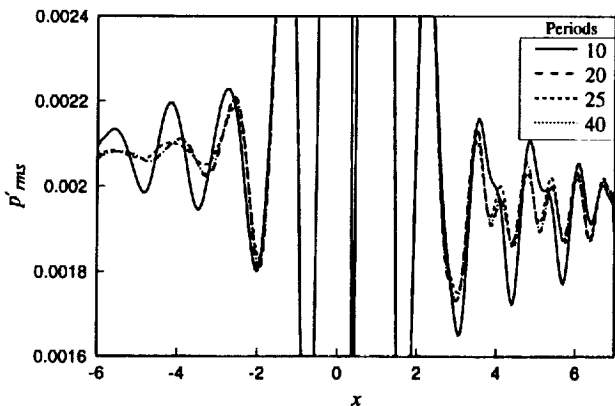
(a) Sampling from $t = 15T$ to $t = 19T$



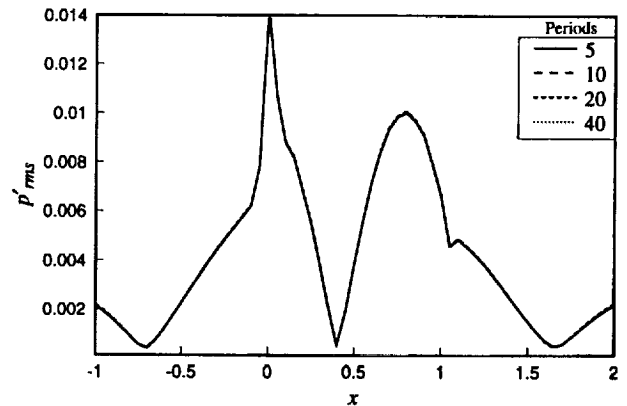
(b) Sampling from $t = 100T$ to $t = 120T$

Figure 3: Variation of rms pressure values along $y = 0$ with domain length for $\omega = 5\pi/2$. 88 points in the y direction and 20 points per unit length in the x direction.

resolve all of the waves, this is not feasible because of the computer costs. Figure 4(b) shows that although the radiated noise is sensitive to the sampling duration, the relatively large fluctuations on the plate are not.



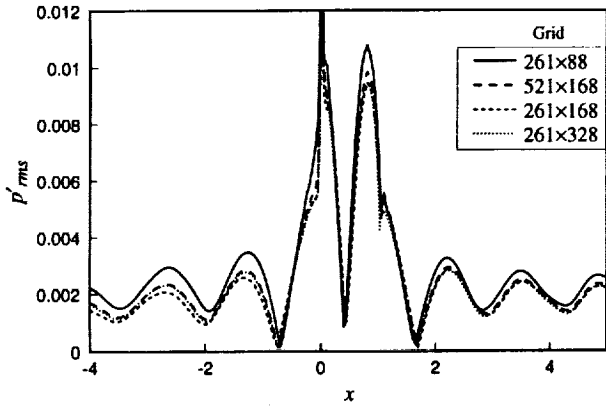
(a)



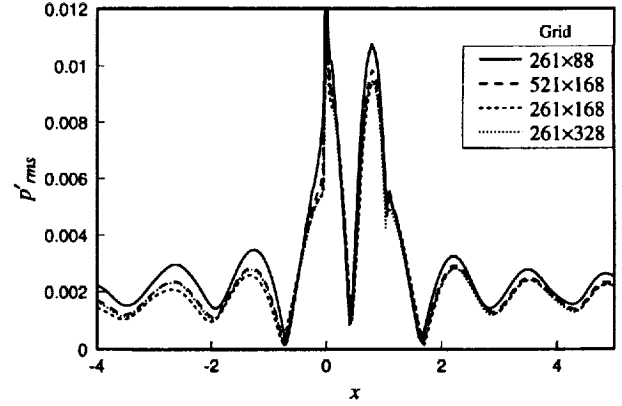
(b)

Figure 4: Variation of rms values with sampling time along $y = 0$ for $\omega = 5\pi/2$. 261×88 grid for $x = -6$ to 7 .

Figures 5 and 6 examine the effect of the grid size on the solution for a domain length of 13. It actually appears that the change in the interblade spacing with grid size has a greater effect on the solution than the change in resolution. The solutions on the 521×168 and 261×168 grids in figure 5 are very similar, but solutions for different grids in the y direction yield different amplitudes. Increasing the number of points in the streamwise direction does help to resolve the singularities at the leading and trailing edges, but the influence of the blade spacing is the dominant effect. The amplitude of the oscillations of the modes within the cascade change with the blade spacing. Hence, it is important to simulate the correct blade spacing in the simulation. A similar modification of the amplitude of the noise is shown in figure 6 for the rms values at $x = -2$ and $x = 3$.

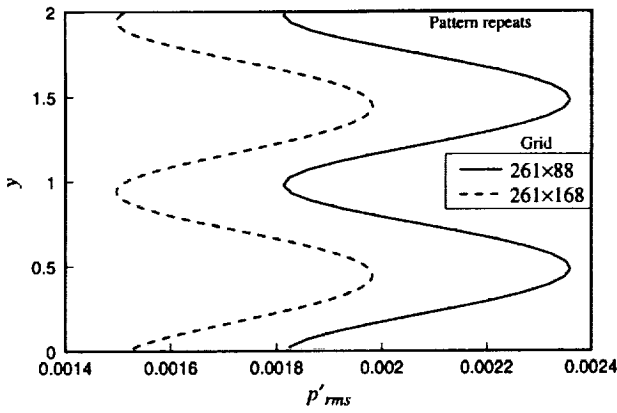


(a) Sampling from $t = 15T$ to $t = 19T$

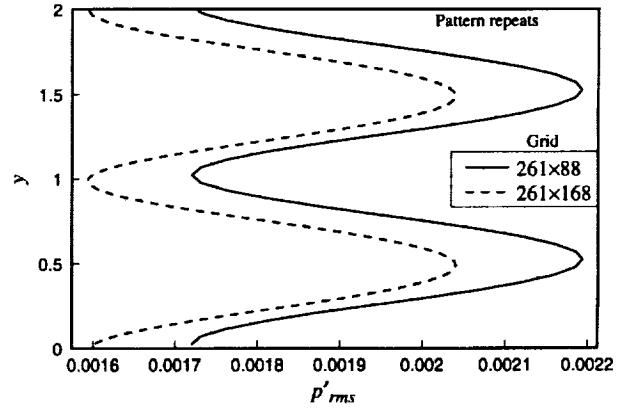


(b) Sampling from $t = 100T$ to $t = 120T$

Figure 5: Variation of rms pressure along $y = 0$ with grid size for $\omega = 5\pi/2$.



(a) $x = -2$



(b) $x = 3$

Figure 6: rms pressure values upstream and downstream of the cascade for $\omega = 5\pi/2$. Sampling from $t = 100T$ to $t = 120T$.

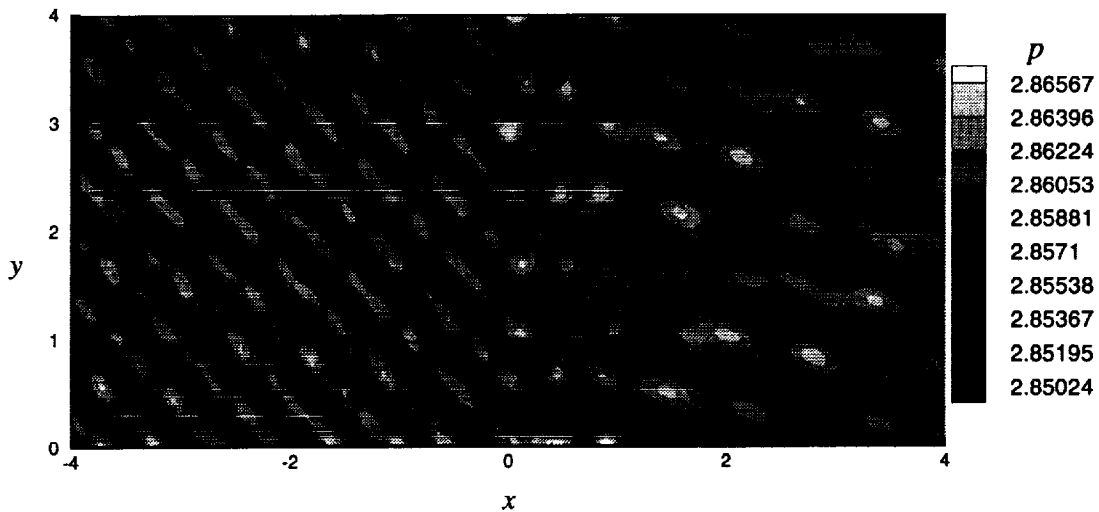
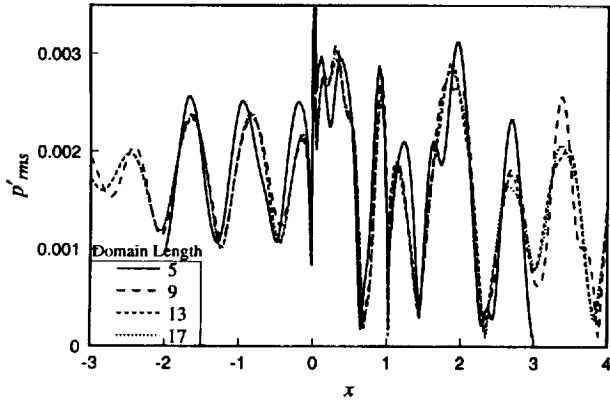


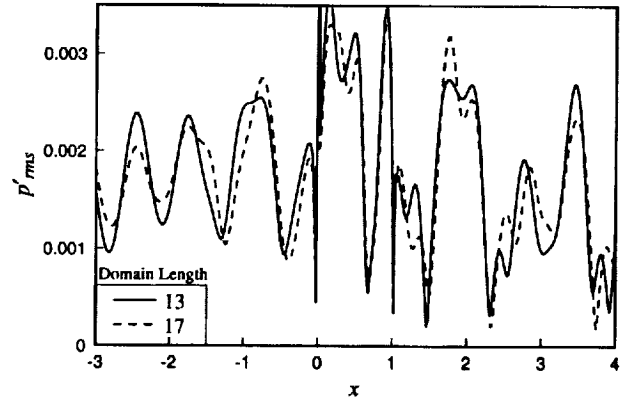
Figure 7: Instantaneous total pressure distribution for $\omega = 13\pi/2$.

High Frequency

The instantaneous total pressure distribution for $\omega = 13\pi/2$ at the beginning of a period is given in figure 7. The pattern is considerably more complicated than the one for the low frequency case, indicating more modal content.



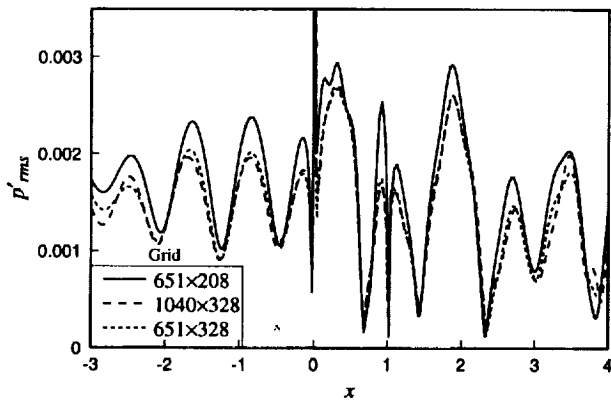
(a) Sampling from $t = 40T$ to $t = 53T$



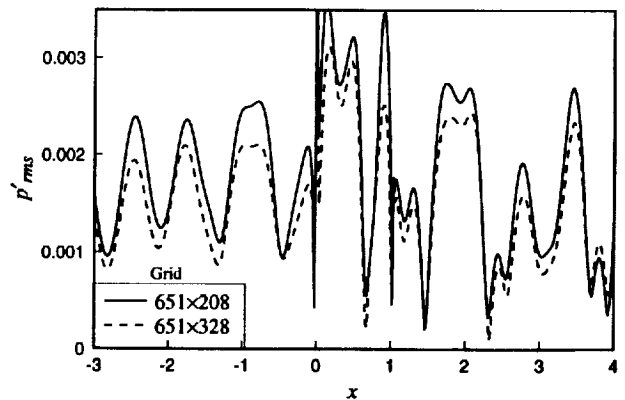
(b) Sampling from $t = 195T$ to $t = 208T$

Figure 8: Variation of rms pressure values along $y = 0$ with domain length for $\omega = 13\pi/2$. 2088 points in the y direction and 50 points per unit length in the x direction.

The trend in the variation of the solution with domain length shown in figure 8 is similar to that found in the low frequency case. Although the solutions for domain lengths of 13 and 17 look similar in 8(a), there is a significant variation in 8(b). This may be caused by reflections and other errors having time to contaminate the entire domain. Also, The solution on the blade surface is much smaller than in the low frequency case and is much more susceptible to being altered by either the cascade effect or errors. Figure 8(a) shows that the solutions on the blade are different for the two sampling times, so it is not surprising that the radiated sound field also exhibits some variation.



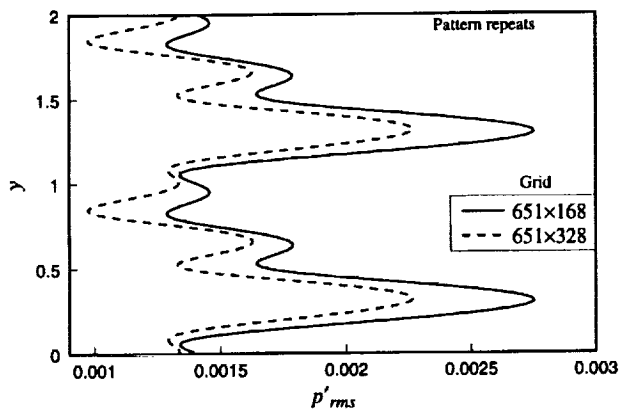
(a) $x = -2$



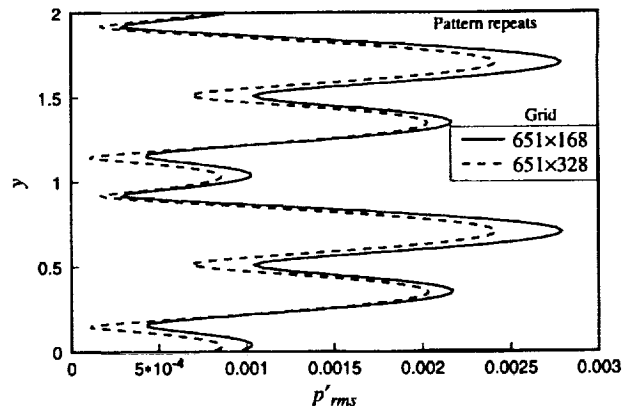
(b) $x = 3$

Figure 9: Variation of rms pressure along $y = 0$ with grid size for $\omega = 13\pi/2$.

Figures 9 and 10 examine the effect of the grid size on the solution for a domain length of 13. As in the low frequency case, there appears to be sufficient resolution with the coarsest mesh, but the change in the blade spacing changes the amplitudes of the oscillations.



(a) Sampling from $t = 40T$ to $t = 53T$



(b) Sampling from $t = 195T$ to $t = 208T$

Figure 10: rms pressure values upstream and downstream of the cascade for $\omega = 13\pi/2$. Sampling from $t = 195T$ to $t = 208T$.

Performance

The Fortran 90 code used in this research was executed on an IBM SP2 with power2 nodes. It is written for parallel computers using the message passing interface (MPI). A detailed description of the parallel implementation can be found in a previous paper by the authors[9]. Table 1 summarizes the computational resources used for some of the cases. The nominal value for the CPU/grid point/time step is 40 microseconds.

ω	Domain size	Grid Size	T	CPU (s)	CPU/ T (s)	Nodes
$5\pi/2$	13×4	261×88	100	708	7.08	10
$5\pi/2$	17×4	341×88	100	834	8.34	10
$13\pi/2$	13×4	651×208	195	8584	44	7
$13\pi/2$	13×4	1040×328	75	11640	155	12

Table 1: Performance numbers for the cascade problem.

CONCLUSIONS

Numerical solutions of the sound radiated from a vortical gust encountering a cascade of flat plate airfoils have been obtained using a finite-difference algorithm implemented for parallel computers. The periodic nature of the problem makes convergence to a periodic state very slow. Thus, longer run times than are needed for unbounded flows are required. Furthermore, better inflow and outflow boundary conditions are needed. Reflections from the boundaries cause significant changes in the solution even when the outer boundaries are moved relatively far from the noise sources. These issues must be addressed before such calculations can be performed efficiently in the time domain.

REFERENCES

- [1] Hu, F. Q., Hussaini, M. Y., and Manthey, J. Low-dissipation and -dispersion Runge-Kutta schemes for computational aeroacoustics. *Journal of Computational Physics*, **124**, pp. 177–191, 1995.
- [2] Tam, C. K. W., and Webb, J. C. Dispersion-relation-preserving finite difference schemes for computational aeracoustics. *Journal of Computational Physics*, **107**, pp. 262–281, 1993.
- [3] Lockard, D. P., Brentner, K. S., and Atkins, H. L. High-accuracy algorithms for computational aeroacoustics. *AIAA Journal*, **33(2)**, pp. 246–251, 1995.
- [4] Jameson, A., Schmidt, W., and Turkel, E. Numerical solution of the Euler equations by finite-volume methods using Runge-Kutta time-stepping schemes. AIAA-81-1259, 1981.
- [5] Tam, C. K. W., and Dong, Z. Radiation and outflow boundary conditions for direct computation of acoustic and flow disturbances in a nonuniform mean flow. CEAS/AIAA Paper-95-007, 1995.
- [6] Lockard, D. P., and Morris, P. J. The radiated noise from airfoils in realistic mean flows. AIAA Paper-97-0285, 1997.
- [7] Giles, M. B. Nonreflecting boundary conditions for euler equation calculations. *AIAA Journal*, **28(12)**, pp. 2050–2057, 1990.
- [8] Thompson, K. W. Time-dependent boundary conditions for hyperbolic systems, II. *Journal of Computational Physics*, **89**, pp. 439–461, 1989.
- [9] Lockard, D. P., and Morris, P. J. A parallel implementation of a computational aeroacoustic algorithm for airfoil noise. AIAA Paper-96-1754, 1996 (to appear *Journal of Computational Acoustics*, 1997).

1000000

1000000

1000000

1000000

1000000

1000000

1000000

526-71

043484

294014

COMPUTATION OF SOUND GENERATED BY FLOW OVER A CIRCULAR CYLINDER: AN ACOUSTIC ANALOGY APPROACH

Kenneth S. Brentner
NASA Langley Research Center
Hampton, Virginia

Christopher L. Rumsey
NASA Langley Research Center
Hampton, Virginia

Jared S. Cox
The George Washington University, JIAFS
Hampton, Virginia

Bassam A. Younis
City University
London, England

SUMMARY

The sound generated by viscous flow past a circular cylinder is predicted via the Lighthill acoustic analogy approach. The two dimensional flow field is predicted using two unsteady Reynolds-averaged Navier-Stokes solvers. Flow field computations are made for laminar flow at three Reynolds numbers ($Re = 1000$, $Re = 10,000$, and $Re = 90,000$) and two different turbulent models at $Re = 90,000$. The unsteady surface pressures are utilized by an acoustics code that implements Farassat's formulation 1A to predict the acoustic field. The acoustic code is a 3-D code—2-D results are found by using a long cylinder length. The 2-D predictions overpredict the acoustic amplitude; however, if correlation lengths in the range of 3 to 10 cylinder diameters are used, the predicted acoustic amplitude agrees well with experiment.

INTRODUCTION

The sound generated by a viscous flow over a cylinder has been widely studied but is still difficult to compute at moderate and high Reynolds numbers. This flow is characterized by the von Karman vortex street—a train of vortices alternately shed from the upper and lower surface of the cylinder. This vortex shedding produces an unsteady force acting on the cylinder which generates the familiar aeolian tones. This problem is representative of several bluff body flows found in engineering applications (e.g., automobile antenna noise, aircraft landing gear noise, etc.). For the workshop category 4 problem, a freestream velocity of Mach number $M = 0.2$ was specified with a Reynolds number based on cylinder diameter of $Re = 90,000$. This Reynolds number is just below the drag crisis, hence, the flow is very sensitive to freestream turbulence, surface roughness, and other factors in the experiment. Numerical calculations of the flow at this Reynolds number are also very sensitive—2-D laminar calculations are nearly chaotic and the transition of the boundary layer from laminar to turbulent flow occurs in the same region that vortex shedding takes place. These aspects of the workshop problem significantly increases the difficulty of prediction and interpretation of results.

In this work, the unsteady, viscous flow over a two-dimensional circular cylinder is computed by two different flow solvers, CFL3D and CITY3D. Two-dimensional (2-D) flow-field calculations were performed at this stage of the investigation to reduce the computational resources required. The noise prediction utilizes the Lighthill acoustic analogy as implemented in a modified version of the helicopter rotor noise prediction program WOPWOP. The 2-D flow field data is utilized in WOPWOP by assuming that the loading does not vary in the spanwise direction.

In the remainder of this paper we will first briefly describe both the aerodynamic and acoustic predictions for both laminar flow and turbulent flows. The Lighthill acoustic analogy [1] utilized in this work effectively separates the flow field and acoustic computations, hence, the presentation is divided in this manner. This paper focuses on the acoustic predictions. More emphasis placed on the computational fluid dynamics (CFD) calculations in a companion paper written by the authors [2].

FLOW-FIELD PREDICTIONS

CFD Methodology

Two unsteady Reynolds-averaged Navier-Stokes (RANS) solvers (CFL3D and CITY3D) were utilized in this work. Note that the term *Reynolds averaged* is used here not in its conventional sense (which implies averaging over an infinite time interval) but, rather, to denote averaging over a time interval which is longer than that associated with the slowest turbulent motions but is much smaller than the vortex shedding period. Thus it is possible to cover a complete vortex shedding cycle with a reasonable number of time steps (typically 2000 or less) without the need to resolve the details of the turbulent motions as would be necessary, for example, with either Direct or Large-Eddy Simulations.

The first code, CFL3D [3], is a 3-D thin-layer compressible Navier-Stokes code which employs the finite volume formulation in generalized coordinates. It employs upwind-biased spatial differencing for the convective and pressure terms, and central differencing for the viscous terms. It is globally second order accurate in space, and employs Roe's flux difference splitting. The code is advanced implicitly in time using 3-factor approximate factorization. Temporal subiterations with multigrid are employed to reduce the linearization and factorization errors. For the current study, CFL3D was run in a 2-D time-accurate mode which is up to second-order accurate in time. Viscous derivative terms are turned on in both coordinate directions, but the cross-coupling terms are neglected as part of the thin-layer assumption.

CFL3D has a wide variety of turbulence models available, including zero-equation, one-equation, and two-equation (linear as well as nonlinear). For the current study, the code was run either laminar-only (i.e., no Reynolds averaging), or else employed the shear stress transport (SST) two-equation $k-\omega$ turbulence model of Menter [4]. This model is a blend of the $k-\omega$ and $k-\epsilon$ turbulence models, with an additional correction to the eddy viscosity to account for the transport of the principal turbulent shear stress. It has been demonstrated to yield good results for a wide variety of steady separated turbulent aerodynamic flows [5], but its capabilities for unsteady flows remain relatively untested.

CITY3D is a finite-volume code for the solution of the incompressible, 3-D Navier-Stokes equations in generalized coordinates. A pressure-correction technique is used to satisfy mass and momentum conservation simultaneously. Temporal and spatial discretization are first- and third-order accurate, respectively. The turbulence model used in this study is the $k-\epsilon$ model modified as described in [6] to account for the effects of superimposing organized mean-flow periodicity on the random turbulent motions. The modification takes the form of an additional source to the ϵ equation which represents the direct energy input into the turbulence spectrum at the Strouhal frequency. Further details are reported in [2] which also gives details of the high Reynolds-number treatment adopted in specifying the near-wall boundary conditions.

CFD Results

Both the shedding frequency and mean drag coefficient for flow past a circular cylinder are known to exhibit only small Reynolds number dependence in the range $1000 < Re < 100,000$. A little above $Re = 100,000$ the drag crisis occurs and the mean drag coefficient \bar{C}_d decreases significantly (from $\bar{C}_d \approx 1.2$ to $\bar{C}_d \approx 0.3$ - see [7] for representative figures). The exact Reynolds number where the drag crisis occurs can decrease significantly with any increase in free-stream turbulence intensity or surface roughness. Because the workshop problem specified $Re = 90,000$, we decided it would be prudent to make a series of computations for both laminar and turbulent flow. Laminar computations were made for $Re = 1000$, $Re = 10,000$, and $Re = 90,000$ with a flow Mach number $M = 0.2$, cylinder diameter $D = 0.019$ m, and freestream speed of sound 340 m/s. Turbulent calculations at $Re = 90,000$ were made for both the SST turbulence model in CFL3D and for the modified $k-\epsilon$ model in CITY3D. A portion of the lift and drag coefficient time history is shown in figure 1. The predicted Strouhal number St and mean drag coefficient \bar{C}_d values are given in the legend of figure 1.

Figure 1 shows that the laminar C_l time histories have approximately the same amplitude, but the laminar $Re = 90,000$ computation is somewhat irregular. The turbulent computations have both lower

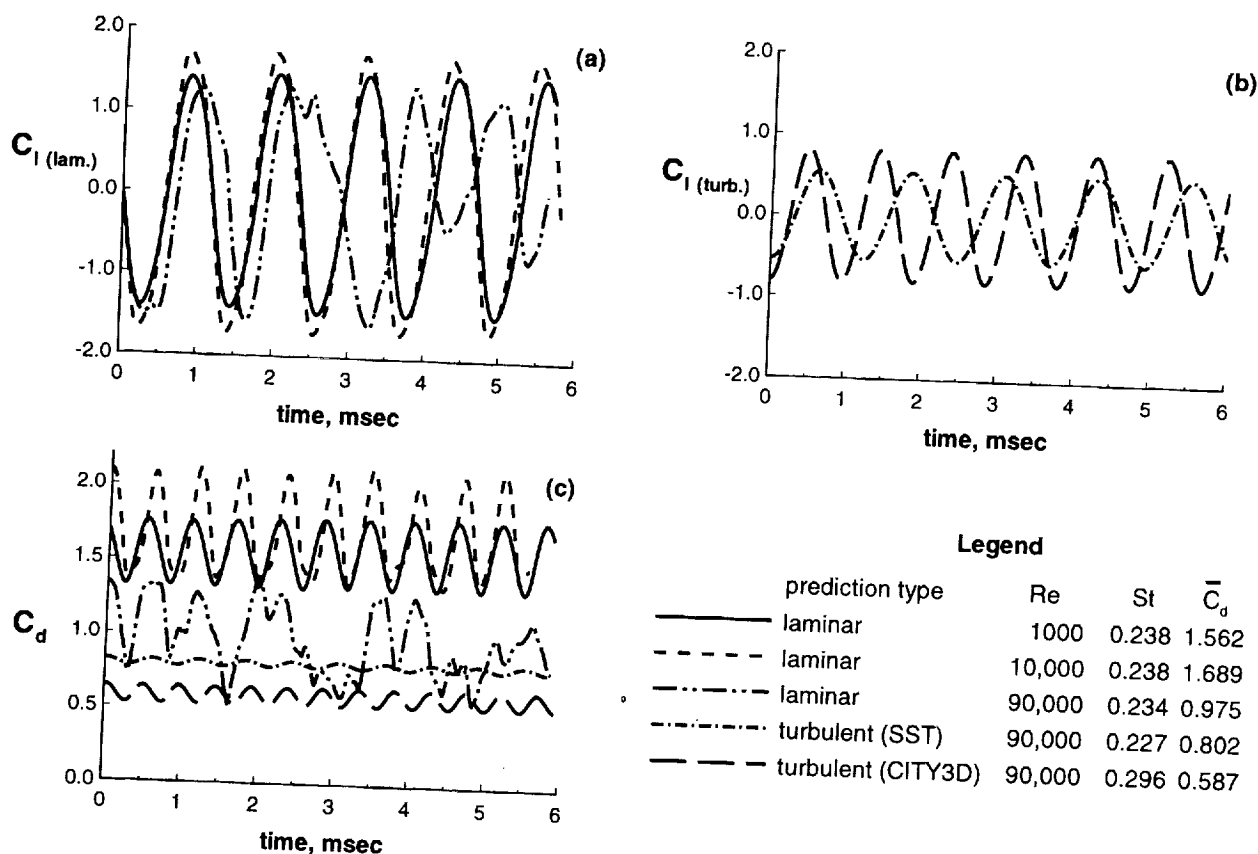


Figure 1. Comparison of predicted C_l and C_d time histories for $M = 0.2$ flow past a 2-D circular cylinder. (a) laminar C_l predictions; (b) turbulent C_l predictions; (c) C_d predictions.

C_l fluctuation amplitude and lower mean and fluctuating drag levels. These lower levels are in general agreement with experiments which have a higher level of turbulence. For example, Revell et al. [8] measured $\bar{C}_d = 1.312$ for a smooth cylinder and $\bar{C}_d = 0.943$ for a rough cylinder, both at $M = 0.2$ and $Re = 89,000$. Notice that the CITY3D codes calculates a Strouhal number somewhat higher than CFL3D and more in the range of a higher Reynolds number data. This is probably related to the fact that CITY3D used a 'wall function' and hence has a turbulent boundary layer profile throughout (as would be the case for flow at a higher Reynolds number). More discussion of these results is given in reference [2].

ACOUSTIC PREDICTIONS

Acoustic Prediction Methodology

The unsteady flow-field calculation from CFL3D or CITY3D is used as input into an acoustic prediction code WOPWOP [9] to predict the near- and far-field noise. WOPWOP is a rotor noise prediction code based upon Farassat's retarded-time formulation 1A [10], which is a solution to the Ffowcs Williams - Hawkins (FW-H) equation [11] with the quadrupole source neglected. Formulation 1A may be written as

$$p'(\mathbf{x}, t) = p'_T(\mathbf{x}, t) + p'_L(\mathbf{x}, t) \quad (1)$$

where

$$4\pi p'_T(\mathbf{x}, t) = \int_{f=0} [\frac{\rho_0(\dot{v}_n + v_{\dot{n}})}{r(1 - M_r)^2}]_{ret} dS + \int_{f=0} [\frac{\rho_0 v_n(r\dot{M}_r + c(M_r - M^2))}{r^2(1 - M_r)^3}]_{ret} dS$$

$$4\pi p'_L(\mathbf{x}, t) = \frac{1}{c} \int_{f=0} [\frac{\dot{\ell}_r}{r(1-M_r)^2}]_{ret} dS + \int_{f=0} [\frac{\ell_r - \ell_M}{r^2(1-M_r)^2}]_{ret} dS + \frac{1}{c} \int_{f=0} [\frac{\ell_r(r\dot{M}_r + c(M_r - M^2))}{r^2(1-M_r)^3}]_{ret} dS$$

Here p' is the acoustic pressure, v_n is the normal velocity of the surface, ℓ_i are the components of the local force intensity that act on the fluid, M is the velocity of the body divided by the freestream sound speed c , and r is the distance from the observer position \mathbf{x} to the source position \mathbf{y} . The subscripts r and n indicate a dot product of the main quantity with unit vectors in the radiation and surface normal directions, respectively. The dot over variables indicates source-time differentiation. The square brackets with the subscript *ret* indicates that the integrands are evaluated at the retarded (emission) time.

Notice that the integration in equation (1) is carried out on the surface $f = 0$ which describes the body—in our case a circular cylinder. Unlike the CFD calculations, the integration performed for the acoustic calculation is over a three-dimensional cylinder that is translating in a stationary fluid. For the predictions in this paper, we assume that the surface pressures are constant along the span at any source time. To model a 2-D cylinder in the 3-D integration, we use a long cylinder length and do not integrate over the ends of the cylinder. Experiments and computational work (e.g., [12–15]) have shown that vortex shedding is not two-dimensional and the shedding is correlated only over some length (typically $< 10D$). We have modeled the effect of vortex shedding correlation length by truncating the cylinder used in the acoustics prediction.

Acoustic Results

To test the coupling of the CFD and acoustic codes, we chose to predict the noise generated by flow past the circular cylinder for an observer position at a location 90 deg from the freestream direction and 128 cylinder diameters away from the cylinder. This corresponds to a microphone location in the experiment conducted by Revell et al. [8]. The predicted acoustic spectra for each of the CFD inputs are compared with experimental data in figure 2. One period of surface pressure data (repeated as necessary) was used to predict the noise. (Approximately 62 cycles of input data were used in the noise calculation of the laminar $Re = 90,000$ case because the loading time history was irregular.) A 0.5 m (26.3D) cylinder length was used in the prediction, matching the physical length of the cylinder used in the experiment. In figure 2 we see that both the Strouhal number and the amplitude are overpredicted. The CFL3D turbulent (SST model) prediction yields a slightly lower amplitude and Strouhal number, but the CITY3D turbulent prediction again has a high Strouhal value at the fundamental frequency and overpredicts the amplitude. The first harmonic of the vortex shedding frequency can be clearly seen in the predictions, but the experimental data is lower in amplitude and frequency.

One explanation for the discrepancy in the noise predictions is that the vortex shedding has been modeled as completely coherent in figure 2. In experiments, however, the vortex shedding has been found to be coherent only over a relatively short length, usually less than $10D$. To investigate the effect of vortex shedding correlation length on predicted noise levels, we varied the length of the cylinder L over the range $3D < L < 250D$ and plotted the overall sound pressure level predicted at the 90 deg, 128D microphone location. Figure 3 show that the length of the cylinder has a strong effect on the peak noise level. For example, a cylinder length of $10D$ (which is a long correlation length) yields a peak amplitude at the 90 deg observer location that is within 2 dB of the experiment. Clearly then a true 2-D noise prediction should be *expected* to overpredict the measured noise, possibly by as much as 25 dB!

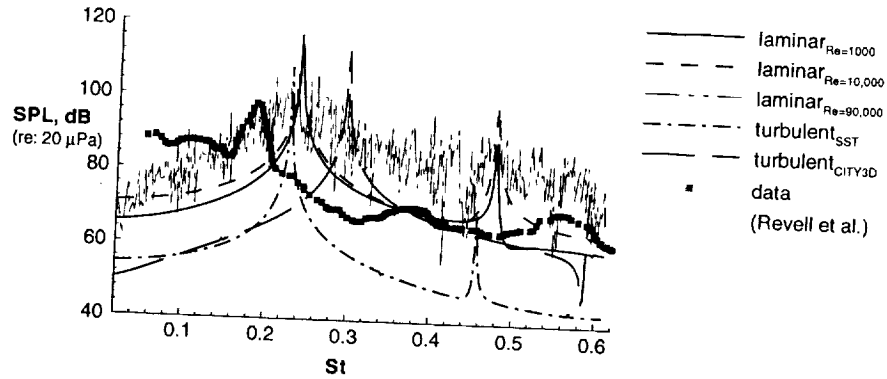


Figure 2. Comparison of predicted and measured sound pressure level for a microphone located $128D$ away from the cylinder at a 90 deg angle to the freestream flow.

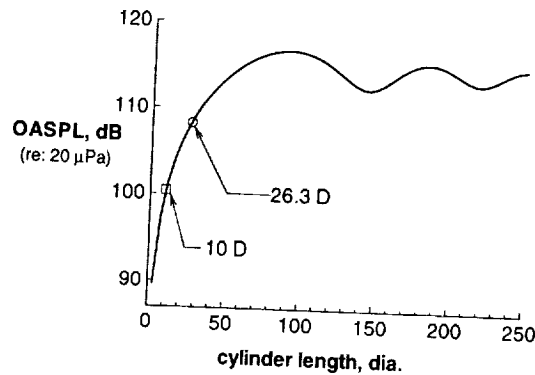


Figure 3. Overall sound pressure level (OASPL) plotted versus cylinder length in the 3-D acoustic computation. The 2-D CFD input data for the turbulent case with the SST model was used for this plot. The CFD data was assumed to be constant along the span for any given source time.

Requested Workshop Predictions

Now that the noise prediction procedure has been compared with experimental data we have enough confidence to present the results requested for the workshop. For these predictions, a cylinder length of $10D$ is used and the microphone locations are set to $35D$ away from the cylinder. Rather than just show the spectra at a few angles we have chosen to plot the entire directivity pattern around the cylinder for the laminar $Re = 1000$ and turbulent SST cases, which are representative. The overall sound pressure level, fundamental frequency, first harmonic are shown in figure 4. In the figure, the cylinder is at the origin and the flow moves from left to right. The 90 deg location is at the top of the figure and the axes units are in dB (re: $20\mu\text{Pa}$). Figure 4(b) and (c) show the expected dipole directivity pattern. The dipole shape in figure 4(c) is not symmetric right and left because of the left-to-right direction of the flow.

The dipole directivity pattern in figure 4 can be understood in more detail if we assume that the cylinder cross section is acoustically compact, that is that the acoustic wavelength is large compared to the diameter of the cylinder. This is actually a very good approximation in this flow condition. By assuming the cylinder has a compact cross section, we can predict the noise by using the section lift and drag directly rather than integrating the pressure over the cylinder surface. Figure 5 shows the directivity of the lift and drag separately for both the fundamental and first harmonic. By separating the lift and drag, we can see clearly in the figure that the noise produced at the fundamental frequency is entirely from the lift dipole (except

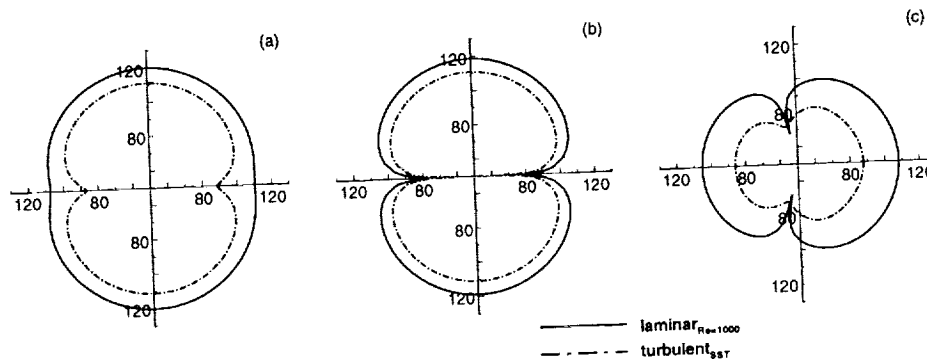


Figure 4. Predicted directivity patterns for $M = 0.2$ flow traveling left to right. Axes units are decibels (dB, re: $20\mu\text{Pa}$). (a) overall sound pressure level; (b) fundamental frequency; (c) first harmonic.

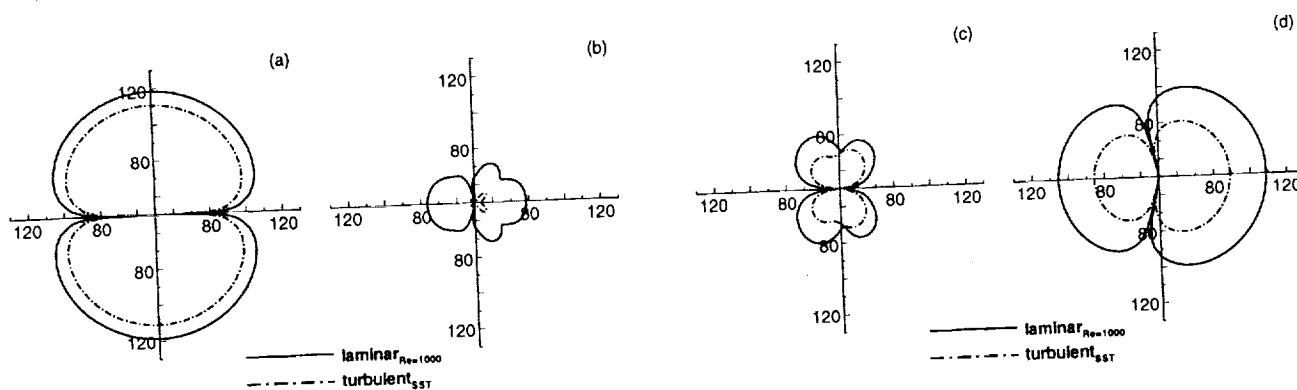


Figure 5. Comparison of the C_l and C_d noise components directivity pattern for $M = 0.2$ flow traveling left to right. Axes units are decibels (dB, re: $20\mu\text{Pa}$). (a) C_l fundamental frequency; (b) C_d fundamental frequency; (c) C_l first harmonic; (d) C_d first harmonic.

at the nulls of the dipole), while the drag completely dominates the first harmonic frequency. This is what should be expected because the period of the drag oscillation is half the lift oscillation period.

CONCLUDING REMARKS

The choice of Reynolds number $Re = 90,000$ makes the calculation of noise generated by flow past a circular cylinder particularly difficult. This difficulty is due to the transitional nature of the flow at this Reynolds number. Laminar flow calculations at such a high Reynolds number are irregular and nearly chaotic. The turbulent calculations are sensitive to both grid and turbulence model (See reference [2]).

Although we have performed only 2-D flow calculations in this paper, the amplitude of the noise prediction seems to agree fairly well with experimental data if a reasonable correlation length of the cylinder is used. To understand all of the details of the flow the problem must ultimately be solved as a 3-D problem to properly account for partial coherence of vortex shedding. The acoustic model does not require any changes for 3-D computations, but the CFD calculations will be very demanding. The CFL3D calculations for two dimensions already require approximately 4.5 CPU hrs on a Cray Y/MP (CITY3D - 80 hrs on workstation) to reach a periodic solution. This will be much longer for an adequately resolved 3-D computation. In contrast the acoustic calculation for a single observer position required about 70 CPU sec on a workstation.

REFERENCES

1. Lighthill, M. J., "On Sound Generated Aerodynamically, I: General Theory," *Proceedings of the Royal Society*, Vol. A221, 1952, pp. 564-587.
2. Cox, J. S., Rumsey, C. L., Brentner, K. S., and Younis, B. A., "Computation of Sound Generated by Viscous Flow Over A Circular Cylinder," *Proceedings of the ASME/ JSME/ IMechE/ CSME/ IAHR 4th International Symposium on Fluid-Structure Interactions, Aeroelasticity, Flow-Induced Vibration & Noise*, Nov. 1997. To appear.
3. Rumsey, C. L., Sanetrik, M. D., Biedron, R. T., Melson, N. D., and Parlette, E. B., "Efficiency and Accuracy of Time-Accurate Turbulent Navier-Stokes Computations," *Computers and Fluids*, Vol. 25, No. 2, 1996, pp. 217-236.
4. Menter, F. R., "Improved Two-Equation $k - \omega$ Turbulence Models for Aerodynamic Flows," NASA TM 103975, Oct. 1992.
5. Menter, F. R., and Rumsey, C. L., "Assessment of Two-Equation Turbulence Models for Transonic Flows," AIAA Paper 94-2343, 1994.
6. Przulj, V., and Younis, B. A., "Some Aspects of the Prediction of Turbulent Vortex Shedding from Bluff Bodies," *Symposium on Unsteady Separated Flows, 1993 ASME Fluids Engineering Division Annual Summer Meeting*, Vol. 149, Washington, DC, 1993.
7. Schlichting, H., *Boundary-Layer Theory*, McGraw-Hill Series in Mechanical Engineering, McGraw-Hill, New York, Seventh edition, 1979. Translated by J. Kestin.
8. Revell, J. D., Prydz, R. A., and Hays, A. P., "Experimental Study of Airframe Noise vs. Drag Relationship for Circular Cylinders," Lockheed Report 28074, Feb. 1977. Final Report for NASA Contract NAS1-14403.
9. Brentner, K. S., "Prediction of Helicopter Discrete Frequency Rotor Noise—A Computer Program Incorporating Realistic Blade Motions and Advanced Formulation," NASA TM 87721, Oct. 1986.
10. Farassat, F., and Succi, G. P., "The Prediction of Helicopter Discrete Frequency Noise," *Vertica*, Vol. 7, No. 4, 1983, pp. 309-320.
11. Ffowcs Williams, J. E., and Hawkings, D. L., "Sound Generated by Turbulence and Surfaces in Arbitrary Motion," *Philosophical Transactions of the Royal Society*, Vol. A264, No. 1151, 1969, pp. 321-342.
12. Alemdaroğlu, N., Rebillat, J. C., and Goethals, R., "An Aeroacoustic Coherence Function Method Applied to Circular Cylinder Flows," *Journal of Sound and Vibration*, Vol. 69, No. 3, 1980, pp. 427-439.
13. Blackburn, H. M., and Melbourne, W. H., "The Effect of Free-Stream Turbulence on Sectional Lift Forces on a Circular Cylinder," *Journal of Fluid Mechanics*, Vol. 306, Jan. 1996, pp. 267-292.
14. Kacker, S. C., Pennington, B., and Hill, R. S., "Fluctuating Lift Coefficient For a Circular Cylinder in Cross Flow," *Journal of Mechanical Engineering Science*, Vol. 16, No. 4, 1974, pp. 215-224.
15. Mittal, R., and Balachandar, S., "Effect of Three-Dimensionality on the Lift and Drag of Nominally Two-Dimensional Cylinders," *Physics of Fluids*, Vol. 7, No. 8, Aug. 1995, pp. 1841-1865.



527-71

043485

COMPUTATION OF NOISE DUE TO THE FLOW OVER A CIRCULAR CYLINDER

294017

P8

Sanjay Kumarasamy¹, Richard A. Korpus² and Jewel B. Barlow³

ABSTRACT

Noise due to the flow over a circular cylinder at a Reynolds number of 90,000 and Mach Number of 0.2 is computed using a two step procedure. As the first step, the flow is computed using an incompressible, time dependent Reynolds Averaged Navier-Stokes (RANS) solver. The resulting unsteady pressures are used as input to a two dimensional frequency domain acoustic solver, and 3D effects are studied using the Lighthill-Curle equation. Grid and time step dependency studies were performed to ascertain the accuracy of the flow computation. Computed acoustic results are compared to experimental values and agree well over much of the spectrum although the computed peak values corresponding to 2D acoustic simulations differ substantially from the available experimental measurements. Three dimensional acoustic simulation reduce the 2D noise level by 10dB.

INTRODUCTION

The most general way to compute noise radiation by a turbulent flow is to numerically solve the Navier-Stokes equations. The computation needs to be performed over a large spatial domain for long time intervals, simultaneously resolving small scales. This requirement overwhelms present day computing power. However, depending on the speed and nature of the flow certain simplifications can be made to make the computations feasible. In the case of low Mach number flows, there are many interesting cases in which there is no back reaction of the acoustic pressures on the flow. Hence, the computations can be split into two parts, namely, the computation of the flow, and the computation of noise. One advantage of this splitting is that computational methods and grids can be optimized separately for the vastly different scales involved.

Flow over a circular cylinder shows a variety of features which vary with Reynolds number. Williamson¹ reviewed the current state of understanding on the subject. The flow regime in the Reynolds number region of 1,000 to 200,000 is termed the "Shear-Layer Transition Regime". In this regime, transition develops in the shear layer characterized by an increase in the base pressure. As the Reynolds number increases, the turbulent transition point in the separated shear layer moves upstream and at 200,000 the flow becomes fully turbulent. At 90,000 it is believed the wake is fully turbulent but the attached boundary layer is essentially laminar. Unfortunately, the RANS solver used in the present work does not have a transition model. Since the extent of turbulent and laminar flow affects the unsteady pressures, three separate simulations were performed to ascertain the effect of the turbulence on the overall sound intensity predicted:

- Case 1. Laminar flow over the entire domain
- Case 2. Laminar flow + Turbulent wake (Base line Study)
- Case 3. Turbulent flow over the entire domain.

Once the underlying flow is computed, noise due to the flow can be computed by a two step procedure. Hardin *et al*² analyzed the sound generation due to the flow over a cavity at low Reynolds and Mach number using an incompressible, two dimensional time dependent Navier Stokes solver to drive the acoustic radiation using the method outlined by Hardin and Pope³. The present work employs a similar two step approach. First, the high Reynolds number, low Mach number flow is computed by an incompressible, time dependent, Reynolds Averaged Navier-Stokes solver. Second, the acoustic radiation is determined by solving the wave equation from the Lighthill Acoustic Analogy (LAA). The acoustic solver was previously validated against test cases for which closed form solutions exist^{4,5,6}.

The Computations reported in the present work refer to the Category 4 problem of the Second Computational Aeroacoustics Workshop¹⁵. The problem is restated for completeness. Consider uniform flow at Mach number of 0.2 over a two-dimensional cylinder of diameter $D=1.9$ cm. The Reynolds number based on the diameter of the cylinder is 90,000.

1. Research Associate, Glenn L. Martin Wind Tunnel, University of Maryland, College Park.

2. Senior Research Scientist, Science Application International Corporation, Annapolis.

3. Director, Glenn L. Martin Wind Tunnel, University of Maryland, College Park.

Perform numerical simulations to estimate the power spectra of the radiated sound in dB (per 20Hz bandwidth) at $r/D=35$ and $\theta = 60^\circ, 90^\circ, 120^\circ$ over the Strouhal number, $St = \frac{fD}{U_0}$, range of $0.01 \leq St \leq 0.61$ at $\Delta St = 0.002$.

MATHEMATICAL FORMULATION

RANS Solver

Computations were performed to obtain numerical solutions of the two dimensional Reynolds-Averaged Navier-Stokes equations,

$$\frac{\partial U_i}{\partial x_i} = 0; \quad \frac{\partial U_i}{\partial t} + U_j \frac{\partial U_i}{\partial x_j} + \frac{\partial P}{\partial x_i} - \frac{1}{Re} \frac{\partial^2 U_i}{\partial x_j \partial x_j} + \frac{\partial}{\partial x_j} (\overline{u_i u_j}) = 0 \quad (1)$$

where U_i , $(\overline{u_i u_j})$, and P represent the Cartesian mean velocities, Reynolds stresses, and pressure, respectively, and repeated indices indicate summation. The equations are solved using the Finite Analytic (FA) Technique^{7,8} on a body fitted grid, and Pressure/velocity coupling is accomplished using a hybrid SIMPLER/PISO method. Closure is accomplished by employing a one-equation $k-l$ for the near-wall viscous sublayer and the standard $k-\epsilon$ model for the rest of the domain. The solver is second order accurate in space, and first order accurate in time.

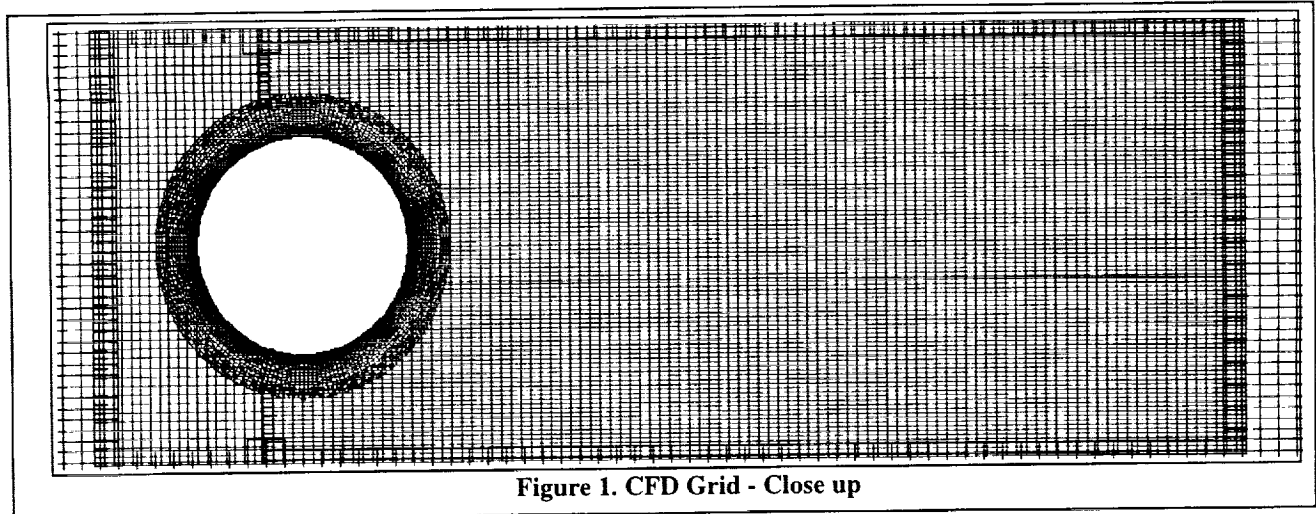


Figure 1. CFD Grid - Close up

The two dimensional circular cylinder and surrounding domain are discretized using a grid such as shown in Fig.(1). The Reynolds number based on diameter is 90,000. The physical domain extends 10 diameters upstream, 20 diameters downstream and 10 diameters above and below the body. Boundary layer spacing was used normal to the body with 40 points in the boundary layer, and a near wall spacing sufficient to resolve $y^+=1$ (smallest spacing = $O(10^{-5}D)$). Grid density was increased to a spacing of $0.02D$, and then held constant up to $4D$ downstream in the wake region to more adequately resolve the vortices. There are approximately 40,000 points in the domain. Uniform flow boundary conditions were applied on the inflow plane. A no slip condition was applied on the body with a Neumann boundary condition on pressure, $\frac{\partial p}{\partial n} = -\frac{2\partial k}{3\partial n}$ where k is the turbulent kinetic energy. For the outflow, top, and bottom boundaries, a radiation boundary condition, Han *et al*⁹, was applied for u , v and p and turbulence quantities.

Acoustic Solver

Lighthill's Acoustic Analogy: The governing equation for acoustic propagation based on Lighthill's Acoustic Analogy^{10,11}, is

$$\frac{1}{c_0^2} \frac{\partial^2 p}{\partial t^2} - \nabla^2 p = \frac{\partial^2}{\partial x_i \partial x_j} (T_{ij}) + \frac{\partial^2}{\partial t^2} \left(\frac{p}{c_0^2} - \rho \right) \quad (2)$$

where p is the pressure, c_o is the speed of sound, u_j is the velocity in the j direction, and $T_{ij} = \rho u_i u_j + \text{viscous}$ is the Lighthill's stress tensor. Neglecting viscous terms and for linear acoustics, $(p - p_o) = (\rho - \rho_o)c_o^2$ equation (2) becomes

$$\frac{1}{c_o^2} \frac{\partial^2 p}{\partial t^2} - \nabla^2 p = \frac{\partial^2}{\partial x_i \partial x_j} (\rho u_i u_j) \quad (3)$$

Non-dimensionalizing the variables, and applying Fourier transformation, leads to

$$\nabla^2 \bar{p} + \omega_s^2 M_\infty^2 \bar{p} = -\frac{\partial^2}{\partial x_i \partial x_j} u_i u_j \quad (4)$$

where M_∞ is the free stream Mach number and ω_s is the Strouhal number. It is noted here that the Mach number in equation (4) is a free parameter and for a consistent formulation it should be small so that the incompressibility assumption is valid for solving the flow. For the present work, the quadrupole noise was not computed. Hence the right hand side of Equation (4) is zero. Equation (4) is transformed to general curvilinear coordinates and discretized using the FA technique. A first order Bayliss-Turkel boundary condition for the Helmholtz equation^{12,13},

$$\frac{\partial p}{\partial r} - \left(ik - \frac{1}{2r} \right) p = 0 \quad (5)$$

where r is the radial distance, was applied on the far-field boundary. The Fourier transformed unsteady pressures from the RANS simulations are applied on the body as Dirichlet boundary conditions. Equation (5) is transformed into computational coordinates, discretized to second order accuracy, and solved implicitly. The discretized form of (4) with boundary conditions (5) constitute a non-positive definite complex system of linear equations. Conventional relaxation methods like Gauss-Seidal and Line relaxation fail due to the non-positive definitiveness and hence Bi-Conjugate Gradient Stabilized (BICG-STAB), Vorst¹⁴, is applied. The acoustic grid topology is shown in Fig.(2). The grid is a polar grid with the far field located at 20 times the wavelength of the acoustic wave. There are 20 grid points per wave length with a total of 400 grid points radially and 36 grid points in the θ direction.

Lighthill -Curle Equation: The acoustic computations were also performed using the Lighthill-Curle¹⁸ integral formulation. The governing equation is given by

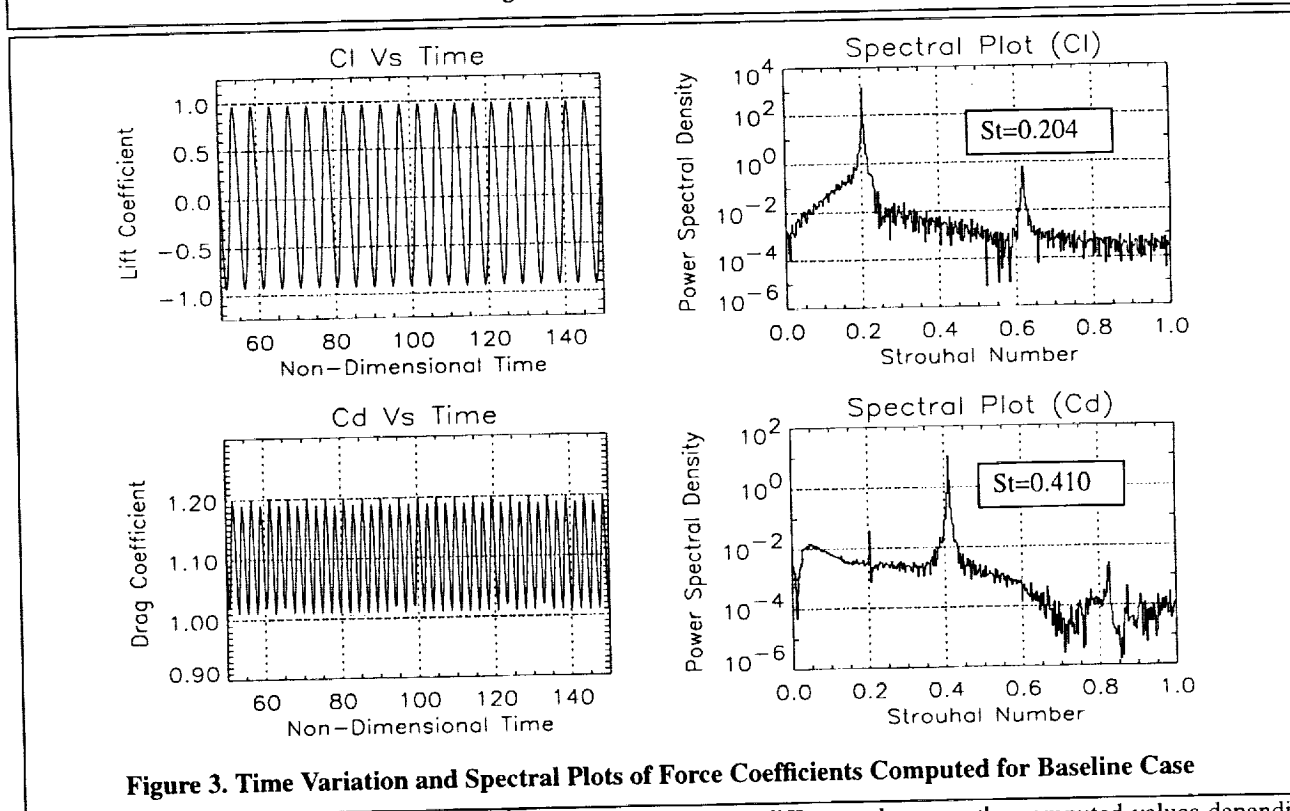
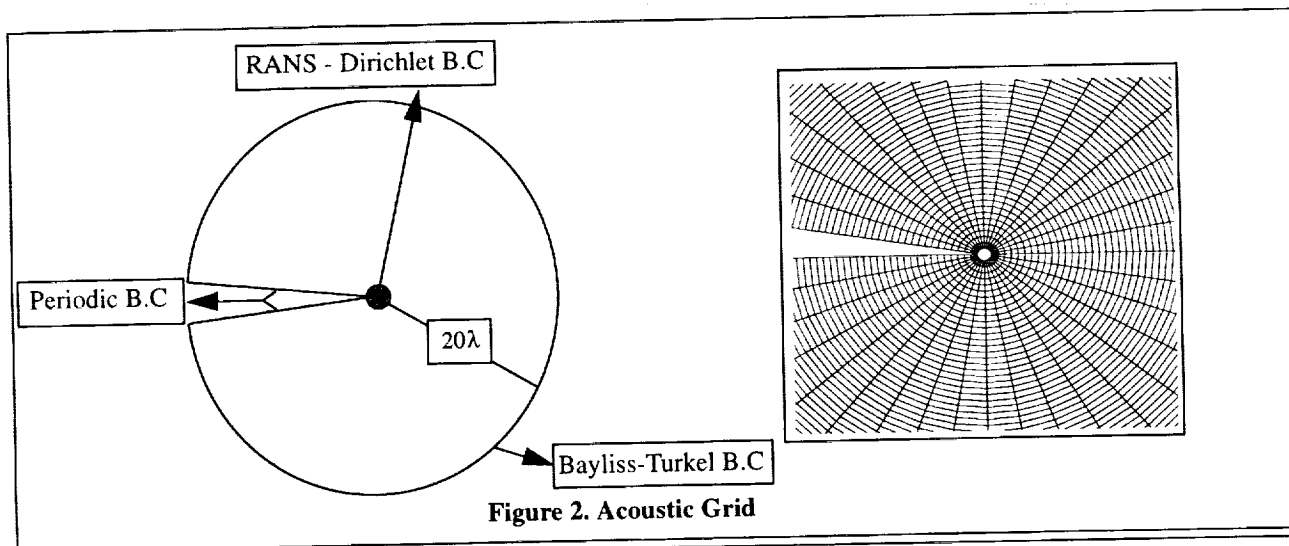
$$p(\vec{r}, t) = \int_{-l}^l \frac{1}{4\pi c} \left(\oint \frac{(\vec{n} \cdot \vec{r})}{r^2} \frac{\partial P_s}{\partial t} \right) (ds) dz \quad (6)$$

where c is the speed of sound, $p(\vec{r}, t)$ is the acoustic pressure at \vec{r} and time t , \vec{n} is the surface normal, P_s is the surface pressure and \vec{r} is the position vector from the surface to the point of observation. The integral along the spanwise direction is neglected for the 2D simulation and l is set to the experimental value for the 3D simulation. The acoustic pressures are Fourier transformed to obtain the acoustic spectrum.

RESULTS

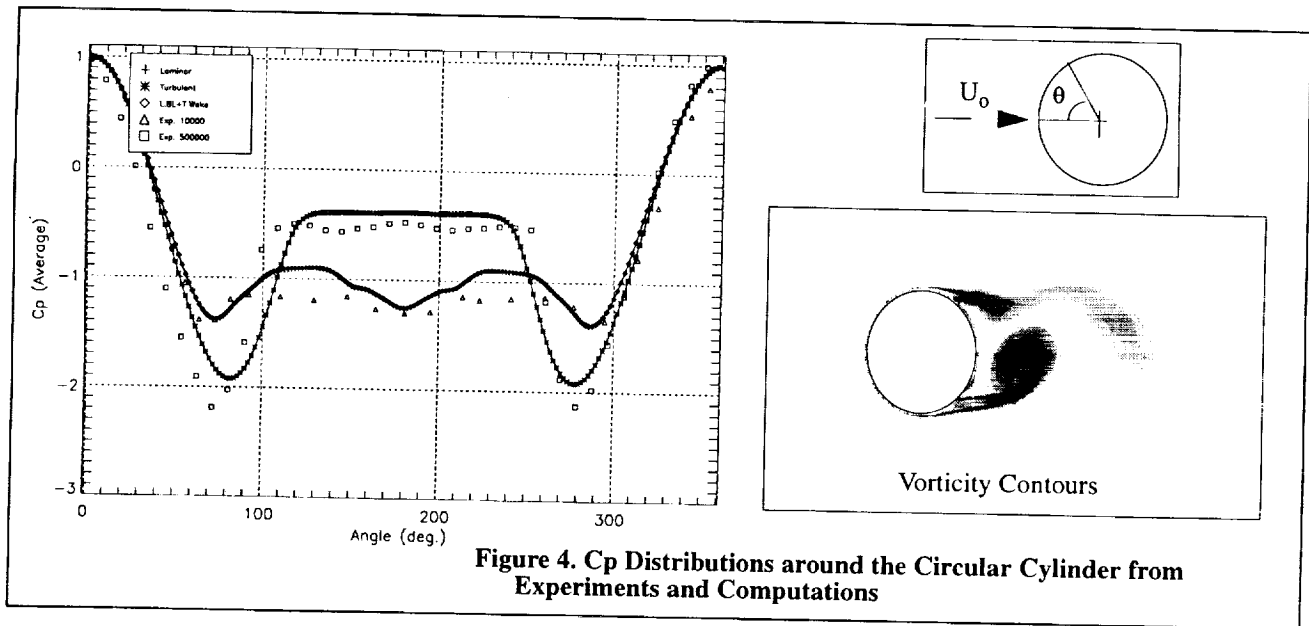
RANS Results

A baseline simulation was first performed using laminar boundary layer and turbulent wake configuration. The simulation used 40,000 point grid and a non-dimensional time step of 0.005. Laminar and turbulent flow in the entire domain were performed. There is no difference between the baseline and laminar flow results but the fully turbulent results show little in common with available experimental data. It is therefore decided to use laminar boundary layer + turbulent wake case for all further studies. Fig.(3) shows a partial time history of the force coefficients. It takes about 5000 iterations for the initial transients to vanish. From the spectral plot it is clear that the lift coefficient varies with a Strouhal number of 0.204 with a total variation of approximately 2.0. The drag coefficient varies at approximately twice the frequency of lift with total variation of 0.2. Since the acoustic pressures are driven by the time dependent variation of the pressures, it is expected that the acoustic pressure at the Strouhal number of 0.2 will be significantly higher than any other frequency. Fig.(4) shows time averaged C_p distributions around the circular cylinder for three computed cases and two experimental cases. $\theta=0$ or 2π corresponds to the front stagnation point. The experimental data corresponds to a Reynolds number of



10,000 (Laminar)¹⁶ and 500,000 (Turbulent)⁴. There is a significant difference between the computed values depending on whether the flow is laminar or turbulent but not much between the laminar and laminar boundary layer + turbulent wake simulations. Computational results show good agreement with the experimental data for the laminar simulation and for the turbulent case. No experimental data is available for the time variation of the pressures or force coefficients.

Table (1) shows the results of the time step and grid refinement studies. Three main parameters, namely, the lift variation, drag coefficient and Strouhal numbers are compared for the various simulations. Apart from the base line grid of 40,000 points, two other grids with 10,000 points (Coarse Grid) and 160,000 points (Fine Grid) were used for the grid refinement studies. Time accuracy studies were performed by changing the time steps from the base line non-dimensional time step of 0.005 to 0.01 and 0.001. The maximum time step for the fine grid was 0.001 and computations become unstable for any value greater. For the base line grid, there is a substantial change (30%) in the lift coefficient as the time step is reduced while the drag shows much smaller variation. Strouhal number is relatively unaffected by the choice of time step



	$\Delta t=0.01$	$\Delta t=0.005$	$\Delta t=0.001$
Coarse	-	0.96	-
Baseline	1.17	1.10	1.12
Fine	Unstable	Unstable	1.13

Drag Coefficient - Experimental Value = 1.15

	$\Delta t=0.01$	$\Delta t=0.005$	$\Delta t=0.001$
Coarse	-	0.60	-
Baseline	0.84	0.90	1.25
Fine	Unstable	Unstable	1.35

Half Amplitude of Lift Coefficient Variation

	$\Delta t=0.01$	$\Delta t=0.005$	$\Delta t=0.001$
Coarse	-	0.18	-
Baseline	0.21	0.21	0.21
Fine	Unstable	Unstable	0.22

Lift St. No. - Experimental Value = 0.2

	$\Delta t=0.01$	$\Delta t=0.005$	$\Delta t=0.001$
Coarse	-	0.36	-
Baseline	0.42	0.42	0.47
Fine	Unstable	Unstable	0.43

Drag St. No. - Experimental Value = 0.4

Table 1. Grid Dependency and Time Accuracy Studies

or the grid size. Grid refinement studies for a time step of 0.001 reveals that the baseline grid is adequate for resolving the flow features and further refinement does not show any significant benefits.

Acoustic Results

The computed pressures on the body were Fast Fourier Transformed and applied as Dirichlet boundary conditions for the acoustic solver. The acoustic solution is computed in the frequency domain so that each frequency constituted one simulation. About 200 simulations for Strouhal numbers ranging from 0.0121 to 0.608 in steps of 0.003 were performed.

Fig.(5) shows the power spectra of the radiated sound at $\theta=90$ degrees over the Strouhal number range of 0.01 to 0.6. The experimental data has been scaled according to the relation, $Sr^2 = cons$, where S is the spectrum, to arrive at the data corresponding to a distance of 35D. The trends are captured correctly for a substantial portion of the spectrum. The experimental data has a spectral resolution of 0.01 in Strouhal number compared to the computation bin size of 0.003. Computational Strouhal number of 0.204 ± 0.003 compares well with the experimental value of 0.186 ± 0.01^{17} . The magnitude of the sound pressure level corresponding to the dominant shedding frequency (0.204) is over predicted by 13 dB. Fig.(5) shows the comparison between the Lighthill-Curle calculations and the experimental data. From the plot it is clear that

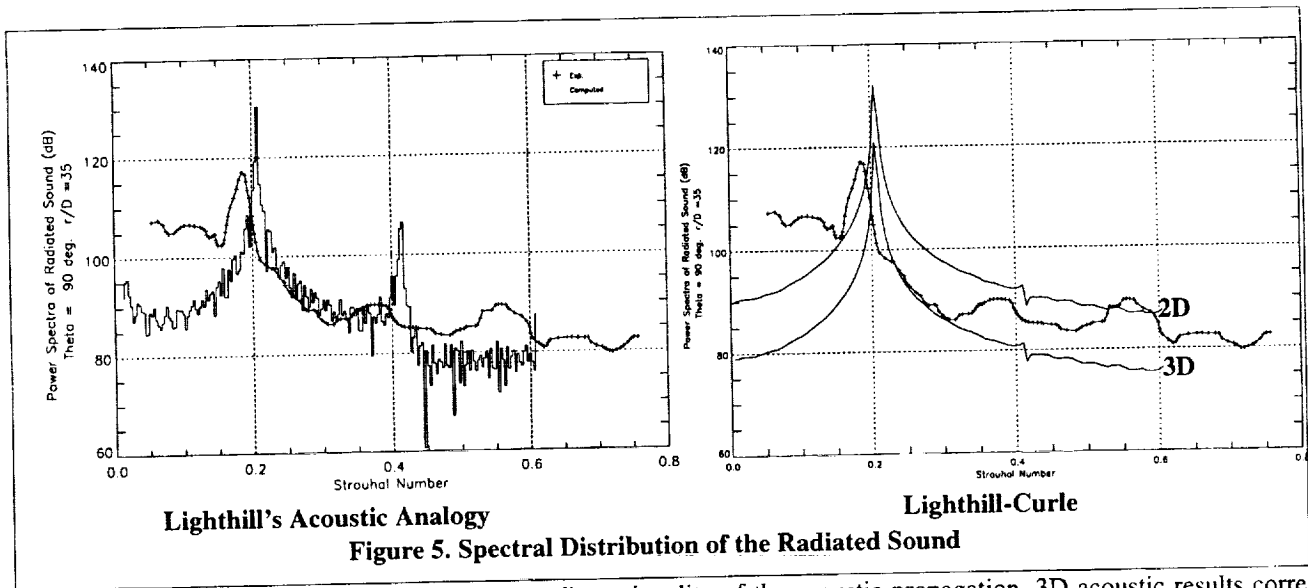


Figure 5. Spectral Distribution of the Radiated Sound

there is at least 10 dB reduction due to the three dimensionality of the acoustic propagation. 3D acoustic results corre-

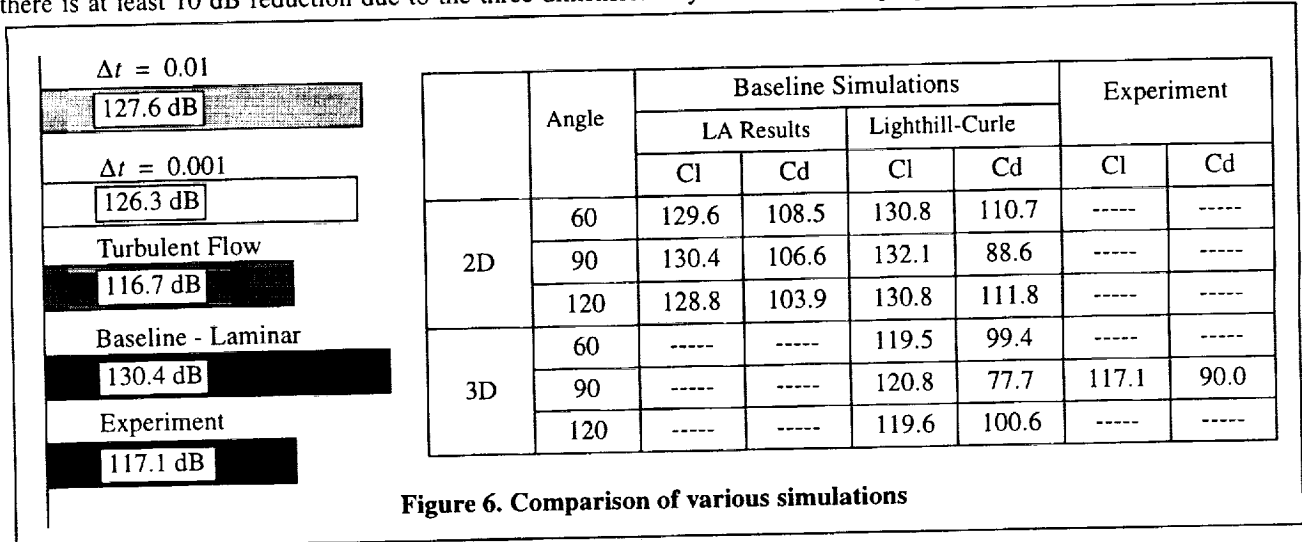


Figure 6. Comparison of various simulations

spond to a cylinder of 25D span with a correlation of 1.0 across the span.

As noted before, three flow simulations were performed. Laminar flow and Laminar flow with turbulent wake did not affect the results as shown in Fig.(6) and the solutions were found to be grid independent for the base line study of Laminar flow with turbulent wake. The effect of turbulent flow and different time steps for the base line studies have considerable impact on the flow properties. The sound pressure levels for various cases are compared in Fig.(6) corresponding to dominant shedding frequency. The time step reduction shows a change of -3dB from the baseline value. The table in Fig.(6) summarizes the results from LAA and Lighthill-Curle simulations corresponding to 60,90 and 120 degrees.

CONCLUSIONS

Sound generated due to the flow over a circular cylinder at a Reynolds number of 90,000 was computed. The Strouhal number associated with the primary shedding was captured quite accurately by the computations. Grid dependency studies were performed to demonstrate the convergence. Time accuracy studies were also performed and show a significant change in the overall results due to the limitation of the first order time accuracy. Acoustic computations were performed using the unsteady pressures to drive the LAA and Lighthill-Curle simulations. The computed noise levels compared reasonably well with the experimental values. The trends are captured quite correctly by the computational solution. Sound pressure level corresponding to the dominant shedding frequency is over predicted in the case of 2D simulation and 3D

results show a reduction of 10 dB. It is demonstrated that the turbulent flow will produce much less cyclic variation leading to a change of -13dB. The present work underlines the need for benchmark experiments that provide more information on the flow properties as well as the acoustic properties to help in ascertaining and refining the computations in both steps, namely, source evaluation and acoustic propagation.

REFERENCES

1. Williamson, C.H.K., "Vortex dynamics in the cylinder wake", *Ann. Rev. of Fluid Mech.*, vol. 28, 1996
2. Hardin, J.C., Pope, S., "Sound Generation by Flow over a Two-Dimensional Cavity", *AIAA Jou.*, Vol.33 No.3. p 407, 1995
3. Hardin, J.C., Pope, S., "A new technique for Aerodynamic Noise Calculation" *Proceedings of the DGLR/AIAA 14th Aeroacoustics Conference*, AIAA, Washington, D.C., pp 448-456, 1992.
4. Kumarasamy, S., "Incompressible Flow Simulation Over a Half Cylinder with Results Used to Compute Associated Acoustic Radiation", Ph.D Thesis, UM-AERO-95-68, Dept. of Aero. Engg., University of Maryland, College Park, 1995.
5. Kumarasamy, S. and Barlow, J.B., "Computation of the noise due to the flow over a half cylinder in ground effect", Presented in the 17th AIAA Aeroacoustics Conference, State College, Penn State, PA, 1996.
6. Kumarasamy, S., Barlow, J.B., "Computational Aeroacoustics of the Flow over a Half Cylinder", AIAA-96-0873, Presented at 34th Aerospace Sciences Meeting and Exhibit, Reno, 1996.
7. Chen, H.C. and Korpus, R., "A Multiblock Finite-Analytic Reynolds-Averaged Navier-Stokes Method for 3D Incompressible Flows," *ASME Summer Fluid Dynamic Conference*, 1993.
8. Korpus, R.A. and Falzarano, J.M., "Prediction of viscous ship roll damping by unsteady Navier-Stokes techniques", To be published in *Offshore Mechanics and Arctic Engineering Journal*, March, 1997.
9. Han, T.Y., Meng, J.C.S., and Innis, G.E., "An Open Boundary Condition for Incompressible Stratified Flows" *J.Comp.Phy.* 49, 276-297, 1983.
10. Lighthill, M.J., "On sound generated aerodynamically I. General Theory", *Proc. Roy. Soc. A* 211, pp. 564, 1952
11. Lighthill, M.J., "On sound generated aerodynamically II. Turbulence as a source of Sound", *Proc. Roy. Soc. A* 222, pp. 114, 1952
12. Bayliss, A., Turkel, E., "Radiation Boundary Conditions for Wave like equations", *Comm. Pure. Appl. Math.*, vol.33, pp. 707-725, 1980.
13. Bayliss, A., Gunzburger, Turkel, E., "Boundary conditions for the numerical solution of elliptic equations in exterior regions", *SIAM J. Appl. Math.*, vol.42, pp 430, 1982.
14. Vorst, H.V.D, et al., "Iterative solution methods for certain sparse linear systems with a non-symmetric matrix arising from PDE-problems", *J. Comp. Phys.*, 44, pp 1-19, 1981.
15. Second Computational Aeroacoustics (CAA) Workshop on Benchmark Problems, Florida State University, Florida, Nov. 1996.
16. Kato, C, Iida, A., Takano, Y., Fujita, H., and Ikegawa, M. "Numerical Prediction of Aerodynamic Noise Radiated from Low Mach Number Turbulent Wake," *AIAA 31st Aerospace Sciences Meeting*, Reno, NV, 1993 (AIAA #93-0145).
17. Revell, J.D., Roland, A.P., and Hays, P.A., "Experimental Study of Airframe Noise vs. Drag Relationship for Circular Cylinders", *Lockheed Report LR28074* Feb 28, 1977 (NASA Contract NAS1-14403).
18. Blake, W.K., "Mechanics of Flow-Induced Sound and Vibration Volume 1. General Concepts and Elementary Sources", Academic Press, Inc., 1986.



528-71
043487
294018
p 14

**A VISCOUS/ACOUSTIC SPLITTING
TECHNIQUE FOR AEOLIAN
TONE PREDICTION**

D. Stuart Pope
Lockheed Martin Engineering and Sciences Company
Hampton, Virginia

INTRODUCTION

In an attempt to better understand noise generated by various airframe components such as landing gear and antennas, a precursor problem was formulated in which noise due to the passage of a steady inflow around a two-dimensional circular cylinder was examined using a viscous/acoustic splitting method. It is believed that this preliminary problem will lead to wider application of the method to more complex geometries of interest. Sample calculations illustrate that separate treatment of the associated hydrodynamics and acoustics leads to better understanding of the noise generation process, easier management of the overall computational effort, and provides results that agree well with experimental work.

Problem Description and Geometry

Consider a two-dimensional cylinder of radius r_0 immersed in a steady, uniform flowfield of velocity U_0 (see figure 1). The flow Reynolds number (based on cylinder diameter and U_0) is taken to be 20,000. Associated with this flow is the well-known von Karmann vortex street which occurs in the cylinder wake due to alternating vortex shedding from the top and bottom cylinder surfaces. The formation and subsequent motion of these vortex structures generate noise often referred to as Aeolian tones at a characteristic Strouhal number of approximately 0.21. The goal of this work is to properly model the generation of these vortices, accurately track their motions, and predict their associated noise for distant observers.

Viscous/Acoustic Splitting Method

For several reasons, Hardin¹ has proposed treating the acoustic calculation separate from the hydrodynamics by regarding the total primitive fluids quantities ρ, u, v, p as composed of an incompressible mean flow and a perturbation about that mean. It can be shown that while the perturbations represent in the nearfield the difference between the fully compressible flow and the assumed incompressible mean flow, they are, in the farfield, purely acoustic (see Hardin for details). By splitting the problem in this fashion, separate methods may be used to calculate the perturbations and the mean flow. This has advantages both in terms of gridding and in application of appropriate boundary conditions. In addition, this allows greater flexibility in the independent choice of solution method. In particular, the method can be illustrated by first considering the governing continuity and momentum equations for the cylinder flow just described:

$$\frac{\partial \rho}{\partial t} + \frac{\partial(\rho u)}{\partial r} + \frac{1}{r} \frac{\partial(\rho v)}{\partial \theta} + \frac{\rho u}{r} = 0$$

$$\frac{\partial u}{\partial t} + u \frac{\partial u}{\partial r} + \frac{v}{r} \frac{\partial u}{\partial \theta} - \frac{v^2}{r} = -\frac{1}{\rho} \frac{\partial p}{\partial r} + v \left[\frac{\partial^2 u}{\partial r^2} + \frac{1}{r} \frac{\partial u}{\partial r} + \frac{1}{r^2} \frac{\partial^2 u}{\partial \theta^2} - \frac{u}{r^2} - \frac{2}{r^2} \frac{\partial v}{\partial \theta} \right]$$

$$\frac{\partial v}{\partial t} + u \frac{\partial v}{\partial r} + \frac{v}{r} \frac{\partial v}{\partial \theta} + \frac{uv}{r} = -\frac{1}{\rho r} \frac{\partial p}{\partial \theta} + v \left[\frac{\partial^2 v}{\partial r^2} + \frac{1}{r} \frac{\partial v}{\partial r} + \frac{1}{r^2} \frac{\partial^2 v}{\partial \theta^2} - \frac{v}{r^2} + \frac{2}{r^2} \frac{\partial u}{\partial \theta} \right]$$

We also assume that for low-speed flows, the isentropic relation between pressure and density may be used:

$$\frac{\partial p}{\partial t} = c^2 \frac{\partial \rho}{\partial t}$$

$$c^2 = \frac{\gamma p}{\rho} .$$

The total variables are now decomposed into incompressible mean flow quantities (which are, in general, time varying) and perturbations:

$$u = U + u'$$

$$v = V + v'$$

$$p = P + p'$$

$$\rho = \rho_o + \rho' .$$

In terms of these quantities, continuity becomes

$$\frac{\partial \rho'}{\partial t} + \rho \frac{\partial u'}{\partial r} + u \frac{\partial \rho'}{\partial r} + \frac{\rho}{r} \frac{\partial v'}{\partial \theta} + \frac{v}{r} \frac{\partial \rho'}{\partial \theta} + \frac{\rho u'}{r} + \rho \left(\frac{\partial U}{\partial r} + \frac{1}{r} \frac{\partial V}{\partial \theta} + \frac{U}{r} \right) = 0 .$$

Noting that the terms in parentheses are identically those of the incompressible continuity equation and sum to zero, we obtain

$$\frac{\partial \rho'}{\partial t} + \rho \left(\frac{\partial u'}{\partial r} + \frac{1}{r} \frac{\partial v'}{\partial \theta} + \frac{u'}{r} \right) + u \frac{\partial \rho'}{\partial r} + \frac{v}{r} \frac{\partial \rho'}{\partial \theta} = 0 .$$

Similar treatment of the momentum equations leads to

$$\frac{\partial u'}{\partial t} + u \frac{\partial u'}{\partial r} + \frac{v}{r} \frac{\partial u'}{\partial \theta} - \frac{v^2}{r} + u' \frac{\partial U}{\partial r} + \frac{v'}{r} \frac{\partial U}{\partial \theta} - \frac{2Vv'}{r} =$$

$$= v \left(\frac{\partial^2 u'}{\partial r^2} + \frac{1}{r} \frac{\partial u'}{\partial r} + \frac{1}{r^2} \frac{\partial^2 u'}{\partial \theta^2} - \frac{u'}{r^2} - \frac{2}{r^2} \frac{\partial v'}{\partial \theta} \right) - \frac{\rho'}{1+\rho'} \left(\frac{\partial U}{\partial t} + U \frac{\partial U}{\partial r} + \frac{V}{r} \frac{\partial U}{\partial \theta} - \frac{V^2}{r} \right) +$$

$$+ \frac{v\rho'}{1+\rho'} \left(\frac{\partial^2 U}{\partial r^2} + \frac{1}{r} \frac{\partial U}{\partial r} + \frac{1}{r^2} \frac{\partial^2 U}{\partial \theta^2} - \frac{U}{r^2} - \frac{2}{r^2} \frac{\partial V}{\partial \theta} \right) - \frac{1}{1+\rho'} \frac{\partial p'}{\partial r}$$

and

$$\begin{aligned}
& \frac{\partial v'}{\partial t} + u \frac{\partial v'}{\partial r} + \frac{v}{r} \frac{\partial v'}{\partial \theta} + \frac{u'v'}{r} + u' \frac{\partial v'}{\partial r} + \frac{v'}{r} \frac{\partial v'}{\partial \theta} + \frac{Uv'}{r} + \frac{Vu'}{r} = \\
& = v \left(\frac{\partial^2 v'}{\partial r^2} + \frac{1}{r} \frac{\partial v'}{\partial \theta} + \frac{1}{r^2} \frac{\partial^2 v'}{\partial \theta^2} - \frac{v'}{r^2} + \frac{2}{r^2} \frac{\partial u'}{\partial \theta} \right) - \frac{\rho'}{1+\rho'} \left(\frac{\partial v'}{\partial t} + U \frac{\partial v'}{\partial r} + \frac{v}{r} \frac{\partial v'}{\partial \theta} + \frac{Uv'}{r} \right) + \\
& + \frac{v\rho'}{1+\rho'} \left(\frac{\partial^2 V}{\partial r^2} + \frac{1}{r} \frac{\partial V}{\partial r} + \frac{1}{r^2} \frac{\partial^2 V}{\partial \theta^2} - \frac{V}{r^2} + \frac{2}{r^2} \frac{\partial U}{\partial \theta} \right) - \frac{1}{r(\rho_o + \rho')} \frac{\partial p'}{\partial \theta} .
\end{aligned}$$

Finally, the relation between pressure and density becomes

$$\frac{\partial p'}{\partial t} = c^2 \frac{\partial \rho'}{\partial t} - \frac{\partial P}{\partial t}$$

These expressions constitute four equations in the four unknown quantities ρ', u', v', p' . The incompressible terms which also appear are determined separately and act as forcing functions to the equations. Prior to solving, the above equations are first made nondimensional. The perturbation quantities are nondimensionalized by cylinder radius, r_o , the ambient speed of sound c_o , and incompressible density, ρ_o . The incompressible terms are treated similarly, but freestream velocity U_o is used in the nondimensionalization rather than c_o . The resulting expressions are

$$\begin{aligned}
M_o \frac{\partial \rho'}{\partial t} + (1+\rho') \frac{\partial u'}{\partial r} + (M_o U + u') \frac{\partial \rho'}{\partial r} + \frac{1+\rho'}{r} \frac{\partial v'}{\partial \theta} + \frac{M_o V + v'}{r} \frac{\partial \rho'}{\partial \theta} + \frac{(1+\rho')u'}{r} &= 0 \\
M_o \frac{\partial u'}{\partial t} + (M_o U + u') \frac{\partial u'}{\partial r} + \frac{M_o V + v'}{r} \frac{\partial u'}{\partial \theta} + M_o \left(u' \frac{\partial U}{\partial r} + \frac{v'}{r} \frac{\partial U}{\partial \theta} - \frac{2Vv'}{r} \right) - \frac{v'^2}{r} &= \\
= \frac{M_o}{\text{Re}} \left(\frac{\partial^2 u'}{\partial r^2} + \frac{1}{r} \frac{\partial u'}{\partial \theta} + \frac{1}{r^2} \frac{\partial^2 u'}{\partial \theta^2} - \frac{u'}{r^2} - \frac{2}{r^2} \frac{\partial v'}{\partial \theta} \right) - \frac{\rho' M_o^2}{1+\rho'} \left(\frac{\partial U}{\partial t} + U \frac{\partial U}{\partial r} + \frac{v}{r} \frac{\partial U}{\partial \theta} - \frac{V^2}{r} \right) + \\
+ \frac{M_o^2 \rho'}{\text{Re}(1+\rho')} \left(\frac{\partial^2 U}{\partial r^2} + \frac{1}{r} \frac{\partial U}{\partial r} + \frac{1}{r^2} \frac{\partial^2 U}{\partial \theta^2} - \frac{U}{r^2} - \frac{2}{r^2} \frac{\partial V}{\partial \theta} \right) - \frac{1}{1+\rho'} \frac{\partial p'}{\partial r} \\
M_o \frac{\partial v'}{\partial t} + (M_o U + u') \frac{\partial v'}{\partial r} + \frac{M_o V + v'}{r} \frac{\partial v'}{\partial \theta} + M_o \left(u' \frac{\partial V}{\partial r} + \frac{v'}{r} \frac{\partial V}{\partial \theta} + \frac{Uv'}{r} + \frac{Vu'}{r} \right) + \frac{u'v'}{r} &= \\
= \frac{M_o}{\text{Re}} \left(\frac{\partial^2 v'}{\partial r^2} + \frac{1}{r} \frac{\partial v'}{\partial \theta} + \frac{1}{r^2} \frac{\partial^2 v'}{\partial \theta^2} - \frac{v'}{r^2} + \frac{2}{r^2} \frac{\partial u'}{\partial \theta} \right) - \frac{\rho' M_o^2}{1+\rho'} \left(\frac{\partial V}{\partial t} + U \frac{\partial V}{\partial r} + \frac{v}{r} \frac{\partial V}{\partial \theta} + \frac{UV}{r} \right) + \\
+ \frac{M_o^2 \rho'}{\text{Re}(1+\rho')} \left(\frac{\partial^2 V}{\partial r^2} + \frac{1}{r} \frac{\partial V}{\partial r} + \frac{1}{r^2} \frac{\partial^2 V}{\partial \theta^2} - \frac{V}{r^2} + \frac{2}{r^2} \frac{\partial U}{\partial \theta} \right) - \frac{1}{r(1+\rho')} \frac{\partial p'}{\partial \theta}
\end{aligned}$$

and lastly,

$$\frac{\partial p'}{\partial t} = c^2 \frac{\partial \rho'}{\partial t} - M_o^2 \frac{\partial P}{\partial t}$$

where

$$c^2 = \frac{\gamma(M_o^2 P + p')}{1 + \rho'}$$

In the above equations, M_o refers to the freestream Mach number and Reynolds number is based on cylinder radius. All variables are considered nondimensional throughout the remainder of this work.

Incompressible Mean Flow Calculation

The forcing terms appearing in the above equations may be found by any convenient method. In this work, since the flowfield is two-dimensional, a vorticity-stream function approach is used. The governing equations are, in nondimensional variables

$$\left(\frac{\partial^2}{\partial r^2} + \frac{1}{r} \frac{\partial}{\partial \theta} + \frac{1}{r^2} \frac{\partial^2}{\partial \theta^2} \right) \psi = -\Omega$$

and

$$\left(\frac{\partial}{\partial t} + \frac{1}{r} \frac{\partial \psi}{\partial \theta} \frac{\partial}{\partial r} - \frac{1}{r} \frac{\partial \psi}{\partial r} \frac{\partial}{\partial \theta} \right) \Omega = \frac{1}{\text{Re}} \left(\frac{\partial^2}{\partial r^2} + \frac{1}{r} \frac{\partial}{\partial r} + \frac{1}{r^2} \frac{\partial^2}{\partial \theta^2} \right) \Omega .$$

The effects of viscosity strongly dominate the character of the incompressible flowfield. These effects are especially important at the cylinder surface and their accurate calculation requires a fine grid. A coordinate transformation is employed which finely spaces grid points at the cylinder surface while sparsely spacing points in the farfield. This transformation is

$$r = e^{a\zeta}$$

$$\eta = \frac{\theta}{a}$$

where $a = \ln(r_{\max})$, r_{\max} being the outer boundary of the computational domain. In these coordinates, transformed equations for ψ and Ω may be solved on a uniformly spaced ζ, η grid, yet the surface grid point clustering necessary in the physical domain can be realized. The transformed equations are

$$\left(\frac{\partial^2}{\partial \zeta^2} + \frac{\partial^2}{\partial \eta^2} \right) \psi = -E^2 \Omega$$

$$\left(E^2 \frac{\partial}{\partial t} + \frac{\partial \psi}{\partial \eta} \frac{\partial}{\partial \zeta} - \frac{\partial \psi}{\partial \zeta} \frac{\partial}{\partial \eta} \right) \Omega = \frac{1}{\text{Re}} \left(\frac{\partial^2}{\partial \zeta^2} + \frac{\partial^2}{\partial \eta^2} \right) \Omega$$

where

$$E = ae^{a\zeta}.$$

Note that an additional relation is required to specify P which appears in the perturbation equations. This relation can be found by differentiation of the momentum equations and adding the two. The result is, in transformed coordinates,

$$a^2 \left[\left(\frac{\partial \psi}{\partial \zeta} \right)^2 + \left(\frac{\partial \psi}{\partial \eta} \right)^2 \right] + a \left[\frac{\partial \psi}{\partial \zeta} \left(\frac{\partial^2 \psi}{\partial \eta^2} - \frac{\partial^2 \psi}{\partial \zeta^2} \right) - 2 \frac{\partial \psi}{\partial \eta} \frac{\partial^2 \psi}{\partial \zeta \partial \eta} \right] + \left[\frac{\partial^2 \psi}{\partial \zeta^2} \frac{\partial^2 \psi}{\partial \eta^2} + \left(\frac{\partial^2 \psi}{\partial \zeta \partial \eta} \right)^2 \right] = -\frac{E^2}{2} \left(\frac{\partial^2 P}{\partial \zeta^2} + \frac{\partial^2 P}{\partial \eta^2} \right)$$

The solution procedure is initiated by assuming that the flowfield is everywhere both potential and irrotational. Thus, at $t = 0$,

$$\begin{aligned} \psi(r, \theta) &= \left(r - \frac{1}{r} \right) \sin \theta \\ \Omega(r, \theta) &= 0 \\ P(r, \theta) &= P_o - \frac{1}{2r^4} + \frac{1}{r^2} \cos 2\theta - \frac{1}{r} \sin^2 \theta \end{aligned}$$

where P_o is nondimensional ambient pressure given by

$$P_o = \frac{1}{\gamma M_o^2} .$$

These potential flow conditions are maintained throughout the simulation at the outer boundary which is far from the cylinder. At the cylinder surface, the no-slip conditions

$$\begin{aligned} \psi(1, \eta) &= 0 \\ \Omega(1, \eta) &= -\left(\frac{1}{E^2} \frac{\partial^2 \psi}{\partial \zeta^2} \right)_{1, \eta} \\ \left(\frac{\partial P}{\partial \zeta} \right)_{1, \eta} &= \left(\frac{1}{\text{Re } E} \frac{\partial^3 \psi}{\partial \zeta^2 \partial \eta} \right)_{1, \eta} \end{aligned}$$

are imposed. The vorticity transport equation is advanced in time at interior points using a 'donor cell' method² in which finite differencing of the advection terms is chosen in such a way as to ensure the transfer of information in the locally windward direction. Hence, vorticity is advanced to time step $n + 1$ via

$$\begin{aligned} \Omega_{i,j}^{n+1} &= \Omega_{i,j}^n + \frac{\Delta t}{\text{Re } E_{i,j}^2} \left[\frac{\Omega_{i+1,j}^n - 2\Omega_{i,j}^n + \Omega_{i-1,j}^n}{(\Delta \zeta)^2} + \frac{\Omega_{i,j+1}^n - 2\Omega_{i,j}^n + \Omega_{i,j-1}^n}{(\Delta \eta)^2} \right] + \\ &+ \frac{\Delta t}{E_{i,j}^2} \left[\frac{u_{\zeta E} \Omega_E - u_{\zeta W} \Omega_W}{\Delta \zeta} + \frac{u_{\eta N} \Omega_N - u_{\eta S} \Omega_S}{\Delta \eta} \right] \end{aligned}$$

where

$$\begin{aligned}
u_{\zeta E} &= \frac{1}{2} \left(\frac{\psi_{i,j+2}^n - \psi_{i,j}^n}{2\Delta\eta} + \frac{\psi_{i,j+1}^n - \psi_{i,j-1}^n}{2\Delta\eta} \right) \\
u_{\zeta W} &= \frac{1}{2} \left(\frac{\psi_{i,j}^n - \psi_{i,j-2}^n}{2\Delta\eta} + \frac{\psi_{i,j+1}^n - \psi_{i,j-1}^n}{2\Delta\eta} \right) \\
u_{\eta N} &= \frac{1}{2} \left(\frac{\psi_{i+2,j}^n - \psi_{i,j}^n}{2\Delta\zeta} + \frac{\psi_{i+1,j}^n - \psi_{i-1,j}^n}{2\Delta\zeta} \right) \\
u_{\eta S} &= \frac{1}{2} \left(\frac{\psi_{i,j}^n - \psi_{i-2,j}^n}{2\Delta\zeta} + \frac{\psi_{i+1,j}^n - \psi_{i-1,j}^n}{2\Delta\zeta} \right)
\end{aligned}$$

and

$$\begin{aligned}
\Omega_E &= \begin{cases} \Omega_{i,j}^n, & u_{\zeta E} \geq 0 \\ \Omega_{i+1,j}^n, & u_{\zeta E} < 0 \end{cases} \\
\Omega_W &= \begin{cases} \Omega_{i-1,j}^n, & u_{\zeta W} \geq 0 \\ \Omega_{i,j}^n, & u_{\zeta W} < 0 \end{cases} \\
\Omega_N &= \begin{cases} \Omega_{i,j}^n, & u_{\eta N} \geq 0 \\ \Omega_{i,j+1}^n, & u_{\eta N} < 0 \end{cases} \\
\Omega_S &= \begin{cases} \Omega_{i,j-1}^n, & u_{\eta S} \geq 0 \\ \Omega_{i,j}^n, & u_{\eta S} < 0 \end{cases}
\end{aligned}$$

After obtaining updated values $\Omega_{i,j}^{n+1}$ at all interior points, the poisson equation for $\psi_{i,j}^{n+1}$ is solved using successive over-relaxation(SOR), i.e.,

$$\psi_{i,j}^{k+1} = (1 - \omega)\psi_{i,j}^k + \frac{\omega}{2(1 + \beta^2)} \left[\psi_{i+1,j}^k + \psi_{i-1,j}^{k+1} + \beta^2(\psi_{i,j+1}^k + \psi_{i,j-1}^{k+1}) + E_{i,j}^2 (\Delta\zeta)^2 \Omega_{i,j}^{n+1} \right]$$

where

$$\beta = \frac{\Delta\zeta}{\Delta\eta}$$

and ω is a relaxation parameter which can be chosen arbitrarily to speed convergence so long as $0 < \omega < 2$ is maintained. The superscript k in the above equation refers to the SOR iterates. Iteration continues until successive iterates $\psi_{i,j}^k$ and $\psi_{i,j}^{k+1}$ differ by less than some specified tolerance over the entire flowfield which is then considered converged.

The final step in obtaining the incompressible solution at the new time step consists of solution of the poisson equation for pressure using a cyclic reduction algorithm to solve a set of simultaneous linear equations. The SOR approach just described could also have been used.

Perturbation Flow Calculation

Having obtained the mean flow in terms of $\psi_{i,j}^{n+1}$ and $P_{i,j}^{n+1}$, a different algorithm can be used to solve the perturbation equations at the new time step. In this work, a second-order explicit MacCormack predictor-

corrector method was chosen. It is important that the algorithm selected minimize damping and dispersion in order to accurately capture the acoustic waves. The effects of viscosity on the perturbations can be shown to be almost negligible so that for this calculation, a stretched grid is not required. Rather, a grid uniform in both radial and azimuthal directions is chosen. The incompressible terms necessary for the perturbation equations are simply interpolated from the stretched onto the uniform grid. The perturbation equations may then be solved by first defining the viscous and incompressible contributions to the perturbed velocity temporal fluxes

$$\begin{aligned} \left(\frac{\delta u'}{\delta t}\right)_{visc+inc} &\equiv \frac{M_o}{\text{Re}} \left(\frac{\bar{\delta}^2 u'}{\bar{\delta} r^2} + \frac{1}{r} \frac{\bar{\delta} u'}{\bar{\delta} r} + \frac{1}{r^2} \frac{\bar{\delta}^2 u'}{\bar{\delta} \theta^2} - \frac{u'}{r^2} - \frac{2}{r^2} \frac{\bar{\delta} v'}{\bar{\delta} \theta} \right) \\ &\quad + \frac{M_o \rho'}{\rho} \left(\frac{\bar{\delta}^2 U}{\bar{\delta} r^2} + \frac{1}{r} \frac{\bar{\delta} U}{\bar{\delta} r} + \frac{1}{r^2} \frac{\bar{\delta}^2 U}{\bar{\delta} \theta^2} - \frac{U}{r^2} - \frac{2}{r^2} \frac{\bar{\delta} V}{\bar{\delta} \theta} \right) \\ \left(\frac{\delta v'}{\delta t}\right)_{visc+inc} &\equiv \frac{M_o}{\text{Re}} \left(\frac{\bar{\delta}^2 v'}{\bar{\delta} r^2} + \frac{1}{r} \frac{\bar{\delta} v'}{\bar{\delta} r} + \frac{1}{r^2} \frac{\bar{\delta}^2 v'}{\bar{\delta} \theta^2} - \frac{v'}{r^2} + \frac{2}{r^2} \frac{\bar{\delta} u'}{\bar{\delta} \theta} \right) \\ &\quad + \frac{M_o \rho'}{\rho} \left(\frac{\bar{\delta}^2 V}{\bar{\delta} r^2} + \frac{1}{r} \frac{\bar{\delta} V}{\bar{\delta} r} + \frac{1}{r^2} \frac{\bar{\delta}^2 V}{\bar{\delta} \theta^2} - \frac{V}{r^2} + \frac{2}{r^2} \frac{\bar{\delta} U}{\bar{\delta} \theta} \right) \end{aligned}$$

where

$$\rho = 1 + \rho'$$

so that the predictor step may be written

$$\begin{aligned} \left(\frac{\partial \rho'}{\partial t}\right)_{i,j}^* &= -\frac{1}{M_o} \left[\bar{\rho} \left(\frac{\delta u'}{\delta r} + \frac{1}{r} \frac{\delta v'}{\delta \theta} + \frac{u'}{r} \right) + \bar{u} \frac{\delta \rho'}{\delta r} + \frac{\bar{v}}{r} \frac{\delta \rho'}{\delta \theta} \right]_{i,j}^n \\ \left(\frac{\partial u'}{\partial t}\right)_{i,j}^* &= -\frac{1}{M_o} \left[\bar{u} \frac{\delta u'}{\delta r} + \frac{\bar{v}}{r} \frac{\delta u'}{\delta \theta} - \frac{v'^2}{r} + M_o \left(u' \frac{\bar{\delta} U}{\bar{\delta} r} + \frac{v'}{r} \frac{\bar{\delta} U}{\bar{\delta} \theta} - \frac{2Vv'}{r} \right) \right. \\ &\quad \left. - M_o^2 \frac{\rho'}{\bar{\rho}} \left(\frac{\delta U}{\delta t} + U \frac{\bar{\delta} U}{\bar{\delta} r} + \frac{V}{r} \frac{\bar{\delta} U}{\bar{\delta} \theta} - \frac{V^2}{r} \right) - \frac{1}{\bar{\rho}} \frac{\partial \rho'}{\partial r} + \left(\frac{\delta u'}{\delta t}\right)_{visc+inc} \right]_{i,j}^n \\ \left(\frac{\partial v'}{\partial t}\right)_{i,j}^* &= -\frac{1}{M_o} \left[\bar{u} \frac{\delta v'}{\delta r} + \frac{\bar{v}}{r} \frac{\delta v'}{\delta \theta} + \frac{u'v'}{r} + M_o \left(u' \frac{\bar{\delta} V}{\bar{\delta} r} + \frac{v'}{r} \frac{\bar{\delta} V}{\bar{\delta} \theta} + \frac{Uv'}{r} + \frac{Vu'}{r} \right) \right. \\ &\quad \left. - M_o^2 \frac{\rho'}{\bar{\rho}} \left(\frac{\delta V}{\delta t} + U \frac{\bar{\delta} V}{\bar{\delta} r} + \frac{V}{r} \frac{\bar{\delta} V}{\bar{\delta} \theta} + \frac{UV}{r} \right) - \frac{1}{r\bar{\rho}} \frac{\partial \rho'}{\partial r} + \left(\frac{\delta v'}{\delta t}\right)_{visc+inc} \right]_{i,j}^n \\ \left(\frac{\partial p'}{\partial t}\right)_{i,j}^* &= c^2 \left(\frac{\partial \rho'}{\partial t}\right)_{i,j}^* - M_o^2 \left(\frac{\delta P}{\delta t}\right)_{i,j}^n \end{aligned}$$

followed by

$$(\rho')_{i,j}^* = (\rho')_{i,j}^n + \left(\frac{\partial \rho'}{\partial t} \right)_{i,j}^* \Delta t$$

$$(u')_{i,j}^* = (u')_{i,j}^n + \left(\frac{\partial u'}{\partial t} \right)_{i,j}^* \Delta t$$

$$(v')_{i,j}^* = (v')_{i,j}^n + \left(\frac{\partial v'}{\partial t} \right)_{i,j}^* \Delta t$$

$$(p')_{i,j}^* = (p')_{i,j}^n + \left(\frac{\partial p'}{\partial t} \right)_{i,j}^* \Delta t$$

In these expressions, the notations $\frac{\delta}{\delta r}, \frac{\delta}{\delta \theta}, \frac{\delta}{\delta t}$ refer to one-sided differences while expressions $\frac{\bar{\delta}}{\delta r}, \frac{\bar{\delta}}{\delta \theta}$ denote centered differences. A corrector step is next implemented in which the terms

$\left(\frac{\partial \rho'}{\partial t} \right)_{i,j}^{n+1}, \left(\frac{\partial u'}{\partial t} \right)_{i,j}^{n+1}, \left(\frac{\partial v'}{\partial t} \right)_{i,j}^{n+1}, \left(\frac{\partial p'}{\partial t} \right)_{i,j}^{n+1}$ are computed in the same manner as in the predictor step. However, in this computation, one-sided differences are performed in the sense opposite to their application in the predictor step, i.e., if forward differences were used in the predictor, backward differences are used in the corrector and vice versa. Also, bracketed terms in the corrector expressions are evaluated using the * quantities rather than level n quantities as in the predictor step. The updates for level $n+1$ are written finally as

$$(\rho')_{i,j}^{n+1} = \frac{1}{2} \left[(\rho')_{i,j}^n + (\rho')_{i,j}^* + \left(\frac{\partial \rho'}{\partial t} \right)_{i,j}^{n+1} \Delta t \right]$$

$$(u')_{i,j}^{n+1} = \frac{1}{2} \left[(u')_{i,j}^n + (u')_{i,j}^* + \left(\frac{\partial u'}{\partial t} \right)_{i,j}^{n+1} \Delta t \right]$$

$$(v')_{i,j}^{n+1} = \frac{1}{2} \left[(v')_{i,j}^n + (v')_{i,j}^* + \left(\frac{\partial v'}{\partial t} \right)_{i,j}^{n+1} \Delta t \right]$$

$$(p')_{i,j}^{n+1} = \frac{1}{2} \left[(p')_{i,j}^n + (p')_{i,j}^* + \left(\frac{\partial p'}{\partial t} \right)_{i,j}^{n+1} \Delta t \right].$$

Perturbation Boundary Conditions

At inflow, a radiation condition is applied which is expressed nondimensionally by

$$\left(\frac{1}{\Lambda(\theta)} \frac{\partial}{\partial t} + \frac{\partial}{\partial r} + \frac{1}{2r} \right) \begin{bmatrix} \rho' \\ u' \\ v' \\ p' \end{bmatrix} = 0$$

where $\Lambda(\theta) = M_o \cos \theta + \sqrt{1 - M_o^2 \sin^2 \theta}$. Practically, this condition is implemented using a one-sided difference

$$\phi_{i,j}^{n+1} = \phi_{i,j}^n - \Lambda(\theta) \left[\frac{\delta\phi}{\delta r} + \frac{1}{2r} \right]_{i,j}^n \Delta t$$

where $\phi = \rho', u', v', p'$. At the outer computational boundary, conditions obtained by Tam and Dong³ are applied. Although these conditions were originally derived for steady nonuniform flow, they are used here with slight modification arising from the unsteadiness of the mean flow. Nondimensionally, they are written

$$M_o \frac{\partial \rho'}{\partial t} + \bar{u} \frac{\partial \rho'}{\partial x} + \bar{v} \frac{\partial \rho'}{\partial y} = M_o \frac{\partial p'}{\partial t} + M_o \frac{\partial P}{\partial t} + \bar{u} \frac{\partial p'}{\partial x} + \bar{v} \frac{\partial p'}{\partial y}$$

$$M_o \frac{\partial \bar{u}'}{\partial t} + \bar{u} \frac{\partial \bar{u}'}{\partial x} + \bar{v} \frac{\partial \bar{u}'}{\partial y} = -\frac{\partial p'}{\partial x} - M_o^2 \frac{\partial \bar{U}}{\partial t}$$

$$M_o \frac{\partial \bar{v}'}{\partial t} + \bar{u} \frac{\partial \bar{v}'}{\partial x} + \bar{v} \frac{\partial \bar{v}'}{\partial y} = -\frac{\partial p'}{\partial y} - M_o^2 \frac{\partial \bar{V}}{\partial t}$$

$$\frac{1}{\Lambda(\theta)} \frac{\partial p'}{\partial t} + \frac{\partial p'}{\partial r} + \frac{p'}{2r} = -\frac{M_o^2}{\Lambda(\theta)} \frac{\partial P}{\partial t}$$

where an overbar denotes that the quantity is Cartesian rather than polar. The relation between the two is

$$\bar{u}' = u' \cos \theta - v' \sin \theta$$

$$\bar{v}' = u' \sin \theta + v' \cos \theta.$$

Also needed in the above are the relations

$$\frac{\partial}{\partial x} = \cos \theta \frac{\partial}{\partial r} - \frac{\sin \theta}{r} \frac{\partial}{\partial \theta}$$

$$\frac{\partial}{\partial y} = \sin \theta \frac{\partial}{\partial r} + \frac{\cos \theta}{r} \frac{\partial}{\partial \theta}$$

Once again, one-sided differences are used in the implementation so that Cartesian velocity components are first updated according to

$$(\bar{u}')_{i,j}^{n+1} = (\bar{u}')_{i,j}^n - \frac{1}{M_o} \left(\frac{\delta p'}{\delta x} + M_o^2 \frac{\delta U}{\delta t} + \bar{u} \frac{\delta \bar{u}'}{\delta x} + \bar{v} \frac{\delta \bar{u}'}{\delta y} \right)_{i,j}^n \Delta t$$

$$(\bar{v}')_{i,j}^{n+1} = (\bar{v}')_{i,j}^n - \frac{1}{M_o} \left(\frac{\delta p'}{\delta y} + M_o^2 \frac{\delta V}{\delta t} + \bar{u} \frac{\delta \bar{v}'}{\delta x} + \bar{v} \frac{\delta \bar{v}'}{\delta y} \right)_{i,j}^n \Delta t$$

which is then followed by conversion of these values to the polar updates

$$(u')_{i,j}^{n+1} = (\bar{u}')_{i,j}^{n+1} \cos \theta + (\bar{v}')_{i,j}^{n+1} \sin \theta$$

$$(v')_{i,j}^{n+1} = -(\bar{u}')_{i,j}^{n+1} \sin \theta + (\bar{v}')_{i,j}^{n+1} \cos \theta.$$

In application, radiation conditions are applied when $\pi/2 \leq \theta \leq 3\pi/2$ while the outflow conditions are used when $-\pi/2 \leq \theta \leq \pi/2$.

At the surface of the cylinder, we require that the total velocities u, v obey the no-slip condition. Since we also enforce $U, V = 0$ in the mean flow calculation, it is then required that both $u', v' = 0$ on the surface. These values are substituted into the governing equations to obtain surface conditions for both ρ' and p' :

$$\frac{\partial \rho'}{\partial t} = -\frac{\bar{\rho}}{M_o} \frac{\partial u'}{\partial r}$$

$$\frac{\partial p'}{\partial t} = c^2 \frac{\partial \rho'}{\partial t} - M_o^2 \frac{\partial P}{\partial t}$$

or,

$$(\rho')_{1,j}^{n+1} = (\rho')_{1,j}^n - \left(\frac{\bar{\rho}}{M_o} \frac{\delta u'}{\delta r} \right)_{1,j}^n \Delta t$$

$$(p')_{1,j}^{n+1} = (p')_{1,j}^n + \left(c^2 \frac{\partial \rho'}{\partial t} - M_o^2 \frac{\delta P}{\delta t} \right)_{1,j}^n \Delta t$$

Results

A sample problem was chosen in which a circular cylinder of diameter 1.9 cm is immersed in an oncoming uniform stream of $M_o = 0.2$. Observers are placed 70 cylinder radii away from the cylinder's center at azimuthal locations of $\theta = 60^\circ, 90^\circ, 120^\circ$. After nondimensionalizing the problem geometry, a stretched grid of 146 x 91 (radial x azimuthal) grid points with $r_{\max} = 75$ was used in the mean flow calculations. With this grid, nondimensional Δr varied from 0.03 next to the cylinder surface to 2.2 at the outer computational boundary. Azimuthal spacing was constant at 0.0698. Both grid and Δt refinement studies were done and confirmed the adequacy of the grid and good convergence for the incompressible calculations with a time step of $\Delta t = 0.01$. Prior to acoustic computation, the mean flow calculations are allowed to evolve until transients no longer appear. Typical flowfield snapshots of this condition appear in figure 2. In order to monitor the evolution of the mean flowfield, an additional nearfield observer was placed just aft in the cylinder wake and incompressible quantities monitored. These time histories appear as figure 3 and indicate that indeed, the periodic shedding had achieved the desired regularity during the accompanying acoustic calculations.

The acoustic calculations were performed on a 401 x 91 uniformly spaced grid ($\Delta r = 0.185$, $\Delta \theta = 0.0698$) using the same $\Delta t = 0.01$. The perturbed quantities monitored at the nearfield observer appear as figure 4 and clearly illustrate the presence of transients due to the initial condition $\rho', u', v', p' = 0$. However, these quantities eventually assume regularity. Figure 5 shows time histories of p' for the additional three farfield observers and contain transient behavior. Note that in the nearfield, the dominant frequency in this time history is twice that associated with the farfield observers, which is as expected.

Finally, the latter portions of the perturbation pressure histories were extracted (to eliminate the transients which dominate the early half of the history) and spectral analyzed. Figure 6 gives the SPL in dB for these observers as a function of frequency. The calculated SPL shows agreement with experimental data (figure 7). This sample calculation required approximately 20 hours of CPU time on a DEC-Alpha machine wherein 97% of the CPU was dedicated to this task.

Conclusion

The viscous/acoustic splitting method has been implemented and shows acceptable agreement with experimental data for the problem selected. This approach allows the investigator wide latitude in independently choosing particular methods appropriate to each portion of the problem which may have competing consideration in terms of numerics, efficiency, or application of boundary conditions. Though not shown here, comparisons of the acoustic formulation results show excellent agreement with simple problems having analytic solutions which gives hope for wider application of the method to more complex and realistic problems associated with airframe or automobile noise. The major difficulty encountered in this work was in the application of Tam and Dong's outflow conditions (derived for steady flow) at boundaries where the flow was unsteady. In particular, a very long-term weak instability manifests itself and eventually destabilizes the calculations. Development of robust conditions for these boundaries is a pressing need and offers opportunity for future study.

References

- ¹Hardin, J.C. and Pope, D.S. An Acoustic/Viscous Splitting Technique for Computational Aeroacoustics, Theoretical and Computational Fluid Dynamics, Vol. 6, No. 5-6, October 1994.
- ²Gentry, R.A., Martin, R.E., and Daly, B.J. An Eulerian Differencing Method for Unsteady Compressible Flow Problems, J. of Computational Physics, Vol. 1, pp. 87-118, 1966.
- ³Tam, C.K. and Dong, Z. Radiation and Outflow Boundary Conditions for Direct Computation of Acoustic and Flow Disturbances in a Nonuniform Mean Flow, AIAA Paper 95-007, 1995.

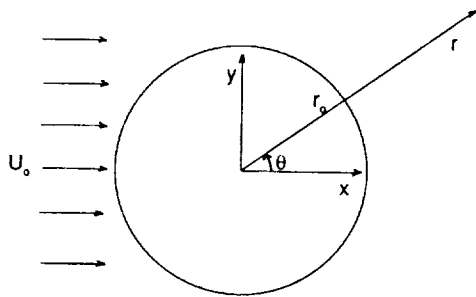


Figure 1 - Cylinder Geometry

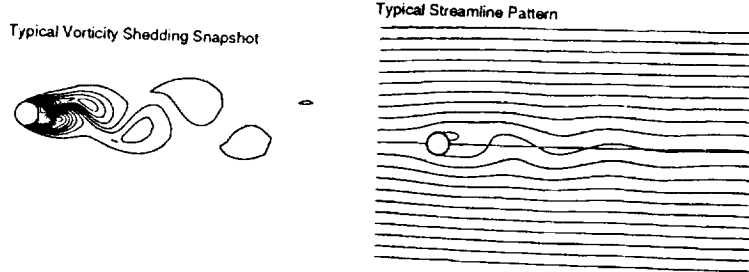


Figure 2 - Typical Incompressible Flowfield Snapshots

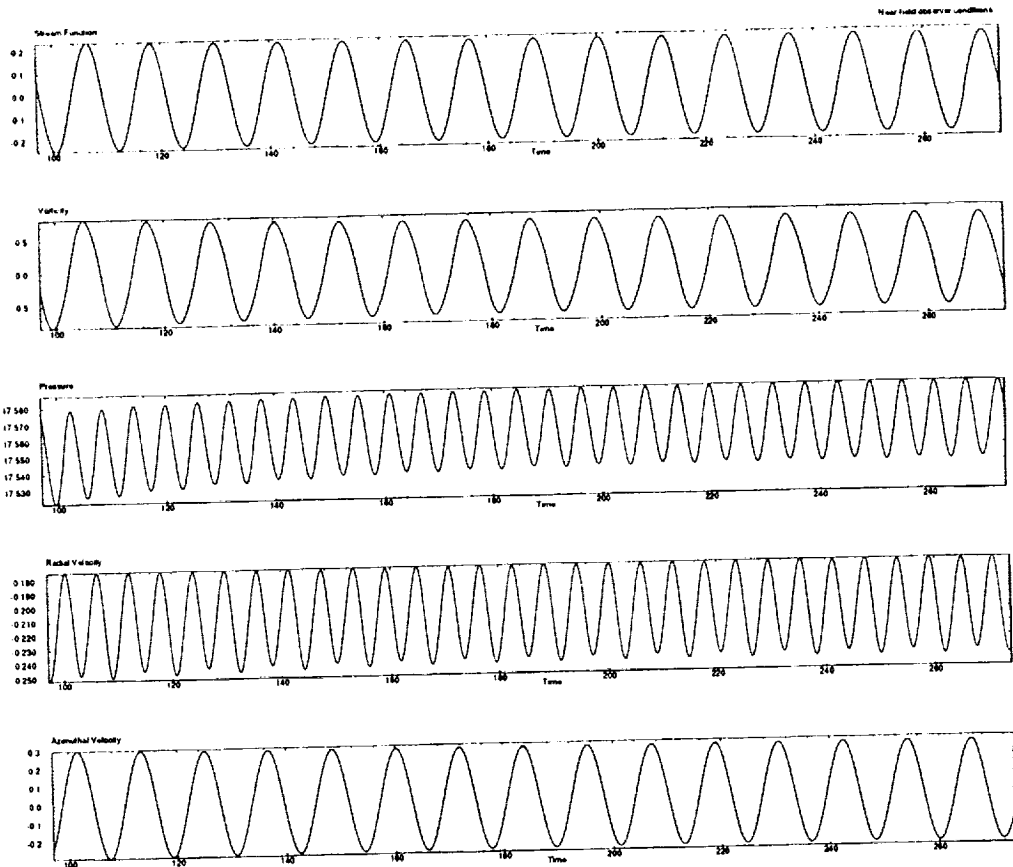


Figure 3 - Nearfield Incompressible Quantities

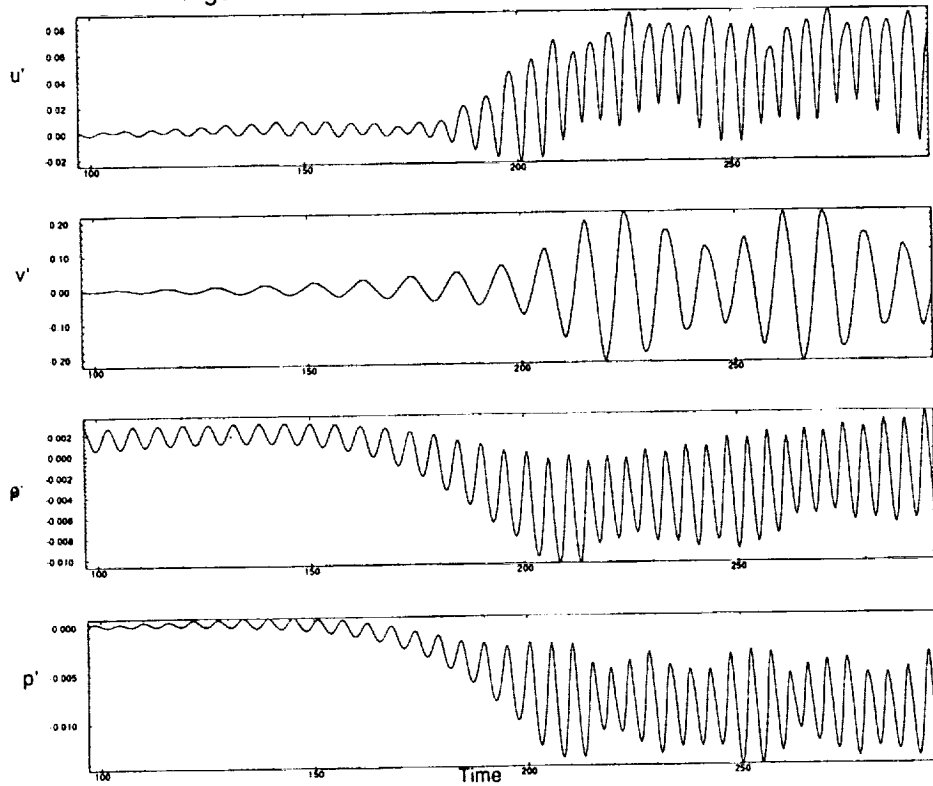


Figure 4 - Nearfield Perturbation Quantities

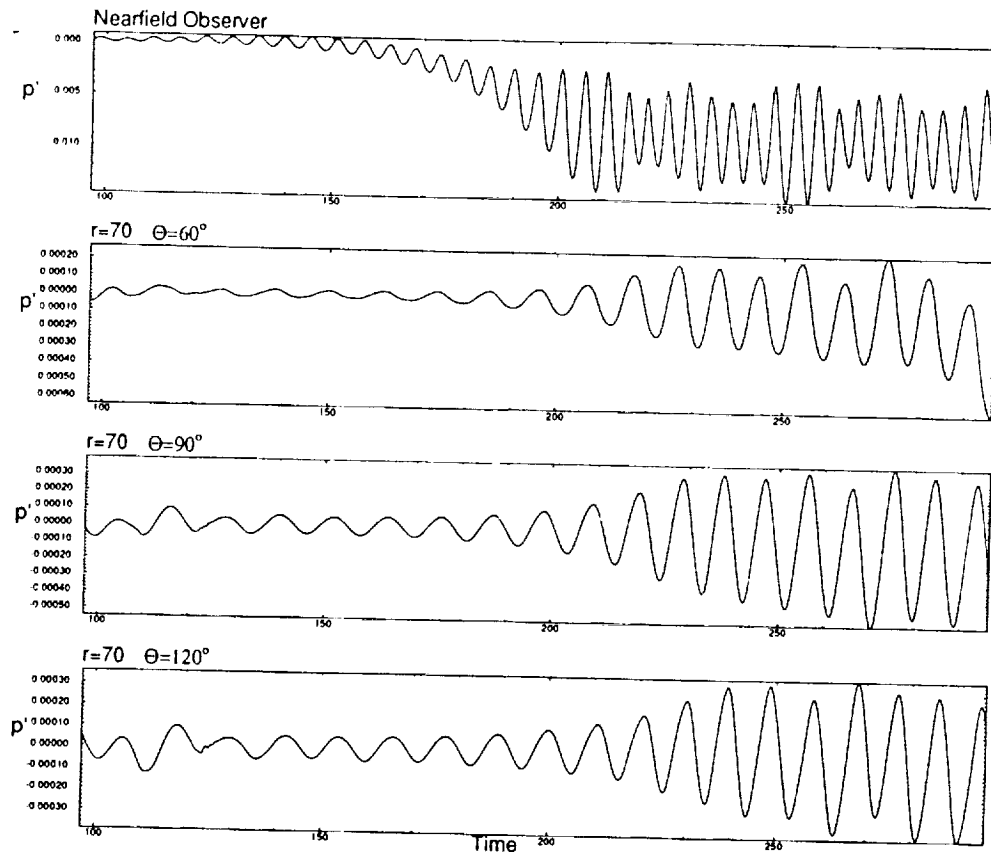


Figure 5 - Perturbed Pressure at Distant Observers

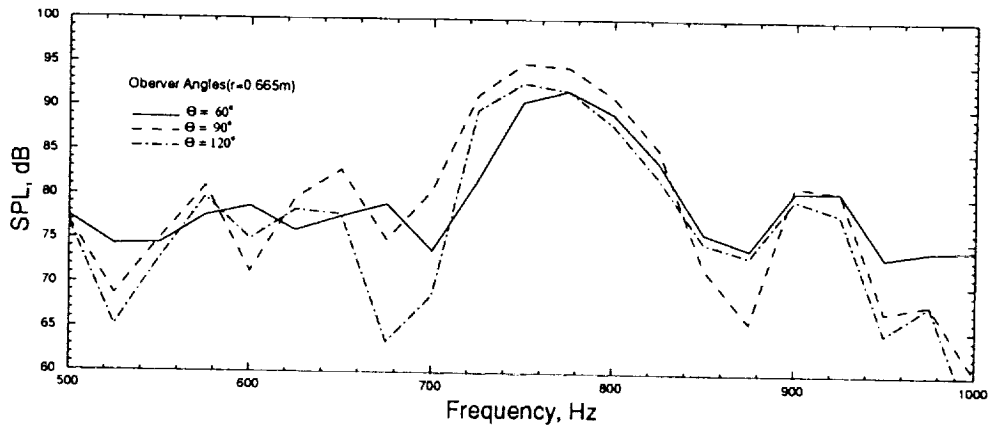


Figure 6 - SPL of Perturbed Pressure for Distant Observers

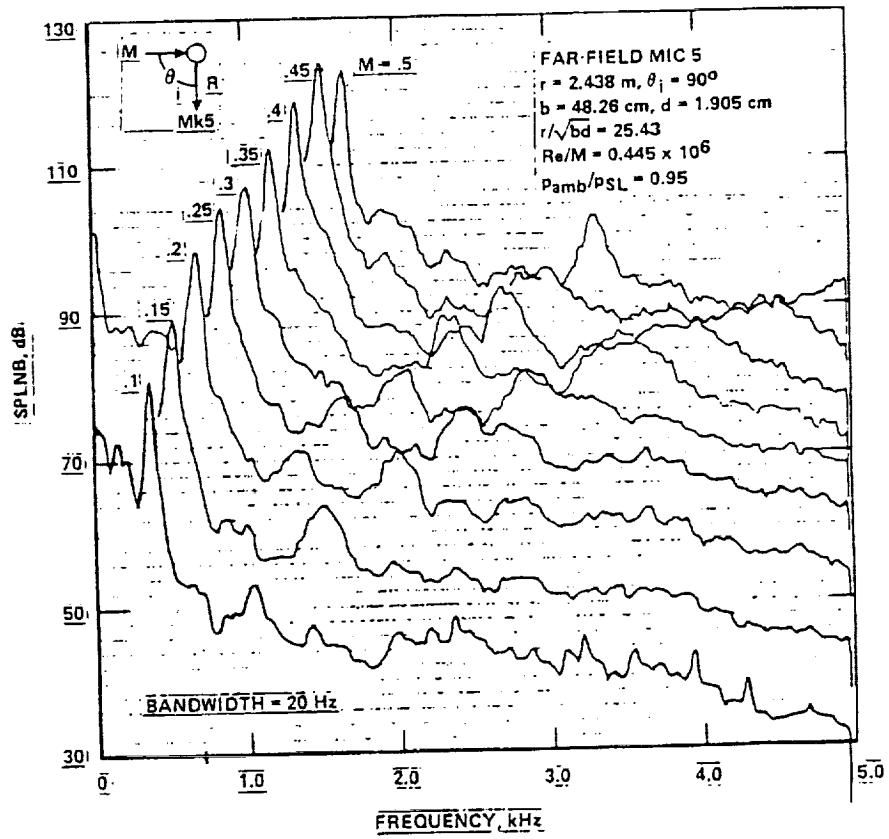


Figure 7 - Experimental Data for Sample Calculation

529-71
043 488
294020 p 10

LARGE-EDDY SIMULATION OF A HIGH REYNOLDS NUMBER FLOW AROUND A CYLINDER INCLUDING AEROACOUSTIC PREDICTIONS

Evangelos T. Spyropoulos and Bayard S. Holmes
Centric Engineering Systems, Inc., Santa Clara, CA 95054-3004

ABSTRACT

The dynamic subgrid-scale model is employed in large-eddy simulations of flow over a cylinder at a Reynolds number, based on the diameter of the cylinder, of 90,000. The Centric SPECTRUMTM finite element solver is used for the analysis. The far field sound pressure is calculated from Lighthill-Curle's equation using the computed fluctuating pressure at the surface of the cylinder. The sound pressure level at a location 35 diameters away from the cylinder and at an angle of 90° with respect to the wake's downstream axis was found to have a peak value of approximately 110 db. Slightly smaller peak values were predicted at the 60° and 120° locations. A grid refinement study suggests that the dynamic model demands mesh refinement beyond that used here.

I. Introduction

In the past few years, there has been a resurgence of interest in performing large-eddy simulations (LES) of flows of engineering interest. There are two roles for LES to play in the computation of complex flows. First, it can be used to study the physics of turbulence at higher Reynolds numbers than can currently be achieved with direct numerical simulation (DNS), and can aid in the testing and improvement of lower order engineering turbulence models. Second, it is hoped that LES can be used as an engineering tool rather than as a research tool. Although it remains expensive, it may be the only means of accurately computing complex flows for which lower order models fail.

The dynamic subgrid-scale (SGS) modeling concept was introduced by Germano *et al.*¹ for LES of incompressible flows and has attracted a lot of attention in the LES community during the recent years. The main advantage of the dynamic model over other models used in the past is that it requires little prior experience with the type of flow being considered. The model (dynamically) adjusts to the flow conditions by employing the resolved large-scale information to predict the effects of the small scales.

In this study, the far-field noise due to a high Reynolds number flow over a cylinder is predicted numerically using the SPECTRUMTM finite element solver. First, the LES method with the dynamic model is used to compute the turbulent flowfields. The results from the CFD analysis are then used in Lighthill-Curle's⁴ acoustic analogy equation to predict the sound pressure level at several locations.

II. Numerical Method

A. Flow Analysis

The unsteady flow calculations were all performed using the SPECTRUMTM finite element solver. The LES method was employed to compute the velocity and pressure turbulent fields assuming incompressible flow conditions. In LES one computes explicitly only the motion of the large-scale structures. The effects of the small-scales are not captured but are modeled. The governing equations for the large eddies are obtained after filtering the continuity and momentum equations. The filtering operation (denoted by an overbar) maintains only the large-scales and can be written in terms of a convolution integral,

$$\bar{f}(x_1, x_2, x_3) = \int_D \prod_{i=1}^3 G_i(x_i - x'_i) f(x'_1, x'_2, x'_3) dx'_1 dx'_2 dx'_3, \quad (1)$$

where f is a turbulent field, G_i is some spatial filter that operates in the i -th direction and has a filter width Δ_i , and D is the flow domain.

The effects of the small-scales are present in the filtered momentum equation through the SGS stress tensor

$$\tau_{ij} = (\overline{u_i u_j} - \bar{u}_i \bar{u}_j), \quad (2)$$

and require modeling. The dynamic SGS model introduced by Germano *et al.*,¹ and later refined by Lilly,² is used in this study. The model is based on Smagorinsky's³ eddy-viscosity SGS model. The model constant, however, is allowed to vary in space and time, and is computed dynamically, as the simulation progresses, from the energy content of the smallest of the resolved large-scales. This approach for calculating the model constant has been found to substantially improve the accuracy and robustness of the LES method, since the model constants adjust dynamically to the local structure of the flow and do not have to be specified *a priori*. In addition, it has been found that the dynamic model provides the correct limiting behavior near solid boundaries, and adjusts properly by itself in the transitional or laminar regimes. Although it can not properly predict backscatter, it allows for some reverse energy cascade.

Dynamic modeling is accomplished with the aid of a second filter (referred to as the test filter, \hat{G}) that has a filter width $\hat{\Delta}_i$ in the i -th direction ($\hat{\Delta}_i > \Delta_i$). The model parameterization for the SGS stresses is given by

$$\tau_{ij} = -2\nu_t \bar{S}_{ij}, \quad (3)$$

where $\nu_t = C \Delta^2 \bar{S}$, $\Delta = \sqrt[3]{\Delta x \Delta y \Delta z}$, $\bar{S}_{ij} = \frac{1}{2} \left(\frac{\partial \bar{u}_i}{\partial x_j} + \frac{\partial \bar{u}_j}{\partial x_i} \right)$, and $\bar{S} = \sqrt{2 \bar{S}_{ij} \bar{S}_{ij}}$. The model coefficient is computed from

$$C(x, y, z, t) = \frac{\langle \mathcal{L}_{ij} M_{ij} \rangle}{\langle M_{pq} M_{pq} \rangle}, \quad (4)$$

where $\hat{\cdot}$ denotes test-filtered quantities, $\hat{\Delta} = \sqrt[3]{\hat{\Delta}_1 \hat{\Delta}_2 \hat{\Delta}_3}$, and

$$\mathcal{L}_{ij} = \widehat{\overline{u_i u_j}} - \widehat{\bar{u}_i \bar{u}_j}, \quad (5)$$

$$M_{ij} = -2\hat{\Delta}^2 \widehat{\bar{S}_M \bar{S}_{ij}} + 2\Delta^2 \widehat{\bar{S} \bar{S}_{ij}}, \quad (6)$$

In the implementation of the model in the SPECTRUM solver, negative values for the eddy viscosity, μ_t , are allowed, as long as the total viscosity ($\mu_T = \bar{\mu} + \mu_t$) is non-negative. This restricts the amount of energy back-scatter allowed, but avoids numerical instabilities due to anti-dissipation. A top-hat filter is employed for the test filtering.

The filtered equations of motion for the large eddies are numerically solved using a segregated solution strategy. In this approach, the equations for pressure and velocity are solved in an uncoupled fashion in that within each time step, the pressure is at first held fixed (in the first equation group or stagger) and an iterative solution is obtained on the velocity variable. This is followed by a stagger in which the velocity is fixed and a solution is obtained for the pressure. The velocities are then updated to reflect the pressure solution.

B. Aeroacoustic Predictions

A simple acoustic model was employed to predict the sound pressure level at points away from the cylinder. This prediction was based on the Lighthill-Curle acoustic analogy.⁴ A rigid body surrounded by a fluid acts as a dipole source and the sound pressure for this source at a given distance away is given by

$$p(r_i, t) = \frac{1}{4\pi c} \int \frac{n_i r_i}{r^2} \frac{\partial p_s}{\partial t} dS, \quad (7)$$

where n_i is the surface normal, r_i is the vector from the surface to the point of observation, p_s is the surface pressure (obtained from the LES), and dS is the differential surface area. The speed of sound, c , is approximated here in meters per second from $c = 331 + 0.6T$, where T is the temperature in degrees Celcius.

In addition, since only a part of the cylinder was modeled along the spanwise direction (see section III for details), the sound pressure level radiated from the portion of the cylinder outside the computational domain was calculated as proposed by Kato *et al.*⁵:

$$SPL = SPL_S + 20 \log \left(\frac{L_C}{L_S} \right) + 10 \log \left(\frac{L}{L_C} \right), \quad (8)$$

where L and L_S is the length of the actual cylinder and of the simulated domain, respectively, and SPL_S is the sound pressure level radiated from the simulated domain. Also, L_C is an equivalent coherent length defined such that the pressure fluctuations on the surface of the cylinder can be assumed to be in the same phase angle within L_C , and in a completely independent phase outside L_C .

III. Results

Several LES were conducted on different finite element grids using the dynamic model to simulate the near wake of a circular cylinder. The diameter of the cylinder, D , was 0.019m, and the Reynolds number (based on D) was 90,000. The computational domain employed in the first LES (case 1) was 20 cylinder diameters long along the streamwise x-direction, 10 diameters long along the y-direction and 2 diameters long along the spanwise z-direction. The large eddies of the near wake structure are known to be typified by a length scale of about half diameter. Therefore, the modeling of only 2 diameters of the cylinder's length is expected to be sufficient for the LES. The cylinder was placed 5 diameters from the inlet

boundary. A top view of the numerical grid is shown in figure 1a. The spanwise discretization uses 8 elements placed at a uniform spacing. A close view of the grid around the cylinder is also shown in figure 1a. The total number of elements used in this case is 31,000. A larger computational domain was used in the other two cases, which was 70 cylinder diameters long along the streamwise x-direction, 40 diameters long along the y-direction and 2 diameters long along the spanwise z-direction. The cylinder was placed 20 diameters from the inlet boundary. Cases 2 employed 44,970 of elements (14 elements along the span), whereas case 3 used 244,980 elements (30 elements along the span). Top views of the finite element grids for these cases are shown in figure 1. This figure includes also a magnification of each grid in the vicinity of the cylinder. The following boundary conditions were employed: A uniform velocity profile was imposed at the inlet boundary ($\bar{u} = U_\infty, \bar{v} = \bar{w} = 0$). A no-slip condition was imposed at the surface of the cylinder, a traction-free condition was applied at the outlet boundary, and a slip condition was applied at the side boundaries. In order to facilitate the aeroacoustic analysis, the time step was kept constant ($\Delta t = 0.00001$ seconds). In cases 1 and 2 the velocity and pressure fields were initially set to be uniform based on their freestream values. The initial transients, however, were eliminated by allowing the flow to convect throughout the computational domain before employing any of the data in the aeroacoustic analysis. In order to save on computational effort, case 3 was initiated after interpolating a solution from the coarse grid simulation of case 2.

Figures 2 and 3 show instantaneous contour plots of the pressure field and of the x-component of the velocity, respectively, for all three cases at a time approximately equal to one shedding period. The near wake structure and patterns of vortex shedding are clearly visible. As expected, the quality of the results improved with grid refinement. Contours of the y- and z-components of the velocity are shown for case 3 in figure 4. The existence of three-dimensionality in the flowfield due to turbulence is evident (figure 4b). The ability of the dynamic model to turn itself off in the laminar regions and adjust the eddy viscosity based on the local turbulence level is shown in figure 4c.

Finally, the predicted sound pressure levels for all cases are compared in figure 5. It should be noted that the length correction, described in section IIb, increased the peak noise level by about 15% (this correction is included in the results of figure 5). Also, the equivalent coherent length, L_C , was set equal to three diameters, as suggested by the experimental findings of Schmidt⁶ for $Re=90,000$ flow around a cylinder. Three microphone locations are considered, located at 35 diameters away from the cylinder's centerline and at a 60° , 90° and 120° angle with respect to the wake's downstream axis. In all cases, the peak of the noise spectra is slightly higher at the 90° location. For cases 2 and 3, this peak is about 110 dB and occurs at a frequency of approximately 550 Hz. Higher noise levels, however, are predicted for case 1. This is believed to be mainly due the fact a smaller in size computational domain was used in this case (see figure 1), which may have amplified the amount of vortex shedding, and, consequently, the noise level, because of the slip condition applied at the side walls. The peak of this spectrum is approximately 120 dB at a frequency of about 750 Hz. The most striking feature of the results from the three meshes is the change in frequency with the mesh used. In fact, the Strouhal number based on the primary shedding frequency for case 1 is about 0.198, while the Strouhal number for cases 2 and 3 is about 0.13. The expected value is about 0.2. Because of these discrepancies, some of these calculations were repeated using all three meshes and the Smagorinsky SGS model with a Smagorinsky constant equal

to $C_S = C^{1/2} = 0.1$. These LES gave more consistent results with shedding frequencies corresponding to Strouhal numbers of about 0.2 (results from these computations are not presented here due to space limitations). So, it is possible that the meshes used here are too coarse for the dynamic model and hence have produced inconsistent results. We plan to investigate this issue more thoroughly in the future.

IV. Conclusions

The far-field sound due to vortex shedding in the turbulent wake of a $Re=90,000$ flow around a cylinder is predicted based on Lighthill-Curle's Acoustic Analogy concept. The history of the fluctuating pressure at the surface of the cylinder, required by the acoustic analysis, was obtained by conducting LES using the dynamic SGS model. Several numerical grids were used, the finest of which contained a total of about 245,000 finite elements. The maximum sound pressure level at a distance of 35 diameters away from the cylinder's centerline was found to be equal to 105 dB, 110 dB and 108 dB at the 60° , 90° and 120° angle location, with respect to the wake's downstream axis, respectively. The meshes used, however, may not be sufficiently fine for the dynamic SGS model, as is suggested by inconsistencies in the results found as the grid was refined.

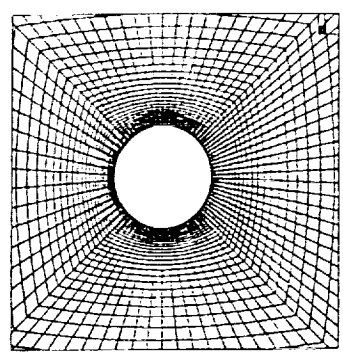
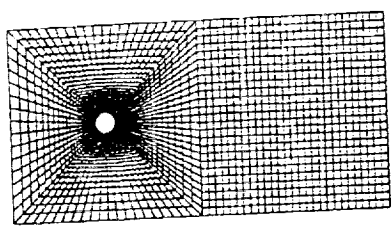
Acknowledgements

This work was supported by the NASA Langley Research Center under SBIR contract NAS1-20584. The authors wish to acknowledge the support of the contract monitor, Kristine Meadows.

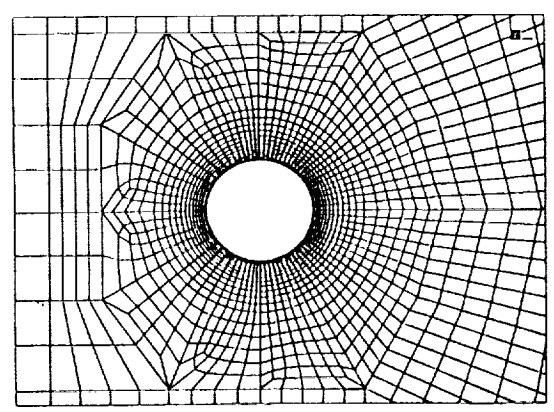
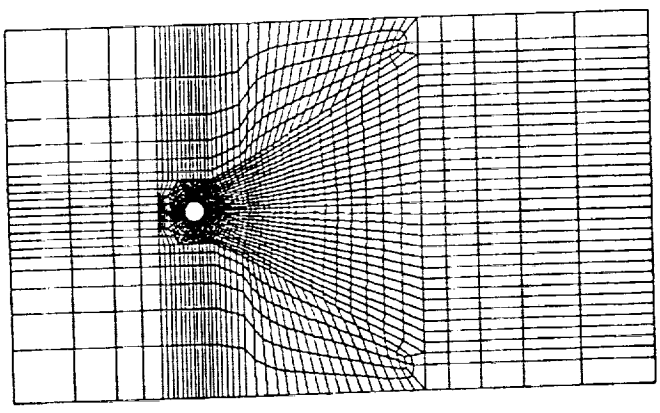
References

- ¹ Germano, M., Piomelli, U., Moin, P. and Cabot, W., 1991. "A dynamic subgrid-scale eddy-viscosity model," *Physics of Fluids A*, **3**, pp. 1760-1765.
- ² Lilly, D. K., 1992. "A proposed modification of the Germano subgrid-scale closure method," *Physics of Fluids A*, **4**, pp. 633-635.
- ³ Smagorinsky, J. S., 1963. "General circulation experiments with the primitive equations. I. The basic experiment," *Monthly Weather Review*, **91**, pp. 99-164.
- ⁴ Pierce, A., 1991. *Acoustics: An Introduction to its Physical Principals and Applications*, McGraw-Hill, New York.
- ⁵ Kato, C., Iida, A., Fujita, H. and Ikegawa, M. 1993. "Numerical prediction of aerodynamic noise from low Mach Number turbulent wake," AIAA Paper 93-0145, 31st AIAA Aerospace Sciences Meeting, Reno, NV.
- ⁶ Schmidt, L. V. 1965. "Measurements of Fluctuating Air Loads on a circular cylinder," *Journal of Aircraft*, **2**, pp. 49-55.

a)



b)



c)

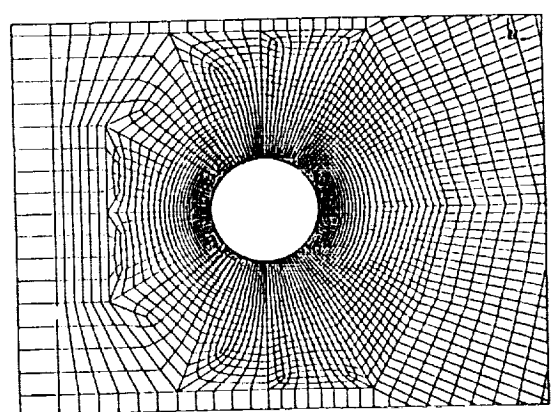
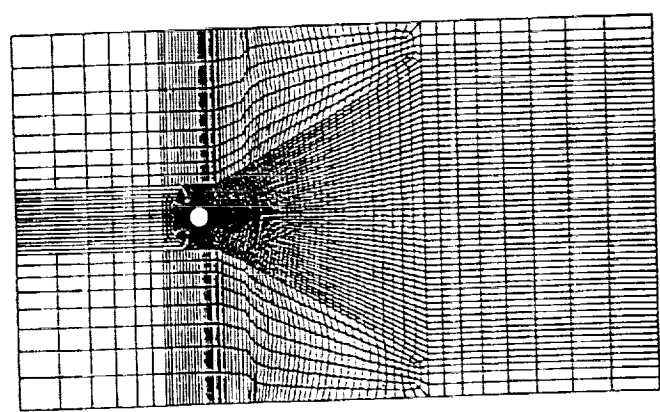


Figure 1. Top view of the finite element mesh with magnification around the vicinity of the cylinder; a) case 1, b) case 2, and c) case 3.

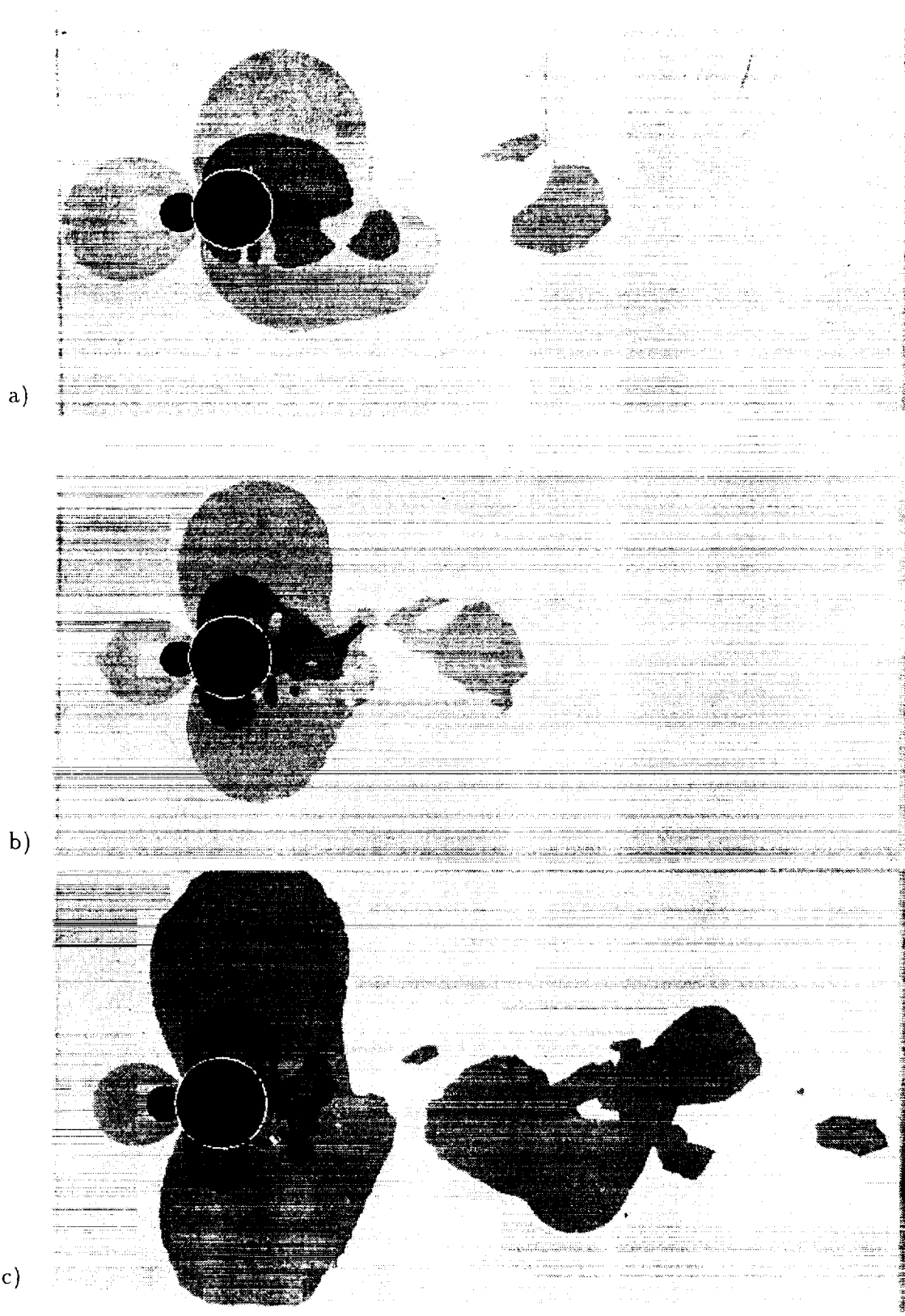


Figure 2. Contours of the instantaneous pressure fields after one shedding period; a) case 1, b) case 2, and c) case 3.

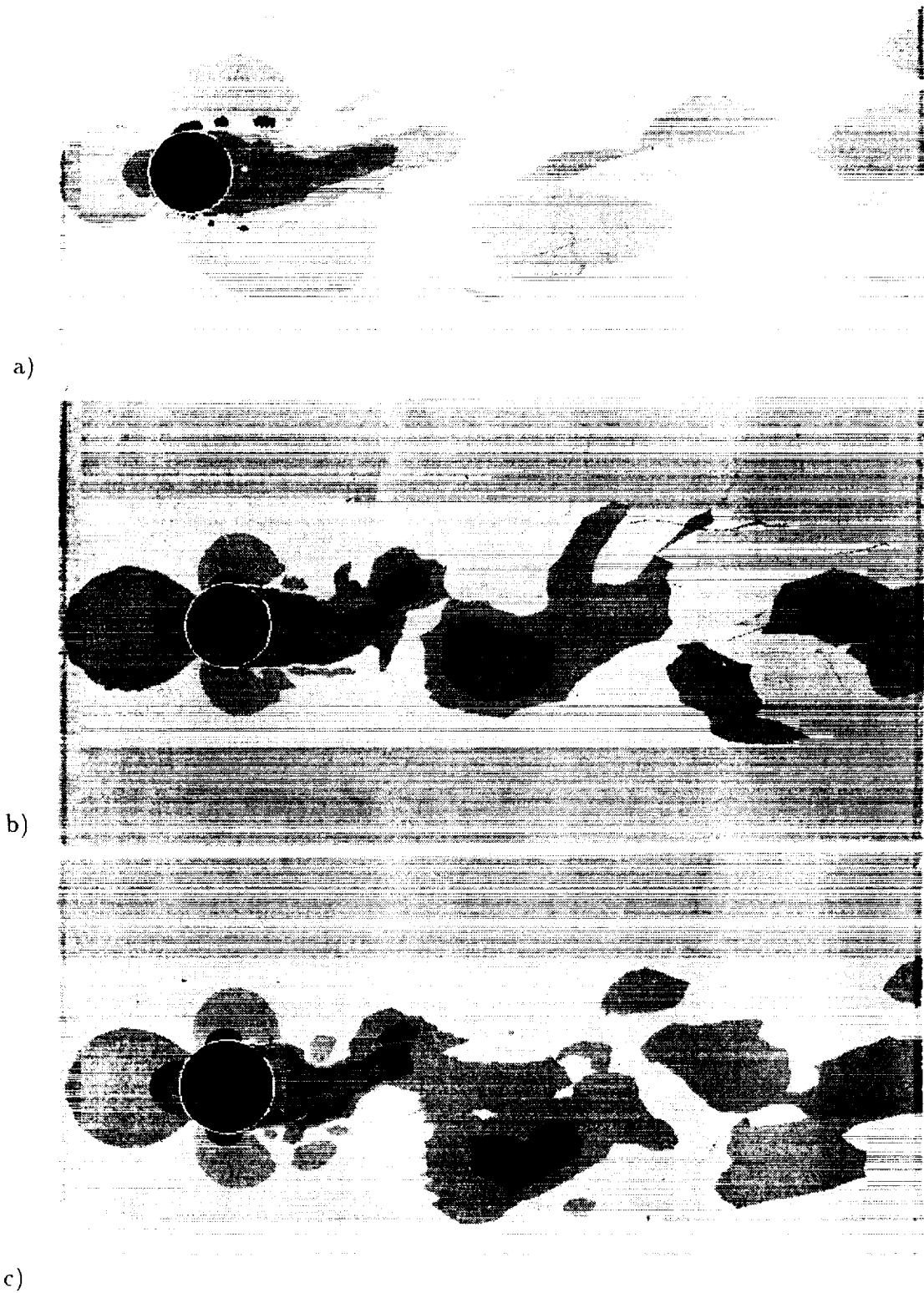


Figure 3. Contours of the x-component of velocity after one shedding period; a) case 1, b) case 2, and c) case 3.

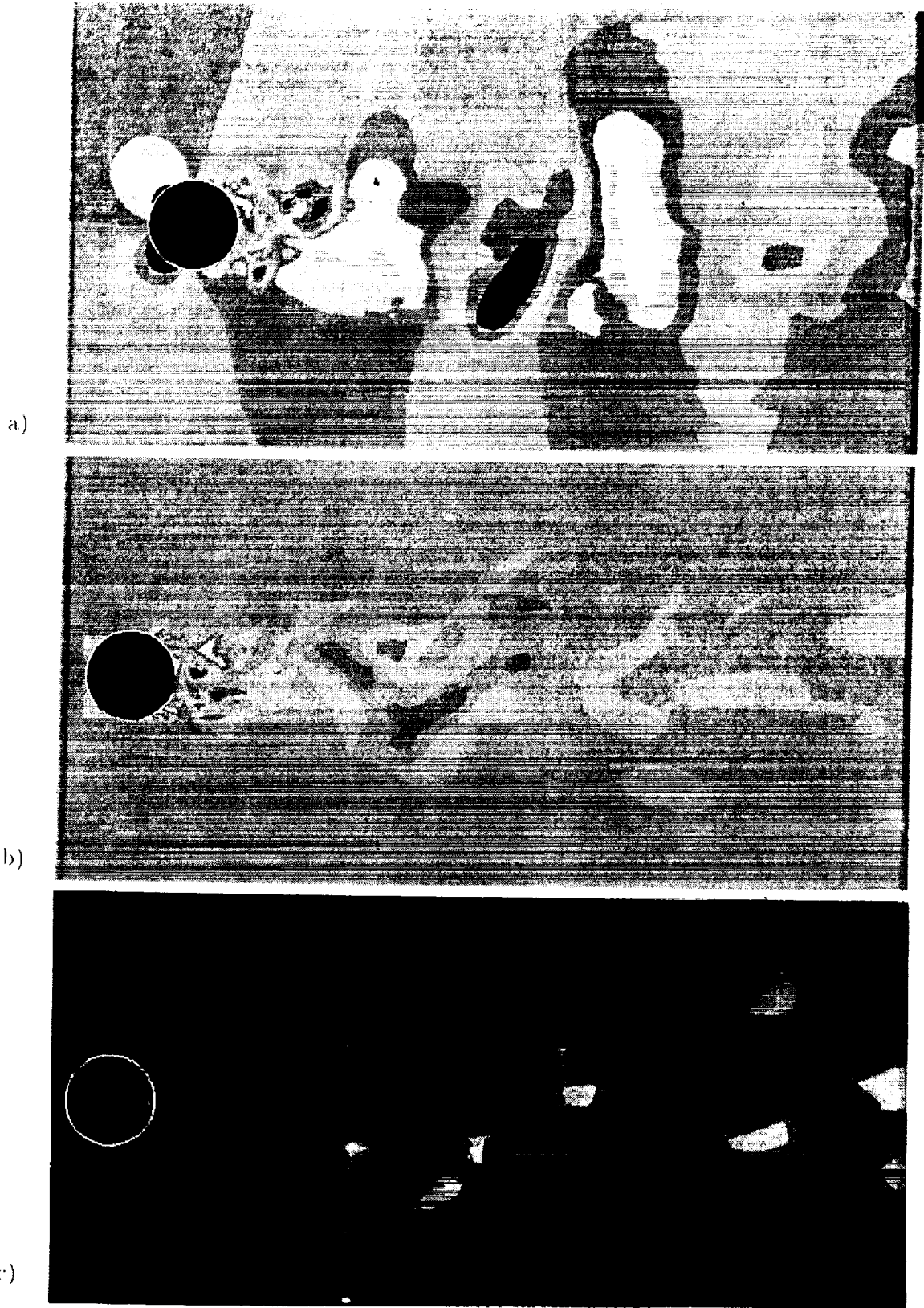


Figure 4. (Contours after one shedding period for case 3; a) y-component of velocity, b) z-component of velocity, and c) eddy viscosity.

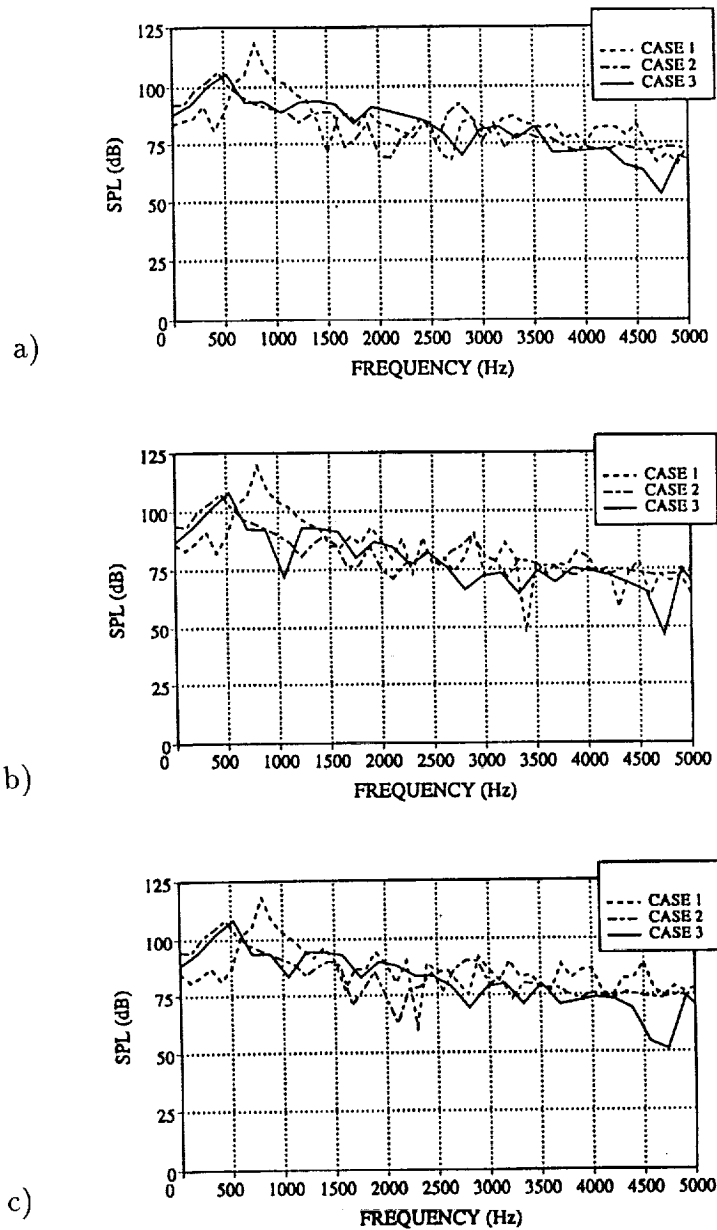


Figure 5. Sound pressure level spectra at a location 35 diameters away from the cylinder and at an angle with respect to the wake's downstream axis of; a) 60°, b) 90°, and c) 120°.

530-71
043489
294022 p20

A COMPARATIVE STUDY OF LOW DISPERSION FINITE VOLUME
SCHEMES FOR CAA BENCHMARK PROBLEMS

CL05E

D. V. Nance
USAF Wright Laboratory
Eglin AFB, FL 32542-6810

L. N. Sankar
Georgia Institute of Technology
Atlanta, GA 30332

K. Viswanathan
Dynacs Engineering Company, Inc.
Renton, WA 98055

SUMMARY

Low dispersion finite volume schemes have been developed to combine the dispersion matching characteristics of classical dispersion relation preserving schemes with the flexibility and ease of applicability of finite volume schemes. In this study, three types of low dispersion finite volume schemes are applied to a series of problems selected from the first and second NASA/ICASE workshops in computational aeroacoustics for benchmark problems. Our schemes are cast in a general framework designed to account for advection of the main flow field by permitting upwinding at the cell interfaces. The application of these schemes to the linear problems of acoustics is also straightforward. The low dispersion finite volume schemes presented here are designed to be fourth order accurate in space. However, these schemes are easily extended to higher spatial orders. For the first workshop, results are presented for problems in Categories 1, 2, and 4. We also present results for Categories 1 and 4 of the second workshop. Comparisons are made with exact solutions where available.

INTRODUCTION

Aerodynamic noise prediction and control are gaining increased attention from the aerospace research community. This shift in emphasis is motivated by society's demand for quieter aircraft, quieter not only in the sense of propulsion noise, but in the sense of aerodynamic noise as well. Aeroacoustic noise is particularly difficult to resolve computationally. The numerical "noise" created by the solution of the main flow field tends to overwhelm subtle acoustic waves.¹ As a result, higher order numerical schemes are needed to preserve the physics of the acoustic field. Low

dispersion finite volume (LDFV) schemes have been developed for this purpose. These schemes are easily implemented in upwind, finite volume solvers. Engendered with the characteristics of flux splitting methods, LDFV schemes do not require the addition of artificial viscosity. By using the finite volume discretization method, LDFV schemes handle arbitrary geometries easily, and boundary conditions are easily implemented. Below, three versions of the LDFV method are applied to a number of aeroacoustics problems. The basic LDFV methods we discuss are fourth order accurate in space, and in time, our equations are integrated by using second and fourth order Runge-Kutta schemes.

NUMERICAL SCHEMES AND SOLUTION PROCEDURE

The LDFV discretization procedure is best illustrated through a simple model problem, the linear wave equation in one dimension

$$\frac{\partial q}{\partial t} + \frac{\partial q}{\partial x} = 0. \quad (1)$$

By dividing a one-dimensional domain into cells, we may write

$$\left(\frac{\partial q}{\partial t}\right)_i = -\frac{q_{i+1/2} - q_{i-1/2}}{\Delta x} = -\frac{q_R - q_L}{\Delta x}. \quad (2)$$

The variables q_R and q_L may be endowed with upwind character through the use of asymmetric stencils. For instance, we may construct a five-point upwind formula for q_R . In Figure 1, consider the stencil centered at $i + 1/2$.

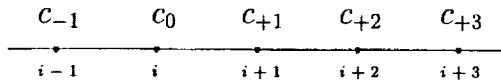


Figure 1: Stencil Representation for $q_{i+1/2}$

Accordingly,

$$q_R = q_{i+1/2} = \sum_{j=-1}^3 c_j q(\xi_{i+1/2} + \Delta_j \xi), \quad (3)$$

where

$$\Delta_j \xi = \left(-\frac{1}{2} + j\right) \Delta \xi. \quad (4)$$

Naturally, a left upwinded formula can be derived at $i + 1/2$ for use with flux splitting schemes. Moreover, we can derive centered formulas, without upwinding, for $q_{i+1/2}$ by using the same procedure. Centered LDFV formulas are useful with certain linear acoustics problems. The discretization involving $q_{i+1/2}$ and $q_{i-1/2}$, given in equation (2), is also suited for use with linear problems. For flux splitting schemes, we create both left and right upwinded formulas for $q_{i+1/2}$ at each cell interface. These formulas serve as upwind interpolants similar to those used in Van Leer's Monotone Upwind Schemes for Conservation Laws (MUSCL). However, LDFV schemes are designed to improve numerical dispersion and dissipation performance as well as increase accuracy.

Type 1 LDFV Scheme

The Type 1 LDFV scheme requires optimizing the coefficients c_j in equation (3) in order to preserve the dispersion relation for q . The optimization procedure is conducted in the computational plane. Therefore, for nonuniform grids, the order of accuracy is quoted formally. This statement is true for all versions of the LDFV method. By taking the Fourier integral transform of equation (3), we have

$$\hat{q}_{i+1/2}^{Num} = \sum_{j=-1}^3 c_j \exp(i\alpha\Delta_j\xi). \quad (5)$$

To grant the best dispersion matching performance, equation (5) should remain as close as possible to unity through the range of $\alpha\Delta\xi$. Type 1 optimization attempts to satisfy this requirement using a weakly constrained least squares procedure. By applying least squares directly to equation (5), we can obtain an individual dispersion relation corresponding to each coefficient c_j . We can combine each of these relations with a set of Taylor-series-based accuracy equations; the resulting system is determinate and easily solved. Hence, we obtain a set of coefficients c_j for each of these systems. By using (5), each set of the c_j can be analyzed graphically to determine its dispersion performance.

Type 2 LDFV Scheme

The Type 2 LDFV scheme exploits an algebraic decomposition of the classical Dispersion Relation Preserving (DRP) finite difference stencil.³ This procedure concentrates DRP optimization on the difference in a given flow property across a cell interface. That is, we optimize Δq at the cell interface as opposed to q . This strategy has its advantages for linear problems and for non-limited flux difference splitting schemes.

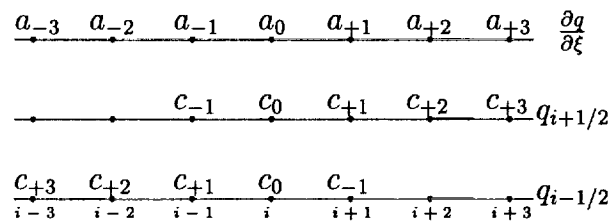


Figure 2: Stencil Decomposition

Recall that flux difference splitting schemes are driven by a numerical flux generated by using the differences in characteristic wave properties taken across a cell interface. As is shown above, the symmetric DRP stencil developed by Tam and Webb can be decomposed into two asymmetric upwind stencils. The stencil expression for $q_{i+1/2}$ has the same form as equation (3). The decomposition relation is alone indeterminate for the coefficients c_j . We can make this relation determinate by including a set of Taylor-series-based accuracy constraints for $q_{i+1/2}$. As a result, we have created a set of upwinded interpolation formulas that are accurate in terms of both q and Δq .

Type 3 LDFV Scheme

Obtaining the Type 3 LDFV coefficients also involves optimizing the dispersion relation for $q_{i+1/2}$. The Type 3 interpolation expression has the same form as equation (3). Again the optimization is performed in the computational plane using equation (5). To determine the c_j , we use a strong, constrained least squares analysis. We begin by writing a set of Taylor-series-based accuracy equations for the stencil (3); one less equation is necessary than the number of coefficients. Alone these equations form an indeterminate system, so we choose one coefficient, say c_k , and solve the now determinate system for the c_j , i.e.,

$$c_j = c_j(c_k), \quad k \neq j. \quad (6)$$

These relations for c_j are used in the least squares analysis of (5). The coefficients are obtained through solution of the equation

$$\frac{d}{da_k} \int_{-\pi/2}^{\pi/2} \left\| \hat{q}_{i+1/2}^{Num} - 1 \right\|^2 d(\alpha \Delta \xi) = 0. \quad (7)$$

The coefficients for the Type 1, 2, and 3 LDFV schemes are given in Table 1 for our basic five point stencil.

Table 1: LDFV Coefficients

c_j	LDFV-1	LDFV-2	LDFV-3
c_{-1}	-0.0325305	-0.0185071	-0.0413084
c_0	0.442622	0.407362	0.477734
c_1	0.742317	0.763958	0.680649
c_2	-0.182378	-0.175972	-0.147266
c_3	0.0299695	0.0231596	0.0211916

Discretizing the Linearized Euler Equations

Since many of our chosen aeracoustics problems occur in two dimensions, we will briefly discuss discretization of the linearized Euler equations. This system of governing equations is well-suited for modeling linear acoustics. We begin with the nonlinear Euler equations

$$\frac{\partial q}{\partial t} + \frac{\partial F}{\partial x} + \frac{\partial G}{\partial y} = 0, \quad (8)$$

where F and G are flux vectors, and

$$q = (\rho, \rho u, \rho v, e)^T.$$

To linearize (8), as suggested by Hardin⁴, we assume that acoustic fluctuations may be modeled as small perturbations on the main flow field, so

$$q = \bar{q} + \acute{q}, \quad \acute{q} \ll \bar{q}. \quad (9)$$

Also, we make use of the quasi-linear form of the flux vectors, i.e.,

$$\frac{\partial F}{\partial x} = A \frac{\partial q}{\partial x}; \quad \frac{\partial G}{\partial y} = B \frac{\partial q}{\partial y}, \quad (10)$$

where A and B are flux Jacobian matrices given by

$$A = \frac{\partial F}{\partial q}; \quad B = \frac{\partial G}{\partial q}. \quad (11)$$

By using (10) and (11) in equation (8) and by applying (9), we can show that

$$\frac{\partial \bar{q}}{\partial t} + \frac{\partial(\bar{A}\bar{q})}{\partial x} + \frac{\partial(\bar{B}\bar{q})}{\partial y} + \frac{\partial \acute{q}}{\partial t} + \frac{\partial(\bar{A}\acute{q})}{\partial x} + \frac{\partial(\bar{B}\acute{q})}{\partial y} = 0, \quad (12)$$

having neglected terms of the second and higher orders. The first three terms represent the Euler equations for the main flow field, so the sum of these terms is identically zero. The remaining terms are the linearized Euler equations

$$\frac{\partial \acute{q}}{\partial t} + \frac{\partial(\bar{A}\acute{q})}{\partial x} + \frac{\partial(\bar{B}\acute{q})}{\partial y} = 0; \quad (13)$$

\bar{A} and \bar{B} depend strictly upon the main flow field properties.⁵ To perform a spatial discretization of (13), we integrate (13) over a given cell area and apply the divergence theorem.

$$\frac{\partial}{\partial t} \int_{\text{Cell}} \acute{q} dV + \oint_{\partial(\text{Cell})} (\bar{A}i + \bar{B}j)\acute{q} \cdot \hat{n} dS = 0. \quad (14)$$

The boundary term can be discretized as follows.

$$\frac{\partial}{\partial t} \int_{Cell} \dot{q} dV + \sum_{Sides}^{Cell} (\bar{A}\hat{n}_x + \bar{B}\hat{n}_y) \dot{q} \Delta S = 0. \quad (15)$$

$\bar{A}\hat{n}_x + \bar{B}\hat{n}_y$ is a diagonalizable matrix suitable for upwinding⁶, i.e.,

$$(\bar{A}\hat{n}_x + \bar{B}\hat{n}_y) \dot{q} = C^+ \dot{q}_L + C^- \dot{q}_R. \quad (16)$$

C^+ is the upwind matrix for "right" traveling waves in the nonlinear flowfield. Accordingly, it is used with the left upwinded \dot{q}_L . C^- and \dot{q}_R are quantities associated with the remaining upwind direction. Hence, the semi-discrete form is

$$\frac{d(\dot{q}_{Cell})}{dt} = -\frac{1}{V_{Cell}} \sum_{Sides}^{Cell} (C^+ \dot{q}_L + C^- \dot{q}_R) \Delta S. \quad (17)$$

Temporal Discretization

Equation (17) must be integrated in time to render a numerical solution. To accomplish this integration, we recognize that (17) is in the form

$$\frac{\partial \dot{q}}{\partial t} = R(\dot{q}). \quad (18)$$

Equation (18) may be numerically integrated in time by using the two-step Runge-Kutta scheme

$$\begin{aligned} \dot{q}^p &= \dot{q}^n + \Delta t R^n; \\ \dot{q}^{(n+1)} &= \frac{1}{2}(\dot{q}^n + \dot{q}^p) + \frac{\Delta t}{2} R^p. \end{aligned} \quad (19)$$

Of course, higher order Runge-Kutta schemes may be used in lieu of (19). Hirsch is a suitable reference for these methods.⁶

Discretization of the Navier-Stokes Equations

The laminar Navier-Stokes equations are applied in the vortex-shedding noise problem, so we will briefly discuss their two-dimensional form here. In vector form, these equations can be written

$$\frac{\partial q}{\partial t} + \frac{\partial F}{\partial x} + \frac{\partial G}{\partial y} = \frac{\partial R}{\partial x} + \frac{\partial S}{\partial y}. \quad (20)$$

The left side of (20) is identical to the Euler equations; however, vectors R and S contain viscous and heat conduction terms. This system is solved in full nonlinear simulation. The advective terms are solved using Roe's flux difference splitting and LDFV interpolation. The viscous/heat conduction terms are discretized in finite volume form using classical DRP formulas for differentials occurring in the stress terms and in Fourier's Law. A four-stage Runge-Kutta scheme is used for

temporal integration of the semi-discrete form.

RESULTS AND DISCUSSION

The First Workshop

Results for the first workshop are submitted in this report, because the work on LDFV schemes did not begin until after the publication date for the first workshop. For the linear wave equation, Figure 3 contains the time 100 results for all three types of LDFV schemes. Clearly, the Type 1 and 3 results are poor, because neither Type 1 nor 3 optimization is tied to the spatial differencing operator. The Type 2 results are excellent, because the Type 2 scheme optimizes Δu at the cell interface. In fact, on uniform grids, the Type 2 LDFV scheme algebraically reduces to the classical DRP scheme.

The spherical wave equation was also solved in Category 1. Our results are computed for an angular frequency of $\omega = \frac{\pi}{4}$. As with the preceding problem, the space derivatives are discretized as in (2). The numerical results are presented at time 200 in Figure 4. All of the LDFV schemes outperform the MacCormack and upwind schemes in the solution of this problem.⁷ The Type 2 solution demonstrates the best performance among the LDFV schemes. Still, the Type 1 and 3 schemes show some improved dissipative performance while limiting group velocity errors.

For the Category 2 submission, we have solved the nonlinear Euler equations in one dimension. The system is initiated by a Gaussian pressure pulse. In Figure 5, the results are compared with an upwind scheme of the fifth order. A limiter was used to remove oscillations from the solution. The Type 1 and 3 LDFV schemes perform very well, comparable with the fifth order upwind solution. On the other hand, the Type 2 solution, omitted from Figure 5, does not perform well when used with the limiter. The Type 1 and 3 solutions capture the shock wave very well except near the discontinuity where small oscillations exist. These oscillations may be removed through the use of an improved limiting strategy for the stencil.

The reflection of a Gaussian acoustic pulse from a wall in a uniform flow was chosen as a problem from Category 4. The solutions for this problem at times 60 and 75 are shown in Figures 6 and 7, respectively. The linearized Euler equations are used in this problem, so the Type 2 LDFV scheme performs best. In fact, this scheme performs comparably well to MacCormack's method.⁷ The Type 1 and 3 schemes perform well on the smoother sections of the pulse; however, these schemes are more dissipative near the pulse extrema. Still, the Type 1 and 3 solutions perform better than the upwind scheme almost everywhere along the pulse profile.⁷ By examining a series of Type 2 LDFV solutions in time, it becomes apparent that the quality of the solutions improves with time. This behavior is a desirable trait of algorithms for computational aeroacoustics (CAA).

The Second Workshop

The problems specified within the second workshop have presented an opportunity for testing the LDFV schemes on curvilinear geometries. Problems 1 and 2 are appropriate for study since

they are easily cast on polar grids. Before solving Problem 1, our LDFV solver was validated for the interaction of a plane acoustic wave with a rigid circular cylinder. The time $t = \frac{\pi}{2}$ numerical solution, calculated in two dimensions, is compared against the exact solution in Figure 8. A 41 by 63 grid was employed for the calculation along with $\Delta t = 0.01$. The comparison between the exact and numerical solutions is quite good although the solution quality does fluctuate in time. In this case, all of the LDFV schemes outperform the MUSCL scheme.

All three LDFV schemes were used to compute solutions for Problem 1, the scattering of periodic acoustic waves generated by a Gaussian source term in the linearized Euler equations. The grid used for this problem is 153 by 159; it has uniform spacing in the azimuthal direction. Radially, the grid stretches in the region adjacent to the body but then adopts uniform spacing in the midfield and farfield. The minimum radial spacing is 0.01, and $\Delta t = 0.005$. Graphical snapshots of the pressure field are presented in Figures 9 and 10 for solution times 5.0 and 7.5, respectively. The Type 2 LDFV scheme was used to generate these solutions. The mean-squared pressure plots for the farfield are given in Figure 11.

Problem 2 is an initial value problem; unlike the system in Problem 1, the nonhomogeneous terms are set equal zero. In this case, a Gaussian pressure wave is initiated in the field at time zero. As the solution evolves, the pulse reflects from the cylinder and propagates out of the domain. The grid specification and time step are identical to those used for Problem 1. All three LDFV schemes were used to solve Problem 2. Snapshots of the acoustic field calculated by the Type 2 scheme are presented in Figures 12 and 13 for solution times 5.0 and 7.5. The pressure time history plots for the Type 1, Type 2, and Type 3 solutions are presented in Figures 14, 15, and 16, respectively.

The Category 4 problem involved the greatest expenditure of computing resources and time among all of the workshop problems. In order to reduce the computer memory and time requirements as much as practicable, we have diverged from the problem specifications by selecting Reynolds number 200 and 5000 for our simulations. Also, our calculations are performed using dimensionless quantities at Mach 0.2. The flow solver is a compressible, laminar Navier-Stokes code that employs Roe's flux difference splitting scheme with fourth order LDFV interpolation in space. The temporal integration routine uses a fourth order Runge-Kutta scheme. This program has been validated using archival data on this geometry; the validation information will be published elsewhere.

The calculations for both Reynolds numbers were performed on cylindrical grids. A 95 by 125 grid was used for the Reynolds number 200 case. For the Reynolds number 5000 case, a slightly larger grid was used with dimensions 95 by 136. In both cases, the first radial increment is set at 0.01. The initial stretching ratio is 1.08, but in the nearfield, the stretching ratio is increased additively by 0.001 at each successive radial increment. The radial grid is progressively stretched until the radial increment exceeds 0.25; the increment is then held constant through the midfield and farfield. For the Reynolds number 200 case, acoustic sampling is conducted 23 diameters away from the cylinder, and for the Reynolds number 5000 case, samples were taken 25 diameters away from the body. In both cases, acoustic sampling is performed at locations above the cylinder and in the cylinder wake. Nonreflecting boundary conditions are implemented in the farfield to pre-

vent reflected numerical waves from damaging the solution. The calculations were performed on a CRAY-YMP with two processors. The program is optimized for vector processing and executes at 195 MFLOPs. A further computational increase in speed is obtained through autotasking. In order to resolve the power spectral density for the radiated noise to $\Delta St = 0.003$, an average of 113 CRAY CPU-HOURS is required for each Reynolds number.

For the calculation at Reynolds number 200, a vorticity field plot is provided as Figure 17. The power spectral density (PSD) for acoustic pressure squared taken above the cylinder is given in Figure 18. The vortex-shedding frequency is captured correctly, and a harmonic is predicted at twice the fundamental frequency. Figure 19 contains the wake spectrum at this Reynolds number. A single wake tone is predicted at $St = 0.39$.

The power spectral density (PSD) for the simulation at Reynolds number 5000 is subject to a large amount of numerical noise. The extraneous noise may be caused by poorer grid resolution for this Reynolds number. Finer grids are usually employed for higher Reynolds numbers, because the excessive dissipation caused by coarse grids can damp smaller motions significantly. As a result, numerical noise may begin to create spurious fluctuations of the same order as the acoustic fluctuations of interest. Still, the vortex-shedding frequency is captured well at the sampling point above the cylinder. The simulation also reveals a peak at $St = 0.13$. There is some experimental evidence supporting the existence of a peak in this Strouhal number range; however, the experimental data was taken, naturally, for a turbulent flow.⁸ Due to the presence of turbulent fluctuations, this peak is not clearly resolved throughout the spectra for the range of experimental Reynolds numbers. At Reynolds number 5000, the experimental data does nonetheless indicate a peak in this range. The wake spectrum for Reynolds number 5000 is given in Figure 21. This spectrum predicts a strong peak at $St = 0.1$ with a strong one-third harmonic. As with the preceding spectrum, there is a great deal of numerical noise present, so the positions of the peaks in these spectra are subject to question. Still, the results of this analysis show that LDFV schemes can be used for predicting the vortex-shedding noise produced by bluff bodies and complex configurations. This method is also useful for higher Mach number flows.

CONCLUSIONS

The low dispersion finite volume schemes have been demonstrated for a number of aeroacoustic problems selected from the first and second computational aeroacoustics workshops for benchmark problems. These schemes possess the dispersion relation matching characteristics of classical dispersion relation preserving schemes while retaining the flexibility and versatility of finite volume schemes. The viability of these schemes has also been demonstrated for a first principles analysis of vortex-shedding noise. The low dispersion finite volume techniques can readily be retrofitted into many current finite volume flow solvers.

REFERENCES

- [1] Tam, C.K.W., "Computational Aeroacoustics: Issues and Methods", *AIAA Journal*, Vol. 33, No. 10, October 1995, pp. 1788-1796.
- [2] Van Leer, B., "Towards the Ultimate Conservative Difference Scheme, IV: A New Approach to Numerical Convection", *Journal of Computational Physics*, Vol. 23, 1977, pp. 276-299.
- [3] Tam, C.K.W. and Webb, J. C., "Dispersion-Relation-Preserving Schemes for Computational Aeroacoustics", *Journal of Computational Physics*, Vol. 107, 1993, pp. 262-281.
- [4] Hardin, J., Invited Lecture Given at the ASME Forum on Computational Aeroacoustics and Hydroacoustics, June 1993.
- [5] Viswanathan, K. and Sankar, L.N., "Toward the Direct Calculation of Noise: Fluid/Acoustic Coupled Simulation", *AIAA Journal*, Vol. 33, No. 12, December 1995, pp. 2271-2279.
- [6] Hirsch, C., *Numerical Computation of Internal and External Flows*, Vol. 2. John Wiley & Sons, New York, 1990.
- [7] Nance, D.V., Viswanathan, K., and Sankar, L.N., "A Low Dispersion Finite Volume Scheme for Aeroacoustic Applications", AIAA Paper 96-0278, 34th Aerospace Sciences Meeting and Exhibit, 1996.
- [8] Chambers, F. W., "Isolated Component Testing for the Identification of Automotive Wind Noise Sources", ASME Noise Control and Acoustics Division (NCA), Winter Annual Meeting Dallas, TX, 1990.

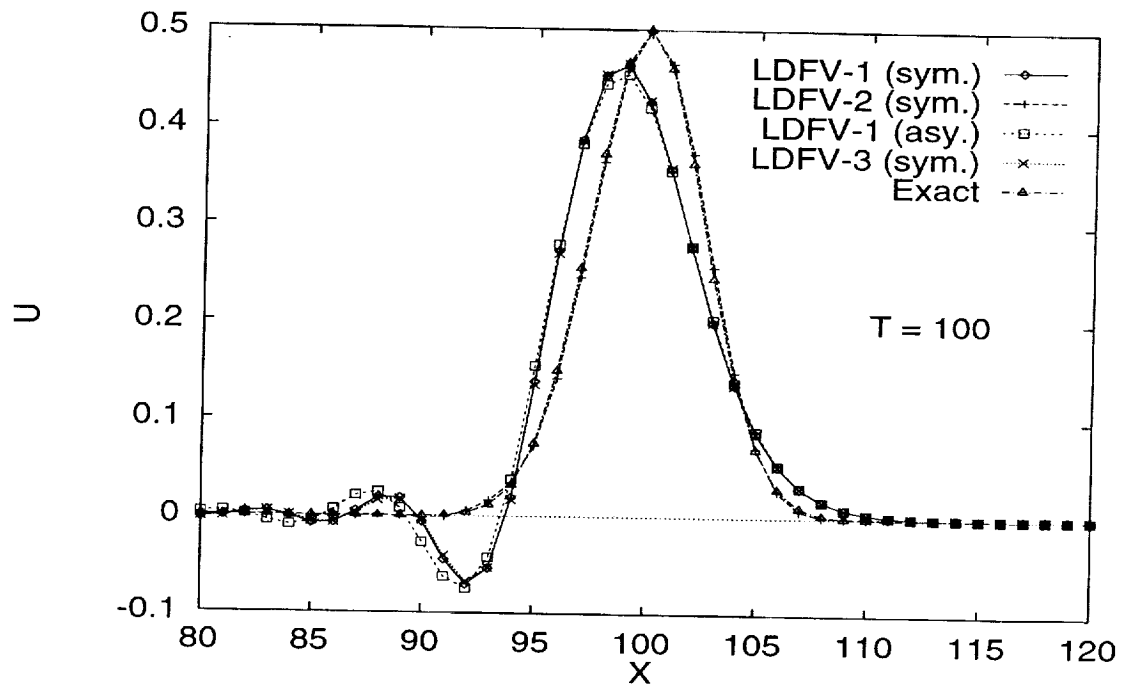


Figure 3: Linear Wave Equation Solutions $T = 100$

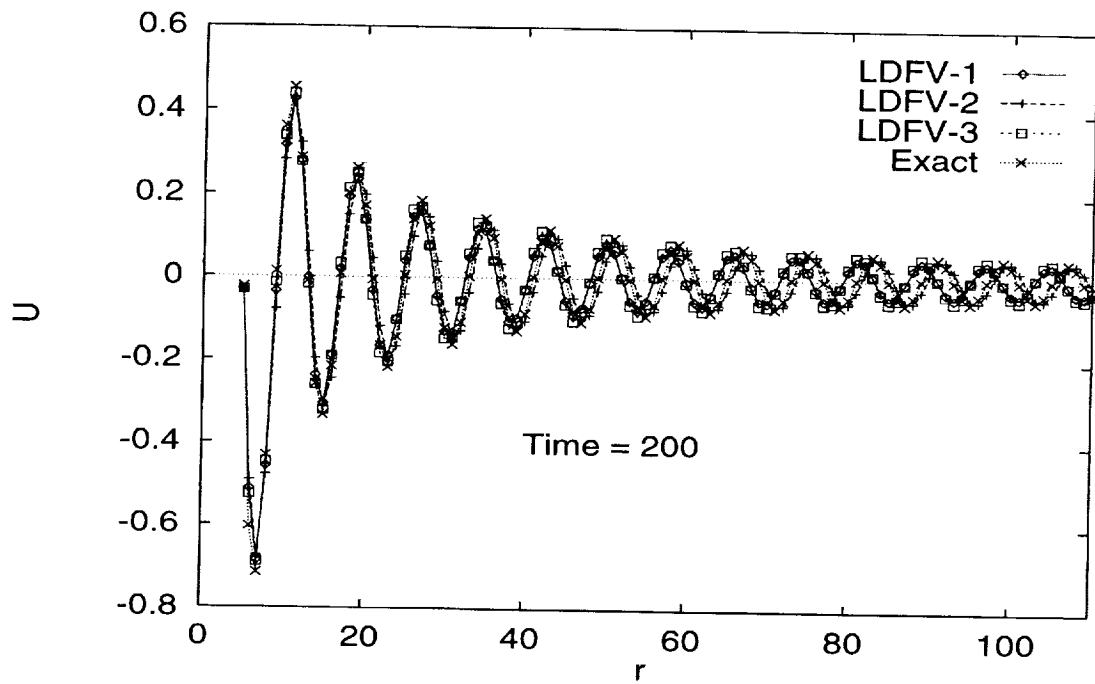


Figure 4: Spherical Wave Equation Solutions $T = 200$

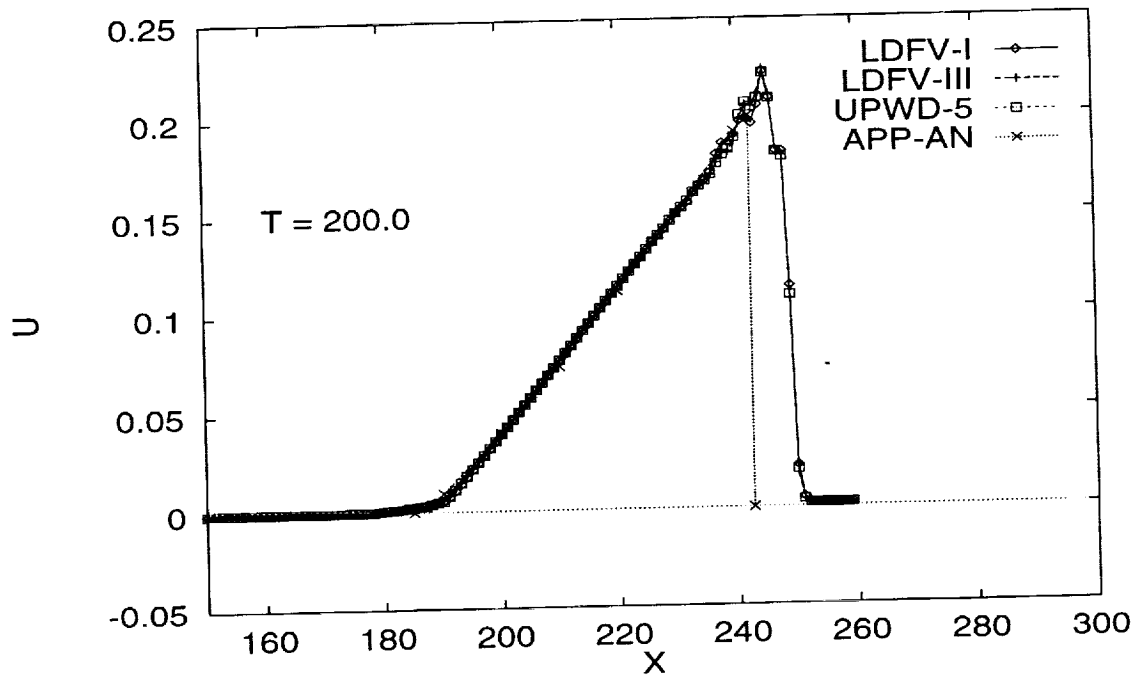


Figure 5: Nonlinear Pulse Solutions $T = 200$

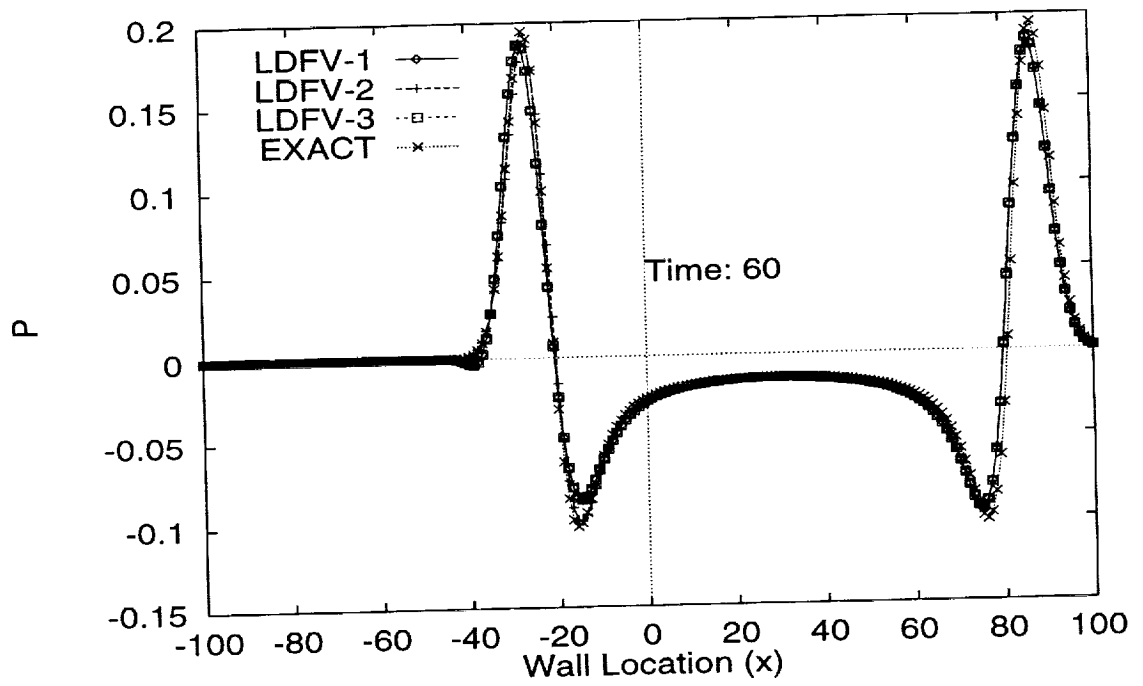


Figure 6: Wall-Reflected Pulse Solutions $T = 60$

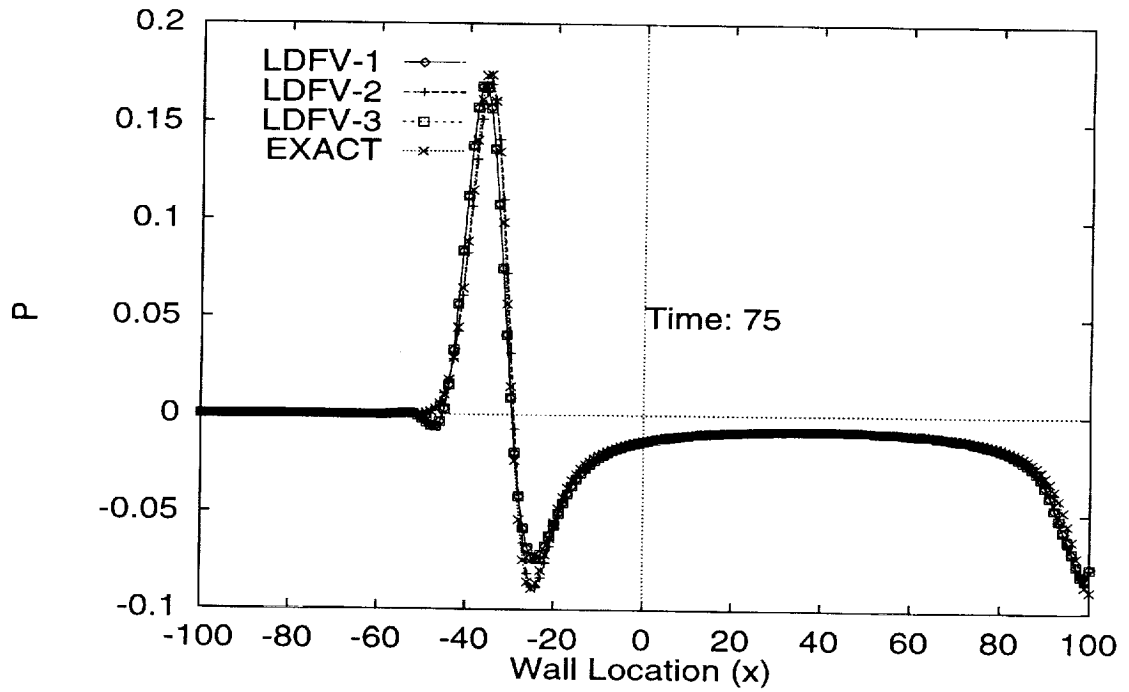


Figure 7: Wall-Reflected Pulse Solutions $T = 75$

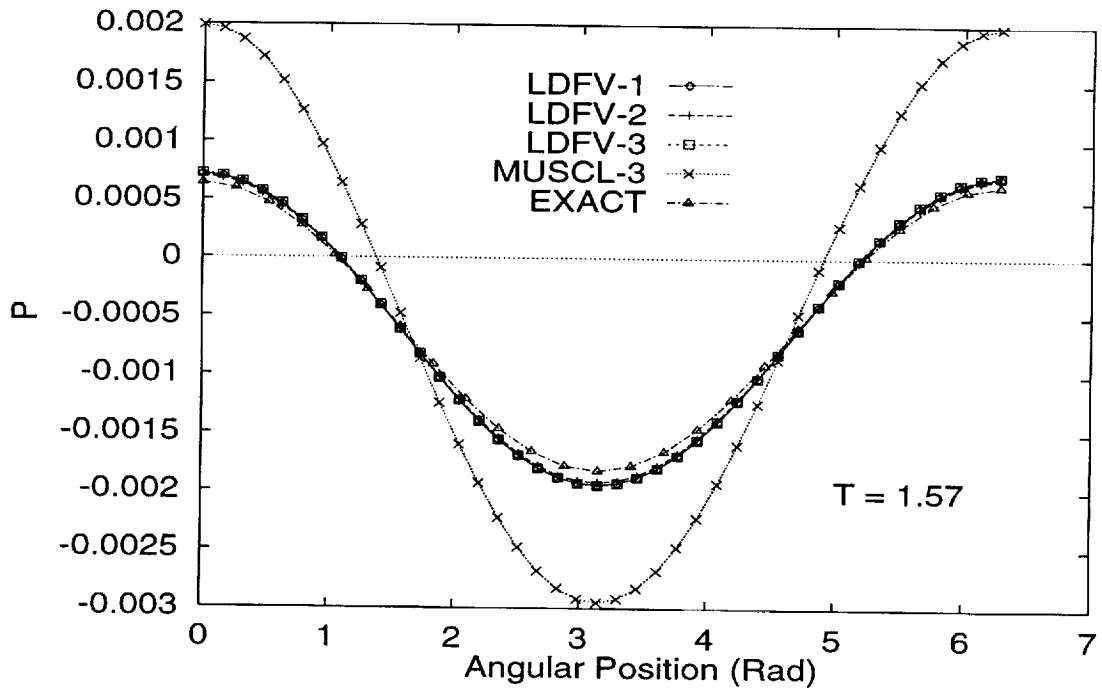


Figure 8: Plane Wave Cylindrical Scattering Solutions
 $T = \frac{\pi}{2}$

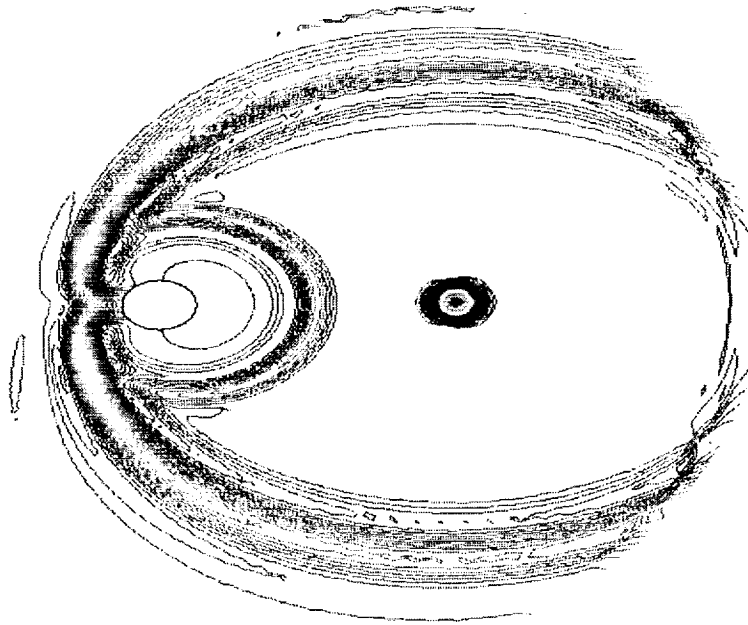


Figure 9: Nonhomogeneous Cylindrical Scattering Problem $T = 5$

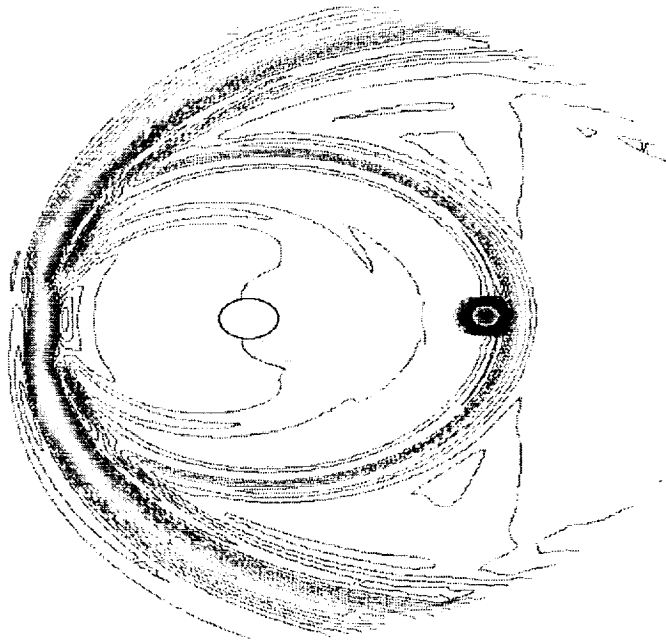


Figure 10: Nonhomogeneous Cylindrical Scattering Problem $T = 7.5$

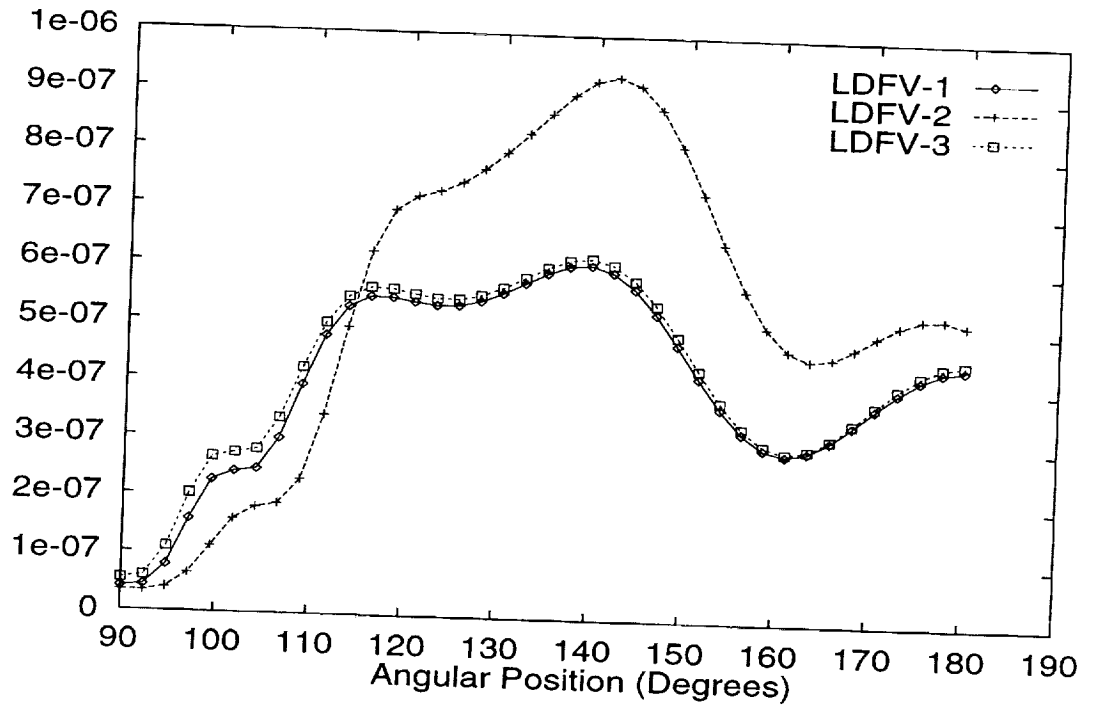


Figure 11: Time-Averaged Acoustic Pressure
Nonhomogeneous Cylindrical Scattering Problem

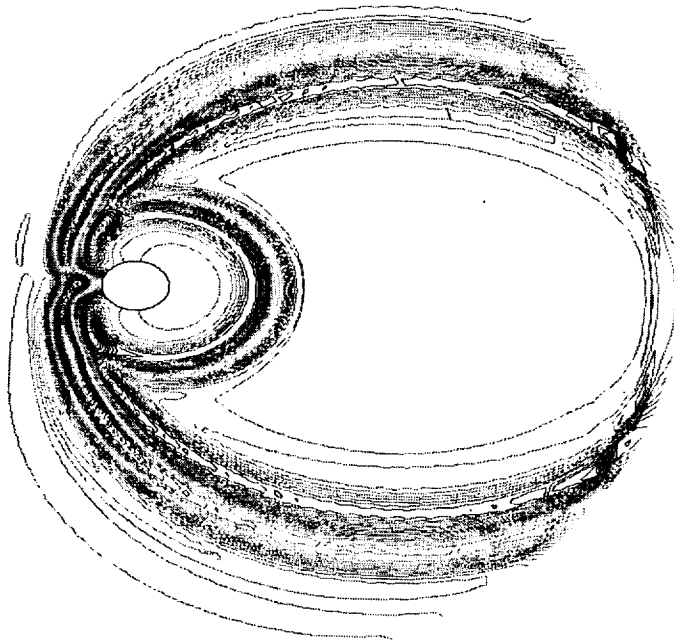


Figure 12: Cylindrical Scattering Initial Value Problem $T = 5.0$

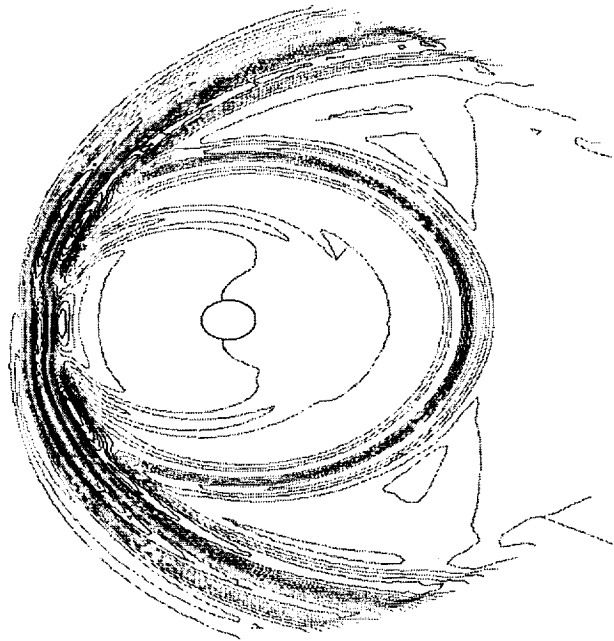


Figure 13: Cylindrical Scattering Initial Value Problem $T = 7.5$

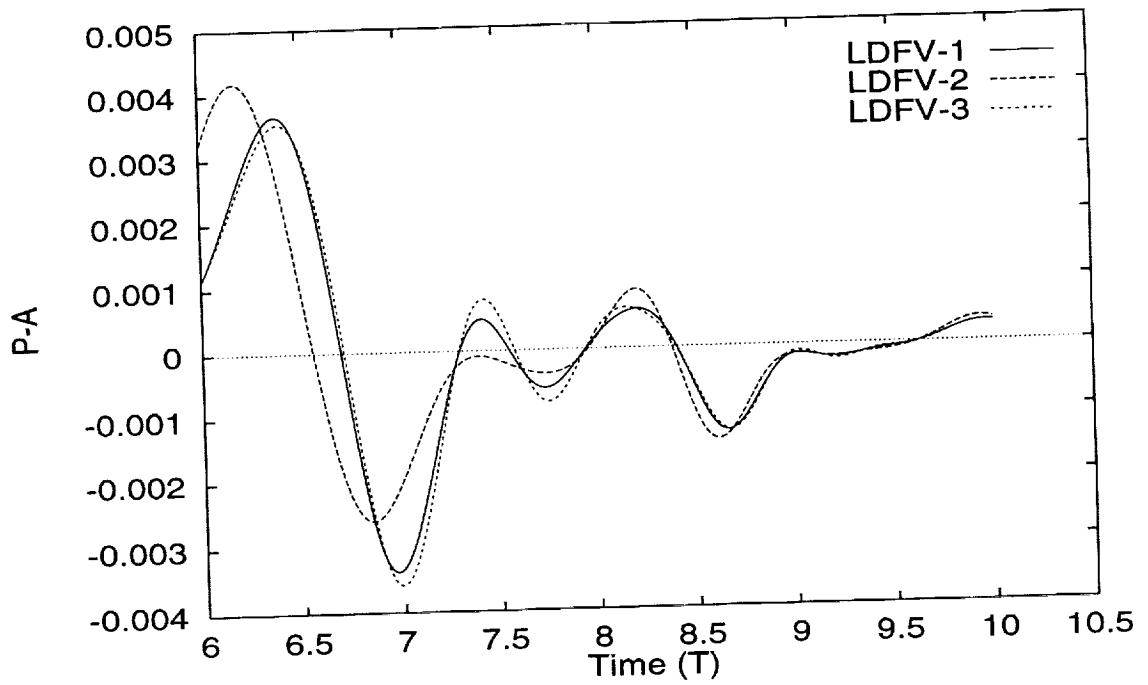


Figure 14: Cylindrical Scattering Initial Value Problem
Pressure Time History at Point A

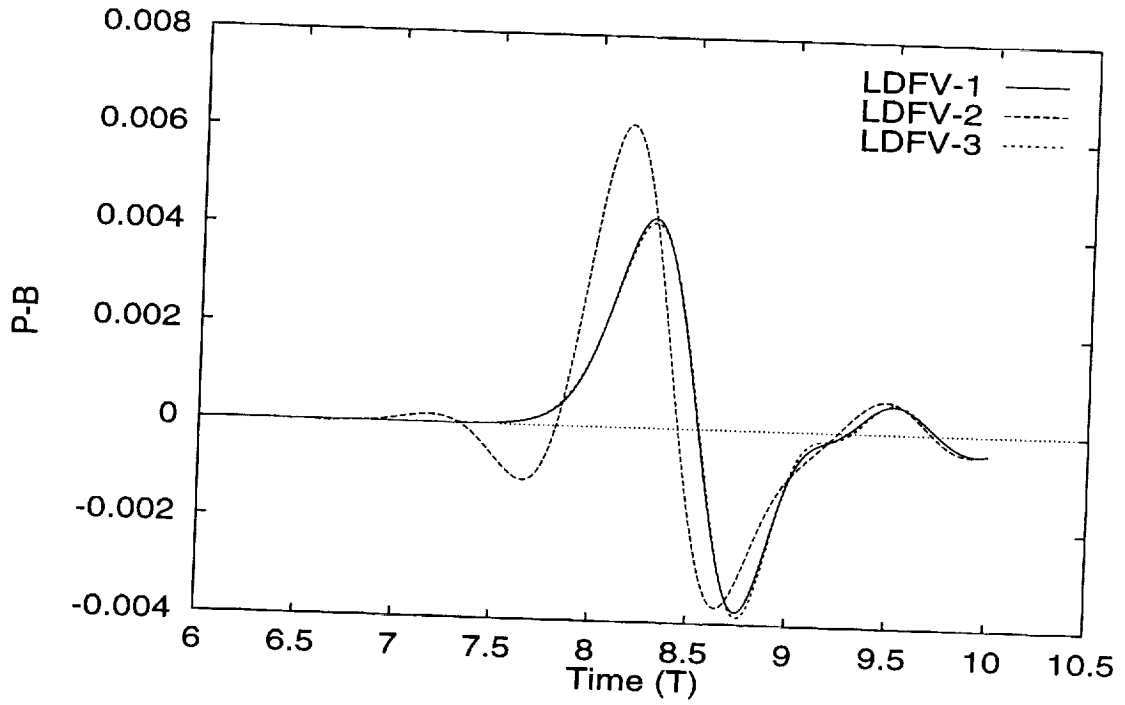


Figure 15: Cylindrical Scattering Initial Value Problem
Pressure Time History at Point B

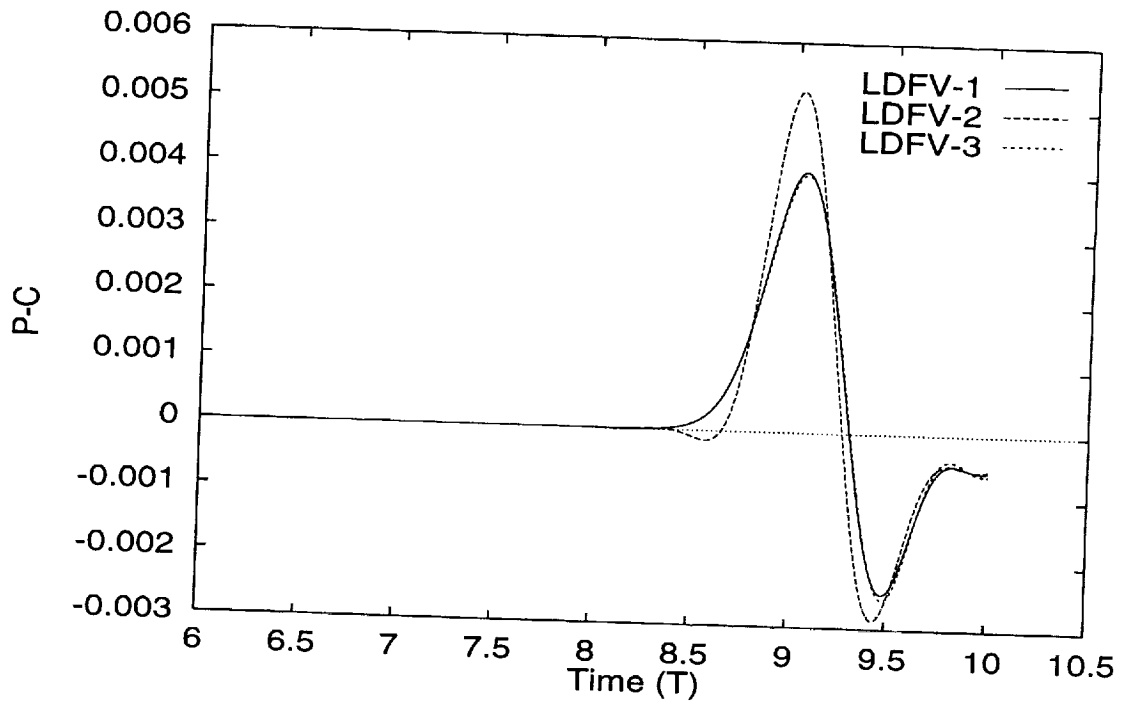


Figure 16: Cylindrical Scattering Initial Value Problem
Pressure Time History at Point C

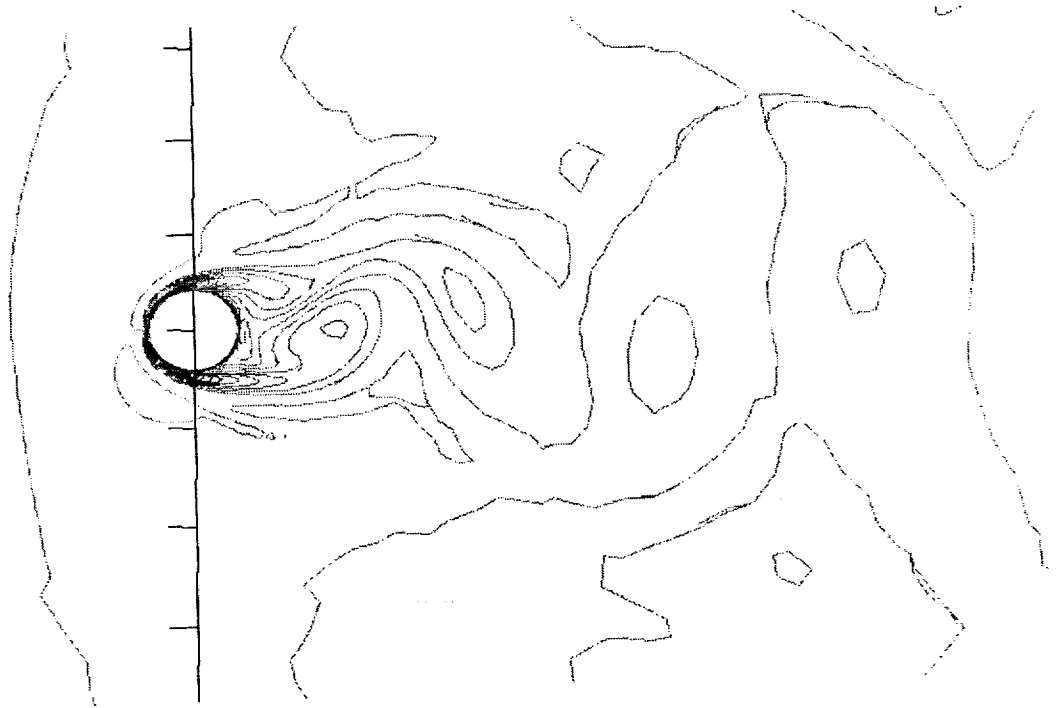


Figure 17: Vorticity Field Re 200

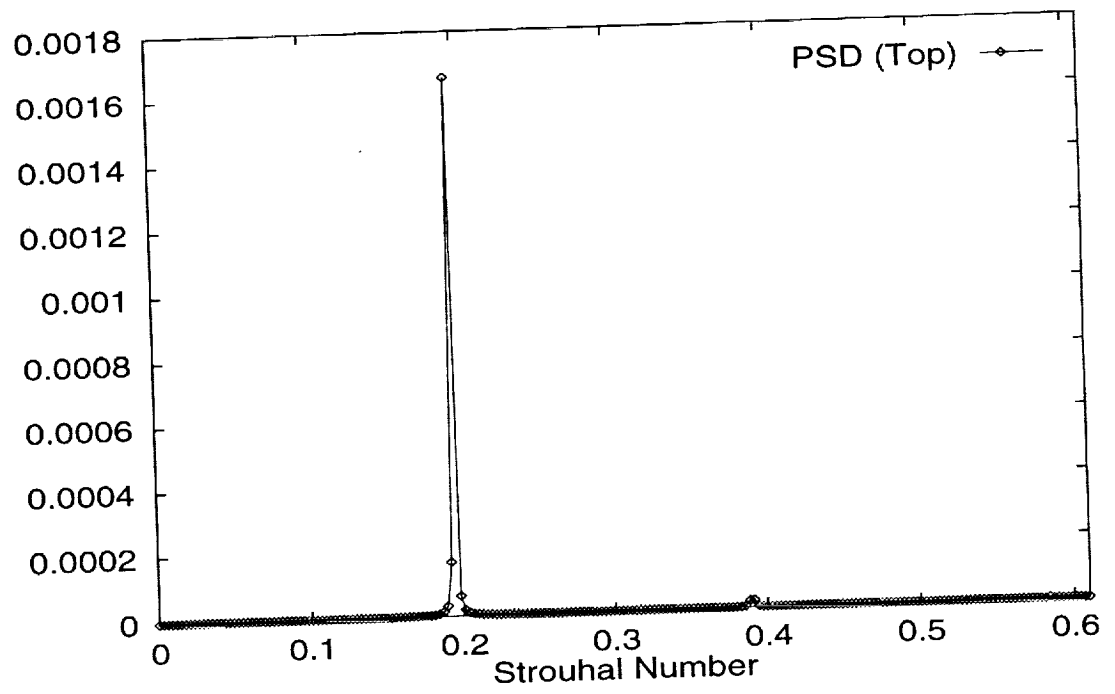


Figure 18: Power Spectral Density Above Cylinder Re 200

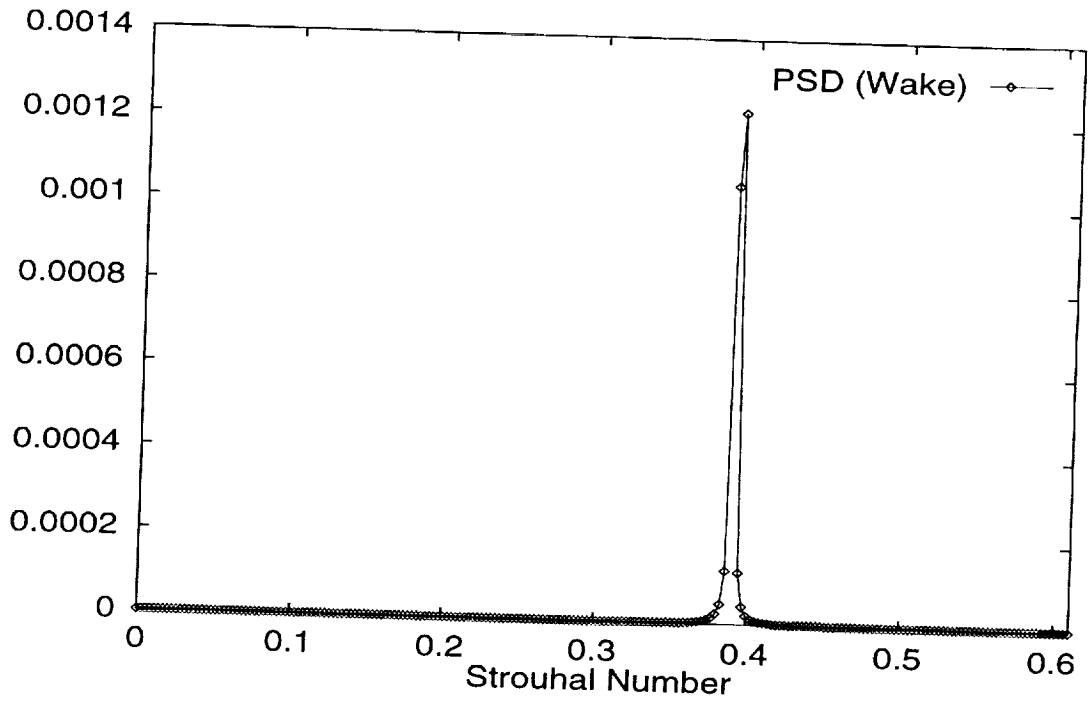


Figure 19: Power Spectral Density in Cylinder Wake Re 200

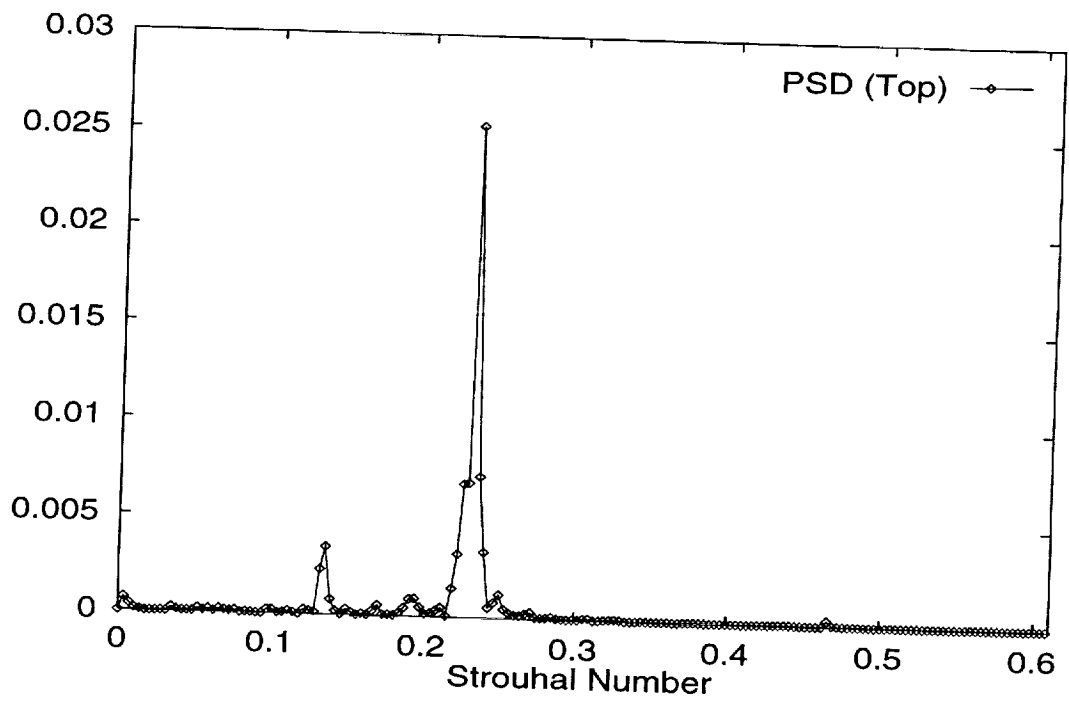


Figure 20: Power Spectral Density Above Cylinder Re 5000

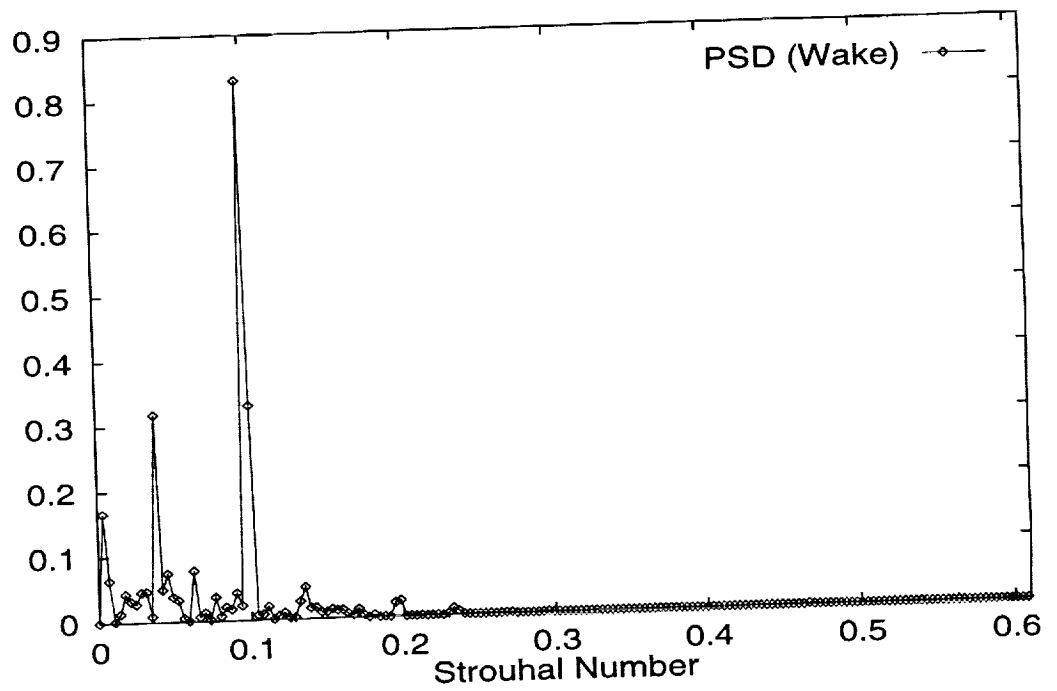


Figure 21: Power Spectral Density in Cylinder Wake Re 5000

OMIT TO
END

OVERVIEW OF COMPUTED RESULTS

Christopher K.W. Tam
Florida State University

One distinctive feature of the CAA Workshops on benchmark problems is that all participants are required to submit a set of their computed data to the Scientific Committee for comparisons with the exact (nearly exact) solutions or experimental measurements. The purpose of the comparisons is to provide a measure of the quality of the numerical results. Also it is hoped that the comparisons would offer feedback to the participants to encourage improvements on their computational algorithms.

The benchmark problems of the First CAA Workshop were designed mainly to test the dispersion, dissipation and anisotropy characteristics of the computational schemes. They are, therefore, somewhat idealized and simple. The benchmark problems of the Second CAA Workshop are more realistic and hence more difficult and challenging. The first three categories of problems are formulated to test the design and implementation of boundary conditions. They include open boundary conditions (radiation condition) wall boundary conditions and radiation boundary conditions in ducted environments. Based on the submitted data and their comparisons with exact (nearly exact) solutions, it appears that significant advances in the development of numerical boundary conditions for CAA have been made over the last few years. The Category 4 problem is the first benchmark problem involving viscous flow. Viscous flow problems, by nature, have multiple length scales. They are much more difficult to solve computationally. Perhaps, because of the intrinsic complexity of the problem, all the contributors have chosen not to compute the radiated sound directly. Direct computation of the radiated sound remains a challenge for the future.

The Scientific Committee wishes to thank the following individuals for their time and effort in carrying out the comparisons on its behalf.

Category 1.

Problems 1 & 2. Konstantin A. Kurbatskii and Christopher K.W. Tam, Florida State University.

Problems 3 & 4. Philip J. Morris, Penn State University.

Category 2.

Problem 1. Philip J. Morris, Penn State University.

Problems 2. Konstantin A. Kurbatskii and Christopher K.W. Tam, Florida State University.

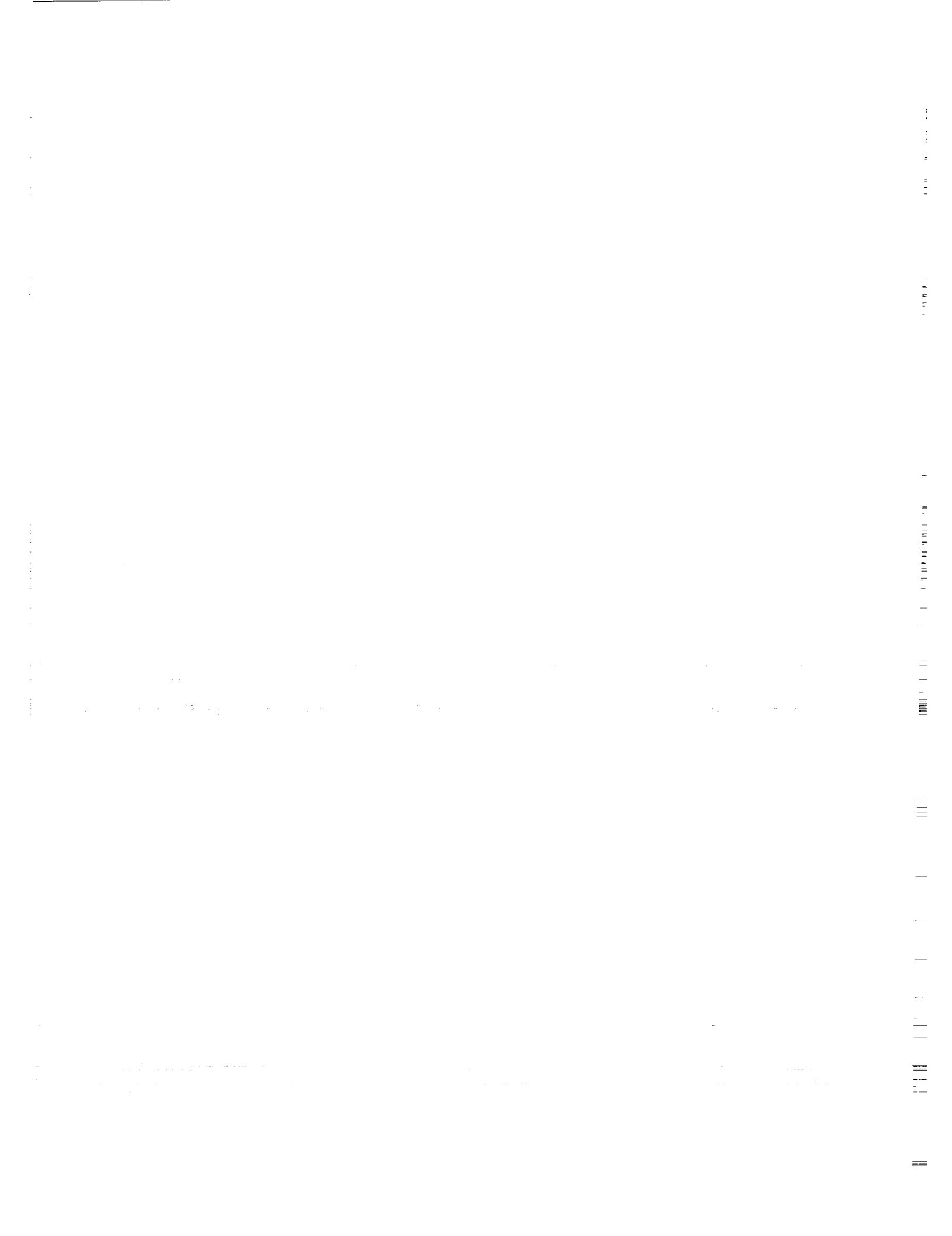
Category 3.

Problems 1, 2 & 3. Kenneth C. Hall, Duke University.

Category 4.

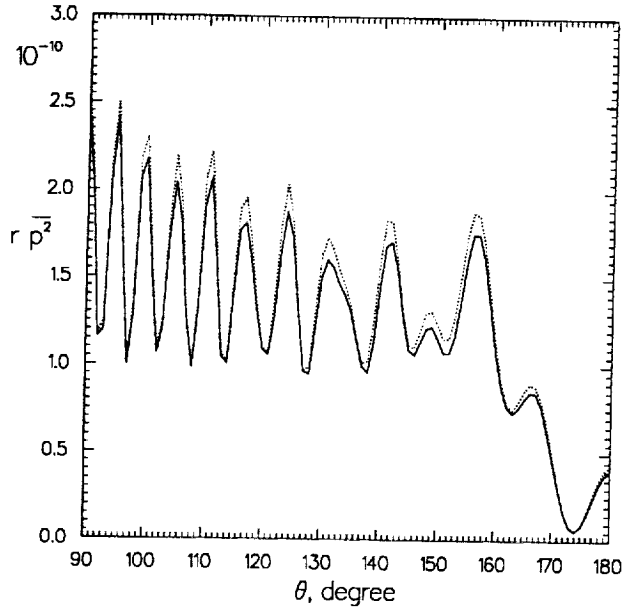
Problem 1. Jay C. Hardin, NASA Langley Research Center.

The Committee also wishes to thank Dennis L. Huff (NASA Lewis Research Center) for his contribution to the formulation of the Category 3 problems.

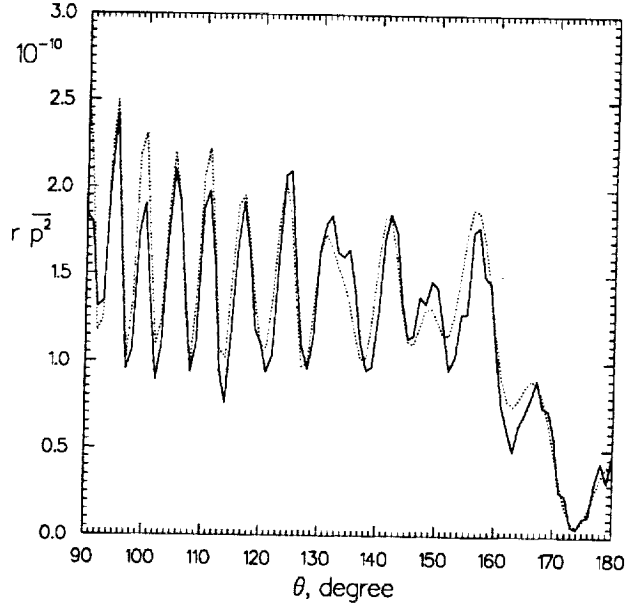


Category 1, Problem 1

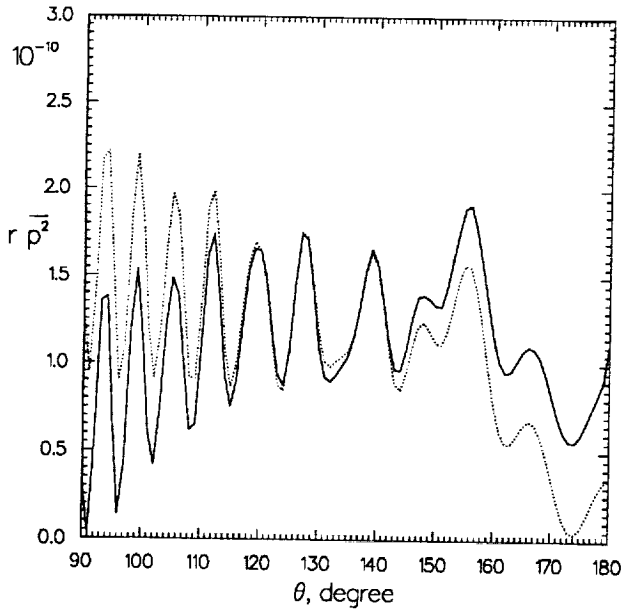
Konstantin A. Kurbatskii and Christopher K.W. Tam



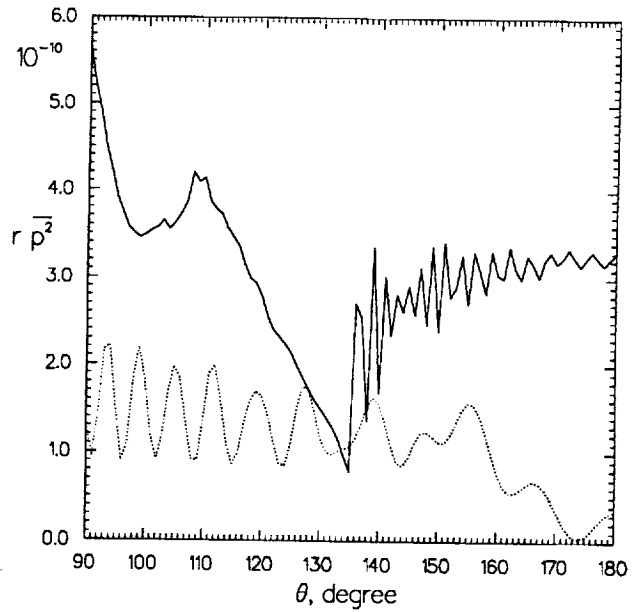
— solution by Atkins
($r=7.0$), exact.



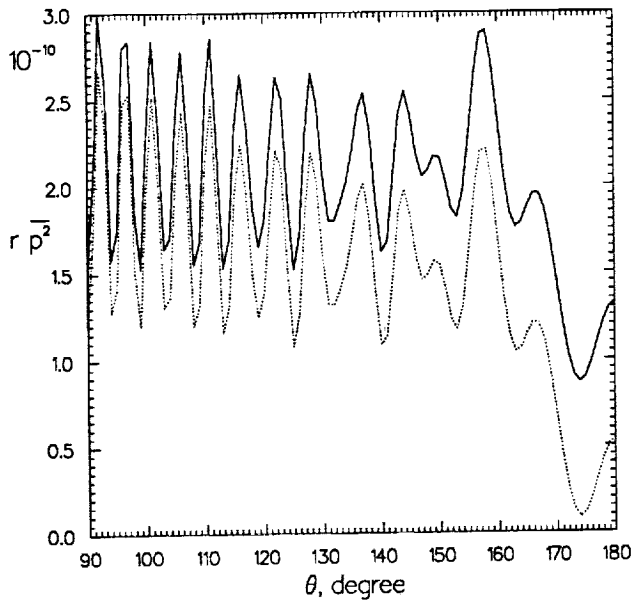
— solution by Djambazov
($r=7.0$), exact.



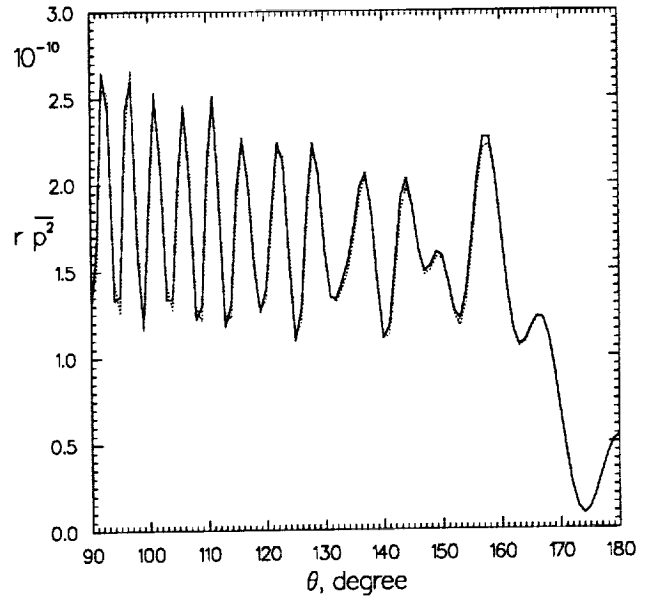
— solution by Baysal and Kaushik
($r=5.0$), exact.



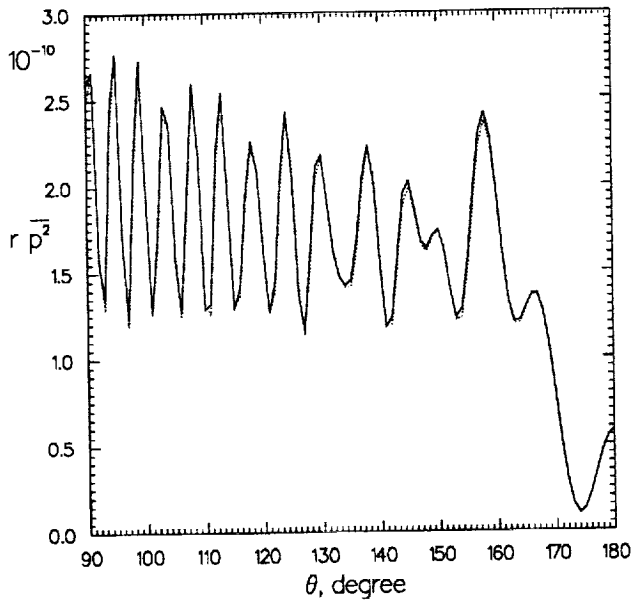
— solution by Fung
($r=5.0$), exact.



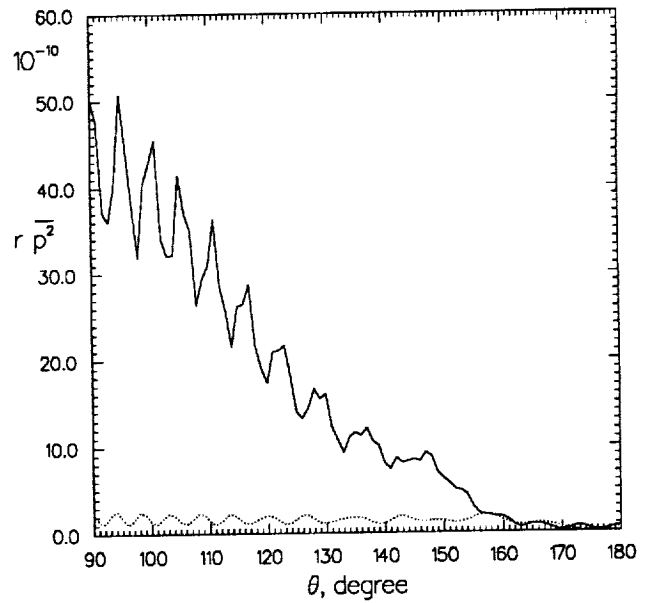
———— solution by Hayder
($r=11.4423$), exact.



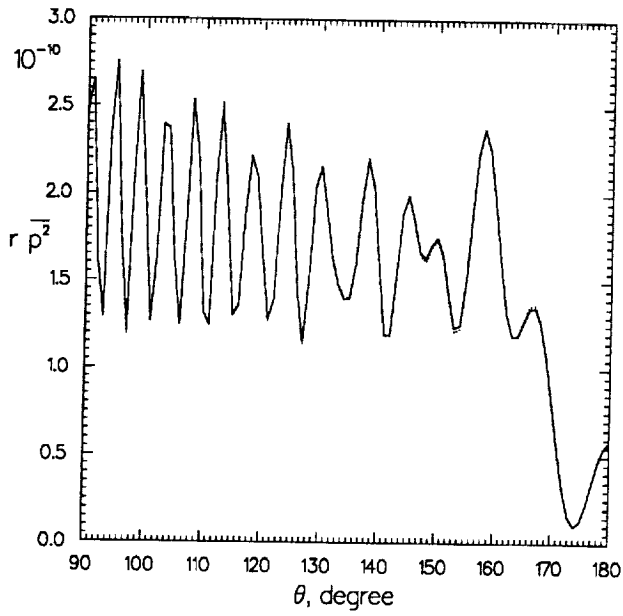
———— solution by Hu
($r=11.6875$), exact.



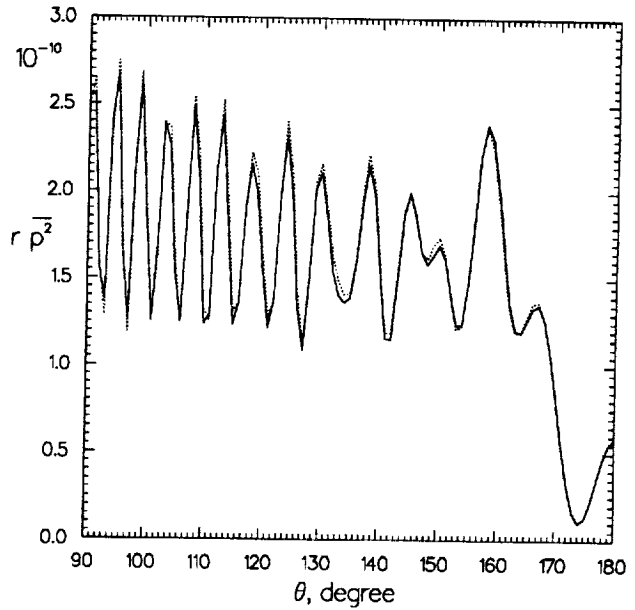
———— solution by Hixon
($r=15.0$), exact.



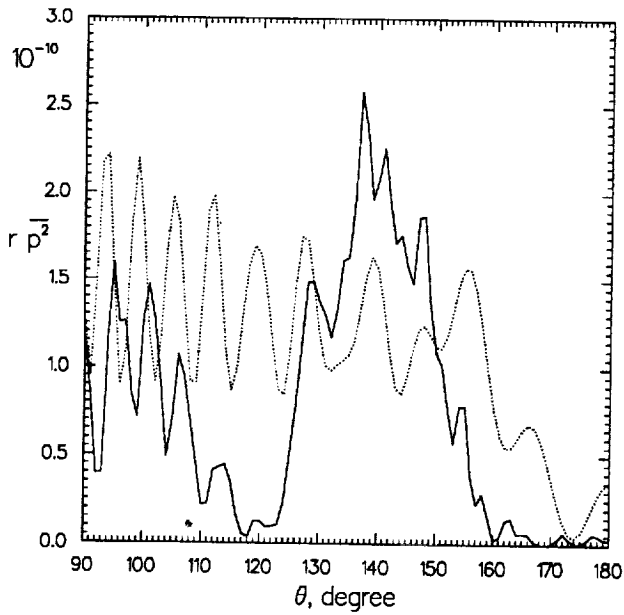
———— solution by Kim and Roe
($r=9.0$), exact.



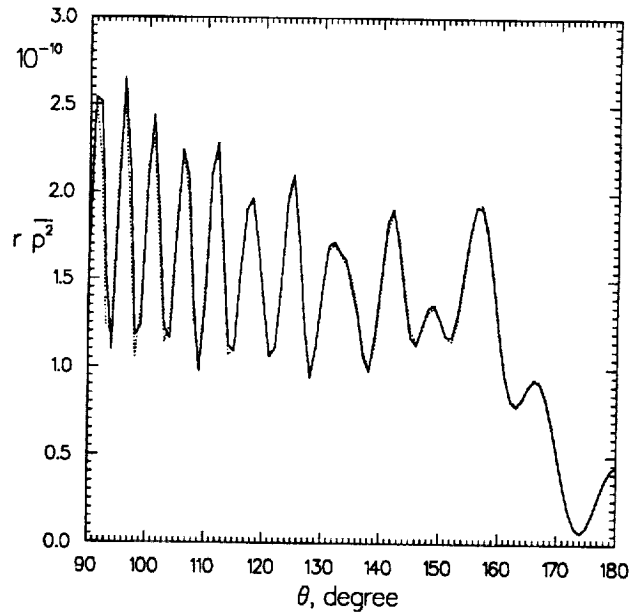
— solution by Kopriva
($r=15.0$), exact.



— solution by Tam
($r=15.0$), exact.

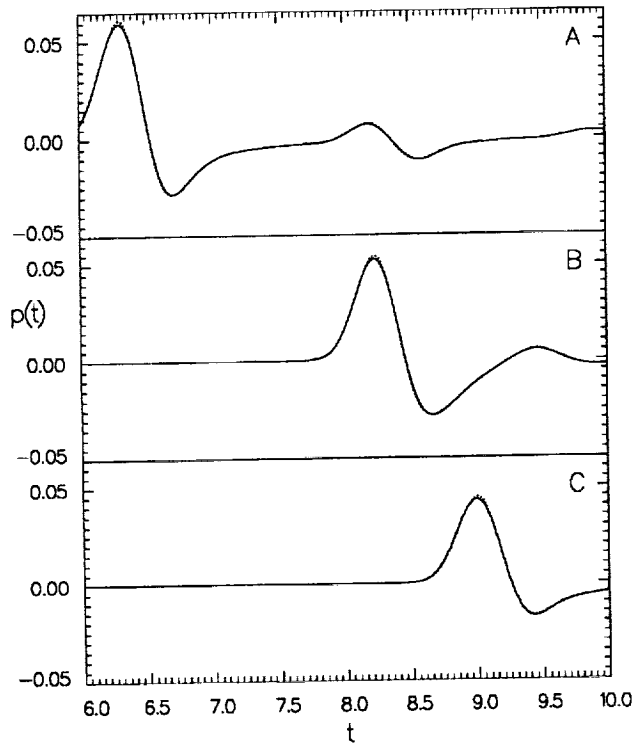


— solution by Morris Hsi
($r=5.0$), exact.

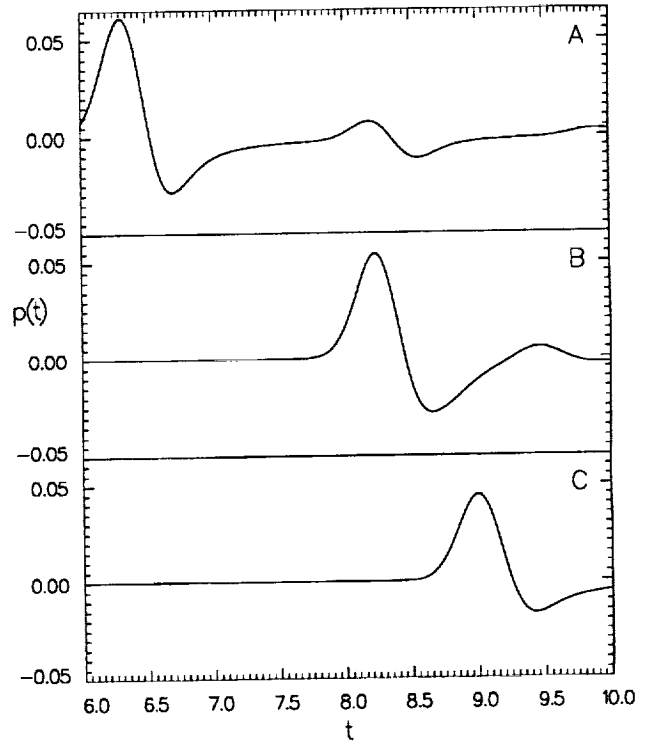


— solution by Zhuang
($r=7.5$), exact.

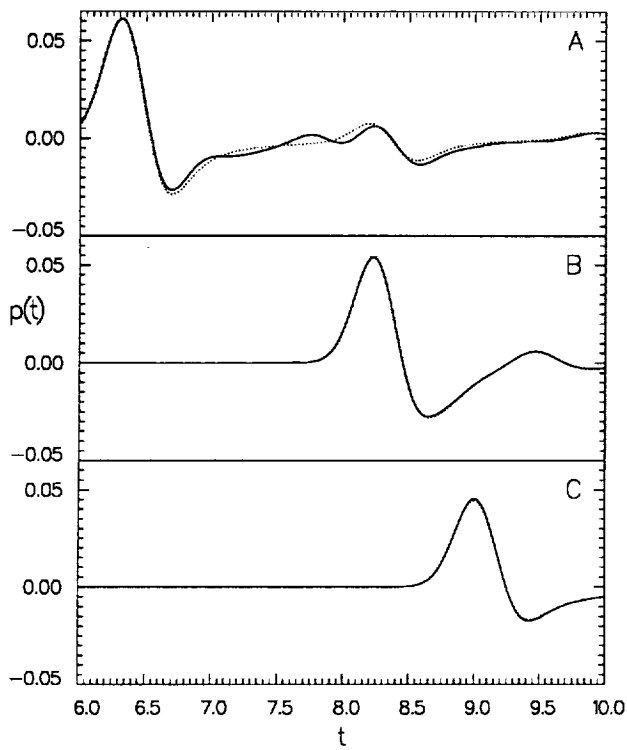
Category 1, Problem 2



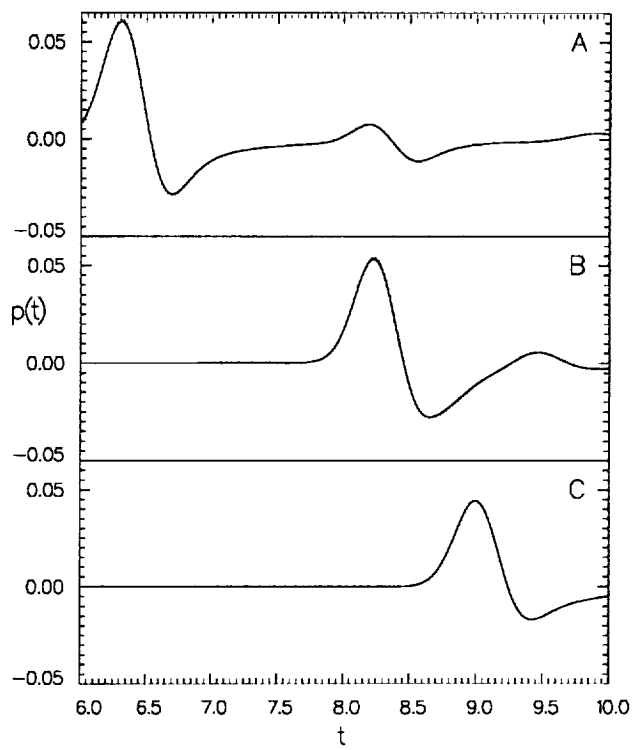
— solution by Atkins,
..... exact.



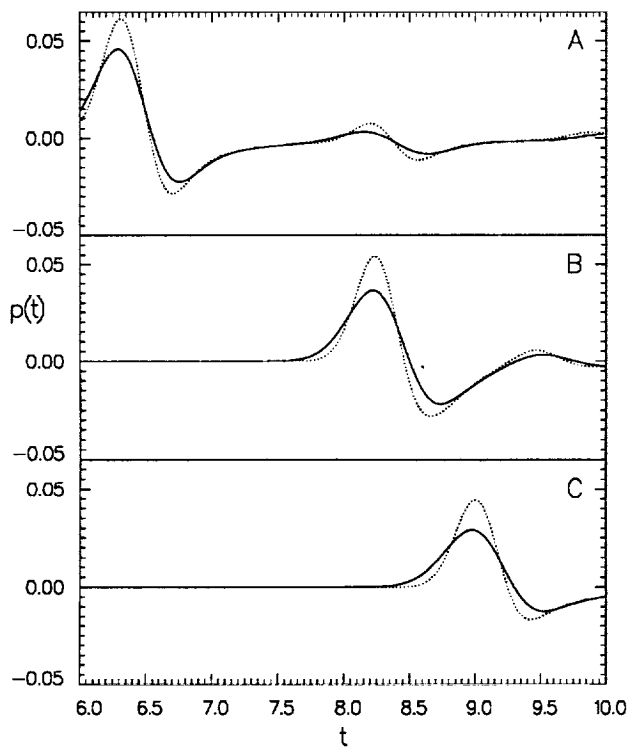
— solution by Baysal,
..... exact.



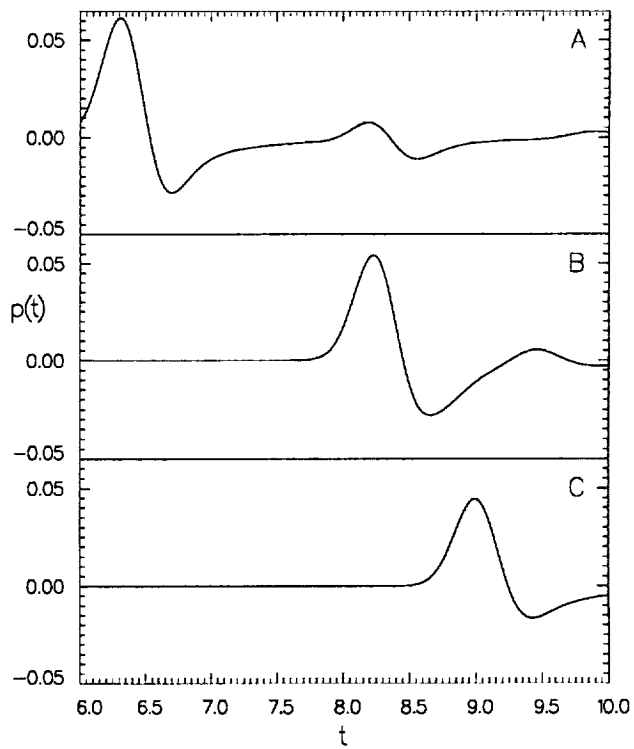
—— solution by Djambazov,
 exact.



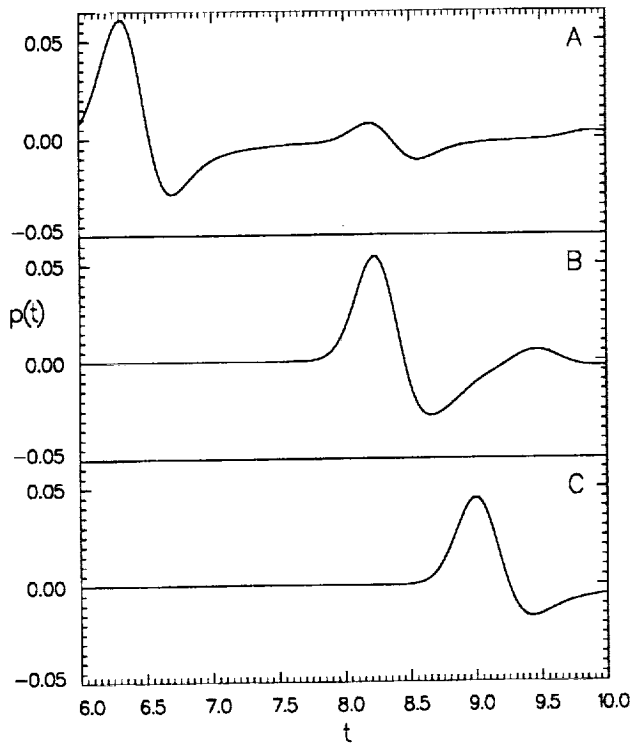
—— solution by Hayder,
 exact.



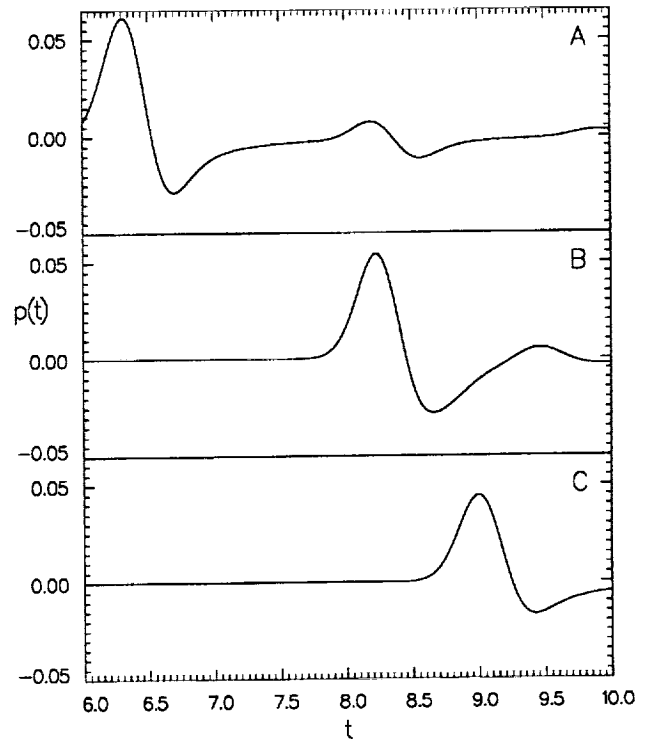
—— solution by Fung,
 exact.



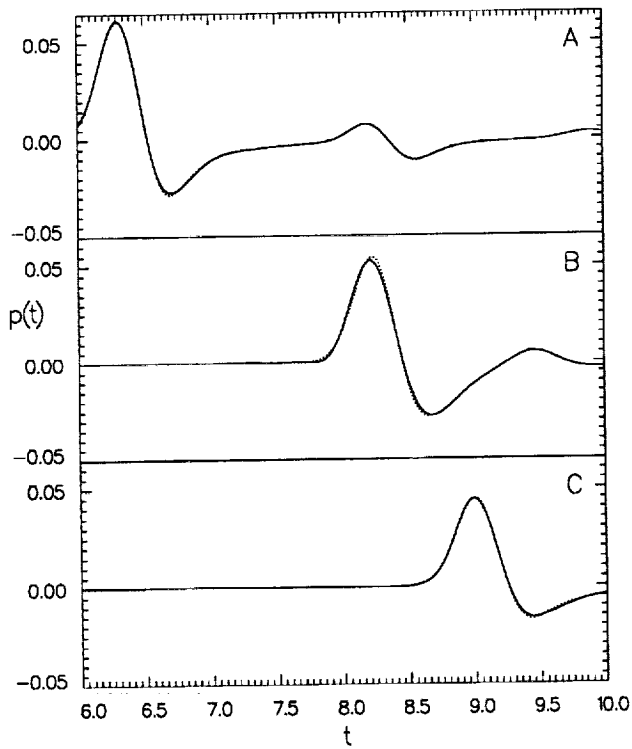
—— solution by Hixon,
 exact.



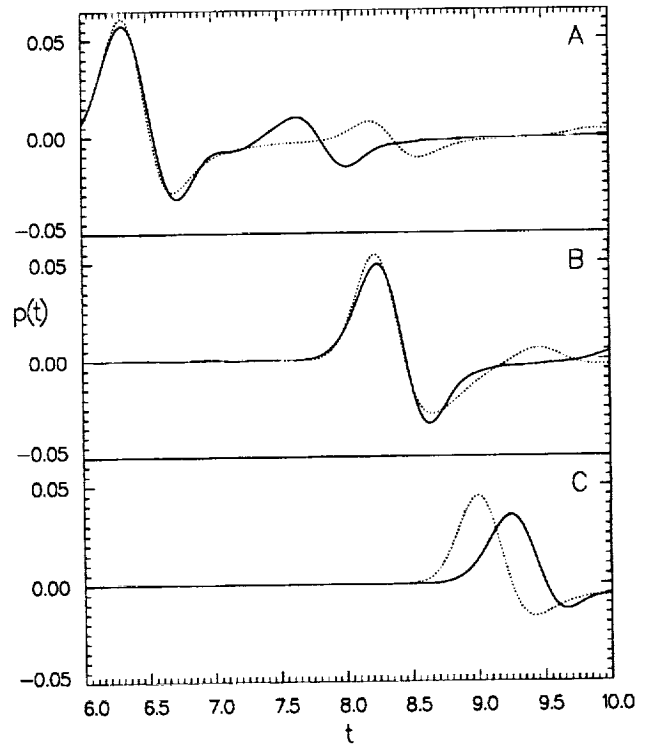
— solution by Hu,
 exact.



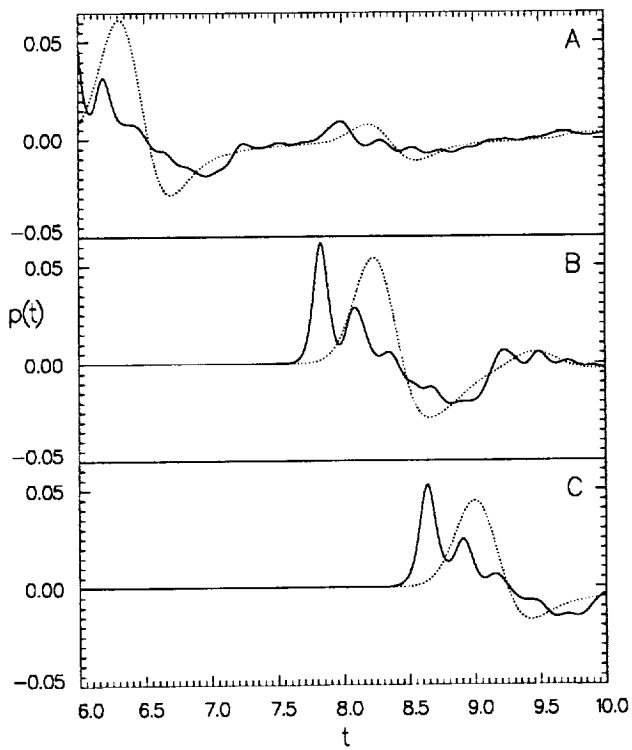
— solution by Kopriva,
 exact.



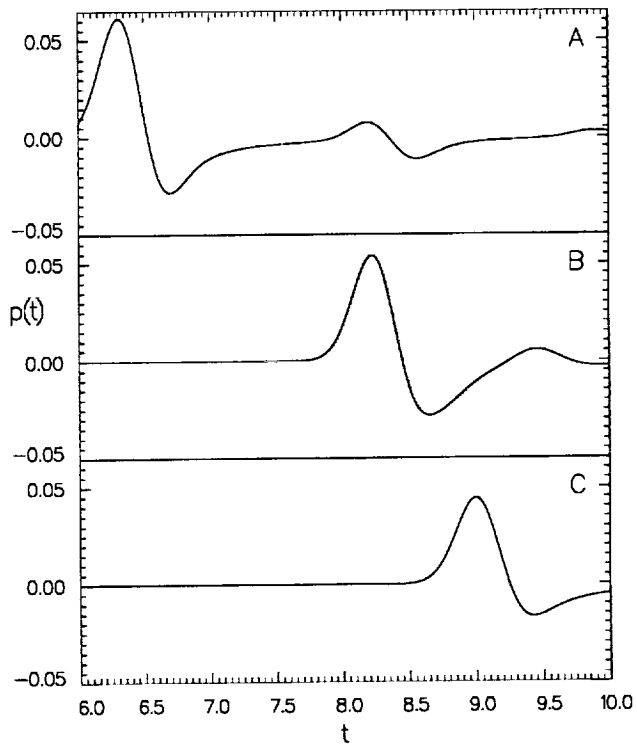
— solution by Kim and Roe,
 exact.



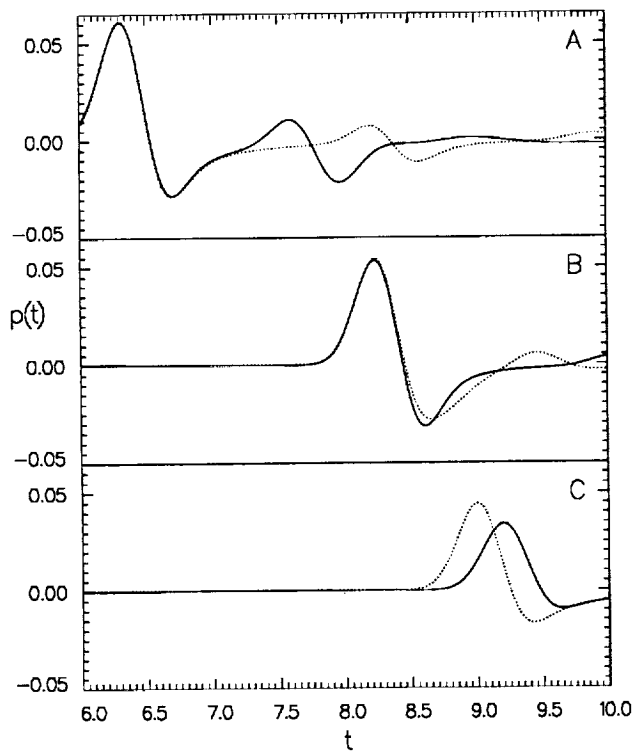
— solution by Lin,
 exact.



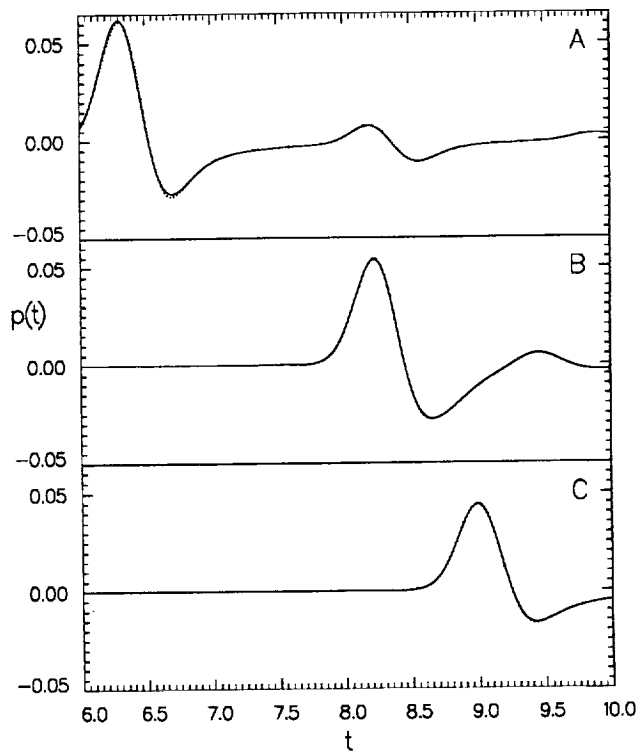
— solution by Morris Hsi,
 exact.



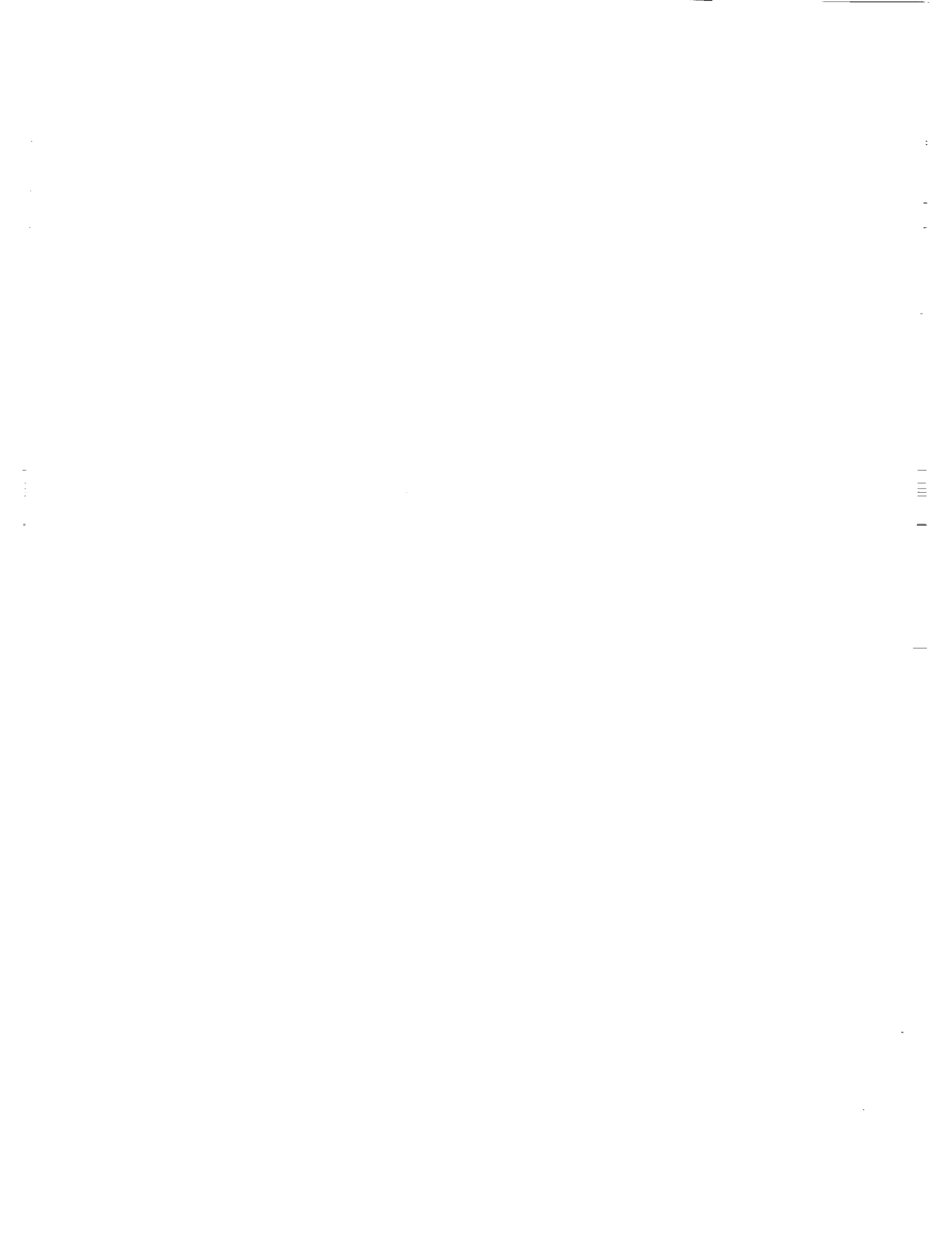
— solution by Tam,
 exact.



— solution by Radvugin,
 exact.



— solution by Zhuang,
 exact.



SOLUTION COMPARISONS. CATEGORY 1: PROBLEMS 3 AND 4. CATEGORY 2: PROBLEM 1

Philip J. Morris*

Department of Aerospace Engineering
The Pennsylvania State University
University Park, PA 16802

CATEGORY 1: PROBLEM 3

Only Ozyoruk and Long submitted a complete solution to the axisymmetric sphere scattering problem. The agreement between the numerical and exact solution is very good. Only one example solution is shown below. Other solutions, with different grids and Kirchhoff surface definitions gave similar agreement.

CATEGORY 1: PROBLEM 4

Only Shieh and Morris submitted a solution for the three-dimensional sphere scattering problem. The comparison between the numerical and exact solutions is shown in the contributed paper.

CATEGORY 2: PROBLEM 1

Four groups contributed solutions to the problem of sound radiation from a distributed source inside an open-ended, cylindrical duct. The agreement between each of the numerical solutions is good, with only minor differences in both the low and high frequency cases. Some differences occur between the numerical solutions and the model problem solution, particularly at high frequencies. This is likely to be due to the use of a point, rather than a distributed, source in the model problem. The fine structure of the interference between the scattered fields outside the cylinder is captured very well by the numerical solutions.

*Boeing/A. D. Welliver Professor of Aerospace Engineering

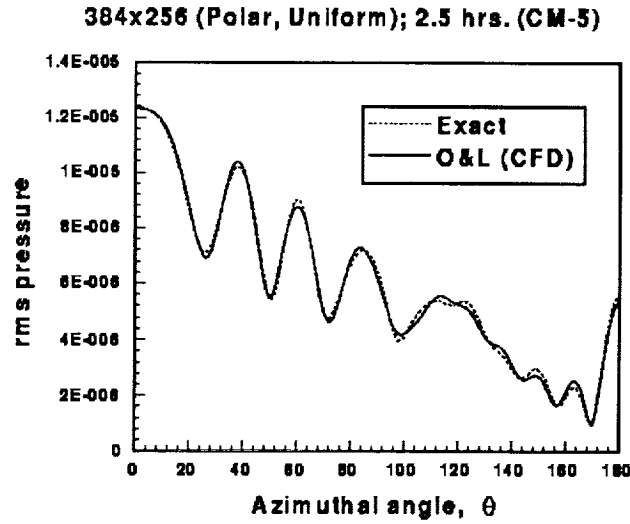


Figure 1: Category 1: Problem 3. Numerical solution by Ozyoruk and Long.

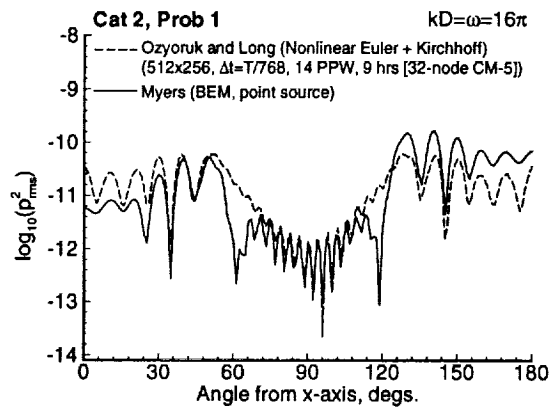


Figure 2: Category 2: Problem 1. High frequency solution by Ozyoruk and Long.

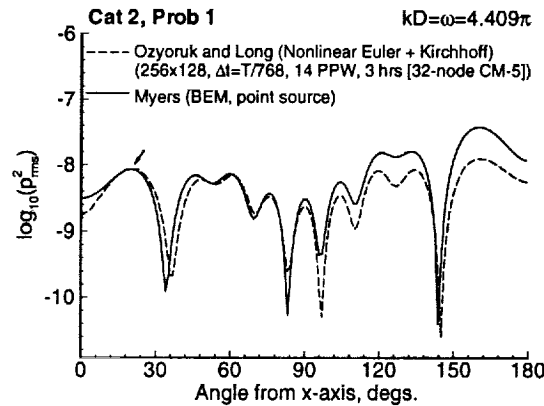


Figure 3: Category 2: Problem 1. Low frequency solution by Ozyoruk and Long.

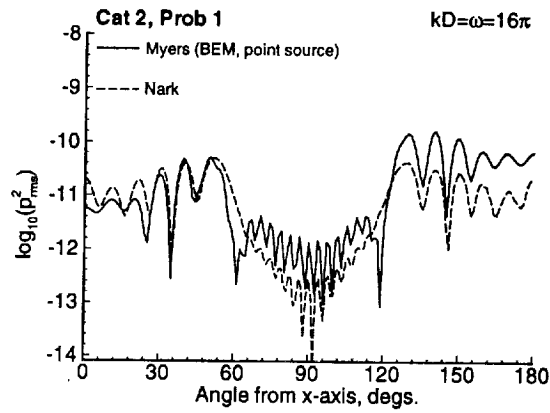


Figure 4: Category 2: Problem 1. High frequency solution by Nark.

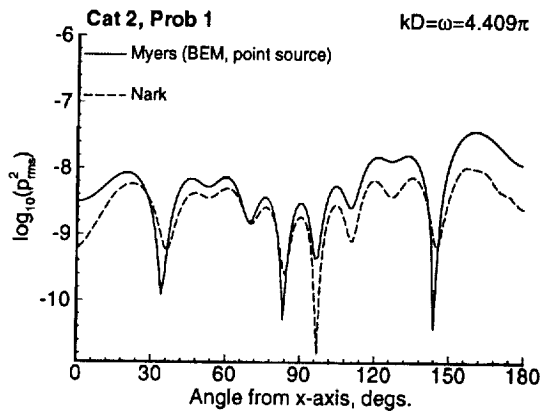


Figure 5: Category 2: Problem 1. Low frequency solution by Nark.

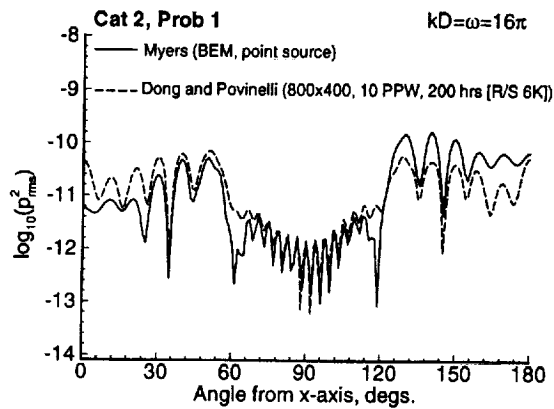


Figure 6: Category 2: Problem 1. High frequency solution by Dong and Povinelli.

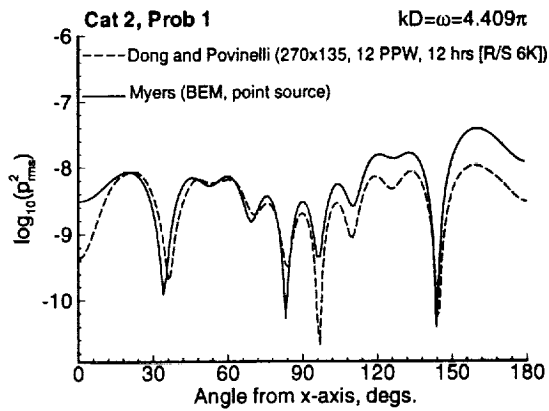


Figure 7: Category 2: Problem 1. Low frequency solution by Dong and Povinelli.

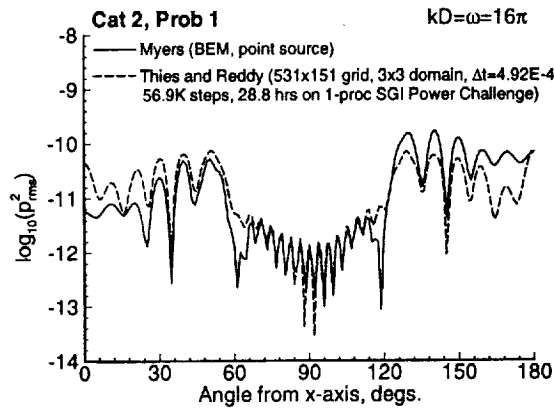


Figure 8: Category 2: Problem 1. High frequency solution by Thies and Reddy.

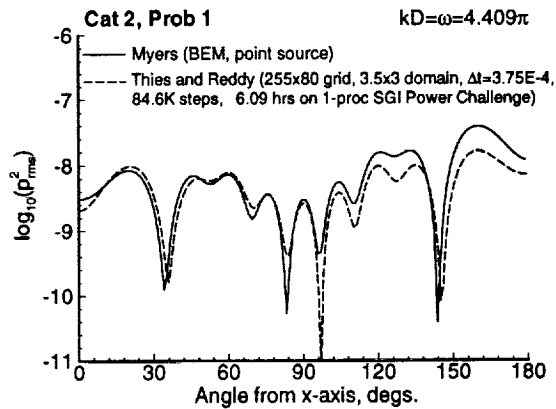
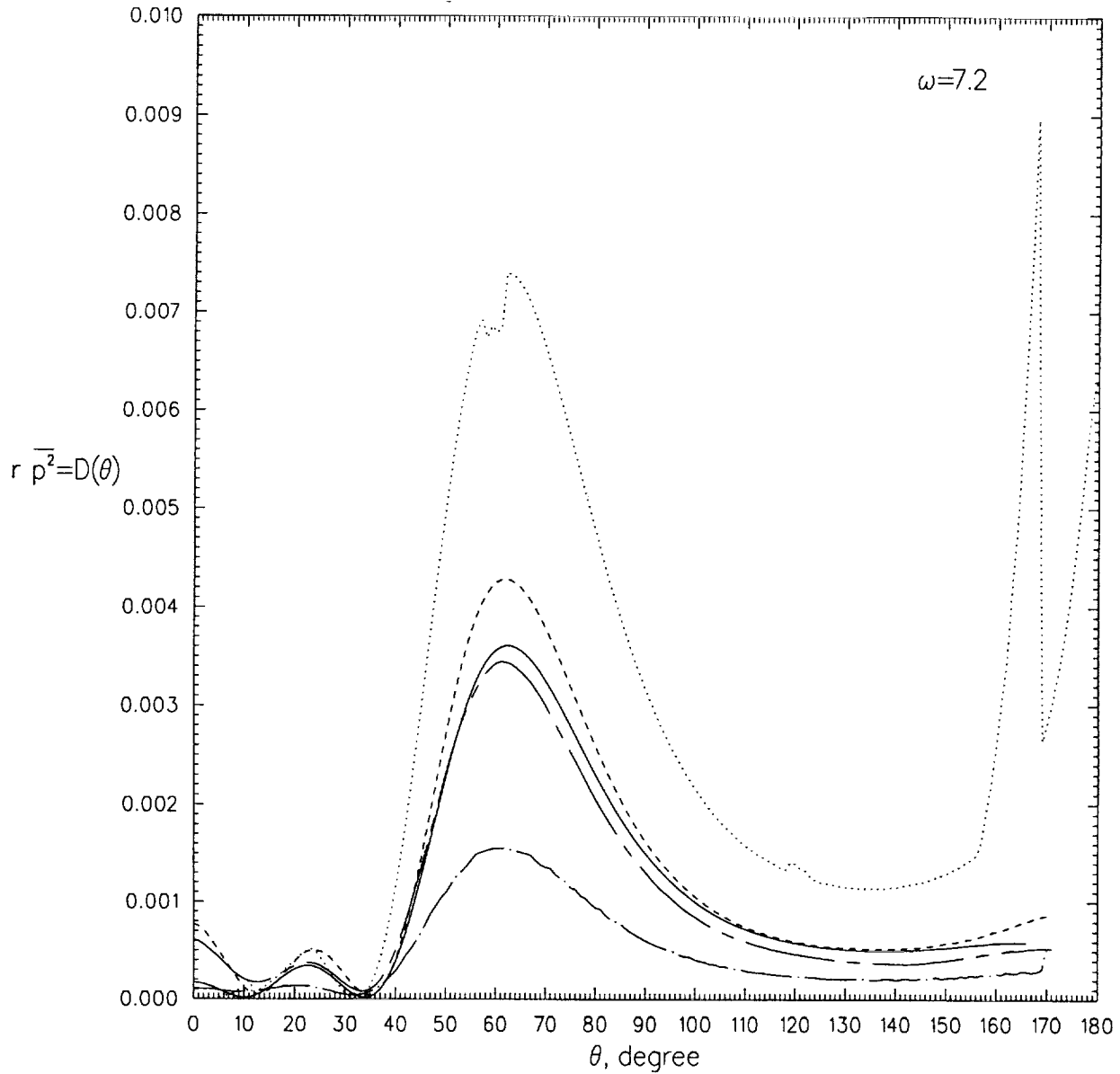


Figure 9: Category 2: Problem 1. Low frequency solution by Thies and Reddy.

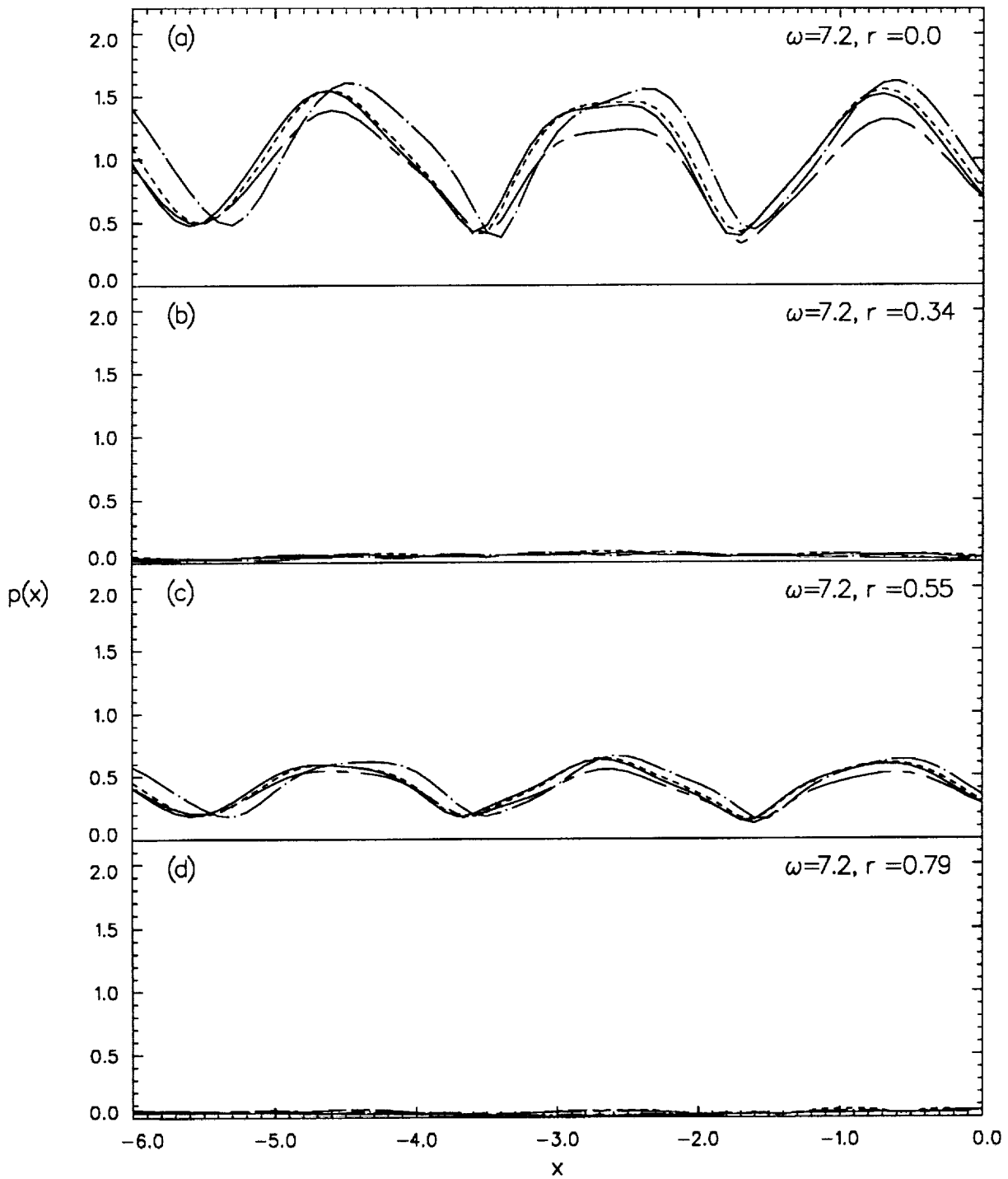
Category 2, Problem 2

Konstantin A. Kurbatskii and Christopher K.W. Tam



Directivity of radiated sound at $\omega = 7.2$,

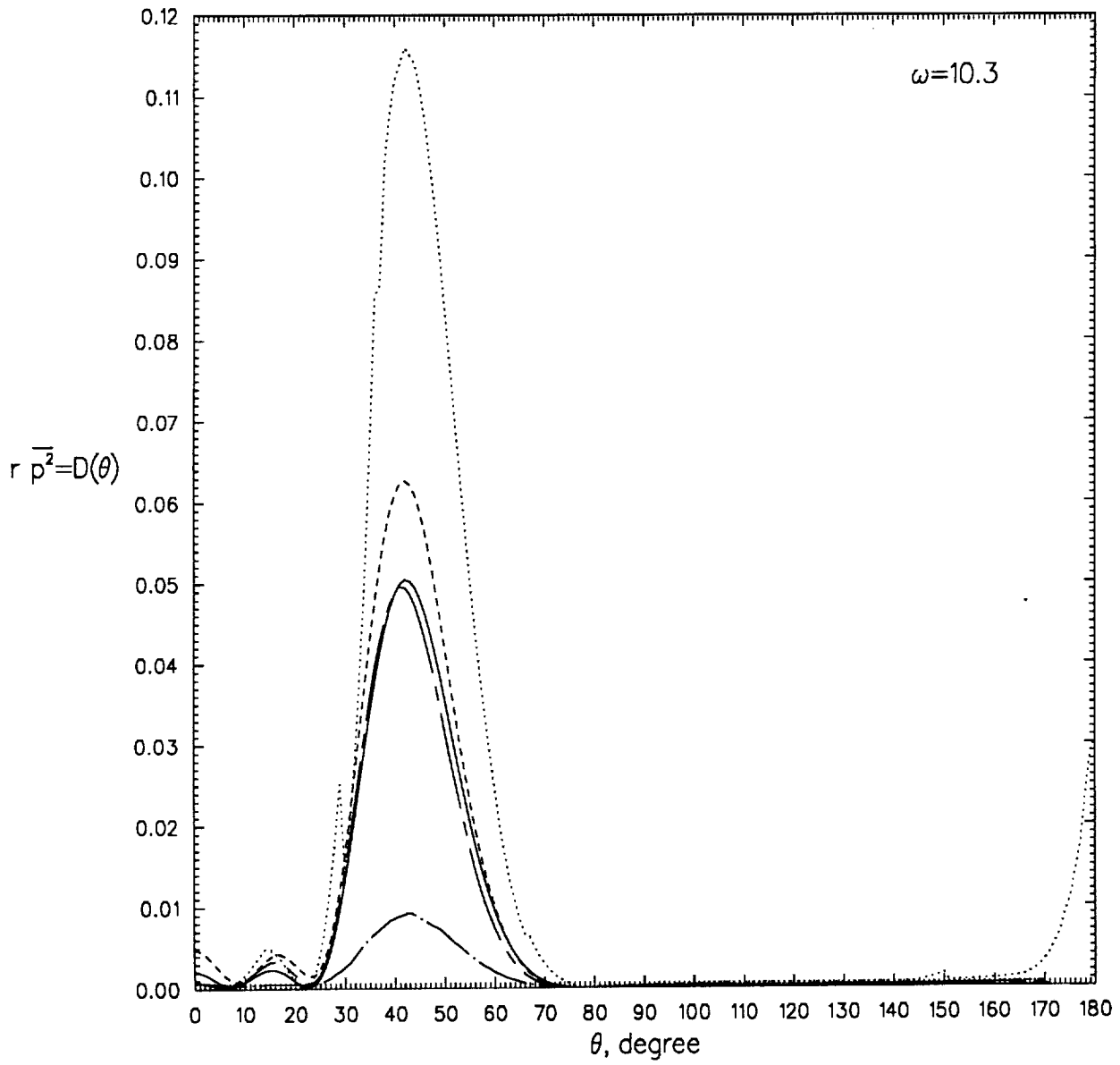
- · — · — solution by Dong,
- - - - - solution by Hu,
- · - · - solution by Nark,
- solution by Tam,
- Wiener-Hopf solution by Cho.



Pressure envelope inside the duct at $\omega = 7.2$.

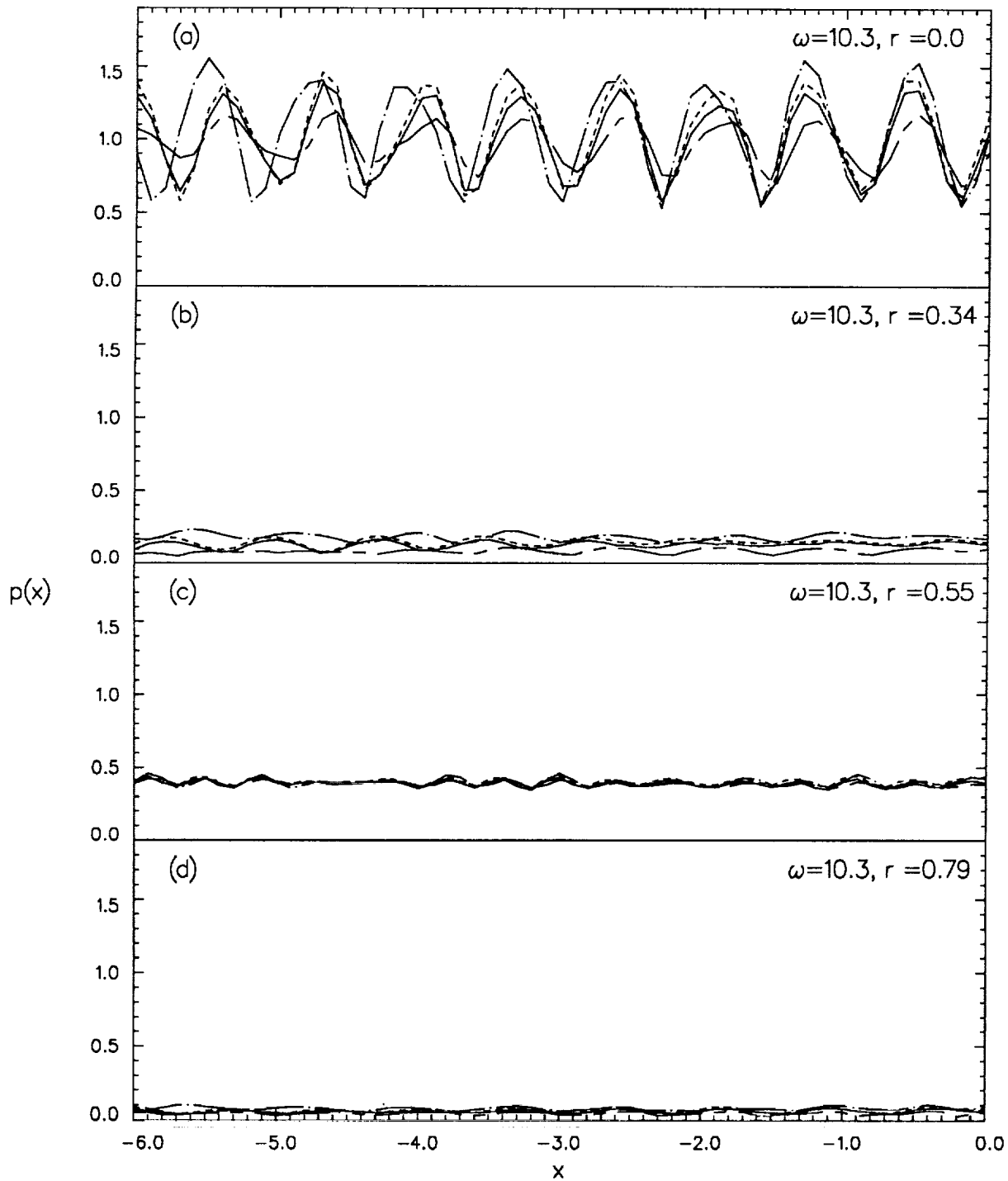
(a) $r = 0.0$, (b) $r = 0.34$, (c) $r = 0.55$, (d) $r = 0.79$,

- - - - - solution by Dong, solution by Hu,
 - . - . - solution by Nark, ——— solution by Tam.



Directivity of radiated sound at $\omega = 10.3$,

- · — · — solution by Dong,
- - - - - solution by Hu,
- · - · - solution by Nark,
- solution by Tam,
- Wiener-Hopf solution by Cho.



Pressure envelope inside the duct at $\omega = 10.3$.

(a) $r = 0.0$, (b) $r = 0.34$, (c) $r = 0.55$, (d) $r = 0.79$,

- · - · - solution by Dong, - - - - - solution by Hu,
 - · · · - solution by Nark, - - - - - solution by Tam.

CATEGORY 3.

Kenneth C. Hall

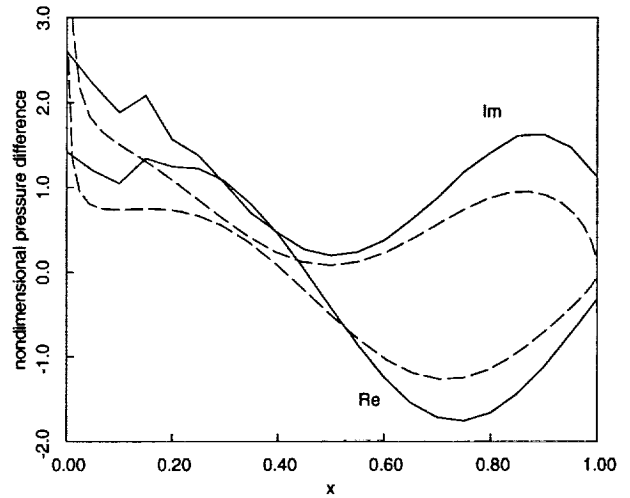
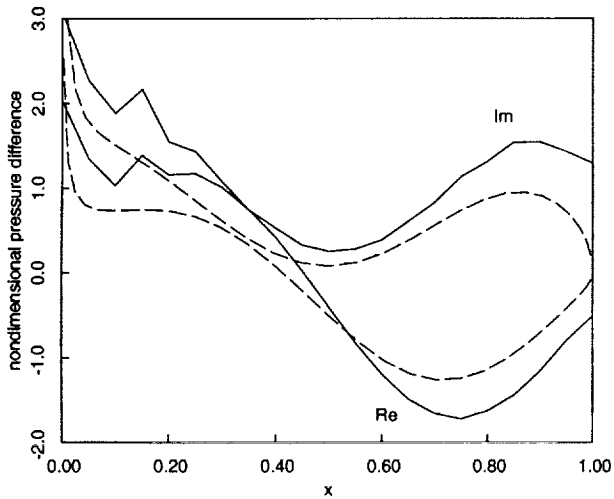


Figure 1: Nondimensional pressure loading on airfoil, $\omega = \sigma = 5\pi/2$ (Fang Hu, Problem 1). Note, pressures are normalized by the gust velocity v_g . In all cases, the dashed line is the “exact” LIN-SUB solution, while the solid line is the submitted numerical solution.

Figure 3: Nondimensional pressure loading on airfoil, $\omega = \sigma = 5\pi/2$ (Fang Hu, Problem 3).

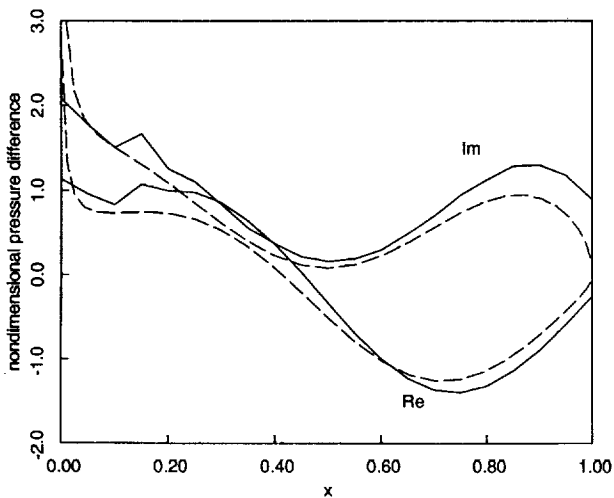


Figure 2: Nondimensional pressure loading on airfoil, $\omega = \sigma = 5\pi/2$ (Fang Hu, Problem 2).

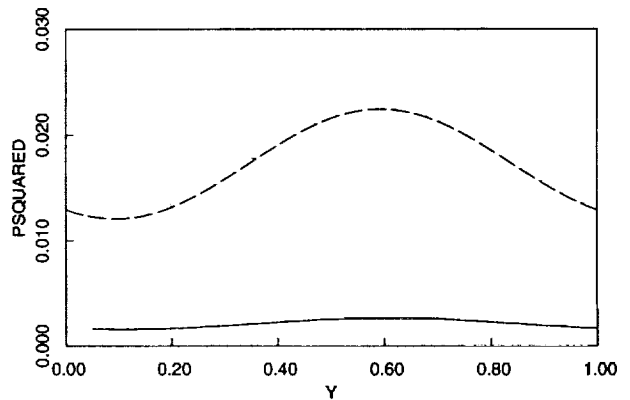


Figure 4: Mean square pressure upstream ($x = -2$) of cascade, $\omega = \sigma = 5\pi/2$ (Fang Hu, Problem 2).

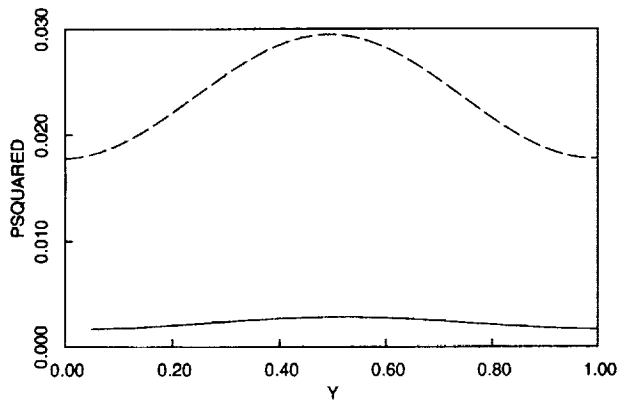


Figure 5: Mean square pressure downstream ($x = 3$) of cascade, $\omega = \sigma = 5\pi/2$ (Fang Hu, Problem 2).

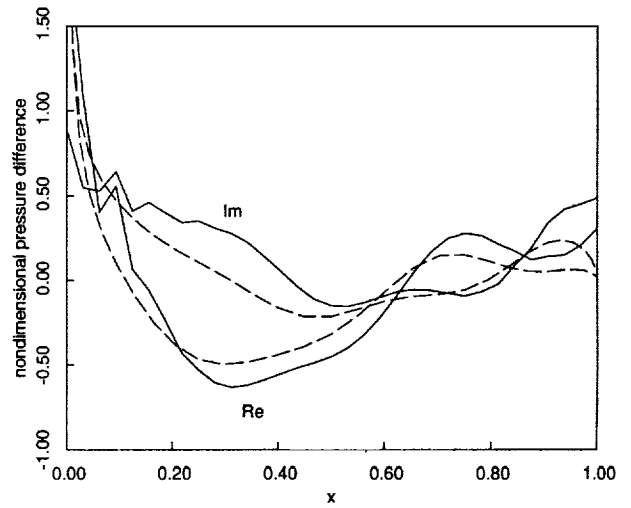


Figure 7: Nondimensional pressure loading on airfoil, $\omega = \sigma = 13\pi/2$ (Fang Hu, Problem 2).

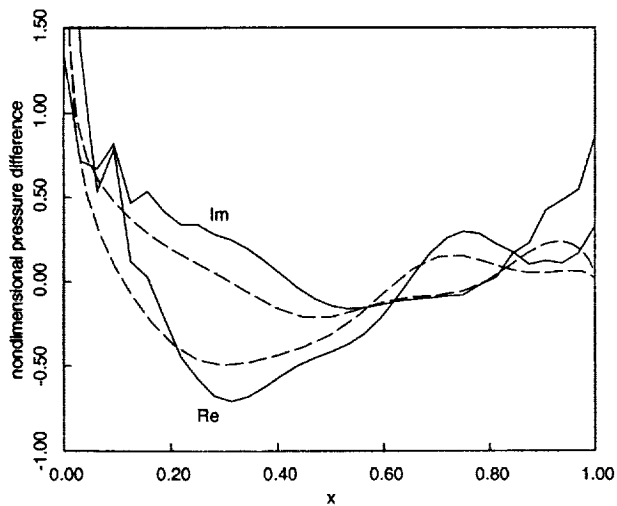


Figure 6: Nondimensional pressure loading on airfoil, $\omega = \sigma = 13\pi/2$ (Fang Hu, Problem 1).

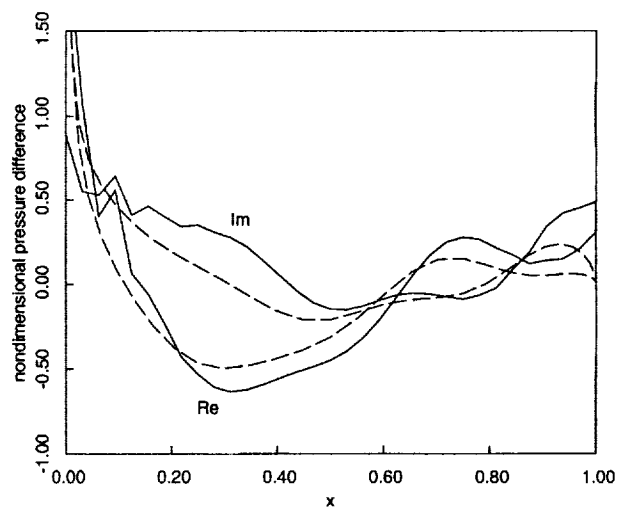


Figure 8: Nondimensional pressure loading on airfoil, $\omega = \sigma = 13\pi/2$ (Fang Hu, Problem 3).

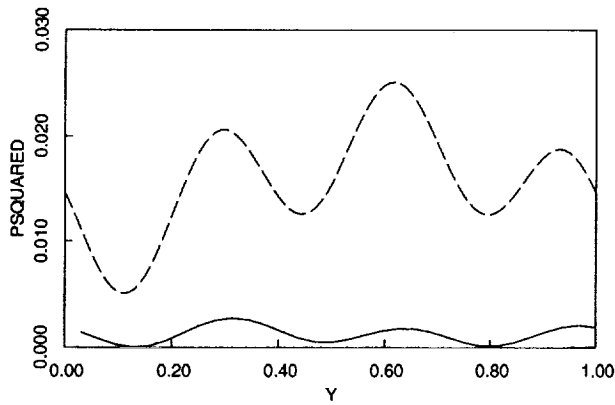


Figure 9: Mean square pressure upstream ($x = -2$) of cascade, $\omega = \sigma = 13\pi/2$ (Fang Hu, Problem 2).

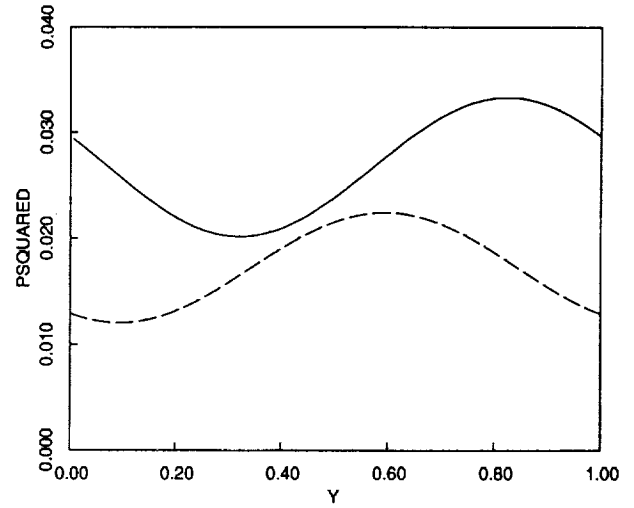


Figure 12: Mean square pressure upstream ($x = -2$) of cascade, $\omega = \sigma = 5\pi/2$ (Lockard and Morris, Problem 2).

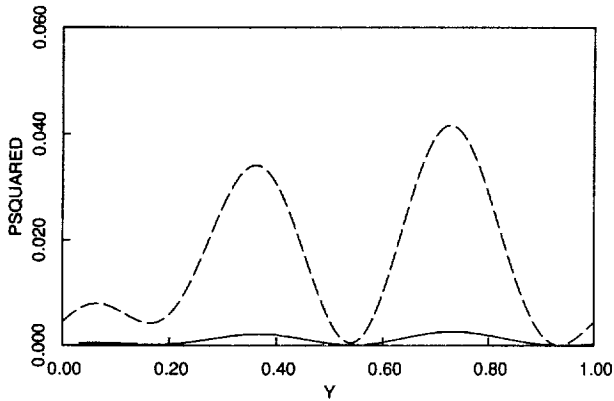


Figure 10: Mean square pressure downstream ($x = 3$) of cascade, $\omega = \sigma = 13\pi/2$ (Fang Hu, Problem 2).

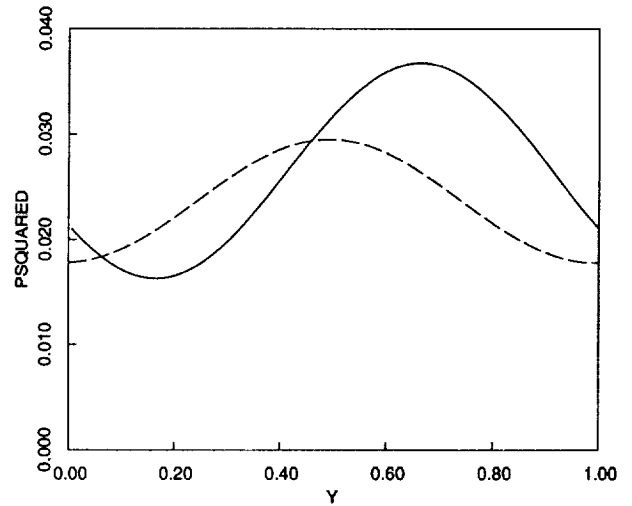


Figure 13: Mean square pressure downstream ($x = 3$) of cascade, $\omega = \sigma = 5\pi/2$ (Lockard and Morris, Problem 2).

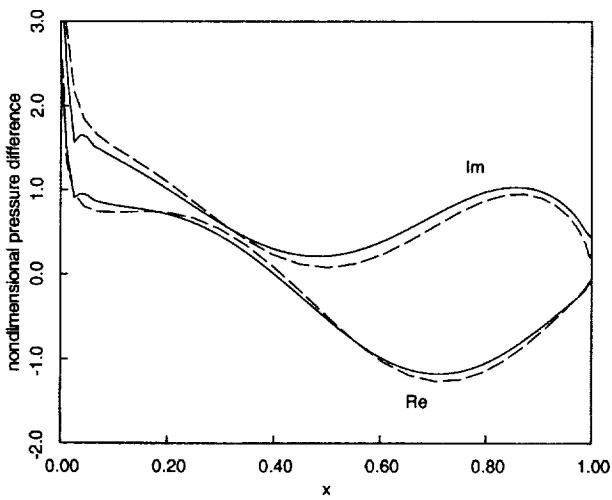


Figure 11: Nondimensional pressure loading on air-foil, $\omega = \sigma = 5\pi/2$ (Lockard and Morris, Problem 2).

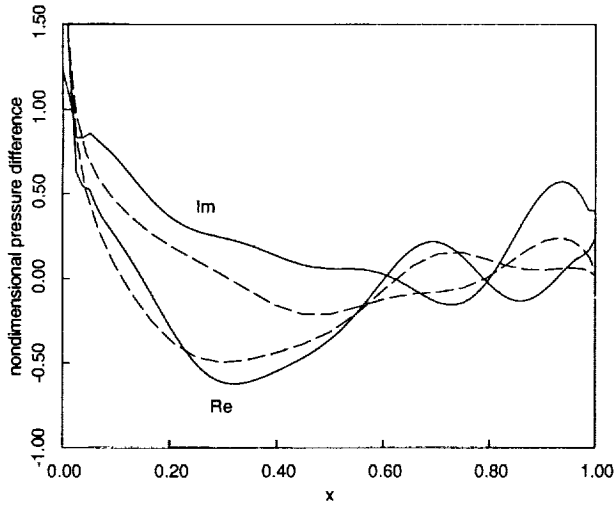


Figure 14: Nondimensional pressure loading on airfoil, $\omega = \sigma = 13\pi/2$ (Lockard and Morris, Problem 2).

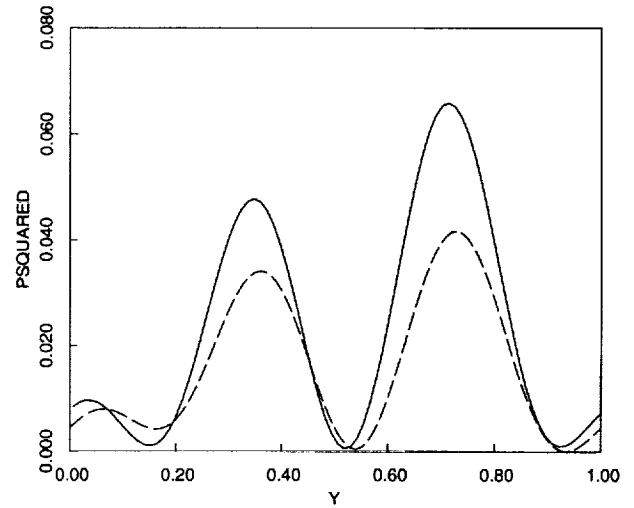


Figure 16: Mean square pressure downstream ($x = 3$) of cascade, $\omega = \sigma = 13\pi/2$ (Lockard and Morris, Problem 2).

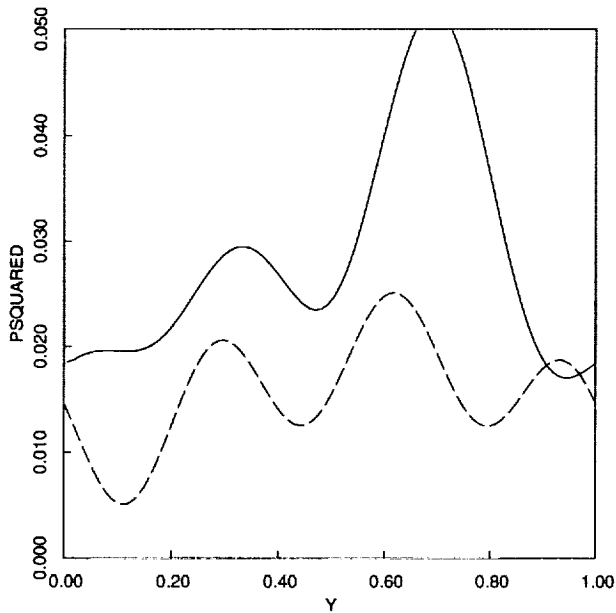


Figure 15: Mean square pressure upstream ($x = -2$) of cascade, $\omega = \sigma = 13\pi/2$ (Lockard and Morris, Problem 2).

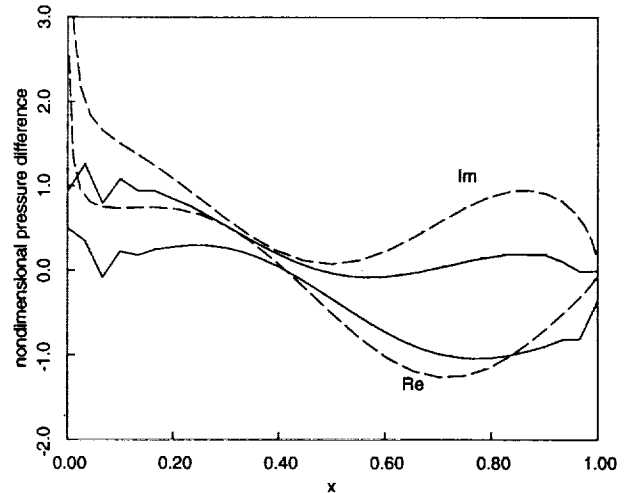


Figure 17: Nondimensional pressure loading on airfoil, $\omega = \sigma = 5\pi/2$ (Tam, Problem 2).

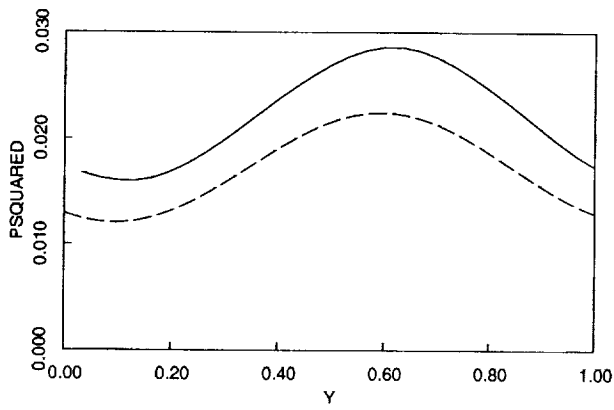


Figure 18: Mean square pressure upstream ($x = -2$) of cascade, $\omega = \sigma = 5\pi/2$ (Tam, Problem 2).

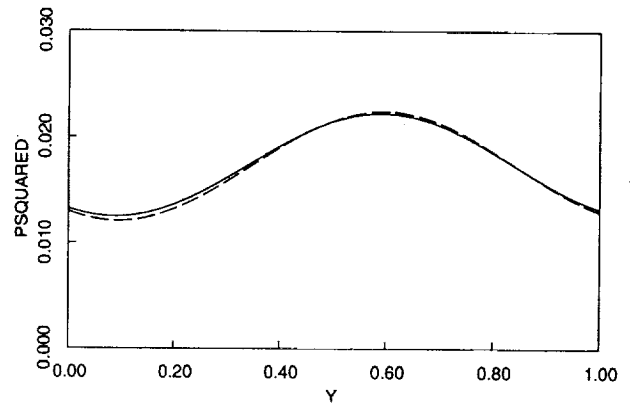


Figure 21: Mean square pressure upstream ($x = -2$) of cascade, $\omega = \sigma = 5\pi/2$ (Hall, Problem 1).

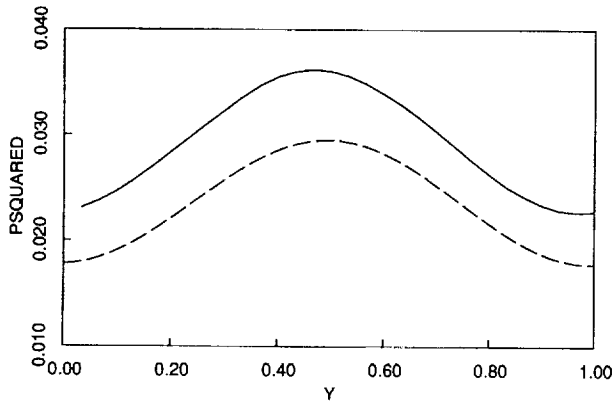


Figure 19: Mean square pressure downstream ($x = 3$) of cascade, $\omega = \sigma = 5\pi/2$ (Tam, Problem 2).

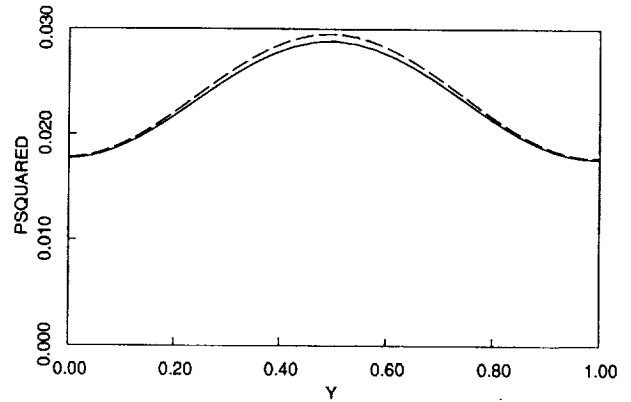


Figure 22: Mean square pressure downstream ($x = 3$) of cascade, $\omega = \sigma = 5\pi/2$ (Hall, Problem 1).

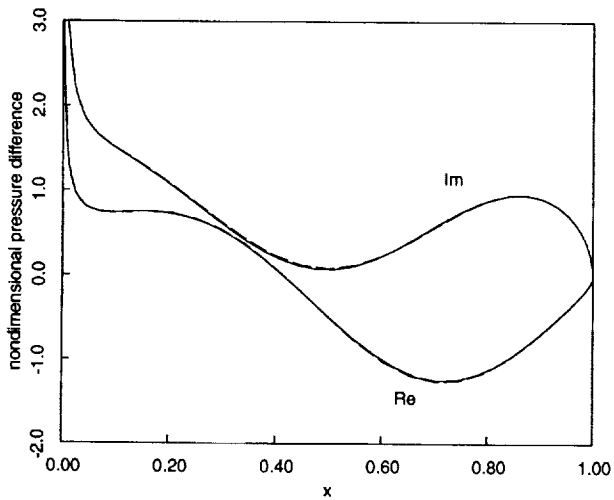


Figure 20: Nondimensional pressure loading on airfoil, $\omega = \sigma = 5\pi/2$ (Hall, Problem 1).

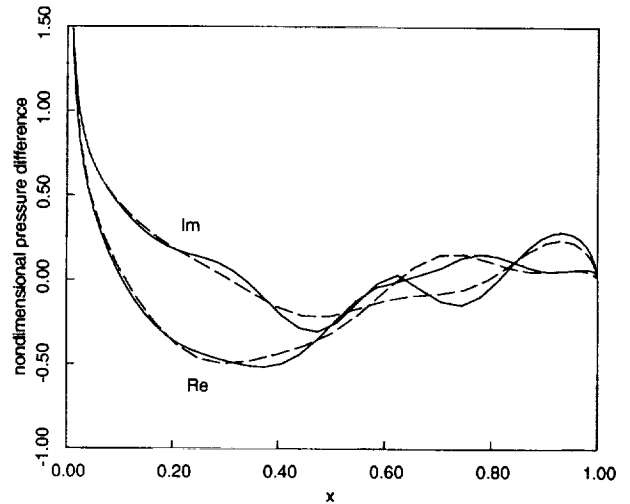


Figure 23: Nondimensional pressure loading on airfoil, $\omega = \sigma = 13\pi/2$ (Hall, Problem 1).

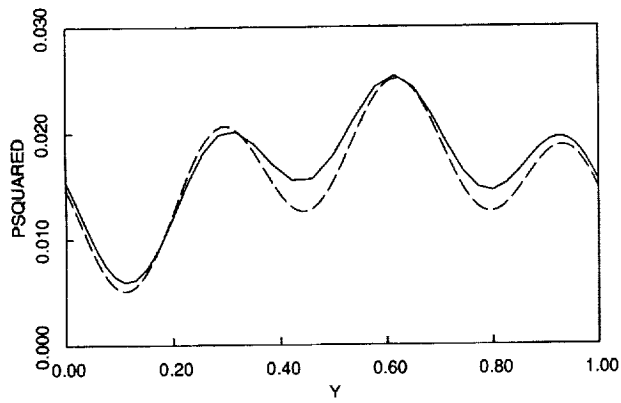


Figure 24: Mean square pressure upstream ($x = -2$) of cascade, $\omega = \sigma = 13\pi/2$ (Hall, Problem 1).

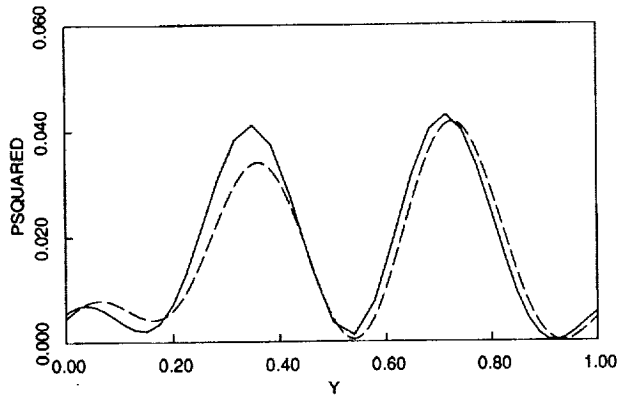


Figure 25: Mean square pressure downstream ($x = 3$) of cascade, $\omega = \sigma = 13\pi/2$ (Hall, Problem 1).

SOLUTION COMPARISONS: CATEGORY 4

Jay C. Hardin
NASA Langley Research Center
Hampton, VA 23681

The Category 4 problem was proposed as an example of the technologically important class of massively separated flow noise generators. Since the CAA community is presently being asked to attack such sources, it was deemed appropriate to include one as a benchmark problem. Such flows are viscous, turbulent, and the source of the sound arises from the dynamics of the flow itself. Thus, no exact solution is available for this category. However, for the Aeolian tone produced by a cylinder in a uniform flow, a substantial amount of unambiguous experimental data exists, albeit much of it for higher Reynolds and Mach numbers than the problem proposed.

The Mach number of the flow in this benchmark problem was chosen because many of the technologically important applications (automobiles, aircraft on landing approach, high speed trains, etc) have Mach numbers in this range. The Reynolds number chosen was taken as a compromise--high enough to be realistic and for which good quality data existed, yet low enough that one could resolve most of the important scales without too fine a grid. In hindsight, it might have been better to specify a higher Reynolds number, as the flow is still transitional at $Re=90,000$ whereas the turbulent models have been developed for fully turbulent flows.

The inherent challenge of this problem lies in choosing the numerical approach within the limits of the computational facilities available. The flow is experimentally found to be three dimensional with a finite correlation length in the spanwise direction. However, a 3-D Direct Numerical Simulation (DNS) at a Reynolds number of 90,000 is out of the question due to the range of scales which must be resolved in three directions. Thus, one must fall back on an approach such as Large Eddy Simulation (LES) or Reynolds Averaged (short-time) Navier-Stokes (RANS) to reduce the range of scales which must be resolved. This leads one into the realm of turbulent modeling, such as the Dynamic Sub-Grid Scale (DSGS) model, in order to retain the effect of the sub-grid scales on those resolved. Even this approach is very computationally demanding. One is tempted to reduce the dimensionality of the problem to two, as the geometry is two-dimensional. However, one runs into two problems: First, turbulence is inherently three dimensional and the use of turbulent models in two dimensions is problematic. Second, a 2-D acoustic field falls off like $r^{1/2}$ with distance in the farfield rather than r as would be the case in 3-D.

In addition, there is the question of compressibility. Does one compute a compressible flow solution in which the flow and acoustic fields can be solved simultaneously? Or, noting the low Mach number requested, does one break the problem into two parts, solving first for the flowfield (either compressibly or incompressibly) and then using an acoustic analogy, i.e. Lighthill (Helmholtz in the frequency domain), Curle, or Ffowcs Williams-Hawkings (FW-H) which integrate the flow induced pressures over the surface of the cylinder, or the acoustic/viscous split (A/VS), which solves a forced set of Euler equations, for the acoustic field?

In the event, all of the contributors chose to break the problem into two parts. However, their other choices varied considerably. The following table compares the approaches employed:

Contributor	Flow Solver	Re	Turbulent Model	Acoustic Solver
Brentner et al	2-D Comp. and Incomp. RANS	1,000 10,000 90,000	$k-\omega$	2-D and 3-D FW-H
Kumarasamy et al	2-D Incomp. RANS	90,000	$k-\epsilon$	2-D Helmholtz 3-D Curle
Pope	2-D Incomp. DNS	20,000	None	A/VS
Spyropoulos and Holmes	3-D Incomp. LES	90,000	DSGS	3-D Curle

Table 1: Comparison of Contributor's Approaches

The 3-D acoustic solutions with 2-D flow solutions were achieved by assuming the 2-D flow solution to be valid everywhere over the finite span of the 3-D acoustic integral. Of course, the amplitude of the resulting noise predictions is very much dependent upon the span assumed.

The experimental data for this case indicates that the Aeolian tone occurs at a Strouhal number of 0.1846 which corresponds to a frequency of 643 Hz. The amplitude at $\theta = 90$ degrees and $r/D=35$ is approximately 111dB. Spectral shapes obtained by all the contributors are shown in their respective papers, while their predictions of the frequency and amplitude of the Aeolian tone are shown in the following table:

Contributor	Peak St	Peak Level (dB)
Brentner et al	0.234-0.296	120
Kumarasamy et al	0.204	120.8
Pope	0.219	2-D
Spyropoulos and Holmes	0.158	110

Table 2: Aeolian Tone Predictions

Only 3-D noise calculations are shown in this table due to the problem with the fall-off of the 2-D calculations. The amplitude predictions are sensitive to the assumed span of the cylinder. Assignment of a span to the experimental data is not straightforward due to the

presence of the wind tunnel walls. The variation in the Strouhal number predictions of Brentner et al depended upon the turbulent model employed.

All of the contributors found the expected dipole directivity pattern with peak at $\theta = 90$ degrees and all predicted a reasonable spectral shape out to the maximum Strouhal number requested of 0.6. Thus, the DNS, LES and RANS approaches all seem to retain the relevant scales. The variation of the peak Strouhal number predictions is somewhat disappointing, but may be due to the transitional nature of the flow. Further work by Brentner et al indicates that, at higher Reynolds numbers where the flow is fully turbulent, the predictions produced by the various turbulence models coincide. The variation in the amplitude predictions is not of as much concern due to the ambiguity of the cylinder length and the inherent bias and uncertainty of spectral estimates near peaks.

11/11/11

11/11/11

11/11/11

11/11/11

11/11/11

11/11/11

INDUSTRY PANEL PRESENTATIONS AND DISCUSSIONS

N. N. Reddy
Lockheed Martin Aeronautical Systems
Marietta, GA 30063

The workshop organizers invited representative from aircraft and automobile industry to organize an industry panel to participate in the workshop. The purpose of the panel is to present and discuss the needs for the computational aeroacoustics and provide guidance to the researchers and scientists by identifying the important issues related to acoustic technology.

The following representatives attended the workshop and participated in the panel discussions moderated by N. N. Reddy.

Thomas Barber	United Technologies Research Center
Philip Gliebe	G E Aircraft Engines
Mahendra Joshi	McDonnell Douglas Aerospace
N. N. Reddy	Lockheed Martin Aeronautical Systems
Rahul Sen	Boeing Commercial Airplane Group
Gary S. Strumolo	Ford Research Laboratory
Agnes Wozniha	Boeing Helicopters

Ed Hall of Allison Engine Company, Ram Janakairaman of McDonnell Douglas Helicopter Systems, and Donald Weir of Allied Signal Engines were also invited but unable to attend the workshop. Mahendra Joshi presented the computational aeroacoustic needs from the airframe manufacturer's point of view, Philip Gliebe presented from aircraft engine manufacturer's point of view, and Gary Strumolo presented from automobile point of view. The following paragraphs summarizes the noise issues and how Computational Aeroacoustics can help in understanding the noise sources and some of the complex issues.

NOISE SOURCES

The noise generation mechanisms of a typical turbofan is shown in Figure 1. Fan generated noise propagates through engine inlet and fan exhaust. The turbine and combustion noise propagates through primary nozzle. In addition, there are jet mixing noise from fan jet and primary core jet. The relative importance of these sources as a function of bypass ratio is shown in Figure 2. It is clear that as bypass ratio increases, the turbomachinery noise dominates over the jet noise. Some of the noise reduction features that are currently practiced are shown in Figure 3.

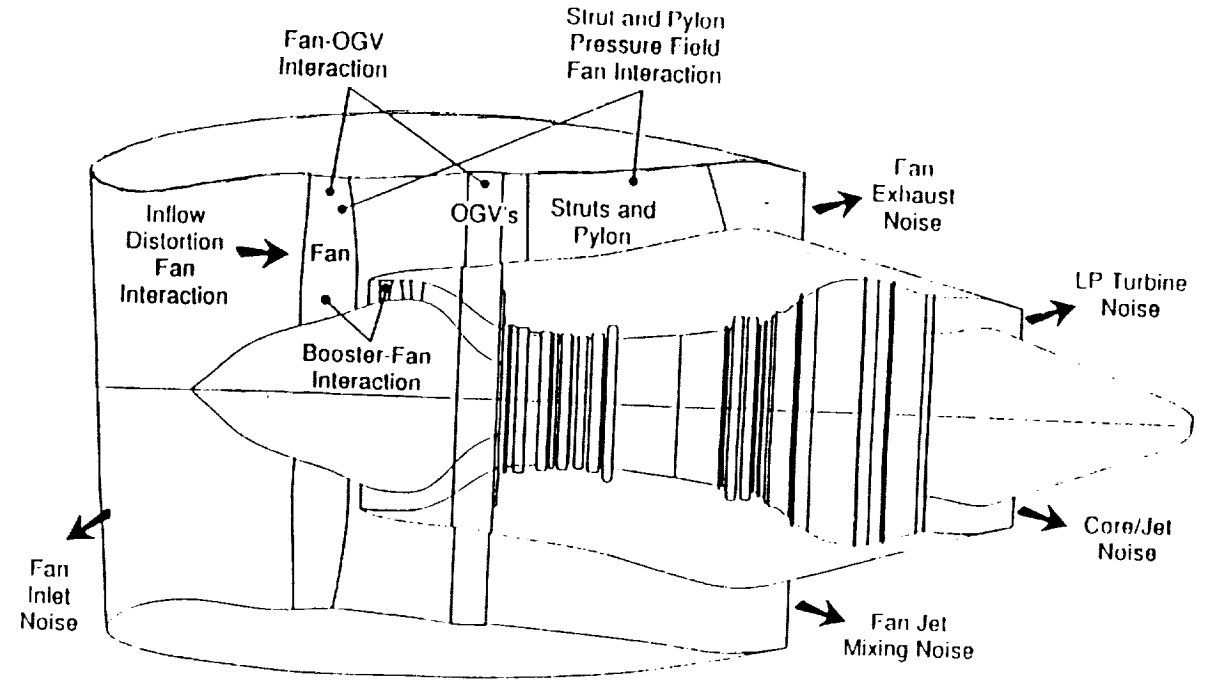


Figure 1. Noise Generating Mechanisms in Turbofan Engines

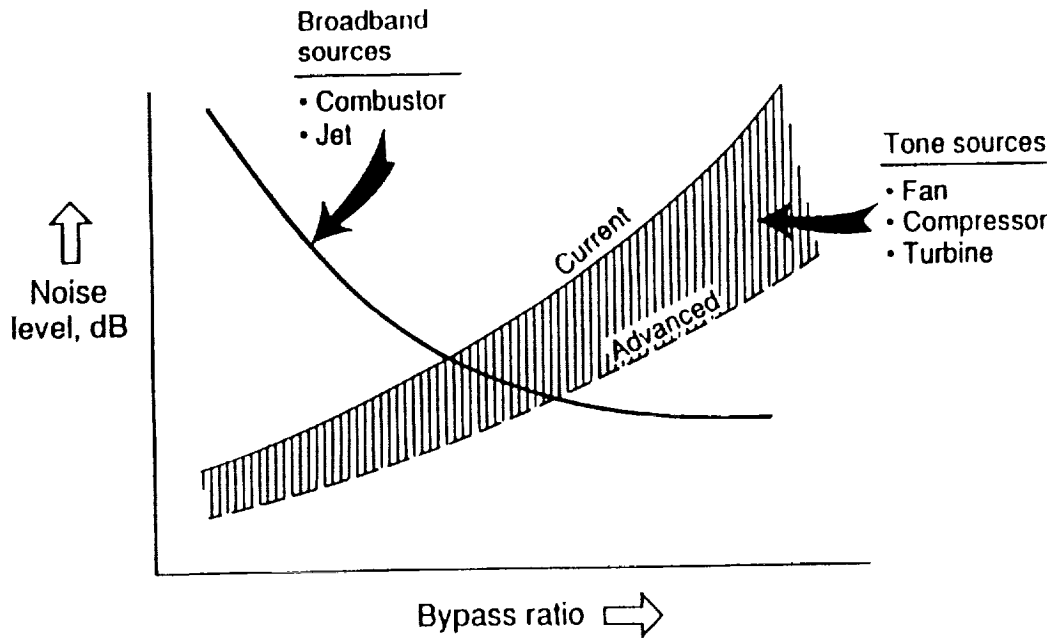


Figure 2. Relative Importance of Turbofan Engine Noise Sources

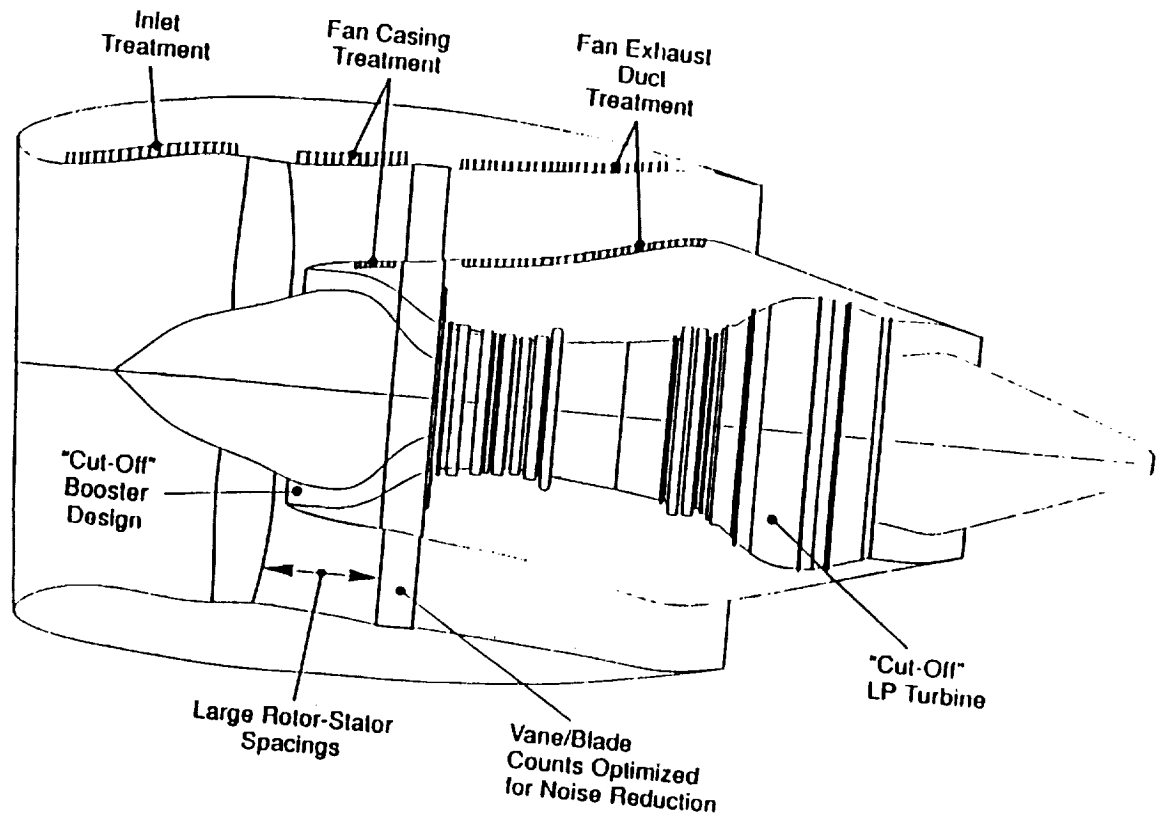


Figure 3. Current Noise Reduction Features in Turbofan Engines

The airframe noise sources that are generated by the aerodynamic flow interacting with the aircraft surfaces during flight are illustrated in Figure 4. The interaction between wing and flap, landing gear and flap, and jet exhaust and flap are also important sources. The relative strength of these sources depends on the flight speed, the geometry, and the relative position of the components.

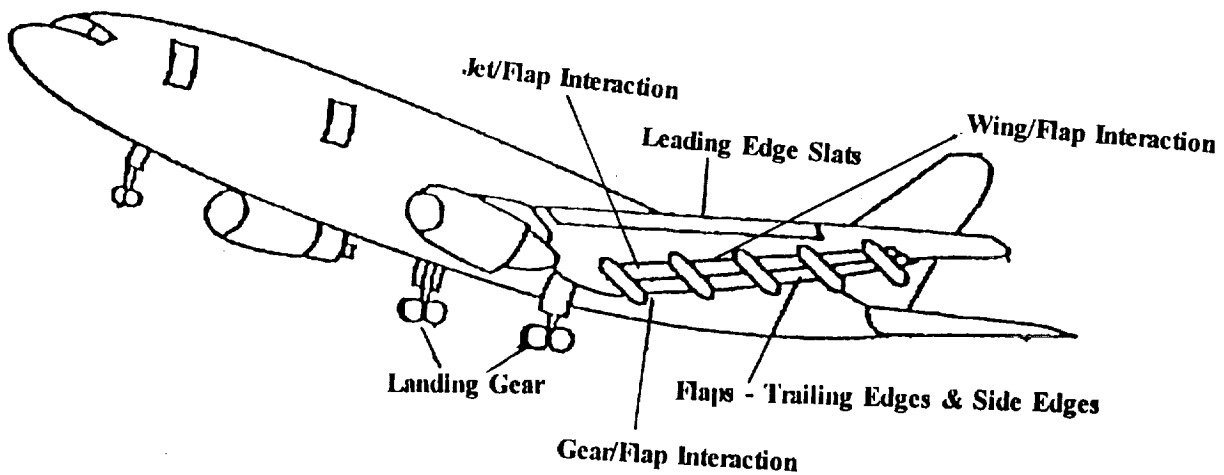


Figure 4. Airframe Noise Sources

Some of noise sources are complex, because of the wake flow from one component interacting with the other component will influence the noise source. For example, the flap noise may depend on the leading edge slat configurations. Recently some progress was made in development of CAA to understand wing/flap sources. The numerical simulation of 2-D wing/flap configuration shown in Figure 5 illustrates the location of sources and their propagation characteristics.

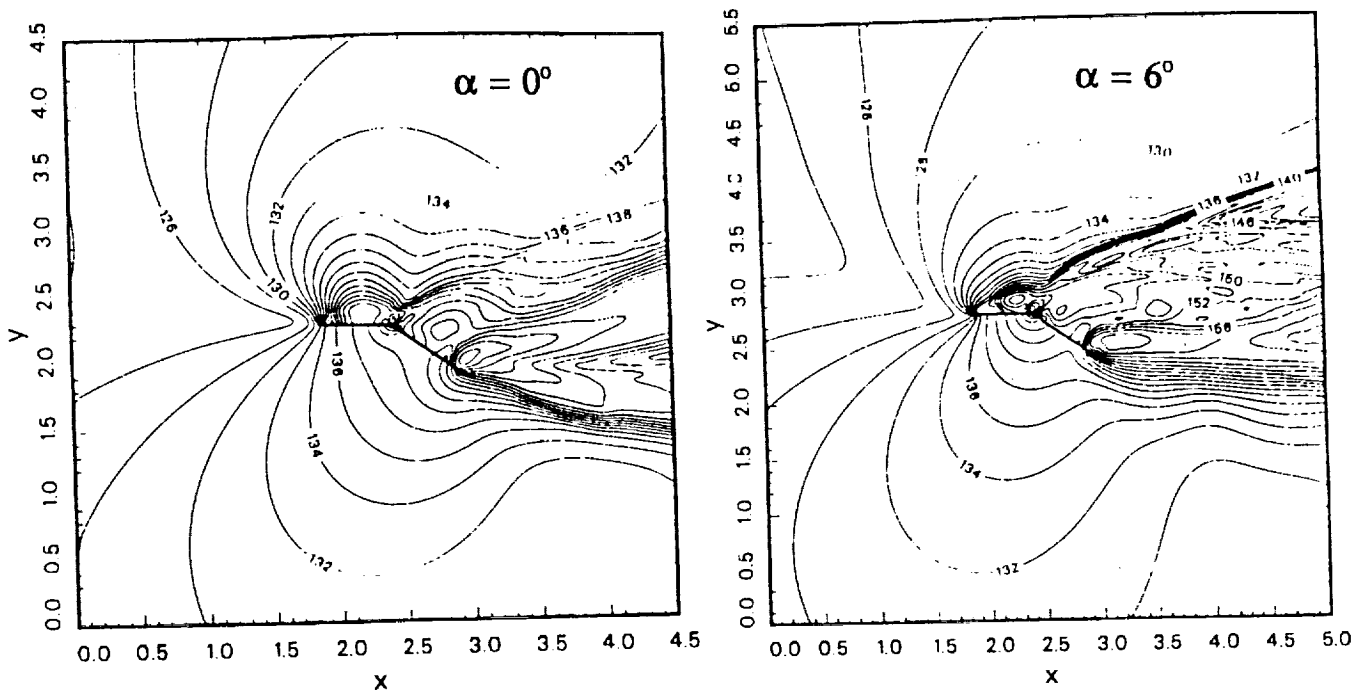


Figure 5. Numerical Simulation of 2-D Wing/Flap Noise (OASPL Contours)

NOISE GENERATION PROCESS MODELING - CAA ROLE

Computational Aeroacoustics (CAA) will be extremely helpful in resolving physical modeling issues which seemingly escape resolution by theoretical and experimental methods. CAA models with appropriate boundary conditions for turbomachinery noise, jet noise and airframe noise in conjunction with experiments will be useful in developing accurate noise prediction methods and viable noise reduction concepts. CAA will also enhance the understanding of the wind noise in the automobiles. The mean flow characteristics from CFD may be utilized in developing CAA models.

REPORT DOCUMENTATION PAGE			Form Approved OMB No. 0704-0188	
Public reporting burden for this collection of information is estimated to average 1 hour per response, including the time for reviewing instructions, searching existing data sources, gathering and maintaining the data needed, and completing and reviewing the collection of information. Send comments regarding this burden estimate or any other aspect of this collection of information, including suggestions for reducing this burden, to Washington Headquarters Services, Directorate for Information Operations and Reports, 1215 Jefferson Davis Highway, Suite 1204, Arlington, VA 22202-4302, and to the Office of Management and Budget, Paperwork Reduction Project (0704-0188), Washington, DC 20503.				
1. AGENCY USE ONLY (Leave blank)	2. REPORT DATE June 1997	3. REPORT TYPE AND DATES COVERED Conference Publication		
4. TITLE AND SUBTITLE Second Computational Aeroacoustics (CAA) Workshop on Benchmark Problems		5. FUNDING NUMBERS 522-31-21-04		
6. AUTHOR(S) C.K.W. Tam and J.C. Hardin, Editors		8. PERFORMING ORGANIZATION REPORT NUMBER L-17641		
7. PERFORMING ORGANIZATION NAME(S) AND ADDRESS(ES) NASA Langley Research Center Hampton, VA 23681-0001		10. SPONSORING/MONITORING AGENCY REPORT NUMBER NASA CP-3352		
9. SPONSORING/MONITORING AGENCY NAME(S) AND ADDRESS(ES) National Aeronautics and Space Administration Washington, DC 20546-0001 and Florida State University Tallahassee, Florida		11. SUPPLEMENTARY NOTES C.K.W. Tam: Florida State University, Tallahassee, Florida J.C. Hardin: NASA Langley Research Center, Hampton, Virginia		
12a. DISTRIBUTION/AVAILABILITY STATEMENT Unclassified-Unlimited Subject Category 71 Availability: NASA CASI (301) 621-0390		12b. DISTRIBUTION CODE		
13. ABSTRACT (Maximum 200 words) The proceedings of the Second Computational Aeroacoustics (CAA) Workshop on Benchmark Problems held at Florida State University are the subject of this report. For this workshop, problems arising in typical industrial applications of CAA were chosen. Comparisons between numerical solutions and exact solutions are presented where possible.				
14. SUBJECT TERMS Aeroacoustics; Numerical methods; Wave propagation; Sound sources			15. NUMBER OF PAGES 390	
			16. PRICE CODE A17	
17. SECURITY CLASSIFICATION OF REPORT Unclassified	18. SECURITY CLASSIFICATION OF THIS PAGE Unclassified	19. SECURITY CLASSIFICATION OF ABSTRACT Unclassified	20. LIMITATION OF ABSTRACT	

